

The background of the entire page features a stylized brain composed of numerous small, interconnected triangles. Each triangle is filled with a different color, creating a vibrant, multi-colored effect. The colors include shades of yellow, orange, red, purple, blue, and green. A network of thin, light gray lines connects the vertices of these triangles, forming a complex web that covers the entire brain shape. The top half of the image has a solid blue background, while the bottom half is white.

# **THE ROLE OF ASTROGLIA AND OLIGODENDROGLIA IN CNS DEVELOPMENT, PLASTICITY, AND DISEASE – NOVEL TOOLS AND INVESTIGATIVE APPROACHES**

**EDITED BY:** Enrica Boda, Francesca Boscia and Christian Lohr  
**PUBLISHED IN:** Frontiers in Cellular Neuroscience



# frontiers

## Frontiers eBook Copyright Statement

The copyright in the text of individual articles in this eBook is the property of their respective authors or their respective institutions or funders. The copyright in graphics and images within each article may be subject to copyright of other parties. In both cases this is subject to a license granted to Frontiers.

The compilation of articles constituting this eBook is the property of Frontiers.

Each article within this eBook, and the eBook itself, are published under the most recent version of the Creative Commons CC-BY licence.

The version current at the date of publication of this eBook is CC-BY 4.0. If the CC-BY licence is updated, the licence granted by Frontiers is automatically updated to the new version.

When exercising any right under the CC-BY licence, Frontiers must be attributed as the original publisher of the article or eBook, as applicable.

Authors have the responsibility of ensuring that any graphics or other materials which are the property of others may be included in the CC-BY licence, but this should be checked before relying on the CC-BY licence to reproduce those materials. Any copyright notices relating to those materials must be complied with.

Copyright and source acknowledgement notices may not be removed and must be displayed in any copy, derivative work or partial copy which includes the elements in question.

All copyright, and all rights therein, are protected by national and international copyright laws. The above represents a summary only. For further information please read Frontiers' Conditions for Website Use and Copyright Statement, and the applicable CC-BY licence.

ISSN 1664-8714

ISBN 978-2-88976-285-9

DOI 10.3389/978-2-88976-285-9

## About Frontiers

Frontiers is more than just an open-access publisher of scholarly articles: it is a pioneering approach to the world of academia, radically improving the way scholarly research is managed. The grand vision of Frontiers is a world where all people have an equal opportunity to seek, share and generate knowledge. Frontiers provides immediate and permanent online open access to all its publications, but this alone is not enough to realize our grand goals.

## Frontiers Journal Series

The Frontiers Journal Series is a multi-tier and interdisciplinary set of open-access, online journals, promising a paradigm shift from the current review, selection and dissemination processes in academic publishing. All Frontiers journals are driven by researchers for researchers; therefore, they constitute a service to the scholarly community. At the same time, the Frontiers Journal Series operates on a revolutionary invention, the tiered publishing system, initially addressing specific communities of scholars, and gradually climbing up to broader public understanding, thus serving the interests of the lay society, too.

## Dedication to Quality

Each Frontiers article is a landmark of the highest quality, thanks to genuinely collaborative interactions between authors and review editors, who include some of the world's best academicians. Research must be certified by peers before entering a stream of knowledge that may eventually reach the public - and shape society; therefore, Frontiers only applies the most rigorous and unbiased reviews. Frontiers revolutionizes research publishing by freely delivering the most outstanding research, evaluated with no bias from both the academic and social point of view. By applying the most advanced information technologies, Frontiers is catapulting scholarly publishing into a new generation.

## What are Frontiers Research Topics?

Frontiers Research Topics are very popular trademarks of the Frontiers Journals Series: they are collections of at least ten articles, all centered on a particular subject. With their unique mix of varied contributions from Original Research to Review Articles, Frontiers Research Topics unify the most influential researchers, the latest key findings and historical advances in a hot research area! Find out more on how to host your own Frontiers Research Topic or contribute to one as an author by contacting the Frontiers Editorial Office: [frontiersin.org/about/contact](https://frontiersin.org/about/contact)



## THE ROLE OF ASTROGLIA AND OLIGODENDROGLIA IN CNS DEVELOPMENT, PLASTICITY, AND DISEASE – NOVEL TOOLS AND INVESTIGATIVE APPROACHES

Topic Editors:

**Enrica Boda**, University of Turin, Italy

**Francesca Boscia**, University of Naples Federico II, Italy

**Christian Lohr**, University of Hamburg, Germany

**Citation:** Boda, E., Boscia, F., Lohr, C., eds. (2022). The Role of Astroglia and Oligodendroglia in CNS Development, Plasticity, and Disease – Novel Tools and Investigative Approaches. Lausanne: Frontiers Media SA.  
doi: 10.3389/978-2-88976-285-9

# Table of Contents

- 05 Editorial: The Role of Astroglia and Oligodendroglia in CNS Development, Plasticity, and Disease – Novel Tools and Investigative Approaches**  
Enrica Boda, Francesca Boscia and Christian Lohr
- 08 A Dual Nanosensor Approach to Determine the Cytosolic Concentration of ATP in Astrocytes**  
Susanne Köhler, Hartmut Schmidt, Paula Fülle, Johannes Hirrlinger and Ulrike Winkler
- 22 Deletion of LRP1 From Astrocytes Modifies Neuronal Network Activity in an in vitro Model of the Tripartite Synapse**  
Ramona Romeo, Kristin Glotzbach, Anja Scheller and Andreas Faissner
- 43 Low-Density Lipoprotein Receptor-Related Protein 1 (LRP1) as a Novel Regulator of Early Astroglial Differentiation**  
Ramona Romeo, Damian Boden-El Mourabit, Anja Scheller, Melanie D. Mark and Andreas Faissner
- 63 Approaches to Study Gap Junctional Coupling**  
Jonathan Stephan, Sara Eitelmann and Min Zhou
- 78 C21orf91 Regulates Oligodendroglial Precursor Cell Fate—A Switch in the Glial Lineage?**  
Laura Reiche, Peter Göttle, Lydie Lane, Paula Duek, Mina Park, Kasum Azim, Jana Schütte, Anastasia Manousi, Jessica Schira-Heinen and Patrick Küry
- 96 Automated in vivo Tracking of Cortical Oligodendrocytes**  
Yu Kang T. Xu, Cody L. Call, Jeremias Sulam and Dwight E. Bergles
- 112 Specialized Pro-resolving Lipid Mediators and Glial Cells: Emerging Candidates for Brain Homeostasis and Repair**  
Marta Tiberi and Valerio Chiurchiù
- 123 Novel Tools and Investigative Approaches for the Study of Oligodendrocyte Precursor Cells (NG2-Glia) in CNS Development and Disease**  
Christophe Galichet, Richard W. Clayton and Robin Lovell-Badge
- 141 Heterogeneity and Development of Fine Astrocyte Morphology Captured by Diffraction-Limited Microscopy**  
Daniel Minge, Cátia Domingos, Petr Unichenko, Charlotte Behringer, Alberto Pauletti, Stefanie Anders, Michel K. Herde, Andrea Delekate, Polina Gulakova, Susanne Schoch, Gabor C. Petzold and Christian Henneberger
- 157 Calcium Signals in Astrocyte Microdomains, a Decade of Great Advances**  
Annamaria Lia, Vanessa Jorge Henriques, Micaela Zonta, Angela Chiavegato, Giorgio Carmignoto, Marta Gómez-Gonzalo and Gabriele Losi
- 164 Auxiliary Subunits Control Function and Subcellular Distribution of AMPA Receptor Complexes in NG2 Glia of the Developing Hippocampus**  
Stefan Hardt, Dario Tascio, Stefan Passlick, Aline Timmermann, Ronald Jabs, Christian Steinhäuser and Gerald Seifert

- 181** *Using Genetically Encoded Calcium Indicators to Study Astrocyte Physiology: A Field Guide*  
Christian Lohr, Antonia Beiersdorfer, Timo Fischer, Daniela Hirnet, Natalie Rotermund, Jessica Sauer, Kristina Schulz and Christine E. Gee
- 191** *Versatile Surface Electrodes for Combined Electrophysiology and Two-Photon Imaging of the Mouse Central Nervous System*  
Michael Schweigmann, Laura C. Caudal, Gebhard Stopper, Anja Scheller, Klaus P. Koch and Frank Kirchhoff
- 208** *Neuronal and Astrocytic Regulations in Schizophrenia: A Computational Modelling Study*  
Lea Fritschi, Johanna Hedlund Lindmar, Florian Scheidl and Kerstin Lenk
- 225** *Novel in vitro Experimental Approaches to Study Myelination and Remyelination in the Central Nervous System*  
Davide Marangon, Nicolò Caporale, Marta Boccazzi, Maria P. Abbracchio, Giuseppe Testa and Davide Lecca
- 244** *Novel Toolboxes for the Investigation of Activity-Dependent Myelination in the Central Nervous System*  
Jack Kent Heflin and Wenjing Sun



# Editorial: The Role of Astroglia and Oligodendroglia in CNS Development, Plasticity, and Disease – Novel Tools and Investigative Approaches

Enrica Boda<sup>1\*</sup>, Francesca Boscia<sup>2†</sup> and Christian Lohr<sup>3†</sup>

<sup>1</sup> Department of Neuroscience Rita Levi-Montalcini, Neuroscience Institute Cavalieri Ottolenghi (NICO), University of Turin, Turin, Italy, <sup>2</sup> Division of Pharmacology, Department of Neuroscience, Reproductive Sciences and Dentistry, School of Medicine, Federico II University of Naples, Naples, Italy, <sup>3</sup> Division of Neurophysiology, University of Hamburg, Hamburg, Germany

**Keywords:** astrocytes, oligodendrocytes, methods, experimental models, CNS development, CNS plasticity, CNS disease

## Editorial on the Research Topic

### The Role of Astroglia and Oligodendroglia in CNS Development, Plasticity, and Disease – Novel Tools and Investigative Approaches

## OPEN ACCESS

### Edited and reviewed by:

Marie-Ève Tremblay,  
University of Victoria, Canada

### \*Correspondence:

Enrica Boda  
enrica.boda@unito.it

<sup>†</sup>These authors have contributed  
equally to this work

### Specialty section:

This article was submitted to  
Non-Neuronal Cells,  
a section of the journal  
Frontiers in Cellular Neuroscience

**Received:** 22 March 2022

**Accepted:** 22 April 2022

**Published:** 09 May 2022

### Citation:

Boda E, Boscia F and Lohr C (2022)  
Editorial: The Role of Astroglia and  
Oligodendroglia in CNS Development,  
Plasticity, and Disease – Novel Tools  
and Investigative Approaches.  
Front. Cell. Neurosci. 16:901820.  
doi: 10.3389/fncel.2022.901820

The development of novel tools and methodologies to probe and manipulate glial cell functions and signaling has recently allowed an unprecedented level of comprehension of astro- and oligodendroglia contribution to CNS development, homeostasis, and plasticity. Both cell types critically contribute to neuronal function throughout the lifespan by providing metabolic support, promoting synchronization of neuronal networks and being involved in the homeostasis of ions, neurotransmitters, reactive oxygen species, and metabolites. Astroglia support synaptogenesis and synapse plasticity, whereas oligodendroglia assure developmental myelination, sustain axon maturation and integrity, and plastically respond to experience with *de-novo* myelin deposition or remodeling (Verkhratsky and Nedergaard, 2018; Kuhn et al., 2019). Studies have also provided evidence of a remarkable level of functional, molecular and developmental heterogeneity (Marques et al., 2016; Cerrato et al., 2018; Khakh and Deneen, 2019; Batiuk et al., 2020; Sherafat et al., 2021; Seeker and Williams, 2022) and unexpected interactions with immune cells (including microglia, peripheral macrophages, and T cells) for both astrocytes and oligodendroglia (Ponath et al., 2018; Kirby and Castelo-Branco, 2021). This latter aspect contributes to astro-/oligodendroglia response to injury. In this respect, recent technological advances also allowed to understand that dysregulations affecting the crosstalk between astro-/oligodendroglia and other cellular partners, including neurons, can be primarily involved in the initiation and progression of neurodevelopmental, psychiatric and neurodegenerative disorders, revealing their potential as therapeutic targets (Salmaso et al., 2014; Boda, 2021; Boscia et al., 2021; Healy et al., 2022; Lee et al., 2022).

This Research Topic Issue consists of 16 articles, i.e., seven literature reviews/minireviews, 8 original research articles and one “Technology and Code” manuscript, presenting or exploiting state-of-the-art methodological approaches as well as novel tools and experimental models to understand the diverse roles of astrocytes and oligodendroglia in CNS development, function and dysfunction.

Specifically, as regards novel methods to study astrocyte physiology and morphology, in their research article, Köhler et al. provide a new approach to study ATP metabolism in brain cells using a combination of two ATP nanosensors with different affinities that allow for the measurement of basal cytosolic concentration at rest as well as changes following challenges. In Minge et al., high resolution microscopy is employed to study the morphology of fine astrocyte processes by analyzing the tissue volume fraction occupied by astrocytes and the astrocytic process density. Schweigmann et al. design new liquid crystal polymer surface electrodes for recording and stimulating neuronal activity with a central window that allows for simultaneous imaging. They combine the surface electrodes with two-photon  $\text{Ca}^{2+}$  imaging in *in vivo* experiments, in which they stimulate neurons and record  $\text{Ca}^{2+}$  signals in astrocytes.

Three reviews summarize methodological aspects to study astrocyte properties. Stephan et al. provide an overview of state-of-the-art techniques to record, visualize and analyze gap junctions coupling astrocytes or established between astrocytes and other types of glial cells, so-called panglial coupling.  $\text{Ca}^{2+}$  signaling is a key feature of astrocytes and the development of highly sensitive genetically encoded  $\text{Ca}^{2+}$  indicators has boosted physiological research on astrocytes. While the review by Lia et al. focusses on recent advances regarding mechanisms and functions of  $\text{Ca}^{2+}$  signaling, in particular in astrocytic microdomains, Lohr et al. present a brief compendium of genetically encoded  $\text{Ca}^{2+}$  indicators used in glial cell research that compares the most important properties of the indicators.

By generating novel mouse mutants, Romeo et al. show that the astrocyte-specific deletion of the low-density lipoprotein receptor-related protein 1 (LRP1), a transmembrane receptor with multiple possible ligands, causes a transient delay in hippocampal astrocyte maturation at an early developmental timepoint, which in turn results in a reduced activity of neurons within the hippocampus. Moreover, by exploiting an *in vitro* model of the tripartite synapses, the same group, Romeo et al. show that the astrocyte-specific deletion of LRP1 negatively influences neuronal network activity and synaptogenesis, and propose that this effect may be mediated by an alteration of the expression of the glutamate transporter and of the release of cytokines in LRP1-deleted astrocytes.

Finally, in an *in silico* study, Fritschi et al. address the question of how astrocytes and neurons are involved in schizophrenia.

The “oligodendrocyte” section includes three reviews summarizing current and cutting-edge approaches. Heflin and Sun review state-of-art approaches for studying neuron-oligodendrocyte interactions and activity-dependent myelination with both temporal and spatial precision. They specifically highlight novel transgenic mouse models and techniques such as electrophysiology, *in vivo* imaging, and 2-photon uncaging. Marangon et al. provide an extensive overview of the advantages and limitations of the current and emerging techniques to study (re)myelination *in vitro*. Beside the classical (re)myelination assays with rodent oligodendrocyte precursor cell (OPC)-neuron co-cultures and *ex vivo* organotypic cultures, the authors discuss the most recent approaches based on the use of human iPSC-derived OPCs and 3D organoids. The

implications of the use of personalized humanized models and their optimization for the identification of remyelinating agents are also discussed. Galichet et al. provide a collection of recently used approaches including functional genetics, transcriptomics, imaging, electrophysiology and optogenetics, to study OPC biology, as well as their morphological, functional and molecular heterogeneity. They also discuss the multitude of culture systems used to generate and maintain OPCs *in vitro*, including 2D and 3D techniques, using primary animal or human cell lines or OPCs derived from induced pluripotent stem cells.

In a “Technology and Code” manuscript, Xu et al. describe a novel software tool (Oligo-Track) for an automated image analysis and *in vivo* tracking of oligodendrocytes over time in the mammalian brain with multi-photon microscopy. The method described has significant advantages in speeding up the analysis of oligodendrocyte number, distribution, and size over other approaches and will be available to the community.

Reiche et al. exploit a combination of data mining/bioinformatic analyses, histological analyses and *in vitro* assays to investigate the role of C21ORF91, found overexpressed in Down Syndrome (DS) iPSCs and considered a key modulator of aberrant CNS development in DS, in oligodendroglia. By reproducing C21orf91 overexpression in cultured primary OPCs, the authors show that C21orf91 critically regulates OPC myelination capacity. Further, C21orf91 overexpression results in the appearance of cells endowed with both oligodendroglia and astroglia features, rising the hypothesis that a developmental fate switch could contribute to white matter alterations in DS.

In their research article, Hardt et al. investigate the expression changes of auxiliary transmembrane AMPA receptor related proteins (TARPs) during postnatal maturation and the functional consequences on AMPA receptor properties and  $\text{Ca}^{2+}$  permeability in NG2 glia. The increased proportion of  $\text{Ca}^{2+}$  permeable AMPA receptors at the soma during postnatal maturation is accompanied by the downregulation of TARP  $\gamma 8$ , suggesting that AMPA receptors  $\text{Ca}^{2+}$  permeability during postnatal maturation may be affected by the interaction with TARPs.

Finally, Tiberi and Chiurchiù review the role of a new class of intercellular mediators, i.e., the specialized pro-resolving lipid mediators (SPMs), formerly studied in the context of the resolution of peripheral inflammation, in the regulation of astrocytes/oligodendroglia state and cross-talk with microglia and neurons, highlighting their relevance and therapeutic potential in the context of neuroinflammatory and neurodegenerative diseases.

In summary, the manuscripts gathered in this Research Topic provide an updated insight into *in silico*/bioinformatic, *in vitro*, *ex vivo*, and *in vivo* approaches that have been recently developed to study the functions of astro-/oligodendroglia, and highlight the potency of these cutting-edge approaches to address novel questions about the role of these cells in CNS development, function and disease. We hope that this Research Topic will stimulate discussion and new research directions to move forward on glial cell studies with relevant implications for the development of glia-focused therapeutic

approaches for CNS disease. As Guest Editors, we thank all the colleagues who accepted the invitation to participate in this Research Topic and share their manifold expertise and insights and to the Editorial Staff of Frontiers in Cellular Neuroscience—Section Non-Neuronal Cells for their assistance.

## AUTHOR CONTRIBUTIONS

EB, FB, and CL contributed to the manuscript conceptualization, writing, review and editing, and to funding acquisition. All authors contributed to the article and approved the submitted version.

## REFERENCES

- Batiuk, M. Y., Martirosyan, A., Wahis, J., de Vin, F., Marneffe, C., Kusserow, C., et al. (2020). Identification of region-specific astrocyte subtypes at single cell resolution. *Nat. Commun.* 11, 1220. doi: 10.1038/s41467-019-14198-8
- Boda, E. (2021). Myelin and oligodendrocyte lineage cell dysfunctions: new players in the etiology and treatment of depression and stress-related disorders. *Eur. J. Neurosci.* 53, 281–297. doi: 10.1111/ejn.14621
- Boscia, F., Elkjaer, M. L., Illes, Z., and Kukley, M. (2021). Altered expression of ion channels in white matter lesions of progressive multiple sclerosis: what do we know about their function? *Front. Cell Neurosci.* 15, 685703. doi: 10.3389/fncel.2021.685703
- Cerrato, V., Parmigiani, E., Figueres-Oñate, M., Betizeau, M., Aprato, J., and Nanavaty, I. (2018). Multiple origins and modularity in the spatiotemporal emergence of cerebellar astrocyte heterogeneity. *PLoS Biol.* 16, e2005513. doi: 10.1371/journal.pbio.2005513
- Healy, L. M., Stratton, J. A., Kuhlmann, T., and Antel, J. (2022). The role of glial cells in multiple sclerosis disease progression. *Nat. Rev. Neurol.* 18, 237–248. doi: 10.1038/s41582-022-00624-x
- Khakh, B. S., and Deneen, B. (2019). The emerging nature of astrocyte diversity. *Ann. Rev. Neurosci.* 42, 187–207. doi: 10.1146/annurev-neuro-070918-050443
- Kirby, L., and Castelo-Branco, G. (2021). Crossing boundaries: interplay between the immune system and oligodendrocyte lineage cells. *Semin. Cell Dev. Biol.* 116:45–52. doi: 10.1016/j.semcdb.10, 013.
- Kuhn, S., Gritti, L., Crooks, D., and Dombrowski, Y. (2019). Oligodendrocytes in development, myelin generation and beyond. *Cell* 8, 1424. doi: 10.3390/cells8111424
- Lee, H. G., Wheeler, M. A., and Quintana, F. J. (2022). Function and therapeutic value of astrocytes in neurological diseases. *Nat. Rev. Drug Discov.* doi: 10.1038/s41573-022-00390-x. Available online at: <https://www.nature.com/articles/s41573-022-00390-x#citeas>
- Marques, S., Zeisel, A., Codeluppi, S., van Bruggen, D., Mendanha Falcão, A., and Xiao, L. (2016). Oligodendrocyte heterogeneity in the mouse juvenile and adult central nervous system. *Science* 352, 1326–1329. doi: 10.1126/science.aaf6463
- Ponath, G., Park, C., and Pitt, D. (2018). The role of astrocytes in multiple sclerosis. *Front. Immunol.* 9, 217. doi: 10.3389/fimmu.2018.00217
- Salmaso, N., Jablonska, B., Scafidi, J., Vaccarino, F. M., and Gallo, V. (2014). Neurobiology of premature brain injury. *Nat. Neurosci.* 17, 341–346. doi: 10.1038/nn.3604
- Seeker, L. A., and Williams, A. (2022). Oligodendroglia heterogeneity in the human central nervous system. *Acta Neuropathol.* 143, 143–157. doi: 10.1007/s00401-021-02390-4
- Sherafat, A., Pfeiffer, F., and Nishiyama, A. (2021). Shaping of regional differences in oligodendrocyte dynamics by regional heterogeneity of the pericellular microenvironment. *Front. Cell Neurosci.* 15, 721376. doi: 10.3389/fncel.2021.721376
- Verkhratsky, A., and Nedergaard, M. (2018). Physiology of astroglia. *Physiol. Rev.* 98, 239–389. doi: 10.1152/physrev.00042.2016

## FUNDING

This work was supported by the Fondazione Italiana Sclerosi Multipla (FISM) 2019/PR-Multi/003 grant, the Cassa di Risparmio di Torino (CRT) Foundation grant (ID 2021.0657), and local funds of University of Turin, to EB; Fondazione Italiana Sclerosi Multipla FISM 2015/R/6 and Italian Ministry for University and Research PRIN 2017, 20175SA5JJ to FB. This study was also supported by the Italian Ministero dell'Istruzione, dell'Università e della Ricerca -MIUR project Dipartimenti di Eccellenza 2018–2022 to Department of Neuroscience Rita Levi Montalcini and by the Deutsche Forschungsgemeinschaft (SFB 1328, project number 335447717).

**Conflict of Interest:** The authors declare that the research was conducted in the absence of any commercial or financial relationships that could be construed as a potential conflict of interest.

**Publisher's Note:** All claims expressed in this article are solely those of the authors and do not necessarily represent those of their affiliated organizations, or those of the publisher, the editors and the reviewers. Any product that may be evaluated in this article, or claim that may be made by its manufacturer, is not guaranteed or endorsed by the publisher.

Copyright © 2022 Boda, Boscia and Lohr. This is an open-access article distributed under the terms of the Creative Commons Attribution License (CC BY). The use, distribution or reproduction in other forums is permitted, provided the original author(s) and the copyright owner(s) are credited and that the original publication in this journal is cited, in accordance with accepted academic practice. No use, distribution or reproduction is permitted which does not comply with these terms.





# A Dual Nanosensor Approach to Determine the Cytosolic Concentration of ATP in Astrocytes

Susanne Köhler<sup>1</sup>, Hartmut Schmidt<sup>1</sup>, Paula Fülle<sup>1,2</sup>, Johannes Hirrlinger<sup>1,3\*†</sup> and Ulrike Winkler<sup>1</sup>

<sup>1</sup> Carl-Ludwig-Institute for Physiology, Faculty of Medicine, University Leipzig, Leipzig, Germany, <sup>2</sup> Wilhelm-Ostwald-Schule, Gymnasium der Stadt Leipzig, Leipzig, Germany, <sup>3</sup> Department of Neurogenetics, Max-Planck-Institute for Experimental Medicine, Göttingen, Germany

## OPEN ACCESS

### Edited by:

Christian Lohr,  
University of Hamburg, Germany

### Reviewed by:

Ignacio Fernández-Moncada,  
INSERM U1215 Neurocentre  
Magendie, France  
Takeharu Nagai,  
Osaka University, Japan

### \*Correspondence:

Johannes Hirrlinger  
johannes.hirrlinger@  
medizin.uni-leipzig.de;  
hirrlinger@em.mpg.de

### †ORCID:

Johannes Hirrlinger  
orcid.org/0000-0002-6327-0089

### Specialty section:

This article was submitted to  
Non-Neuronal Cells,  
a section of the journal  
Frontiers in Cellular Neuroscience

**Received:** 26 May 2020

**Accepted:** 26 August 2020

**Published:** 18 September 2020

### Citation:

Köhler S, Schmidt H, Fülle P,  
Hirrlinger J and Winkler U (2020) A  
Dual Nanosensor Approach  
to Determine the Cytosolic  
Concentration of ATP in Astrocytes.  
Front. Cell. Neurosci. 14:565921.  
doi: 10.3389/fncel.2020.565921

Adenosine triphosphate (ATP) is the central energy carrier of all cells and knowledge on the dynamics of the concentration of ATP ([ATP]) provides important insights into the energetic state of a cell. Several genetically encoded fluorescent nanosensors for ATP were developed, which allow following the cytosolic [ATP] at high spatial and temporal resolution using fluorescence microscopy. However, to calibrate the fluorescent signal to [ATP] has remained challenging. To estimate basal cytosolic [ATP] ([ATP]<sub>0</sub>) in astrocytes, we here took advantage of two ATP nanosensors of the ATeam-family (ATeam1.03; ATeam1.03YEMK) with different affinities for ATP. Altering [ATP] by external stimuli resulted in characteristic pairs of signal changes of both nanosensors, which depend on [ATP]<sub>0</sub>. Using this dual nanosensor strategy and epifluorescence microscopy, [ATP]<sub>0</sub> was estimated to be around 1.5 mM in primary cultures of cortical astrocytes from mice. Furthermore, in astrocytes in acutely isolated cortical slices from mice expressing both nanosensors after stereotactic injection of AAV-vectors, 2-photon microscopy revealed [ATP]<sub>0</sub> of 0.7 mM to 1.3 mM. Finally, the change in [ATP] induced in the cytosol of cultured cortical astrocytes by application of azide, glutamate, and an increased extracellular concentration of K<sup>+</sup> were calculated as −0.50 mM, −0.16 mM, and 0.07 mM, respectively. In summary, the dual nanosensor approach adds another option for determining the concentration of [ATP] to the increasing toolbox of fluorescent nanosensors for metabolites. This approach can also be applied to other metabolites when two sensors with different binding properties are available.

**Keywords:** ATeam, ATP, astrocyte, calibration, genetically encoded sensors for metabolites

## INTRODUCTION

The metabolism of the brain is realized by a joint effort of all cell types including neurons, glial cells as well as cells constituting the blood vessels. Almost all aspects of metabolism in the brain involve several types of cells, including energy metabolism (Pellerin and Magistretti, 1994; Guzmán and Blázquez, 2001; Barros and Deitmer, 2010; Nave, 2010a; Hirrlinger and Nave, 2014; Barros et al., 2018b; Díaz-García and Yellen, 2019; Vicente-Gutierrez et al., 2019; Zuend et al., 2020), and neurotransmitter metabolism (van den Berg et al., 1978; Waagepetersen et al., 2003; Bak et al., 2006; Le Douce et al., 2020). Furthermore, brain cells are structurally intermingled, heavily interdigitating their numerous cellular processes (Somjen, 1988; Grosche et al., 1999; Bushong et al., 2002; Nave, 2010b). Therefore, to study the dynamics of brain metabolism

in detail, methods allowing to assess metabolites at high spatial and temporal resolution are required. These requirements are not fulfilled by most of the classical biochemical methods, as well as by techniques like PET or fMRI.

However, fluorescence nanosensors for metabolites are well suited to follow the concentration of a growing set of metabolites at high spatial and temporal resolution *in vitro*, *in situ*, and *in vivo* (Imamura et al., 2009; Hung et al., 2011; San Martín et al., 2014; Lange et al., 2015; Mächler et al., 2016; Mongeon et al., 2016; Trevisiol et al., 2017; Winkler et al., 2017; Köhler et al., 2018; Barros et al., 2018a; Díaz-García et al., 2019; Zuend et al., 2020). Conceptually, these sensors are proteins composed of a domain which specifically binds the metabolite of interest as well as one or more fluorescent proteins, which change their fluorescent properties upon metabolite binding. Different types of such sensors have been described. In single fluorophore sensors the fluorophore changes its fluorescence intensity upon metabolite binding. In ratiometric sensors the signal change is either derived from Förster resonance energy transfer (FRET) involving two fluorescent proteins. Alternatively, a second “reference fluorophore” is integrated in the sensor protein, which is unaffected by metabolite binding. Examples of such sensors include sensors for adenosine triphosphate (ATP; e.g., sensors of the ATeam family, Imamura et al., 2009; Queen, Yaginuma et al., 2014; Takaine et al., 2019), the ATP/ADP ratio (Perceval, Berg et al., 2009; PercevalHR, Nguyen et al., 2019), the NADH/NAD<sup>+</sup>-redox ratio (Peredox, Hung et al., 2011; Sonar, Zhao et al., 2015), NADPH (iNap family, Zhao et al., 2016), glucose (FlipGlu, Fehr et al., 2003; SweetieTS, Díaz-García et al., 2019), lactate (Laconic, San Martín et al., 2013), and pyruvate (Pyronic, San Martín et al., 2014; PyronicSF, Arce-Molina et al., 2020).

Fluorescent nanosensors for metabolites can be used to monitor relative changes of the respective metabolite within a cell or cellular compartment during an experiment by monitoring the time course of the fluorescent signal. However, the fluorescence signal is often not linearly related to the concentration of the metabolite (or only in a small concentration range). Furthermore, all sensors show a basal, metabolite independent fluorescence. Therefore, to calculate the concentration of the metabolite from this fluorescence signal has remained challenging and several different approaches have been employed (San Martín et al., 2014; Yellen and Mongeon, 2015; Barros et al., 2018a). All of these different approaches have their own advantages, but also limitations (see discussion section and **Table 1**). We here add a novel approach to the toolbox of fluorescent nanosensors for metabolites, which allows estimating the intracellular concentration of a metabolite under basal conditions by combining two nanosensors for the same metabolite with different binding equilibrium constants. This approach is exemplified using two ATP sensitive nanosensors (ATeam1.03, abbreviated AT, and ATeam1.03YEMK, abbreviated ATY) which differ in their dissociation constants ( $k_D$ ; Imamura et al., 2009). The feasibility of this approach is shown in cultured cortical astrocytes as well as in cortical astrocytes *in situ* in acutely isolated brain slices.

## MATERIALS AND METHODS

### Ethics Statement

In accordance with the guidelines for the welfare of experimental animals issued by the European Communities Council Directive (2010/63/EU) and with the German Protection of Animals Act (Tierschutzgesetz), mice were bred in the animal facility of the Medical Faculty of the University of Leipzig. Mice were housed in individually ventilated cages in a specific pathogen free environment in a 12 h/12 h light dark cycle with access to food and water *ad libitum*. Experiments were approved by the animal welfare office of the Faculty of Medicine, University of Leipzig and the governmental authorities of Saxony (Landesdirektion Sachsen, registration number T20/16; TVV62/15).

### Cell Culture and Transfection

Plasmids pDR-GW AT1.03, pDR-GW AT1.03YEMK, and pDR-GW AT1.03R122K/R126K (Bermejo et al., 2010) were obtained from Wolf Frommer (via Addgene; plasmids 28003, 28004, and 28005). The open reading frames of ATeam1.03, ATeam1.03YEMK, and AT1.03<sup>R122K/R126K</sup> (Imamura et al., 2009) were subcloned into pDEST expression vectors using Gateway cloning. Primary cortical astrocytes were prepared from the brains of newborn mice of the C57Bl/6J background as described (Requardt et al., 2010, 2012; Winkler et al., 2017). Cells were seeded on glass coverslips (30 mm diameter) with custom made silicon rings, which allow splitting the surface of the coverslip into two independent chambers (**Supplementary Figure 1**), and were cultured in DMEM/10% FCS/25 mM glucose for 1 week. The medium was exchanged to DMEM/10% FCS/5 mM glucose and cells were further cultured for at least 7 days with exchange of the medium twice per week. Cells on one coverslip were transfected with expression plasmids encoding ATeam1.03 in one chamber and ATeam1.03YEMK in the other chamber using lipofectamine (Thermo Fisher Scientific, Schwerte, Germany) and the standard protocol suggested by the supplier. Cells were used for experiments 1 day after transfection.

### Epifluorescence Imaging

Epifluorescence live cell imaging was performed as essentially described before (Winkler et al., 2017). In brief, coverslips were mounted into a custom-made flow chamber which was continuously perfused at 37°C with incubation medium containing (in mM) 145 NaCl, 5.4 KCl, 1 MgCl<sub>2</sub>, 1.8 CaCl<sub>2</sub>, 20 HEPES, 0.8 Na<sub>2</sub>HPO<sub>4</sub>, 5 glucose; pH 7.4; bubbled with 20% O<sub>2</sub>, 80% N<sub>2</sub> to ensure a constant O<sub>2</sub> partial pressure in all experiments. Cells were observed using an Axio-ObserverZ1 microscope (Zeiss, Jena, Germany) using a Plan-Apochromat 20x/0.8 objective and an AxioCam 506 camera (688 × 552 pixels, 4 × 4 binning, pixel size 0.91 μm × 0.91 μm) with acquisition times of 150 ms (CFP) and 100 ms (FRET). The two channels were recorded with the following filter sets: CFP: excitation 436/25 nm, beam splitter 455 nm, and emission 480/40 nm; and FRET: excitation 436/25 nm, beam splitter 455 nm, and emission 535/30 nm. Using the motorized x-y stage of the microscope, images of cells in both chambers were recorded

**TABLE 1** | Comparison of the dual nanosensor approach to other methods for calibrating nanosensors.

	Dual nanosensor	Single point calibration	Full calibration
Requirements	2 Sensors with different $k_D$	1 Sensor	Precise control of the [metabolite] within the cellular compartment of interest, e.g., via - transporters - permeabilization - dialysis
Parameters to be obtained from other experimental systems	$k_D$ $n_H$ (for both sensors)	$k_D$ $n_H$ $R_{\max}$	None
Parameters to be measured in each experiment <sup>1</sup>	$R_{\min}$	$R_{\min}$	None <sup>2</sup>
Single cell data available	Yes <sup>3</sup>	Yes	Yes

Notes: <sup>1</sup>in addition to  $R$ . <sup>2</sup>If the signal is very stable between experiments. However, at least one "anchor point" (e.g.,  $R_0$ ) might be necessary to relate the established calibration curve to the specific experiment. <sup>3</sup>needs second step of calculation.

almost simultaneously with only the time delay necessary to move the stage to the other positions (<1 s). Images were obtained every 20 s. At the end of each experiment, iodoacetate (1 mM; Applichem, Darmstadt, Germany) and sodium azide (10 mM; Serva, Heidelberg, Germany) were applied. This treatment blocks all ATP-producing pathways allowing to normalize the sensor signal to nominally [ATP] = 0.

## AAV Injection and 2-Photon Imaging in Acute Brain Slices

To image the dynamics of ATP in cortical astrocytes in acute brain slices, ATeam1.03 or ATeam1.03YEMK-open reading frames (Imamura et al., 2009) were cloned into a vector for packaging into adeno-associated viruses (AAV) and astrocyte-specific expression was driven by GFAP-promoter elements (Lee et al., 2008; Mächler et al., 2016; Stobart et al., 2018). The plasmids were packaged into AAV serotype 5 by the Viral Vector Facility at the Neuroscience Center Zurich, University of Zurich, Switzerland. 0.5  $\mu$ l of AAV containing solution (virus titer:  $2.2 \times 10^{12}$  vg/ml (AT);  $2.75 \times 10^{12}$  vg/ml (ATY) were stereotactically injected into cortex of 2 to 3 month old mice (coordinates: 0.5 mm caudal to bregma, lateral 2.0 mm, and ventral 1.1 mm), i.e., in the primary somatosensory cortex. 4 weeks later, mice were sacrificed and 250  $\mu$ m thick acute coronal brain slices were prepared (Pätz et al., 2018). Slices were transferred to the stage of a 2-photon laser scanning microscope (Olympus FV1000) equipped with a XLPlan N 25x/1.05 W objective (Olympus) and a Mai Tai DeepSee laser (Spectra-Physics, Darmstadt, Germany) and continuously superfused at room temperature with aCSF solution (in mM): 130 NaCl, 2.5 KCl, 1 MgCl<sub>2</sub>, 2 CaCl<sub>2</sub>, 1.25 NaH<sub>2</sub>PO<sub>4</sub>, 26 NaHCO<sub>3</sub>, 10 glucose, pH 7.4. The medium was continuously bubbled with carbogen. Imaging was performed within 500  $\mu$ m of the site of AAV injection. The following imaging parameters were used: excitation: 810 nm; emission 510 DC XR (F33-511 OD, 266685; AHF, Germany); pixel size:  $0.552 \times 0.552$   $\mu$ m;  $512 \times 512$  pixels; pixel dwell time: 2  $\mu$ s; time resolution: 60 s; stack of 23 single  $z$ -planes. All experiments were started by perfusing the slice with aCSF for 20 min followed by aCSF containing 1  $\mu$ M TTX (Tocris, Bristol, United Kingdom) to prevent neuronal activity and to define the sensor signals under baseline conditions. Afterward, glutamate (100  $\mu$ M in aCSF) was applied for 20 min. At the end of each experiment, 1 mM iodoacetate and 10 mM azide was added

to deplete the cells of ATP. All solutions were adjusted to same pH and osmolality.

## Data Analysis and Analytical Solution

For a detailed description of the variables and indices used for this calculation see **Supplementary Table 1**. Regions of interest (ROI), each containing a single cell, were defined manually using Fiji (Schindelin et al., 2012). Background subtracted mean fluorescence intensities averaged over all pixels within a ROI were determined for the FRET ( $I_{\text{FRET}}$ ) and the CFP ( $I_{\text{CFP}}$ ) channel. The ratio of the intensities ( $I$ ) was calculated as  $I = I_{\text{FRET}}/I_{\text{CFP}}$ . The relative sensor signal ratio ( $R$ ) was calculated as

$$R = \frac{I - I_{\min}}{I_0 - I_{\min}} \quad (1)$$

where  $I_{\min}$  is  $I$  at [ATP] of 0 mM and  $I_0$  being the pre-treatment baseline  $I$  at the unknown baseline [ATP]<sub>0</sub>. This results in a minimum  $R$  ( $R_{\min}$ ) of 0 for [ATP] of 0 mM and a pre-treatment  $R$  value ( $R_0$ ) of 1 at the unknown baseline [ATP]<sub>0</sub>. Notably,  $R$  as defined by Eq. 1, does not directly relate to the sensor occupancy  $B$ , defined as

$$B = \frac{[\text{ATP bound sensor}]}{[\text{sensor}]_{\text{total}}} = \frac{[\text{ATP}]^{n_H}}{[\text{ATP}]^{n_H} + k_D^{n_H}} \quad (2)$$

with  $n_H$  being the Hill-coefficient and  $k_D$  the dissociation constant.  $B$  scales between 0 (at [ATP] = 0) and 1 (at full saturation of the sensor; **Figures 1A,B**). However, while at [ATP] = 0 both,  $B$  and  $R$  are equal to 0,  $R = 1$  at [ATP]<sub>0</sub> for each experiment but  $B = 1$  at full saturation of the sensor (**Figures 1A,B**). As [ATP]<sub>0</sub> within a cell is not known, the value of  $B_0$  at baseline conditions is also not known; therefore, a direct calculation of changes in [ATP] ( $d[\text{ATP}]$ ) from changes in  $R$  ( $dR$ ) is not possible.

If  $R$  values at full saturation ( $R_{\max}$ ) can be measured, it is possible to relate  $R$  to the metabolite concentration, as has been done for the ATeam-type ATP sensors using purified sensor proteins (Imamura et al., 2009):

$$R = \frac{R_{\max} \times [\text{ATP}]^{n_H}}{[\text{ATP}]^{n_H} + k_D^{n_H}} \quad (3)$$

Different from this  $R_{\max}$  approach, the dual nanosensor approach introduced here avoids the necessity to determine  $R_{\max}$ . Yet, it still relies on knowledge about  $k_D$  and  $n_H$  (**Table 1**).

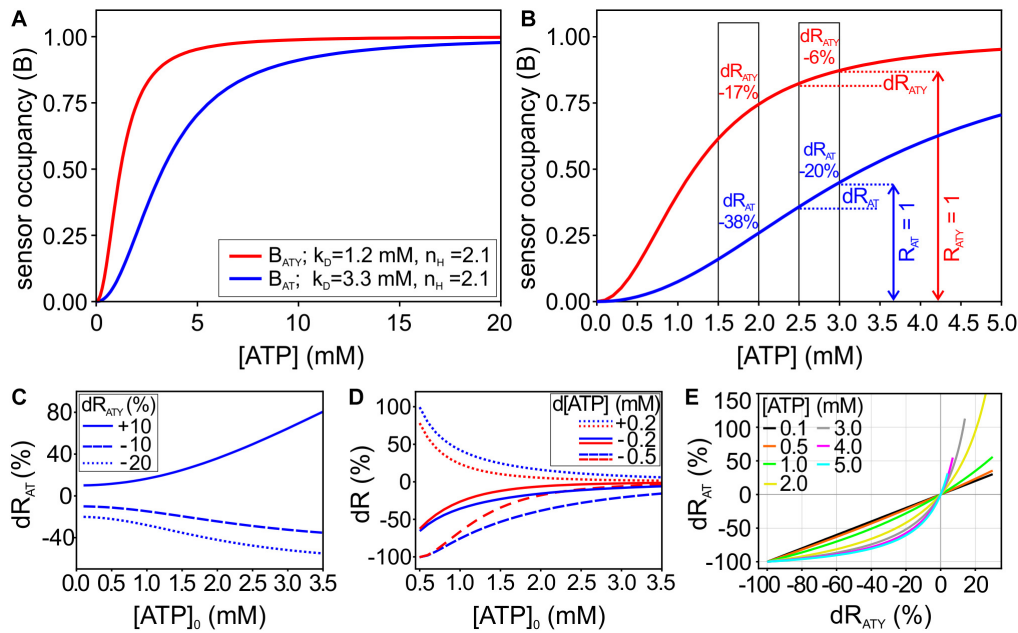


**FIGURE 1** | Mathematical framework of the dual nanosensor approach. **(A)** Binding curves for the ATP sensors ATeam1.03 (AT; blue) and ATeam1.03YEMK (ATY; red), showing the sensor occupancy ( $B$ ) at different cytosolic  $[ATP]$ . **(B)** Enlargement of A for  $[ATP]$  from 0 to 5 mM. The boxes highlight two examples with  $d[ATP] = -0.5$  mM starting at  $[ATP]_0 = 2$  mM and  $[ATP]_0 = 3$  mM, respectively. Note that  $R_{AT} = 1$  and  $R_{ATY} = 1$  (i.e., the sensor signal at the starting  $[ATP]_0$ , indicated by the vertical arrows for the example of  $[ATP]_0 = 3$  mM) correspond to different values of sensor occupancy ( $B$ ) for both sensors. The resulting relative changes of the sensor signals  $dR_{AT}$  and  $dR_{ATY}$  are given within the boxes. **(C)** Changes of  $R_{AT}$  ( $dR_{AT}$ ) depending on  $[ATP]_0$  at given values of  $dR_{ATY}$  ( $dR_{ATY} = -10\%$ ,  $-20\%$ , and  $+10\%$ ). **(D)** A change in  $[ATP]$  results in a characteristic pair of signal changes  $dR_{AT}$  and  $dR_{ATY}$ , which depend also on  $[ATP]_0$ . Shown are examples of  $d[ATP] = -0.2$  mM,  $d[ATP] = -0.5$  mM, and  $d[ATP] = +0.2$  mM. **(E)** For each  $[ATP]_0$ , unique pairs of  $dR_{AT}$  and  $dR_{ATY}$  describe a given  $d[ATP]$ . Therefore,  $[ATP]_0$  can be deduced from pairs of  $dR_{AT}$  and  $dR_{ATY}$  obtained experimentally.

To calculate  $[ATP]_0$  and  $[ATP]$  during treatment ( $[ATP]_{treat}$ ),  $dR$  values for measurements with AT and ATY, respectively, were obtained experimentally for different treatments;  $k_D$  and  $n_H$  values for the indicators were taken from the literature. The following sets of parameters were used:

$k_{D,AT} = 3.3$  mM,  $k_{D,ATY} = 1.2$  mM,  $n_{H,AT} = n_{H,ATY} = 2.1$  (Imamura et al., 2009).

$k_{D,AT} = 9.4$  mM,  $k_{D,ATY} = 2.7$  mM,  $n_{H,AT} = n_{H,ATY} = 1.0$  (Lerchundi et al., 2020).

To calculate  $[ATP]_0$  and  $[ATP]_{treat}$  from  $dR_{AT}$  and  $dR_{ATY}$  measured in the experiments, a system of two non-linear equations was used which allowed deriving analytical solutions:

$$dR_{AT} = \frac{R_{AT,treat}}{R_{AT,0}} - 1 \quad (4a)$$

$$dR_{ATY} = \frac{R_{ATY,treat}}{R_{ATY,0}} - 1 \quad (4b)$$

Introducing  $R$  according to Eq. 3 into Eqs 4a,b the following equations result (for simplicity “ $n_H$ ” is replaced by “ $n$ ” in Eqs 5a,b and 6a,b):

$$dR_{AT} = \left( \frac{R_{max,AT} \times [ATP]_{treat}^n}{[ATP]_{treat}^n + k_{D,AT}^n} \right) / \left( \frac{R_{max,AT} \times [ATP]_0^n}{[ATP]_0^n + k_{D,AT}^n} \right) - 1 \quad (5a)$$

$$dR_{ATY} = \left( \frac{R_{max,ATY} \times [ATP]_{treat}^n}{[ATP]_{treat}^n + k_{D,ATY}^n} \right) / \left( \frac{R_{max,ATY} \times [ATP]_0^n}{[ATP]_0^n + k_{D,ATY}^n} \right) - 1 \quad (5b)$$

Solving Eqs 5a,b as a system of non-linear equations using “Solve” of Mathematica 12.1. yielded the following analytical expressions for  $[ATP]_0$  and  $[ATP]_{treat}$ :

$$[ATP]_0 = \left( \frac{(dR_{AT} - dR_{ATY}) \times k_{D,AT}^n \times k_{D,ATY}^n}{dR_{ATY} \times k_{D,AT}^n + dR_{AT} \times k_{D,ATY}^n - dR_{AT} \times k_{D,ATY}^n - dR_{ATY} \times k_{D,AT}^n} \right)^{\frac{1}{n}} \quad (6a)$$

$$[ATP]_{treat} = \left( \frac{(dR_{AT} - dR_{ATY}) \times k_{D,AT}^n \times k_{D,ATY}^n}{dR_{ATY} \times k_{D,AT}^n - dR_{AT} \times k_{D,ATY}^n} \right)^{\frac{1}{n}} \quad (6b)$$

Of note, this analytical solution requires that  $n_{H,AT} = n_{H,ATY}$ , a prerequisite met by the ATeam sensors. If  $n_{H,1} \neq n_{H,2}$ , solving the system of non-linear equations results in expressions involving complex numbers. In this case, numerical solving of Eqs 5a,b using “NSolve” of Mathematica is preferable.



Having established the mean  $[ATP]_0$  of all cells observed in a given experiment according to Eq. 6a,  $R$  values (Eq. 1) can be correlated to sensor occupancy  $B$ . First,  $B_0$  is calculated from  $[ATP]_0$  using Eq. 2. Then, all  $R$  values are multiplied by  $B_0$  resulting in  $R$  values reflecting sensor occupancy with a range of  $R = 0$  at  $[ATP] = 0$  to  $R = R_{max} = 1$  at saturation of the sensor. Consecutively,  $[ATP]$  for each single cell at any time point during an experiment (including  $[ATP]_0$ ) is revealed by

$$[ATP] = k_D \times \left( \frac{R}{R_{max} - R} \right)^{\frac{1}{n_H}} \quad (7)$$

Using Eq. 7,  $[ATP]$  can be calculated for both sensors separately. Finally, rates of  $[ATP]$  changes were calculated by linear regression of  $[ATP]$  over the time period of interest.

## Data Processing and Presentation

Microscopic images were processed using Zeiss ZEN software, Fiji and Corel Draw X4 Graphic. Data were analyzed and calculated using Fiji and Microsoft Excel. Analytical solutions of the system of non-linear equations as well as values for  $[ATP]_0$  and  $[ATP]_{treat}$  according to Eqs. 6a,b were obtained using Mathematica. Diagrams were generated using Sigma Plot. In the boxplots, the box spans from the 25th to 75th percentile, the whiskers span from the 10th to the 90th percentile and dots highlighting the 5th to the 95th percentile. In addition, in **Figures 5A,B** all outliers are indicated by light blue and light red circles. Within the box dashed lines represent the mean value, solid lines show the median. In **Figure 2A**, lines represent the mean and the shaded area indicates the standard deviation (SD). In **Figures 2B–D** circles and associated error bars represent the mean  $\pm$  SD. All data presented in **Figures 1–5** are obtained on 3 independent astrocytic cell cultures. Data in the text are given as mean  $\pm$  SD. Final illustrations were arranged using Corel Draw X4 Graphic.

## RESULTS

The ATP sensors ATeam1.03 (abbreviated AT in the following) and ATeam1.03YEMK (abbreviated as ATY) are two cytosolic, ATP specific nanosensors, which differ in their affinity for ATP (Imamura et al., 2009). Dissociation constants ( $k_D$ ) of 3.3 mM and 1.2 mM were described for AT and ATY, respectively; for both sensors a Hill coefficient  $n_H$  of 2.1 was found (Imamura et al., 2009). Therefore, the occupancy of the sensor (i.e., the ratio of ATP bound sensor/total sensor; referred to as  $B$  here; see Eq. 2) is different for both sensors at a given cytosolic concentration of ATP ( $[ATP]$ ; **Figure 1A**). The  $[ATP]$  of a cell under baseline resting conditions ( $[ATP]_0$ ) is a very important parameter for cellular energy metabolism, which is difficult to determine and not known in many cases. We reasoned that a treatment of cells, which results in a given change in  $[ATP]$  ( $d[ATP]$ ), will cause different relative changes of the sensor signal for AT ( $dR_{AT}$ ) and ATY ( $dR_{ATY}$ ; **Figure 1B**). For example, at  $[ATP]_0 = 2$  mM a change in  $[ATP]$  of  $-0.5$  mM will result in  $dR_{AT} = -38\%$  and  $dR_{ATY} = -17\%$ ; while at  $[ATP]_0 = 3$  mM the same change in

ATP will result in  $dR_{AT} = -20\%$  and  $dR_{ATY} = -6\%$  (**Figure 1B**). Therefore, at a given  $dR_{ATY}$ , the corresponding  $dR_{AT}$  correlates to  $[ATP]_0$ , or else, depending on  $[ATP]_0$  a change in  $[ATP]$  will result in a characteristic pair of values for  $dR_{AT}$  and  $dR_{ATY}$  (**Figures 1C,D**). Accordingly,  $[ATP]_0$  can be derived from pairs of  $dR_{AT}$  and  $dR_{ATY}$  obtained by treating cells with conditions which change  $[ATP]$  (**Figure 1E**). Importantly, for this approach prior knowledge of the actual  $d[ATP]$  caused by these conditions is not necessary.

To test this approach experimentally, primary cultured cortical astrocytes were studied, which have been reported before to respond to different stimuli with changes in  $[ATP]$  (Winkler et al., 2017). After transfection with either AT or ATY, cells were imaged by epifluorescence microscopy in a custom-made system allowing to image cells transfected with the different plasmids in parallel in the same experiment. Cells readily responded to treatments with a change in  $[ATP]$  reflected by both AT and ATY (**Figure 2A**). At the end of each experiment, cells were incubated with iodoacetate (IA) and azide to block cellular ATP production thereby depleting cellular ATP, allowing to normalize the sensor signal to the sensor signal at  $[ATP] = 0$  mM (**Figure 2A**).

Cells were treated with three different conditions: (a) 10 mM azide (**Figure 2B**); (b) 100  $\mu$ M glutamate (**Figure 2C**); and (c) by increasing the extracellular concentration of potassium ( $[K^+]_e$ ) from 5.4 mM to 12 mM (**Figure 2D**). From the resulting pairs of  $dR_{AT}$  and  $dR_{ATY}$ ,  $[ATP]_0$  was calculated both for the single experiments with simultaneous imaging of both AT and ATY as well as for the data pooled from all experiments using the same condition (**Figure 2E**, Eq. 6a). Both types of analysis revealed a resting, basal  $[ATP]_0$  of about 1.5 mM (**Figure 2E**;  $1.51 \pm 0.35$  mM,  $n = 9$  experiments/ $1.47 \pm 0.06$  mM;  $N = 3$  conditions).

The calculation of  $[ATP]_0$  using this dual nanosensor approach depends on knowledge of the  $k_D$  values of the two versions of the sensor. In the original description of ATP sensors of the ATeam family  $k_D$  values of 3.3 mM and 1.2 mM (and  $n_{H,AT} = n_{H,ATY} = 2.1$ ) have been reported for AT and ATY, respectively (Imamura et al., 2009). However, based on calibration of the sensors in astrocytes and neurons in organotypic brain slice cultures, recently  $k_D$  values of 9.4 mM and 2.7 mM were determined (Gerka et al., 2019; Lerchundi et al., 2020). The latter studies used a Michaelis–Menten equation for fitting the data, which inherently implies  $n_H = 1$ .  $[ATP]_0$  calculated using these parameters (**Figure 2F**) revealed  $18.10 \pm 29.23$  mM ( $n = 9$  experiments) and  $8.04 \pm 1.54$  mM ( $N = 3$  conditions). These values are substantially higher compared to previously published data on astrocytes and neurons (1 mM to 4 mM; Fukuda et al., 1983; Ainscow et al., 2002; Mollajew et al., 2013; Rangaraju et al., 2014; Toloe et al., 2014; Pathak et al., 2015), suggesting that this set of parameters might not be fully applicable on the experimental system used here. Despite these uncertainties regarding the  $k_D$  values, these analyses show that the dual nanosensor approach is well suited to estimate the intracellular cytosolic  $[ATP]$  within cells. We note, that for further analysis of the data obtained on cultured astrocytes (**Figures 4, 5**) the original  $k_D$  and  $n_H$

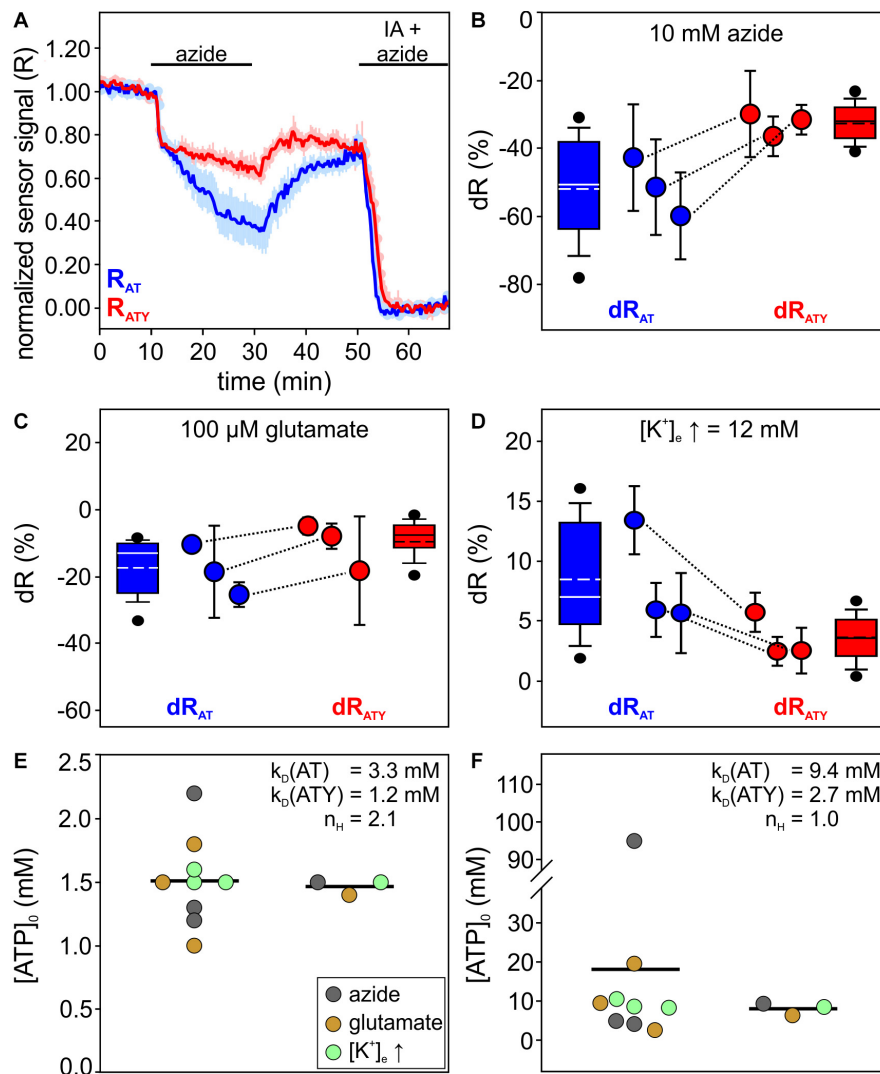


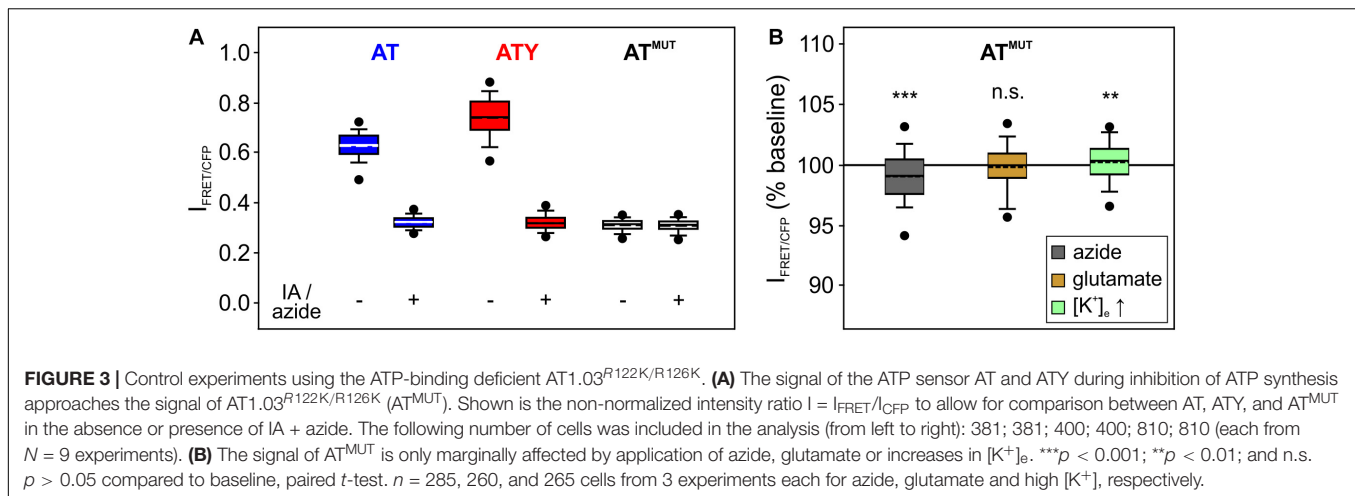
**FIGURE 2 |** Determination of  $[ATP]_0$  in primary cultured cortical astrocytes using the dual nanosensor approach. **(A)** Time course of the signal of AT (blue) and ATY (red) during an experiment exposing the cells to azide (10 mM). At the end of the experiment, cells were treated with iodoacetate (IA) and azide to deplete cellular ATP. Shown is the normalized sensor signal R for all cells of one representative experiment ( $n = 25$  cells for both AT and ATY; mean  $\pm$  SD). **(B–D)** Signal changes  $dR$  obtained for AT ( $dR_{AT}$ ; blue) and ATY ( $dR_{ATY}$ ; red) during incubation of astrocytes with azide (**B**; 10 mM, 20 min), glutamate (**C**; 100  $\mu$ M, 15 min) or an increase in  $[K^+]_e$  (**D**; from 5.4 mM to 12 mM, 10 min). Shown is the distribution of  $dR$  of all cells (box plots), as well as the mean  $\pm$  SD of each experiment (circles and error bars). Corresponding means of both sensors from the paired experiments are connected with lines. Each condition was replicated in  $N = 3$  independent experiments. In each experiment, the following number of cells were analyzed: B, AT: 50, 50, 40. B, ATY: 48, 50, 47. C, AT: 50, 17, 40; C, ATY: 49, 44, 34. D, AT: 43, 46, 44; and D, ATY: 44, 46, 36. **(E)**  $[ATP]_0$  values calculated from the  $dR_{AT} - dR_{ATY}$  pairs shown in panels (B–D), using the parameters indicated within the graph. On the left, values calculated from the  $dR_{AT} - dR_{ATY}$  pairs from the paired experiments (circles) as well as the mean (line) are shown. Right: values obtained from the  $dR_{AT} - dR_{ATY}$  pairs obtained from the pooled cells of all experiments. **(F)** Same calculation as in (E), but with different values of  $k_D$  and  $n_H$  as indicated within the graph.

values will be used (i.e.,  $k_{D,AT} = 3.3$  mM,  $k_{D,ATY} = 1.2$  mM,  $n_{H,AT} = n_{H,ATY} = 2.1$ ; Imamura et al., 2009).

Two crucial assumptions are inherent in this approach: (a) treatment of the cells with iodoacetate + azide depletes the cell of cytosolic ATP; (b) no other factors, like, e.g., pH, affect the sensor signal during treatment of the cells. To test the validity of these assumptions, experiments were repeated with cells expressing AT1.03<sup>R122K/R126K</sup> (abbreviated AT<sup>MUT</sup>), a mutated version of the ATeam sensors consisting of the same fluorophores and the same ATP binding protein, but which does not bind ATP due to

two point mutations within the ATP binding domain (Imamura et al., 2009). First, the signal of AT<sup>MUT</sup> is very similar to the signal of AT and ATY during application of iodoacetate + azide (Figure 3A), suggesting that cytosolic  $[ATP]$  reaches nominally zero and confirming previous observations (Trevisiol et al., 2017; Winkler et al., 2017). Secondly, when cells expressing AT<sup>MUT</sup> were treated with azide, glutamate or with increased  $[K^+]_e$ , only a minor change in the AT<sup>MUT</sup> signal was observed (Figure 3B; azide:  $-0.9 \pm 2.9\%$ ;  $n = 285$  cells; glutamate:  $-0.2 \pm 2.2\%$ ;  $n = 260$  cells;  $[K^+]_e$ :  $0.2 \pm 2.2\%$ ;  $n = 265$  cells). As AT<sup>MUT</sup> has

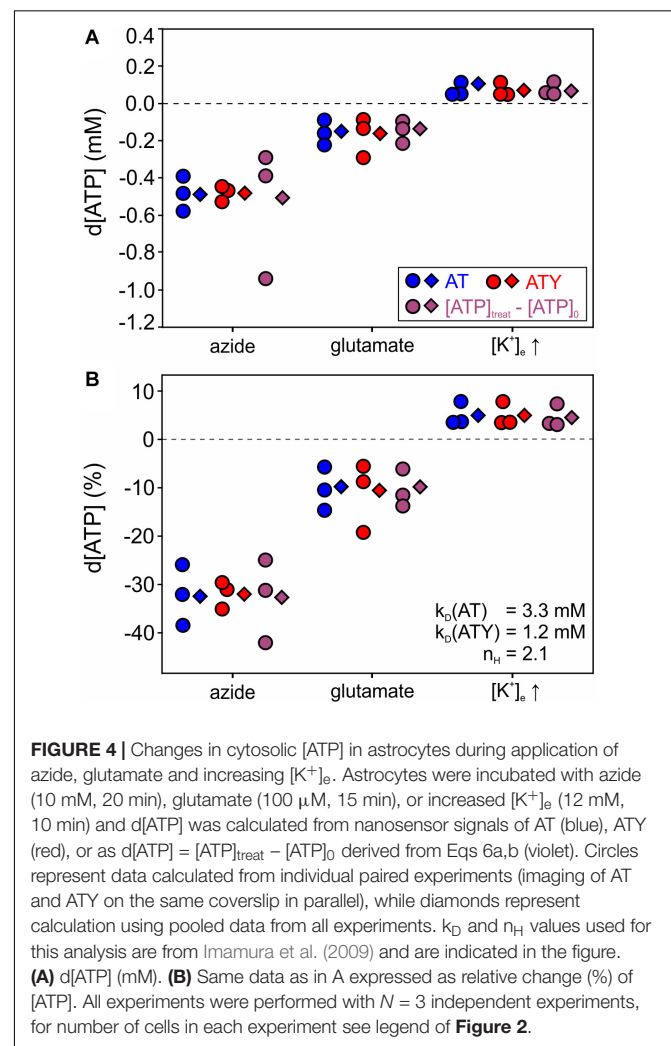




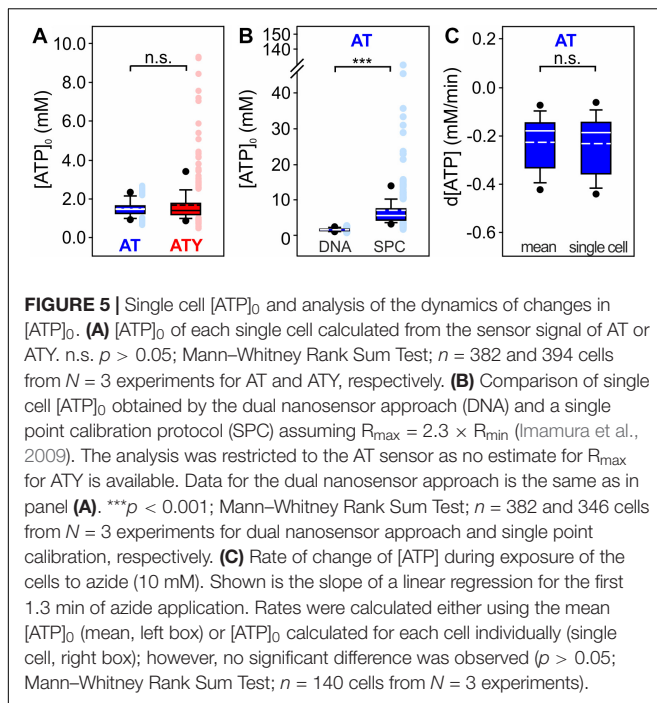
the same properties as AT and ATY with the exception of ATP binding, these data indicate that other factors than  $[ATP]$  do not contribute substantially to the change of the sensor signal of AT and ATY under the conditions of these experiments.

Having established  $[ATP]_0$  using the dual nanosensor approach, the changes in  $[ATP]$  induced by the different treatments were calculated (Figure 4, Eq. 6b). Exposure of astrocytes to azide, which blocks the respiratory chain, reduced  $[ATP]$  by  $-0.50 \pm 0.15$  mM reflecting  $-32.4 \pm 5.2\%$  of  $[ATP]_0$  (Figure 4;  $n = 3$  experiments with 285 cells analyzed), indicating that astrocytes maintain the cytosolic  $[ATP]$  at about 70% of the basal value in the absence of oxidative phosphorylation. Of note, vice versa this finding also implies that glycolysis alone is not sufficient to maintain  $[ATP]$  at control levels. Furthermore, application of glutamate (100  $\mu$ M, 15 min) resulted in a reduction of  $[ATP]$  of about  $-0.16 \pm 0.06$  mM ( $-10.8 \pm 5.0\%$ ;  $n = 3$  experiments with 234 cells analyzed; Figure 4). Finally, increasing  $[K^+]_e$  induced a rise in  $[ATP]$  of  $0.07 \pm 0.04$  mM, i.e.,  $4.7 \pm 2.4\%$  ( $n = 3$  experiments with 259 cells analyzed; Figure 4). The results were very similar irrespective of whether each experiment was analyzed separately, or whether all data from all cells were pooled prior to analysis (compare circles and diamonds in Figure 4), suggesting that paired experiments are not a prerequisite of the dual nanosensor approach. Furthermore, similar results were obtained when calculating  $d[ATP]$  from the AT or ATY signal (blue and red symbols in Figure 4), or by calculating  $d[ATP] = [ATP]_{\text{treat}} - [ATP]_0$  using the equations derived from solving the system of non-linear equations (Eqs 6a,b; violet symbols in Figure 4).

Astrocytes are a heterogeneous cell population which also includes heterogeneity of metabolism (Bittner et al., 2010; Matyash and Kettenmann, 2010; Zhang and Barres, 2010; Bayraktar et al., 2015; Farmer and Murai, 2017; Köhler et al., 2018, 2019; Miller, 2018; Morel et al., 2018; Batiuk et al., 2020). Therefore, information on the heterogeneity of  $[ATP]_0$  within the astrocytic cell population is of major interest. While calculating  $[ATP]_0$  using the dual nanosensor method initially results in the mean  $[ATP]_0$  of all cells included in the analysis,  $[ATP]_0$  for each single cell can be obtained in a second calculation step using



the mean  $[ATP]_0$  as additional parameter. This analysis revealed similar results when calculated either from the AT or ATY signals (Figure 5A; AT:  $1.51 \pm 0.40$  mM;  $n = 382$  cells from  $N = 9$



experiments; ATY:  $1.70 \pm 1.06$  mM;  $n = 394$  cells from  $N = 9$  experiments). However, the ATY-based calculation resulted in more cells with very high  $[ATP]_0$ , most likely because the ATY binding curve (Figure 1A) is flat in this concentration range and even very small differences in  $R_{ATY}$  result in a rather large difference in  $[ATP]_0$ .

Another method to obtain single cell data from fluorescent nanosensor imaging is the single point calibration protocol (e.g., Sotelo-Hitschfeld et al., 2012; Fernández-Moncada and Barros, 2014; Arce-Molina et al., 2020). Only one nanosensor is needed for this approach, and  $k_D$  and  $n_H$  are derived from other experimental systems like in the dual nanosensor approach (Table 1). In addition, an estimate for  $R_{max}$  needs to be included in the calculation. For AT, a dynamic range of  $R_{max} = 2.3 \times R_{min}$  has been reported (Imamura et al., 2009). As no explicit information on  $R_{max}$  of ATY is available, only data obtained by imaging of AT were reanalyzed using the single point calibration protocol (Figure 5B). This analysis revealed a higher mean  $[ATP]_0$  and a larger variability of  $[ATP]_0$  compared to the dual nanosensor approach (Figure 5B;  $7.00 \pm 8.08$  mM;  $n = 346$  cells from  $N = 9$  experiments).

Calibration of fluorescent nanosensors to the concentration of the metabolite also allows assessing kinetic changes of the concentration of the metabolite. As an example, the rate of the  $[ATP]$  decrease during inhibition of oxidative phosphorylation by azide was calculated, using either  $[ATP]_0$  obtained as the mean  $[ATP]_0$  of all cells within an experiment or  $[ATP]_0$  calculated for each cell individually (Figure 5C). No significant differences were observed between the two modes of calculation ( $p > 0.05$ ; Mann–Whitney Rank Sum Test).  $[ATP]$  decreased with a rate of  $-0.23 \pm 0.11$  mM/min (Figure 5C; data calculated with mean  $[ATP]_0$ ;  $n = 140$  cells from  $N = 3$  experiments).

Finally, to validate the dual nanosensor approach in a more intact system than primary cultured cortical astrocytes, AT and ATY were expressed in cortical astrocytes *in vivo* by stereotactic injection of AAV vectors, in which expression of the sensor is driven by the GFAP promoter. Acute brain slices were prepared from these mice and imaged using 2-photon microscopy (Figures 6A,B). Application of glutamate induced changes in  $[ATP]$  and corresponding values of  $dR_{AT}$  and  $dR_{ATY}$  were recorded (Figure 6C). As the two sensors were not expressed within the same mice, no pairing of experiments was possible. Based on the two different sets of  $k_D$ -values (Imamura et al., 2009; Lerchundi et al., 2020), a basal  $[ATP]_0$  of  $0.7$  mM or  $1.3$  mM was calculated, respectively (Figure 6D), showing that the dual nanosensor approach can also be applied to more intact preparations like acute brain slices as well as to other imaging techniques like 2-photon laser scanning microscopy.

## DISCUSSION

Fluorescent nanosensors for metabolites have strongly contributed to a much deeper knowledge on the metabolism and its dynamics of the mammalian brain (and of other organs and organisms; Deuschle et al., 2006; Tsuyama et al., 2013; Yaginuma et al., 2014; Masia et al., 2018; Volkenhoff et al., 2018; Nguyen et al., 2019; Takaine et al., 2019; Arce-Molina et al., 2020; Kioka et al., 2020). As these sensors are proteins which can be genetically encoded, they allow cell type specific expression using specific promoters as well as subcellular targeting using appropriate targeting sequences. Combined with different state-of-the-art microscopy technologies, the dynamics of metabolites can be followed in cultured cells, in tissue preparations like brain slices or the isolated optic nerve, but also *in vivo* in living and even awake animals (Bittner et al., 2011; Ruminot et al., 2011; Mächler et al., 2016; Díaz-García et al., 2017, 2019; Trevisiol et al., 2017; Köhler et al., 2018; Baeza-Lehnert et al., 2019; Gerkau et al., 2019; Lerchundi et al., 2019; Arce-Molina et al., 2020; Zuend et al., 2020). However, while these nanosensors readily allow for monitoring relative changes of the metabolite concentration, deduction of absolute concentrations and absolute concentration changes (i.e., in mol/l) during treatments has remained challenging as calibration of the signal of the nanosensors to the actual concentration of the metabolite is hampered by both, theoretical and practical problems (Barros et al., 2018a). We here introduce the dual nanosensor approach, a novel strategy to determine  $[ATP]_0$  using two nanosensors for ATP with different binding equilibrium constants  $k_D$ .

## Properties, Assumptions and Limitations of the Dual Nanosensor Approach

The dual nanosensor approach requires the availability of two nanosensors sensitive to the concentration of the metabolite of interest (here ATP), which differ in their binding equilibrium constants  $k_D$  (Table 1). Parallel experiments with cells expressing one or the other sensor reveal the signal change  $dR$  of both sensors (Figure 2). If both sensors would differ in their spectral properties, which is unfortunately not the case for

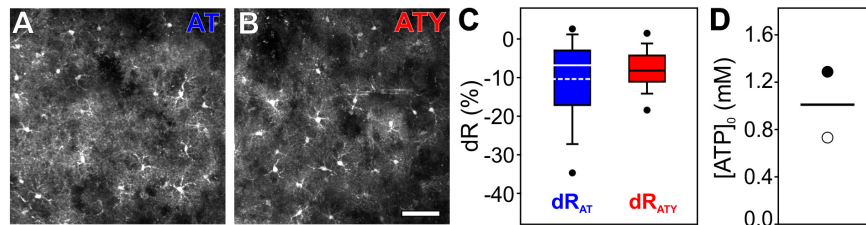


**FIGURE 6 |** Determination of  $[ATP]_0$  in cortical astrocytes in acutely isolated brain slices using 2-photon imaging. AT or ATY were expressed in astrocytes in the primary somatosensory cortex *in vivo* by stereotactic injections of AAV-based vectors and acutely isolated brain slices were prepared. **(A, B)** 2-photon images showing expression of AT **(A)** or ATY **(B)** in cortical astrocytes. Scale bar: 50  $\mu$ m. **(C)** dR values obtained for AT (blue) and ATY (red) during incubation of the slices with glutamate (100  $\mu$ M) for 20 min. **(D)**  $[ATP]_0$  values obtained from the  $dR_{AT}$ - $dR_{ATY}$  pair shown in C calculated using the following sets of parameters:  $k_{D,AT} = 3.3$  mM,  $k_{D,ATY} = 1.2$  mM,  $n_H = 2.1$  (open circle; Imamura et al., 2009); and  $k_{D,AT} = 9.4$  mM,  $k_{D,ATY} = 2.7$  mM,  $n_H = 1$  (filled circle; Lerchundi et al., 2020).  $n = 80, 92$  cells from  $N = 4, 6$  mice were included in the analysis shown in **(C and D)** for AT and ATY, respectively.

AT and ATY (but has been reported for ATP sensors using a single fluorophore; Arai et al., 2018), both sensors could even be recorded within a single cell. Values for  $k_D$  and  $n_H$  need to be obtained from other experimental systems, e.g., from measurements of the purified sensor protein (Imamura et al., 2009), assuming that these values can be applied to the indicators in the cytosolic environment of the cells of interest (**Table 1**). While such transfer of parameters is often used also for other calibration strategies (e.g., Sotelo-Hitschfeld et al., 2012; Fernández-Moncada and Barros, 2014; Arce-Molina et al., 2020), several studies indicate that parameters of various genetically encoded nanosensors can be affected by the cellular environment (Hires et al., 2008; Pérez Koldenkova and Nagai, 2013; Yaginuma et al., 2014; Lerchundi et al., 2019, 2020). Moreover, care has to be taken that these values are determined by appropriate methods including similar or –ideally– identical excitation and emission wavelengths (Pomorski et al., 2013). In addition,  $R_{min}$  needs to be measured for each cell during the experiments (**Table 1**), thereby requiring a method to deplete the cells from ATP. Application of azide, which blocks oxidative phosphorylation at complex IV of the respiratory chain, and iodoacetate, which blocks glycolysis at glyceraldehyde-3-phosphate dehydrogenase (GAPDH), resulted in a decrease of the AT- and ATY-sensor signal reaching the signal of the ATP-binding deficient  $AT1.03^{R122K/R126K}$  ( $AT^{MUT}$ ; **Figure 3A**), suggesting that the fluorescence signal observed under these conditions is at least close to  $R_{min}$  and reflects a concentration of cytosolic ATP of nominally zero. This observation is in line with previous observations using the same treatment to deplete ATP (Trevisiol et al., 2017; Winkler et al., 2017), but also with a different approach blocking glycolysis using 2-deoxyglucose and oxidative phosphorylation by oligomycin (Shulman et al., 2015). Finally, it has to be assumed that a given treatment of a cell results in the same change of  $[ATP]$  when either AT or ATY is expressed. This might be of special importance if the concentration of the analyte of interest is within the same range (or lower) as the concentration of the sensor, e.g., in the case of  $Ca^{2+}$ -sensors. However,  $[ATP]_0$  is at least one to two orders of magnitude higher than the typical concentration of genetically expressed sensor proteins (Barros et al., 2018a), suggesting that the difference in  $k_D$

of the two sensors does not have a major influence on the dynamics of  $[ATP]$ .

The dual nanosensors approach adds another option to the list of strategies for quantifying metabolite concentrations from fluorescent signals. The approach eliminates the necessity to determine  $R_{max}$  (or  $dR_{max}$ ) of the nanosensor (**Table 1**) and is applicable to complex tissues like, e.g., the highly myelinated axons in the optic nerve (Trevisiol et al., 2017) or the brain *in vivo*, because it does not require experimental control of the metabolite concentration within the cell compartment of interest. Furthermore, any stimulation, which results in a reproducible change of the concentration of the metabolite, can be used to calculate  $[ATP]_0$  without prior knowledge of the actual concentration change  $d[ATP]$ . Finally, once the mean  $[ATP]_0$  of the observed cells was determined,  $[ATP]_0$  of each single cell can be calculated (**Table 1** and **Figure 5A**). Therefore, this approach will be an interesting option for determining basal metabolite concentrations based on fluorescence imaging.

## Comparison to Other Methods for Calibration of Nanosensors

In the following, two other methods of calibration of metabolic nanosensors will be discussed and compared to the dual nanosensor approach: (a) single point calibration (e.g., Sotelo-Hitschfeld et al., 2012; Fernández-Moncada and Barros, 2014; Arce-Molina et al., 2020); and (b) full calibration within the cell(-compartment) of interest (used, e.g., in Bittner et al., 2010; Hung et al., 2011; San Martín et al., 2013; Mongeon et al., 2016; Köhler et al., 2018).

For calculating the metabolite concentration using the single point calibration method,  $k_D$  and  $n_H$  obtained in other experimental systems are needed and  $R_{min}$  has to be determined in each experiment (**Table 1**) similar to the dual nanosensor approach. While only one nanosensor is needed, additionally an estimate of  $R_{max}$  is required. However,  $R_{max}$  of, for example, the lactate sensor Laconic and the pyruvate sensor Pyronic differs by a factor of two between purified protein and when expressed in cells (San Martín et al., 2013, 2014). Therefore, a determination of  $R_{max}$  within the cell of interest is preferable, but requires experimental access to increase the concentration of the



metabolite to saturating levels. Such a saturation of the sensor is feasible for metabolites for which endogenous transporters with favorable kinetic properties are expressed allowing equilibration of the extra- and intracellular concentration of the metabolite under appropriate experimental conditions, as exemplified, e.g., for glucose, lactate and pyruvate (Bittner et al., 2010; San Martín et al., 2013, 2014; Mächler et al., 2016; Arce-Molina et al., 2020). However, cells do not express transporters for ATP. Therefore, one option to increase [ATP] would be to inhibit all ATP consuming processes and to rely on cellular ATP production. However, inhibition of all ATP consuming enzymes is not feasible, and the total amount of adenine nucleotides, which can be phosphorylated to ATP, might be insufficient to achieve sensor saturation. Alternatively, cell membranes are permeabilized without leakage of the sensor protein to allow access of ATP from the extracellular environment (Gerkauf et al., 2019; Lerchundi et al., 2020). However, the permeabilizing agent itself or changes of the intracellular ion composition might also affect the sensor signal. Taken together, reliable determination of  $R_{\max}$  for the ATP sensor in the cell of interest is a difficult task; therefore, one advantage of the dual nanosensor approach is to avoid the need of estimating  $R_{\max}$ . Reevaluation of our imaging data for the AT sensor by the single point calibration method revealed mean  $[ATP]_0 = 7 \text{ mM}$  (Figure 5B), i.e., higher as calculated by the dual nanosensor approach as well as higher than previously reported for glial cells in culture (1.4 mM; Ainscow et al., 2002), suggesting that the  $R_{\max}$  value obtained for the purified protein ( $2.3 \times R_{\min}$ ; Imamura et al., 2009) does not reflect  $R_{\max}$  in cells. Taken together, compared to the dual nanosensor approach, the single point calibration method (Bittner et al., 2010; Mollajew et al., 2013; San Martín et al., 2013; Takaine, 2019; Arce-Molina et al., 2020) provides direct single cell information on the metabolite concentration with only a single nanosensor, but requires an additional estimate of  $R_{\max}$  (Table 1).

Ideally, nanosensors are calibrated within the cell of interest at the subcellular location of interest by applying the metabolite of interest at (numerous) different defined concentrations without interfering with the cellular environment (full calibration; Table 1). Unfortunately, at present this is feasible only in a very limited set of experimental systems. First, controlling the metabolite concentration within the cell requires good accessibility to the cell of interest which is limited in more complex systems like in axons of a highly myelinated nerve or in the brain *in vivo*. In addition, access of the metabolite to the inside of the cell requires either endogenous transporters or permeabilization. Such an approach has been used, e.g., for calibration of glucose sensors (Bittner et al., 2010), the lactate sensor Laconic (San Martín et al., 2013), or Peredox reporting the NADH/NAD<sup>+</sup> ratio (Hung et al., 2011; Hung and Yellen, 2014; Köhler et al., 2018). These studies took advantage of the inherent permeability of the cells to either glucose, or lactate and pyruvate due to the expression of appropriate transporters. In contrast, cell membranes are not permeable for ATP and a plethora of reactions consume ATP within the cell. Nevertheless, also ATP sensors have recently been calibrated in organotypic

brain slice cultures using permeabilization of cell membranes (Gerkauf et al., 2019; Lerchundi et al., 2020). On the other hand, full calibration of nanosensors in readily accessible systems like purified proteins relies on the assumption that these calibration curves are valid also in cellular and/or more complex systems, but such approaches have successfully been used for obtaining quantitative information in various settings (e.g., San Martín et al., 2013; Fernández-Moncada and Barros, 2014; Mongeon et al., 2016). Furthermore, full calibration of metabolic nanosensors in combination with fluorescence life time imaging (FLIM) allows quantifying metabolite concentrations as, e.g., shown for Peredox, a sensor for the NADH/NAD<sup>+</sup>-redox ratio, or the glucose sensor SweetieTS (Mongeon et al., 2016; Díaz-García et al., 2017, 2019).

In summary, the dual nanosensor approach is a novel method for quantifying [ATP] from fluorescence data with its own advantages and limitations when compared to other methods (Table 1). Nevertheless, for certain applications like, e.g., complex and difficult to access tissues, it will provide an alternative/additional way for obtaining quantitative data.

## ATP in Astrocytes

The dual nanosensor approach was employed to determine the basal concentration of ATP in the cytosol of astrocytes both in primary cultures and acutely isolated brain slices.  $[ATP]_0$  was determined at around 1.5 mM for cultured cells (Figure 2) as well as between 0.7 mM and 1.3 mM for cortical astrocytes in brain slices (Figure 6). These values are well within the range of [ATP] reported for glial cells in culture (1.4 mM; Ainscow et al., 2002) as well as other cells like, e.g., neurons (1 mM to 4 mM; Fukuda et al., 1983; Ainscow et al., 2002; Mollajew et al., 2013; Rangaraju et al., 2014; Toloe et al., 2014; Pathak et al., 2015). However, the values are lower than data obtained from biochemical assays (3–7.5 mM; Schousboe et al., 1975; Silver and Erecinska, 1997; 10 mM calculated from ATP content: 40 nmol/mg protein, Winkler et al., 2017; and cytosolic volume of cultured astrocytes: 4.1  $\mu\text{L}/\text{mg}$  protein, Dringen and Hamprecht, 1998). This difference is most likely due to the fact that nanosensors measure the concentration of free cytosolic ATP, while biochemical assays measure the total amount of ATP within a cell including organelles as well as ATP bound to proteins.

Based on the dual nanosensor approach, changes of [ATP] induced by the three different incubation conditions were calculated. Importantly, the resulting  $d[ATP]$  did not differ between the different methods of calculation (Figure 4). Furthermore, the values obtained using the calculation from each paired experiment, but also from the pooled data of all experiments yielded very similar results suggesting that this approach is robust against these experimental variables. In cultured cortical astrocytes, glutamate application induced a  $d[ATP]$  of  $-0.16 \text{ mM}$ , amounting to about 11% of  $[ATP]_0$  (Figure 4), consistent with previous reports showing a (non-quantified) decrease in [ATP] (Magistretti and Chatton, 2005; Langer et al., 2017; Winkler et al., 2017). Uptake of glutamate released from synapses during neurotransmission is a major task for gray matter astrocytes (van den Berg et al., 1978; Bak et al., 2006) and the associated decrease in

[ATP] has been implicated in the stimulation of astrocytic metabolism to support neighboring neurons (astrocyte-neuron-lactate shuttle hypothesis; Pellerin and Magistretti, 1994; Voutsinos-Porche et al., 2003).

Another sign of neuronal activity relevant for regulation of astrocytic metabolism is an increase of the concentration of extracellular  $K^+$  ( $[K^+]_e$ ; Rash, 2010; Bittner et al., 2011; Ruminot et al., 2019).  $K^+$  is released from all neurons during repolarization and is, therefore, not restricted to glutamatergic neurons (Rash, 2010; MacVicar and Choi, 2017). An increase in  $[K^+]_e$  induces glycogenolysis and activates astrocytic metabolism (Hof et al., 1988; Ruminot et al., 2011; Choi et al., 2012; MacVicar and Choi, 2017; Fernandez-Moncada et al., 2018; Köhler et al., 2018). Previously, an increase in the ATY signal induced by increasing  $[K^+]_e$  from 3 mM to 8 mM or 12 mM was reported for astrocytes in culture and acutely isolated brain slices (Fernandez-Moncada et al., 2018; Lerchundi et al., 2019). Using the dual nanosensor approach and increasing  $[K^+]_e$  from 5.4 mM to 12 mM,  $d[ATP]$  was quantified here as 0.07 mM or about 5% of  $[ATP]_0$  in cultured cortical astrocytes (**Figure 4**). The  $K^+$  induced increase of [ATP] is likely limited by the availability of free ADP within the cell and, therefore, the rather small increase in [ATP] might underestimate the level of activation of metabolism.

Finally, when blocking mitochondrial ATP production using azide, a decrease of [ATP] of about  $-0.5$  mM (i.e.,  $-32\%$  of  $[ATP]_0$ ; **Figure 4**) with an initial rate of  $d[ATP]$  of  $-0.23$  mM/min (**Figure 5C**) was observed, consistent with our previous biochemical measurements on the same culture preparations (Winkler et al., 2017). Astrocytes express all enzymes of glycolysis at rather high levels, but are also equipped with the enzymes necessary for fully oxidizing pyruvate and generating ATP in mitochondria (Lovatt et al., 2007). Nevertheless, astrocytes tolerate inhibition of mitochondrial ATP production well by upregulating glycolysis resulting in an increased NADH/NAD<sup>+</sup>-redox ratio and increased lactate production (Dringen et al., 1993; Bittner et al., 2010; Wilhelm and Hirrlinger, 2011; San Martín et al., 2013; Supplie et al., 2017; Westhaus et al., 2017), consistent with the surprising finding that mice lacking functional mitochondria in astrocytes survive for more than a year without any phenotype (Supplie et al., 2017). However, because numerous mechanisms can contribute to an increase of the glycolytic rate including, e.g., upregulation of glucose transport, upregulation of glycolytic enzymes or activation by allosteric regulators like, e.g., fructose-2,6-bisphosphate, the precise mechanism remains to be elucidated.

In summary, the dual nanosensor approach allows estimating the basal concentration of a metabolite of interest (here ATP) based on the signal changes of two nanosensors with different equilibrium constants. It adds an option to the toolbox for quantifying changes in cellular metabolite concentrations from fluorescence changes, which is particularly useful if determination of  $R_{max}$  is difficult or impeded since the dual sensor approach is independent of this parameter. Finally, this method is not only applicable to metabolic nanosensors, but also

for other sensors reporting, e.g., pH or the concentration of ions or second messengers (San Martín et al., 2014; Zhang et al., 2018; Bischof et al., 2019; Depaoli et al., 2019).

## DATA AVAILABILITY STATEMENT

All datasets presented in this study are included in the article/**Supplementary Material**.

## ETHICS STATEMENT

The animal study was reviewed and approved by Animal Welfare Office of the Faculty of Medicine, University of Leipzig and Landesdirektion Sachsen.

## AUTHOR CONTRIBUTIONS

JH conceptualized and designed the study. SK, PF, and UW acquired data. SK, PF, HS, JH, and UW analyzed and interpreted the data. HS performed analysis using Mathematica. JH and UW supervised the project. JH acquired funding. SK, JH, and UW wrote the manuscript. All authors contributed to manuscript revision, read, and approved the submitted version.

## FUNDING

This work was supported by grants from the Deutsche Forschungsgemeinschaft (DFG; HI1414/6-1, HI1414/7-1). The funding sources were not involved in study design, data collection and interpretation, or the decision to submit the work for publication.

## ACKNOWLEDGMENTS

JH would like to thank Klaus-Armin Nave, Göttingen, for longstanding collaboration and ongoing support. We thank Eva Kendzia, Christopher Wolff and Marit Sicker for help with cell culture, Grit Marx for help with mouse management, the Medizinisch-Experimentelles Zentrum of the Medical Faculty, University of Leipzig for excellent mouse husbandry as well as the mechanics workshop of the Max-Planck-Institute for Experimental Medicine for developing the silicon devices and flow-chambers used for cell culture. We acknowledge support from the German Research Foundation (DFG) and Universität Leipzig within the program of Open Access Publishing.

## SUPPLEMENTARY MATERIAL

The Supplementary Material for this article can be found online at: <https://www.frontiersin.org/articles/10.3389/fncel.2020.565921/full#supplementary-material>

## REFERENCES

- Ainscow, E. K., Mirshamsi, S., Tang, T., Ashford, M. L. J., and Rutter, G. A. (2002). Dynamic imaging of free cytosolic ATP concentration during fuel sensing by rat hypothalamic neurones: evidence for ATP-independent control of ATP-sensitive  $K^+$  channels. *J. Physiol.* 544, 429–445. doi: 10.1113/jphysiol.2002.022434
- Arai, S., Kriszt, R., Harada, K., Looi, L.-S., Matsuda, S., Wongso, D., et al. (2018). RGB-Color intensimetric indicators to visualize spatiotemporal dynamics of ATP in single cells. *Angew. Chem.* 57, 10873–10878. doi: 10.1002/anie.201804304
- Arce-Molina, R., Cortés-Molina, F., Sandoval, P. Y., Galaz, A., Alegria, K., Schirmeier, S., et al. (2020). A highly responsive pyruvate sensor reveals pathway-regulatory role of the mitochondrial pyruvate carrier MPC. *eLife* 9:e53917. doi: 10.7554/eLife.53917
- Baeza-Lehnert, F., Saab, A. S., Gutierrez, R., Larenas, V., Diaz, E., Horn, M., et al. (2019). Non-canonical control of neuronal energy status by the  $Na^+$  Pump. *Cell Metab.* 29, 668.e4–680.e4. doi: 10.1016/j.cmet.2018.11.005
- Bak, L. K., Schousboe, A., and Waagepetersen, H. S. (2006). The glutamate/GABA-glutamine cycle: aspects of transport, neurotransmitter homeostasis and ammonia transfer. *J. Neurochem.* 98, 641–653. doi: 10.1111/j.1471-4159.2006.03913.x
- Barros, L. F., Bolaños, J. P., Bonvento, G., Bouzier-Sore, A.-K., Brown, A., Hirrlinger, J., et al. (2018a). Current technical approaches to brain energy metabolism. *Glia* 66, 1138–1159. doi: 10.1002/glia.23248
- Barros, L. F., Brown, A., and Swanson, R. A. (2018b). Glia in brain energy metabolism: a perspective. *Glia* 66, 1134–1137. doi: 10.1002/glia.23316
- Barros, L. F., and Deitmer, J. W. (2010). Glucose and lactate supply to the synapse. *Brain Res. Rev.* 63, 149–159. doi: 10.1016/j.brainresrev.2009.10.002
- Batiuk, M. Y., Martirosyan, A., Wahis, J., Vin, F., de Marneffe, C., and Kusserow, C. (2020). Identification of region-specific astrocyte subtypes at single cell resolution. *Nat. Commun.* 11:1220. doi: 10.1038/s41467-019-14198-8
- Bayraktar, O. A., Fuentealba, L. C., Alvarez-Buylla, A., and Rowitch, D. H. (2015). Astrocyte development and heterogeneity. *Cold Spring Harb. Perspect. Biol.* 7:a020362. doi: 10.1101/cshperspect.a020362
- Berg, J., Hung, Y. P., and Yellen, G. (2009). A genetically encoded fluorescent reporter of ATP:ADP ratio. *Nat. Methods* 6, 161–166. doi: 10.1038/nmeth.1288
- Bermejo, C., Haerizadeh, F., Takanaga, H., Chermak, D., and Frommer, W. B. (2010). Dynamic analysis of cytosolic glucose and ATP levels in yeast using optical sensors. *Biochem. J.* 432, 399–406. doi: 10.1042/BJ20100946
- Bischof, H., Burgstaller, S., Waldeck-Weiermair, M., Rauter, T., Schinagl, M., Ramadan-Muja, J., et al. (2019). Live-cell imaging of physiologically relevant metal ions using genetically encoded FRET-based probes. *Cells* 8:492. doi: 10.3390/cells8050492
- Bittner, C. X., Loaiza, A., Ruminot, I., Larenas, V., Sotelo-Hitschfeld, T., Gutiérrez, R., et al. (2010). High resolution measurement of the glycolytic rate. *Front. Neuroenerget.* 2:26. doi: 10.3389/fnene.2010.00026
- Bittner, C. X., Valdebenito, R., Ruminot, I., Loaiza, A., Larenas, V., Sotelo-Hitschfeld, T., et al. (2011). Fast and reversible stimulation of astrocytic glycolysis by  $K^+$  and a delayed and persistent effect of glutamate. *J. Neurosci.* 31, 4709–4713. doi: 10.1523/JNEUROSCI.5311-10.2011
- Bushong, E. A., Martone, M. E., Jones, Y. Z., and Ellisman, M. H. (2002). Protoplastic astrocytes in CA1 stratum radiatum occupy separate anatomical domains. *J. Neurosci.* 22, 183–192. doi: 10.1523/jneurosci.22-01-00183.2002
- Choi, H. B., Gordon, G. R. J., Zhou, N., Tai, C., Rungta, R. L., Martinez, J., et al. (2012). Metabolic communication between astrocytes and neurons via bicarbonate-responsive soluble adenylyl cyclase. *Neuron* 75, 1094–1104. doi: 10.1016/j.neuron.2012.08.032
- Depaoli, M. R., Bischof, H., Eroglu, E., Burgstaller, S., Ramadan-Muja, J., Rauter, T., et al. (2019). Live cell imaging of signaling and metabolic activities. *Pharmacol. Therapeut.* 202, 98–119. doi: 10.1016/j.pharmthera.2019.06.003
- Deuschle, K., Chaudhuri, B., Okumoto, S., Lager, I., Lalonde, S., and Frommer, W. B. (2006). Rapid metabolism of glucose detected with FRET glucose nanosensors in epidermal cells and intact roots of Arabidopsis RNA-silencing mutants. *Plant Cell* 18, 2314–2325. doi: 10.1105/tpc.106.044073
- Díaz-García, C. M., Lahmann, C., Martínez-François, J. R., Li, B., Koveal, D., Nathwani, N., et al. (2019). Quantitative in vivo imaging of neuronal glucose concentrations with a genetically encoded fluorescence lifetime sensor. *J. Neurosci. Res.* 97, 946–960. doi: 10.1002/jnr.24433
- Díaz-García, C. M., Mongeon, R., Lahmann, C., Koveal, D., Zucker, H., and Yellen, G. (2017). Neuronal stimulation triggers neuronal glycolysis and not lactate uptake. *Cell Metab.* 26, 361–374. doi: 10.1016/j.cmet.2017.06.021
- Díaz-García, C. M., and Yellen, G. (2019). Neurons rely on glucose rather than astrocytic lactate during stimulation. *J. Neurosci. Res.* 97, 883–889. doi: 10.1002/jnr.24374
- Dringen, R., Gebhardt, R., and Hamprecht, B. (1993). Glycogen in astrocytes: possible function as lactate supply for neighboring cells. *Brain Res.* 623, 208–214. doi: 10.1016/0006-8993(93)91429-V
- Dringen, R., and Hamprecht, B. (1998). Glutathione restoration as indicator for cellular metabolism of astroglial cells. *Dev. Neurosci.* 20, 401–407. doi: 10.1159/000017337
- Farmer, W. T., and Murai, K. (2017). Resolving astrocyte heterogeneity in the CNS. *Front. Cell Neurosci.* 11:300. doi: 10.3389/fncel.2017.00300
- Fehr, M., Lalonde, S., Lager, I., Wolff, M. W., and Frommer, W. B. (2003). In vivo imaging of the dynamics of glucose uptake in the cytosol of COS-7 cells by fluorescent nanosensors. *J. Biol. Chem.* 278, 19127–19133. doi: 10.1074/jbc.M301333200
- Fernández-Moncada, I., and Barros, L. F. (2014). Non-preferential fuelling of the  $Na^+/K^+$ -ATPase pump. *Biochem. J.* 460, 353–361. doi: 10.1042/BJ20140003
- Fernandez-Moncada, I., Ruminot, I., Robles-Maldonado, D., Alegria, K., Deitmer, J. W., and Barros, L. F. (2018). Neuronal control of astrocytic respiration through a variant of the Crabtree effect. *Proc. Natl. Acad. Sci. U. S. A.* 115, 1623–1628. doi: 10.1073/pnas.1716469115
- Fukuda, J., Fujita, Y., and Ohsawa, K. (1983). ATP content in isolated mammalian nerve cells assayed by a modified luciferin-luciferase method. *J. Neurosci. Methods* 8, 295–302. doi: 10.1016/0165-0270(83)90042-0
- Gerkau, N. J., Lerchundi, R., Nelson, J. S. E., Lantermann, M., Meyer, J., Hirrlinger, J., et al. (2019). Relation between activity-induced intracellular sodium transients and ATP dynamics in mouse hippocampal neurons. *J. Physiol.* 597, 5687–5705. doi: 10.1111/JP278658
- Grosche, J., Matyash, V., Moller, T., Verkhratsky, A., Reichenbach, A., and Kettenmann, H. (1999). Microdomains for neuron-glia interaction: parallel fiber signaling to Bergmann glial cells. *Nat. Neurosci.* 2, 139–143. doi: 10.1038/5692
- Guzmán, M., and Blázquez, C. (2001). Is there an astrocyte–neuron ketone body shuttle? *Trends Endocrinol. Metab.* 12, 169–173. doi: 10.1016/S1043-2760(00)00370-2
- Hires, S. A., Tian, L., and Looger, L. L. (2008). Reporting neural activity with genetically encoded calcium indicators. *Brain Cell Biol.* 36, 69–86. doi: 10.1007/s11068-008-9029-4
- Hirrlinger, J., and Nave, K. A. (2014). Adapting brain metabolism to myelination and long-range signal transduction. *Glia* 62, 1749–1761. doi: 10.1002/glia.22737
- Hof, P. R., Pascale, E., and Magistretti, P. J. (1988).  $K^+$  at concentrations reached in the extracellular space during neuronal activity promotes a  $Ca^{2+}$ -dependent glycogen hydrolysis in mouse cerebral cortex. *J. Neurosci.* 8, 1922–1928. doi: 10.1523/JNEUROSCI.08-06-01922.1988
- Hung, Y. P., Albeck, J. G., Tantama, M., and Yellen, G. (2011). Imaging cytosolic NADH-NAD $^{+}$  redox state with a genetically encoded fluorescent biosensor. *Cell Metab.* 14, 545–554. doi: 10.1016/j.cmet.2011.08.012
- Hung, Y. P., and Yellen, G. (2014). Live-cell imaging of cytosolic NADH-NAD $^{+}$  redox state using a genetically encoded fluorescent biosensor. *Methods Mol. Biol.* 1071, 83–95. doi: 10.1007/978-1-62703-622-1\_7
- Imamura, H., Nhat, K. P., Togawa, H., Saito, K., Iino, R., Kato-Yamada, Y., et al. (2009). Visualization of ATP levels inside single living cells with fluorescence resonance energy transfer-based genetically encoded indicators. *Proc. Natl. Acad. Sci. U.S.A.* 106, 15651–15656.
- Kioka, H., Kato, H., Fujita, T., Asano, Y., Shintani, Y., Yamazaki, S., et al. (2020). In vivo real-time ATP imaging in zebrafish hearts reveals G0s2 induces ischemic tolerance. *FASEB J.* 34, 2041–2054. doi: 10.1096/fj.201901686R
- Köhler, S., Winkler, U., Sicker, M., and Hirrlinger, J. (2018). NBCe1 mediates the regulation of the NADH/NAD $^{+}$  redox state in cortical astrocytes by neuronal signals. *Glia* 66, 2233–2245. doi: 10.1002/glia.23504



- Köhler, S., Winkler, U., and Hirrlinger, J. (2019). Heterogeneity of astrocytes in grey and white matter. *Neurochem. Res.* doi: 10.1007/s11064-019-02926-x [Epub ahead of print].
- Lange, S. C., Winkler, U., Andresen, L., Byhro, M., Waagepetersen, H. S., Hirrlinger, J., et al. (2015). Dynamic changes in cytosolic ATP levels in cultured glutamatergic neurons during NMDA-induced synaptic activity supported by glucose or lactate. *Neurochem. Res.* 40, 2517–2526. doi: 10.1007/s11064-015-1651-9
- Langer, J., Gerkau, N. J., Derouiche, A., Kleinhaus, C., Moshrefi-Ravassdani, B., Friedrich, M., et al. (2017). Rapid sodium signaling couples glutamate uptake to breakdown of ATP in perivascular astrocyte endfeet. *Glia* 65, 293–308. doi: 10.1002/glia.23092
- Le Douce, J., Maugard, M., Veran, J., Matos, M., Jégo, P., Vigneron, P.-A., et al. (2020). Impairment of glycolysis-derived l-serine production in astrocytes contributes to cognitive deficits in Alzheimer's Disease. *Cell Metab.* 31, 503.e8–517.e8. doi: 10.1016/j.cmet.2020.02.004
- Lee, Y., Messing, A., Su, M., and Brenner, M. (2008). GFAP promoter elements required for region-specific and astrocyte-specific expression. *Glia* 56, 481–493. doi: 10.1002/glia.20622
- Lerchundi, R., Huang, N., and Rose, C. R. (2020). Quantitative imaging of changes in astrocytic and neuronal ATP using two different variants of ATeam. *Front. Cell. Neurosci.* 14:80. doi: 10.3389/fncel.2020.00080
- Lerchundi, R., Kafitz, K. W., Winkler, U., Färfers, M., Hirrlinger, J., and Rose, C. R. (2019). FRET-based imaging of intracellular ATP in organotypic brain slices. *J. Neurosci. Res.* 97, 933–945. doi: 10.1002/jnr.24361
- Lovatt, D., Sonnewald, U., Waagepetersen, H. S., Schousboe, A., He, W., Lin, J. H., et al. (2007). The transcriptome and metabolic gene signature of protoplasmic astrocytes in the adult murine cortex. *J. Neurosci.* 27, 12255–12266. doi: 10.1523/jneurosci.3404-07.2007
- Mächler, P., Wyss, M. T., Elsayed, M., Stobart, J., Gutierrez, R., von Faber-Castell, A., et al. (2016). In vivo evidence for a lactate gradient from astrocytes to neurons. *Cell Metab.* 23, 94–102. doi: 10.1016/j.cmet.2015.10.010
- MacVicar, B. A., and Choi, H. B. (2017). Astrocytes provide metabolic support for neuronal synaptic function in response to extracellular K<sup>+</sup>. *Neurochem. Res.* 42, 2588–2594. doi: 10.1007/s11064-017-2315-8
- Magistretti, P. J., and Chatton, J. Y. (2005). Relationship between L-glutamate-regulated intracellular Na<sup>+</sup> dynamics and ATP hydrolysis in astrocytes. *J. Neural. Transm.* 112, 77–85. doi: 10.1007/s00702-004-0171-6
- Masia, R., McCarty, W. J., Lahmann, C., Luther, J., Chung, R. T., Yarmush, M. L., et al. (2018). Live cell imaging of cytosolic NADH/NAD<sup>+</sup> ratio in hepatocytes and liver slices. *Am. J. Physiol. Gastrointest. Liver Physiol.* 314, G97–G108. doi: 10.1152/ajpgi.00093.2017
- Matyash, V., and Kettenmann, H. (2010). Heterogeneity in astrocyte morphology and physiology. *Brain Res. Rev.* 63, 2–10. doi: 10.1016/j.brainresrev.2009.12.001
- Miller, S. J. (2018). Astrocyte heterogeneity in the adult central nervous system. *Front. Cell. Neurosci.* 12:401. doi: 10.3389/fncel.2018.00401
- Mollajew, R., Toloe, J., and Mironov, S. L. (2013). Single KATP channel opening in response to stimulation of AMPA/kainate receptors is mediated by Na<sup>+</sup> accumulation and submembrane ATP and ADP changes. *J. Physiol.* 591, 2593–2609. doi: 10.1113/jphysiol.2012.248369
- Mongeon, R., Venkatachalam, V., and Yellen, G. (2016). Cytosolic NADH-NAD<sup>+</sup> Redox visualized in brain slices by two-photon fluorescence lifetime biosensor imaging. *Antioxid. Redox Signal.* 25, 553–563. doi: 10.1089/ars.2015.6593
- Morel, L., Men, Y., Chiang, M. S. R., Tian, Y., Jin, S., Yelick, J., et al. (2018). Intracortical astrocyte subpopulations defined by astrocyte reporter Mice in the adult brain. *Glia* 67, 171–181. doi: 10.1002/glia.23545
- Nave, K. A. (2010a). Myelination and support of axonal integrity by glia. *Nature* 468, 244–252. doi: 10.1038/nature09614
- Nave, K.-A. (2010b). Myelination and the trophic support of long axons. *Nat. Rev. Neurosci.* 11, 275–283. doi: 10.1038/nrn2797
- Nguyen, P. T. M., Ishiwaata-Kimata, Y., and Kimata, Y. (2019). Monitoring ADP/ATP ratio in yeast cells using the fluorescent-protein reporter PercevalHR. *Biosci. Biotechnol. Biochem.* 83, 824–828. doi: 10.1080/09168451.2019.1574204
- Pathak, D., Shields, L. Y., Mendelsohn, B. A., Haddad, D., Lin, W., Gerencser, A. A., et al. (2015). The role of mitochondrially derived ATP in synaptic vesicle recycling. *J. Biol. Chem.* 290, 22325–22336. doi: 10.1074/jbc.M115.656405
- Pätz, C., Brachtendorf, S., and Eilers, J. (2018). The transgenic mouse line Igsf9-eGFP allows targeted stimulation of inferior olive efferents. *J. Neurosci. Methods* 296, 84–92. doi: 10.1016/j.jneumeth.2017.12.024
- Pellerin, L., and Magistretti, P. J. (1994). Glutamate uptake into astrocytes stimulates aerobic glycolysis: a mechanism coupling neuronal activity to glucose utilization. *Proc. Natl. Acad. Sci. U.S.A.* 91, 10625–10629. doi: 10.1073/pnas.91.22.10625
- Pérez Koldenkova, V., and Nagai, T. (2013). Genetically encoded Ca<sup>2+</sup> indicators: properties and evaluation. *Biochim. Biophys. Acta* 1833, 1787–1797. doi: 10.1016/j.bbamcr.2013.01.011
- Pomorski, A., Kochańczyk, T., Miłoch, A., and Krężel, A. (2013). Method for accurate determination of dissociation constants of optical ratiometric systems: chemical probes, genetically encoded sensors, and interacting molecules. *Anal. Chem.* 85, 11479–11486. doi: 10.1021/ac402637h
- Rangaraju, V., Calloway, N., and Ryan, T. A. (2014). Activity-driven local ATP synthesis is required for synaptic function. *Cell* 156, 825–835. doi: 10.1016/j.cell.2013.12.042
- Rash, J. E. (2010). Molecular disruptions of the panglial syncytium block potassium siphoning and axonal saltatory conduction: pertinence to neuromyelitis optica and other demyelinating diseases of the central nervous system. *Neuroscience* 168, 982–1008. doi: 10.1016/j.neuroscience.2009.10.028
- Requardt, R. P., Hirrlinger, P. G., Wilhelm, F., Winkler, U., Besser, S., and Hirrlinger, J. (2012). Ca<sup>2+</sup> signals of astrocytes are modulated by the NAD<sup>+</sup>/NADH redox state. *J. Neurochem.* 120, 1014–1025. doi: 10.1111/j.1471-4159.2012.07645.x
- Requardt, R. P., Wilhelm, F., Rillich, J., Winkler, U., and Hirrlinger, J. (2010). The biphasic NAD(P)H fluorescence response of astrocytes to dopamine reflects the metabolic actions of oxidative phosphorylation and glycolysis. *J. Neurochem.* 115, 483–492. doi: 10.1111/j.1471-4159.2010.06940.x
- Ruminot, I., Gutiérrez, R., Peña-Münzenmayer, G., Añazco, C., Sotelo-Hitschfeld, T., Lerchundi, R., et al. (2011). NBCE1 mediates the acute stimulation of astrocytic glycolysis by extracellular K<sup>+</sup>. *J. Neurosci.* 31, 14264–14271. doi: 10.1523/JNEUROSCI.2310-11.2011
- Ruminot, I., Schmälzle, J., Leyton, B., Barros, L. F., and Deitmer, J. W. (2019). Tight coupling of astrocyte energy metabolism to synaptic activity revealed by genetically encoded FRET nanosensors in hippocampal tissue. *J. Cereb. Blood Flow Metabol.* 39, 513–523. doi: 10.1177/0271678X17737012
- San Martín, A., Ceballo, S., Baeza-Lehnert, F., Lerchundi, R., Valdebenito, R., Contreras-Baeza, Y., et al. (2014). Imaging mitochondrial flux in single cells with a FRET sensor for pyruvate. *PLoS One* 9:e85780. doi: 10.1371/journal.pone.0085780
- San Martín, A., Ceballo, S., Ruminot, I., Lerchundi, R., Frommer, W. B., and Barros, L. F. (2013). A genetically encoded FRET lactate sensor and its use to detect the Warburg effect in single cancer cells. *PLoS One* 8:e0057712. doi: 10.1371/journal.pone.0057712
- San Martín, A., Sotelo-Hitschfeld, T., Lerchundi, R., Fernandez-Moncada, I., Ceballo, S., Valdebenito, R., et al. (2014). Single-cell imaging tools for brain energy metabolism: a review. *Neurophotonics* 1:11004. doi: 10.1117/1.NPh.1.1.011004
- Schindelin, J., Arganda-Carreras, I., Frise, E., Kaynig, V., Longair, M., Pietzsch, T., et al. (2012). Fiji: an open-source platform for biological-image analysis. *Nat. Methods* 9, 676–682. doi: 10.1038/nmeth.2019
- Schousboe, A., Fosmark, H., and Hertz, L. (1975). High content of glutamate and of ATP in astrocytes cultured from rat brain hemispheres: effect of serum withdrawal and of cyclic AMP. *J. Neurochem.* 25, 909–911. doi: 10.1111/j.1471-4159.1975.tb04429.x
- Shulman, Y., Stavsky, A., Fedorova, T., Mikulincer, D., Atias, M., Radinsky, I., et al. (2015). ATP binding to synapsin IIa regulates usage and clustering of vesicles in terminals of hippocampal neurons. *J. Neurosci.* 35, 985–998. doi: 10.1523/JNEUROSCI.0944-14.2015
- Silver, I. A., and Erecinska, M. (1997). Energetic demands of the Na<sup>+</sup>/K<sup>+</sup> ATPase in mammalian astrocytes. *Glia* 21, 35–45. doi: 10.1002/(SICI)1098-1136(199709)21:1<35::AID-GLIA4<3.0.CO;2-0
- Somjen, G. G. (1988). Nervenkit: notes on the history of the concept of neuroglia. *Glia* 1, 2–9. doi: 10.1002/glia.440010103

- Sotelo-Hitschfeld, T., Fernandez-Moncada, I., and Barros, L. F. (2012). Acute feedback control of astrocytic glycolysis by lactate. *Glia* 60, 674–680. doi: 10.1002/glia.22304
- Stobart, J. L., Ferrari, K. D., Barrett, M. J. P., Stobart, M. J., Looser, Z. J., Saab, A. S., et al. (2018). Long-term in vivo calcium imaging of astrocytes reveals distinct cellular compartment responses to sensory stimulation. *Cereb. Cortex* 28, 184–198. doi: 10.1093/cercor/bhw366
- Supplie, L. M., Düking, T., Campbell, G., Diaz, F., Moraes, C. T., Götz, M., et al. (2017). Respiration-deficient astrocytes survive as glycolytic cells in vivo. *J. Neurosci.* 37, 4231–4242. doi: 10.1523/JNEUROSCI.0756-16.2017
- Takaine, M. (2019). QUEEN-based spatiotemporal ATP imaging in budding and fission yeast. *Bio Protoc.* 9:e3320. doi: 10.21769/BioProtoc.3320
- Takaine, M., Ueno, M., Kitamura, K., Imamura, H., and Yoshida, S. (2019). Reliable imaging of ATP in living budding and fission yeast. *J. Cell Sci.* 132:jcs.230649. doi: 10.1242/jcs.230649
- Toloe, J., Mollajew, R., Kugler, S., and Mironov, S. L. (2014). Metabolic differences in hippocampal 'Rett' neurons revealed by ATP imaging. *Mol. Cell Neurosci.* 59, 47–56. doi: 10.1016/j.mcn.2013.12.008
- Trevisiol, A., Saab, A. S., Winkler, U., Marx, G., Imamura, H., Mobius, W., et al. (2017). Monitoring ATP dynamics in electrically active white matter tracts. *eLife* 6:e24241. doi: 10.7554/eLife.24241
- Tsuyama, T., Kishikawa, J.-I., Han, Y.-W., Harada, Y., Tsubouchi, A., Noji, H., et al. (2013). In vivo fluorescent adenosine 5'-triphosphate (ATP) imaging of *Drosophila melanogaster* and *Caenorhabditis elegans* by using a genetically encoded fluorescent ATP biosensor optimized for low temperatures. *Anal. Chem.* 85, 7889–7896. doi: 10.1021/ac4015325
- van den Berg, C. J., Matheson, D. F., and Nijemanting, W. V. (1978). "Compartmentation of amino acids in brain: the GABA glutamine-glutamate cycle," in *Amino Acids and Chemical Transmitters*, ed. F. Fonnum (New York, NY: Plenum Press), 709–723. doi: 10.1007/978-1-4613-4030-0\_50
- Vicente-Gutierrez, C., Bonora, N., Bobo-Jimenez, V., Jimenez-Blasco, D., Lopez-Fabuel, I., Fernandez, E., et al. (2019). Astrocytic mitochondrial ROS modulate brain metabolism and mouse behaviour. *Nat. Metab.* 1, 201–211. doi: 10.1038/s42255-018-0031-6
- Volkenhoff, A., Hirrlinger, J., Kappel, J. M., Klämbt, C., and Schirmeier, S. (2018). Live imaging using a FRET glucose sensor reveals glucose delivery to all cell types in the *Drosophila* brain. *J. Insect. Physiol.* 106, 55–64. doi: 10.1016/j.jinsphys.2017.07.010
- Voutsinos-Porche, B., Bonvento, G., Tanaka, K., Steiner, P., Welker, E., Chatton, J. Y., et al. (2003). Glial glutamate transporters mediate a functional metabolic crosstalk between neurons and astrocytes in the mouse developing cortex. *Neuron* 37, 275–286. doi: 10.1016/s0896-6273(02)01170-4
- Waagepetersen, H. S., Sonnewald, U., and Schousboe, A. (2003). Compartmentation of glutamine, glutamate, and GABA metabolism in neurons and astrocytes: functional implications. *Neuroscientist* 9, 398–403. doi: 10.1177/1073858403254006
- Westhaus, A., Blumrich, E. M., and Dringen, R. (2017). The antidiabetic drug metformin stimulates glycolytic lactate production in cultured primary rat astrocytes. *Neurochem. Res.* 42, 294–305. doi: 10.1007/s11064-015-1733-8
- Wilhelm, F., and Hirrlinger, J. (2011). The NAD<sup>+</sup>/NADH redox state in astrocytes: independent control of the NAD<sup>+</sup> and NADH content. *J. Neurosci. Res.* 89, 1956–1964. doi: 10.1002/jnr.22638
- Winkler, U., Seim, P., Enzbrenner, Y., Kohler, S., Sicker, M., and Hirrlinger, J. (2017). Activity-dependent modulation of intracellular ATP in cultured cortical astrocytes. *J. Neurosci. Res.* 95, 2172–2181. doi: 10.1002/jnr.24020
- Yaginuma, H., Kawai, S., Tabata, K. V., Tomiyama, K., Kakizuka, A., Komatsuzaki, T., et al. (2014). Diversity in ATP concentrations in a single bacterial cell population revealed by quantitative single-cell imaging. *Sci. Rep.* 4:6522. doi: 10.1038/srep06522
- Yellen, G., and Monge, R. (2015). Quantitative two-photon imaging of fluorescent biosensors. *Curr. Opin. Chem. Biol.* 27, 24–30. doi: 10.1016/j.cbpa.2015.05.024
- Zhang, Y., and Barres, B. A. (2010). Astrocyte heterogeneity: an underappreciated topic in neurobiology. *Curr. Opin. Neurobiol.* 20, 588–594. doi: 10.1016/j.conb.2010.06.005
- Zhang, Z., Chen, W., Zhao, Y., and Yang, Y. (2018). Spatiotemporal imaging of cellular energy metabolism with genetically-encoded fluorescent sensors in brain. *Neurosci. Bull.* 34, 875–886. doi: 10.1007/s12264-018-0229-3
- Zhao, F.-L., Zhang, C., Zhang, C., Tang, Y., and Ye, B.-C. (2016). A genetically encoded biosensor for in vitro and in vivo detection of NADP<sup>+</sup>. *Biosens. Bioelectron.* 77, 901–906. doi: 10.1016/j.bios.2015.10.063
- Zhao, Y., Hu, Q., Cheng, F., Su, N., Wang, A., Zou, Y., et al. (2015). SoNar, a highly responsive NAD<sup>+</sup>/NADH sensor, allows high-throughput metabolic screening of anti-tumor agents. *Cell Metab.* 21, 777–789. doi: 10.1016/j.cmet.2015.04.009
- Zuend, M., Saab, A. S., Wyss, M. T., Ferrari, K. D., Hösl, L., Looser, Z. J., et al. (2020). Arousal-induced cortical activity triggers lactate release from astrocytes. *Nat. Metab.* 2, 179–191. doi: 10.1038/s42255-020-0170-4

**Conflict of Interest:** The authors declare that the research was conducted in the absence of any commercial or financial relationships that could be construed as a potential conflict of interest.

Copyright © 2020 Köhler, Schmidt, Fülle, Hirrlinger and Winkler. This is an open-access article distributed under the terms of the Creative Commons Attribution License (CC BY). The use, distribution or reproduction in other forums is permitted, provided the original author(s) and the copyright owner(s) are credited and that the original publication in this journal is cited, in accordance with accepted academic practice. No use, distribution or reproduction is permitted which does not comply with these terms.



# Deletion of LRP1 From Astrocytes Modifies Neuronal Network Activity in an *in vitro* Model of the Tripartite Synapse

Ramona Romeo<sup>1</sup>, Kristin Glotzbach<sup>1</sup>, Anja Scheller<sup>2</sup> and Andreas Faissner<sup>1\*</sup>

<sup>1</sup> Department of Cell Morphology and Molecular Neurobiology, Ruhr-University Bochum, Bochum, Germany, <sup>2</sup> Department of Molecular Physiology, Center for Integrative Physiology and Molecular Medicine (CIPMM), University of Saarland, Homburg, Germany

## OPEN ACCESS

### Edited by:

Renato Socodato,  
Institute for Molecular and Cellular  
Biology (IBMC), Portugal

### Reviewed by:

Takahisa Kanekiyo,  
Mayo Clinic Florida, United States  
Ciaran Murphy-Royal,  
University of Montreal Hospital Centre  
(CRCHUM), Canada

### \*Correspondence:

Andreas Faissner  
andreas.faissner@rub.de

### Specialty section:

This article was submitted to  
Non-Neuronal Cells,  
a section of the journal  
Frontiers in Cellular Neuroscience

**Received:** 29 May 2020

**Accepted:** 30 November 2020

**Published:** 14 January 2021

### Citation:

Romeo R, Glotzbach K, Scheller A  
and Faissner A (2021) Deletion  
of LRP1 From Astrocytes Modifies  
Neuronal Network Activity in an *in vitro*  
Model of the Tripartite Synapse.  
*Front. Cell. Neurosci.* 14:567253.  
doi: 10.3389/fncel.2020.567253

The low-density lipoprotein receptor-related protein 1 (LRP1) is a transmembrane receptor that binds over 40 potential ligands and is involved in processes such as cell differentiation, proliferation, and survival. LRP1 is ubiquitously expressed in the organism and enriched among others in blood vessels, liver, and the central nervous system (CNS). There, it is strongly expressed by neurons, microglia, immature oligodendrocytes, and astrocytes. The constitutive LRP1 knockout leads to embryonic lethality. Therefore, previous studies focused on conditional LRP1-knockout strategies and revealed that the deletion of LRP1 causes an increased differentiation of neural stem and precursor cells into astrocytes. Furthermore, astrocytic LRP1 is necessary for the degradation of A $\beta$  and the reduced accumulation of amyloid plaques in Alzheimer's disease. Although the role of LRP1 in neurons has intensely been investigated, the function of LRP1 with regard to the differentiation and maturation of astrocytes and their functionality is still unknown. To address this question, we generated an inducible conditional transgenic mouse model, where LRP1 is specifically deleted from GLAST-positive astrocyte precursor cells. The recombination with resulting knockout events was visualized by the simultaneous expression of the fluorescent reporter tdTomato. We observed a significantly increased number of GLT-1 expressing astrocytes in LRP1-depleted astrocytic cultures in comparison to control astrocytes. Furthermore, we investigated the influence of astrocytic LRP1 on neuronal activity and synaptogenesis using the co-culture of hippocampal neurons with control or LRP1-depleted astrocytes. These analyses revealed that the LRP1-deficient astrocytes caused a decreased number of single action potentials as well as a negatively influenced neuronal network activity. Moreover, the proportion of pre- and postsynaptic structures was significantly altered in neurons co-cultured with LRP1-depleted astrocytes. However, the number of structural synapses was not affected. Additionally, the supernatant of hippocampal neurons co-cultured with LRP1-deficient astrocytes showed an altered set of cytokines in comparison to the control condition, which potentially contributed to the altered

neuronal transmission and synaptogenesis. Our results suggest astrocytic LRP1 as a modulator of synaptic transmission and synaptogenesis by altering the expression of the glutamate transporter on the cell surface on astrocytes and the release of cytokines *in vitro*.

**Keywords:** astrocytes, astrocytic heterogeneity, synaptogenesis, *in vitro* knockout model LRP1, neuronal plasticity, tripartite synapse

## INTRODUCTION

The low-density lipoprotein receptor-related protein 1 (LRP1) is a transmembrane receptor and part of the low-density lipoprotein receptor (LDL) family (May and Herz, 2003; Boucher and Herz, 2011). LRP1 consists of two covalently bound subunits, an 85 kDa intracellular  $\beta$ -chain and the 515 kDa extracellular  $\alpha$ -chain with four ligand-binding sites. The physiological relevance of LRP1 becomes apparent through the more than 40 potential ligands (Boucher and Herz, 2011; Bres and Faissner, 2019), including Apolipoprotein E (ApoE),  $\alpha$ 2-macroglobulin, tissue plasminogen activator (tPa), and amyloid precursor protein (APP), just to name a few (Orth et al., 1992; Lillis et al., 2008). Binding of the ligand to LRP1 leads to endocytosis of the whole receptor–ligand–complex (Willnow et al., 2012). Therefore, LRP1 is involved in several cellular processes such as cell proliferation, differentiation and lipid metabolism. In general, LRP1 is ubiquitously expressed, but strongly enriched in the liver, lung, blood vessels, and in the central nervous system (CNS). There, it is expressed by neurons, microglia, immature oligodendrocytes, and astrocytes (May et al., 2004; Liu et al., 2010; Boucher and Herz, 2011; Auderset et al., 2016; Schäfer et al., 2019). LRP1 is critical for development, proved by the constitutive knockout causing embryonic lethality (Herz et al., 1993). Therefore, several targeted LRP1-knockout models have been developed. The conditional knockout of LRP1 in cortical and spinal cord-derived neural stem and precursor cells (NSPCs) *in vitro* produced an increased number of glial fibrillary acidic protein (GFAP)-positive astrocytes, as well as a decreased number of oligodendrocytes and neurons (Safina et al., 2016). Furthermore, the deletion of LRP1 in neurons caused hyperactivity, dystonia, and increased neurodegeneration in the cortex and hippocampus of mice (May et al., 2004; Liu et al., 2010). The functions of LRP1 in regard to differentiation and functionality of astrocytes have, however, not been intensively investigated so far. It is known that astrocytic LRP1 plays a critical role in brain A $\beta$  clearance involved in Alzheimer's disease (AD) pathogenesis (Liu et al., 2017). The knockdown of LRP1 in primary astrocytes resulted in decreased cellular A $\beta$  uptake and degradation. Furthermore, the silencing of LRP1 was accompanied by the downregulation of several A $\beta$ -degrading enzymes, like matrix metalloproteases MMP2 and MMP9. The impaired A $\beta$  clearance caused by the astrocytic LRP1 knockdown led to an accelerated amyloid plaque deposition (Liu et al., 2017). The authors concluded that the expression of LRP1 and its function in astrocytes could be an effective strategy to counter the amyloid plaque accumulation in AD. Furthermore, Bres et al. (2020) investigated the deletion of *Lrp1* from embryonic cortical radial glia stem cells located in the telencephalon

and observed a severe epileptic phenotype accompanied by an altered differentiation of astrocytic subpopulations. This resulting epileptic phenotype had not been described in knockout models where *Lrp1* had been deleted from other cell types, such as neurons or oligodendrocytes. Therefore, we aimed to investigate whether the deletion of LRP1 in the postnatal astrocytic lineage might alter neuronal transmission, eventually leading to hyperexcitability and epilepsy. The physiological functions of LRP1 in the astrocyte lineage had not been addressed so far.

Therefore, we generated a new mouse model, where LRP1 was specifically deleted from glutamate aspartate transporter (GLAST)-positive astrocyte precursor cells. We mated the floxed reporter mouse line (Mori et al., 2006; Madisen et al., 2010) with the LRP1<sup>fl/fl</sup> mice (Rohlmann et al., 1996) to obtain an inducible conditional transgenic mouse model. The reporter tdTomato allowed tracing of recombination and therefore knockout events. We analyzed the maturation of astrocytes *in vitro* via the expression of stage-specific astrocytic markers. To investigate the influence of astrocytic LRP1 on neuronal activity and synaptogenesis, we co-cultured hippocampal wild-type neurons with either wild-type or LRP1-depleted astrocytes. In this approach, we analyzed the number of pre- and postsynapses, as well as neuronal network activity and spontaneous action potentials using microelectrode arrays (MEAs). Our results highlight astrocytic LRP1 as a novel regulator of directed neuronal network activity and modulator of synaptogenesis *in vitro*.

## MATERIALS AND METHODS

### Animals

This study was performed under the animal license of the State Agency for Nature, Environment and Consumer Protection Northrhine-Westphalia (Landesamt fuer Umweltschutz, Naturschutz und Verbraucherschutz; file number: 84-02.04.2016.A482). The animals were housed under a 12-h light–dark cycle with constant access to food and water.

LRP1<sup>fl/fl</sup> (B6;129S7-LRP1<sup>TM2Her/J</sup>; Jackson Laboratories; Catalog No. JAX:012604; RRID: IMSR\_JAX:012604; MGI: J:76281) were obtained from Jackson Laboratory. Knockin GLAST-Cre<sup>ERT2</sup> mice [Slc1a3<sup>TM1(Cre/ERT2)Mgoe</sup>; MGI: 3830051] were mated with Rosa26 reporter mice [Ai14, Gt(ROSA)26Sor<sup>TM14(CAG-tdTomato)Hze</sup>; MGI: 3809524] to visualize recombination events (see **Supplementary Figure 1**). To generate the new LRP1-depleted mouse line, the LRP1<sup>fl/fl</sup> mice were crossbred with the GLAST<sup>Cre/ERT2</sup>Rosa26<sup>fl/fl</sup> mice. The genotyping was performed as already described



in Ulc et al. (2019). Briefly, genomic DNA was isolated out of tail biopsies with 200  $\mu$ l of *DirectPCR*<sup>®</sup> *Lysis Reagent Tail* (Peqlab, VWR Life Science, Radnor, PA, United States) and 0.2 mg/ml Proteinase-K (Sigma-Aldrich, Chemie GmbH, Munich, Germany) at 55°C and 350 rpm overnight. The digestion was stopped at 85°C for 45 min and 350 rpm. The *Lrp1* gene was amplified according to the Jackson Laboratory protocol (forward primer: 5'-C ATACCCTCTTCAAACCCCTTCCTG-3'; reverse primer: 5'-GC AAGCTCTCCTGCTCAGACCTGGA-3'). The *Glast* wild-type allele was amplified with specific GLAST primer (forward: 5'-GAGGCACTTGGCTAGGCTCTGAGGA-3'; reverse: 5'-GA GGAGATCCTGACCGATCAGTTGG-3). The expression of the Cre recombinase was detected with a Cre primer (5'-GGTGTACGGTCAGTAAATTGGACAT-3'). The floxed Rosa26 alleles were amplified with the specific primer forward (5'-CCGAAAATCTGTGGGAAGTC-3') and reverse (5'-CTGTT CCTGTACGGCATGG-3'), whereas the wild-type alleles were amplified with the forward (5'-AAGGGAGCTG CAGTGGAGTA-3') and reverse primer (5'-GGCATTA AAGCAGCGTATCC-3'). Animals referred to as knockout animals displayed the genotype GLAST<sup>Cre/wt</sup>Rosa26<sup>fl/fl</sup>LRP1<sup>fl/fl</sup>, whereas control animals had the genotype GLAST<sup>Cre/wt</sup>Rosa26<sup>fl/fl</sup>LRP1<sup>wt/wt</sup>.

For the co-culture of hippocampal neurons together with either LRP1-deficient or wild-type astrocytes, the newly generated LRP1-knockout line as well as C57BL/6J (Jackson Laboratories; Catalog No. JAX:000664; RRID: IMSR\_JAX:000664; and MGI: 3028467) wild-type animals were compared.

## Isolation and Cultivation of Primary Murine Astrocytes

Astrocytes were obtained by the dissection of the cortex of postnatal day P0–P3 knockout or control animals following an established protocol (Gottschling et al., 2016a, 2019), with minor alterations. Cortices of one animal were cultured in a T25 flask (Sarstedt, Nuembrecht, Germany), separately according to the respective genotype. Recombination could not be induced in early postnatal pups via lactating mothers; therefore, reporter-positive astrocytes were not available for FACS sorting. For this reason, confluent genetically modified astrocytes were treated with 1  $\mu$ M of 4-hydroxy-tamoxifen (4-OH-TAM; Sigma-Aldrich, Catalog No. t5648) via the application to the medium once a day for four consecutive days to induce the activation of the Cre recombinase in culture.

## Cultivation of Hippocampal Neurons

For the cultivation of hippocampal neurons, wild-type brains from E15.5 embryos were dissected and the hippocampi were prepared. The cultured neurons were cultured with either wild-type or LRP1-deficient astrocytes in an insert co-culture model as described previously (Gottschling et al., 2016a, 2019).

## Multielectrode Array (MEA)

The neuronal activity of hippocampal neurons co-cultured with astrocytes was measured 14 and 21 days *in vitro* (div).

The spontaneous activity was measured for 10 min using the MC\_Rack software (Version 3.9.0, Multi Channel Systems, Reutlingen, Germany). The spikes, spontaneous single action potentials, and bursts were analyzed. Therefore, we used the already established protocol by Geissler and Faissner (2012) and Hales et al. (2010).

## Differentiation Assay

Directly after the treatment with 4-OH-TAM for four consecutive days, astrocytes were plated on poly-D-lysine (PDL; 10  $\mu$ g/ $\mu$ l, Sigma-Aldrich, Catalog No. PD899)-coated four-well dishes at a density of 5,000 cells per well. The medium was exchanged every 7 days. After 3, 5, 7, 14, and 21 days post plating (dpp), cells were fixed for 10 min with 4% (v/v) paraformaldehyde (PFA, Carl Roth, Karlsruhe Germany) and intensively washed with phosphate-buffered saline (PBS; 137 mM sodium chloride, 3 mM kalium chloride, 6.5 mM disodium hydrogen phosphate, and 1.5 mM potassium dihydrogen phosphate; pH 7.3) and used for immunocytochemical analysis. Alternatively, 4-OH-TAM-treated astrocytes were also plated at a density of 580,000 cells per cm<sup>2</sup> in PDL-coated cell culture dishes for analogous time periods and lysed for either Western blot or PCR analysis.

## Immunocytochemistry of the Differentiation Assay

The astrocytes were immunocytochemically stained as previously described (Safina et al., 2016; Ulc et al., 2019). Briefly, fixed astrocytes were washed three times with PBT-1 [10% (w/v) bovine serum albumin (BSA; Sigma-Aldrich, Catalogue-No.: A7030), 0.1% (v/v) Triton-X 100 in PBS] for 10 min. Afterward, primary antibodies were diluted in PBT-1 and the fixed astrocytes were incubated for 30 min at room temperature. As primary antibodies, we used the following: LRP1 (1:500, Abcam, Catalog No. ab92544; RRID: AB\_2234877), GFAP (1:300, DAKO, Catalog No. Z0334; RRID: AB\_10013382), GLT-1 (EAAT1; 1:100, Santa Cruz, Catalog No. sc-365634; RRID: AB\_10844832), and phospho-Histone H3 (PH3; 1:100, Millipore, Catalog No. 06-570; RRID: AB\_310177). Further on, the cells were washed thrice with PBS/A [0.1% bovine serum albumin (w/v) (BSA; Sigma-Aldrich, Catalog No. A7030) in PBS] for 10 min. Species-specific secondary antibodies coupled with Cy2 (1:250; Goat anti-mouse Cy2, Jackson Immuno Research Labs, Catalog No. 115-545-044; RRID: AB\_2338844; Goat anti-rabbit Cy2, Jackson Immuno Research Labs, Catalog No. 111-545-045; RRID: AB\_2338049) and the nuclear marker Hoechst (Sigma-Aldrich, Catalog No. 94403) were diluted in PBS/A and added to the cells for 30 min at room temperature in the dark. Next, the cells were washed three times with PBS for 10 min and mounted with 50% (v/v) PBS and 50% (v/v) of glycerol (PBS/glycerol) for microscopy. Pictures were taken with the Axioplan 2 imaging from Zeiss (Oberkochen, Germany). For one N, six pictures were taken at a 100-fold magnification. Therefore, two peripheral areas on the left side of the well and two peripheral areas on the right side of the well were chosen. Additionally, two pictures were taken in the center of the well. The area of GFAP-positive astrocytes was analyzed with ImageJ. Hence, five GFAP- and tdTomato-positive astrocytes were randomly chosen

in one well. Following from this, 30 randomly chosen astrocytes were analyzed per N.

## Immunocytochemistry of Synapses

To stain the pre- and postsynapses of hippocampal neurons, the cells were fixed with 4% (v/v) PFA for 10 min after 14 and 21 div. The staining procedure was performed as already described in Gottschling et al. (2016b). Briefly, the neurons were washed with PBS and subsequently incubated with 25 mM glycine for 20 min before the cells were blocked with blocking buffer [10% (v/v) horse serum (Gibco, Catalog No. 16050-122), 0.1% (v/v) Triton X-100 in PBS] for 1 h. Afterward, the primary antibodies (Bassoon; 1:1000; Synaptic Systems, Catalog No. 141003; RRID: AB\_887697 and PSD95; 1:500; Millipore, Catalog No. MAB1598; RRID: AB\_1121285) were diluted in blocking buffer and the incubation occurred for 1 h at room temperature in a wet chamber. Next on, the neurons were washed thrice with blocking buffer before the cells were incubated with the species-specific secondary antibodies (Goat anti-mouse Cy2, 1:250, Jackson Immuno Research Labs, Catalog No. 115-545-044; RRID: AB\_2338844; Goat anti-rabbit Cy3, 1:500, Jackson Immuno Research Labs, Catalog No. 111-165-045; RRID: AB\_2338003) for 1 h in a dark wet chamber. Afterward, the cells were washed twice with blocking buffer, once with PBS and distilled water. At last, the neurons were covered with Immu-Mount (Thermo Scientific, Waltham, MA, Catalog No. 9990402). Images were taken with Laser Scanning Microscope Axiovert 200 M by Zeiss using a 630-fold magnification.

## RNA Isolation, cDNA Synthesis, and Real-Time PCR Analysis

Cells were lysed at specific timepoints with lysis buffer (Gene Elute Mammalian Total RNA Miniprep Kit; Sigma-Aldrich, Catalog No. RTN350-1KT) for RNA isolation. The total RNA was extracted as described in the manufacturer's manual. Next, the whole RNA was used to synthesize cDNA with the First-Strand cDNA Synthesis Kit (Fermentas, Waltham, MA, Catalog No. K1612) following the instructions. Real-time PCR analysis was performed with specific primers (see Table 1). For normalization and as a housekeeping gene,  $\beta$ -actin was used and the analysis was performed with the PCR cyclers Mastercycler gradient by Eppendorf AG (Hamburg, Germany).

## Western Blotting

The astrocytes were lysed at specific timepoints with radioimmunoprecipitation assay buffer [RIPA; 10 mM Tris-HCl (pH 8.0), 1 mM ethylenediaminetetraacetic acid (EDTA), 0.5 mM ethylene glycol-bis( $\beta$ -aminoethyl ether)-N,N,N',N'-tetraacetic acid (EGTA), 1% (v/v) Triton X-100, 0.1% (w/v) sodium deoxycholate, 0.1% (v/v) sodium dodecyl sulfate (SDS), and 140 mM NaCl, Sigma-Aldrich] with 1% (v/v) of the protease inhibitor phenylmethylsulfonyl fluoride (PMSF) and 1% (v/v) aprotinin (APR). Cell scrapers were used to detach the cells from the cell culture dishes. The cell lysates were stored at  $-20^{\circ}\text{C}$  until further use. The Western blot analysis was performed as

**TABLE 1 |** Genes monitored in the expression profile analysis of LRP1-deficient astrocytes in comparison to control astrocytes and hippocampal neurons *in vitro*.

Gene	Primer sequence	GenBank nos.
$\beta$ -actin	F: 5'-TATGCCAACACAGTGTCTGCTGGTGG-3' R: 5'-TAGAAGCATTGCGGTGGACAATGG-3'	NM_007393.5
<i>Aldh1l1</i>	F: 5'-GGAAGTTGAGAGGGGAGGAC-3' R: 5'-GGAAGTTGAGAGGGGAGGAC-3'	BC030730.1
<i>Aquaporin-4</i>	F: 5'-TTGCTTTGGATCAGCATTG-3' R: 5'-TGAGCTCCACATCAGGACAG-3'	NM_009700.3
<i>C2</i>	F: 5'-GCGGAGATCCCCAGGTAGTA-3' R: 5'-GTGGAAGTCCCTTGGCAGAA-3'	NM_013484.2
<i>C3</i>	F: 5'-GCCCATCCCTACAGCACTAT-3' R: 5'-ATCCACCCACACAGAGTCAG-3'	NM_009778.3
<i>Fgfr3</i>	F: 5'-GTCCTGTTCTGGCCAATGTT-3' R: 5'-GTTTCTGGCAGCCCAAGTCTC-3'	NM_001205270.1
<i>Gfap</i>	F: 5'-CGACTATCGCCGCCAACTGC-3' R: 5'-GCGATCTCGATGTCCAGGGCT-3'	NM_001131020.1
<i>Glast</i>	F: 5'-GGCGGCCCTAGATAGTAAGG-3' R: 5'-AGAGTCTCCATGGCCTCTGA-3'	XM_021208184.2
<i>Glt-1</i>	F: 5'-ATGATCATGTGTTACTCCCTC-3' R: 5'-TTGTCGTGTAATAGGACTGC-3'	NM_001077514.4
<i>Gria1</i>	F: 5'-CCGTTGACACATCCAATCAG-3' R: 5'-GTTGGCGAGGATGATAGTGGT-3'	NM_001113325.2
<i>Gria2</i>	F: 5'-AACGCGCTGTATCCTTGAC-3' R: 5'-CTCCTGCATTCTCTCTCTG-3'	NM_013540.3
<i>Grin1</i>	F: 5'-CGGCTCTTGGAAGATACAGC-3' R: 5'-TTGTAGACGCGCATCATCTC-3'	NM_008169.3
<i>Grin2a</i>	F: 5'-GCTGTCAGCACTGAATCCAA-3' R: 5'-ATCCCTGGGAGAACTTGCTT-3'	NM_008170.3
<i>Grin2b</i>	F: 5'-GTGAGAGCTCCTTTGCCAAC-3' R: 5'-GGGTTGGACTGGTTCCTAT-3'	NM_008171.3
<i>Lcn2</i>	F: 5'-ACTTGATCCCTGCCCATCT-3' R: 5'-AAGCGGGTGAAACGTTCTCT-3'	NM_008491.1
<i>Lrp1</i>	F: 5'-GGTAGTTGTTTCTCAATGCTC-3' R: 5'-TGTTGCTGACTAACAACTGCT-3'	NM_008512.2
<i>Lrp2</i>	F: 5'-CTTCTGATGAGTCCGCTTGC-3' R: 5'-AGTTCCCATGCTGCACCTTG-3'	NM_001081088.2
<i>Lrp4</i>	F: 5'-AGAAGTGTGAGATGGTGCGA-3' R: 5'-TTAAGGTTGGCAGCGAGGAT-3'	NM_172668.3
<i>Nestin</i>	F: 5'-CTCGAGCAGGAAGTGGTAGG-3' R: 5'-GTTAGCGCTGCCRCRAGACC-3'	NM_016701.3
<i>S100</i>	F: 5'-TGCTTCCACCACTACTCCG-3' R: 5'-ACTCCTGGAGTCACTACCTCC-3'	NM_009115.3
<i>Serpina3n</i>	F: 5'-AGAAGACTTCCCTGATGCC-3' R: 5'-AGAAGACTTCCCTGATGCC-3'	NM_009252.2

The used primers were self-designed with the according nucleotide sequence (see GenBank nos.).

already described in Hennen et al. (2011). To further validate the downregulation of LRP1, we used anti-LRP1 primary antibody (1:10,000, Abcam, Catalog No. ab92544; RRID: AB\_2234877) as well as  $\beta$ -actin (1:10,000; Sigma-Aldrich, Catalog No. A2228; RRID: AB\_476697) as a control for normalization. The protein expression was visualized with the Clarity<sup>TM</sup> Western ECL Substrate by BioRad (Feldkirchen, Germany, Catalog No. 1705061) and detected with the MicroChemie chemiluminescence device with Gel Capture Software by biostep (Burkhardtshof, Germany, Version 6.6).



Cytokine Array

Hippocampal neurons were either co-cultured with wild-type or LRP1-deficient astrocytes for 21 days *in vitro*. Afterward, the cell culture supernatants were centrifuged for 10 min at 16,000 relative centrifugal force (rcf) to remove particles. Cytokine screening was performed with the Proteome Profiler™ Mouse Cytokine Array Panel A (see **Table 2**; R&D Systems, Minneapolis, Minnesota, United States, Catalog No. ARY006).

**TABLE 2 |** Coordinates of the 40 analyzed cytokines on the filter membrane of the assay.

Coordinate	Target cytokine
A1, A2	Reference spot
A3, A4	Reference spot
B1, B2	BLC
B3, B4	C5/C5a
B5, B6	G-CSF
B7, B8	GM-CSF
B9, B10	I-309
B11, B12	Eotaxin
B13, B14	sICAM-1
B15, B16	IFN- $\gamma$
B17, B18	IL-1 $\alpha$
B19, B20	IL-1 $\beta$
B21, B22	IL-1ra
B23, B24	IL-2
C1, C2	IL-3
C3, C4	IL-4
C5, C6	IL-5
C7, C8	IL-6
C9, C10	IL-7
C11, C12	IL-10
C13, C14	IL-13
C15, C16	IL-12 p70
C17, 18	IL-16
C19, C20	IL-17
C21, C22	IL-23
C23, C24	IL-27
D1, D2	IP-10
D3, D4	I-TAC
D5, D6	KC
D7, D8	M-CSF
D9, D10	JE
D11, D12	MCP-5
D13, D14	MIG
D15, D16	MIP-1 $\alpha$
D17, D18	MIP-1 $\beta$
D19, D20	MIP-2
D21, D22	RANTES
D23, D24	SDF-1
E1, E2	TARC
E3, E4	TIMP-1
E5, E6	TNF- $\alpha$
E7, E8	TREM-1
F1, F2	Reference spot
F23, F24	Negative control

Each coordinate represents an analyzed cytokine. The reference spots were positive controls, detectable after the application of the supernatant.

Statistical Analyses

Immunocytochemical stainings were quantified with ImageJ. All positive cells were counted with the cell counter plug-in. To investigate the influence of LRP1 on the differentiation of astrocytes, we quantified the number of tdTomato- and marker-double positive cells to compare the recombined subpopulations in both conditions. For the analysis of the pre- and postsynaptic puncta, the puncta analyzer with a rolling ball radius of 50 pixel was used. The size of a single puncta was defined as size (pixel<sup>2</sup>) = 2-infinity. The intensity of the bands of the PCR and Western blot analyses as well as the pixel densities of the cytokine array were evaluated with ImageJ. The band intensities were normalized to the expression of  $\beta$ -actin in both cases. We used the endpoint-PCR analysis as a semi-quantitative method to investigate differentially expressed genes upon LRP1 deletion. The number of cycles was below the level of amplificate saturation. The represented figures are exemplary pictures. The shown PCR results were repeated for representation and do not belong to the data shown in the diagram. Results are shown as the mean  $\pm$  the standard error of the mean (SEM). After confirmation that the data were normally distributed, two-way ANOVA with *post hoc* Bonferroni test was performed to investigate the level of significance ( $p \leq 0.05$ ). If the data were not normally distributed, we used the Friedman test to assess the level of significance.

RESULTS

Knockout Induction Was Successful in Astrocytic Cultures

We have previously shown that the deletion of *Lrp1* in NSPCs leads to an increased number of GFAP-positive astrocytes *in vitro* (Safina et al., 2016). To further validate the functions of LRP1 in astrocytes, we generated a new transgenic mouse line, where LRP1 can specifically be deleted from astrocytes via the expression of the Cre recombinase under the control of the GLAST promotor. Our control cells were lacking floxed LRP1, but expressing CreERT2 leading to recombined tdTomato expression after control cells were also treated with 4-OH-TAM. The recombination events were visualized via the reporter gene *Tdtomato* (**Figure 1A**). For this purpose, primary astrocytic cultures were treated exogenously with 4-hydroxy-tamoxifen (4-OH-TAM) to induce the activation of the Cre DNA recombinase. The recombination rate was evaluated via the quantification of all tdTomato-positive cells divided by the number of Hoechst-positive cell nuclei. The knockout efficiency was calculated as the number of LRP1- and tdTomato-double positive cells divided by the total number of tdTomato-positive cells. During the cultivation time from three up to 21 dpp, no differences in the recombination rates of control and knockout cells could be identified (**Figure 1B**). The expression of LRP1 in recombined cells was investigated in both conditions over the cultivation period (**Figure 1C**) to document the deletion of *Lrp1* in the knockout cultures. The statistical evaluation showed that the number of LRP1-positive cells was significantly decreased in the

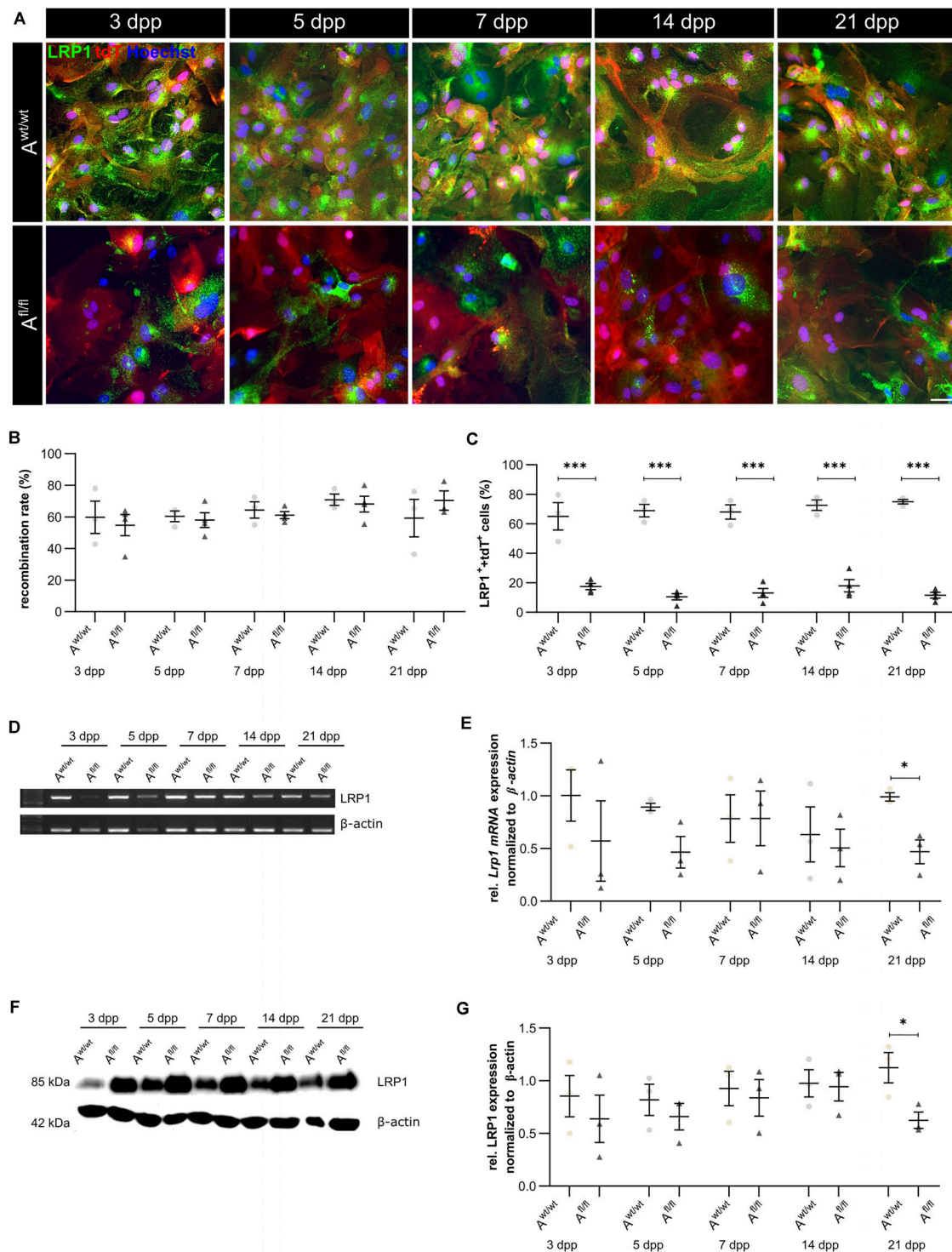


**FIGURE 1 |** Knockout induction was successful *in vitro*. Immunocytochemical staining against LRP1 (green) and tdTomato (red) showed a decreased expression of LRP1 in recombined knockout astrocytes in comparison to recombined control astrocytes during the whole cultivation time (**A**). The recombination rate of both conditions was similar, ranging between 60 and 70% of all astrocytes (**B**). The deletion of *Lrp1* was assessed by the quantification of LRP1- and tdTomato-expressing cells (**C**). The statistical evaluation showed that the number of LRP1-positive cells was significantly decreased in the knockout condition. Furthermore, the deletion of *Lrp1* was evaluated via PCR and compared to the expression in control astrocytes during the cultivation time up to 21 dpp (**D**). The quantification revealed a significant downregulation of *Lrp1* in knockout astrocytes (**E**). Additionally, the protein expression of LRP1 was significantly downregulated in knockout astrocytes in comparison to control astrocytes (**F,G**). The PCR and Western blot analysis depict exemplary results (scale bar: 100  $\mu$ m; mean  $\pm$  SEM;  $N = 3$ ; two-way ANOVA with *post hoc* Bonferroni test). \* $p < 0.05$ ; \*\*\* $p < 0.001$ .

knockout condition compared to the control condition (3 dpp:  $A^{wt/wt}$   $65.05 \pm 7.59\%$ ,  $A^{fl/fl}$   $17.47 \pm 1.81\%$ ,  $p \leq 0.0001$ ; 5 dpp:  $A^{wt/wt}$   $68.88 \pm 3.46\%$ ,  $A^{fl/fl}$   $10.51 \pm 1.86\%$ ,  $p \leq 0.0001$ ; 7 dpp:  $A^{wt/wt}$   $68.01 \pm 4.00\%$ ,  $A^{fl/fl}$   $13.04 \pm 2.62\%$ ,  $p \leq 0.0001$ ; 14 dpp:  $A^{wt/wt}$   $72.60 \pm 2.95\%$ ,  $A^{fl/fl}$   $17.96 \pm 3.62\%$ ,  $p \leq 0.0001$ ; 21 dpp:  $A^{wt/wt}$   $74.99 \pm 1.25\%$ ,  $A^{fl/fl}$   $11.61 \pm 1.68\%$ ,  $p \leq 0.0001$ ). To further validate the downregulation of LRP1 in the astrocyte culture after induction with 4-OH-TAM, the expression of *Lrp1* on mRNA level was analyzed. Here, a decreased expression of *Lrp1* was observed in the knockout culture compared to the control culture. This effect was stable over the whole cultivation time and significant at 21 dpp ( $A^{wt/wt}$   $1.007 \pm 0.028$ ,  $A^{fl/fl}$   $0.468 \pm 0.072$ ,  $p \leq 0.05$ ;  $N = 3$ ; **Figures 1D,E**). The quantification of the Western blot showed a decreased expression of LRP1 on the protein level in the knockout cultures during the whole cultivation time in comparison to the control condition. After 21 dpp, there was a significant decrease of astrocytic LRP1 in the depleted condition ( $0.625 \pm 0.049$ ) compared to the control ( $1.124 \pm 0.144$ ;  $p \leq 0.05$ ;  $N = 3$ ) (**Figures 1F,G**). It is known that the knockout or downregulation of one member of the LDL family can cause increased expression of other members. Therefore, the expression of *Lrp2* and *Lrp4* was measured after the induction of the knockout. There were no alterations in the expression pattern of both receptors after the treatment with 4-OH-TAM in the LRP1-depleted cultures compared to the control condition (data not shown).

## LRP1 Was Not Implicated in the Proliferation of Early Postnatal Astrocytes

Due to the high number of potential ligands and the influence of LRP1 on cellular processes, we investigated the proliferation capacity of astrocytes lacking LRP1. Therefore, we used the proliferation marker phospho-Histone H3 (PH3) (**Figure 2A**). At the beginning of the culture period, the immunocytochemical staining did not reveal significant differences between PH3- and tdTomato-double positive cells in LRP1-deficient astrocytes in comparison to control astrocytes. With ongoing differentiation, the number of proliferative cells decreased under both conditions (**Figure 2B**).

## Astrocyte Maturation Was Altered in Absence of LRP1

Next, the question was addressed if the deletion of *Lrp1* can cause an altered maturation of astrocytes. Therefore, a gene expression profile analysis was performed. We used stage-specific markers of the astrocytic maturation to determine the effect of LRP1 on the differentiation via RT-PCR. At first, late precursor cell genes were investigated. The expression of *Glast* was decreased at an early cultivation time in LRP1-deficient cultures in comparison to the control condition. With ongoing cultivation time, this effect was compensated and both conditions showed a similar expression

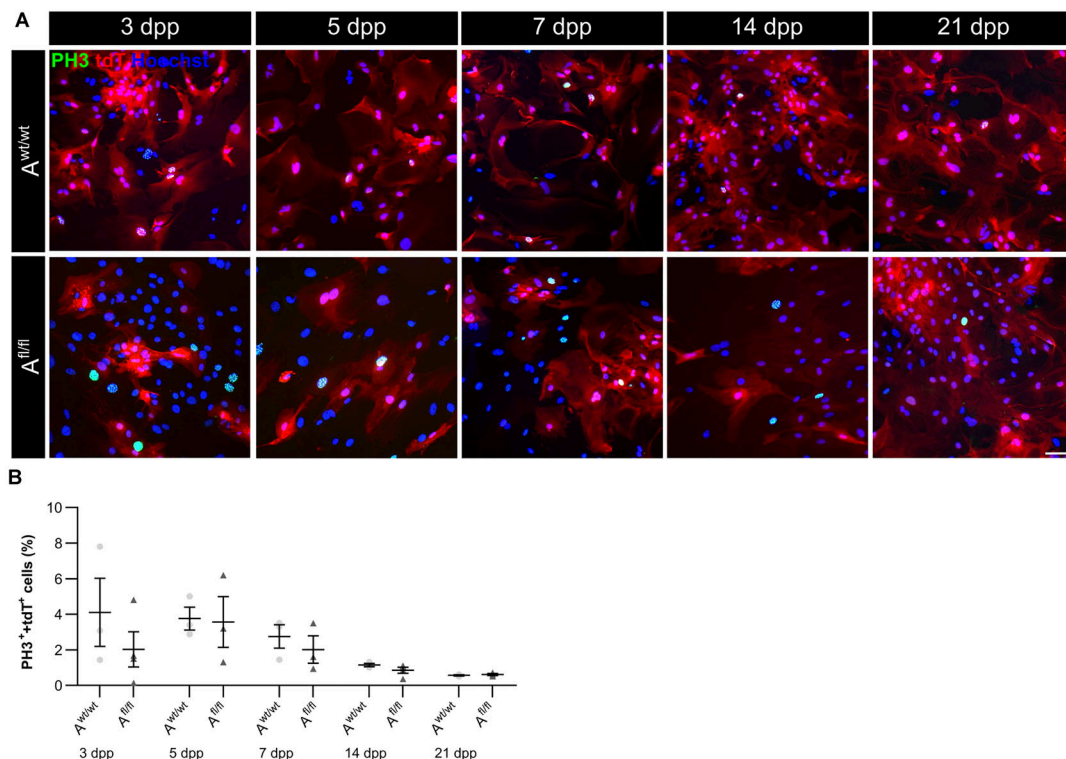


**FIGURE 2 |** Proliferation rate was not significantly altered upon *Lrp1* deletion. The proliferation rate was evaluated with the marker phospho-histone H3 (PH3; green) and tdTomato (red) (**A**). The quantification showed that with ongoing cultivation time, the proliferation rate was similar in both conditions (**B**) (scale bar: 100  $\mu$ m; mean  $\pm$  SEM;  $N = 3$ ; two-way ANOVA with *post hoc* Bonferroni test).



of *Glast*. At the end of the cultivation time, LRP1-deficient astrocytes showed an increased expression of *Glast* in comparison to the control condition (**Figures 3A,B**). Next, the expression of the late precursor gene *Nestin* was analyzed (**Figures 3A,C**). Here, the PCR revealed a similar effect of LRP1 on the *Nestin* expression as on the *Glast* expression. At the beginning of the cultivation, LRP1-depleted astrocytes expressed a decreased amount of *Nestin* in comparison to the control astrocytes. After a longer period of time, the expression profile was adapted in both conditions. After 14 and 21 dpp, the expression of *Nestin* was slightly enhanced in LRP1-deficient astrocytes compared to control astrocytes (**Figure 3C**). Afterward, the levels of the *fibroblast growth factor receptor-3* (FGFR-3) were analyzed as a marker for late precursor cells, which will eventually differentiate into astrocytes (**Figure 3A**). At early cultivation timepoints, control astrocytes showed an increased *Fgfr-3* expression compared to LRP1-depleted astrocytes. The absence of LRP1 in the astrocytes caused slightly increased levels of *Fgfr-3* after a longer cultivation time in comparison to the control condition (**Figure 3D**).

Immature astrocytes are characterized by the expression of aquaporin-4 (Aqp-4) as well as aldehyde dehydrogenase 1 family member L1 (AldH1L1). The expression of *Aldh1l1* was slightly decreased in LRP1-deficient astrocytes at an early timepoint compared to control astrocytes. With ongoing differentiation, the gene expression increased in knockout astrocytes and was similar to the amount of *Aldh1l1* in control astrocytes (**Figures 3A,E**). At the beginning of the cultivation time, *Aqp-4* was slightly decreased in LRP1-deficient astrocytes in comparison to control astrocytes. One week after plating, the amount of *Aqp-4* was similar in the control and knockout condition. With increasing cultivation time, the expression of *Aqp-4* increased in LRP1-lacking astrocytes in comparison to control astrocytes (**Figures 3A,F**).

To evaluate the differentiation from LRP1-deficient astrocytes into mature astrocytes, we used the S100 calcium binding protein (S100). Here, the analysis revealed no alterations in the amount of *S100* on mRNA level in knockout astrocytes compared to the control group (**Figures 3A,G**).

The analysis revealed that late precursor and immature genes showed the same shift in LRP1-deficient astrocytes. At early cultivation timepoints, LRP1-knockout astrocytes showed a decreased expression of these genes in comparison to control astrocytes. However, with ongoing differentiation, LRP1-deficient astrocytes compensated the decreased expression and showed an increased amount of gene expression compared to the control condition. In conclusion, we observed a shifted expression pattern of late precursor and immature astrocytic genes in LRP1-depleted astrocytes.

## LRP1-Deficient Astrocytes Did Not Show a Reactive Phenotype

It is known that astrocytes react to stress with an increased expression of GFAP. Besides an increased number of GFAP-positive cells, the area of the astrocytes can increase as well. Therefore, we were interested in the number of GFAP-positive cells in the absence of LRP1, as well as in the GFAP-positive

area covered by these astrocytes. The immunocytochemical staining did not reveal any changes in the number of GFAP- and tdTomato-double positive astrocytes in LRP1-lacking cultures compared to the control condition (**Figure 4B**). The measurement of the area covered by GFAP-positive astrocytes was not increased in the absence of LRP1 compared to control astrocytes (**Figure 4C**). The evaluation of the expression of *Gfap* mRNA via PCR revealed the same tendency. The ablation of LRP1 caused no alterations in comparison to the control condition (**Figures 4D,E**). The deletion of LRP1 did not cause a reactive phenotype in regard to the number of GFAP-positive cells as well as on the area covered by GFAP-positive astrocytes.

## LRP1-Deletion Resulted in Increased Number of the Glutamate Transporter 1-Positive Astrocytes (GLT-1)

Beside various functions, astrocytes can also influence synaptic transmission via the uptake of neurotransmitters such as glutamate out of the synaptic cleft. One glutamate transporter in mature astrocytes is the glutamate transporter 1 (GLT-1). We investigated the number of GLT-1-positive astrocytes via immunocytochemistry and the amount of *Glt-1* expression via PCR analysis. Here, we observed an increased number of GLT-1-positive astrocytes in the absence of LRP1 in comparison to control astrocytes (**Figures 5A,B**). The difference between the knockout and control situation was more pronounced in the beginning of the cultivation time. At 5 dpp, the number of GLT-1- and tdTomato-double positive astrocytes were significantly increased in LRP1-depleted astrocytes ( $50.27 \pm 2.20\%$ ) compared to control astrocytes ( $24.835 \pm 0.09\%$ ;  $p \leq 0.05$ ;  $N = 3$ ). With increasing cultivation, the number of GLT-1- and tdTomato-double positive astrocytes was slightly diminished in control cultures compared to LRP1-knockout astrocytes. However, the gene expression of *Glt-1* was not altered in LRP1-depleted astrocytes in contrast to control astrocytes (**Figures 5C,D**). The deletion of LRP1 in astrocytic cultures resulted in an increased number of GLT-1-positive astrocytes. Because the control and the LRP1-deficient astrocytes have the same genetic background as a consequence of our breeding strategy, the phenotype observed can directly be traced back to the receptor and most probably implicates LRP1-coupled signaling pathways.

## LRP1-Deficient Astrocytes Promote the Generation of Presynapses and Decreased the Activity of Hippocampal Neurons

To further elucidate the influence of LRP1 on the functionality of astrocytes, we co-cultured embryonic wild-type hippocampal neurons (further referred to as N) either with wild-type astrocytes (N/A<sup>wt/wt</sup>) or with LRP1-deficient astrocytes (N/A<sup>l/h</sup>). The synaptogenesis was investigated with immunocytochemical stainings using the presynapse marker Bassoon and the postsynaptic marker PSD-95 (**Figure 6A**). The colocalization of both signals was pictured in yellow puncta, highlighting a structurally complete synapse. The total number of pre- as

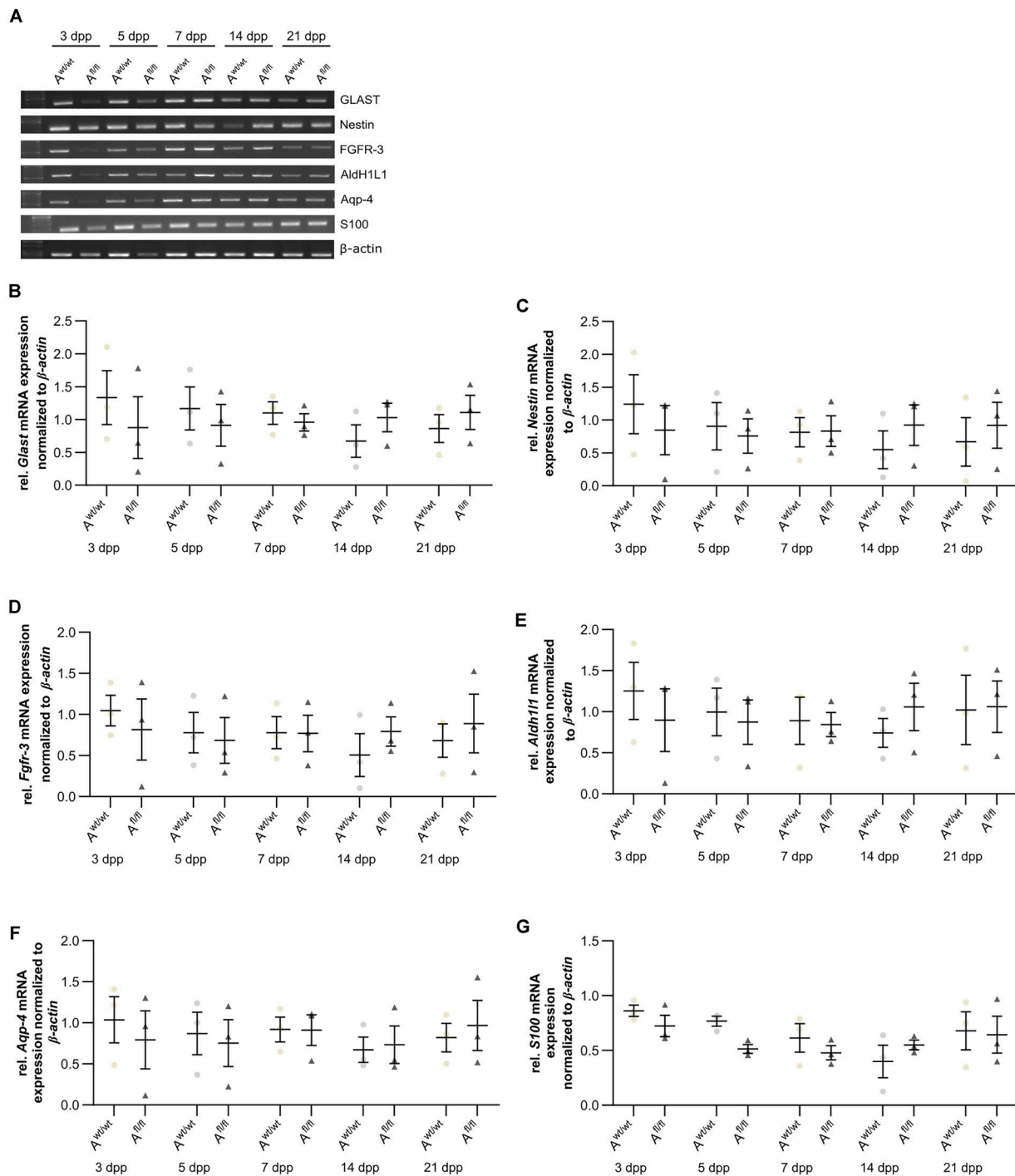


**FIGURE 3 |** Expression of late precursor and immature genes was slightly altered at the beginning of the cultivation time in LRP1-deficient astrocytes. The expression of *Glaxt* was slightly decreased in LRP1-deficient astrocytes at 3 and 5 dpp (**A**). With ongoing cultivation time, the expression increased in LRP1-depleted astrocytes and was comparable to control astrocytes (**B**). The expression of *Nestin* showed a similar result (**A**). First, the expression was slightly decreased in LRP1-knockout astrocytes and with ongoing maturation the amount increased and showed similar levels to control astrocytes (**C**). As a last precursor gene, *Fgfr-3* was investigated (**A,D**). Again, the expression was slightly decreased in depleted astrocytes, but with ongoing cultivation, the amount of *Fgfr-3* was increasing. The expression of *Aldh1l1* was slightly decreased in LRP1-depleted astrocytes 3 dpp compared to control astrocytes (**A,E**). However, with ongoing maturation of the astrocytes, the amount of *Aldh1l1* was comparable between both genotypes. At the end of the cultivation time, the expression of *Aldh1l1* was slightly enhanced in LRP1-depleted astrocytes. The expression profile of *Aqp-4* was similar to the profile of *Aldh1l1* (**A,F**). In immature cultures, the amount of *Aqp-4* was slightly decreased in knockout astrocytes and on a similar level with ongoing cultivation. The gene expression of *S100* was similar in LRP1-deficient astrocytes as well as in control astrocytes during the whole cultivation time (**A,G**). The PCR analysis depicts exemplary results (mean  $\pm$  SEM;  $N = 3$ ; two-way ANOVA with *post hoc* Bonferroni test).

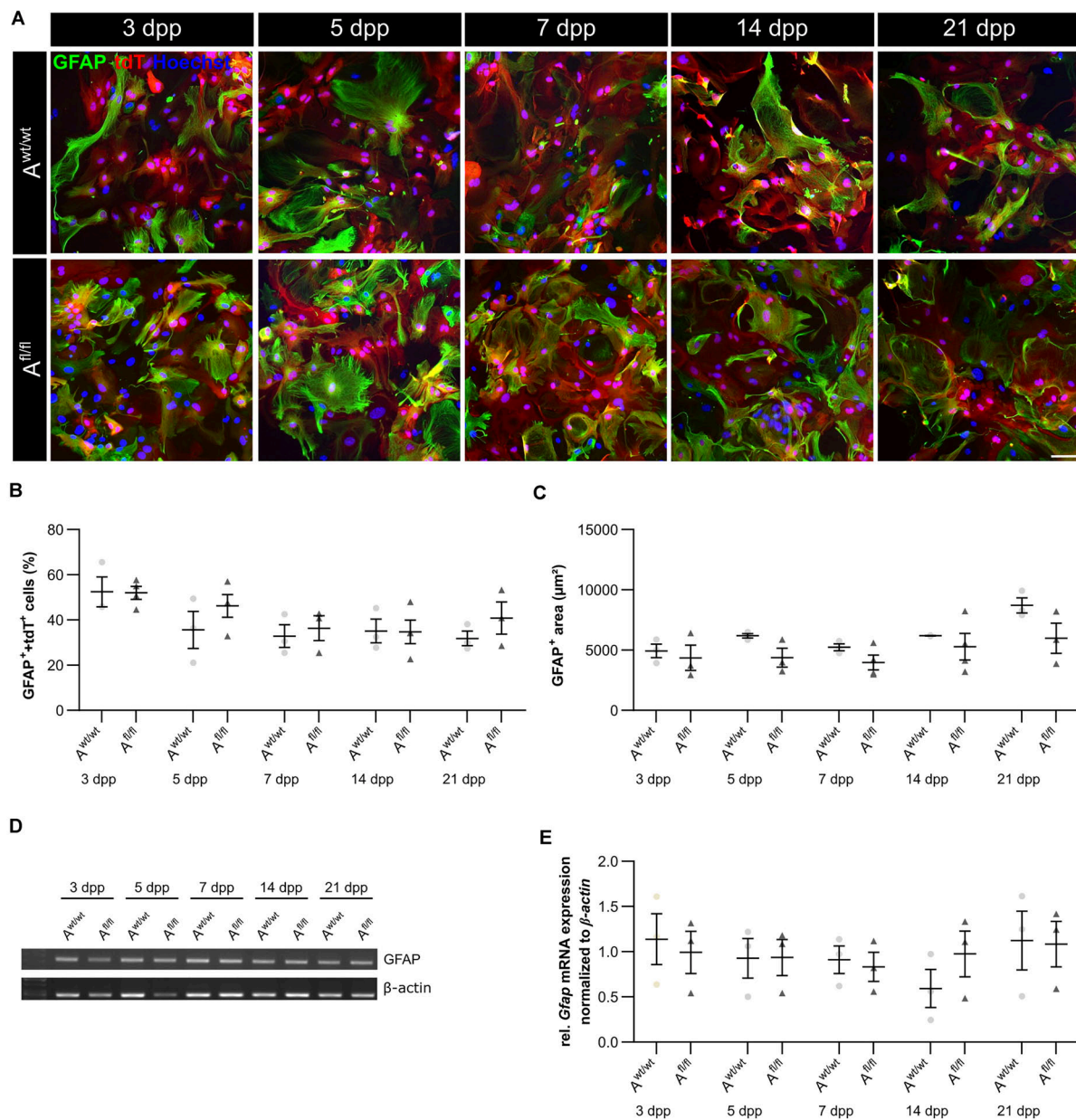


**FIGURE 4 |** LRP1-deficient astrocytes showed no reactive phenotype. The immunocytochemical staining against GFAP (green) and tdTomato (red) revealed no alterations in the morphology of astrocytes (**A**). The quantification of the staining showed no changes in the number of GFAP- and tdTomato-double positive astrocytes in the LRP1-depleted condition compared to the control condition (**B**). Reactive astrocytes showed an increased GFAP-positive area compared to non-reactive astrocytes. However, the GFAP-positive area was similar in both conditions and showed no changes (**C**). Additionally, the gene expression of *Gfap* was investigated (**D**). The statistical evaluation showed no alterations in both conditions (**E**). The PCR analysis depicts exemplary results (scale bar: 100 μm; mean ± SEM; *N* = 3; two-way ANOVA with *post hoc* Bonferroni test).

well as postsynapses and the number of structurally complete synapses were quantified after 14 and 21 days *in vitro* (div). After 14 div, the number of presynapses was significantly decreased in *N/A<sup>fl/fl</sup>* ( $4188.938 \pm 261.4586$ ) when compared with *N/A<sup>wt/wt</sup>* ( $4969.669 \pm 171.561$ ;  $p \leq 0.05$ ; *N* = 5; *n* = 130). In contrast, the number of postsynapses was significantly increased in *N/A<sup>fl/fl</sup>* ( $3035.577 \pm 131.638$ ) compared to *N/A<sup>wt/wt</sup>* ( $2676.801 \pm 105.416$ ;  $p \leq 0.05$ ; *N* = 5; *n* = 130). However, the

number of structurally complete synapses as indicated by the number of yellow puncta revealed no changes in both conditions after 14 div. After 21 div, the number of Bassoon-positive puncta was again significantly decreased in *N/A<sup>fl/fl</sup>* ( $4567.228 \pm 129.309$ ) when compared to *N/A<sup>wt/wt</sup>* ( $5137.953 \pm 151.525$ ;  $p \leq 0.05$ ; *N* = 5; *n* = 130). However, the number of postsynapses as well as of colocalization was not altered in *N/A<sup>fl/fl</sup>* in respect to *N/A<sup>wt/wt</sup>* (**Figure 6B**). The neuronal activity of neurons



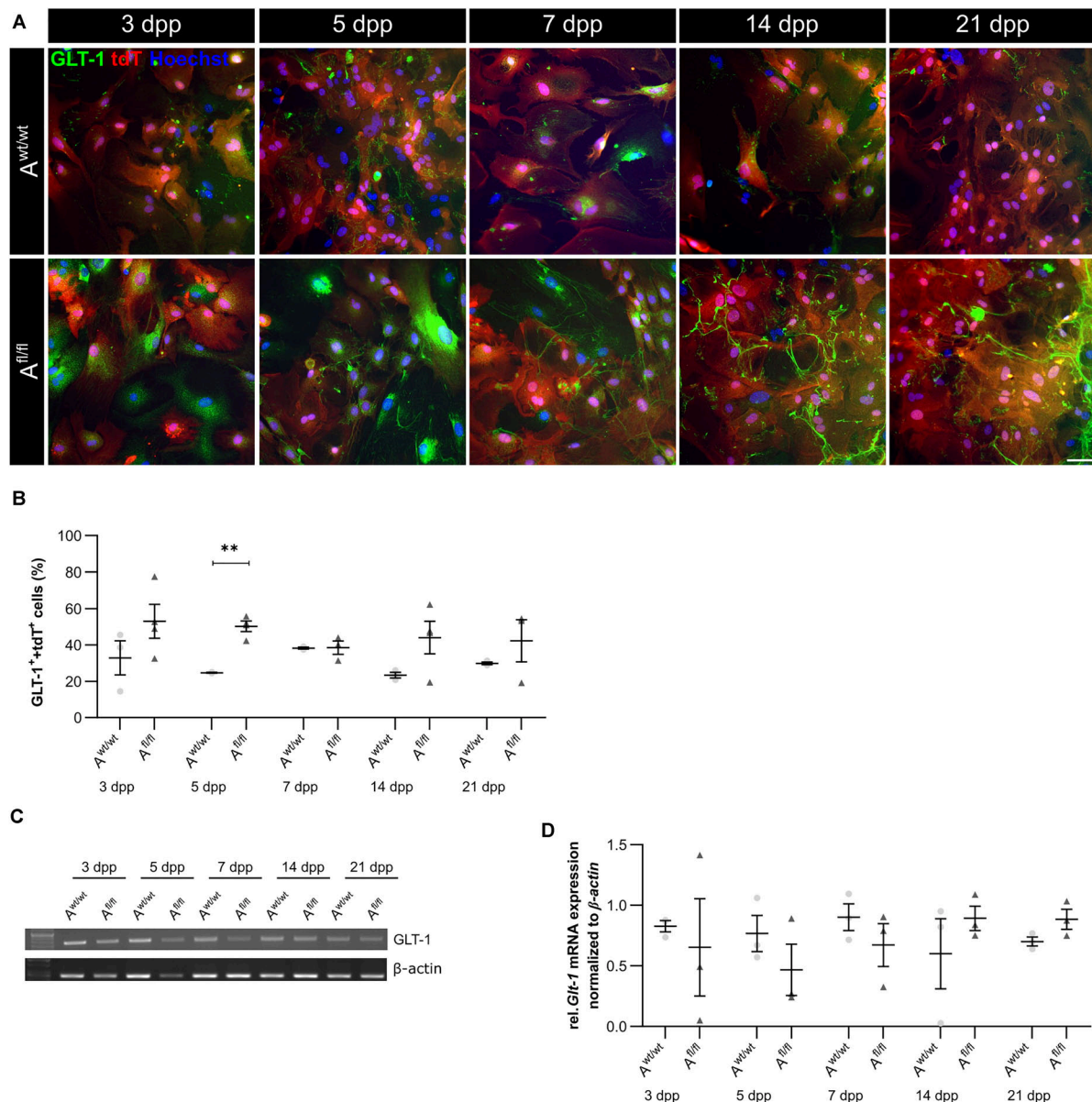


**FIGURE 5 |** *Lrp1* deletion resulted in increased number of GLT-1-positive astrocytes. The number of GLT-1 (green)- and tdTomato (red)-double positive astrocytes was evaluated via immunocytochemistry (A). The quantification showed a significantly increased number of GLT-1- and tdTomato-double positive astrocytes upon LRP1 deletion. With ongoing cultivation time, the number of double-positive cells decreased slightly in the LRP1-depleted culture, but remained higher than in the control condition (B). Additionally, the gene expression of *Glut-1* was investigated (C) but the quantification revealed no changes between both conditions (D). The PCR analysis depicts exemplary results (scale bar: 100  $\mu$ m; mean  $\pm$  SEM;  $N = 3$ ; two-way ANOVA with *post hoc* Bonferroni test). \*\* $p < 0.01$ .

co-cultured with either wild-type or LRP1-deficient astrocytes was evaluated with a MEA. The investigated parameters were the number of spikes, defined as spontaneous single action potential, as well as bursts, an organized sequence of several action potentials, and the percentage of spikes in bursts as well as the duration of bursts. These parameters are highlighting the neuronal activity. After 14 div, the number of spikes was significantly decreased in  $N/A^{fl/fl}$  ( $1308.387 \pm 110.463$ ) compared to  $N/A^{wt/wt}$  ( $2168.304 \pm 161.824$ ;  $p \leq 0.0001$ ;  $N = 4$ ;  $n = 240$ ) (Figure 7A). Moreover, this effect was visible with

increasing cultivation time, where the number of spikes was significantly decreased in  $N/A^{fl/fl}$  ( $1259.662 \pm 137.21$ ) when compared to  $N/A^{wt/wt}$  ( $1951.156 \pm 153.940$ ;  $p \leq 0.001$ ;  $N = 4$ ;  $n = 240$ ). The organized activation of neurons, defined as bursts, was significantly decreased in  $N/A^{fl/fl}$  ( $28.334 \pm 4.55$ ) in contrast to  $N/A^{wt/wt}$  ( $47.217 \pm 3.739$ ;  $p \leq 0.0001$ ;  $N = 4$ ;  $n = 240$ ) after 14 div. Furthermore, the number of bursts remained similar in  $N/A^{fl/fl}$  after 21 div and was slightly decreased compared to  $N/A^{wt/wt}$  (Figure 7B). The percentage of spikes in bursts highlights the organization of the activity of the whole neuronal

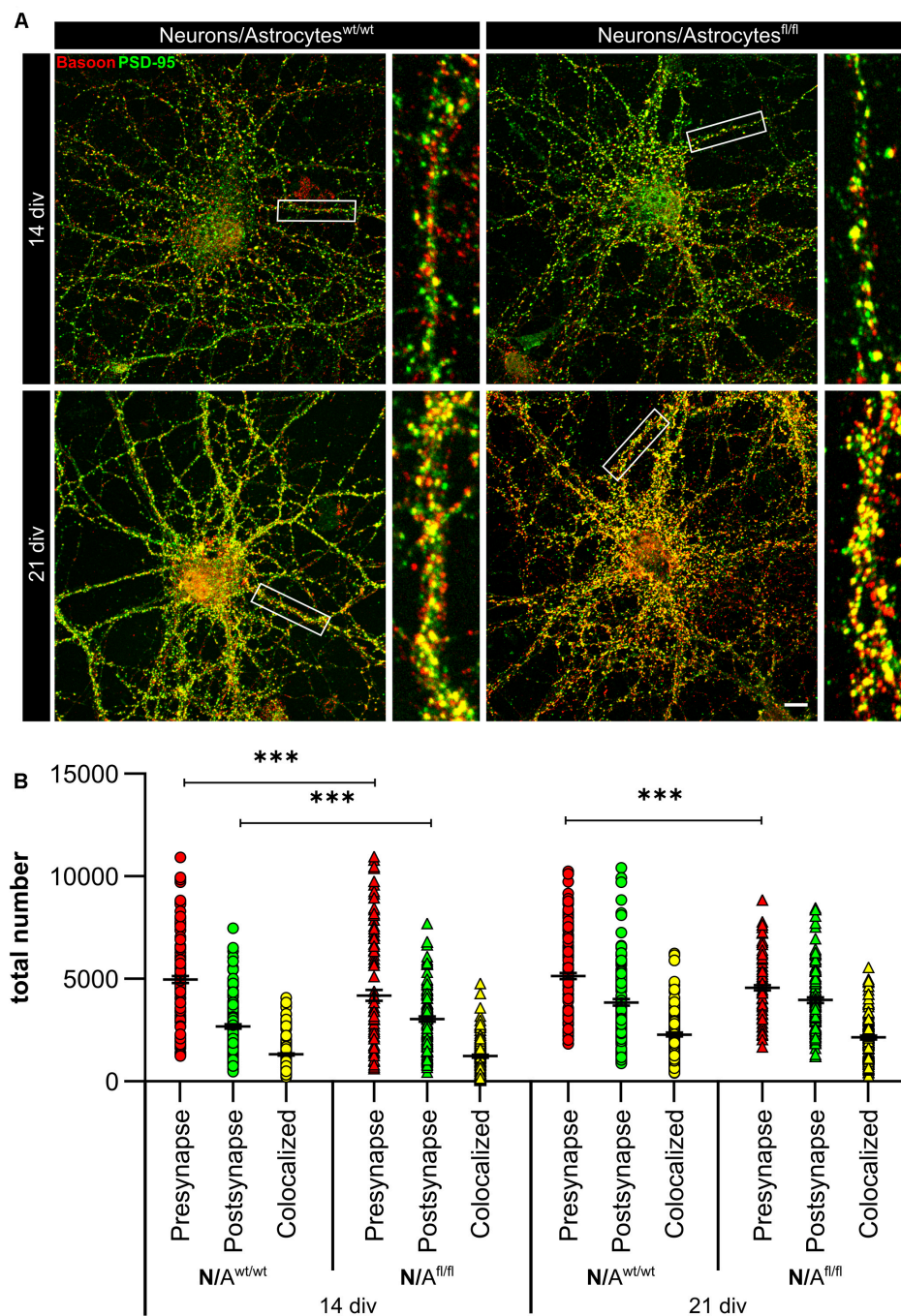
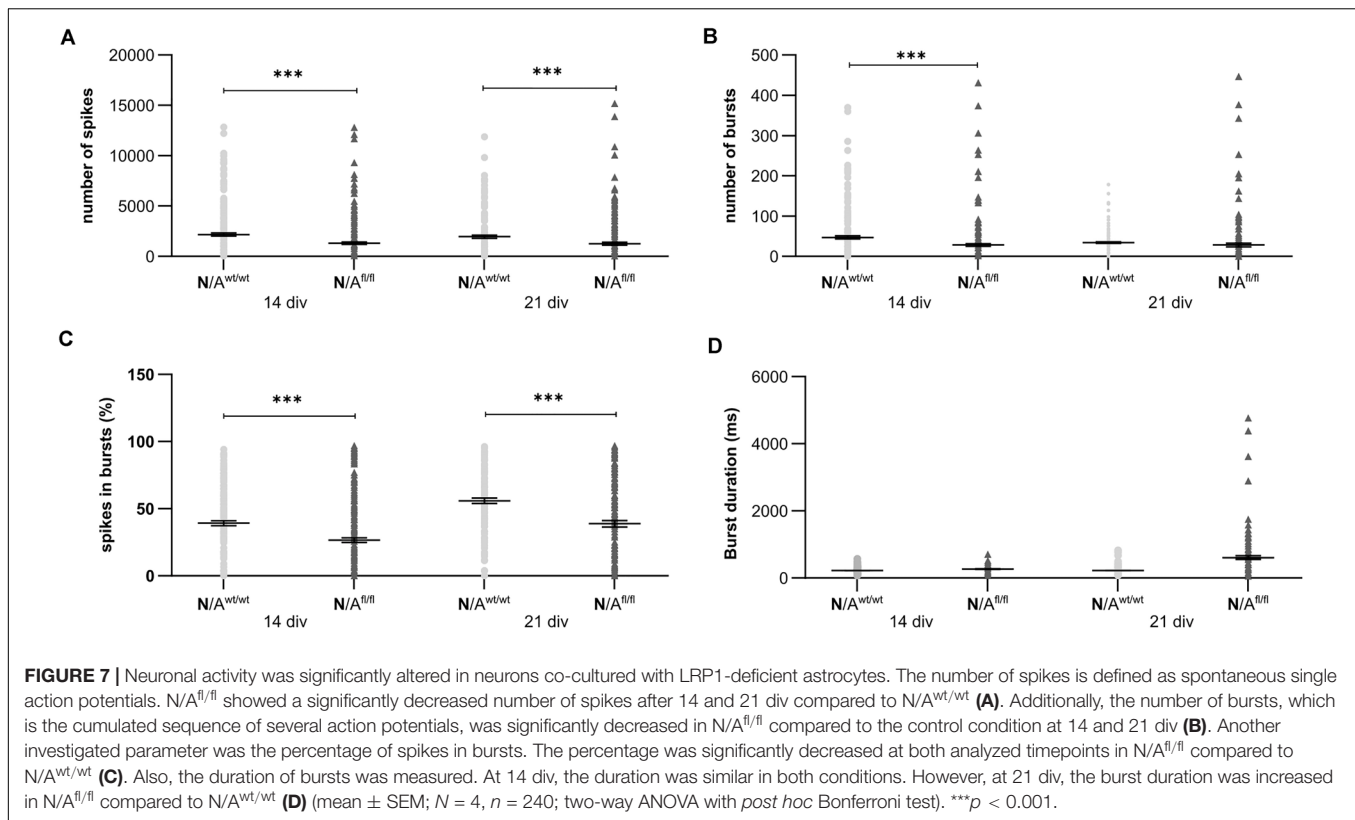


**FIGURE 6 |** *Lrp1* deletion in astrocytes altered neuronal synaptogenesis significantly. Hippocampal neurons (N) were either co-cultured with wild-type (N/A<sup>wt/wt</sup>) or LRP1-depleted (N/A<sup>fl/fl</sup>) astrocytes for 14 and 21 div to evaluate the number of presynapses (Bassoon, red), postsynapses (PSD-95, green), and structurally complete synapses (colocalization, yellow) (**A**). The quantification showed that the number of presynapses was significantly decreased in N/A<sup>fl/fl</sup> compared to N/A<sup>wt/wt</sup> during the whole cultivation time. Additionally, the number of postsynapses was significantly increased in N/A<sup>fl/fl</sup> at 14 div compared to N/A<sup>wt/wt</sup>. However, the amount of structurally complete synapses was not influenced by the LRP1-depleted astrocytes in comparison to the control condition (**B**) (scale bar: 100  $\mu$ m; mean  $\pm$  SEM; N/A<sup>wt/wt</sup>  $N = 6$ ,  $n = 151$ ; N/A<sup>fl/fl</sup>  $N = 5$ ,  $n = 130$ ; two-way ANOVA with *post hoc* Bonferroni test). \*\*\* $p < 0.001$ .

network. Here, the measurements showed that the co-culture of LRP1-deficient astrocytes together with hippocampal neurons resulted in a significantly decreased percentage of spikes in bursts over the whole cultivation time (14 div:  $26.60 \pm 1.93\%$ ;

21 div:  $38.79 \pm 2.52\%$ ), when compared to neurons co-cultured with wild-type astrocytes (14 div:  $39.22 \pm 1.86\%$ ; 21 div:  $55.92 \pm 2.04\%$ ;  $p \leq 0.0001$ ;  $N = 4$ ;  $n = 240$ ) (**Figure 7C**). At the first investigated timepoint, the burst duration was comparable



in  $N/A^{wt/wt}$  and  $N/A^{fl/fl}$ . After 21 div, the burst duration was increased in  $N/A^{fl/fl}$  in contrast to  $N/A^{wt/wt}$  (Figure 7D). The deletion of astrocytic LRP1 resulted in a decreased number of single action potential and number of bursts in hippocampal neurons as well as in an altered synaptogenesis. This result was more remarkable because the  $N/A^{fl/fl}$  culture system contained a minor fraction of wild-type astrocytes (section “Knockout Induction Was Successful in Astrocytic Cultures”, see above), which may partially alleviate the impact of LRP1 elimination. These findings highlight the importance of astrocytic LRP1 in regard to the directed neuronal network activity *in vitro*.

### Astrocytic *Lrp1* Deletion Did Not Cause Altered Glutamate Transporter and Glutamate Receptor Expression

To further investigate the molecular influence of LRP1 on astrocytic functions in regard to neuronal transmission, we analyzed the expression of both glutamate transporter GLAST and GLT-1 in either LRP1-depleted or control astrocytes co-cultured with hippocampal neurons for 14 and 21 div. Here, the expression pattern of *Glut* was not altered on mRNA level in the knockout condition when compared to wild-type astrocytes co-cultured with neurons (Figures 8A,B). Also, the expression of *Glt-1* was similar in both conditions after 14 and 21 div (Figures 8A,C).

Next, we were interested in the expression profile of glutamate receptor subunits of the AMPA and NMDA receptors (AMPA and NMDAR). Therefore, we performed a mRNA analysis of

hippocampal neurons, which were co-cultured with either wild-type or LRP1-depleted astrocytes for 14 and 21 div. The analysis revealed no alterations in the expression of the analyzed AMPAR subunits *Gria1* and *Gria2* in neurons co-cultured with wild-type astrocytes after 14 and 21 div (Figures 9A,B and Figures 9A,C), when compared to neurons co-cultured with LRP1-deficient astrocytes. Next, we investigated the obligatory subunit *Grin1* of the NMDAR. Again, the expression profile of the neurons was not influenced by LRP1-depleted astrocytes after 14 and 21 div when compared to the neurons co-cultured with wild-type astrocyte (Figures 9A,D). The relative expression of the alternative NMDAR subunit *Grin2a* was comparable in neurons co-cultured with wild-type or with LRP1-deficient astrocytes (Figures 9A,E). The relative expression of *Grin2b* was slightly increased at 14 div in neurons co-cultured with wild-type astrocytes, whereas the relative expression in neurons co-cultured with LRP1-deficient astrocytes was slightly decreased. Nevertheless, the alterations in the relative expression of *Grin2b* after 21 div were not detectable anymore (Figures 9A,F). In conclusion, the decreased neuronal network activity of hippocampal neurons co-cultured with LRP1-deficient astrocytes was caused by neither the altered expression of NMDAR- or AMPAR-subunits in neurons nor the expression of glutamate transporters on the astrocytic cell surface.

### LRP1-Deficient Astrocytes Showed no A1 Astrocyte-Specific Phenotype

To further validate whether the deletion of LRP1 in astrocytes caused neurotoxic properties, we investigated the expression of



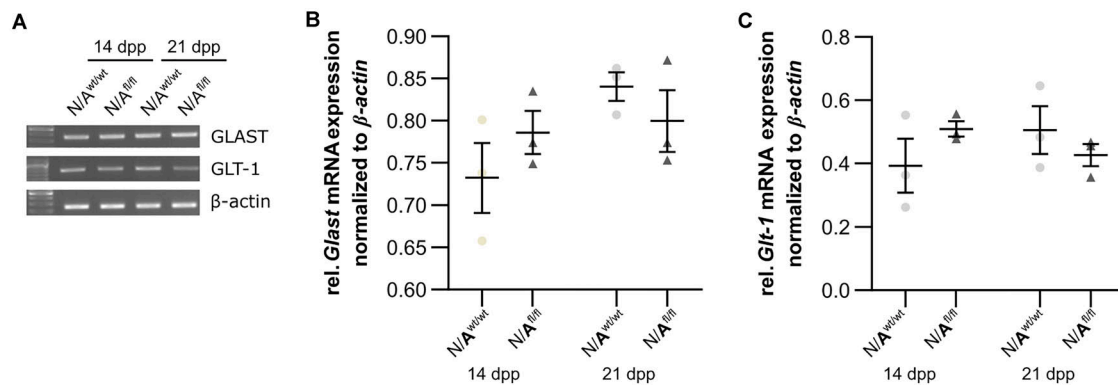


**FIGURE 8 |** LRP1 did not alter astrocytic functions in regard to glutamate transport. Both astrocytic glutamate transporters were investigated in either LRP1-deficient or wild-type astrocytes co-cultured with hippocampal neurons. The gene expression profile of *Glst* was comparable in N/A<sup>wt/wt</sup> and N/A<sup>fl/fl</sup> at both timepoints (A,B). Moreover, the relative expression of *Glt-1* was also not altered in N/A<sup>wt/wt</sup> compared to N/A<sup>fl/fl</sup> (A,C). The PCR analysis depicts exemplary results (mean  $\pm$  SEM;  $N = 3$ ; two-way ANOVA with *post hoc* Bonferroni test).

factors that are known to be expressed by type A1 astrocytes (Clarke et al., 2018). Therefore, we used lysates of wild-type or LRP1-deficient astrocytes that had been co-cultured with hippocampal neurons for 14 and 21 div. Firstly, the expression profile of *lipocalin-2* (*Lcn2*) was analyzed. *Lcn2* expression was not altered in LRP1-deficient astrocytes when compared to wild-type astrocytes (Figures 10A,B). Another factor expressed by A1 astrocytes is the serine protease inhibitor A3A (Serpina3A). Here, the analysis revealed no alterations in the absence of astrocytic LRP1 in comparison to wild-type astrocytes co-cultured with neurons (Figures 10A,C). The over-activation of the complement system can have a negative impact on synaptogenesis and neuronal activity, which can be influenced by A1 astrocytes. Therefore, we also investigated the expression of the complement components C2 and C3, which are known to be highly upregulated in A1 astrocytes. The expression of C2 was slightly decreased in LRP1-deficient astrocytes when compared to wild-type astrocytes (Figures 10A,D). Another component of the complement system that was analyzed was C3. During the whole cultivation time, the deletion of LRP1 had no influence on the relative expression of C3, when compared to the wild-type situation (Figures 10A,E). In summary, LRP1-depleted astrocytes did not show the expression pattern of neurotoxic A1 astrocytes.

### Expression of Cytokines Were Altered in Cell Culture Supernatant of LRP1-Deficient Astrocytes Co-Cultured With Hippocampal Neurons

To further investigate the influence of astrocytic LRP1 on synaptogenesis and neuronal activity, we were interested in the expression of cytokines in the supernatant of hippocampal neurons either co-cultured with wild-type or LRP1-deficient astrocytes after 21 div. Both conditions expressed the same cytokines, however, with differing amounts (Figures 11A,B). The analysis showed that the cytokines KC and TIMP-1 were slightly increased in N/A<sup>fl/fl</sup> in comparison to other upregulated

cytokines. A strong increased expression of siCAM-1 and IL-6 was observed in the knockout condition. The cytokines IP-10, MIP-1 $\alpha$ , JE, and SDF-1 were slightly decreased in the supernatant of N/A<sup>fl/fl</sup> compared to N/A<sup>wt/wt</sup> (Figure 11C). However, some cytokines were strongly downregulated in the knockout condition. IL-1 $\alpha$  showed a decreased expression in the knockout condition compared to the control condition. Furthermore, MIP-1 $\beta$  and M-CSF as well as MIP-2, RANTES, and TNF $\alpha$  were strongly downregulated upon deletion of *Lrp1* in astrocytes co-cultured with hippocampal neurons compared to the control condition (Figure 11C).

## DISCUSSION

We generated an inducible conditional transgenic mouse model where *Lrp1* was specifically deleted in GLAST-positive astrocyte precursor cells. With this approach, we wanted to investigate the influence of LRP1 on the maturation and functionality in astrocytes. Additionally, we wanted to unravel the functions of astrocytic LRP1 on synaptogenesis and neuronal activity *in vitro*. Our data provide evidence that LRP1-deficient astrocytes caused a significantly altered synaptogenesis of hippocampal neurons as well as a decreased number of single action potentials and neuronal network activity.

Lipoprotein receptor-related protein 1 regulates the availability of the tPA at synapses via endocytosis and releases tPA in a controlled manner (Cassé et al., 2012). The inhibition of LRP1 via its inhibitor receptor related protein (RAP) reduced the amount of tPA uptake by astrocytes. However, the release of neuronal tPA was not influenced by a decreased astrocytic tPA uptake (Cassé et al., 2012). We hypothesize that the increased number of postsynapses in our experimental setup was caused by an increased amount of tPA in the synaptic cleft, because the endocytosis by LRP1-deficient astrocytes was impaired. As already described, one of the multiple ligands of LRP1 is ApoE, which is involved in cholesterol transport. Neurons alone are able to produce enough cholesterol to survive and



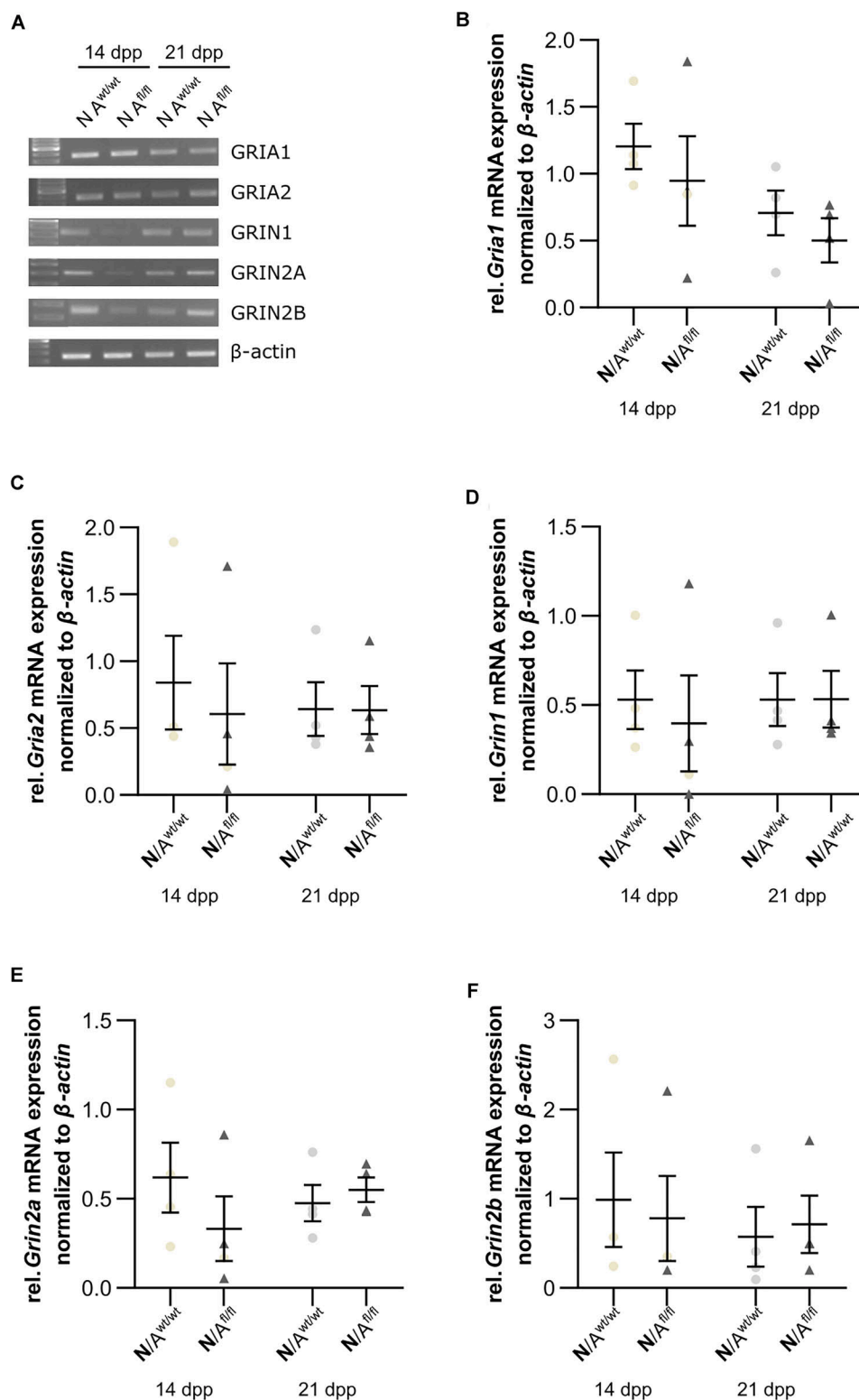


**FIGURE 9 |** Glutamate receptor subunits were not influenced by astrocytic LRP1 deletion. **(A)** The AMPA receptor subunits *Gria1* and *Gria2* showed no changes in the gene expression profile of N co-cultured either with A<sup>wt/wt</sup> or with A<sup>fl/fl</sup> at 14 or 21 div **(B,C)**. Additionally, the expression profile of the obligatory NMDA receptor subunit *Grin1* was investigated and again the absence of astrocytic LRP1 had no influence of the amount of *Grin1* **(D)**. Moreover, two NMDA receptor subunits were investigated, which are known to be influenced by LRP1. However, the amount of *Grin2a* and *Grin2b* were not significantly influenced by astrocytic LRP1 **(E,F)**. The PCR analysis depicts exemplary results (mean ± SEM; *N* = 4; Friedman test).

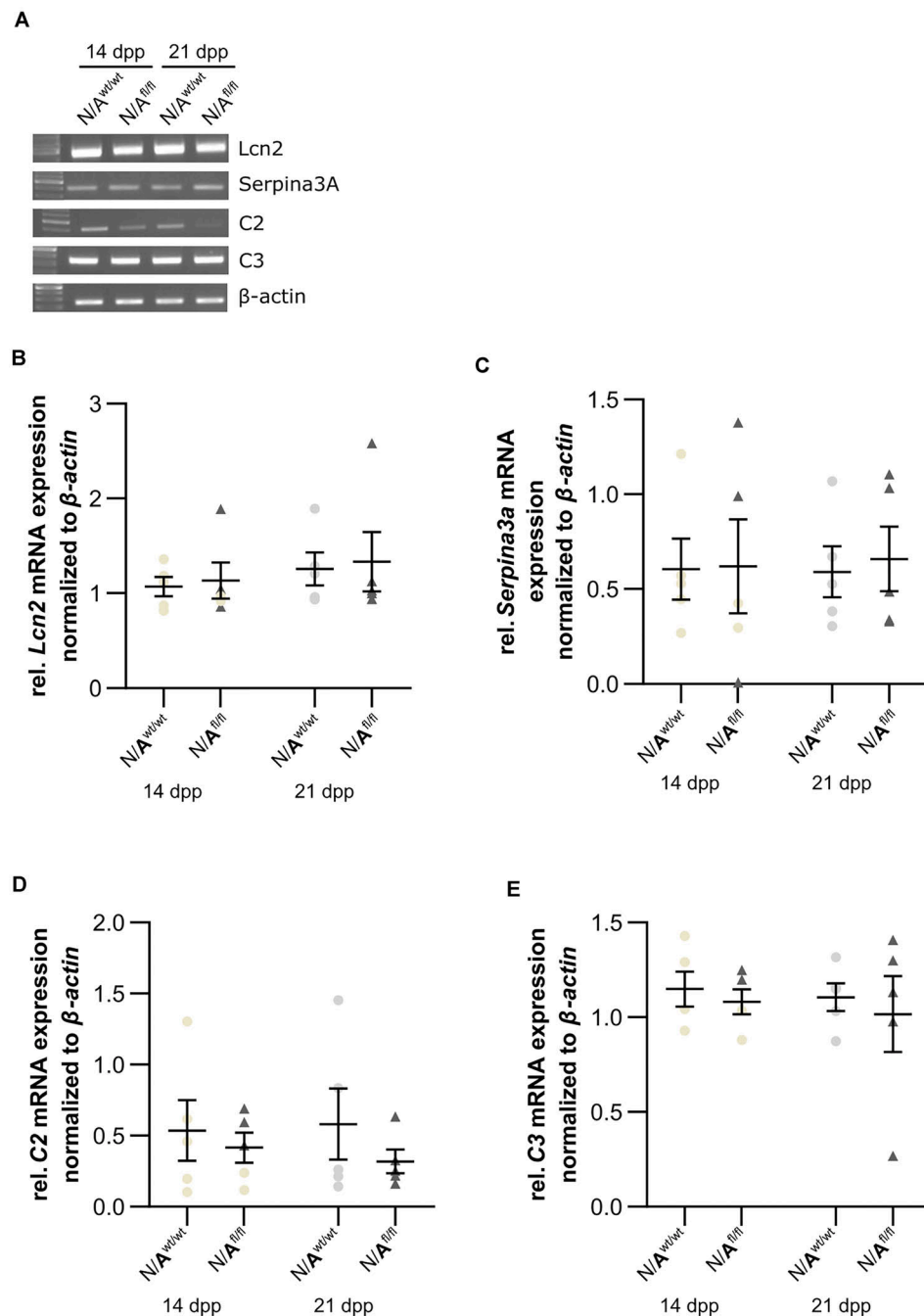


**FIGURE 10 |** LRP1-deficient astrocytes did not express neurotoxic factors. The relative expression of *lipocalin-2* (*Lcn2*) was not altered in N/A<sup>fl/fl</sup> compared to N/A<sup>wt/wt</sup> (A,B). Another factor secreted by neurotoxic astrocytes is the serine protease inhibitor A3A (*Serpina3A*) (C). The gene expression profile was not altered in N/A<sup>fl/fl</sup> compared to N/A<sup>wt/wt</sup> during the cultivation time. Additionally, two components of the complement system were analyzed (D,E). Again, both components, C2 and C3, were similarly expressed in both conditions. The PCR analysis depicts exemplary results (mean ± SEM; N = 5; Friedman test).

differentiate to some extent, but their synapse formation is inefficient (Pfrieger, 2003). Neurons need to be supplied with cholesterol via astrocytes and ApoE-containing lipoproteins to form structural and functional synapses. Massive synaptogenesis requires large amounts of cholesterol, which may represent a link between synaptogenesis and the differentiation of astrocytes

in the developing brain (Mauch et al., 2001). The study of Liu et al. (2010) showed that the deletion of *Lrp1* in the brain resulted in increased levels of ApoE but decreased levels of cholesterol. The availability of cholesterol can impair the development of presynapses in our co-culture system with LRP1-deficient astrocytes. We propose that the deletion of *Lrp1*

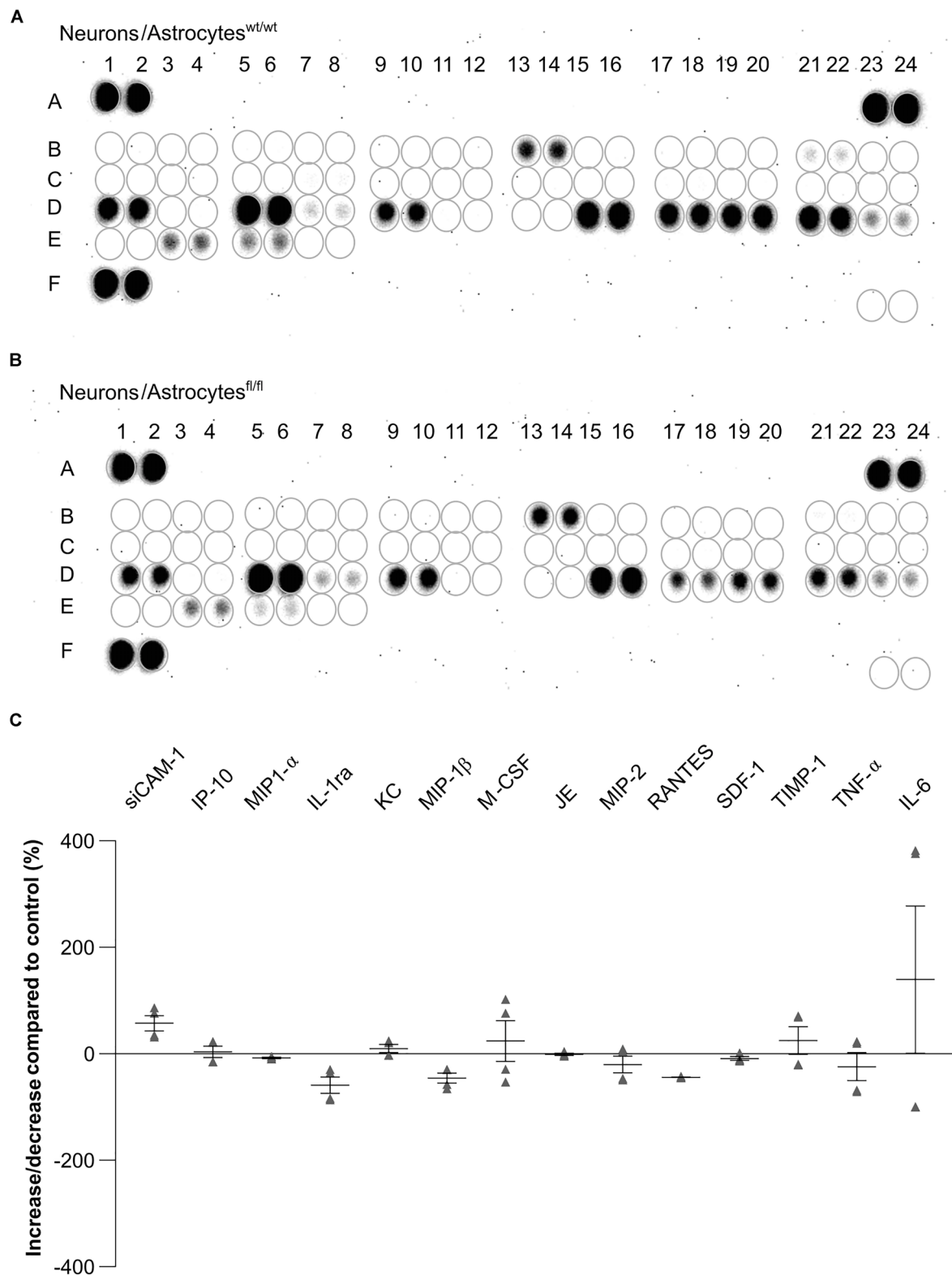


**FIGURE 11** | Expression of cytokines in the supernatant of hippocampal neurons co-cultured with wild-type (A) or LRP1-deficient astrocytes (B) after 21 div. The quantification revealed that the cytokines KC and TIMP-1 were slightly increased expressed in N/A<sup>fl/fl</sup> compared to the control condition (C). Additionally, siCAM-1 and IL-6 were strongly expressed in the knockout condition, whereas IP-10, MIP-1 $\alpha$ , JE, MIP-2, and SDF-1 were slightly decreased in the knockout condition compared to the control. Strongly reduced were the cytokines IL-1ra, MIP-1 $\beta$ , M-CSF, RANTES, and TNF- $\alpha$  (mean  $\pm$  SEM;  $N = 2$ ,  $n = 4$ ).

in astrocytes co-cultured with hippocampal neurons caused an altered pre- and postsynapse formation due to modified uptake and degradation of tPA and ApoE. This presumably resulted in altered cholesterol availability for neurons and affected ongoing synaptogenesis.

The analysis of the neuronal activity revealed that the deletion of astrocytic LRP1 resulted in a decreased number of single action potential as well as a decreased network activity in general. Among other things, astrocytes remove glutamate out of the synaptic cleft via glutamate transporters, e.g., GLT-1, which is significantly increased in our *in vitro* model. Furthermore, they supply the presynaptic terminal with glutamate, as well as with the precursor glutamine, and astrocytes support the efficient uptake of glutamate following synaptic transmission (Papouin et al., 2017). Rehman et al. (2017) have shown that glutamine augments neuronal activity in rat hippocampal slices. Therefore, we conclude that the deletion of LRP1 in astrocytes might cause an altered supply of glutamine at the presynaptic terminal, which resulted in a decreased neuronal activity and weakened presynaptic terminals.

Additionally, we investigated if the maturation and differentiation of astrocytes were influenced by the deletion of LRP1. The analyses showed that LRP1-deficient astrocytes had a reduced proliferation rate at the beginning of the cultivation. This effect was already described in neural stem and progenitor cells (NSPCs), which were lacking LRP1 (Safina et al., 2016). It was reported that astrocytes *in vitro* showed a density-dependent proliferation (Nakatsuji and Miller, 1998), explaining the similar proliferation rates observed in our model at later cultivation timepoints. However, our findings suggest that the absence of LRP1 also has an impact on the proliferation of astrocytes *in vitro*.

The next focus was the influence of LRP1 on the maturation of astrocytes. Therefore, we used stage-specific markers to address this question. Here, we used several tools to investigate the impact. Firstly, we analyzed the expression of late precursor, immature, and mature astrocyte genes via PCR analysis. All investigated genes have in common that at the beginning of the cultivation time, the expression of these genes was decreased in the LRP1-depleted astrocytes in comparison to the control astrocytes. Subsequently, with ongoing differentiation, the expression of the genes was increased in the deficient cultures in comparison to the control. These findings lead to the suggestion that LRP1 might be important for the early-onset differentiation of astrocytes *in vitro*. This is supported by the results of Herz et al. (1992, 1993) where it was shown that the deletion of *Lrp1* in the embryo is lethal, highlighting the importance of LRP1 in the early development of the CNS. Additionally, the altered or decreased expression of stage-specific markers corresponds to the decreased proliferation rate observed in the LRP1-deficient astrocytes. A decreased proliferation rate might result in an altered or delayed differentiation of astrocytes. However, neither the number of GFAP-positive astrocyte nor the GFAP-positive area was altered in the absence of LRP1.

Astrocytes are known as the most abundant cell type in the CNS (Zuchero and Barres, 2015; Liddelov and Barres, 2017) and mediate diverse functions. They are involved in energy supply

(Chuquet et al., 2010), maintenance of ion and pH homeostasis (Mahmoud et al., 2019), and the uptake of neurotransmitters, e.g.,  $\gamma$ -aminobutyric acid (GABA), glycine, and glutamate. Thereby, astrocytes are also involved in the regulation of synaptic transmission (Renzel et al., 2013). The concept of the tripartite synapse, where astrocytes in conjunction with the pre- and postsynapse form the functional synapse, is a well-established model (Farhy-Tselnicker and Allen, 2018). Astrocytic protrusions, including those that contact synapses, express several proteins, which are involved in synaptic transmission (Papouin et al., 2017). For example, astrocytic protrusions express the GLAST and the glutamate transporter-1 (GLT-1) (Chaudhry et al., 1995), glutamine synthetase (Derouiche and Frotscher, 1991), aquaporins (Thrane et al., 2011), potassium channels (Higashi et al., 2001), cell adhesion molecules, and lactate transporters (Zhuang et al., 2011). These factors contribute to the controlled and effective neuronal transmission by resupplying the presynaptic terminal with glutamate and glutamate precursor glutamine via glutamate transporters and glutamine synthetase. Additionally, astrocytes are removing glutamate out of the synaptic cleft to ensure an efficient synaptic transmission. Lastly, they provide neurons with energy substrates to support the neuronal transmission, as well as plasticity (Papouin et al., 2017). An altered astrocyte functionality, e.g., a decreased expression of glutamate transporters on the cell surface, can cause pathological conditions. Regan et al. (2007) have reported that the decreased expression of glutamate transporters resulted in an increased amount of glutamate in the synaptic cleft. An increased amount of glutamate above the threshold is neurotoxic and causes hyperexcitability of neurons. The immunocytochemical staining against GLT-1 showed that the deletion of *Lrp1* caused an increased number of GLT-1-positive astrocytes in comparison to the control condition. Previous studies reported that the expression of GLT-1 or number of GLT-1-positive astrocytes decreased after the onset of seizures or *status epilepticus* (SE) (Hubbard et al., 2016). However, recently, Peterson and Binder (2019) have demonstrated that GLT-1 and GLAST, both glutamate transporters, were significantly upregulated shortly after SE but were decreased at later timepoints. They conclude that this was a compensatory response to the large amount of glutamate during SE. We already hypothesized that the altered neuronal activity was caused by an inefficient supply of glutamine at the presynaptic terminal and the decreased replenishment of glutamate via the LRP1-deficient astrocytes, which might result in an increased number of GLT-1-positive astrocytes.

Our recent data demonstrated that the proliferation rate was decreased in LRP1-depleted astrocytes, which resulted in a delayed maturation of the cells *in vitro*. Additionally, the number of GLT-1-positive astrocytes was significantly increased in the absence of LRP1.

To investigate the influence of astrocytic LRP1 on the functionality of neurons, we analyzed the gene expression of NMDA and AMPA receptor subunits in neurons co-cultured with LRP1-deficient or wild-type astrocytes, as previous studies reported that the activation of NMDA and AMPA receptors can be influenced by astrocytic properties (Xu et al., 2010; Allen, 2014; Jolly et al., 2018; Neame et al., 2019). However, we did not see an



alteration in the expression of receptor subunits when neurons were co-cultured with LRP1-deficient astrocytes. Clarke et al. (2018) have shown that astrocyte reactivity is accompanied by the expression of specific genes. Therefore, we investigated if the deletion of *Lrp1* in astrocytes contributes to a reactive phenotype in the presence of hippocampal neurons, which might lead to the release of neurotoxic factors. Here we chose, in accordance with Clarke et al. (2018), lipocalin-2 (*Lcn2*), serine protease inhibitor A3A (*Serpina3A*), as well as the two complement components, C2 and C3. The quantification revealed no altered expression of any of these genes in LRP1-deficient astrocytes. This leads to the assumption that the absence of LRP1 had no influence on the reactivity of astrocytes on mRNA level. This is consistent with the observation that the number of GFAP-positive astrocytes and their surface area was not altered upon the deletion of *Lrp1*. So, we conclude that a reactive phenotype of the astrocytes is not the reason for the altered activity of the neurons co-cultured with LRP1-deficient astrocytes.

Finally, to investigate the influence of astrocytic LRP1 on neuronal activity and synaptogenesis, we assessed the cytokine release into the co-culture supernatant of LRP1-deficient or wild-type astrocytes with hippocampal neurons. However, we did not observe a significantly altered expression in the cytokine profiles of hippocampal neurons co-cultured with LRP1-deficient astrocytes in comparison to the control condition.

In summary, our results have shown that the deletion of *Lrp1* in astrocytes did not cause a reactive phenotype as characterized by an increased number of GFAP-positive astrocytes. However, other properties were altered, for example, the proliferation rate and the increased number of GLT-1-positive astrocytes. We did not observe a causal context in our investigated parameters and the decreased neuronal activity of hippocampal neurons co-cultured with LRP1-deficient astrocytes, which might relate to the limitation of this mouse model. As already described, the recombination rate and the knockout efficiency were around 55 to 77% and 82 to 90% of the cells, respectively. The proportion of non-recombined and LRP1-deficient cells still influenced the results. For the immunocytochemical stainings, only recombined cells were quantified, whereas the candidate gene expression profile analysis was performed with cell lysates of the whole cell population including non-recombined cells, which might conceal alterations between the conditions.

Despite these limitations, we identified astrocytic LRP1 as a novel modulator of astrocyte functions in the context of the tripartite synapse.

## DATA AVAILABILITY STATEMENT

The raw data supporting the conclusions of this article will be made available by the authors, without undue reservation.

## ETHICS STATEMENT

The animal study was reviewed and approved by the Landesamt fuer Umweltschutz, Naturschutz und

Verbraucherschutz. Written informed consent was obtained from the owners for the participation of their animals in this study.

## AUTHOR CONTRIBUTIONS

RR and KG performed the experiments. RR, KG, and AF wrote and revised the manuscript. AS kindly provided the GLAST:CreERT2 mouse line and revised the manuscript. All authors contributed to the article and approved the submitted version.

## FUNDING

We are grateful for grant support by the German Research Foundation (DFG, SPP 1172, FA 159/20-1,2 to AF and a junior research support grant to RR). We acknowledge support from the DFG Open Access Publication Funds of the Ruhr-Universität Bochum.

## ACKNOWLEDGMENTS

We would like to thank M.Sc. David Wegrzyn for his advice concerning the co-culture of hippocampal neurons, the MEA measurements, and the immunocytochemistry procedure for pre- and postsynapse staining. Additionally, we would like to thank Prof. Frank Kirchhoff for providing us the GLAST:CreERT2 mouse line and his critical comments on our manuscript.

## SUPPLEMENTARY MATERIAL

The Supplementary Material for this article can be found online at: <https://www.frontiersin.org/articles/10.3389/fncel.2020.567253/full#supplementary-material>

**Supplementary Figure 1** | Mating scheme for the newly generated inducible conditional transgenic mouse line GLAST:CreERT2xLRP1fl/fl. For the generation of the LRP1-depleted astrocyte mouse model we mated the GLAST:CreERT2 mouse line with the LRP1fl/fl mouse line. In the F1 generation triple heterozygous animals were used for further breeding. Upon the mating of the heterozygous animals of the F1 generation, 27 different genotypes of the offspring could potentially be generated. The knockout animals were characterized by the heterozygous expression of the Cre recombinase under the GLAST promotor and double floxed alleles of the tdTomato reporter and LRP1. The control has the same genetic profile, except the LRP1 alleles were not flanked by loxP sites.

**Supplementary Figure 2** | Exemplary recordings of MEA analysis of hippocampal neurons co-cultured with LRP1-deficient astrocytes for 21 div. The recordings of 60 electrodes on one MEA device were visualized via a heat map (A). Each electrode was depicted as a rectangle and the activity was coded in a color scheme (black-strong activity; red-active; yellow-medium activity; and blue-no activity). Additionally, all occurring spikes were recorded for each electrode over the investigated time (B). Furthermore, the activity of single electrodes was magnified (C). The intensity of single spikes in micro Volt ( $\mu$ V) was presented. The number and duration of bursts were deduced by the number and frequency of spikes as it was characterized as the organized sequence of action potentials.

## REFERENCES

- Allen, N. J. (2014). Astrocyte regulation of synaptic behavior. *Ann. Rev. Cell Dev. Biol.* 30, 439–463. doi: 10.1146/annurev-cellbio-100913-013053
- Auderset, L., Cullen, C. L., and Young, K. M. (2016). Low density lipoprotein-receptor related protein 1 is differentially expressed by neuronal and glial populations in the developing and mature mouse central nervous system. *PLoS One* 11:155878. doi: 10.1371/journal.pone.0155878
- Boucher, P., and Herz, J. (2011). Signaling through LRP1: Protection from atherosclerosis and beyond. *Biochem. Pharmacol.* 81, 1–5. doi: 10.1016/j.bcp.2010.09.018
- Bres, E. E., and Faissner, A. (2019). Low density receptor-related protein 1 interactions with the extracellular matrix: more than meets the eye. *Front. Cell Dev. Biol.* 7:31. doi: 10.3389/fcell.2019.00031
- Bres, E. E., Safina, D., Müller, J., Bedner, P., Yang, H., Helluy, X. et al. (2020). Lipoprotein receptor loss in forebrain radial glia results in neurological deficits and severe seizures. *Glia* 68, 2517–2549. doi: 10.1002/glia.23869
- Cassé, F., Bardou, I., Danglot, L., Briens, A., Montagne, A., Parcq, J., et al. (2012). Glutamate controls tPA recycling by astrocytes, which in turn influences glutamatergic signals. *J. Neurosci.* 32, 5186–5199. doi: 10.1523/JNEUROSCI.5296-11.2012
- Chaudhry, F. A., Lehre, K. P., van Lookeren Campagne, M., Ottersen, O. P., Danbolt, N. C., and Storm-Mathisen, J. (1995). Glutamate transporters in glial plasma membranes: highly differentiated localizations revealed by quantitative ultrastructural immunocytochemistry. *Neuron* 15, 711–720. doi: 10.1016/0896-6273(95)90158-2
- Chuquet, J., Quilichini, P., Nimchinsky, E. A., and Buzsáki, G. (2010). Predominant enhancement of glucose uptake in astrocytes versus neurons during activation of the somatosensory cortex. *J. Neurosci.* 30, 15298–15303. doi: 10.1523/JNEUROSCI.0762-10.2010
- Clarke, L. E., Liddel, S. A., Chakraborty, C., Münch, A. E., Heiman, M., Barres, B. A. et al. (2018). Normal aging induces A1-like astrocyte reactivity. *Proc. Natl. Acad. Sci. U S A.* 115, E1896–E1905. doi: 10.1073/pnas.1800165115
- Derouiche, A., and Frotscher, M. (1991). Astroglial processes around identified glutamatergic synapses contain glutamine synthetase: evidence for transmitter degradation. *Brain Res.* 552, 346–350. doi: 10.1016/0006-8993(91)90103-3
- Farhy-Tselnick, I., and Allen, N. J. (2018). Astrocytes, neurons, synapses: a tripartite view on cortical circuit development. *Neural Dev.* 13:7. doi: 10.1186/s13064-018-0104-y
- Geissler, M., and Faissner, A. (2012). A new indirect co-culture set up of mouse hippocampal neurons and cortical astrocytes on microelectrode arrays. *J. Neurosci. Method* 204, 262–272. doi: 10.1016/j.jneumeth.2011.11.030
- Gottschling, C., Dzyubenko, E., Geissler, M., and Faissner, A. (2016a). The indirect neuron-astrocyte coculture assay: an in vitro set-up for the detailed investigation of neuron-glia interactions. *J. Vis. Exp.* 117:54757. doi: 10.3791/54757
- Gottschling, C., Geissler, M., Springer, G., Wolf, R., Juckel, G., and Faissner, A. (2016b). First and second generation antipsychotics differentially affect structural and functional properties of rat hippocampal neuron synapses. *Neuroscience* 337, 117–130. doi: 10.1016/j.neuroscience.2016.08.055
- Gottschling, C., Wegrzyn, D., Denecke, B., and Faissner, A. (2019). Elimination of the four extracellular matrix molecules tenascin-C, tenascin-R, brevican and neurocan alters the ratio of excitatory and inhibitory synapses. *Sci. Rep.* 9:13939. doi: 10.1038/s41598-019-50404-9
- Hales, C. M., Rolston, J. D., and Potter, S. M. (2010). How to culture, record and stimulate neuronal networks on micro-electrode arrays (MEAs). *J. Vis. Exp.* 39:2056. doi: 10.3791/2056
- Hennen, E., Czopka, T., and Faissner, A. (2011). Structurally distinct lewisX glycans distinguish subpopulations of neural stem/progenitor cells. *J. Biol. Chem.* 286, 16321–16331. doi: 10.1074/jbc.M110.201095
- Herz, J., Clouthier, D. E., and Hammer, R. E. (1992). LDL receptor-related protein internalizes and degrades uPA-PAI-1 complexes and is essential for embryo implantation. *Cell* 71, 411–421.
- Herz, J., Clouthier, D. E., and Hammer, R. E. (1993). Correction: LDL receptor-related protein internalizes and degrades uPA-PAI-1 complexes and is essential for embryo implantation. *Cell* 73:428. doi: 10.1016/0092-8674(93)90130-I
- Higashi, K., Fujita, A., Inanobe, A., Tanemoto, M., Doi, K., Kubo, T. et al. (2001). An inwardly rectifying K(+) channel, Kir4.1, expressed in astrocytes surrounds synapses and blood vessels in brain. *Am. J. Physiol. Cell Physiol.* 281, C922–C931. doi: 10.1152/ajpcell.2001.281.3.C922
- Hubbard, J. A., Szu, J. I., Yonan, J. M., and Binder, D. K. (2016). Regulation of astrocyte glutamate transporter-1 (GLT1) and aquaporin-4 (AQP4) expression in a model of epilepsy. *Exp. Neurol.* 283, 85–96. doi: 10.1016/j.expneurol.2016.05.003
- Jolly, S., Bazargani, N., Quiroga, A. C., Pringle, N. P., Attwell, D., Richardson, W. D., et al. (2018). G protein-coupled receptor 37-like 1 modulates astrocyte glutamate transporters and neuronal NMDA receptors and is neuroprotective in ischemia. *Glia* 66, 47–61. doi: 10.1002/glia.23198
- Liddel, S. A., and Barres, B. A. (2017). Reactive astrocytes: production, function, and therapeutic potential. *Immunity* 46, 957–967. doi: 10.1016/j.immuni.2017.06.006[snm]}
- Lillis, A. P., Van Duyn, L. B., Murphy-Ullrich, J. E., and Strickland, D. K. (2008). LDL receptor-related protein 1: unique tissue-specific functions revealed by selective gene knockout studies. *Physiol. Rev.* 88, 887–918. doi: 10.1152/physrev.00033.2007
- Liu, C.-C., Hu, J., Zhao, N., Wang, J., Wang, N., Cirrito, J. R., et al. (2017). Astrocytic LRP1 mediates brain A $\beta$  clearance and impacts amyloid deposition. *J. Neurosci.* 37, 4023–4031. doi: 10.1523/JNEUROSCI.3442-16.2017
- Liu, Q., Trotter, J., Zhang, J., Peters, M. M., Cheng, H., Bao, J., et al. (2010). Neuronal LRP1 knockout in adult mice leads to impaired brain lipid metabolism and progressive, age-dependent synapse loss and neurodegeneration. *J. Neurosci.* 30, 17068–17078. doi: 10.1523/JNEUROSCI.4067-10.2010
- Madisen, L., Zwingman, T. A., Sunken, S. M., Oh, S. W., Zariwala, H. A., Gu, H., et al. (2010). A robust and high-throughput Cre reporting and characterization system for the whole mouse brain. *Nat. Neurosci.* 13, 133–140. doi: 10.1038/nn.2467
- Mahmoud, S., Gharagzloo, M., Simard, C., and Gris, D. (2019). Astrocytes maintain glutamate homeostasis in the CNS by controlling the balance between glutamate uptake and release. *Cells* 8:184. doi: 10.3390/cells8020184
- Mauch, D. H., Nägler, K., Schumacher, S., Göritz, C., Müller, E.-C., Otto, A., et al. (2001). CNS synaptogenesis promoted by glia-derived cholesterol. *Science* 294, 1354–1357. doi: 10.1126/science.294.5545.1354
- May, P., and Herz, J. (2003). LDL receptor-related proteins in neurodevelopment. *Traffic* 4, 291–301. doi: 10.1034/j.1600-0854.2003.00086\_4\_5.x
- May, P., Rohlmann, A., Bock, H. H., Zurhove, K., Marth, J. D., Schomburg, E. D., et al. (2004). Neuronal LRP1 functionally associates with postsynaptic proteins and is required for normal motor function in mice. *Mol. Cell. Biol.* 24, 8872–8883. doi: 10.1128/MCB.24.20.8872-8883.2004
- Mori, T., Tanaka, K., Buffo, A., Wurst, W., Kühn, R., and Götz, M. (2006). Inducible gene deletion in astroglia and radial glia—a valuable tool for functional and lineage analysis. *Glia* 54, 21–34. doi: 10.1002/glia.20350
- Nakatsuji, Y., and Miller, R. H. (1998). Homotypic cell contact-dependent inhibition of astrocyte proliferation. *Glia* 22, 379–389. doi: 10.1002/(SICI)1098-1136(199804)22:4<379::AID-GLIA7>3.0.CO;2-Z
- Neame, S., Safory, H., Radziszewsky, I., Touitou, A., Marchesani, F., Marchetti, M., et al. (2019). The NMDA receptor activation by d-serine and glycine is controlled by an astrocytic Phgdh-dependent serine shuttle. *Proc. Natl. Acad. Sci. U.S.A.* 116, 20736–20742. doi: 10.1073/pnas.1909458116
- Orth, K., Madison, E. L., Gething, M. J., Sambrook, J. F., and Herz, J. (1992). Complexes of tissue-type plasminogen activator and its serpin inhibitor plasminogen-activator inhibitor type 1 are internalized by means of the low density lipoprotein receptor-related protein/alpha 2-macroglobulin receptor. *Proc. Natl. Acad. Sci. U S A.* 89, 7422–7426. doi: 10.1073/pnas.89.16.7422
- Papouin, T., Dunphy, J., Tolman, M., Foley, J. C., and Haydon, P. G. (2017). Astrocytic control of synaptic function. *Philos. Transac. Royal Soc. B Biol. Sci.* 372:20160154. doi: 10.1098/rstb.2016.0154
- Peterson, A. R., and Binder, D. K. (2019). Regulation of synaptosomal GLT-1 and GLAST during epileptogenesis. *Neuroscience* 411, 185–201. doi: 10.1016/j.neuroscience.2019.05.048
- Pfrier, F. W. (2003). Role of cholesterol in synapse formation and function. *Biochimica et Biophys. Acta Biomem.* 1610, 271–280. doi: 10.1016/S0005-2736(03)00024-5

- Regan, M. R., Huang, Y. H., Kim, Y. S., Dykes-Hoberg, M. I., Jin, L., Watkins, A. M., et al. (2007). Variations in promoter activity reveal a differential expression and physiology of glutamate transporters by glia in the developing and mature CNS. *J. Neurosci.* 27, 6607–6619. doi: 10.1523/JNEUROSCI.0790-07.2007
- Rehman, M. U., Mushtaq, M., and Sherkheli, M. A. (2017). Glutamine augments neuronal network activity in Rat hippocampal slices. *J. Ayub. Med. Coll. Abbottabad.* 29, 388–392.
- Renzel, R., Sadek, A.-R., Chang, C.-H., Gray, W. P., Seifert, G., and Steinhäuser, C. (2013). Polarized distribution of AMPA, but not GABAA, receptors in radial glia-like cells of the adult dentate gyrus. *Glia* 61, 1146–1154. doi: 10.1002/glia.22505
- Rohlmann, A., Gotthardt, M., Willnow, T. E., Hammer, R. E., and Herz, J. (1996). Sustained somatic gene inactivation by viral transfer of Cre recombinase. *Nat. Biotechnol.* 14, 1562–1565. doi: 10.1038/nbt1196-1562
- Safina, D., Schlitt, F., Romeo, R., Pflanzner, T., Pietrzik, C. U., Narayanaswami, V. et al. (2016). Low-density lipoprotein receptor-related protein 1 is a novel modulator of radial glia stem cell proliferation, survival, and differentiation. *Glia* 64, 1363–1380. doi: 10.1002/glia.23009
- Schäfer, I., Kaisler, J., Scheller, A., Kirchhoff, F., Haghighi, A., and Faissner, A. (2019). Conditional deletion of LRP1 leads to progressive loss of recombined NG2-expressing oligodendrocyte precursor cells in a novel mouse model. *Cells* 8:1550. doi: 10.3390/cells8121550
- Thrane, A. S., Rappold, P. M., Fujita, T., Torres, A., Bekar, L. K., Takano, T. et al. (2011). Critical role of aquaporin-4 (AQP4) in astrocytic Ca<sup>2+</sup> signaling events elicited by cerebral edema. *Proc. Natl. Acad. Sci. U S A.* 108, 846–851. doi: 10.1073/pnas.1015217108
- Ulc, A., Zeug, A., Bauch, J., van Leeuwen, S., Kuhlmann, T., Ffrench-Constant, C., et al. (2019). The guanine nucleotide exchange factor Vav3 modulates oligodendrocyte precursor differentiation and supports remyelination in white matter lesions. *Glia* 67, 376–392. doi: 10.1002/glia.23548
- Willnow, T. E., Christ, A., and Hammes, A. (2012). Endocytic receptor-mediated control of morphogen signaling. *Development* 139, 4311–4319. doi: 10.1242/dev.084467
- Xu, J., Xiao, N., and Xia, J. (2010). Thrombospondin 1 accelerates synaptogenesis in hippocampal neurons through neuroligin 1. *Nat. Neurosci.* 13, 22–24. doi: 10.1038/nn.2459
- Zhuang, Z., Huang, J., Cepero, M. L., and Liebl, D. J. (2011). Eph signaling regulates gliotransmitter release. *Commun. Integr. Biol.* 4, 223–226. doi: 10.4161/cib.4.2.14507
- Zuchero, J. B., and Barres, B. A. (2015). Glia in mammalian development and disease. *Development* 142, 3805–3809. doi: 10.1242/dev.129304.

**Conflict of Interest:** The authors declare that the research was conducted in the absence of any commercial or financial relationships that could be construed as a potential conflict of interest.

Copyright © 2021 Romeo, Glotzbach, Scheller and Faissner. This is an open-access article distributed under the terms of the Creative Commons Attribution License (CC BY). The use, distribution or reproduction in other forums is permitted, provided the original author(s) and the copyright owner(s) are credited and that the original publication in this journal is cited, in accordance with accepted academic practice. No use, distribution or reproduction is permitted which does not comply with these terms.



# Low-Density Lipoprotein Receptor-Related Protein 1 (LRP1) as a Novel Regulator of Early Astroglial Differentiation

Ramona Romeo<sup>1</sup>, Damian Boden-El Mourabit<sup>2</sup>, Anja Scheller<sup>3</sup>, Melanie D. Mark<sup>2</sup> and Andreas Faissner<sup>1\*</sup>

<sup>1</sup> Department of Cell Morphology and Molecular Neurobiology, Ruhr-University Bochum, Bochum, Germany, <sup>2</sup> Behavioral Neuroscience, Ruhr-University Bochum, Bochum, Germany, <sup>3</sup> Department of Molecular Physiology, Center for Integrative Physiology and Molecular Medicine (CIPMM), University of Saarland, Homburg, Germany

## OPEN ACCESS

### Edited by:

Christian Lohr,  
University of Hamburg, Germany

### Reviewed by:

Gustavo Alberto Chiabrando,  
National University of Córdoba,  
Argentina

Kyung Seok Han,  
Dongguk University Gyeongju,  
South Korea

### \*Correspondence:

Andreas Faissner  
andreas.faissner@rub.de

### Specialty section:

This article was submitted to  
Non-Neuronal Cells,  
a section of the journal  
Frontiers in Cellular Neuroscience

**Received:** 16 December 2020

**Accepted:** 26 January 2021

**Published:** 18 February 2021

### Citation:

Romeo R, Boden-El Mourabit D, Scheller A, Mark MD and Faissner A (2021) Low-Density Lipoprotein Receptor-Related Protein 1 (LRP1) as a Novel Regulator of Early Astroglial Differentiation. *Front. Cell. Neurosci.* 15:642521. doi: 10.3389/fncel.2021.642521

Astrocytes are the most abundant cell type within the central nervous system (CNS) with various functions. Furthermore, astrocytes show a regional and developmental heterogeneity traceable with specific markers. In this study, the influence of the low-density lipoprotein receptor-related protein 1 (LRP1) on astrocytic maturation within the hippocampus was analyzed during development. Previous studies mostly focused on the involvement of LRP1 in the neuronal compartment, where the deletion caused hyperactivity and motor dysfunctions in knockout animals. However, the influence of LRP1 on glia cells is less intensively investigated. Therefore, we used a newly generated mouse model, where LRP1 is specifically deleted from GLAST-positive astrocytes co-localized with the expression of the reporter tdTomato to visualize recombination and knockout events *in vivo*. The influence of LRP1 on the maturation of hippocampal astrocytes was assessed with immunohistochemical stainings against stage-specific markers as well as on mRNA level with RT-PCR analysis. The examination revealed that the knockout induction caused a significantly decreased number of mature astrocytes at an early developmental timepoint compared to control animals. Additionally, the delayed maturation of astrocytes also caused a reduced activity of neurons within the hippocampus. As previous studies showed that the glial specification and maturation of astrocytes is dependent on the signaling cascades Ras/Raf/MEK/Erk and PI3K/Akt, the phosphorylation of the signaling molecules Erk1/2 and Akt was analyzed. The hippocampal tissue of LRP1-deficient animals at P21 showed a significantly decreased amount of activated Erk in comparison to control tissue leading to the conclusion that the activation of this signaling cascade is dependent on LRP1 in astrocytes, which in turn is necessary for proper maturation of astrocytes. Our results showed that the deletion of LRP1 at an early developmental timepoint caused a delayed maturation of astrocytes in the hippocampus based on an altered activation of the Ras/Raf/MEK/Erk signaling



pathway. However, with ongoing development these effects were compensated and the number of mature astrocytes was comparable as well as the activity of neurons. Therefore, LRP1 acts as an early regulator of the differentiation and maturation of astrocytes within the hippocampus.

**Keywords:** astrocyte heterogeneity, differentiation, astrocyte functions, hippocampus, *in vivo* knockout model, LRP1

## INTRODUCTION

Astrocytes are the most abundant cell type within the central nervous system (CNS) and were formerly known as passive players supplying neurons with energy substrates and providing structural support (Yong et al., 1998; Gordon et al., 2007; Iadecola and Nedergaard, 2007; Sofroniew and Vinters, 2010). However, more recent studies prove that astrocytes are actively contributing to the neuronal transmission in forming the tripartite synapse with pre- and postsynapse (Bushong et al., 2004; Freeman, 2010; Savtchouk and Volterra, 2018). The majority of astrocytes are generated postnatally after the generation of neurons (Kriegstein and Alvarez-Buylla, 2009). The postnatal and terminal differentiation into astrocytes seem to be dependent on intracellular signaling cues (Qian et al., 2000; Shen et al., 2006). Previous studies have shown that the glial specification is influenced by the activation of the Ras/Raf/MEK/Erk pathway (Franzdóttir et al., 2009; Li et al., 2012). The activity of these signaling pathways is regulated by the formation of cell surface receptor complexes causing intracellular signaling cascades. One known activator of the Ras/Raf/MEK/Erk pathway is the complex formation between the low-density lipoprotein receptor-related protein 1 (LRP1) with the platelet-derived growth factor receptor  $\beta$  (PDGFR $\beta$ ) (Boucher et al., 2002; Loukinova et al., 2002) or tropomyosin receptor kinase A (trkA) (Spuch et al., 2012). Furthermore, the association of LRP1 with PDGFR $\beta$  also influences the activation of the PI3K/Akt pathway, another important signaling cascade involved in glia specification (Muratoglu et al., 2010).

LRP1 is a member of the low-density lipoprotein receptor (LDL) superfamily and is also known as CD91 or  $\alpha$ 2-macroglobulin receptor (Binder et al., 2000; Liu et al., 2000; Marschang et al., 2004). The receptor is ubiquitously expressed but enriched in liver, blood vessels and the CNS (Lillis et al., 2005). The receptor consists of an extracellular, 515 kDa  $\alpha$ -chain and an intracellular, 85 kDa  $\beta$ -chain, non-covalently bound on the cell surface (Lillis et al., 2005). Over 40 potential ligands are known for LRP1 and ligand binding to LRP1 leads to endocytosis of the whole complex, making LRP1 formerly known for its endocytic function (Lillis et al., 2005; Bres and Faissner, 2019). In addition, LRP1 can form complexes with other receptors leading to the activation of intracellular pathways. Thereby, LRP1 was unraveled as a regulator for different cellular processes, such as proliferation (Zhang and Liu, 2002), differentiation (Seger and Krebs, 1995; Ortega and Alcántara, 2010; Safina et al., 2016) and apoptosis (Burris, 2013; Kumar et al., 2013). Total loss of LRP1 within the whole organism leads to embryonic lethality, highlighting the importance of LRP1 (Herz et al., 1992, 1993).

However, the influence of LRP1 in regard to astrocyte function was not intensively studied. The deletion of LRP1 in astrocytes caused a negatively influenced cellular uptake of A $\beta$  and degradation involved in Alzheimer's Disease (AD) progression (Liu et al., 2017). The deletion of LRP1 from radial glia cells resulted in altered numbers of astroglial subpopulations *in vivo* (Bres et al., 2020). Furthermore, we investigated the influence of LRP1 on astrocytes *in vitro*, where we observed that the knockout of LRP1 in primary cortical astrocytes caused an altered expression of mature astrocytic markers. Additionally, the functionality of astrocytes in regard to the neuronal transmission as well as on synaptogenesis of hippocampal neurons was negatively influenced (Romeo et al., 2021).

Based on the findings and preliminary data we decided to investigate the influence of LRP1 on the maturation and functions of hippocampal astrocytes *in vivo*. Therefore, we used our newly generated mouse model (Romeo et al., 2021), where LRP1 is specifically deleted from GLAST-positive astrocytes via the intraperitoneal injection of Tamoxifen into lactating mothers causing the loss of LRP1 in their litters. Via the expression of the reporter tdTomato, we were able to visualize recombination events as well as the deletion of LRP1. The maturation of astrocytes in LRP1-deficient tissue was assessed via immunohistochemical stainings as well as with RT-PCR. Additionally, we wanted to further characterize our knockout model and performed behavioral tests to investigate the motor coordination and cognitive abilities.

## MATERIALS AND METHODS

### Animals

As previously described (Romeo et al., 2021), we generated a new triple transgenic mouse model where *Lrp1* was specifically deleted from GLAST-positive astroglial precursor cells by using the GLAST::CreERT2-mouse line (Mori et al., 2006) bred with the LRP1<sup>flox/flox</sup>-mouse line (Rohlmann et al., 1996). For the mating of control, respectively, knockout animals, animals with a heterozygous expression of the Cre recombinase under the GLAST promotor were used (Romeo et al., 2021). Therefore, not all pups of the litters were suitable for the study as some expressed the Cre recombinase homozygously or not at all. Additionally, the application of Tamoxifen to lactating mothers caused mortality of the pups. This study was performed in approval with the State Agency for Nature, Environment and Consumer Protection Northrhine-Westphalia (Landesamt fuer Umweltschutz, Naturschutz und Verbraucherschutz; file number: 84-02.04.2016.A482). The animals were housed with a

12 h light/dark cycle and access to food and water *ad libitum*. To induce the knockout in the new born pups lactating mothers received 100 mg/kg of bodyweight of a 10 mg/ml stock solution of Tamoxifen (TAM; Sigma Aldrich, Chemie GmbH, Munich, Germany, Catalog-No.: t5648) in corn oil 5 days after birth. TAM was applied for 5 days in a row in accordance to Jahn et al. (2018). The genotyping of the animals was performed as described in Romeo et al. (2021). Briefly, tail biopsies were taken and lysed with 200  $\mu$ l of *DirectPCR® Lysis Reagent Tail* (Peqlab, VWR Life Science, Radnor, PA) and 0.2 mg/ml Proteinase-K (Sigma-Aldrich, Chemie GmbH, Munich, Germany) at 55°C at 350 rpm overnight. The lysis was stopped by heating the samples to 85°C for 45 min at 350 rpm. For the genotyping, gene-specific primers were used.

## Transcardial Perfusion of Animals

For the investigation of the influence of LRP1 on the maturation of astrocytes and their functionality, three developmental stages were analyzed (P21, P28, and P56-P70, summarized as adult). At the stage-specific age either control or knockout animals were anesthetized with 100 mg/kg ketamine (CP-Pharma, Burgdorf, Germany), 10 mg/kg Xylazin (CP-Pharma) in 0.9% NaCl. Afterward, the animals were transcardially perfused with phosphate buffered saline (PBS; 137 mM sodium chloride, 3 mM potassium chloride, 6.5 mM disodium hydrogen phosphate, 1.5 mM potassium dihydrogen phosphate; pH 7.3) and subsequently with 4% (w/v) paraformaldehyde (PFA) when the tissue was used for immunohistochemistry. Tissue for the RNA and protein isolation was prepared and transferred to a dish containing PBS. Then the hippocampus was removed and frozen in liquid nitrogen until further use.

## Immunohistochemistry

Prepared tissue was post-fixed in 4% (w/v) PFA for additional 6 h and then dehydrated in a sucrose gradient (10%, 20%, 30% (w/v) sucrose in PBS). Afterward, the tissue was embedded in Tissue Freezing Medium (Leica, Wetzlar, Germany) at  $-80^{\circ}\text{C}$  until further use. Cryosections of 14  $\mu\text{m}$  were prepared. The cryosections were stained as previously described (Schäfer et al., 2019; Ulc et al., 2019). Shortly, cryosections were transferred to citric acid buffer (solution A: 0.1 M citric acid-1-hydrate, solution B: 0.1 M Na-citrate-dihydrate; 1 mM of solution A and 4 mM of solution B in *aqua dest.*) for 1 h at  $70^{\circ}\text{C}$ . After cooling and blocking (10% (v/v) normal goat serum (NGS; Jackson Immuno Research Labs, Catalog-No.: 005-00-121; AB\_2336990) in PBT-1 [10% (v/v) BSA, 0.1% (v/v) Triton-X 100 in PBS]) for 1 h, primary antibodies were diluted in blocking solution and sections were incubated over night at  $4^{\circ}\text{C}$ . For our analysis we used the following primary antibodies: LRP1 (1:500, Abcam, Catalog-No.: ab92544; AB\_2234877), GFAP (1:300, DAKO, Catalog-No.: Z0334; AB\_10013382), GLT-1 (EAAT2; 1:100, Santa Cruz, Catalog-No.: sc-365634; AB\_10844832), S100 (1:750, Sigma-Aldrich, Catalog-No.: ab868; AB\_306716), c-Fos (1:500, Abcam, Catalog-No.: ab208942; AB\_2747772), CC1 (APC; 1:100, Abcam, Catalog-No.: ab16794; AB\_443473), NeuN (1:500, Millipore, Catalog-No.: MAB377; AB\_2298772) and phospho-Histone H3 (PH3; 1:300, Millipore, Catalog-No.:

06-570; AB\_310177). Further on, sections were washed thrice with PBS for 20 min, followed by incubation with appropriate secondary antibodies diluted in PBS/A (0.1% bovine serum albumin (w/v; BSA; Sigma-Aldrich, Catalog-No.: A7030) in PBS) for 2 h at room temperature. We used the following secondary antibodies coupled with Cy2: Goat anti-mouse Cy2, Jackson Immuno Research Labs, Catalog-No.: 115-545-044; AB\_2338844 and Goat anti-rabbit Cy2, Jackson Immuno Research Labs, Catalog-No.: 111-545-045; AB\_2338049 (1:250) and the cell nuclei marker Hoechst (1:100). Further on, the washing steps with PBS were repeated in the dark and the sections were covered with Immu-Mount (Thermo Fisher Scientific, Waltham, Massachusetts, United States; Catalog-No.: 9990402). Images were taken with the AxioZoom by Zeiss (Oberkochen, Germany).

## RNA Isolation, cDNA Synthesis and Real-Time PCR Analysis

One hippocampal half of animals was lysed with lysis buffer of the Gene Elute Mammalian Total RNA Miniprep Kit (Sigma Aldrich; Catalog-No.: RTN350-1KT) and RNA was isolated according to manufacturer's manual. To synthesize cDNA, 1  $\mu\text{g}$  of RNA was used in accordance to the First Strand cDNA-synthesis Kit (Fermentas, Waltham, MA, United States; Catalog-No.: K1612). To investigate the maturation of astrocytes within astrocyte-specific LRP1-depleted hippocampi, stage-specific astroglial markers were used (see Table 1) with  $\beta$ -actin as reference gene.

## Sample Synthesis and Western Blotting

The other hippocampal half was lysed with radioimmunoprecipitation assay buffer (RIPA; 10 mM Tris-HCl (pH 8.0), 1 mM ethylenediaminetetraacetic acid (EDTA), 0.5 mM ethylene glycol-bis( $\beta$ -aminoethyl ether)-N,N,N',N'-tetraacetic acid (EGTA), 1% (v/v) Triton X-100, 0.1% (w/v) sodium deoxycholate, 0.1% (v/v) sodium dodecyl sulphate (SDS), 140 mM NaCl, Sigma) with 1% (v/v) of protease inhibitors phenylmethylsulfonyl fluoride (PMSF) and 1% (v/v) aprotinin (APR). The tissue was manually lysed and further on triturated with pipettes to dissolve the tissue. Protein concentration was measured with the Pierce™ BCA™ Protein Assay (Thermo Fisher Scientific). For the western blot analysis 30  $\mu\text{g}$  of protein was applied to a 12% sodium dodecyl sulfate polyacrylamide (SDS) gel as described in Hennen et al. (2011). We used following primary antibodies: LRP1 (1:10,000, Abcam, Catalog-No.: ab92544; AB\_2234877), pAkt (1:5,000, Cell Signaling Technologies, Catalog-No.: #4,060, AB\_2315049), tAkt (1:5,000; Cell Signaling Technologies, Catalog-No.: #4,691, AB\_915783), pErk1/2 (1:5,000; Santa Cruz, Catalog-No.: sc-7383, AB\_627545), tErk1/2 (1:5,000; Santa Cruz, Catalog-No.: sc-514302, AB\_2571739), GLT-1 (EAAT2; 1:200, Santa Cruz, Catalog-No.: sc-365634; AB\_2571739) and  $\alpha$ -tubulin (1:5,000, Sigma Aldrich, Catalog-No.: T9026, AB\_477593), used as control and for normalization. The protein expression was detected with the Clarity™ Western ECL Substrate by BioRad (Feldkirchen, Germany) and visualized with the MicroChemie chemiluminescence device with the Gel Capture Software by biostep (Burkhardtsdorf, Germany; Version: 6.6).

**TABLE 1** | Investigated genes in the expression profile analysis of hippocampal tissue of either LRP1-deficient animals compared to control animals *in vivo*.

Gene	Primer sequence	GenBank no.
<i>β-actin</i>	F: 5'-TATGCCAACACAGTGTCTGTGGTGG-3' R: 5'-TAGAAGCATTGCGGTGGACAATGG-3'	NM_007393.5
<i>Akt1</i>	F: 5'-5'-CGACGTAGCCATTGTGAAGG-3' R: 5'-CTTCCTGCCTCTTGAGTCCA-3'	NM_009652.3
<i>Aldh1l1</i>	F: 5'-GGAAGTTGAGAGGGGAGGAC-3' R: 5'-GGAAGTTGAGAGGGGAGGAC-3'	BC030730.1
<i>Aquaporin-4</i>	F: 5'-TTGCTTTGATCAGCATTG-3' R: 5'-TGAGCTCCACATCAGGACAG-3'	NM_009700.3
<i>Fgfr3</i>	F: 5'-GTCCTGTTCTGGCCAATGTT-3' R: 5'-GTTTCTGGCAGCCAAGTCTC-3'	NM_001205270.1
<i>Gfap</i>	F: 5'-CGACTATCGCCGCAACTGC-3' R: 5'-GCGATCTCGATGTCAGGGCT-3'	NM_001131020.1
<i>Glast</i>	F: 5'-GGCGGCCCTAGATAGTAAGG-3' R: 5'-AGAGTCTCCATGGCCTCTGA-3'	XM_021208184.2
<i>Glt-1</i>	F: 5'-ATGATCATGTGGTACTCCCTC-3' R: 5'-TTGTCGTCGTAATGGACTGC-3'	NM_001077514.4
<i>Gria1</i>	F: 5'-CCGTTGACACATCCAATCAG-3' R: 5'-GTTGGCGAGGATGTAGTGGT-3'	NM_001113325.2
<i>Gria2</i>	F: 5'-AACGGCGTGAATCCTTGAC-3' R: 5'-CTCCTGCATTTCCTCTCTG-3'	NM_013540.3
<i>Grin1</i>	F: 5'-CGGCTCTTGAAGATACAGC-3' R: 5'-TTGTAGACGCGCATCATCTC-3'	NM_008169.3
<i>Grin2a</i>	F: 5'-GCTGTCAGCACTGAATCCAA-3' R: 5'-ATCCCTGGGAGAACTTGCTT-3'	NM_008170.3
<i>Grin2b</i>	F: 5'-GTGAGAGCTCCTTTGCCAAC-3' R: 5'-GGGTTGGAAGTGTCCCTAT-3'	NM_008171.3
<i>Lrp1</i>	F: 5'-GGTAGTTGTTTCTCAATGCTC-3' R: 5'-TGTTGCTGACTAACAACCTGCT-3'	NM_008512.2
<i>Lrp2</i>	F: 5'-CTTCTGATGAGTCCGCTTGC-3' R: 5'-AGTTCCATTGCTGCACTTG-3'	NM_001081088.2
<i>Mtor</i>	F: 5'-CTTGCTGATCCTCAACGAGC-3' R: 5'-CTGGATCAGCGAGTTCTTGC-3'	NM_020009.2
<i>Nestin</i>	F: 5'-CTCGAGCAGGAAGTGGTAGG-3' R: 5'-GTTAGCGCTGCCRCRAGACC-3'	NM_016701.3
<i>S100</i>	F: 5'-TGCTTCCACCAGTACTCCG-3' R: 5'-ACTCCTGGAAGTCACACTCC-3'	NM_009115.3

The used primers were self-designed with the according nucleotide sequence (see GenBank No.).

## Motor and Cognitive Behavior Tests

To investigate if the absence of astroglial LRP1 has an influence on the behavior or motor coordination, we used six conditional knockout animals (GLAST<sup>CreERT2/wt</sup>Rosa26<sup>fl/fl</sup>LRP1<sup>fl/fl</sup>; 4 males, 2 females) and five control animals (GLAST<sup>CreERT2/wt</sup>Rosa26<sup>fl/fl</sup>LRP1<sup>wt/wt</sup>; 4 males, 1 female) at the age of 2 months, for all tests. The rotarod test assessed the motor coordination as well as the balance of the knockout animals in comparison to the control animals as described (Mark et al., 2011; Maejima et al., 2013). Briefly, after acclimation to the rotarod device (Columbus Instruments) with four rotations per minute (rpm) for 1 min the rod was accelerated at 0.1 rpm/s up to 40 rpm. Speed and latency to fall were recorded and averaged from three trials per mouse. To test for fine motor coordination mice were tested on the beam walk. Mice were placed on a horizontally 70 cm long beam (1 cm wide and 60 cm above the table surface) with a 20 cm<sup>2</sup> goal box. The animals underwent 2 days of training (six trials per day) before the data was collected. The time to transverse the beam, idle time (immobile time at start), the number of slips of the right and left hindlimbs and falls were investigated. Animals were given a maximum of 120 s to reach the goal box or for a fall. The collected data was averaged over three trials per mouse. The muscle strength of the mice was evaluated with the hangwire test. Mice were placed upside down on a wire screen (1.2 × 1.2 cm) 50 cm above a cage and the latency to fall was recorded. Another test to investigate motor coordination and balance is the vertical pole test. Here, the mice were placed on a 50 cm vertical metal pole (1 cm diameter) facing upwards. The latency to descend down to the cage was recorded. When the animals fell down or slid down the pole rear end first, the maximum of 120 s was given. To assess the cognitive abilities that are related to memory and learning processes the 2-object novel object recognition test (NOR) based on the established

protocol (Lueptow, 2017) was used. Briefly, the test consisted of 3 days, habituation to the arena (50 × 50 cm), testing to two similar objects and testing to one familiar and one novel object. The latency to investigate the new object in comparison to the familiar one was recorded and defined as the preference index. Cognitive functions of the mice were also investigated using the T-maze test (Deacon and Rawlins, 2006). Briefly, mice were placed in a T-shaped arena and explored the left or right arm of the T. The mice chose one arm based on curiosity. When the mouse entered one of the arms in the T a door at the start of the arm was closed to allow 30 s exploration. Then the mice were again placed at the start of the arena and were allowed to choose one arm. Unperturbed animals would explore the previously unknown arm of the arena, whereas impaired animals were not able to remember which part was already explored. Five trials per animal were averaged and the alternation value was evaluated.

For the statistical analyses, we firstly evaluated if the data was normally distributed with the Shapiro-Wilk-Normality test. As the data was normally distributed the Student's *t*-test was used to investigate the level of significance (\**p* ≤ 0.05, \*\**p* ≤ 0.01, \*\*\**p* ≤ 0.001).

## Statistical Analyses

The immunohistochemical stainings were investigated with the cell counter plug-in by Image J. Here, all tdTomato-positive cells were quantified in the spaces between the *Cornu Ammonis* layers of the hippocampus to provide the most accurate quantification of recombined cells (see **Supplementary Figure 1**). Afterward, all marker-specific and tdTomato-double positive cells were quantified to evaluate specificity of recombination. Exemplary double-positive cells, meaning tdTomato- and marker-positive cells, were highlighted with arrowheads in the figures. Additionally, the nuclei within the molecular layers



of the hippocampus were evaluated to investigate the number of recombined cells. Intensity of the bands of the PCR and western blot analyzes were also measured with ImageJ. The band intensities were normalized to the expression of  $\beta$ -actin, respectively,  $\alpha$ -tubulin. The results are shown as the mean  $\pm$  the standard error of the mean (SEM). The endpoint-PCR analysis was used as a semi-quantitative method to analyze potentially differentially expressed genes after knockout indication. The cycle number for the RT-PCR were below the amplificate saturation level. The depicted PCR results are only shown as an example. For the statistical analyses, we firstly evaluated if the data was normally distributed with the Shapiro-Wilk-Normality test. As the data was normally distributed, we used the two-way ANOVA with *post-hoc* Bonferroni test to analyze the level of significance (\* $p \leq 0.05$ , \*\* $p \leq 0.01$ , \*\*\* $p \leq 0.001$ ).

## RESULTS

### Successful Deletion of LRP1 in Hippocampal Astrocytes

We have previously shown that the deletion of *Lrp1* in neural stem and precursor cells leads to an increased number in GFAP-positive astrocytes (Safina et al., 2016) and that the absence of *Lrp1* in astrocytes caused a delayed maturation and an altered neuronal transmission in neurons *in vitro* (Romeo et al., 2021). Here we were interested how the deletion of astroglial *Lrp1* affects the differentiation of astrocytes and the functionality *in vivo*. Therefore, we used the already described triple transgenic mouse line GLAST::CreERT2xLRP1 (Romeo et al., 2021). In this mouse model LRP1 was specifically deleted in GLAST-positive astrocytes and the recombination events were visualized with the expression of the reporter tdTomato. In this study, we used LRP1-deficient animals (GLAST<sup>CreERT2</sup>/wt<sup>Rosa26<sup>fl/fl</sup></sup>LRP1<sup>fl/fl</sup>; further referred to as LRP1<sup>fl/fl</sup> or knockout) and control animals, with expression of tdTomato (GLAST<sup>CreERT2</sup>/wt<sup>Rosa26<sup>fl/fl</sup></sup>LRP1<sup>wt/wt</sup>; further referred to as LRP1<sup>wt/wt</sup> or control). To induce the conditional knockout, tamoxifen (TAM) was applied to lactating mothers. The application of TAM caused release of CreERT2 from HSP90 and translocation to the nucleus, subsequently followed by the excision of loxP-flanked genes, (*Lrp1* and the stop codon upstream of *Tdtomato* to induce the expression of the reporter) (Weber et al., 2001; Mori and Zhang, 2006). First, we evaluated the recombination efficiency in control and conditional knockout mice at three developmental stages via immunohistochemistry (P21, P28 and adult) within the hippocampus. Therefore, we quantified all tdTomato-positive cells divided by the total number of Hoechst-positive cell nuclei in the molecular layers of the hippocampus. The quantification showed that at P21 92.51%  $\pm$  1.73% of the cells in control animals and 94.21%  $\pm$  0.36% of the cells in the conditional knockout were recombined (see **Figures 1A,B**). At P28 the recombination efficiency was similar to P21 (85.48%  $\pm$  1.92% in the control mice and 90.97%  $\pm$  2.13% in the knockout mice, respectively). The number of recombined cells was stable over time. At the adult stage around 96.77%  $\pm$  0.24% of the cells were still tdTomato-positive in LRP1-deficient animals

in comparison to 95.4%  $\pm$  0.35% in control mice. Next, we investigated the number of LRP1- and tdTomato-double positive cells in both conditions to evaluate the knockout efficiency. Therefore, the number of LRP1- and tdTomato-double positive cells were divided by the number of all tdTomato-positive cells. The expression of LRP1 was significantly decreased in the knockout condition compared to the control condition (P21: LRP1<sup>wt/wt</sup> 59.76%  $\pm$  2.48%, LRP1<sup>fl/fl</sup> 5.83%  $\pm$  1.36%,  $p \leq 0.0001$ ; P28: LRP1<sup>wt/wt</sup> 71.05%  $\pm$  3.8%, LRP1<sup>fl/fl</sup> 7.15%  $\pm$  1.88%,  $p \leq 0.0001$ ; adult: LRP1<sup>wt/wt</sup> 63.45%  $\pm$  3.82%, LRP1<sup>fl/fl</sup> 2.51%  $\pm$  0.56%,  $p \leq 0.0001$ ) at all investigated time points (see **Figures 1A,C**). To further validate the downregulation of LRP1 in the knockout animals, we performed PCR and western blot analysis. The relative expression of LRP1 was not affected by the knockout induction (see **Figures 1D,E**). Furthermore, the western blot analysis showed no significant alterations in the protein expression of LRP1 (see **Figures 1F,G**). However, it needs to be considered that hippocampal tissue was used including other cell types expressing LRP1.

To confirm that the deletion of LRP1 only affected the astroglial lineage an immunohistochemical staining against NeuN and CC1 was performed to exclude neurons and oligodendrocytes. Therefore, knockout tissue of P28 mice was used and almost no co-localization of tdTomato with either NeuN-positive neurons or CC1-positive oligodendrocytes were observed, meaning that the vast majority of cells lacking LRP1 were astrocytes (see **Figure 2A**). Additionally, we analyzed the weight of LRP1-deficient animals and compared the values to control animals and we saw no difference (see **Figure 2B**). Due to the similar structure and comparable functions in regard to endocytosis (Auderset et al., 2016), we were interested if the LDL-family member LRP2 was upregulated in hippocampal tissue of LRP1-deficient animals during the development as a compensatory effect. We investigated the expression of the LDL-family member via PCR. The expression of LRP2 was not altered in LRP1-deficient hippocampal tissue in comparison to control tissue (see **Figures 2C,D**).

### LRP1 Did Not Influence Proliferation of Hippocampal Astrocytes at P21

Due to the high number of potential ligands LRP1 is known to influence several cellular processes including proliferation. Therefore, we investigated the proliferation capacity of recombined astrocytes via immunohistochemistry (see **Figure 3A**). The numbers of phospho-Histone H3 (PH3)- and tdTomato-double positive cells were quantified (see **Figure 3B**). The quantification revealed that the absence of LRP1 caused no altered proliferation rate. Therefore, the number of PH3- and tdTomato-positive cells were comparable in both conditions.

### No Changes in Astroglial Maturation After Loss of LRP1

We analyzed whether the deletion of LRP1 had any influence on the gene expression of several markers specific for the late precursor or immature astroglial stage (see **Figure 4**). To identify late precursor cells favoring an astroglial fate, we used *Glaxt*



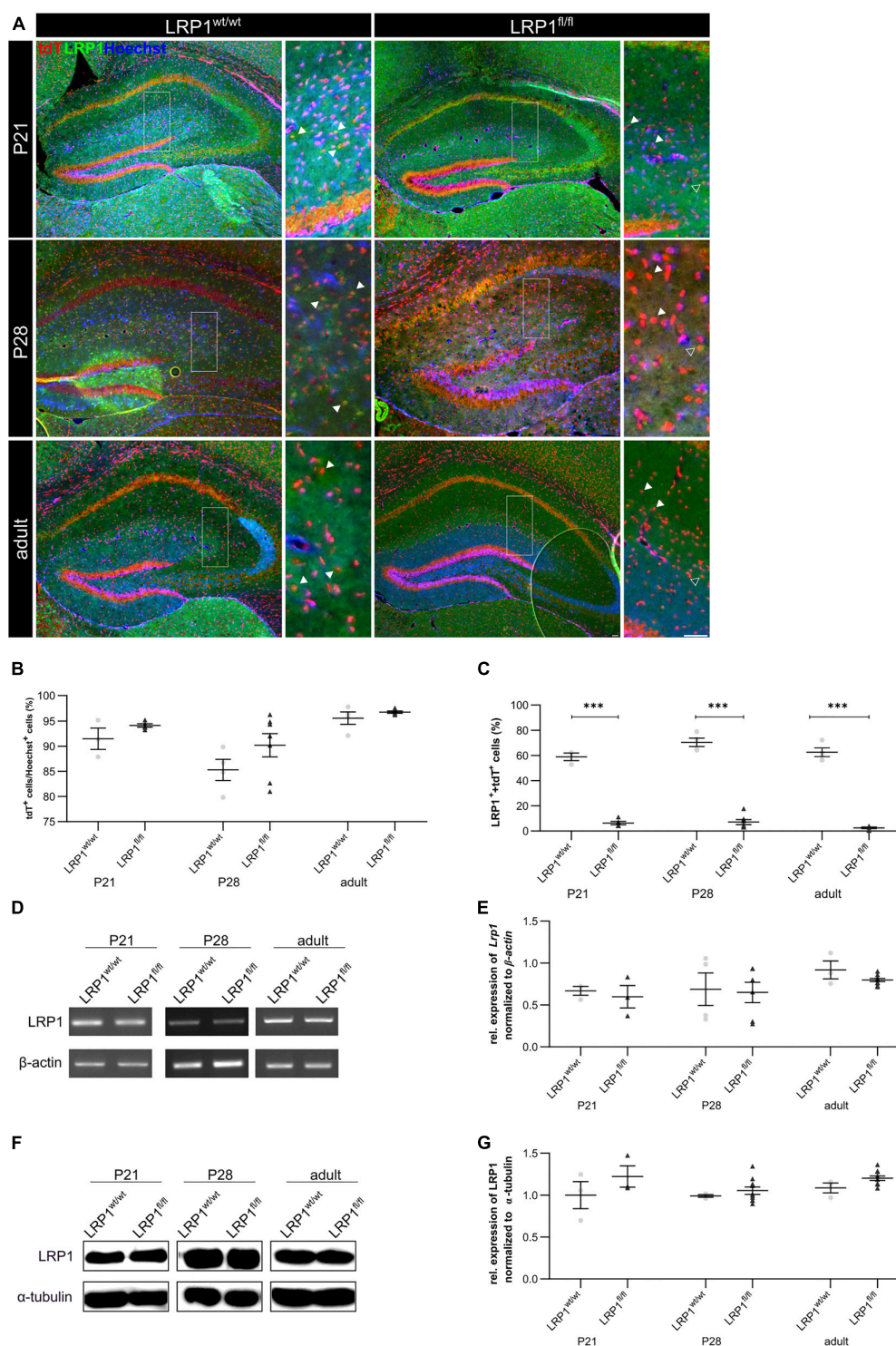


**FIGURE 1 |** Knockout induction via lactating mothers was successful *in vivo*. The immunohistochemical staining against LRP1 (green) and tdTomato (red) revealed the expression of LRP1 by recombined astrocytes during development indicated by the arrowhead (A). The recombination rate differed between 85 and 97% during development in LRP1-deficient and control hippocampi (B). The knockout efficiency was evaluated by the quantification of LRP1- and tdTomato-double positive cells divided by the total number of recombined cells within the hippocampus. Here the quantification showed that the number of LRP1-expressing recombined cells was significantly decreased in the knockout compared to the control (C). Furthermore, the knockout induction was evaluated via RT-PCR (D). The gene expression of *Lrp1* was not altered in LRP1-deficient hippocampi during development compared to control tissue (E). As a last approach the protein expression of LRP1 was analyzed with western blot analysis (F). The protein expression was comparable in both conditions during development (G) (Scale bar is 50 μm; mean ± SEM; two-way ANOVA with *post-hoc* Bonferroni test; \**p* < 0.05, \*\**p* < 0.01, \*\*\**p* < 0.001; for *N*-values see Table 2).

**TABLE 2 |** Number of biological N for each performed experiment.

	LRP1 <sup>wt/wt</sup>	LRP1 <sup>fl/fl</sup>
Immunohistochemistry	P21: N = 3 P28: N = 4 Adult: N = 4	P21: N = 5 P28: N = 7 Adult: N = 6
PCR/western blot	P21: N = 3 P28: N = 4 Adult: N = 3	P21: N = 3 P28: N = 6 Adult: N = 10
Weight	P21: N = 6 P28: N = 3 Adult: N = 9	P21: N = 8 P28: N = 17 Adult: N = 17
Behavioral tests	N = 5	N = 6

The number of samples differed between each genotype and developmental timepoint due to the sample preparation.

(see **Figures 4A,B**) and *Fgfr-3* (see **Figures 4A,C**), whereas immature astrocytes were investigated via the expression of *Aqp-4* (see **Figures 4A,D**) as well as *Aldh1l1* (see **Figures 4A,E**). The gene expression analysis revealed no changes of any marker in hippocampal tissue of LRP1-deficient animals compared to the control condition, highlighting that LRP1 has no influence on astroglial maturation based on the analyzed markers.

## Decreased Quantity of GFAP-Positive Astrocytes in the Hippocampus at P21

We previously reported that the deletion of *Lrp1* in neural stem and progenitor cells (NSPCs) caused an increased number of glial fibrillary acidic protein (GFAP)-positive astrocytes (Safina et al., 2016; Bres et al., 2020). However, LRP1-deficient astrocytes did not show a reactive phenotype *in vitro* (Romeo et al., 2021). Via the immunohistochemical staining against GFAP, we wanted to investigate the influence of the LRP1 deletion in regard to a reactive phenotype and in terms of maturation, where GFAP is mainly expressed by mature astrocytes *in vivo* (see **Figure 5A**). The quantification of GFAP- and tdTomato-double positive cells revealed that the deletion of LRP1 led to a significantly decreased number of double positive cells ( $19.73\% \pm 1.68\%$ ) in comparison to the control tissue ( $39.11\% \pm 2.24\%$ ;  $p \leq 0.01$ ) at P21 (see **Figure 5B**). With ongoing development, the number of GFAP- and tdTomato-positive astrocytes increased in the knockout mice and was comparable to the control condition reaching adulthood where the numbers stabilized.

Furthermore, mRNA expression of *Gfap* was investigated to support the findings of the immunohistochemical staining (see **Figure 5C**). Contrary to immunohistochemical data, the mRNA analysis showed that the astroglial loss of *Lrp1* had no effect on *Gfap* mRNA expression at any developmental stage in the hippocampus compared to the control tissue (see **Figure 5D**).

Additionally, the number of S100 calcium binding protein  $\beta$  (S100)-positive cells was evaluated to investigate the maturation of LRP1-depleted astrocytes (see **Figure 6A**). The immunohistochemical staining showed that the number of S100- and tdTomato-positive cells was significantly downregulated in LRP1-deficient hippocampi ( $16.55\% \pm 2.88\%$ ) when compared to control tissue ( $28.45\% \pm 2.44\%$ ;  $p \leq 0.05$ ) at P21 (see **Figure 6B**). The number of double positive cells was comparable

in control and LRP1-deficient mice with ongoing development. However, similar to GFAP, the mRNA expression of *S100* was not affected by the deletion of LRP1 in astrocytes (see **Figures 6C,D**).

The data indicates that LRP1 mainly influences the maturation of astrocytes in early development in the hippocampus. However, these differences were compensated with increasing age of the animals. Additionally, the regulation by the knockout induction occurred mainly on protein level as the mRNA expression was not affected by the absence of LRP1, contrary to the number of marker-positive cells.

## Expression of Glutamate Transporter GLT-1 Was Not Altered in Astrocytes Upon LRP1 Deletion

Astrocytes have diverse functions and can contribute to different cellular processes. They are involved in synaptic transmission via the uptake of neurotransmitters, like glutamate, out of the synaptic cleft. Therefore, the expression of the glutamate transporter 1 (GLT-1) on the cell surface of LRP1-deficient astrocytes was investigated (see **Figure 7A**). The quantification of the immunohistochemical staining revealed no alterations in the number of GLT-1- and tdTomato-positive cells in early development at P21 (see **Figure 7B**). With increasing age, GLT-1 becomes the main glutamate transporter and the number of GLT-1-positive astrocytes should increase. Our analysis showed that the number of GLT-1- and tdTomato-positive cells increased in controls and LRP1-deficient mice but slightly decreased reaching adulthood. Although, no changes in *Glt-1* mRNA expression were observed (see **Figure 7C**). The analysis showed no alterations in the expression of *Glt-1* in LRP1-deficient hippocampal tissue at all three investigated timepoints in comparison to the control tissue (see **Figure 7D**). Furthermore, the protein expression of GLT-1 was not affected by the depletion of LRP1 as well (see **Supplementary Figures S2A,B**).

## LRP1-Deficient Hippocampal Tissue Showed Significantly Decreased Activity of the Ras/Raf/MEK/Erk-Signaling Pathway at P21

The deletion of LRP1 in astrocytes mainly influenced the maturation at an early developmental timepoint. As previously described the maturation of glial cells is dependent on the Ras/Raf/MEK/Erk and PI3K/Akt signaling cascade. Therefore, we were interested whether the phosphorylation of the signaling molecules Erk1/2 and Akt were influenced by the deletion of LRP1 in astrocytes and therefore might explain the delayed maturation we observed at P21 (see **Figure 8**). The western blot analysis showed a significant downregulation of the active phospho-Erk (pErk) in P21 hippocampal tissue after astroglial loss of LRP1 ( $0.418 \pm 0.197$ ) compared to controls ( $1.138 \pm 0.092$ ;  $p \leq 0.05$ ) (see **Figures 8A,B**). However, with ongoing maturation the protein expression was comparable in both conditions. The activation of pErk in astrocytes was strongly decreased as we investigated hippocampal tissue including other cell types, also expressing several signaling molecules, such as pErk.

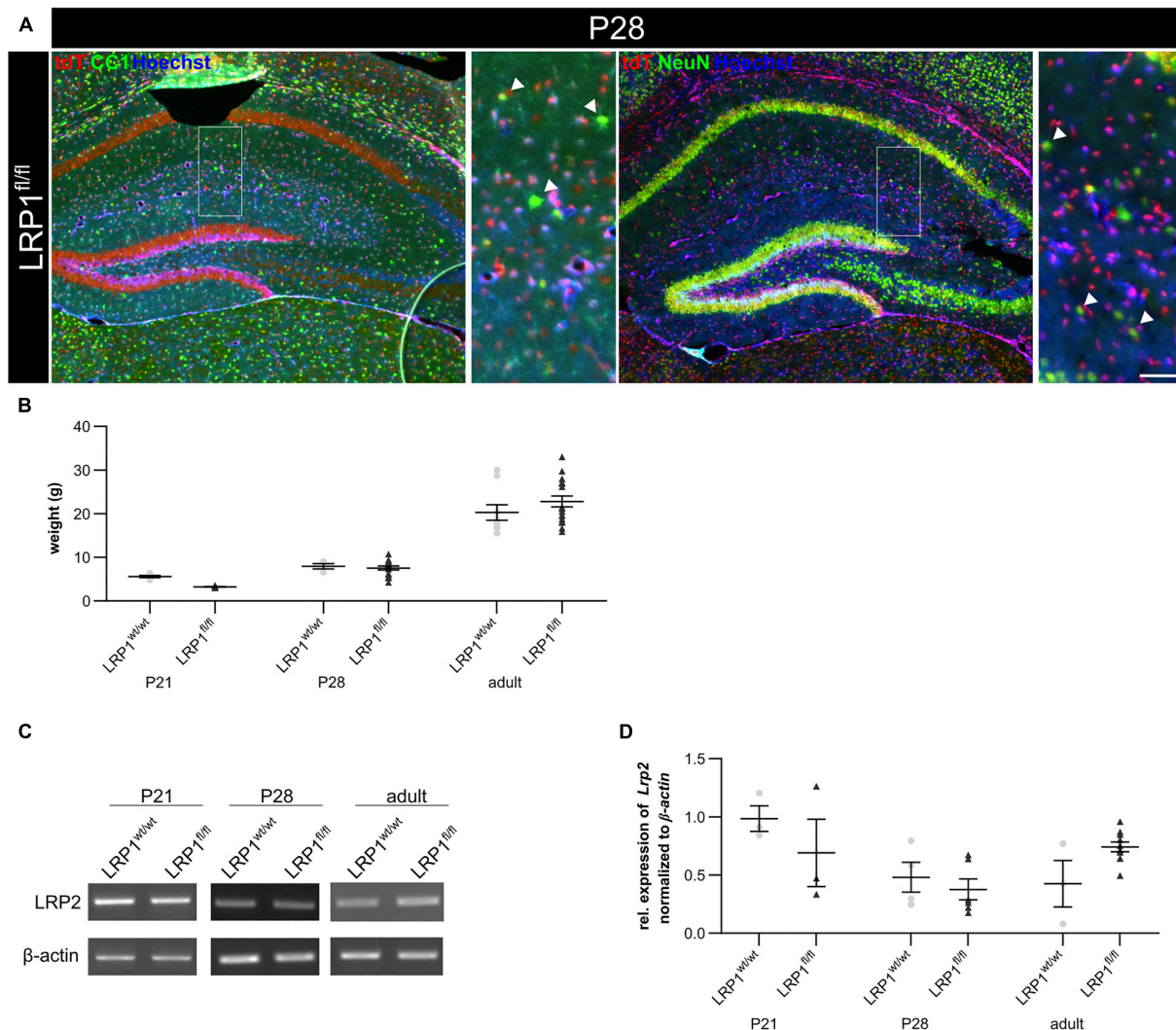


**FIGURE 2 |** Characterization of the knockout *in vivo*. To confirm that the deletion of LRP1 was restricted to the astrocytic lineage, an immunohistochemical staining against neurons (NeuN; green) and oligodendrocytes (CC1; green) was performed (**A**). There was no colocalization of both cell-specific markers with the expression of tdTomato in recombined cells indicated by the arrowhead leading to the assumption that the deletion of LRP1 only occurred in astrocytes. To further characterize the newly generated mouse line, the weights of the TAM-receiving animals were compared (**B**). The statistical analysis revealed no changes in the weight of knockout animals compared to the control. As the deletion of one member of the LDL-family might result in an increased expression of other members, the expression of *Lrp2* (**C,D**) was investigated. However, the knockout induction of LRP1 caused no altered expression of LRP2 (Scale bar is 50  $\mu$ m; mean  $\pm$  SEM; two-way ANOVA with *post-hoc* Bonferroni test; for *N*-values see **Table 2**).

The expression of pAkt was not influenced by the deletion of LRP1 in astrocytes in comparison to the controls at any investigated timepoint (see **Figures 8C,D**) as we could find no alterations in the gene expression of *Akt* and *Mtor* after loss of LRP1 (data not shown).

### Deletion of Astrocytic LRP1 Negatively Influenced Activity of Hippocampal Neurons *in vivo*

To further investigate the effect of LRP1 loss in astrocytes to hippocampal tissue, we investigated the activity of neurons via the staining against c-Fos, marking activated neurons (see

**Figure 9A**). Thereby, we deduced whether the metabolic supply of neurons via astrocytes was influenced by the deletion of *Lrp1*. All c-Fos-positive cells were quantified and the number of positive cells per mm<sup>2</sup> was measured (see **Figure 9B**). The quantification showed a significantly decreased number of c-Fos-positive neurons after loss of LRP1 (10.53 cells/mm<sup>2</sup>  $\pm$  3.15 cells/mm<sup>2</sup>) when compared to the control condition (41.90 cells/mm<sup>2</sup>  $\pm$  3.41 cells/mm<sup>2</sup>;  $p \leq 0.01$ ) at P21. With ongoing maturation, the number of c-Fos-positive neurons were similar in both conditions.

Furthermore, the expression of subunits of the glutamate receptors  $\alpha$ -amino-3-hydroxy-5-methyl-4-isoxazolepropionic acid (AMPA) and N-methyl-D-aspartate (NMDA) were



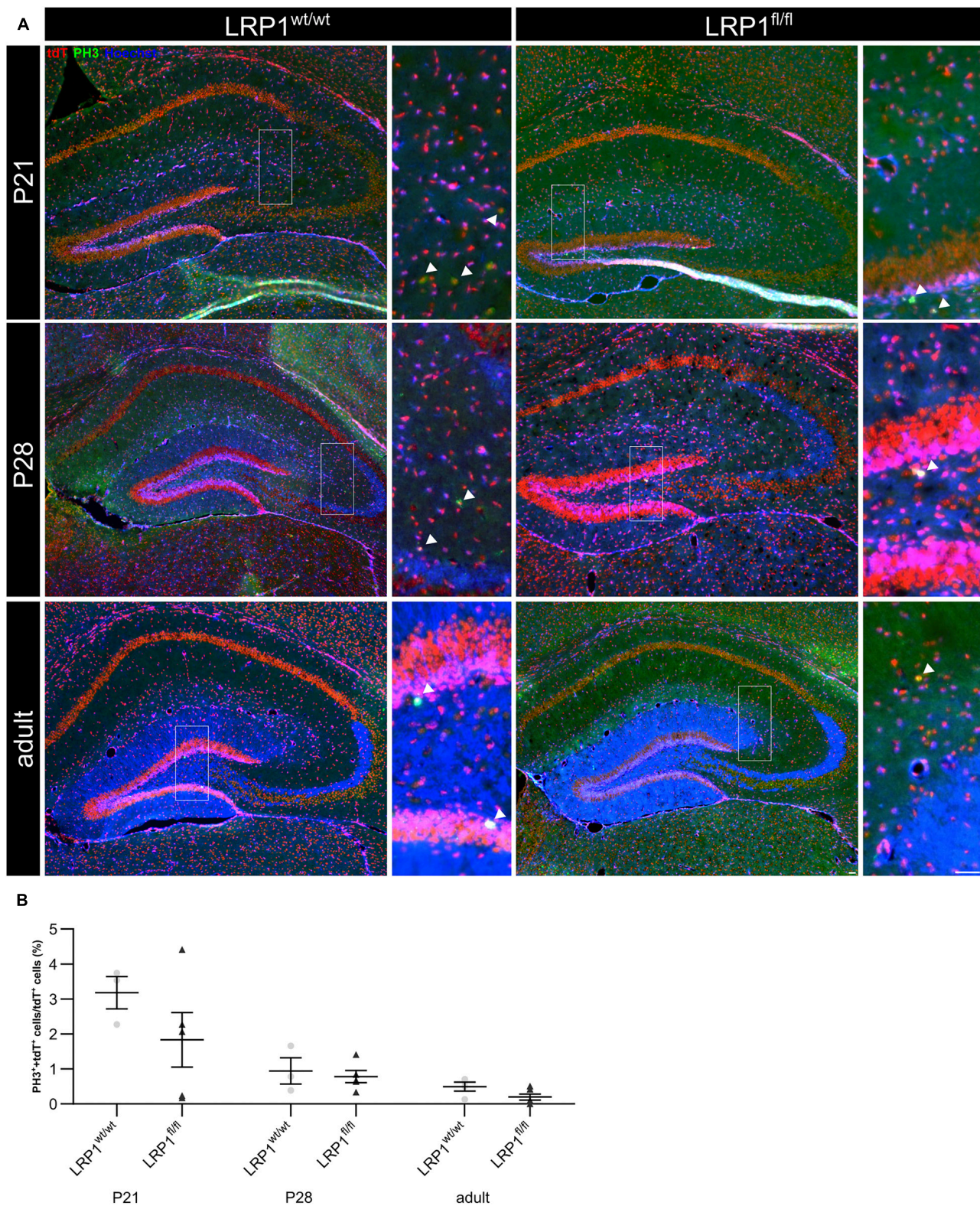
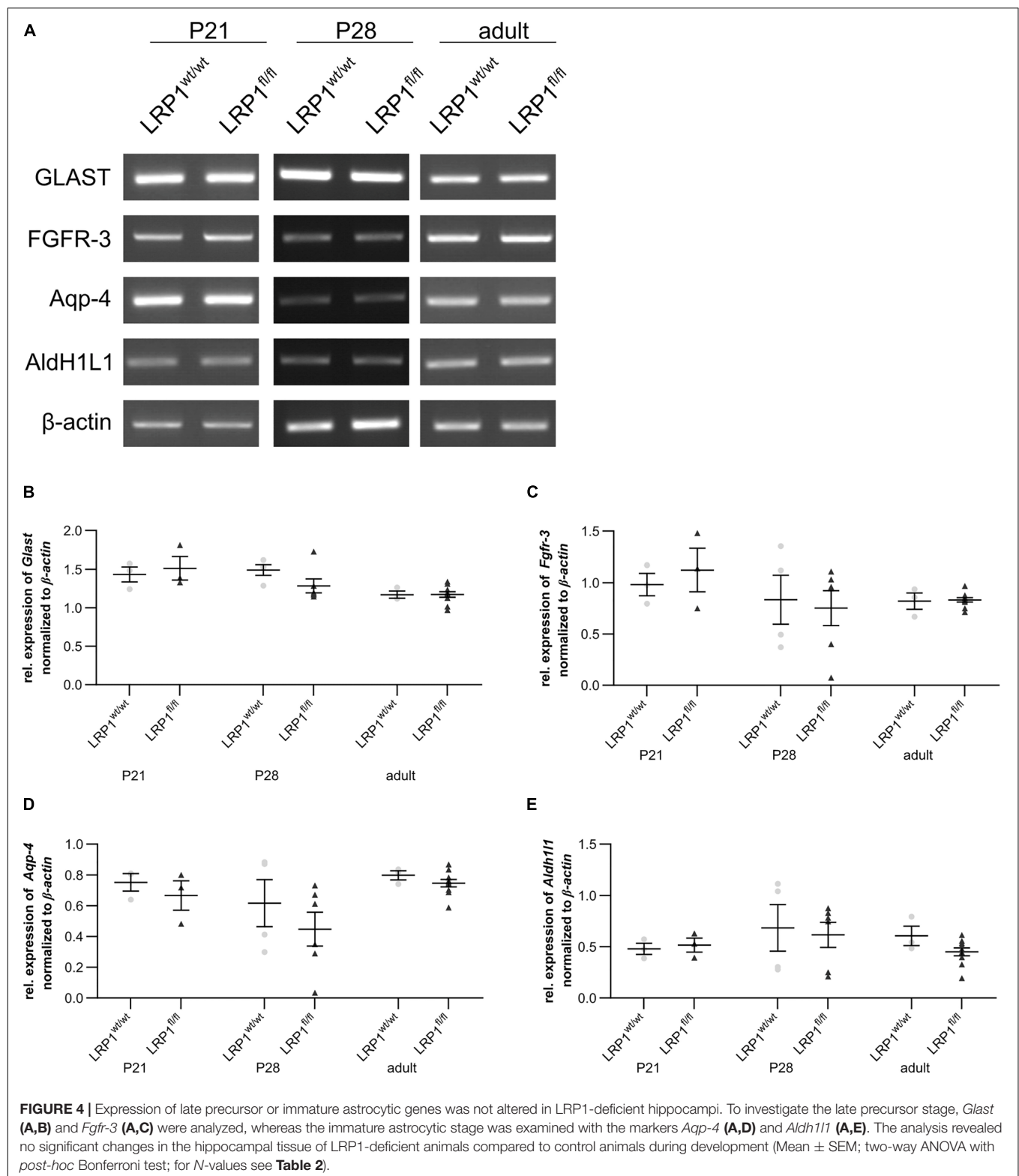


**FIGURE 3 |** Proliferation capacity of LRP1-deficient astrocytes was not affected. The proliferation rate was evaluated with an immunohistochemical staining against phospho-Histone H3 (PH3; green) and tdTomato (**A**, red). Double-positive cells indicated by the arrowhead were quantified and the analysis showed that the numbers of proliferation events were comparable in both conditions (**B**, Scale bar is 50  $\mu$ m; mean  $\pm$  SEM; two-way ANOVA with *post-hoc* Bonferroni test; for *N*-values see **Table 2**).





investigated via RT-PCR (Figure 9C). We investigated the gene expression of the AMPAR subunits *Gria1* and *Gria2* (see Figures 9D,E) as well as the NMDAR subunits *Grin1*, *Grin2a*, and *Grin2b* (see Figures 9F–H) as it was previously proposed

that these subunits can be influenced via LRP1. However, the expression analysis revealed no alterations in the gene expression of the receptor subunits in LRP1-deficient hippocampal tissue compared to the control during development.

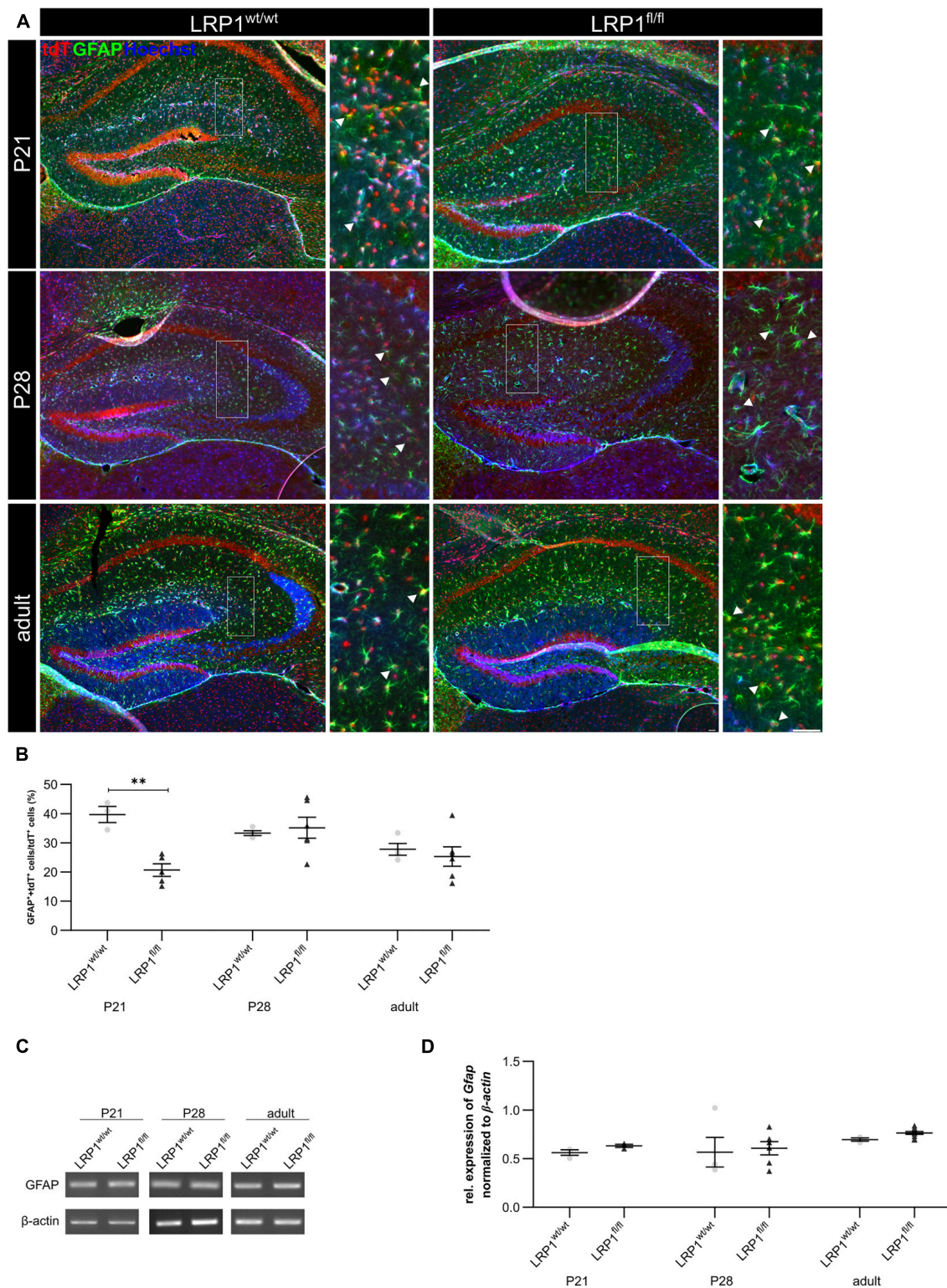


**FIGURE 5 |** LRP1 depletion in astrocytes resulted in no reactive phenotype. The immunohistochemical staining against GFAP (green) and tdTomato (red) revealed no reactive morphology (**A**). The quantification of GFAP- and tdTomato-positive cells indicated by the arrowhead showed no changes in the number of double-positive cells in the hippocampi upon LRP1 deletion during development (**B**). Additionally, RT-PCR analysis was performed to investigate whether the *Gfap* gene expression was altered (**C**). However, the statistical analysis showed no differences between the knockout and control condition at all three investigated timepoints (**D**) (Scale bar is 50  $\mu$ m; mean  $\pm$  SEM; two-way ANOVA with *post-hoc* Bonferroni test; for *N*-values see **Table 2**).



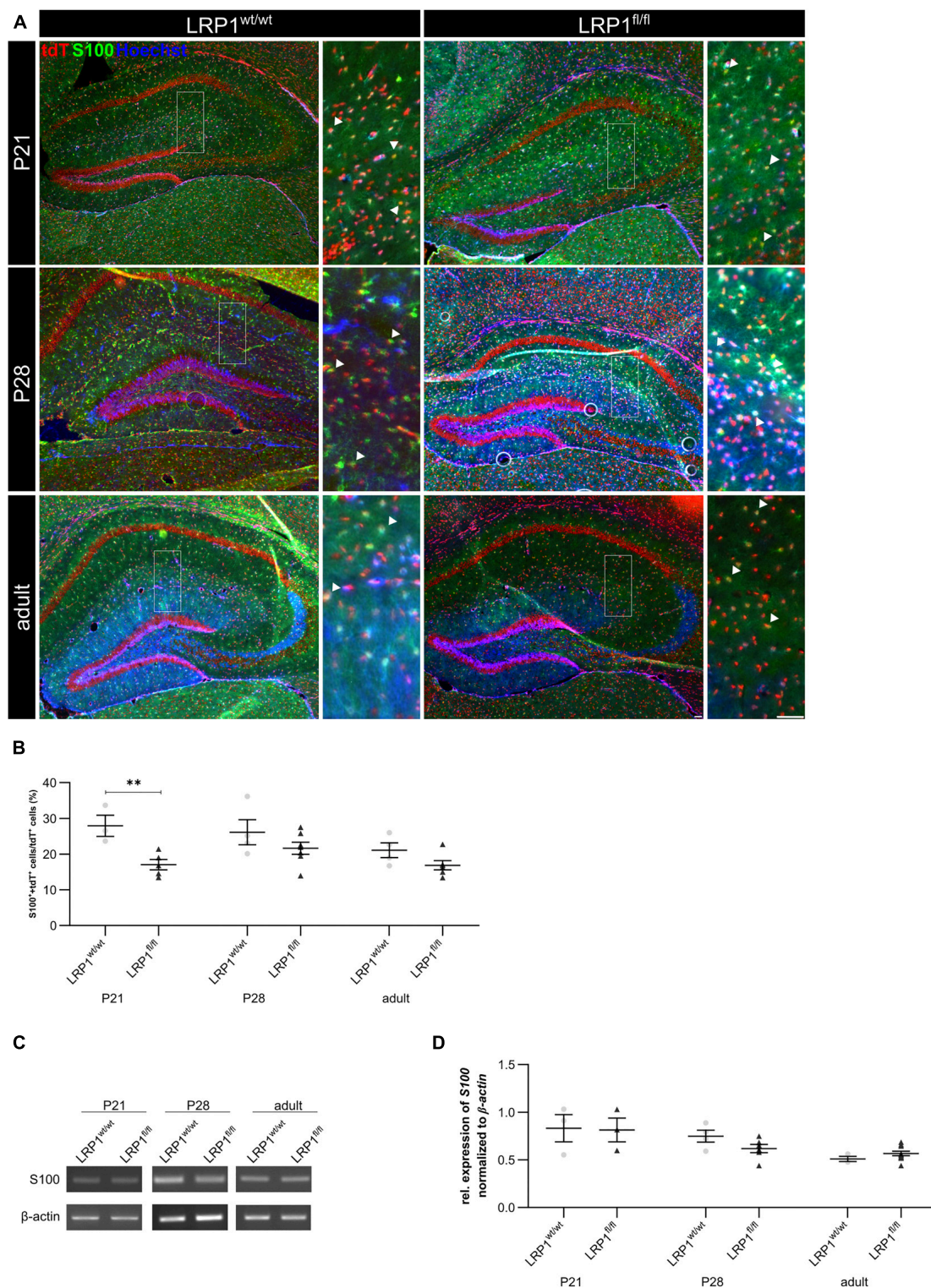


**FIGURE 6 |** Maturation of LRP1-deficient astrocytes was affected at the beginning of development. To further investigate the maturation of astrocytes upon LRP1 deletion, an immunohistochemical staining against S100 (green) and tdTomato was performed (**A**). The quantification showed a significantly decreased number of double-positive cells indicated by the arrowhead within the hippocampi of LRP1-deficient animals at P21 compared to the control condition (**B**). However, with ongoing development the numbers were comparable in both conditions. To support the findings of the staining, RT-PCR analysis was performed to analyze S100 gene expression (**C**). Nevertheless, the expression was not altered upon LRP1 deletion in hippocampal tissue at all three investigated timepoints (**D**) (Scale bar is 50  $\mu$ m; mean  $\pm$  SEM; two-way ANOVA with *post-hoc* Bonferroni test; for *N*-values see **Table 2**).

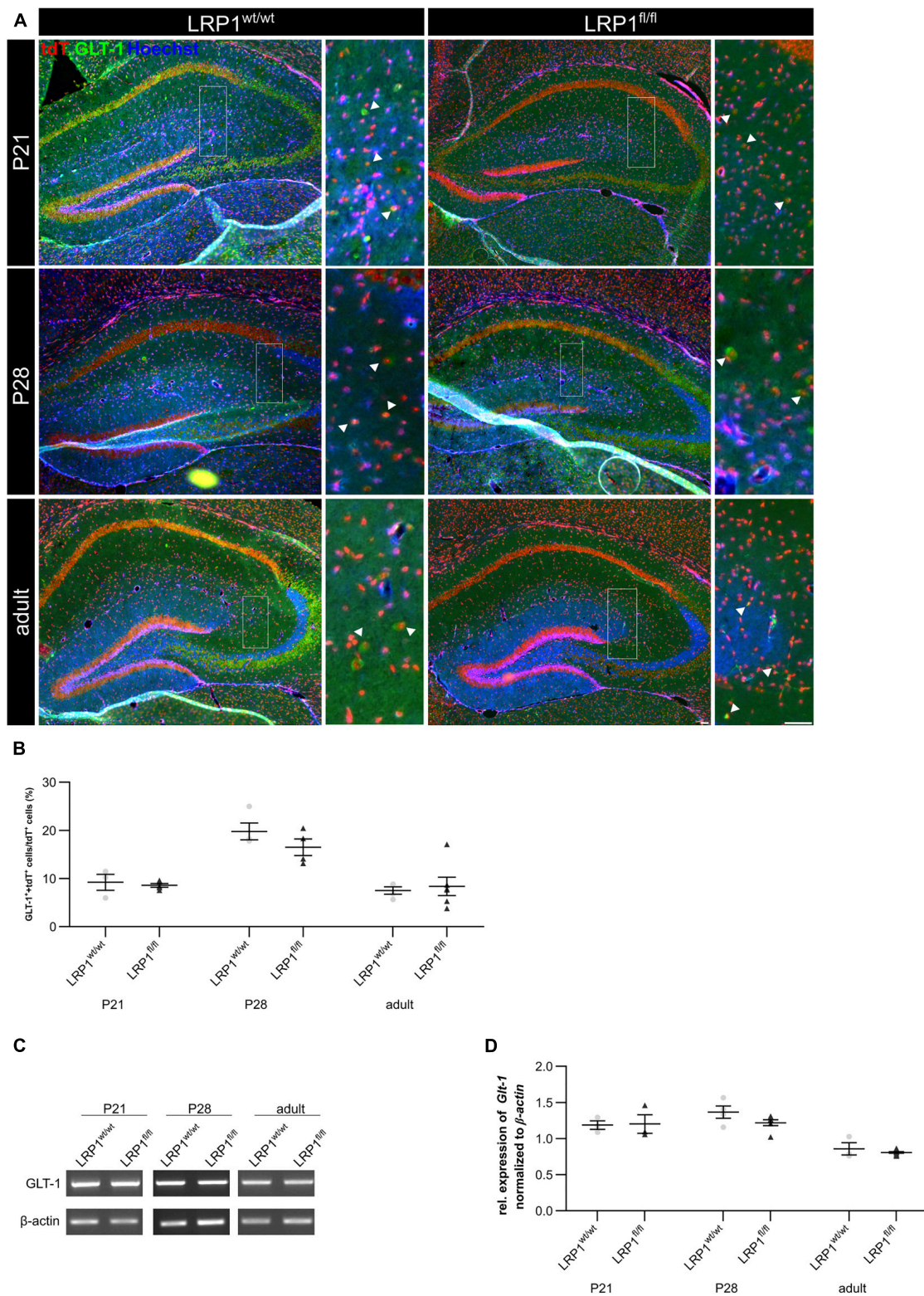
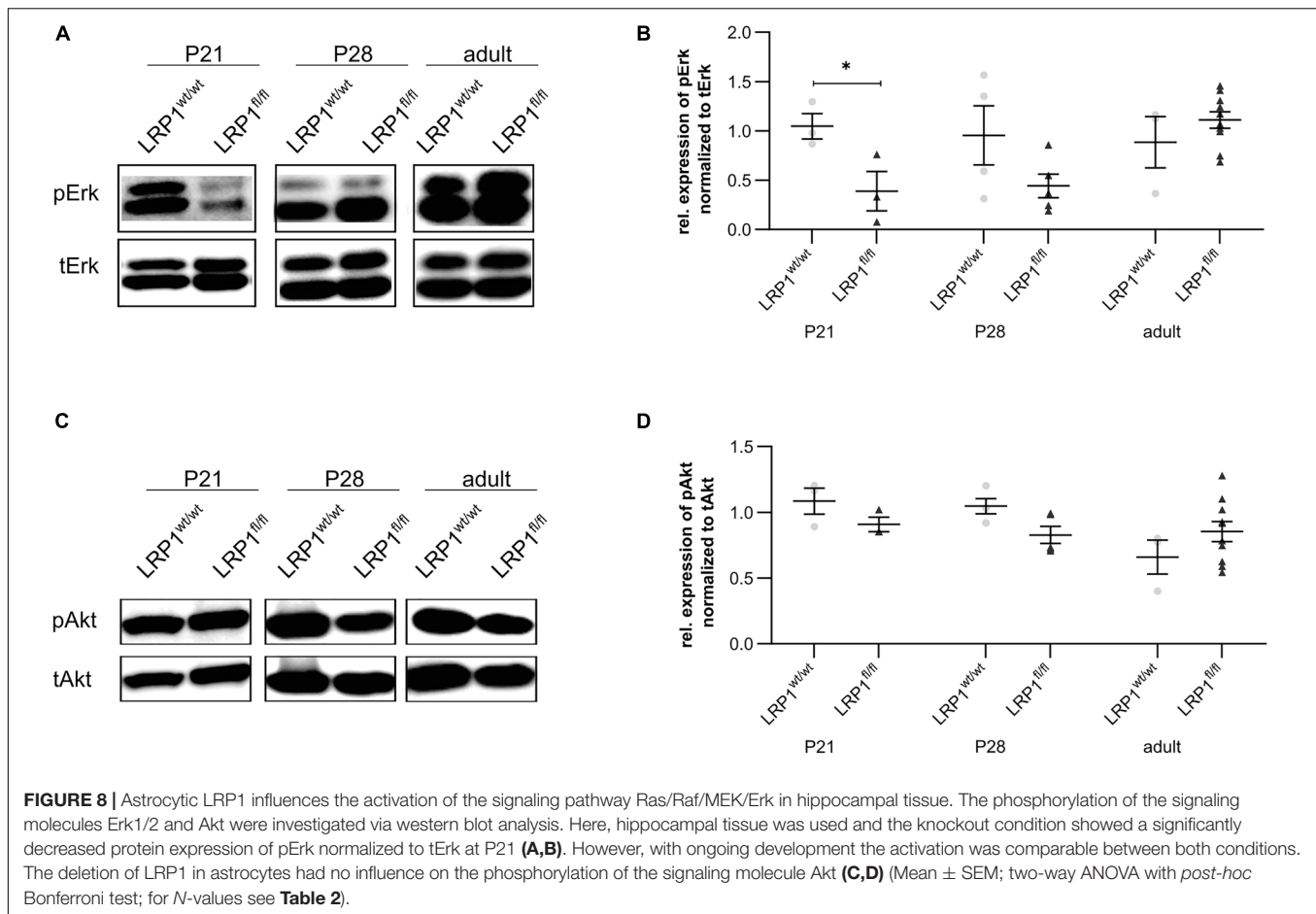


**FIGURE 7 |** Glutamate transporter expression was not influenced by the deletion of LRP1. As a next approach, the number of GLT-1 (green) and tdTomato-expressing (red) cells was analyzed **(A)**. The statistical evaluation showed no alterations in the number of double-positive cells indicated by the arrowhead in LRP1-depleted tissue compared to the control condition during development **(B)**. Also, the gene expression of *Glut-1* was not affected by the deletion of LRP1 in hippocampal tissue **(C,D)** (Scale bar is 50  $\mu$ m; mean  $\pm$  SEM; two-way ANOVA with *post-hoc* Bonferroni test; for *N*-values see **Table 2**).





## Deletion of Astrocytic LRP1 Had No Influence on Motor Coordination or Cognitive Abilities in Adult Animals

To assess if the astrocytic deletion of LRP1 had any influence of the behavior or the motor coordination on adult knockout animals several tests were performed. Fine motor coordination and balance were investigated with the beam walk test. The first investigated parameter was the time that was needed by the animals to cross the beam (see **Figure 10A**), the second parameter was the time left immobile until they started walking on the beam for the first time (see **Figure 10B**) and the last parameter were the slips of the hindlimbs, either right or left, of the animals while crossing the beam (see **Figure 10C**). In general, the LRP1-deficient animals exhibited no motor dysfunctions or imbalance in comparison to the control animals. However, the number of slips of the hindlimbs were slightly decreased compared to the control animals, hinting an increased balance. Next, we used the hangwire test to evaluate strength with little coordination. The knockout animals performed in the same way as the control animals in this task (see **Figure 10D**). Additionally, the motor coordination and balance were analyzed with the pole test. The time needed to descend down to the cage was not altered in the knockout group compared to control animals (see **Figure 10E**). The last motor coordination test was the rotarod.

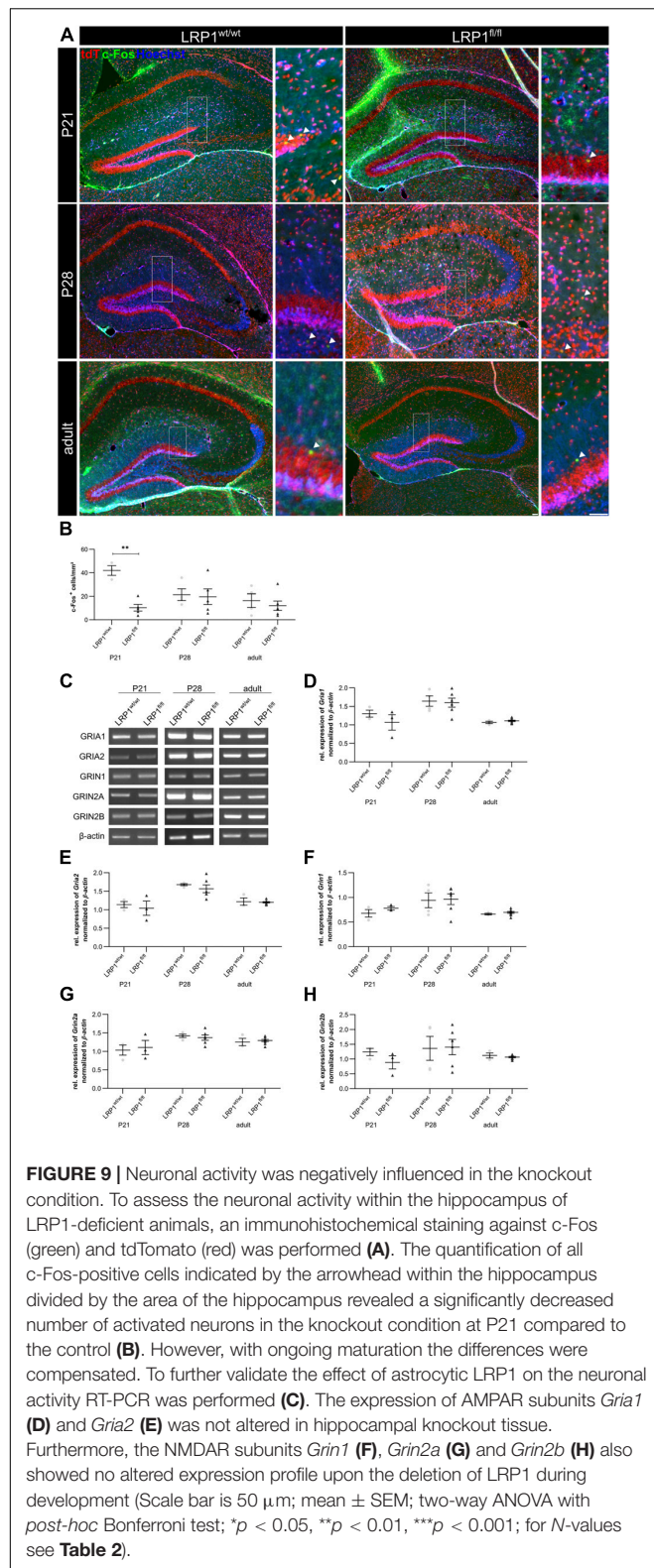
The investigated parameters here were the time when the animals fell down (see **Figure 10F**) as well as the speed of the rod when the animals fell down (see **Figure 10G**). Again, we saw no differences in the motor coordination of LRP1-depleted animals.

The cognitive abilities of the LRP1-deficient animals were assessed with the T-maze test (see **Figure 10H**) and the novel object recognition (NOR) test (see **Figure 10I**). These two tests revealed that the knockout animals showed no cognitive disabilities in comparison to the control group.

These findings lead to the assumption that the astrocytic deletion of LRP1 had no effect on the motor coordination as well as on the cognitive abilities of adult animals.

## DISCUSSION

We used the newly generated mouse model with an inducible loss of astroglial LRP1 to examine how the maturation and maintenance of astrocytes is influenced by astroglial LRP1. Therefore, we decided to investigate the maturation on protein (immunohistochemistry, western blot) and mRNA level (RT-PCR). The application of Tamoxifen caused a significantly decreased number of LRP1-expressing cells in the knockout condition compared to the control condition. However, western blot analysis revealed no significant downregulation.



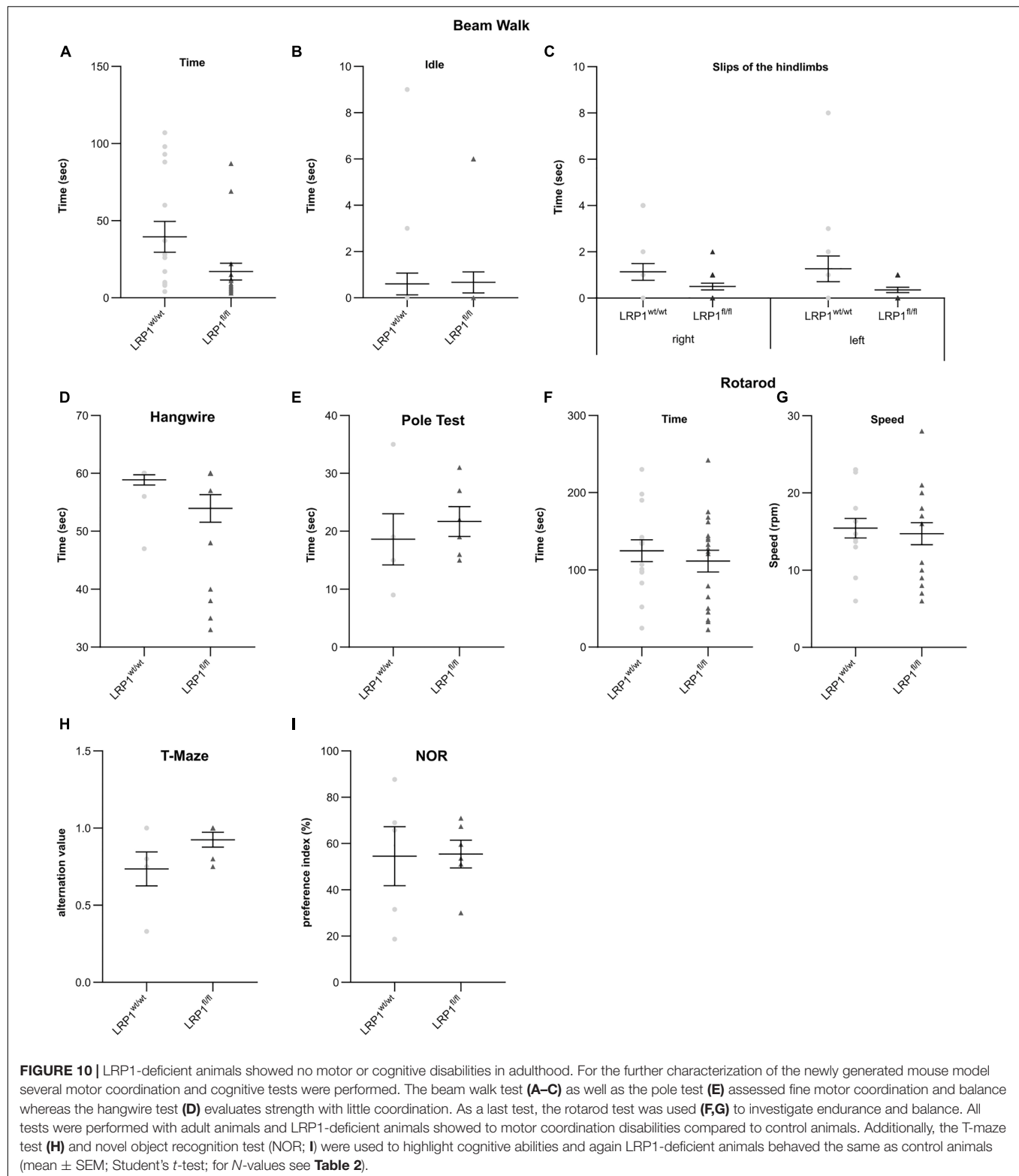
Nevertheless, the analysis was performed with hippocampal tissue, including other cell types, such as neurons and microglia, beside the knockout-affected astrocytes. Previous studies showed

that 50% of LRP1 protein is expressed by neurons (Shinohara et al., 2017; Liu et al., 2019), possibly masking the deletion of LRP1 in astrocytes. The further analysis of the knockout specificity revealed that only negligible amount of either NeuN- or CC1-positive cells were expressing tdTomato. However, previous studies reported that CC1 was detectable in a small proportion of astrocytes (Bhat et al., 1996; Fuss et al., 2000; Mori et al., 2006; Bin et al., 2016). Mori et al. (2005) have reviewed the concurring expression of astrocyte-specific markers also in radial glia cells. Recombination under the GFAP promotor was detectable in neurons derived from radial glia cells (Malatesta et al., 2003). Leading to the assumption that tdTomato- and NeuN-double positive cells observed in the described animal model might resemble newborn neurons derived from radial glia cells located in the dentate gyrus affected by the recombination. However, as neither neurons nor oligodendrocytes are expressing the used astrocyte-specific markers, the analysis performed in this study resembled the effect of LRP1 on the maturation of astrocytes.

After successful confirmation of astroglia-specific LRP1 loss *in vivo*, we investigated the proliferation behavior of recombined cells within the hippocampus during development and observed no changes in astroglial proliferation rate. We previously reported that the proliferation of neural stem and precursor cells *in vitro* was negatively influenced by the deletion of LRP1 (Safina et al., 2016). However, the role of LRP1 in regard to proliferation is opposed, depending on the cell type and tissue.

We tracked the astroglial differentiation with stage-specific markers according to Wiese et al. (2012). However, the gene analysis revealed no significant alterations in regard to the expression of late precursor markers, such as GLAST and FGFR-3, nor to immature astrocytes markers, such as AldH1L1 and Aqp-4. Nevertheless, the protein expression is not always correlating to the mRNA levels, as the relationship between mRNA to protein synthesis is objected to fluctuations caused by different factors, such as resource availability (Liu et al., 2016). Therefore, the number of positive cells might be altered, whereas the mRNA levels were not affected by the LRP1 deletion.

As a next step, we investigated mature astrocytes with immunohistochemistry. Here we used GFAP, a prototypical marker for mature astrocytes and a reliable maker for reactive astrogliosis (Pekny et al., 1995; Pekny and Pekna, 2004; Herrmann et al., 2008). Our analysis showed a significantly decreased number of recombined cells expressing GFAP at P21 in knockout mice compared to controls. Barcelona et al. (2011) showed that the expression of GFAP in retinal Müller glia was induced by application of  $\alpha$ 2-macroglobulin. This effect was abolished by using the LRP1 inhibitor RAP. Therefore, the binding of  $\alpha$ 2-macroglobulin to LRP1 facilitates the expression of GFAP. The deletion of LRP1 in astroglia might cause the same effect, leading to a decreased number of GFAP-positive astrocytes observed in our animal model. Furthermore, we assessed mature astrocytes with S100 and again the number of tdTomato- and S100-double positive cells was significantly decreased in the hippocampus at P21. However, the number of GLT-1- and tdTomato-double positive cells was not affected



by the LRP1-knockout. Nevertheless, we observed a decreased number of GLT-1- and tdTomato-double positive cells in both conditions reaching adulthood. Benediktsson et al. (2012) observed a correlation between the number of GLT-1-positive

astrocytes and neuronal activity. Therefore, we hypothesized that the observed decreased neuronal activity in the adult stage resulted in a reduced number of GLT-1- and tdTomato-positive cells in both conditions.

Our results indicate that LRP1 is mainly essential for astroglial maturation during an early developmental phase causing a decreased maturation at this timepoint, which is compensated with ongoing development. We hypothesized that this effect might be dependent on the activation of signaling cascades as it is known that LRP1 can form complexes with other receptors on the cell surface, which induce downstream activation of signaling cascades (Seger and Krebs, 1995; Zhang and Liu, 2002; Ortega and Alcántara, 2010; Burris, 2013; Kumar et al., 2013).

Previous studies already reported that the postnatal proliferation and terminal differentiation of glial cells is dependent on cell intrinsic cues (Qian et al., 2000; Shen et al., 2006). The Ras/Raf/MEK/Erk pathway was described to be critical for the glial specification as well as for proliferation (Li et al., 2012). The activation of this signaling cascade can be induced by the complex formation of LRP1 with PDGFR $\beta$  (Boucher et al., 2002; Loukinova et al., 2002) or with trkA (Spuch et al., 2012). Therefore, we examined the phosphorylation and therewith the activation of signaling molecules Erk1/2 and Akt. Our analysis showed a significantly downregulated phosphorylation of Erk1/2 in hippocampal tissue of P21 knockout animals, which correlates to the delayed maturation observed at the same developmental stage. Therefore, we conclude that LRP1 is a regulator of the early astrocytic maturation by influencing the activation of the Ras/Raf/MEK/Erk pathway, while the maintenance of astroglial numbers seems to be not influenced by the loss of LRP1.

Based on our findings, we were interested if the delayed maturation of astrocytes had any influence on the activity of neurons as we previously observed that LRP1-depleted astrocytes negatively influenced the activity of hippocampal neurons in a model of the tripartite synapse *in vitro* (Romeo et al., 2021). We used c-Fos to investigate the number of activated neurons within the hippocampus and saw a significantly decreased number of c-Fos-positive cells at P21, which were not accompanied by an altered expression of NMDA or AMPA receptor subunits. This result corresponds to the delayed maturation of astrocytes at the same timepoint. Previous studies showed that the neuronal differentiation as well as neurite outgrowth is dependent on the activation of the Ras/Raf/MEK/Erk pathway induced via astrocytes as it promoted the astrocytic release of laminin (Spohr et al., 2011, 2014). We observed a decreased phosphorylation of the signaling molecule Erk1/2 involved in this signaling pathway, which besides negatively influencing the astroglial maturation also caused an altered neuronal differentiation or neurite outgrowth ultimately resulting in a decreased neuronal activity observed in our model. Further studies might highlight if the observed decreased phosphorylation of Erk1/2 is facilitated via the binding of LRP1 ligands, such as tPA or  $\alpha$ 2-macroglobulin, or the interaction of LRP1 with other receptors, like integrins or PDGFR.

The altered neuronal activity observed in our animal model might also result from other factors, as astrocytes are tightly associated to neuronal synapses by forming the tripartite synapse. Here, astrocytes are able to release gliotransmitters, such as GABA, ATP, and D-serine, directly influencing the

activity of the pre- or postsynapse (Araque et al., 1999; Volterra and Steinhäuser, 2004; Perea et al., 2009). Another neuromodulating factor released by astrocytes is the tissue plasminogen activator (tPA) (Fernández-Monreal et al., 2004; Samson and Medcalf, 2006). It was previously reported that the inhibition of LRP1 via RAP caused a decreased uptake of tPA out of the synaptic cleft facilitated via astrocytes (Cassé et al., 2012). Thereby, astrocytes cannot buffer the potentiated NMDA receptor activity by tPA, ultimately resulting in neurotoxicity due to high levels of glutamate within the synaptic cleft (Cassé et al., 2012; Jeanneret et al., 2016).

To further characterize our new mouse model, we performed several motor coordination and cognitive tests with adult animals. However, the LRP1-deficient animals showed no disabilities or cognitive restrictions in comparison to control animals of the same age.

It is of interest to compare the outcome of the present investigation with results obtained by deleting LRP1 from cortical radial glia stem cells using the Emx1-Cre driver line (Bres et al., 2020). In that model, recombination started at E9.5 and affected both cortex and hippocampus, targeting neurogenesis as well as gliogenesis. The resulting mouse line displayed severe neurological symptoms, expanded ventricles and seizures. As a consequence, astrocytes became reactive starting at P21 and up-regulated GFAP. Unexpectedly, however, the hippocampus at P28 exhibited a reduction of c-fos-positive cells, comparable to the current study. In the present approach, LRP1 was deleted from the astrocyte lineage during the postnatal period, after the phase of neurogenesis had been completed. As consequence, astrocyte maturation in the hippocampus was delayed and neuronal activity in the hippocampus appeared reduced at P14, as judged from c-fos expression. We conclude that elimination of LRP1 from the astrocyte lineage *per se* is not sufficient to explain the hyperactive phenotype observed in our previous study. In this our model is in agreement with a recent report where LRP1 had been removed using a GFAP-driven Cre-recombinase (Liu et al., 2017).

Summarized our results showed that the deletion of LRP1 in astrocytes resulted in a delayed maturation at an early developmental stage, accompanied by a decreased activation of signaling molecules. However, the gene expression of any stage-specific marker related to the astrocytic lineage was not influenced by the knockout induction. Though, the immunohistochemical analysis revealed a decreased number of mature astrocytes. Additionally, the neuronal activity was negatively influenced by the deletion of astroglial LRP1 at the same developmental stage. Nevertheless, the observed effects were compensated with ongoing development resulting in comparable cell numbers and no motor or cognitive deficits in adult conditional knockout mice.

## CONCLUSION

In conclusion, we could identify LRP1 as a novel regulator of the early astroglial differentiation in the hippocampus by promoting



the phosphorylation of Erk1/2 involved in the Ras/Raf/MEK/Erk signaling pathway.

## DATA AVAILABILITY STATEMENT

The raw data supporting the conclusions of this article will be made available by the authors, without undue reservation.

## ETHICS STATEMENT

The animal study was reviewed and approved by the State Agency for Nature, Environment and Consumer Protection Northrhine-Westphalia (Landesamt fuer Umweltschutz, Naturschutz und Verbraucherschutz; file number: 84-02.04.2016.A482). Written informed consent was obtained from the owners for the participation of their animals in this study.

## AUTHOR CONTRIBUTIONS

RR performed the experiments regarding the transcardial perfusion, sample preparation, immunohistochemistry, as well as RT-PCR. RR and AF wrote and revised the manuscript. DM and MM performed the behavioral and cognitive tests. MM and AS revised the manuscript. All authors contributed to the article and approved the submitted version.

## REFERENCES

- Araque, A., Parpura, V., Sanzgiri, R. P., and Haydon, P. G. (1999). Tripartite synapses: glia, the unacknowledged partner. *Trends Neurosci.* 22, 208–215. doi: 10.1016/s0166-2236(98)01349-6
- Auderset, L., Landowski, L. M., Foa, L., and Young, K. M. (2016). Low density lipoprotein receptor related proteins as regulators of neural stem and progenitor cell function. *Stem Cells Int.* 2016:2108495. doi: 10.1155/2016/2108495
- Barcelona, P. F., Ortiz, S. G., Chiabrand, G. A., and Sánchez, M. C. (2011). alpha2-Macroglobulin induces glial fibrillary acidic protein expression mediated by low-density lipoprotein receptor-related protein 1 in Müller cells. *Invest. Ophthalmol. Vis. Sci.* 52, 778–786. doi: 10.1167/iov.10-5759
- Benediktsson, A. M., Marrs, G. S., Tu, J. C., Worley, P. F., Rothstein, J. D., Bergles, D. E., et al. (2012). Neuronal activity regulates glutamate transporter dynamics in developing astrocytes. *Glia* 60, 175–188. doi: 10.1002/glia.21249
- Bhat, R. V., Axt, K. J., Fosnaugh, J. S., Smith, K. J., Johnson, K. A., Hill, D. E., et al. (1996). Expression of the APC tumor suppressor protein in oligodendroglia. *Glia* 17, 169–174. doi: 10.1002/(SICI)1098-1136(199606)17:2<169::AID-GLIA8<3.0.CO;2-Y
- Bin, J. M., Harris, S. N., and Kennedy, T. E. (2016). The oligodendrocyte-specific antibody 'CCI' binds Quaking 7. *J. Neurochem.* 139, 181–186. doi: 10.1111/jnc.13745
- Binder, R. J., Han, D. K., and Srivastava, P. K. (2000). CD91: a receptor for heat shock protein gp96. *Nat. Immunol.* 1, 151–155. doi: 10.1038/77835
- Boucher, P., Liu, P., Gotthardt, M., Hiesberger, T., Anderson, R. G. W., and Herz, J. (2002). Platelet-derived growth factor mediates tyrosine phosphorylation

## FUNDING

We would like to thank the German Research Foundation (DFG) for their support (SPP 1757 FA 159/20-1,2 to AF, a junior research support grant to RR, and MA 5806/2-1 and MA 5806/1-2 to MM).

## ACKNOWLEDGMENTS

We thank M. Sc. Kristin Glotzbach for advice concerning the manuscript and the induction of the knockout. We thank Dr. Frank Kirchhoff for support and critical comments on the manuscript. We are grateful to Dr. Magdalena Goetz for providing the GLAST-CreERT2 mouse line. We acknowledge support by the Open Access Publication funds of the Ruhr-University Bochum.

## SUPPLEMENTARY MATERIAL

The Supplementary Material for this article can be found online at: <https://www.frontiersin.org/articles/10.3389/fncel.2021.642521/full#supplementary-material>

**Supplementary Figure 1** | Exemplary picture of analyzed area. The quantification of recombined and marker-positive cells occurred in the spaces between the *Cornu Ammonis* layers of the hippocampus. Here, the vast majority of cells were tdTomato-positive, leading to the assumption that the vast majority were astroglia.

**Supplementary Figure 2** | Protein expression of GLT-1 was not altered upon knockout induction. The deletion of LRP1 from astrocytes did not cause any changes in the protein expression of GLT-1 (A,B; mean  $\pm$  SEM; two-way ANOVA with *post-hoc* Bonferroni test; for *N*-values see Table 2).

- of the cytoplasmic domain of the low Density lipoprotein receptor-related protein in caveolae. *J. Biol. Chem.* 277, 15507–15513. doi: 10.1074/jbc.M200428200
- Bres, E. E., and Faissner, A. (2019). Low density receptor-related protein 1 interactions with the extracellular matrix: more than meets the eye. *Front. Cell Dev. Biol.* 7:31. doi: 10.3389/fcell.2019.00031
- Bres, E. E., Safina, D., Müller, J., Bedner, P., Yang, H., Helluy, X., et al. (2020). Lipoprotein receptor loss in forebrain radial glia results in neurological deficits and severe seizures. *Glia* 68, 2517–2549. doi: 10.1002/glia.23869
- Burris, H. A. (2013). Overcoming acquired resistance to anticancer therapy: focus on the PI3K/AKT/mTOR pathway. *Cancer Chemother. Pharmacol.* 71, 829–842. doi: 10.1007/s00280-012-2043-3
- Bushong, E. A., Martone, M. E., and Ellisman, M. H. (2004). Maturation of astrocyte morphology and the establishment of astrocyte domains during postnatal hippocampal development. *Int. J. Dev. Neurosci.* 22, 73–86. doi: 10.1016/j.ijdevneu.2003.12.008
- Cassé, F., Bardou, I., Danglot, L., Briens, A., Montagne, A., Parcq, J., et al. (2012). Glutamate controls tPA recycling by astrocytes, which in turn influences glutamatergic signals. *J. Neurosci.* 32, 5186–5199. doi: 10.1523/JNEUROSCI.5296-11.2012
- Deacon, R. M. J., and Rawlins, J. N. P. (2006). T-maze alternation in the rodent. *Nat. Protoc.* 1, 7–12. doi: 10.1038/nprot.2006.2
- Fernández-Monreal, M., López-Atalaya, J. P., Benchenane, K., Léveillé, F., Cacquevel, M., Plawinski, L., et al. (2004). Is tissue-type plasminogen activator a neuromodulator? *Mol. Cell. Neurosci.* 25, 594–601. doi: 10.1016/j.mcn.2003.11.002
- Franzdóttir, S. R., Engelen, D., Yuva-Aydemir, Y., Schmidt, I., Aho, A., and Klämbt, C. (2009). Switch in FGF signalling initiates glial differentiation in the *Drosophila* eye. *Nature* 460, 758–761. doi: 10.1038/nature08167

- Freeman, M. R. (2010). Specification and morphogenesis of astrocytes. *Science* 330, 774–778. doi: 10.1126/science.1190928
- Fuss, B., Mallon, B., Phan, T., Ohlemeyer, C., Kirchhoff, F., Nishiyama, A., et al. (2000). Purification and analysis of in vivo-differentiated oligodendrocytes expressing the green fluorescent protein. *Dev. Biol.* 218, 259–274. doi: 10.1006/dbio.1999.9574
- Gordon, G. R. J., Mulligan, S. J., and MacVicar, B. A. (2007). Astrocyte control of the cerebrovasculature. *Glia* 55, 1214–1221. doi: 10.1002/glia.20543
- Hennen, E., Czopka, T., and Faissner, A. (2011). Structurally distinct LewisX Glycans distinguish subpopulations of neural stem/progenitor cells. *J. Biol. Chem.* 286, 16321–16331. doi: 10.1074/jbc.M110.201095
- Herrmann, J. E., Imura, T., Song, B., Qi, J., Ao, Y., Nguyen, T. K., et al. (2008). STAT3 is a critical regulator of astrogliosis and scar formation after spinal cord injury. *J. Neurosci.* 28, 7231–7243. doi: 10.1523/JNEUROSCI.1709-08.2008
- Herz, J., Clouthier, D. E., and Hammer, R. E. (1992). LDL receptor-related protein internalizes and degrades uPA-PAI-1 complexes and is essential for embryo implantation. *Cell* 71, 411–421. doi: 10.1016/0092-8674(92)90511-A
- Herz, J., Clouthier, D. E., and Hammer, R. E. (1993). Correction: LDL receptor-related protein internalizes and degrades uPA-PAI-1 complexes and is essential for embryo implantation. *Cell* 73:428. doi: 10.1016/0092-8674(93)90130-I
- Iadecola, C., and Nedergaard, M. (2007). Glial regulation of the cerebral microvasculature. *Nat. Neurosci.* 10, 1369–1376. doi: 10.1038/nn2003
- Jahn, H. M., Kasakow, C. V., Helfer, A., Michely, J., Verkhatsky, A., Maurer, H. H., et al. (2018). Refined protocols of tamoxifen injection for inducible DNA recombination in mouse astroglia. *Sci. Rep.* 8:5913. doi: 10.1038/s41598-018-24085-9
- Jeanneret, V., Wu, F., Merino, P., Torre, E., Diaz, A., Cheng, L., et al. (2016). Tissue-type plasminogen activator (tPA) modulates the postsynaptic response of cerebral cortical neurons to the presynaptic release of glutamate. *Front. Mol. Neurosci.* 9:121. doi: 10.3389/fnmol.2016.00121
- Kriegstein, A., and Alvarez-Buylla, A. (2009). The glial nature of embryonic and adult neural stem cells. *Annu. Rev. Neurosci.* 32, 149–184. doi: 10.1146/annurev.neuro.051508.135600
- Kumar, A., Rajendran, V., Sethumadhavan, R., and Purohit, R. (2013). AKT kinase pathway: a leading target in cancer research. *Sci. World J.* 2013:756134. doi: 10.1155/2013/756134
- Li, X., Newbern, J. M., Wu, Y., Morgan-Smith, M., Zhong, J., Charron, J., et al. (2012). MEK Is a key regulator of gliogenesis in the developing brain. *Neuron* 75, 1035–1050. doi: 10.1016/j.neuron.2012.08.031
- Lillis, A. P., Mikhailenko, I., and Strickland, D. K. (2005). Beyond endocytosis: LRP function in cell migration, proliferation and vascular permeability. *J. Thromb. Haemost.* 3, 1884–1893. doi: 10.1111/j.1538-7836.2005.01371.x
- Liu, C.-C., Hu, J., Zhao, N., Wang, J., Cirrito, J. R., et al. (2017). Astrocytic LRP1 mediates brain A $\beta$  clearance and impacts amyloid deposition. *J. Neurosci.* 37, 4023–4031. doi: 10.1523/JNEUROSCI.3442-16.2017
- Liu, C. X., Musco, S., Lisitsina, N. M., Yaklichkin, S. Y., and Lisitsyn, N. A. (2000). Genomic organization of a new candidate tumor suppressor gene. *LRP1B*. *Genomics* 69, 271–274. doi: 10.1006/geno.2000.6331
- Liu, Q., Zhang, J., Zerbinatti, C., Zhan, Y., Kolber, B. J., Herz, J., et al. (2019). Correction: lipoprotein receptor LRP1 regulates leptin signaling and energy homeostasis in the adult central nervous system. *PLoS Biol.* 17:e3000310. doi: 10.1371/journal.pbio.3000310
- Liu, Y., Beyer, A., and Aebersold, R. (2016). On the dependency of cellular protein levels on mRNA abundance. *Cell* 165, 535–550. doi: 10.1016/j.cell.2016.03.014
- Loukinova, E., Ranganathan, S., Kuznetsov, S., Gorlatova, N., Migliorini, M. M., Loukinov, D., et al. (2002). Platelet-derived growth factor (PDGF)-induced tyrosine phosphorylation of the low density lipoprotein receptor-related protein (LRP). Evidence for integrated co-receptor function between LRP and the PDGF. *J. Biol. Chem.* 277, 15499–15506. doi: 10.1074/jbc.M200427200
- Lueprow, L. M. (2017). Novel object recognition test for the investigation of learning and memory in mice. *J. Vis. Exp.* 30:55718. doi: 10.3791/55718
- Maejima, T., Wollenweber, P., Teusner, L. U. C., Noebels, J. L., Herlitze, S., and Mark, M. D. (2013). Postnatal loss of P/Q-type channels confined to rhombic-lip-derived neurons alters synaptic transmission at the parallel fiber to purkinje cell synapse and replicates genomic Cacna1a mutation phenotype of ataxia and seizures in mice. *J. Neurosci.* 33, 5162–5174. doi: 10.1523/JNEUROSCI.5442-12.2013
- Malatesta, P., Hack, M. A., Hartfuss, E., Kettenmann, H., Klinkert, W., Kirchhoff, F., et al. (2003). Neuronal or glial progeny: regional differences in radial glia fate. *Neuron* 37, 751–764. doi: 10.1016/s0896-6273(03)00116-8
- Mark, M. D., Maejima, T., Kuckelsberg, D., Yoo, J. W., Hyde, R. A., Shah, V., et al. (2011). Delayed postnatal loss of P/Q-type calcium channels recapitulates the absence epilepsy, dyskinesia, and ataxia phenotypes of genomic Cacna1a mutations. *J. Neurosci.* 31, 4311–4326. doi: 10.1523/JNEUROSCI.5342-10.2011
- Marschang, P., Brich, J., Weeber, E. J., Sweatt, J. D., Shelton, J. M., Richardson, J. A., et al. (2004). Normal development and fertility of knockout mice lacking the tumor suppressor gene LRP1b suggest functional compensation by LRP1. *Mol. Cell Biol.* 24, 3782–3793. doi: 10.1128/MCB.24.9.3782-3793.2004
- Mori, S., and Zhang, J. (2006). Principles of diffusion tensor imaging and its applications to basic neuroscience research. *Neuron* 51, 527–539. doi: 10.1016/j.neuron.2006.08.012
- Mori, T., Buffo, A., and Götz, M. (2005). The novel roles of glial cells revisited: the contribution of radial glia and astrocytes to neurogenesis. *Curr. Top. Dev. Biol.* 69, 67–99. doi: 10.1016/S0070-2153(05)69004-7
- Mori, T., Tanaka, K., Buffo, A., Wurst, W., Kühn, R., and Götz, M. (2006). Inducible gene deletion in astroglia and radial glia—a valuable tool for functional and lineage analysis. *Glia* 54, 21–34. doi: 10.1002/glia.20350
- Muratoglu, S. C., Mikhailenko, I., Newton, C., Migliorini, M., and Strickland, D. K. (2010). Low density lipoprotein receptor-related protein 1 (LRP1) forms a signaling complex with platelet-derived growth factor receptor-beta in endosomes and regulates activation of the MAPK pathway. *J. Biol. Chem.* 285, 14308–14317. doi: 10.1074/jbc.M109.046672
- Ortega, J. A., and Alcántara, S. (2010). BDNF/MAPK/ERK-induced BMP7 expression in the developing cerebral cortex induces premature radial glia differentiation and impairs neuronal migration. *Cereb. Cortex* 20, 2132–2144. doi: 10.1093/cercor/bhp275
- Pekny, M., Leveen, P., Pekna, M., Eliasson, C., Berthold, C. H., Westermarck, B., et al. (1995). Mice lacking glial fibrillary acidic protein display astrocytes devoid of intermediate filaments but develop and reproduce normally. *EMBO J.* 14, 1590–1598. doi: 10.1002/j.1460-2075.1995.tb07147.x
- Pekny, M., and Pekna, M. (2004). Astrocyte intermediate filaments in CNS pathologies and regeneration. *J. Pathol.* 204, 428–437. doi: 10.1002/path.1645
- Perea, G., Navarrete, M., and Araque, A. (2009). Tripartite synapses: astrocytes process and control synaptic information. *Trends Neurosci.* 32, 421–431. doi: 10.1016/j.tins.2009.05.001
- Qian, X., Shen, Q., Goderie, S. K., He, W., Capela, A., Davis, A. A., et al. (2000). Timing of CNS cell generation: a programmed sequence of neuron and glial cell production from isolated murine cortical stem cells. *Neuron* 28, 69–80. doi: 10.1016/s0896-6273(00)00086-6
- Rohlmann, A., Gotthardt, M., Willnow, T. E., Hammer, R. E., and Herz, J. (1996). Sustained somatic gene inactivation by viral transfer of Cre recombinase. *Nat. Biotechnol.* 14, 1562–1565. doi: 10.1038/nbt1196-1562
- Romeo, R., Grotzbach, K., Scheller, A., and Faissner, A. (2021). Deletion of LRP1 from astrocytes modifies neuronal network activity in an *in vitro* model of the tripartite synapse. *Front. Cell. Neurosci.* 14:567253. doi: 10.3389/fncel.2020.567253
- Safina, D., Schlitt, F., Romeo, R., Pflanzner, T., Pietrzik, C. U., Narayanaswami, V., et al. (2016). Low-density lipoprotein receptor-related protein 1 is a novel modulator of radial glia stem cell proliferation, survival, and differentiation. *Glia* 64, 1363–1380. doi: 10.1002/glia.23009
- Samson, A. L., and Medcalf, R. L. (2006). Tissue-type plasminogen activator: a multifaceted modulator of neurotransmission and synaptic plasticity. *Neuron* 50, 673–678. doi: 10.1016/j.neuron.2006.04.013
- Savtchouk, I., and Volterra, A. (2018). Gliotransmission: beyond black-and-white. *J. Neurosci.* 38, 14–25. doi: 10.1523/JNEUROSCI.0017-17.2017
- Schäfer, I., Kaisler, J., Scheller, A., Kirchhoff, F., Haghighi, A., and Faissner, A. (2019). Conditional deletion of LRP1 leads to progressive loss of recombined NG2-expressing Oligodendrocyte precursor cells in a novel mouse model. *Cells* 8:1550. doi: 10.3390/cells8121550
- Seger, R., and Krebs, E. G. (1995). The MAPK signaling cascade. *FASEB J.* 9, 726–735. doi: 10.1096/fasebj.9.7601337
- Shen, Q., Wang, Y., Dimos, J. T., Fasano, C. A., Phoenix, T. N., Lemischka, I. R., et al. (2006). The timing of cortical neurogenesis is encoded within lineages

- of individual progenitor cells. *Nat. Neurosci.* 9, 743–751. doi: 10.1038/nn1694
- Shinohara, M., Tachibana, M., Kanekiyo, T., and Bu, G. (2017). Role of LRP1 in the pathogenesis of Alzheimer's disease: evidence from clinical and preclinical studies. *J. Lipid Res.* 58, 1267–1281. doi: 10.1194/jlr.R075796
- Sofroniew, M. V., and Vinters, H. V. (2010). Astrocytes: biology and pathology. *Acta Neuropathol.* 119, 7–35. doi: 10.1007/s00401-009-0619-8
- Spohr, T. C. E., Dezone, R. S., Rehen, S. K., and Gomes, F. C. A. (2011). Astrocytes treated by lysophosphatidic acid induce axonal outgrowth of cortical progenitors through extracellular matrix protein and epidermal growth factor signaling pathway. *J. Neurochem.* 119, 113–123. doi: 10.1111/j.1471-4159.2011.07421.x
- Spohr, T. C. E., Dezone, R. S., Rehen, S. K., and Gomes, F. C. A. (2014). LPA-primed astrocytes induce axonal outgrowth of cortical progenitors by activating PKA signaling pathways and modulating extracellular matrix proteins. *Front. Cell Neurosci.* 8:296. doi: 10.3389/fncel.2014.00296
- Spuch, C., Ortolano, S., and Navarro, C. (2012). LRP-1 and LRP-2 receptors function in the membrane neuron. Trafficking mechanisms and proteolytic processing in Alzheimer's disease. *Front. Physiol.* 3:269. doi: 10.3389/fphys.2012.00269
- Ulc, A., Zeug, A., Bauch, J., van Leeuwen, S., Kuhlmann, T., Ffrench-Constant, C., et al. (2019). The guanine nucleotide exchange factor Vav3 modulates oligodendrocyte precursor differentiation and supports remyelination in white matter lesions. *Glia* 67, 376–392. doi: 10.1002/glia.23548
- Volterra, A., and Steinhäuser, C. (2004). Glial modulation of synaptic transmission in the hippocampus. *Glia* 47, 249–257. doi: 10.1002/glia.20080
- Weber, P., Metzger, D., and Chambon, P. (2001). Temporally controlled targeted somatic mutagenesis in the mouse brain. *Eur. J. Neurosci.* 14, 1777–1783. doi: 10.1046/j.0953-816x.2001.01803.x
- Wiese, S., Karus, M., and Faissner, A. (2012). Astrocytes as a source for extracellular matrix molecules and cytokines. *Front. Pharmacol.* 3:120. doi: 10.3389/fphar.2012.00120
- Yong, V. W., Krekoski, C. A., Forsyth, P. A., Bell, R., and Edwards, D. R. (1998). Matrix metalloproteinases and diseases of the CNS. *Trends Neurosci.* 21, 75–80. doi: 10.1016/s0166-2236(97)01169-7
- Zhang, W., and Liu, H. T. (2002). MAPK signal pathways in the regulation of cell proliferation in mammalian cells. *Cell Res.* 12, 9–18. doi: 10.1038/sj.cr.7290105

**Conflict of Interest:** The authors declare that the research was conducted in the absence of any commercial or financial relationships that could be construed as a potential conflict of interest.

Copyright © 2021 Romeo, Boden-El Mourabit, Scheller, Mark and Faissner. This is an open-access article distributed under the terms of the Creative Commons Attribution License (CC BY). The use, distribution or reproduction in other forums is permitted, provided the original author(s) and the copyright owner(s) are credited and that the original publication in this journal is cited, in accordance with accepted academic practice. No use, distribution or reproduction is permitted which does not comply with these terms.



# Approaches to Study Gap Junctional Coupling

Jonathan Stephan<sup>1\*</sup>, Sara Eitelmann<sup>1</sup> and Min Zhou<sup>2\*</sup>

<sup>1</sup> Institute of Neurobiology, Heinrich Heine University Düsseldorf, Düsseldorf, Germany, <sup>2</sup> Department of Neuroscience, Wexner Medical Center, Ohio State University, Columbus, OH, United States

## OPEN ACCESS

### Edited by:

Christian Lohr,  
University of Hamburg, Germany

### Reviewed by:

Gerald Seifert,  
University Hospital Bonn, Germany  
Luc Leybaert,  
Ghent University, Belgium

### \*Correspondence:

Jonathan Stephan  
jonathan.stephan@uni-duesseldorf.de  
Min Zhou  
Zhou.787@osu.edu

### Specialty section:

This article was submitted to  
Non-Neuronal Cells,  
a section of the journal  
Frontiers in Cellular Neuroscience

**Received:** 11 December 2020

**Accepted:** 03 February 2021

**Published:** 10 March 2021

### Citation:

Stephan J, Eitelmann S and  
Zhou M (2021) Approaches to Study  
Gap Junctional Coupling.  
*Front. Cell. Neurosci.* 15:640406.  
doi: 10.3389/fncel.2021.640406

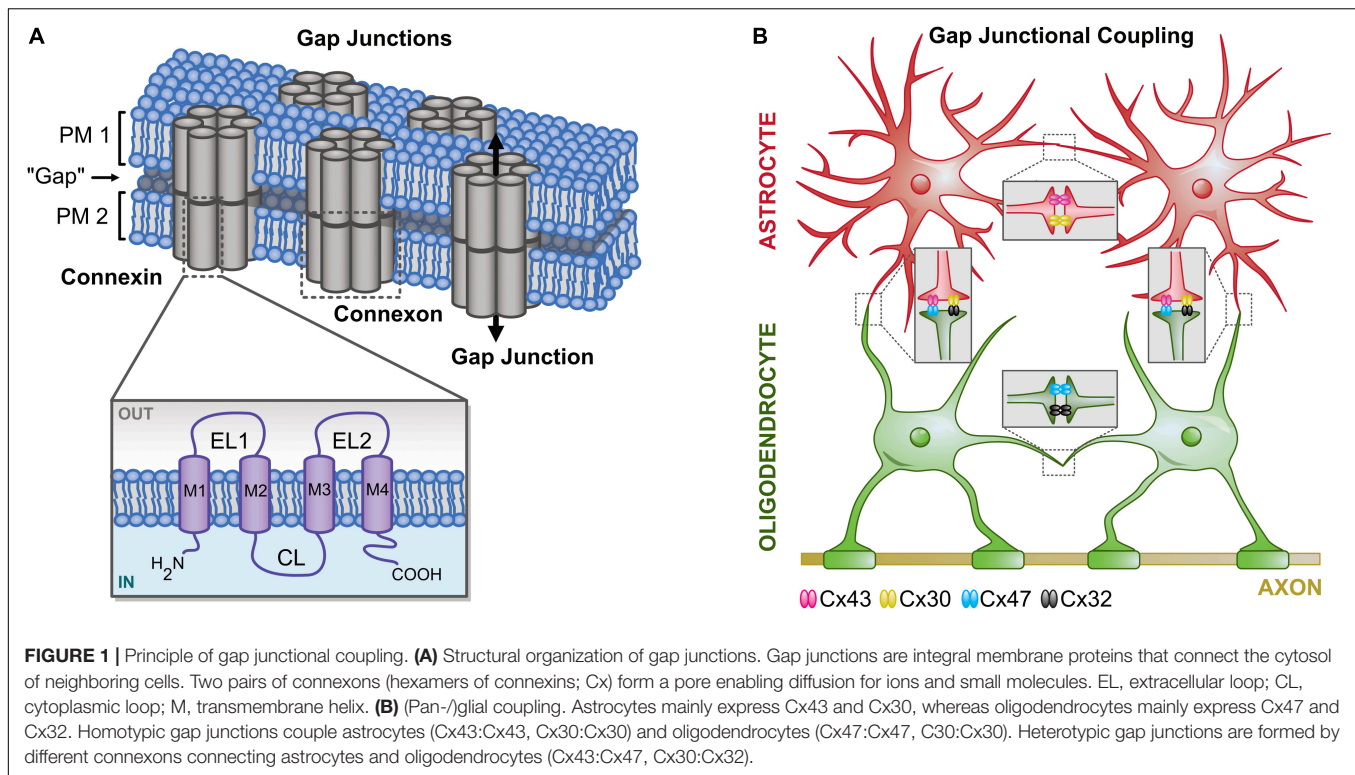
Astrocytes and oligodendrocytes are main players in the brain to ensure ion and neurotransmitter homeostasis, metabolic supply, and fast action potential propagation in axons. These functions are fostered by the formation of large syncytia in which mainly astrocytes and oligodendrocytes are directly coupled. Panglial networks constitute on connexin-based gap junctions in the membranes of neighboring cells that allow the passage of ions, metabolites, and currents. However, these networks are not uniform but exhibit a brain region-dependent heterogeneous connectivity influencing electrical communication and intercellular ion spread. Here, we describe different approaches to analyze gap junctional communication in acute tissue slices that can be implemented easily in most electrophysiology and imaging laboratories. These approaches include paired recordings, determination of syncytial isopotentiality, tracer coupling followed by analysis of network topography, and wide field imaging of ion sensitive dyes. These approaches are capable to reveal cellular heterogeneity causing electrical isolation of functional circuits, reduced ion-transfer between different cell types, and anisotropy of tracer coupling. With a selective or combinatory use of these methods, the results will shed light on cellular properties of glial cells and their contribution to neuronal function.

**Keywords:** patch clamp, paired recordings, astrocyte syncytial isopotentiality, tracer coupling, wide field imaging

## INTRODUCTION

Gap junction channels connect the cytosol of neighboring cells and allow the exchange of ions and small molecules, such as metabolites (Giaume et al., 2010, 2020). Gap junctions form, when two connexons in the membrane of neighboring cells align. Connexons in turn are hexamers that are formed by connexins (Cx; **Figure 1A**). There are 21 Cxs identified so far of which 11 are expressed by neurons and glial cells in the CNS that differ in their mass (Bedner et al., 2012) and expression profile (including developmental and cell type specificity) (Dahl et al., 1996; Kunzelmann et al., 1999; Nagy et al., 1999; Nagy and Rash, 2000; Augustin et al., 2016; Wadle et al., 2018). The composition of gap junctions with different connexons and Cxs defines their properties, for example selectivity and permeability (Bukauskas and Verselis, 2004; Harris, 2007; Abbaci et al., 2008). In addition, post-translational modifications further regulate gap junctional communication (Goodenough and Paul, 2009; Axelsen et al., 2013; Aasen et al., 2018). Homocellular coupling between astrocytes and oligodendrocytes is mediated by homotypic gap junctions (**Figure 1B**; Giaume and Theis, 2010; Maglione et al., 2010). Furthermore, heterocellular (panglial) coupling is observed between both cell types using heterotypic gap junctions (Wasseff and Scherer, 2011; Griemsmann et al., 2015; Augustin et al., 2016; Moshrefi-Ravasdjani et al., 2017; Claus et al., 2018; Wadle et al., 2018; Xin et al., 2019).





In the corpus callosum, astrocytes and NG2 glia form panglial networks (Moshrefi-Ravasdjani et al., 2017). However, in many other brain regions—like the hippocampus, the cortex, and the medial nucleus of the trapezoid body—NG2 glia are neither tracer nor electrically coupled to other glial cells (Wallraff et al., 2004; Houades et al., 2008; Muller et al., 2009; Xu et al., 2014; Bedner et al., 2015; Griemsmann et al., 2015).

Gap junctional coupling is important for homeostasis of  $K^+$  (Wallraff et al., 2006; Pannasch et al., 2011; Breithausen et al., 2020; MacAulay, 2020),  $Na^+$  (Langer et al., 2012; Augustin et al., 2016; Moshrefi-Ravasdjani et al., 2017; Wadle et al., 2018),  $Cl^-$  (Egawa et al., 2013), and neurotransmitters (Pannasch et al., 2011; Chaturvedi et al., 2014). Furthermore, regulated gap junctional coupling is mandatory for activity-dependent redistribution of metabolites, such as glucose (Cruz et al., 2007; Rouach et al., 2008; Giaume et al., 2010). In addition, Cx expression and gap junctional communication are altered under pathophysiological conditions (Cotrino et al., 1998; Nakase et al., 2006; Giaume et al., 2010, 2019, 2020; Xu et al., 2010; Bedner et al., 2015; Lee et al., 2016; Wang Q. et al., 2020). Thus, the basic knowledge about glial gap junctional communication is fundamentally important for our further understanding of the complex neuron-glia interaction in healthy and diseased brains.

Astrocytes can be identified by several approaches. Many astrocytes express marker proteins such as GFAP, S100 $\beta$ , GLAST, or GLT-1 (Eng et al., 2000; Zhou et al., 2006; Kafitz et al., 2008; Schreiner et al., 2014). However, there are subpopulations of astrocytes, which for example do not express GFAP (Kafitz et al., 2008). Additionally, a fraction of NG2 glia are characterized by expression of GFAP and S100 $\beta$

(Nolte et al., 2001; Matthias et al., 2003; Karram et al., 2008). In 2004, the red fluorescent dye sulforhodamine (SR) 101 was introduced as a marker for astrocytes (Nimmerjahn et al., 2004), which allows the *a priori* identification of classical astrocytes in various brain regions, for example, in hippocampus, cortex, and auditory brainstem (Nimmerjahn et al., 2004; Kafitz et al., 2008; Stephan and Friauf, 2014; Ghirardini et al., 2018). Additionally, the use of SR101 is particularly advantageous in astrocyte imaging experiments as it can be combined with ion sensitive dyes such as Fura-2 and sodium-binding benzofuran isophthalate (SBFI; Kafitz et al., 2008; Langer et al., 2012).

Another approach for *a priori* identification of astrocytes is the utilization of reporter mice, such as GFAP-eGFP mice (Nolte et al., 2001). However, the transcript labels only a subset of astrocytes (Nimmerjahn et al., 2004) and, moreover, the transcript is also weakly expressed by NG2 glia (Matthias et al., 2003). Alternatively, ALDH1L1-eGFP mice can be used to identify astrocytes (Heintz, 2004; Yang et al., 2011). These reporter mice exhibit a more accurate labeling pattern of astrocyte populations (Cahoy et al., 2008). Aside this, reporter mice are available to *a priori* identify other glia, such as oligodendrocytes (PLP-GFP mice; Fuss et al., 2000) or NG2 glia (NG2-eYFP mice; Karram et al., 2008). It is worth mentioning that all these reporter mice are suitable to be combined with imaging of ion-sensitive dyes (Moshrefi-Ravasdjani et al., 2017).

A hallmark of classical astrocytes is their large  $K^+$  conductance (Stephan et al., 2012), which results in a highly negative membrane potential (Zhou et al., 2006; Kafitz et al., 2008). Further, astrocyte properties are less

constant as the expression of many astrocyte-typical proteins is regulated during early postnatal development (Felix et al., 2020b). For example, the expression of inwardly rectifying  $K^+$  channels ( $Kir_{4.1}$ ) and two-pore domain  $K^+$  channels ( $K_{2p}$ ) increases (Seifert et al., 2009; Nwaobi et al., 2014; Lunde et al., 2015; Moroni et al., 2015; Olsen et al., 2015) causing a strong decrease in membrane resistance ( $R_M$ ; Zhou et al., 2006; Kafitz et al., 2008; Stephan et al., 2012; Zhong et al., 2016). Simultaneously, the detectable amount of  $K_V$  channel-mediated currents decreases, which together alters the astrocytic current-voltage relationship from non-linear to linear (Zhou et al., 2006; Kafitz et al., 2008; Zhong et al., 2016). In contrast to NG2 glia, astrocytes do not express  $Na_V$  channels (Matthias et al., 2003; Zhou et al., 2006; Kafitz et al., 2008; Zhong et al., 2016).

## ANALYSIS OF GAP JUNCTIONAL COUPLING

There are many different techniques available to study gap junctions. These include but are not limited to whole-cell patch-clamp (paired recordings, analysis of isopotentiality, tracer injection), genetic approaches (FRAP, PARIS, StarTrack, transgenic mice), imaging of ion-sensitive dyes (e.g., SBFI), and expression studies (immunohistochemistry, western blotting) (Abbaci et al., 2008; Giaume and Theis, 2010; Bedner et al., 2012; Langer et al., 2012; Griemsmann et al., 2015; Droguerre et al., 2019; Eitelmann et al., 2019; Gutierrez et al., 2019; Wu et al., 2019; Du et al., 2020; McCutcheon et al., 2020). Here, we focus on approaches to analyze gap junctional communication that can be implemented easily in most electrophysiology and imaging laboratories.

### Patch Clamp-Based Approaches

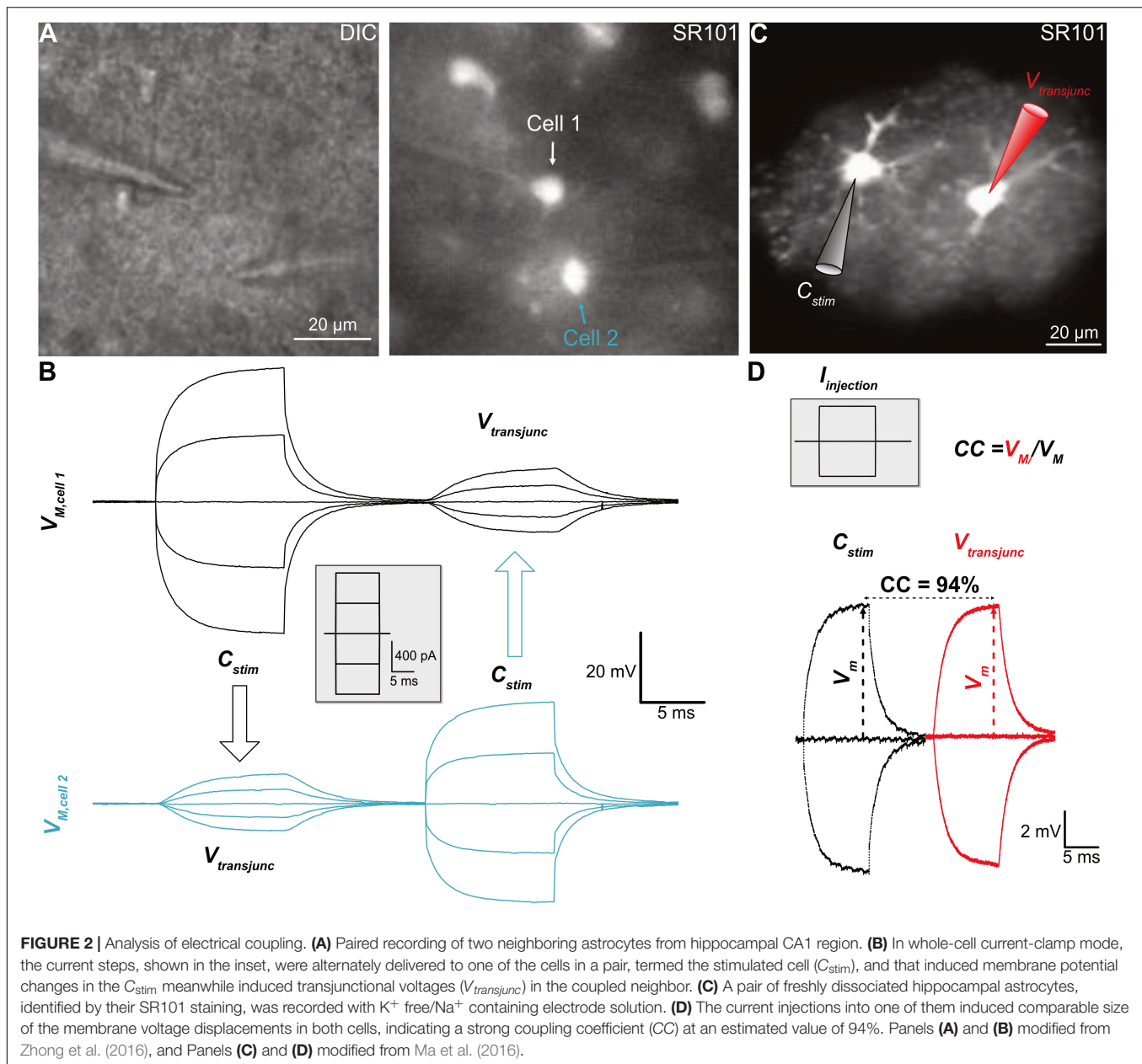
Electrophysiological methods are commonly used to detect gap junctional coupling of cells. In 1966, the first evidence that astrocytes are intercellularly coupled was provided by an electrophysiological study of amphibian optic nerve by Kuffler et al. (1966). In their report, an elegant triple-sharp-electrode recording mode was used to reveal a “low-resistance connection” between neuroglia, which we know now as the gap junctional coupling of fibrous astrocytes in optic nerves. This electrophysiological method was continually used until the 1980s for glial physiology study. For example, Kettenmann and Ransom used it to record cultured astrocytes and oligodendrocytes, confirming that gap junctions were indeed the molecular identities for the functional coupling of these glial subtypes (Kettenmann and Ransom, 1988; Ransom and Kettenmann, 1990).

The advent of patch-clamp in the 1990s ushered electrophysiological studies into a new era. Since the patch-clamp system is able for simultaneous current injection and membrane potential recording, now only two electrodes are used for paired recording. Here, we will limit our discussion to this advanced paired recording mode and its application to analyze the functional connectivity of neighboring astrocytes.

Until now, this technique has been used by several research laboratories for study of gap junctional coupling in native astrocytes in brain slices and freshly isolated astrocytes (Muller et al., 1996; Meme et al., 2009; Xu et al., 2010, 2014; Ma et al., 2016; Zhong et al., 2016; Kiyoshi et al., 2018). These studies demonstrated the paired recording mode as a highly sensitive method for revealing the functional coupling of astrocytes *in situ* and in pairs of freshly dissociated astrocytes. To address the electrical role of gap junctional coupling for astrocyte syncytium, a single electrode method was developed in 2016 with details described in the following “Astrocyte Syncytial Isopotentiality” section. Together with computational modeling, this method allows for monitoring dynamical changes in the coupling strength of an astrocyte syncytium (Ma et al., 2016; Kiyoshi et al., 2018). Another way to assess gap junctional coupling is to add a tracer to the internal solution of patch pipettes and to visualize gap junction-coupled cells. In the following section, we will first discuss the rationale, application, advantage, and limitation of the commonly used paired recording model and the newly developed syncytial isopotentiality measurement. Thereafter, we will highlight, how the addition of gap junction-permeable tracers to the pipette solution can be used to visualize cell-to-cell coupling and to subsequently analyze the topography of tracer-coupled networks.

### Paired Recording Mode

The rationale behind the design of the paired recording model lies in the basic properties of gap junction channels. Gap junctions are large aqueous pores, 8–16 Å, filled with electrolytes that make them ideal electrical conductors for the flow of ionic currents between coupled cells (Weber et al., 2004). In the adjacent cells, the easiness of the ionic current flow is determined by the number of gap junctions aggregated on the plaques in the interface of the adjacent cells, or the intercellular gap junctional resistance ( $R_{gap}$ ). Accordingly, the paired recording mode is designed to examine the  $R_{gap}$  through the passing of injected currents in one of the two coupled cells and to measure subsequently the size of remaining transjunctional voltage arriving at the second cell (Figures 2A,B; Bennett, 1966; Bennett et al., 1991; Ma et al., 2016). There are unique characteristics associated with paired recordings. It is known that the gap junctions formed by different Cxs differ in their permeability properties for endogenous compounds, therefore, differentially regulate the intercellular transfer of metabolites, i.e., glucose, and signaling molecules, such as ATP, glutamate, and  $IP_3$  (Goldberg et al., 1999, 2002; Niessen et al., 2000). It is also known that Cxs vary in pore size and conductivity (~30 to ~300 pS) (Hille, 2001). However, the Cxs ubiquitously exhibit high selectivity to the major intracellular monovalent cation  $K^+$  and  $Na^+$  in the order of  $K^+ > Na^+$  (Wang and Veenstra, 1997), and these ions are charge carriers that mediate current flow between coupled cells. Thus, independent of Cx isoforms, transjunctional voltage measurements stand out as an universal readout of gap junctional coupling (Veenstra et al., 1995; Veenstra, 1996). Additionally, paired recordings are featured by their high detection sensitivity conferred by the



state-of-the-art electronic engineering technology of the patch-clamp amplifier, allowing detection of the ionic currents at the picoampere scale.

Experimentally, two adjacent astrocytes are sequentially recorded in whole-cell mode (**Figures 2A,B**). Subsequently, the current can be alternately injected into one of the recorded cells, defined as the stimulated cell ( $C_{stim}$ ), whereas the transjunctional voltage is recorded in the neighboring recipient cell ( $C_{reci}$ ). Although the  $R_{gap}$  can be calculated from the basic membrane properties and the current-induced membrane voltages, the coupling strength is commonly expressed as the coupling coefficient ( $CC$ )—the ratio of voltages measured from the  $C_{reci}/C_{stim}$ . The higher a  $CC$  value, the stronger the cell-to-cell coupling (Bennett, 1966; Bennett et al., 1991; Ma et al., 2016).

A major advantage of paired recordings is their high sensitivity, which is determined by the open probability that is universally high among gap junctions in the range of 0.6–0.9; whereas the sensitivity of tracer coupling is mostly determined by the pore selectivity that varies among gap junctions (Nielsen et al., 2012). Consequently, in simultaneous transjunctional voltage and dye coupling measurements, it is common to see measurable transjunctional voltages in an absence of detectable dye coupling (Murphy et al., 1983; Ransom and Kettenmann, 1990; Sontheimer et al., 1991; Xu et al., 2010). An example that paired recordings have a higher sensitivity was shown in a study carried out in hippocampal astrocytes *in situ* (Xu et al., 2010). Incubation of brain slices with a gap junction inhibitor, meclofenamic acid (MFA, 100  $\mu M$ ), was able to inhibit astrocyte



gap junctional coupling by 99% (Ma et al., 2016). Interestingly, in the presence of 100  $\mu\text{M}$  MFA, the cross-diffusion of two tracers, Lucifer Yellow (LY) and biocytin, separately loaded into two recording electrodes, were completely inhibited, whereas the transjunctional voltages remained intact (Xu et al., 2010). In the barrel cortex, the Cx43 expression was found to be enriched within the barrels, but largely absent in the inter-barrel space (septa), and this was associated with a restricted dye coupling inside the barrels (Houades et al., 2006). To examine whether such segregated dye coupling indeed indicates a complete absence of gap junctional of astrocytes between barrels and their surrounding septa, the paired recording was carried out between a pair of astrocytes, one inside another outside of the barrel. The results showed that in the transjunctional voltage measurement, astrocytes do communicate inside and outside of the barrels and, therefore, are gap junctional coupled into a syncytium (Kiyoshi et al., 2018). Therefore, the existence of gap junctional coupling can be more sensitively inspected by this method.

Nevertheless, there are also technical challenges and limitations. First of all, still, only a handful of experimenters successfully employed paired recordings in their research. The technical complexity of paired recordings to monitor junctional coupling has limited more researchers to take advantage of this powerful tool in their glial physiology study. The second obstacle that impedes the application of paired recordings is the low  $R_M$  of astrocytes at an estimated level of 6.4  $\text{M}\Omega$  (Du et al., 2015). As a result, the “leaky” membrane shunts most of the injected currents, making it impossible to estimate the current passing through gap junctions resulting in erroneous CC calculation (Du et al., 2020). To make the matters worse, astrocytes are coupled into a syncytial network; each astrocyte is typically directly coupled to 7–9 nearest neighbors across the brain (Xu et al., 2010; Ma et al., 2016; Kiyoshi et al., 2018). Consequently, the injected currents to one of the recorded astrocytes should be redistributed into coupled astrocytes at unknown ratios (in a parallel electrical circuit) (Cotrina et al., 1998). Therefore, the leaking membrane and syncytial coupling make it next to impossible to calculate the actual CC in brain slice recordings. Consequently, rather low CC values in the range from 1.6% to 5.1% were reported from hippocampal astrocytes *in situ* (Meme et al., 2009; Xu et al., 2010).

To solve this problem, the innovative use of paired recordings was applied to freshly dissociated pairs of astrocytes to avoid extensive coupling. To circumvent the shunt of injected currents through abundantly expressed membrane  $\text{K}^+$  channels, the physiological  $\text{K}^+$  content in the electrode solution was substituted equimolarly by  $\text{Na}^+$ ; hence, the electrode  $\text{Na}^+$  equilibrating with the recorded pair of astrocytes will not leak through the membrane  $\text{K}^+$  channels, and measured currents will therefore better reflect junctional coupling (Figures 2C,D). Under these conditions, a strong coupling CC of 94% was revealed. Based on this CC, there was an estimate of 2,000 gap junctions aggregated at the interface of two neighboring astrocytes, and a calculated  $R_{\text{gap}}$  at 4.3  $\text{M}\Omega$  (Ma et al., 2016), which is even lower than the astrocytic  $R_M$  of 6.4  $\text{M}\Omega$  (Du et al., 2015). These results together indicate that the electrical barrier between astrocytes is nearly absent. Recently, ultrastructural

details of astrocyte-astrocyte contacts have been revealed that explain how such a low inter-astrocytic resistance could be biophysically achieved (Kiyoshi et al., 2020).

In summary, the rationale for paired recordings is based on an uniform feature of high open probability of gap junction channels for two intracellular monovalent cations,  $\text{K}^+$  and  $\text{Na}^+$ . Therefore, it offers a rather universal readout to study the functional gap junctional coupling at high sensitivity. For brain slice studies, however, the paired recordings are most valuable for inspecting the existence of functional gap junctional coupling, but are of limited value for quantitative analysis of the CC between astrocytes due to the low  $R_M$  and syncytial coupling. Combinatory use of freshly dissociated pairs of astrocytes and non-physiological  $\text{Na}^+$  or  $\text{Cs}^+$  electrode solution is a powerful alternative to circumvent the above obstacles.

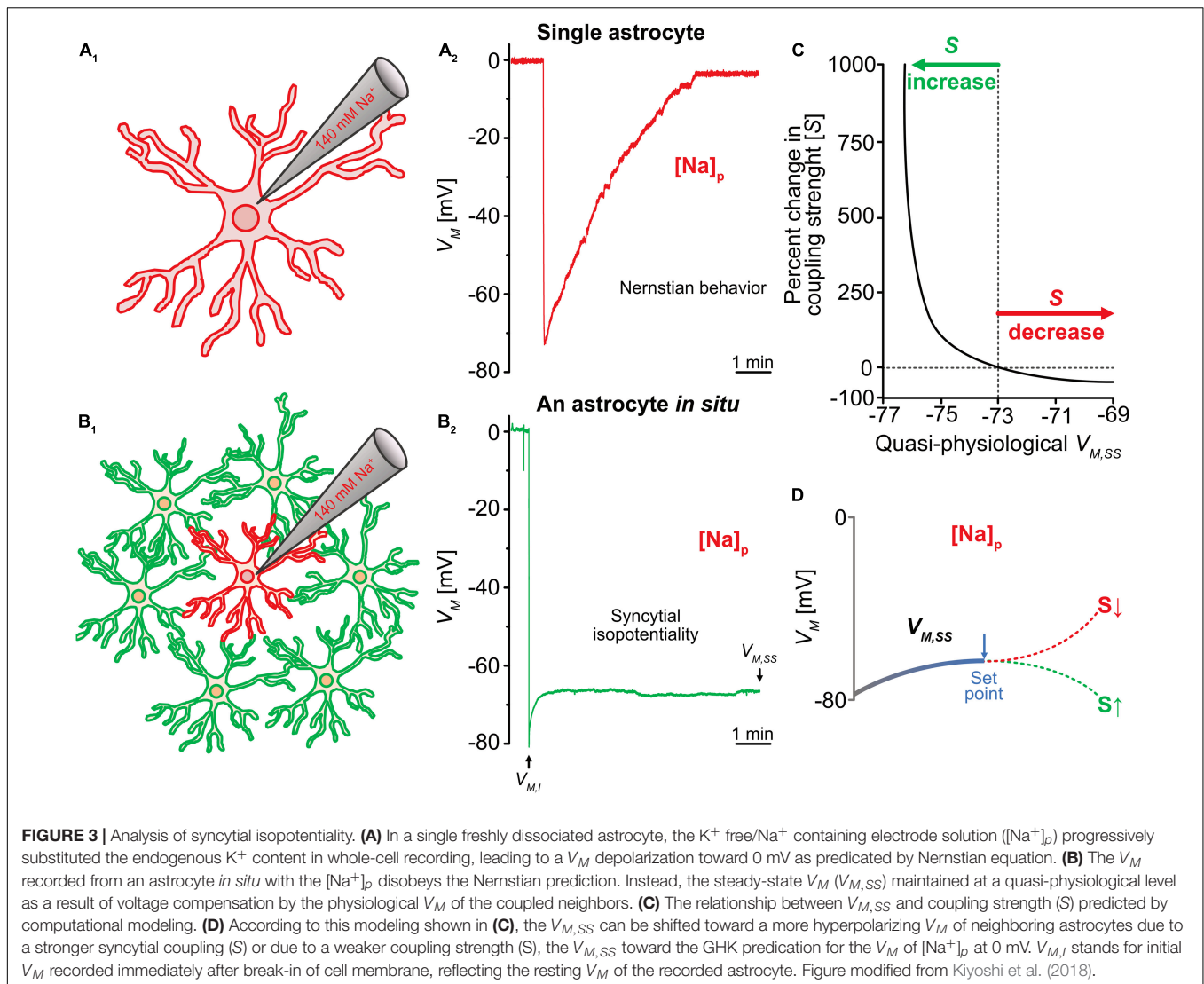
### Astrocyte Syncytial Isopotentiality

As mentioned above, the  $R_{\text{gap}}$  between astrocytes is even lower than astrocytes'  $R_M$ , suggesting that two neighboring astrocytes are able to constantly equalize their membrane potentials and therefore electrically behave as one cell. By extension, the gap junction coupled astrocytes should then be able to balance their membrane potentials to comparable levels so that a syncytial isopotentiality could be achieved. In fact, this possibility was postulated in the past (Muller, 1996) and was discussed by Richard Orkand and his colleagues to be a necessity for the operation of  $\text{K}^+$  spatial buffering in the brain (personal communication with Dr. Serguei Skatchkov). This syncytial isopotentiality was experimentally demonstrated in 2016 (Ma et al., 2016), and a system-wide existence of this feature in the astrocyte networks was confirmed soon after that (Huang et al., 2018; Kiyoshi et al., 2018; Wang W. et al., 2020).

The rationale for the methodological design is based on a basic feature of astrocytes. Physiologically, an astrocyte behaves as a perfect  $\text{K}^+$  electrode (Kuffler et al., 1966; Ransom and Goldring, 1973). Therefore, one can experimentally substitute the intracellular  $\text{K}^+$  concentration ( $[\text{K}^+]_i$ ) through dialysis of the recorded cell with electrode solution containing equimolar (i.e. 140 mM)  $\text{Na}^+$  (or  $\text{Cs}^+$ ) (Ma et al., 2016; Wang W. et al., 2020). This, in turn, alters the  $V_M$  of the recorded astrocyte from  $\text{K}^+$  equilibrium potential ( $E_K$ , -80 mV) to  $\text{Na}^+$  equilibrium potential ( $E_{\text{Na}}$ ,  $\sim 0$  mV) according to the prediction from the Goldman-Hodgkin-Katz (GHK) equation. In single freshly dissociated astrocytes, the  $V_M$  indeed shifts to  $\sim 0$  mV (Figure 3A) (Kiyoshi et al., 2018). However, should the  $R_{\text{gap}}$  be sufficiently low, the associated syncytium can then instantaneously act to compensate for the loss of physiological membrane potential ( $V_M$ ) in the recorded cell, and the level of the compensation should be determined by the coupling strength and the number of directly nearest coupled neighbors (Ma et al., 2016; Kiyoshi et al., 2018).

Experimentally, the syncytial isopotentiality can be detected by the substitution of endogenous  $\text{K}^+$  by a 140 mM  $\text{Na}^+/\text{K}^+$ -free electrode solution ( $[\text{Na}^+]_p$ ) (Figures 3A,B) and recording the astrocyte in current-clamp mode. The breakthrough of the membrane patch shifted the  $V_M$  immediately to a resting membrane potential of -78 mV (Figures 3A,B). Over time, the  $V_M$  reaches a stationary level of -73 mV. This is in sharp contrast to the anticipated depolarization to 0 mV as predicted by the





GHK equation for  $K^+$ -free electrode solution (**Figure 3A**). The initial  $V_M$  recording ( $V_{M,I}$ ) reflects the true resting  $V_M$  of an astrocyte (Ma et al., 2016; Kiyoshi et al., 2018). In hippocampal astrocyte syncytium, the steady-state  $V_M$  ( $V_{M,ss}$ ) in  $[Na^+]_p$  recordings is  $\sim 5$  mV more depolarized than  $V_{M,I}$ .

#### The Ionic Mechanisms Engaged in the Establishment of $V_{M,ss}$

To biophysically explain how the quasi-physiological  $V_{M,ss}$  is established, different size of syncytia, i.e., syncytia containing varying number of astrocytes, were used for  $V_{M,ss}$  recordings, and computational modeling was used to simulate the underlying ionic mechanisms (Ma et al., 2016). The rupture of an astrocyte with  $[Na^+]_p$  initiates dialysis of  $Na^+$  to the recorded astrocyte and associated syncytium (**Figure 3B1**). In the recorded cell, the  $Na^+$  dialysis dissipates the endogenous  $K^+$  content hence abolishes the physiological  $V_M$  established by the across membrane  $K^+$  gradient. To the coupled syncytium, the  $Na^+$  dialysis generates a  $Na^+$  gradient and current flow

across gap junctions that depolarizes neighboring astrocytes and hyperpolarizes the recorded cell. The latter is the major contributor to the quasi-physiological  $V_{M,ss}$ . Additionally, the dissipation of  $K^+$  content in the recorded cell attracts an influx of  $K^+$  from neighboring astrocytes. The accumulated  $K^+$  has the potential to establish a hyperpolarizing potential in the recorded cell therefore additionally contributes to the totality of the quasi-physiological  $V_{M,ss}$  (Ma et al., 2016). As shown in **Figure 3B2**, these two ionic flows take approximately 5 min to reach a steady-state after rupture of whole-cell recording (**Figure 3B2**).

How does the strength of syncytial isopotentiality influence the intensity of the  $Na^+$  and  $K^+$  current flows? As noted above, in the  $[Na^+]_p$  recorded astrocyte, there are two ionic current flows in opposite directions and collectively contribute to the measured  $V_{M,ss}$ ; the outward-going  $Na^+$  current from recorded cell to the coupled cells, and inward-going  $K^+$  current flow from the coupled astrocytes to the recorded cell. To simplify the analysis, we take the outward-going  $Na^+$  ( $I_{Na,out}$ ) to one of the coupled astrocytes as an example, the proximity of the potentials

in these two cells can be expressed as the difference of the voltages between the  $\text{Na}^+$ -loaded astrocyte ( $V_{Na}$ ) and a coupled neighbor ( $V_N$ )

$$(V_N - V_{Na}) = R_{\text{gap}} * I_{\text{Na,out}}$$

where  $(V_N - V_{Na}) = 0$  mV is a theoretically ideal isopotentiality achieved between the two cells. Assuming  $I_{\text{Na,out}}$  is a constant determined by its chemical gradient down the neighboring cell, then a higher strength of isopotentiality, i.e., lower  $(V_N - V_{Na})$ , is correlated to a lower junctional resistance ( $R_{\text{gap}}$ ). Secondly, as  $(V_N - V_{Na})$  approaches the ideal isopotentiality of 0 mV, the  $I_{\text{Na,out}}$  also diminishes to  $\sim 0$  pA. By extension, closer proximity of potentials between the recorded cell and its associated astrocytes, the less outward-going  $\text{Na}^+$  current flow from  $[\text{Na}^+]_p$  recorded astrocyte toward its associated syncytium.

Likewise, the intensity of the inward-going  $\text{K}^+$  current ( $I_{\text{K,in}}$ ) and syncytial coupling strength follows with the same relationship:

$$(V_N - V_{Na}) = R_{\text{gap}} * I_{\text{K,in}}$$

where the inward-going  $\text{K}^+$  current is impeded by increasing proximity of the  $V_{Na}$  to  $V_N$ . It should be noted that  $\text{K}^+$  cannot be substantially buildup due to efflux of  $\text{K}^+$  through membrane  $\text{K}^+$  channels in the  $[\text{Na}^+]_p$  recorded astrocyte; consequently, less hyperpolarizing potential can be built up to make a significant contribution to the recorded  $V_{M,ss}$ .

In summary, we described a method that uses  $[\text{Na}^+]_p$  to disrupt the continuity of a syncytial isopotentiality, and that in turn informs of the existence and the strength of the isopotentiality in an astrocyte syncytium. Biophysically, gap junctional ionic movement occurs during the equalization of the potential differences in a syncytium, therefore a strong syncytial isopotentiality means a less ionic movement inside a syncytium. Additionally, a larger syncytium has a greater capacity to minimize the ionic movement, which has been simulated in a computational model (Ma et al., 2016). Functionally, in the event of local extracellular environment changes, e.g., neuronal firing induced high  $\text{K}^+$ , syncytial isopotentiality provides a sustained driving force to individual astrocytes for high efficient  $\text{K}^+$  uptake, spatial transfer and release of  $\text{K}^+$  to regions where neuronal activity is low (Terman and Zhou, 2019).

### ***$V_{M,ss}$ as a Functional Readout of Coupling Strength (S) of Syncytial Coupling***

Based on the discussion above, the  $V_{M,ss}$  is established and regulated by the  $R_{\text{gap}}$  and the number of astrocytes in a coupled syncytium, therefore can lean to a more hyperpolarizing  $V_M$  in the neighboring astrocytes, or a more depolarizing  $V_M$  established by intracellular  $\text{Na}^+$ . Thus, the  $V_{M,ss}$  serves as a dynamic readout of the strength of syncytial coupling. To be able to quantitatively correlate the changes of  $V_{M,ss}$  with S, a computational model has been established (Figures 3C,D) where a stronger syncytial coupling leads to a stronger compensation of the  $V_{M,ss}$  towards the physiological  $V_M$  of neighboring astrocytes established by

140 mV  $[\text{K}^+]_i$ , whereas a weaker coupling shifts the  $V_{M,ss}$  toward GHK predicted  $E_K$  for the  $\text{Na}^+$  electrode solution. More details about the biophysical principles and assumptions used to build up this computational model are available in this publication (Kiyoshi et al., 2018). In addition, this model can be used for analysis of the dynamic change of coupling strength, for instance, during neuronal activation (Kiyoshi et al., 2018).

This method comprises several advantages. First, differing from paired recordings,  $V_{M,ss}$  is measured from single electrode recordings. Second, this method allows for dynamic monitoring of the coupling strength of a syncytium over time. Third, this method can be incorporated with astrocyte syncytial anatomy studies. For example, ALDH1L1-eGFP reporter mice were used for *a priori* astrocyte identification and examination of syncytial isopotentiality across brain regions. Additionally, the recorded brain slices were then further processed with the tissue-clearing method (Susaki et al., 2014, 2015), i.e., depletion of the brain lipid content, for high-resolution confocal imaging study of the cellular morphology and spatial organization patterns of astrocytes (Kiyoshi et al., 2018). This study showed that in different layers of the visual cortex, the anatomy, in terms of cell density, interastrocytic distance and the number of the nearest neighbors vary in morphometric analysis. However, S does not differ between layers. Additionally, S of the visual cortex was found to be stronger than in the hippocampal CA1 region (Kiyoshi et al., 2018). Fourthly, this method can be incorporated with tracer coupling to map the directionality and spatial coupling of a syncytium (see also “Tracer Coupling”). For example, in the cerebellum, Bergmann glia and velate astrocytes are derived from the same progenitor pool but are strikingly different in their morphology (Kita et al., 2013). Bergmann glia are characterized by having their cell bodies arranged in rows alongside with the soma of Purkinje neurons and extension of their processes along the Purkinje cell layer toward the *pia* of the cerebellum. Velate astrocytes are cerebellar protoplasmic astrocytes that exhibit characteristic velate sheath processes and are more dispersed in arrangement (Chan-Palay and Palay, 1972). S is significantly weaker in Bergmann glia networks than those established by velate astrocytes at the granular layer. In the tracer coupling analysis, the injection of tracer revealed the coupling of Bergmann glia and velate astrocytes. Thus, despite a striking difference in syncytial anatomy, the syncytial isopotentiality occurs to syncytial networks established by both subtypes of astrocytes (Kiyoshi et al., 2018).

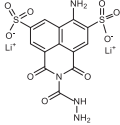
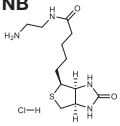
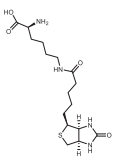
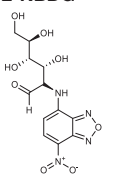
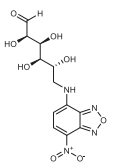
A limitation in this method is the inference of a syncytial isopotentiality based on biophysical principles and electrophysiological measurements. Significant progress has been made in the technique of genetically encoded voltage indicator (Kang et al., 2019). However, this state-of-the-art technique is still below the threshold to detect the subtle variation of voltages in an astrocyte syncytium, and therefore, future optimization of this technique is crucial to recruit advanced imaging techniques to study the physiology and pathology of astrocyte syncytial networks.

Tracer Coupling

Aside this direct measurement of cell-to-cell coupling, tracer coupling can be utilized to mimic diffusion within the network. Tracers are usually loaded for several minutes into a single cell via the backfill of the patch pipette. Simultaneously, tracers diffuse within the gap junction network. The tracer concentration is highest in the patched cell and declines within the network with increasing distance as it diffuses. There are various tracers available comprising different advantages and disadvantages (Table 1; see also Abbaci et al., 2008). An often used tracer is LY (Kawata et al., 1983). It is a fluorescent dye that allows direct observation of diffusion within the network. Subsequently, LY labeling can be combined with immunohistochemistry to determine the identity of coupled cells (Binmoller and Muller, 1992; Konietzko and Muller, 1994). However, it comprises low permeability at gap junctions consisting of Cx30 (Rackauskas et al., 2007). As Cx30 expression increases during early postnatal development (Nagy et al., 1999; Griemsmann et al., 2015; Augustin et al., 2016; Wadle et al., 2018), LY will only highlight a fraction of coupling in more mature tissue. In addition, LY has

a low solubility and tends to clog electrodes. As LY interferes with endogenous electrophysiological properties, it is rather not suitable to be combined with electrophysiological analyses (Tasker et al., 1991). Further fluorophores, e.g., Alexa Fluor (AF) dyes, can be used for tracing coupled cells as well (Han et al., 2013). Like LY, spreading of AF dyes can be assessed directly. However, they do not pass through Cx30 containing gap junctions and just insufficiently through other gap junctions requiring administration at high concentration (Weber et al., 2004). At lower concentrations, there is almost no diffusion to neighboring cells so that AF dyes can be used to label the patch-clamped cell (Augustin et al., 2016; Wadle et al., 2018; Eitelmann et al., 2019). Two other tracers, namely neurobiotin (Nb) and biocytin (Horikawa and Armstrong, 1988; Huang et al., 1992), are colorless and require fixation and further processing of the tissue. Thus, their diffusion cannot be assessed directly. The two tracers are recognized by streptavidin and avidin (Livnah et al., 1993). The latter ones can be linked to either fluorophores or enzymes. Using a fluorophore allows the combination with further immunohistochemical processing of the tissue (Schools

TABLE 1 | Commonly used tracers for analyzing gap junctional coupling.

Tracer	Mass [g/mol]	Fluorescence	Histology required	Advantage	Disadvantage	Reference(s)
<b>LY</b> 	457	✓	✗	Direct imaging	Low Cx30-permeability Alteration of electrophysiological properties	Tasker et al., 1991 Kawata et al., 1983 Rackauskas et al., 2007
<b>NB</b> 	323	✗	(Strept-/) Avidin conjugates	Permeable through all astrocytic Cx	Background labeling of endogenous biotin	Huang et al., 1992 Livnah et al., 1993
<b>Biocytin</b> 	375	✗	(Strept-/) Avidin conjugates	Permeable through all astrocytic Cx	Background labeling of endogenous biotin	Horikawa and Armstrong, 1988 Livnah et al., 1993
<b>2-NBDG</b> 	342	✓	✗	Imaging of glucose distribution	Degradation to non-fluorescent derivative	Yoshioka et al., 1996 Yamada et al., 2000
<b>6-NBDG</b> 	342	✓	✗	Imaging of glucose distribution		Speizer et al., 1985

LY, Lucifer Yellow; NB, neurobiotin; Cx, connexin; NBDG, deoxy-N-(7-nitrobenz-2-oxa-1,3-diazol-4-yl)-aminoglucose; AF, Alexa Fluor.

et al., 2006; Augustin et al., 2016; Eitelmann et al., 2019, 2020). Using peroxidases produces a light-stable product that is not sensitive to photo-bleaching (Konietzko and Muller, 1994; D'Ambrosio et al., 1998). Alternatively, fluorescent glucose analogues can be used (Speizer et al., 1985; Yamada et al., 2000). They allow to visualize activity-dependent, directed glucose redistribution in otherwise spherical networks (Rouach et al., 2008). However, it has to be kept in mind that, for example, 2-NBDG enters the glycolytic pathway and is degraded to a non-fluorescent derivative (Yoshioka et al., 1996).

Gap junctional coupling is not uniform, e.g., it was shown to increase developmentally (Binmoller and Muller, 1992; Schools et al., 2006; Houades et al., 2008; Langer et al., 2012; Griemsmann et al., 2015). Furthermore, there are many examples of spherical networks upon radial tracer diffusion in certain brain regions (Binmoller and Muller, 1992; Houades et al., 2006; Muller et al., 2009). However, in others—in particular in sensory systems—tracer spreading is unequal in different directions (Houades et al., 2008; Augustin et al., 2016; Claus et al., 2018; Condamine

et al., 2018a; Wadle et al., 2018). There, network anisotropy strongly correlates with anatomical and functional organization of the underlying neuronal circuitry. The anisotropy of tracer spreading originates from astrocyte topography (Anders et al., 2014; Augustin et al., 2016; Ghezali et al., 2018; Wadle et al., 2018). Interestingly, in the lateral superior olive—a conspicuous nucleus in the auditory brainstem—absence of spontaneous cochlea-driven neuronal activity leading to disturbed neuronal circuitry (Hirtz et al., 2012; Muller et al., 2019) causes altered astrocyte topography followed by altered orientation of tracer-coupled networks (Eitelmann et al., 2020). In recent years, several different approaches were developed to analyze the anisotropy of tracer-coupled networks (Figure 4). Most approaches are able to reliably detect network anisotropy; however, some are working only in certain brain regions (Eitelmann et al., 2019). The different approaches rely on (1) distance of the farthest cells that are labeled, (2) labeling intensity, (3) position of all coupled cells, or (4) a combination of the aforementioned parameters. Most approaches use the ratio of the diffusion range and/or brightness

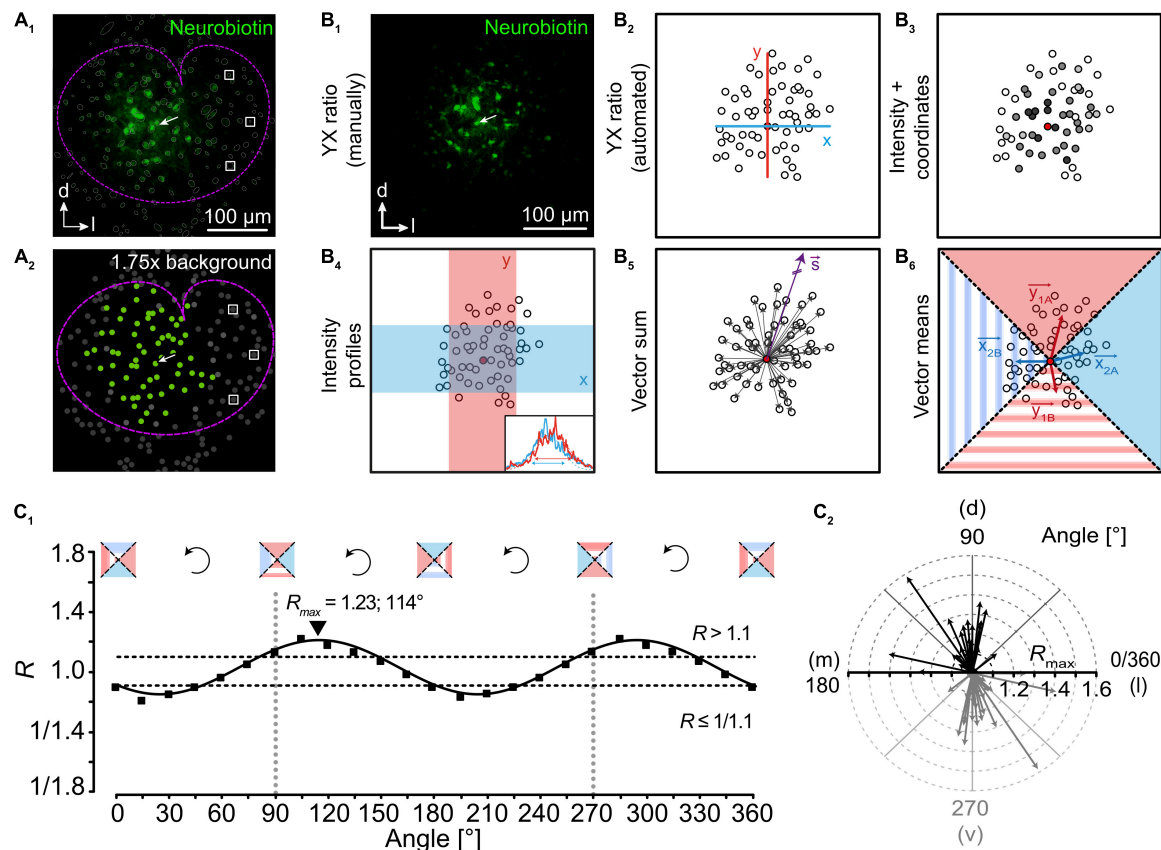


**FIGURE 4 |** Analysis of network topography. **(A)** Detection of coupled cells. Astrocytes in the lateral superior olive (outlined by dotted magenta line) form large tracer-coupled networks (**A<sub>1</sub>**; green). All identified cells are encircled with a thin gray line. Semi-automated detection of coupled cells is achieved by determining background fluorescence levels of cells (white boxes) being far located from the tracer-filled cell (arrow). Setting a threshold allows for unbiased selection of coupled cells (**A<sub>2</sub>**; green: coupled cells; gray: not coupled cells). **(B)** Approaches to study the topography of tracer-coupled networks. Anisotropy is often determined by the ratio of tracer spread (distance and/or intensity) in two directions that are orthogonal to each other (**B<sub>1</sub>–4,6**). Alternatively, a purely vector-based approach can be used (**B<sub>5</sub>**). **(C)** In case of ratio-based analyses, rotation of the coordinate system allows the precise determination of maximal anisotropy and orientation (**C<sub>1</sub>**; exemplarily shown for vector means, **B<sub>6</sub>**). Afterward, results can be gathered in a radar diagram to denote the degree of anisotropy and orientation of networks (**C<sub>2</sub>**). Figure modified from Eitelmann et al. (2019).



of the tracer in two directions. The most convenient approach is to measure the extent of tracer spreading in two directions orthogonal to each other (“YX ratio”). Here, anisotropy is determined by the four outermost cells showing tracer signal (Figure 4B<sub>1,2</sub>; Houades et al., 2006, 2008; Augustin et al., 2016; Ghezali et al., 2018; Wadle et al., 2018). However, since the

tracer signal is declining with distance to the loaded cell, it can be difficult to determine the correct extension of the network. Alternatively, the product of network extension multiplied with the somatic tracer intensity for two directions orthogonal to each other can be calculated (“Intensity + coordinates”; Figure 4B<sub>3</sub>; Anders et al., 2014). However, elevated somatic signal intensities

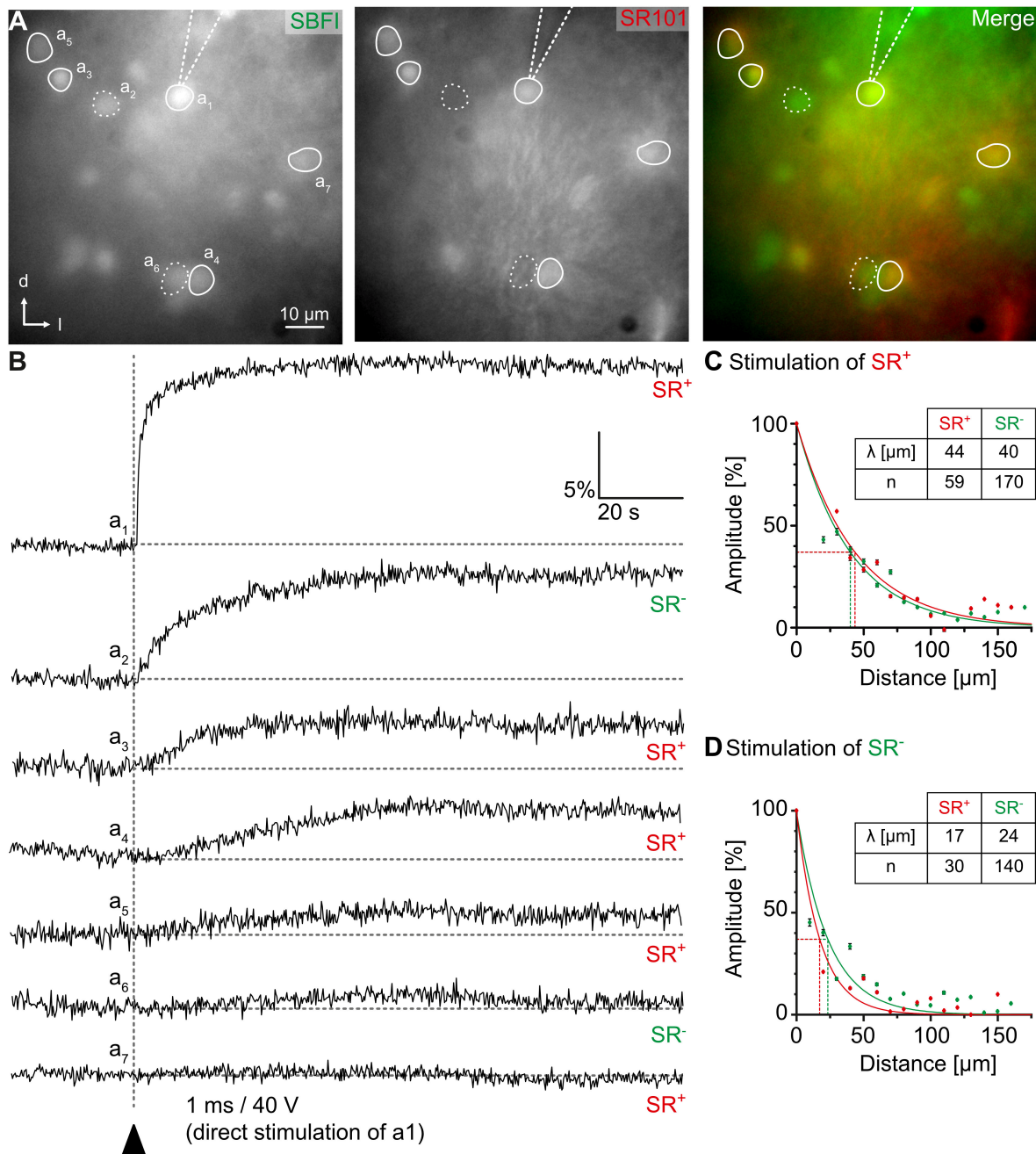


**FIGURE 5 |** Na<sup>+</sup> diffusion in glial networks. **(A)** Cells in the center of the inferior colliculus can be loaded with the fluorescent Na<sup>+</sup> indicator SBFI-AM (left). Astrocytes and *bona fide* oligodendrocytes can be distinguished by sulforhodamine (SR) 101-labeling. **(B)** Electrical stimulation results in Na<sup>+</sup> load of a single astrocyte (**a**<sub>1</sub>). Subsequently, neighboring astrocytes (**a**<sub>3</sub>–**a**<sub>5</sub>, **a**<sub>7</sub>; SR<sup>+</sup>) and *bona fide* oligodendrocytes (**a**<sub>2</sub>, **a**<sub>6</sub>; SR<sup>-</sup>), show elevated Na<sup>+</sup> transients as well. **(C,D)** Na<sup>+</sup> diffusion can be elicited by stimulation of both astrocytes **(C)** and *bona fide* oligodendrocytes **(D)**. The amplitude of Na<sup>+</sup> transients depends on the distance from the stimulated cell. Figure modified from Wadle et al. (2018).

due to expression of endogenous biotin (Bixel and Hamprecht, 2000; Yagi et al., 2002) might result in a distorted ratio. In another approach, the labeling intensity of somata and processes is analyzed to determine network anisotropy (“Intensity profiles”; **Figure 4B<sub>4</sub>**; Claus et al., 2018). Here, intensity plot profiles of two rectangles orthogonal to each other and the ratio of respective full-width at half-maximum (FWHM) are calculated. However, cell number or individual positions are neglected and must be analyzed separately, if required. Finally, there are two vector-based approaches. The first calculates the “Vector sum” (**Figure 4B<sub>5</sub>**; Condamine et al., 2018a,b). However, it only works in brain regions with defined borders, i.e., diffusion barriers resulting from reduced gap junction coupling. Examples of such brain regions are the trigeminal main sensory nucleus and the columns of the barrel cortex. In both, gap junction coupling is stronger within the nucleus and columns compared to areas outside. However, anisotropic tracer diffusion will be visualized only if the tracer is injected into an astrocyte that is not located in the center (Houades et al., 2008; Condamine et al., 2018a) as the “Vector sum” approach is not capable to detect the anisotropy of tracer-coupled networks if they are symmetric with respect to a point (Eitelmann et al., 2019). The second vector-based approach calculates the “Vector means” in four 90° sectors and the ratio of tracer extension is calculated (**Figure 4B<sub>6</sub>**; Eitelmann et al., 2019, 2020). However, analyzing the anisotropy of tracer spreading using only two fixed axes might result in falsified results. For example, if an anisotropic network is turned by 45° from one of the two axes, all ratio-based approaches will postulate spherical network. Therefore, a subsequent analysis using a rotating coordinate system will not only determine the maximal anisotropy of a network, but will also define the preferred orientation (**Figure 4C**; Eitelmann et al., 2019). Taken together, heterogeneity of gap junctional coupling can be visualized excellently by tracer coupling studies. However, they often provide only a snap-shot of coupling using a non-physiological tracer.

## Wide Field (Na<sup>+</sup>) Imaging

Imaging of intracellular ion concentration can be a good tool to supplement tracer coupling studies. For the interpretation of ion diffusion within the gap junction network, it is beneficial to analyze the spread of ions that is less effected by signaling cascades. Thus, Ca<sup>2+</sup> is a less suitable candidate as signaling to neighboring cells is generated by intra- and extracellular pathways (Giaume and Venance, 1998; Bernardinelli et al., 2004; Scemes and Giaume, 2006). However, intercellular Na<sup>+</sup> spread depends on gap junctional coupling as deletion of Cx43 and Cx30 prevents ion exchange between neighboring astrocytes (Wallraff et al., 2006; Langer et al., 2012). However, it has to be kept in mind that intracellular Na<sup>+</sup> is not completely independent from signaling cascades as it is linked to Ca<sup>2+</sup> via the Na<sup>+</sup>/Ca<sup>2+</sup> exchanger (Felix et al., 2020a). For Na<sup>+</sup> imaging, cells are dye-loaded, e.g., with the membrane-permeable form of SBFI (SBFI-acetoxymethyl ester). After cleavage by endogenous esterases SBFI allows ratiometric imaging of [Na<sup>+</sup>]<sub>i</sub> (**Figure 5**; Minta and Tsien, 1989; Meier et al., 2006). Na<sup>+</sup> load into a single cell can be achieved via direct electrical stimulation. This will result in

Na<sup>+</sup> rise in the stimulated and in neighboring cells (**Figure 5B**; Langer et al., 2012; Augustin et al., 2016; Moshrefi-Ravasdjani et al., 2017; Wadle et al., 2018). Measuring the maximal [Na<sup>+</sup>]<sub>i</sub> increase allows for the calculation of the length constant  $\lambda$  using a mono-exponential function (**Figures 5C,D**; Augustin et al., 2016; Moshrefi-Ravasdjani et al., 2017; Wadle et al., 2018), which demonstrates, how efficient Na<sup>+</sup> is redistributed and how strong gap junctional coupling is. It was shown that spatial spread of Na<sup>+</sup> between astrocytes was halfway far in the corpus callosum compared to other brain regions, i.e., hippocampus, lateral superior olive, and inferior colliculus (Langer et al., 2012; Augustin et al., 2016; Moshrefi-Ravasdjani et al., 2017; Wadle et al., 2018). Furthermore, Na<sup>+</sup> diffusion is stronger within homocellular networks. In contrast, in heterocellular (panglial) networks Na<sup>+</sup> redistribution is reduced (**Figure 5D**; Moshrefi-Ravasdjani et al., 2017; Wadle et al., 2018), which likely results from a lower permeability of connexons, which are incorporated into the heterotypic gap junction channels (Bedner et al., 2006). Taken together, imaging of ion sensitive dyes is a good supplement to tracer coupling studies to further characterize gap junctional communication.

## CONCLUSION

Gap junctional communication between glial cells is important for ion and neurotransmitter homeostasis and ensures stabilization of their membrane potential. Though astrocytes throughout the brain share similar properties, they exhibit a considerable amount of region-dependent heterogeneity. To unravel these particular differences suitable approaches are necessary. In this review, we summarized and described well-established and recently developed methods that will allow electrophysiology and imaging laboratories to analyze gap junctional coupling in acute tissue slices.

## AUTHOR CONTRIBUTIONS

JS and MZ designed the study. JS, MZ, and SE wrote the manuscript. SE designed and arranged the figures. All authors contributed to the article and approved the submitted version.

## FUNDING

This study was supported by grants from the German Research Foundation (DFG Priority Program 1608 “Ultrafast and temporally precise information processing: Normal and dysfunctional hearing”: STE 2352/2-1) to JS and the National Institute of Neurological Disorders and Stroke (RO1NS116059) to MZ.

## ACKNOWLEDGMENTS

We acknowledge the support by the Heinrich Heine University Duesseldorf.

## REFERENCES

- Aasen, T., Johnstone, S., Vidal-Brime, L., Lynn, K. S., and Koval, M. (2018). Connexins: synthesis, post-translational modifications, and trafficking in health and disease. *Int. J. Mol. Sci.* 19:1296. doi: 10.3390/ijms19051296
- Abbaci, M., Barberi-Heyob, M., Blondel, W., Guillemin, F., and Didelon, J. (2008). Advantages and limitations of commonly used methods to assay the molecular permeability of gap junctional intercellular communication. *Biotechniques* 45, 56–62.
- Anders, S., Minge, D., Griemsmann, S., Herde, M. K., Steinhauser, C., and Henneberger, C. (2014). Spatial properties of astrocyte gap junction coupling in the rat hippocampus. *Philos. Trans. R. Soc. Lond. B Biol. Sci.* 369:20130600. doi: 10.1098/rstb.2013.0600
- Augustin, V., Bold, C., Wadle, S. L., Langer, J., Jabs, R., Philippot, C., et al. (2016). Functional anisotropic panglial networks in the lateral superior olive. *Glia* 64, 1892–1911. doi: 10.1002/glia.23031
- Axelsen, L. N., Calloe, K., Holstein-Rathlou, N. H., and Nielsen, M. S. (2013). Managing the complexity of communication: regulation of gap junctions by post-translational modification. *Front. Pharmacol.* 4:130. doi: 10.3389/fphar.2013.00130
- Bedner, P., Dupper, A., Huttmann, K., Muller, J., Herde, M. K., Dublin, P., et al. (2015). Astrocyte uncoupling as a cause of human temporal lobe epilepsy. *Brain* 138, 1208–1222. doi: 10.1093/brain/awv067
- Bedner, P., Niessen, H., Odermatt, B., Kretz, M., Willecke, K., and Harz, H. (2006). Selective permeability of different connexin channels to the second messenger cyclic AMP. *J. Biol. Chem.* 281, 6673–6681. doi: 10.1074/jbc.m511235200
- Bedner, P., Steinhauser, C., and Theis, M. (2012). Functional redundancy and compensation among members of gap junction protein families? *Biochim. Biophys. Acta* 1818, 1971–1984. doi: 10.1016/j.bbame.2011.10.016
- Bennett, M. V. (1966). Physiology of electrotonic junctions. *Ann. N. Y. Acad. Sci.* 137, 509–539. doi: 10.1111/j.1749-6632.1966.tb50178.x
- Bennett, M. V., Barrio, L. C., Bargiello, T. A., Spray, D. C., Hertzberg, E., and Saez, J. C. (1991). Gap junctions: new tools, new answers, new questions. *Neuron* 6, 305–320. doi: 10.1016/0896-6273(91)90241-q
- Bernardinelli, Y., Magistretti, P. J., and Chatton, J. Y. (2004). Astrocytes generate Na<sup>+</sup>-mediated metabolic waves. *Proc. Natl. Acad. Sci. U.S.A.* 101, 14937–14942. doi: 10.1073/pnas.0405315101
- Binmoller, F. J., and Muller, C. M. (1992). Postnatal development of dye-coupling among astrocytes in rat visual cortex. *Glia* 6, 127–137. doi: 10.1002/glia.440060207
- Bixel, M. G., and Hamprecht, B. (2000). Immunocytochemical localization of beta-methylcrotonyl-CoA carboxylase in astroglial cells and neurons in culture. *J. Neurochem.* 74, 1059–1067. doi: 10.1046/j.1471-4159.2000.0741059.x
- Breithausen, B., Kautzmann, S., Boehlen, A., Steinhauser, C., and Henneberger, C. (2020). Limited contribution of astroglial gap junction coupling to buffering of extracellular K<sup>+</sup> in CA1 stratum radiatum. *Glia* 68, 918–931. doi: 10.1002/glia.23751
- Bukauskas, F. F., and Verselis, V. K. (2004). Gap junction channel gating. *Biochim. Biophys. Acta* 1662, 42–60.
- Cahoy, J. D., Emery, B., Kaushal, A., Foo, L. C., Zamanian, J. L., Christopherson, K. S., et al. (2008). A transcriptome database for astrocytes, neurons, and oligodendrocytes: a new resource for understanding brain development and function. *J. Neurosci.* 28, 264–278. doi: 10.1523/jneurosci.4178-07.2008
- Chan-Palay, V., and Palay, S. L. (1972). The form of velate astrocytes in the cerebellar cortex of monkey and rat: high voltage electron microscopy of rapid Golgi preparations. *Z. Anat. Entwicklungsgesch.* 138, 1–19. doi: 10.1007/bf00519921
- Chaturvedi, R., Reddig, K., and Li, H. S. (2014). Long-distance mechanism of neurotransmitter recycling mediated by glial network facilitates visual function in *Drosophila*. *Proc. Natl. Acad. Sci. U.S.A.* 111, 2812–2817. doi: 10.1073/pnas.1323714111
- Claus, L., Philippot, C., Griemsmann, S., Timmermann, A., Jabs, R., Henneberger, C., et al. (2018). Barreloid borders and neuronal activity shape panglial gap junction-coupled networks in the mouse thalamus. *Cereb. Cortex* 28, 213–222.
- Condamine, S., Lavoie, R., Verdier, D., and Kolta, A. (2018a). Functional rhythmic domains defined by astrocytic networks in the trigeminal main sensory nucleus. *Glia* 66, 311–326. doi: 10.1002/glia.23244
- Condamine, S., Verdier, D., and Kolta, A. (2018b). Analyzing the size, shape, and directionality of networks of coupled astrocytes. *J. Vis. Exp.* 4, 58116. doi: 10.3791/58116
- Cotrina, M. L., Kang, J., Lin, J. H., Bueno, E., Hansen, T. W., He, L., et al. (1998). Astrocytic gap junctions remain open during ischemic conditions. *J. Neurosci.* 18, 2520–2537. doi: 10.1523/jneurosci.18-07-02520.1998
- Cruz, N. F., Ball, K. K., and Dienel, G. A. (2007). Functional imaging of focal brain activation in conscious rats: impact of [(14)C]glucose metabolite spreading and release. *J. Neurosci. Res.* 85, 3254–3266. doi: 10.1002/jnr.21193
- Dahl, E., Manthey, D., Chen, Y., Schwarz, H. J., Chang, Y. S., Lalley, P. A., et al. (1996). Molecular cloning and functional expression of mouse connexin-30, a gap junction gene highly expressed in adult brain and skin. *J. Biol. Chem.* 271, 17903–17910. doi: 10.1074/jbc.271.30.17903
- D'Ambrosio, R., Wenzel, J., Schwartzkroin, P. A., Mckhann, G. M. II, and Janigro, D. (1998). Functional specialization and topographic segregation of hippocampal astrocytes. *J. Neurosci.* 18, 4425–4438. doi: 10.1523/jneurosci.18-12-04425.1998
- Droguerre, M., Tsurugizawa, T., Duchene, A., Portal, B., Guiard, B. P., Deglon, N., et al. (2019). A new tool for in vivo study of astrocyte connexin 43 in brain. *Sci. Rep.* 9:18292.
- Du, Y., Kiyoshi, C. M., Terman, D., and Zhou, M. (2020). “Analysis of the functional states of an astrocyte syncytium,” in *Basic Neurobiology Techniques*, ed. N. Wright (New York, NY: Humana), 285–313. doi: 10.1007/978-1-4939-9944-6\_12
- Du, Y., Ma, B., Kiyoshi, C. M., Alford, C. C., Wang, W., and Zhou, M. (2015). Freshly dissociated mature hippocampal astrocytes exhibit passive membrane conductance and low membrane resistance similarly to syncytial coupled astrocytes. *J. Neurophysiol.* 113, 3744–3750. doi: 10.1152/jn.00206.2015
- Egawa, K., Yamada, J., Furukawa, T., Yanagawa, Y., and Fukuda, A. (2013). Cl(-) homeodynamics in gap junction-coupled astrocytic networks on activation of GABAergic synapses. *J. Physiol.* 591, 3901–3917. doi: 10.1113/jphysiol.2013.257162
- Eitelmann, S., Hirtz, J. J., and Stephan, J. (2019). A vector-based method to analyze the topography of glial networks. *Int. J. Mol. Sci.* 20:2821. doi: 10.3390/ijms20112821
- Eitelmann, S., Petersilie, L., Rose, C. R., and Stephan, J. (2020). Altered gap junction network topography in mouse models for human hereditary deafness. *Int. J. Mol. Sci.* 21:7376. doi: 10.3390/ijms21197376
- Eng, L. F., Ghirnikar, R. S., and Lee, Y. L. (2000). Glial fibrillary acidic protein: GFAP-thirty-one years (1969–2000). *Neurochem. Res.* 25, 1439–1451.
- Felix, L., Delekate, A., Petzold, G. C., and Rose, C. R. (2020a). Sodium fluctuations in astroglia and their potential impact on astrocyte function. *Front. Physiol.* 11:871. doi: 10.3389/fphys.2020.00871
- Felix, L., Stephan, J., and Rose, C. R. (2020b). Astrocytes of the early postnatal brain. *Eur. J. Neurosci.* [Epub ahead of print]. doi: 10.1111/ejn.14780
- Fuss, B., Mallon, B., Phan, T., Ohlemeyer, C., Kirchhoff, F., Nishiyama, A., et al. (2000). Purification and analysis of in vivo-differentiated oligodendrocytes expressing the green fluorescent protein. *Dev. Biol.* 218, 259–274. doi: 10.1006/dbio.1999.9574
- Ghezali, G., Calvo, C. F., Pillet, L. E., Llense, F., Ezan, P., Pannasch, U., et al. (2018). Connexin 30 controls astroglial polarization during postnatal brain development. *Development* 145:dev155275. doi: 10.1242/dev.155275
- Ghirardini, E., Wadle, S. L., Augustin, V., Becker, J., Brill, S., Hammerich, J., et al. (2018). Expression of functional inhibitory neurotransmitter transporters GlyT1, GAT-1, and GAT-3 by astrocytes of inferior colliculus and hippocampus. *Mol. Brain* 11:4.
- Giaume, C., Koulakoff, A., Roux, L., Holcman, D., and Rouach, N. (2010). Astroglial networks: a step further in neuroglial and gliovascular interactions. *Nat. Rev. Neurosci.* 11, 87–99. doi: 10.1038/nrn2757
- Giaume, C., Saez, J. C., Song, W., Leybaert, L., and Naus, C. C. (2019). Connexins and pannexins in Alzheimer's disease. *Neurosci. Lett.* 695, 100–105. doi: 10.1016/j.neulet.2017.09.006
- Giaume, C., and Theis, M. (2010). Pharmacological and genetic approaches to study connexin-mediated channels in glial cells of the central nervous system. *Brain Res. Rev.* 63, 160–176. doi: 10.1016/j.brainresrev.2009.11.005
- Giaume, C., and Venance, L. (1998). Intercellular calcium signaling and gap junctional communication in astrocytes. *Glia* 24, 50–64. doi: 10.1002/(sici)1098-1136(199809)24:1<50::aid-glia6>3.0.co;2-4



- Giaume, C. B., Naus, C. C., Saez, J. C., and Leybaert, L. (2020). Glial connexins and pannexins in the healthy and diseased brain. *Physiol. Rev.* 101, 93–145. doi: 10.1152/physrev.00043.2018
- Goldberg, G. S., Lampe, P. D., and Nicholson, B. J. (1999). Selective transfer of endogenous metabolites through gap junctions composed of different connexins. *Nat. Cell Biol.* 1, 457–459. doi: 10.1038/15693
- Goldberg, G. S., Moreno, A. P., and Lampe, P. D. (2002). Gap junctions between cells expressing connexin 43 or 32 show inverse permselectivity to adenosine and ATP. *J. Biol. Chem.* 277, 36725–36730. doi: 10.1074/jbc.M109797200
- Goodenough, D. A., and Paul, D. L. (2009). Gap junctions. *Cold Spring Harb. Perspect. Biol.* 1:a002576.
- Griemann, S., Hoft, S. P., Bedner, P., Zhang, J., Von Staden, E., Beinhauer, A., et al. (2015). Characterization of panglial gap junction networks in the thalamus, neocortex, and hippocampus reveals a unique population of glial cells. *Cereb. Cortex* 25, 3420–3433. doi: 10.1093/cercor/bhu157
- Gutierrez, Y., Garcia-Marques, J., Liu, X., Fortes-Marco, L., Sanchez-Gonzalez, R., Giaume, C., et al. (2019). Sibling astrocytes share preferential coupling via gap junctions. *Glia* 67, 1852–1858. doi: 10.1002/glia.23662
- Han, X., Chen, M., Wang, F., Windrem, M., Wang, S., Shanz, S., et al. (2013). Forebrain engraftment by human glial progenitor cells enhances synaptic plasticity and learning in adult mice. *Cell Stem Cell* 12, 342–353. doi: 10.1016/j.stem.2012.12.015
- Harris, A. L. (2007). Connexin channel permeability to cytoplasmic molecules. *Prog. Biophys. Mol. Biol.* 94, 120–143. doi: 10.1016/j.pbiomolbio.2007.03.011
- Heintz, N. (2004). Gene expression nervous system atlas (GENSAT). *Nat. Neurosci.* 7:483. doi: 10.1038/nn0504-483
- Hille, B. (2001). *Ion Channels of Excitable Cells*. Sunderland, MA: Sinauer.
- Hirtz, J. J., Braun, N., Griesemer, D., Hannes, C., Janz, K., Lohrke, S., et al. (2012). Synaptic refinement of an inhibitory topographic map in the auditory brainstem requires functional Cav1.3 calcium channels. *J. Neurosci.* 32, 14602–14616. doi: 10.1523/jneurosci.0765-12.2012
- Horikawa, K., and Armstrong, W. E. (1988). A versatile means of intracellular labeling: injection of biocytin and its detection with avidin conjugates. *J. Neurosci. Methods* 25, 1–11. doi: 10.1016/0165-0270(88)90114-8
- Houades, V., Koulakoff, A., Ezan, P., Seif, I., and Giaume, C. (2008). Gap junction-mediated astrocytic networks in the mouse barrel cortex. *J. Neurosci.* 28, 5207–5217. doi: 10.1523/jneurosci.5100-07.2008
- Houades, V., Rouach, N., Ezan, P., Kirchhoff, F., Koulakoff, A., and Giaume, C. (2006). Shapes of astrocyte networks in the juvenile brain. *Neuron Glia Biol.* 2, 3–14. doi: 10.1017/s1740925x06000081
- Huang, M., Du, Y., Kiyoshi, C., Wu, X., Askwith, C., Mctigue, D., et al. (2018). Syncytial isopotentiality: an electrical feature of spinal cord astrocyte networks. *Neuroglia* 1, 271–279. doi: 10.3390/neuroglia1010018
- Huang, Q., Zhou, D., and Difiglia, M. (1992). Neurobiotin, a useful neuroanatomical tracer for in vivo anterograde, retrograde and transneuronal tract-tracing and in vitro labeling of neurons. *J. Neurosci. Methods* 41, 31–43. doi: 10.1016/0165-0270(92)90121-s
- Kafitz, K. W., Meier, S. D., Stephan, J., and Rose, C. R. (2008). Developmental profile and properties of sulforhodamine 101–Labeled glial cells in acute brain slices of rat hippocampus. *J. Neurosci. Methods* 169, 84–92. doi: 10.1016/j.jneumeth.2007.11.022
- Kang, B. E., Lee, S., and Baker, B. J. (2019). Optical consequences of a genetically-encoded voltage indicator with a pH sensitive fluorescent protein. *Neurosci. Res.* 146, 13–21. doi: 10.1016/j.neures.2018.10.006
- Karram, K., Goebbels, S., Schwab, M., Jennissen, K., Seifert, G., Steinhauser, C., et al. (2008). NG2-expressing cells in the nervous system revealed by the NG2-EYFP knockin mouse. *Genesis* 46, 743–757. doi: 10.1002/dvg.20440
- Kawata, K., Sano, Y., Inenaga, K., and Yamashita, H. (1983). Immunohistochemical identification of lucifer yellow-labeled neurons in the rat supraoptic nucleus. *Histochemistry* 78, 21–26. doi: 10.1007/bf00491107
- Kettenmann, H., and Ransom, B. R. (1988). Electrical coupling between astrocytes and between oligodendrocytes studied in mammalian cell cultures. *Glia* 1, 64–73. doi: 10.1002/glia.440010108
- Kita, Y., Kawakami, K., Takahashi, Y., and Murakami, F. (2013). Development of cerebellar neurons and glia revealed by in utero electroporation: golgi-like labeling of cerebellar neurons and glia. *PLoS One* 8:e70091. doi: 10.1371/journal.pone.0070091
- Kiyoshi, C. M., Aten, S., Arzola, E. P., Patterson, J. A., Taylor, A. T., Du, Y., et al. (2020). Ultrastructural view of astrocyte-astrocyte and astrocyte-synapse contacts within the hippocampus. *BioRxiv* doi: 10.1101/2020.10.28.358200
- Kiyoshi, C. M., Du, Y., Zhong, S., Wang, W., Taylor, A. T., Xiong, B., et al. (2018). Syncytial isopotentiality: a system-wide electrical feature of astrocytic networks in the brain. *Glia* 66, 2756–2769. doi: 10.1002/glia.23525
- Konietzko, U., and Muller, C. M. (1994). Astrocytic dye coupling in rat hippocampus: topography, developmental onset, and modulation by protein kinase C. *Hippocampus* 4, 297–306. doi: 10.1002/hipo.450040313
- Kuffler, S. W., Nicholls, J. G., and Orkand, R. K. (1966). Physiological properties of glial cells in the central nervous system of amphibia. *J. Neurophysiol.* 29, 768–787. doi: 10.1152/jn.1966.29.4.768
- Kunzelmann, P., Schroder, W., Traub, O., Steinhauser, C., Dermietzel, R., and Willecke, K. (1999). Late onset and increasing expression of the gap junction protein connexin30 in adult murine brain and long-term cultured astrocytes. *Glia* 25, 111–119. doi: 10.1002/(sici)1098-1136(19990115)25:2<111::aid-glia2>3.0.co;2-i
- Langer, J., Stephan, J., Theis, M., and Rose, C. R. (2012). Gap junctions mediate intercellular spread of sodium between hippocampal astrocytes in situ. *Glia* 60, 239–252. doi: 10.1002/glia.21259
- Lee, C. Y., Dallerac, G., Ezan, P., Anderova, M., and Rouach, N. (2016). Glucose tightly controls morphological and functional properties of astrocytes. *Front. Aging Neurosci.* 8:82. doi: 10.3389/fnagi.2016.00082
- Linwah, O., Bayer, E. A., Wilchek, M., and Sussman, J. L. (1993). Three-dimensional structures of avidin and the avidin-biotin complex. *Proc. Natl. Acad. Sci. U.S.A.* 90, 5076–5080. doi: 10.1073/pnas.90.11.5076
- Lunde, L. K., Camassa, L. M., Hoddevik, E. H., Khan, F. H., Ottersen, O. P., Boldt, H. B., et al. (2015). Postnatal development of the molecular complex underlying astrocyte polarization. *Brain Struct. Funct.* 220, 2087–2101. doi: 10.1007/s00429-014-0775-z
- Ma, B., Buckalew, R., Du, Y., Kiyoshi, C. M., Alford, C. C., Wang, W., et al. (2016). Gap junction coupling confers isopotentiality on astrocyte syncytium. *Glia* 64, 214–226. doi: 10.1002/glia.22924
- MacAulay, N. (2020). Molecular mechanisms of K(+) clearance and extracellular space shrinkage-Glia cells as the stars. *Glia* 68, 2192–2211.
- Maglione, M., Tress, O., Haas, B., Karram, K., Trotter, J., Willecke, K., et al. (2010). Oligodendrocytes in mouse corpus callosum are coupled via gap junction channels formed by connexin47 and connexin32. *Glia* 58, 1104–1117. doi: 10.1002/glia.20991
- Matthias, K., Kirchhoff, F., Seifert, G., Huttman, K., Matyash, M., Kettenmann, H., et al. (2003). Segregated expression of AMPA-type glutamate receptors and glutamate transporters defines distinct astrocyte populations in the mouse hippocampus. *J. Neurosci.* 23, 1750–1758. doi: 10.1523/jneurosci.23-05-01750.2003
- McCutcheon, S., Stout, R. F. Jr., and Spray, D. C. (2020). The dynamic Nexus: gap junctions control protein localization and mobility in distinct and surprising ways. *Sci. Rep.* 10:17011.
- Meier, S. D., Kovalchuk, Y., and Rose, C. R. (2006). Properties of the new fluorescent Na<sup>+</sup> indicator CoroNa Green: comparison with SBFI and confocal Na<sup>+</sup> imaging. *J. Neurosci. Methods* 155, 251–259. doi: 10.1016/j.jneumeth.2006.01.009
- Meme, W., Vandecasteele, M., Giaume, C., and Venance, L. (2009). Electrical coupling between hippocampal astrocytes in rat brain slices. *Neurosci. Res.* 63, 236–243. doi: 10.1016/j.neures.2008.12.008
- Minta, A., and Tsien, R. Y. (1989). Fluorescent indicators for cytosolic sodium. *J. Biol. Chem.* 264, 19449–19457. doi: 10.1016/s0021-9258(19)47321-3
- Moroni, R. F., Inverardi, F., Regondi, M. C., Pennacchio, P., and Frassoni, C. (2015). Developmental expression of Kir4.1 in astrocytes and oligodendrocytes of rat somatosensory cortex and hippocampus. *Int. J. Dev. Neurosci.* 47, 198–205. doi: 10.1016/j.ijdevneu.2015.09.004
- Moshrefi-Ravaszani, B., Hammel, E. L., Kafitz, K. W., and Rose, C. R. (2017). Astrocyte sodium signalling and panglial spread of sodium signals in brain white matter. *Neurochem. Res.* 42, 2505–2518. doi: 10.1007/s11064-017-2197-9
- Muller, C. M. (1996). “Gap-junctional communication in mammalian cortical astrocytes: development, modifiability and possible functions,” in *Gap Junctions in the Nervous System*, eds D. C. Spray and R. Dermietzel (Austin, TX: RG Landes Company), 203–212. doi: 10.1007/978-3-662-21935-5\_12



- Muller, J., Reyes-Haro, D., Pivneva, T., Nolte, C., Schaette, R., Lubke, J., et al. (2009). The principal neurons of the medial nucleus of the trapezoid body and NG2(+) glial cells receive coordinated excitatory synaptic input. *J. Gen. Physiol.* 134, 115–127. doi: 10.1085/jgp.200910194
- Muller, N. I. C., Sonntag, M., Maraslioglu, A., Hirtz, J. J., and Friauf, E. (2019). Topographic map refinement and synaptic strengthening of a sound localization circuit require spontaneous peripheral activity. *J. Physiol.* 597, 5469–5493. doi: 10.1113/jp277757
- Muller, T., Moller, T., Neuhaus, J., and Kettenmann, H. (1996). Electrical coupling among Bergmann glial cells and its modulation by glutamate receptor activation. *Glia* 17, 274–284. doi: 10.1002/(sici)1098-1136(199608)17:4<274::aid-glia2>3.0.co;2-#
- Murphy, A. D., Hadley, R. D., and Kater, S. B. (1983). Axotomy-induced parallel increases in electrical and dye coupling between identified neurons of *Helisoma*. *J. Neurosci.* 3, 1422–1429. doi: 10.1523/jneurosci.03-07-01422.1983
- Nagy, J. I., Patel, D., Ochalski, P. A., and Stelmack, G. L. (1999). Connexin30 in rodent, cat and human brain: selective expression in gray matter astrocytes, co-localization with connexin43 at gap junctions and late developmental appearance. *Neuroscience* 88, 447–468. doi: 10.1016/s0306-4522(98)00191-2
- Nagy, J. I., and Rash, J. E. (2000). Connexins and gap junctions of astrocytes and oligodendrocytes in the CNS. *Brain Res. Brain Res. Rev.* 32, 29–44. doi: 10.1016/s0165-0173(99)00066-1
- Nakase, T., Yoshida, Y., and Nagata, K. (2006). Enhanced connexin 43 immunoreactivity in penumbral areas in the human brain following ischemia. *Glia* 54, 369–375. doi: 10.1002/glia.20399
- Nielsen, M. S., Axelsen, L. N., Sorgen, P. L., Verma, V., Delmar, M., and Holstein-Rathlou, N. H. (2012). Gap junctions. *Compr. Physiol.* 2, 1981–2035.
- Niessen, H., Harz, H., Bedner, P., Kramer, K., and Willecke, K. (2000). Selective permeability of different connexin channels to the second messenger inositol 1,4,5-trisphosphate. *J. Cell Sci.* 113(Pt 8), 1365–1372.
- Nimmerjahn, A., Kirchhoff, F., Kerr, J. N., and Helmchen, F. (2004). Sulforhodamine 101 as a specific marker of astroglia in the neocortex in vivo. *Nat. Methods* 1, 31–37. doi: 10.1038/nmeth706
- Nolte, C., Matyash, M., Pivneva, T., Schipke, C. G., Ohlemeyer, C., Hanisch, U. K., et al. (2001). GFAP promoter-controlled EGFP-expressing transgenic mice: a tool to visualize astrocytes and astrogliosis in living brain tissue. *Glia* 33, 72–86. doi: 10.1002/1098-1136(20010101)33:1<72::aid-glia1007>3.0.co;2-a
- Nwaobi, S. E., Lin, E., Peramsetty, S. R., and Olsen, M. L. (2014). DNA methylation functions as a critical regulator of Kir4.1 expression during CNS development. *Glia* 62, 411–427. doi: 10.1002/glia.22613
- Olsen, M. L., Khakh, B. S., Skatchkov, S. N., Zhou, M., Lee, C. J., and Rouach, N. (2015). New insights on astrocyte ion channels: critical for homeostasis and neuron-glia signaling. *J. Neurosci.* 35, 13827–13835. doi: 10.1523/jneurosci.2603-15.2015
- Pannasch, U., Vargova, L., Reingruber, J., Ezan, P., Holcman, D., Giaume, C., et al. (2011). Astroglial networks scale synaptic activity and plasticity. *Proc. Natl. Acad. Sci. U.S.A.* 108, 8467–8472. doi: 10.1073/pnas.1016650108
- Rackauskas, M., Verselis, V. K., and Bukauskas, F. F. (2007). Permeability of homotypic and heterotypic gap junction channels formed of cardiac connexins mCx30.2, Cx40, Cx43, and Cx45. *Am. J. Physiol. Heart Circ. Physiol.* 293, H1729–H1736.
- Ransom, B. R., and Goldring, S. (1973). Ionic determinants of membrane potential of cells presumed to be glia in cerebral cortex of cat. *J. Neurophysiol.* 36, 855–868. doi: 10.1152/jn.1973.36.5.855
- Ransom, B. R., and Kettenmann, H. (1990). Electrical coupling, without dye coupling, between mammalian astrocytes and oligodendrocytes in cell culture. *Glia* 3, 258–266. doi: 10.1002/glia.440030405
- Rouach, N., Koulakoff, A., Abudara, V., Willecke, K., and Giaume, C. (2008). Astroglial metabolic networks sustain hippocampal synaptic transmission. *Science* 322, 1551–1555. doi: 10.1126/science.1164022
- Scemes, E., and Giaume, C. (2006). Astrocyte calcium waves: what they are and what they do. *Glia* 54, 716–725. doi: 10.1002/glia.20374
- Schools, G. P., Zhou, M., and Kimelberg, H. K. (2006). Development of gap junctions in hippocampal astrocytes: evidence that whole cell electrophysiological phenotype is an intrinsic property of the individual cell. *J. Neurophysiol.* 96, 1383–1392. doi: 10.1152/jn.00449.2006
- Schreiner, A. E., Durry, S., Aida, T., Stock, M. C., Ruther, U., Tanaka, K., et al. (2014). Laminar and subcellular heterogeneity of GLAST and GLT-1 immunoreactivity in the developing postnatal mouse hippocampus. *J. Comp. Neurol.* 522, 204–224. doi: 10.1002/cne.23450
- Seifert, G., Huttmann, K., Binder, D. K., Hartmann, C., Wyczynski, A., Neusch, C., et al. (2009). Analysis of astroglial K<sup>+</sup> channel expression in the developing hippocampus reveals a predominant role of the Kir4.1 subunit. *J. Neurosci.* 29, 7474–7488. doi: 10.1523/jneurosci.3790-08.2009
- Sontheimer, H., Waxman, S. G., and Ransom, B. R. (1991). Relationship between Na<sup>+</sup> current expression and cell-cell coupling in astrocytes cultured from rat hippocampus. *J. Neurophysiol.* 65, 989–1002. doi: 10.1152/jn.1991.65.4.989
- Speizer, L., Haugland, R., and Kutchai, H. (1985). Asymmetric transport of a fluorescent glucose analogue by human erythrocytes. *Biochim. Biophys. Acta* 815, 75–84. doi: 10.1016/0005-2736(85)90476-6
- Stephan, J., and Friauf, E. (2014). Functional analysis of the inhibitory neurotransmitter transporters GlyT1, GAT-1, and GAT-3 in astrocytes of the lateral superior olive. *Glia* 62, 1992–2003. doi: 10.1002/glia.22720
- Stephan, J., Haack, N., Kafitz, K. W., Durry, S., Koch, D., Hochstrate, P., et al. (2012). Kir4.1 channels mediate a depolarization of hippocampal astrocytes under hyperammonemic conditions in situ. *Glia* 60, 965–978. doi: 10.1002/glia.22328
- Susaki, E. A., Tainaka, K., Perrin, D., Kishino, F., Tawara, T., Watanabe, T. M., et al. (2014). Whole-brain imaging with single-cell resolution using chemical cocktails and computational analysis. *Cell* 157, 726–739. doi: 10.1016/j.cell.2014.03.042
- Susaki, E. A., Tainaka, K., Perrin, D., Yukinaga, H., Kuno, A., and Ueda, H. R. (2015). Advanced CUBIC protocols for whole-brain and whole-body clearing and imaging. *Nat. Protoc.* 10, 1709–1727. doi: 10.1038/nprot.2015.085
- Tasker, J. G., Hoffman, N. W., and Dudek, F. E. (1991). Comparison of three intracellular markers for combined electrophysiological, morphological and immunohistochemical analyses. *J. Neurosci. Methods* 38, 129–143. doi: 10.1016/0165-0270(91)90163-t
- Terman, D., and Zhou, M. (2019). Modeling the role of the astrocyte syncytium and K<sup>+</sup> buffering in maintaining neuronal firing patterns. *Opera Med. Physiol.* 5, 7–16.
- Veenstra, R. D. (1996). Size and selectivity of gap junction channels formed from different connexins. *J. Bioenerg. Biomembr.* 28, 327–337. doi: 10.1007/bf02110109
- Veenstra, R. D., Wang, H. Z., Beblo, D. A., Chilton, M. G., Harris, A. L., Beyer, E. C., et al. (1995). Selectivity of connexin-specific gap junctions does not correlate with channel conductance. *Circ. Res.* 77, 1156–1165. doi: 10.1161/01.res.77.6.1156
- Wadle, S. L., Augustin, V., Langer, J., Jabs, R., Philippot, C., Weingarten, D. J., et al. (2018). Anisotropic panglial coupling reflects tonotopic organization in the inferior colliculus. *Front. Cell Neurosci.* 12:431. doi: 10.3389/fncel.2018.00431
- Wallraff, A., Kohling, R., Heinemann, U., Theis, M., Willecke, K., and Steinhauser, C. (2006). The impact of astrocytic gap junctional coupling on potassium buffering in the hippocampus. *J. Neurosci.* 26, 5438–5447. doi: 10.1523/jneurosci.0037-06.2006
- Wallraff, A., Odermatt, B., Willecke, K., and Steinhauser, C. (2004). Distinct types of astroglial cells in the hippocampus differ in gap junction coupling. *Glia* 48, 36–43. doi: 10.1002/glia.20040
- Wang, H. Z., and Veenstra, R. D. (1997). Monovalent ion selectivity sequences of the rat connexin43 gap junction channel. *J. Gen. Physiol.* 109, 491–507. doi: 10.1085/jgp.109.4.491
- Wang, Q., Wang, W., Aten, S., Kiyoshi, C. M., Du, Y., and Zhou, M. (2020). Epileptiform neuronal discharges impair astrocyte syncytial isopotentiality in acute hippocampal slices. *Brain Sci.* 10:208. doi: 10.3390/brainsci10040208
- Wang, W., Kiyoshi, C. M., Du, Y., Taylor, A. T., Sheehan, E. R., Wu, X., et al. (2020). TREK-1 null impairs neuronal excitability, synaptic plasticity, and cognitive function. *Mol. Neurobiol.* 57, 1332–1346. doi: 10.1007/s12035-019-01828-x
- Wasseff, S. K., and Scherer, S. S. (2011). Cx32 and Cx47 mediate oligodendrocyte-astrocyte and oligodendrocyte-oligodendrocyte gap junction coupling. *Neurobiol. Dis.* 42, 506–513. doi: 10.1016/j.nbd.2011.03.003
- Weber, P. A., Chang, H. C., Spaeth, K. E., Nitsche, J. M., and Nicholson, B. J. (2004). The permeability of gap junction channels to probes of different size is dependent on connexin composition and permeant-pore affinities. *Biophys. J.* 87, 958–973. doi: 10.1529/biophysj.103.036350
- Wu, L., Dong, A., Dong, L., Wang, S. Q., and Li, Y. (2019). PARIS, an optogenetic method for functionally mapping gap junctions. *eLife* 8:e43366.

- Xin, W., Schuebel, K. E., Jair, K. W., Cimbro, R., De Biase, L. M., Goldman, D., et al. (2019). Ventral midbrain astrocytes display unique physiological features and sensitivity to dopamine D2 receptor signaling. *Neuropsychopharmacology* 44, 344–355. doi: 10.1038/s41386-018-0151-4
- Xu, G., Wang, W., Kimelberg, H. K., and Zhou, M. (2010). Electrical coupling of astrocytes in rat hippocampal slices under physiological and simulated ischemic conditions. *Glia* 58, 481–493.
- Xu, G., Wang, W., and Zhou, M. (2014). Spatial organization of NG2 glial cells and astrocytes in rat hippocampal CA1 region. *Hippocampus* 24, 383–395. doi: 10.1002/hipo.22232
- Yagi, T., Terada, N., Baba, T., and Ohno, S. (2002). Localization of endogenous biotin-containing proteins in mouse Bergmann glial cells. *Histochem. J.* 34, 567–572.
- Yamada, K., Nakata, M., Horimoto, N., Saito, M., Matsuoka, H., and Inagaki, N. (2000). Measurement of glucose uptake and intracellular calcium concentration in single, living pancreatic beta-cells. *J. Biol. Chem.* 275, 22278–22283. doi: 10.1074/jbc.m908048199
- Yang, Y., Vidensky, S., Jin, L., Jie, C., Lorenzini, I., Frankl, M., et al. (2011). Molecular comparison of GLT1+ and ALDH1L1+ astrocytes in vivo in astroglial reporter mice. *Glia* 59, 200–207. doi: 10.1002/glia.21089
- Yoshioka, K., Saito, M., Oh, K. B., Nemoto, Y., Matsuoka, H., Natsume, M., et al. (1996). Intracellular fate of 2-NBDG, a fluorescent probe for glucose uptake activity, in *Escherichia coli* cells. *Biosci. Biotechnol. Biochem.* 60, 1899–1901. doi: 10.1271/bbb.60.1899
- Zhong, S., Du, Y., Kiyoshi, C. M., Ma, B., Alford, C. C., Wang, Q., et al. (2016). Electrophysiological behavior of neonatal astrocytes in hippocampal stratum radiatum. *Mol. Brain* 9:34.
- Zhou, M., Schools, G. P., and Kimelberg, H. K. (2006). Development of GLAST(+) astrocytes and NG2(+) glia in rat hippocampus CA1: mature astrocytes are electrophysiologically passive. *J. Neurophysiol.* 95, 134–143. doi: 10.1152/jn.00570.2005

**Conflict of Interest:** The authors declare that the research was conducted in the absence of any commercial or financial relationships that could be construed as a potential conflict of interest.

Copyright © 2021 Stephan, Eitelmann and Zhou. This is an open-access article distributed under the terms of the Creative Commons Attribution License (CC BY). The use, distribution or reproduction in other forums is permitted, provided the original author(s) and the copyright owner(s) are credited and that the original publication in this journal is cited, in accordance with accepted academic practice. No use, distribution or reproduction is permitted which does not comply with these terms.



# C21orf91 Regulates Oligodendroglial Precursor Cell Fate—A Switch in the Glial Lineage?

Laura Reiche<sup>1</sup>, Peter Göttle<sup>1</sup>, Lydie Lane<sup>2,3</sup>, Paula Duek<sup>2,3</sup>, Mina Park<sup>1</sup>, Kasum Azim<sup>1</sup>, Jana Schütte<sup>1</sup>, Anastasia Manousi<sup>1</sup>, Jessica Schira-Heinen<sup>1</sup> and Patrick Küry<sup>1\*</sup>

<sup>1</sup>Department of Neurology, Medical Faculty, Heinrich-Heine-University Düsseldorf, Düsseldorf, Germany, <sup>2</sup>CALIPHO Group, SIB Swiss Institute of Bioinformatics, Geneva, Switzerland, <sup>3</sup>Department of Microbiology and Molecular Medicine, Faculty of Medicine, University of Geneva, Geneva, Switzerland

## OPEN ACCESS

### Edited by:

Christian Lohr,  
University of Hamburg, Germany

### Reviewed by:

Maria Cecilia Angulo,  
Centre National de la Recherche  
Scientifique (CNRS), France  
Yannick Poitelon,  
Albany Medical College,  
United States  
Marta Boccazzi,  
University of Milan, Italy

### \*Correspondence:

Patrick Küry  
kuery@hhu.de

### Specialty section:

This article was submitted to  
Non-Neuronal Cells,  
a section of the journal  
Frontiers in Cellular Neuroscience

**Received:** 13 January 2021

**Accepted:** 22 February 2021

**Published:** 16 March 2021

### Citation:

Reiche L, Göttle P, Lane L, Duek P,  
Park M, Azim K, Schütte J,  
Manousi A, Schira-Heinen J and  
Küry P (2021) C21orf91 Regulates  
Oligodendroglial Precursor Cell  
Fate—A Switch in the Glial Lineage?  
Front. Cell. Neurosci. 15:653075.  
doi: 10.3389/fncel.2021.653075

Neuropathological diseases of the central nervous system (CNS) are frequently associated with impaired differentiation of the oligodendroglial cell lineage and subsequent alterations in white matter structure and dynamics. Down syndrome (DS), or trisomy 21, is the most common genetic cause for cognitive impairments and intellectual disability (ID) and is associated with a reduction in the number of neurons and oligodendrocytes, as well as with hypomyelination and astrogliosis. Recent studies mainly focused on neuronal development in DS and underestimated the role of glial cells as pathogenic players. This also relates to C21ORF91, a protein considered a key modulator of aberrant CNS development in DS. We investigated the role of C21orf91 ortholog in terms of oligodendrogenesis and myelination using database information as well as through cultured primary oligodendroglial precursor cells (OPCs). Upon modulation of *C21orf91* gene expression, we found this factor to be important for accurate oligodendroglial differentiation, influencing their capacity to mature and to myelinate axons. Interestingly, C21orf91 overexpression initiates a cell population coexpressing astroglial- and oligodendroglial markers indicating that elevated C21orf91 expression levels induce a gliogenic shift towards the astrocytic lineage reflecting non-equilibrated glial cell populations in DS brains.

**Keywords:** white matter deficits, gliogenesis, cell fate, down syndrome, neuroregeneration

**Abbreviations:** ACSA-1/GLAST, astrocyte cell surface antigen-1; ACTB,  $\beta$ -actin; aNSC(s), adult neural stem cell(s); APC/CC1, adenomatous polyposis coli protein (antibody clone CC1); BFGF, basic fibroblast growth factor; BSA, bovine serum albumin; CC, corpus callosum; CNS, central nervous system; CNPase, 2',3'-cyclic-nucleotide 3'-phosphodiesterase; DIV, days *in vitro*; DS, Down syndrome; ENPP2/autotaxin, ectonucleotide pyrophosphatase/phosphodiesterase 2; EURL, early undifferentiated retina and lense; FB, forebrain; FBS, fetal bovine serum; GAPDH, glyceraldehyde 3-phosphate dehydrogenase; GEO, Gene Expression Omnibus; GFAP, glial fibrillary acid protein; GFP, green fluorescent protein; GM, gray matter; Gpr17, G protein-coupled receptor-17; Hes1, hairy and enhancer of split-1; HF, hippocampal formation; HOXD1, homeobox protein Hox-D1; HRP, horse radish peroxidase; HS, hemisphere; HSA21, human chromosome 21; HSPA2, heat shock protein family A (Hsp70) member 2; ID, intellectual disability; iPSC, induced pluripotent stem cell; MAG, myelin associated glycoprotein; MBP, myelin basic protein; MMU16, mouse chromosome 16; MOG, myelin oligodendrocyte glycoprotein; MS, multiple sclerosis; Myrf, myelin regulatory factor; NeuN, neuronal nuclei antigen; Nkx2.2, NK2 homeobox 2; Olig2, oligodendrocyte transcription factor 2; OPC(s), oligodendroglial precursor cell(s); PBS, phosphate buffered saline; pcw, post-conceptional weeks; PDGF, platelet-derived growth factor; PDGFR, platelet-derived growth factor receptor; PFA, paraformaldehyde; PKD1, polycystic kidney disease 1/polycystin 1; PLD1, phospholipidase D1; Plp1, proteolipid protein-1; PRRG1, proline rich and gla domain 1; PRR5L, proline rich 5 like; RNA, ribonucleic acid; RNAseq, RNA sequencing; RPKM, reads per kilo base per million mapped reads; RT, room temperature; SLC44A1, solute carrier family 44 member 1; Sox10, sex-determining region Y-box 10; SVZ, subventricular zone; TAP, transiently amplifying progenitor; TBS(-T), Tris-buffered saline (supplemented with Triton); TPM, transcripts per kilobase million; qRT-PCR, quantitative reverse transcription polymerase chain reaction; Wnt, wingless and integration site.

## INTRODUCTION

White matter, which makes up approximately 40% of the human brain, consists of axons, astrocytes, and myelin, the latter of which is imperative for stabilization, protection, and electrical insulation of axons enabling accelerated electrical signal propagation. In the adult central nervous system (CNS), myelin is generated by oligodendrocytes, either deriving from oligodendroglial precursor cells (OPCs) or niche-located adult neural stem cells (aNSCs; Akkermann et al., 2017). The structural integrity of myelin is of crucial importance for CNS function and restoration (Snaidero and Simons, 2014), making it vulnerable to pathological degeneration and inflammation (Waxman, 1992) or genetic intervention (Nave, 1994). Myelin loss, therefore, leads to impaired neuronal signaling, functional deficits, and shortened lifetime (Wilkins et al., 2003). Moreover, axonal nutrition has recently been shown to depend on myelin and oligodendrocytes (Simons and Nave, 2015). Hence, white matter deficits and myelin dysfunctions are considered a main contributing factor for neurodegenerative diseases and malfunctions of the CNS (Bercury and Macklin, 2015).

Down syndrome (DS) results from a trisomy of human chromosome (HSA) 21 and represents the most common genetic cause for cognitive impairments and intellectual disability (ID). The neurological profile of DS patients is characterized by hypotrophy and hypocellularity of neurons (reviewed by Stagni et al., 2017; Baburamani et al., 2019) and oligodendrocytes (Karlsen and Pakkenberg, 2011) accompanied by hypomyelination in the hippocampal formation (Abraham et al., 2012), whereas astroglial cell numbers are increased (Mito and Becker, 1993; Zdaniuk et al., 2011). DS astrocytes also show alterations in the structure and intracellular protein expression (Dossi et al., 2018). Moreover, structural and functional abnormalities of DS white matter were described (Fenoll et al., 2017).

Several studies indicate that white matter malformation contributes to neurological impairment in DS patients (Powell et al., 2014; Fenoll et al., 2017) and that hypomyelination is caused by a cell-autonomous phenomenon in oligodendrocyte development (Olmos-Serrano et al., 2016)—a research focus that has, nevertheless, not been paid much attention so far (Reiche et al., 2019). Olmos-Serrano et al. (2016) revealed a module (termed as M43) enriched in genes associated with oligodendrocyte differentiation and myelination to exhibit a distinct downregulation in several DS brain regions such as the hippocampus throughout development. Among genes such as *CNP*, *PLP1*, *SOX10*, and *GPR17*, also *C21ORF91* is listed within this cluster. Also known as *early undifferentiated retina and lens* (EURL), *C21ORF91* is localized at the centromeric boundary of the DS critical region (DSCR; encompassing 21q21-21q22.3) and was initially described to play a role in defective DS neurogenesis (Li et al., 2016). There, it was shown that *C21ORF91*'s transcript levels within the tested DS brain regions exhibited a spatiotemporal increase compared to equivalent controls. Furthermore, in DS lymphoblastoid cells, *C21ORF91* is overexpressed with a mean ratio close to 1.5, which is proportional to the gene dosage effect of trisomy 21, thus implied

to be involved in the DS phenotype (Ait Yahya-Graison et al., 2007). Indeed, *C21ORF91* has previously been suggested to be relevant for the observed neurodevelopmental disorder and ID arising from HSA21 triplication (Slavotinek et al., 2000; Rost et al., 2004; Korbel et al., 2009; Li et al., 2016). Although expressed ubiquitously in healthy human tissues, *C21orf91* protein was shown to be enriched in oligodendrocytes along with other proteins important for their differentiation such as *Olig2* (Cahoy et al., 2008). Moreover, *C21ORF91* expression in the healthy human brain peaks between birth and adulthood (Li et al., 2016), hence coinciding with the onset and progression of myelination. Interestingly, cognitive deficits and hypomyelinated patterns in DS are thought to arise during these early stages of life and increase during development (Pennington et al., 2003; Rowe et al., 2006; Lanfranchi et al., 2010; Abraham et al., 2012). Based on these parallels as well as on the here presented functional data, a possible correlation between elevated *C21orf91* expression levels and myelination deficits as observed in DS can be suggested.

## MATERIALS AND METHODS

### Data Mining/Human *C21ORF91* Correlations

RNA sequencing (RNAseq) and microarray data for humans were retrieved from Genevestigator (version 7.4.0; Hruz et al., 2008), a curated database that performs meta-analyses of gene expression data on a large panel of tissues and cell types of different experiments. For RNAseq data, 285 human tissues and cells were analyzed for their *C21ORF91* expression level. Gene expression was measured in transcripts per million (TMP). High expression as considered by Genevestigator corresponds to the log(2) of the average of the mean value higher than 3. For microarray data, 416 human tissues and cells were analyzed for their *C21ORF91* expression level. Gene expression is expressed as relative mean values. High expression as considered by Genevestigator corresponds to higher than 12.

*C21ORF91* RNAseq expression data on the human developmental and adult brain for 26 different brain structures expressed as the mean of reads per kilobase million (RPKM) values was retrieved from the Allen Brain Atlas (October 2019 and November 2020). Brain structures were grouped in *allocortex* (hippocampus); *basal ganglia* (striatum); *neural plate* (dorsolateral prefrontal cortex, ventrolateral prefrontal cortex, anterior (rostral) cingulate (medial prefrontal) cortex, orbital frontal cortex, primary motor-sensory cortex, parietal neocortex, posterior (caudal) superior temporal cortex (area 22c), inferolateral temporal cortex (area TEv, area 20), occipital neocortex, amygdaloid complex, upper (rostral) rhombic lip, temporal neocortex, the primary motor cortex (area M1, area 4), the primary somatosensory cortex (area S1, areas 3, 1, 2), posteroventral (inferior) parietal cortex, primary auditory cortex (core), primary visual cortex (striate cortex, area V1/V7), cerebellum, cerebellar cortex) and *thalamus* (dorsal thalamus, mediodorsal nucleus of the thalamus). These grouped brain structures were analyzed for the following grouped ages: 8 and



9 post-conception weeks (pcw), 12 and 13 pcw, 16 and 17 pcw, 19 and 21 pcw, 24–26 pcw (24, 25 and 26 pcw), 35–37 pcw, 4 and 10 months, 1–4 (1, 2, 3 and 4 years), 8–15 (8, 11, 13 and 15 years), 18–23 (18, 19, 21 and 23 years) and 30–40 (30, 36, 37 and 40 years). Data from the *ventricular zone* (lateral ganglionic eminence, medial ganglionic eminence, caudal ganglionic eminence) was available only for 8 and 9 pcw and was therefore omitted.

To obtain additional data on *C21ORF91* expression in the nervous system, we used the Brain EXPression Database (BrainEXP; Jiao et al., 2019), which performs a meta-analysis of microarray and RNAseq data in a subset of nervous system tissues consisting of 4567 samples from 2863 healthy individuals gathered from public databases and their data. The spinal cord, substantia nigra, hippocampus, hypothalamus, amygdala, putamen, caudate nucleus, nucleus accumbens, frontal cortex, BA9, anterior cingulate cortex, cerebellum, and cerebellar hemisphere could be analyzed and compared.

The heatmap displayed in the Allen Brain Atlas database (Sunkin et al., 2013) representing z-scores values of the microarray data for six adult donors was surveyed to identify structures with the highest *C21ORF91* expression. The four probes refer to *C21ORF91* sequences on the microarray chip: A\_23\_P211015 (GGT GAG GTA GAG CAA CTG AAT GCA AAG CTC CTA CAG CAA ATC CAG GAA GTT TTT GAA GAG); A\_24\_P125839 (AGT AGG GCG AAC AGG AAT GAA GTC GCA CCT ACC CAT AAA CAA CTG ACC TAA ACA GAC TT), CUST\_5965\_PI416261804 (ATT CGA TGA CTC TTG GTG AGG TAG AGC AAC TGA ATG CAA AGC TCC TAC AGC AAA TCC AG) and CUST\_5966\_PI416261804 (GAA AAA AGA AGA GAC AAT CTC TAG TCC AGA GGC TAA TGT CCA GAC CCA GCA TCC ACA TTA).

To characterize *C21ORF91* expression on a cellular level, single-nucleus RNAseq data (Allen Brain Atlas) was collected from two sets. The first covers multiple adult human cortical areas (MCA) including the middle temporal gyrus, anterior cingulate cortex, primary visual cortex, primary motor cortex, primary somatosensory cortex, and primary auditory cortex. The second experiment included specifically the adult primary motor cortex (M1). Single-nucleus RNAseq is expressed as counts per million (cpm) trimmed means.

To set-up a coexpressed gene cluster for *C21ORF91*, a list of genes whose expression positively correlates with *C21ORF91* in the adult brain was extracted using the “Correlate Gene Search” functionality appended to the microarray expression data from adult donors provided by the Allen Brain Atlas. Also, coexpression data from the BrainEXP database (Jiao et al., 2019) was retrieved with the default parameters. The genes coexpressing with *C21ORF91* were further analyzed to identify if they coexpress with each other.

Gene ontology (GO) enrichment analysis on the coexpression set from the adult brain microarray from Allen Brain Atlas was performed using PANTHER [(Thomas et al., 2003, 2006); RRID: SCR\_004869; released 20190711] including GO biological process, molecular function and cellular component terms.

*C21ORF91* homologs were searched by protein BLAST at NCBI. Reciprocal best hits were considered as orthologs.

Homology in jawless fishes was searched by tBLASTn with human and zebrafish protein sequences as queries against RefSeq Genome and nucleotide collection databases.

## Gene Expression Heatmap Generation

Bulk transcriptomic datasets assembled as done previously were used for defining the expression of *D16Ert472* mouse *C21orf91* ortholog, further referred to as *C21orf91* across multiple cell types that are present in the forebrain (Azim et al., 2017, 2018), and Gene Expression Omnibus (GEO) repository IDs are stated. These included substages of postnatal oligodendroglia (GSE9566; P16); early postnatal neural stem cells (NSCs) and transiently amplifying progenitors (TAPs; GSE60905); young adult substages of NSCs (GSE54653); young adult neuroblasts and ependymal cells (GSE18765); young adult choroid plexus cells (GSE82308); young adult and postnatal astrocytes (GSE35338, GSE9566); young adult microglia (GSE58483) and embryonic day 14 radial glial cells (vRGs; GSE40582). All analyses were performed in RStudio using publicly available packages installed directly from the Bioconductor consortium<sup>1</sup>. The LIMMA package was used to incorporate all datasets described above systematically which were then subsequently normalized using the standard RMA method. Known oligodendroglial, astrocyte, and NSC lineage markers were additionally studied for heatmap plotting purposes by taking the most significant probes for each gene (differential expression by <0.0001 False Discovery Rate between the individual cell types studied). The selected genes were visualized in an unsupervised heatmap using the pHeatmap package<sup>2</sup>.

## Brain Tissue Preparation, Sectioning, and Immunohistochemistry

For the analysis of transcript and protein levels of *RGD1563888* (rat *C21orf91* ortholog, further referred to as *C21orf91*), embryonic day 16 (E16), postnatal day 0 (P0), P7, P25, and adult (2–3 months) Wistar rats of either sex were deeply anesthetized and killed by an overdose of isoflurane (Piramal-Healthcare, Mumbai, India). Rat brains were isolated, shortly surface-washed with ice-cold Dulbecco's phosphate-buffered saline (PBS; Sigma-Aldrich, St. Louis, USA), and then frozen in  $-35^{\circ}\text{C}$  to  $-50^{\circ}\text{C}$  methyl butane and stored at  $-80^{\circ}\text{C}$  until further processing. Regions of interest including whole hemisphere (HS), forebrain (FB), corpus callosum (CC), hippocampal formation (HF), and cerebellum (CB) were sectioned coronally using a cryostat (Leica CM3050S) at  $-28^{\circ}\text{C}$ . Out of 50–100  $\mu\text{m}$  thick slices, smaller regions (CC and HF) were isolated using a pre-cooled scalpel within the cryostat chamber. Note, that P0 tissue sections were used exclusively for Western blot analysis. Tissues were stored at  $-80^{\circ}\text{C}$ .

For immunohistochemistry, P7 brains were directly processed, while adult rats were transcardially perfused with 150 ml ice-cold Dulbecco's phosphate-buffered saline (PBS; Sigma-Aldrich, St. Louis, MO, USA) followed by 400 ml 4% paraformaldehyde (PFA). Rat brains were harvested and

<sup>1</sup><https://www.bioconductor.org/packages/devel/workflows/vignettes/arrays/inst/doc/arrays.html>

<sup>2</sup><https://cran.r-project.org/web/packages/pheatmap/index.html>

post-fixed for 2 days (P7 brains) or overnight (adult brains) in 4% PFA at 4°C, followed by 48 h cryoprotective dehydration in 30% sucrose (in PBS) at 4°C. Brains were embedded in TissueTek OCT (Sakura Finetek Europe, Netherlands), frozen in −35°C to −50°C methyl butane, and stored at −80°C until preparation of 14 µm coronal sections using a cryostat (Leica CM3050S). Sections were stored at −80°C.

Immunohistochemical staining was performed as previously described (Beyer et al., 2020). Briefly, thawed brain sections were air-dried for at least 15 min at room temperature (RT), rehydrated in distilled water for 5 min, transferred to −20°C acetone for 5 min, and washed in 1× Tris-buffered saline (TBS; pH 7.6) and 1× TBS-T (TBS containing 0.02% Triton X-100) for 5 min each. Non-specific staining was blocked with 10% biotin-free bovine serum albumin (BSA; in TBS-T) for 1 h at RT, followed by application of the following antibodies (in 10% BSA in TBS) and incubation overnight at 4°C: rabbit anti-C21orf91 [1:1,000, Santa Cruz Biotechnology, Cat# sc-83610 (Li et al., 2016)], rabbit anti-C21orf91 (1:200, Bioss, Cat# bs-9983R), rabbit anti-C21orf91 (1:300, Sigma-Aldrich, Cat# HPA049030), mouse anti-neuronal nuclei antigen (NeuN; 1:1,000, Merck Millipore, Cat# MAB377), goat anti-PDGFR (alpha/CD140A, 1:250, Neuromics, Cat# GT15150), mouse anti-oligodendrocyte transcription factor 2 (Olig2; 1:500, Merck Millipore, Cat# MABN50), guinea pig anti-glia fibrillary acidic protein (GFAP; 1:2,000, Synaptic Systems, Cat# 173004), and mouse anti-adenomatous polyposis coli for oligodendrocytes (APC, CC1; 1:500, GeneTex, Cat# GTX16794). Sections were washed two times for 5 min in TBS and incubated with the species-appropriate fluorochrome-conjugated secondary antibodies (1:200 in PBS; donkey: anti-goat; goat: anti-rabbit, anti-mouse, anti-guinea pig; Alexa Fluor488- or Alexa Fluor594-conjugated) and DAPI (4,6-diamidino-2-phenylindole; nuclei labeling, 0.04 µl/ml; Roche Diagnostic GmbH) for 1 h at RT. Slices were mounted with Immu-Mount (Thermo Fisher Scientific, Darmstadt, Germany) and analyzed using a confocal laser scanning microscope 510 (CLSM 510, Zeiss, Jena, Germany) and the ImageJ BioVox software (Schindelin et al., 2012). Z-stacked tile scans on average eight brain slices per marker and time-point (two slices per animal) were fused to a maximum intensity projection *via* ImageJ. C21orf91-positive cells within the whole tile scan projection were counted and normalized to its area [mm<sup>2</sup>], distinguishing between CC and surrounding gray matter structures (GM). Then, on the one hand, the average distribution of C21orf91 expressing cells within the population of marker-positive cells (such as of all GFAP expressing cells within a tile scan) was calculated. To depict the marker-specific population size/density, pie charts vary in size. On the other hand, the mean percentage of marker expressing cells within the C21orf91-positive population was evaluated per animal. Rat brain preparations were approved by the ZETT (Zentrale Einrichtung für Tierforschung und Wissenschaftliche Tierschutzaufgaben; O69/11, V54/09).

## Rat Oligodendroglial Cell Culture

Based on the procedure of McCarthy and de Vellis (1980), the generation of primary OPC cultures from postnatal day

zero to one (P0–1) cerebral rat cortices of Wistar rats (either sex) was performed as previously described (Kremer et al., 2009; Göttle et al., 2018) whereas the cell culture medium was supplemented with fetal bovine serum (FBS) from a different company (Capricorn Scientific, Palo Alto, CA, USA). Primary OPCs (>97% pure) were either seeded onto 0.25 mg/ml poly-D-lysine coated (PDL, Sigma-Aldrich) glass coverslips (13 mm) in 24-well plates (for immunocytochemistry;  $2.5 \times 10^4$  cells/well) or 0.25 mg/ml PDL coated 24-well plates (for quantitative reverse transcription-polymerase chain reaction (qRT-PCR);  $5 \times 10^4$  cells/well) in high-glucose DMEM-based Sato medium. After 1.5 h, cell differentiation was induced by changing medium to differentiation medium (Sato medium supplemented with 0.5% FBS). The medium was exchanged every 3 days. The preparation of rodent primary oligodendroglial cell cultures was approved by the ZETT (O69/11, V54/09).

## Plasmid Construction and OPC Transfection

Plasmid design and generation were conducted by Hybrigenics SA, Paris, France and kindly provided to our lab. Briefly, the complete coding sequence of the rat ortholog *C21orf91* (RGD1563888) was inserted into the company's pV22 vector, which is an equivalent vector to pHTN (Promega France; eucaryotic expression vector containing a HaloTag sequence) with slightly different polylinkers. OPCs were transfected *via* electroporation using the basic glia nucleofector kit and a nucleofector II device (both Lonza, Basel, Switzerland). In detail,  $0.8\text{--}1 \times 10^6$  cells were transfected using the high-efficiency program A-033 resuspended in 100 µl nucleofection solution and a total amount of 2 µg plasmid per  $1 \times 10^6$  cells. For visualization of short-term experiments, control (pHTN) and C21orf91 overexpression vectors were co-transfected with pmaxGFP (Lonza; a green fluorescent protein expression vector) and for visualization of transplanted cells, vectors were co-transfected with the pcDNA3-hyg-citrine vector (yellow fluorescent protein; Kremer et al., 2009) in a ratio of 10:1. Transfected OPCs were seeded onto 0.25 mg/ml PDL coated glass coverslips (13 mm) in 24-well plates (for immunocytochemistry;  $7 \times 10^4$  cells/well) or 0.25 mg/ml PDL coated 24-well plates (for qRT-PCR;  $1.5 \times 10^5$  cells/well) in expansion medium (Sato medium supplemented with 10 ng/ml recombinant human basic fibroblast growth factor (bFGF) and 10 ng/ml recombinant human platelet-derived growth factor-AA (PDGF-AA; both R&D Systems, Wiesbaden-Nordenstadt, Germany). After 4–5 h, the medium was exchanged to a differentiation medium (Kremer et al., 2009).

## RNA Preparation, cDNA Synthesis, and Quantitative RT-PCR

Total RNA purification from tissues was done using Trizol reagent (Invitrogen) while cultured cells were lysed using 350 µl RLT lysis buffer (Qiagen) supplemented with β-mercaptoethanol (1:100, Sigma) and total RNA was purified by using RNeasy Mini Kit (Qiagen, Hilden, Germany) according to manufacturer instructions including DNase digestion. Before quantitative real-time polymerase chain reaction (qPCR), reverse

transcription with 250 ng RNA [measured using a NanoDrop ND 1000 (Peqlab, Erlangen, Germany)] was done using the High-Capacity cDNA Reverse Transcription Kit (ThermoFisher Scientific, Darmstadt, Germany). Gene expression levels were determined on a 7900HT sequence detection system (Applied Biosystems) applying SybrGreen universal master mix (ThermoFisher Scientific, Darmstadt, Germany). For sequence detection, the following forward (fwd) and reverse (rev) primers, generated *via* PrimerExpress 2.0 software (Applied Biosystems), were used, with  $\beta$ -actin (ACTB) and glyceraldehyde 3-phosphate dehydrogenase (GAPDH) serving as reference genes: ACTB\_fwd: AACCTAAGGCCAACCGTGAAG, ACTB\_rev: AGTGGTACGACCAGAGGCAT, C21orf91\_fwd: CTTTCAGCAAGCGTCATCGAATT, C21orf91\_rev: GTATCC TGGGAAGACGCGGATG, CNPase\_fwd: ATGCTGAGCTTG GCGAAGAA, CNPase\_rev: GTACCCCGTGAAGATGGCC, GAPDH\_fwd: GAACGGGAAGCTCACTGGC, GAPDH\_rev: GCATGTTCAGATCCACAACGG, MBP\_fwd: CAATGGACCC GACAGGAAAC, MBP\_rev: TGGCATCTCCAGCGTGTTC, MOG\_fwd: CAGTTGTACGCAGCTACGC, MOG\_rev: AT GCCCTGGCCCTATCACTC. Relative gene expression levels were determined according to the  $\Delta\Delta C_t$  method (ThermoFisher Scientific, Darmstadt, Germany). All measurements were done in duplicates; generated from  $n = 8$  independent experiments and data are shown as mean values  $\pm$  SEM.

## Immunocytochemistry and Assessment of Morphology

To evaluate marker expression and morphological maturation, the immunocytochemical analysis was performed after cells were fixed using 4% paraformaldehyde (PFA) at RT for 10 min. Non-specific binding of antibodies was prevented by incubation in blocking solution [10% normal goat serum (NGS); in PBS containing 0.1% Triton X-100] at RT for 45 min. Subsequently, cells were subjected to primary antibody solution (10% NGS, in PBS containing 0.01% Triton X-100), using the following dilutions overnight at 4°C: rabbit anti-GFAP (1:1,000, DAKO Agilent, Cat# Z0334), mouse anti-GFAP (1:1,000, Merck Millipore, Cat# MAB3402), mouse anti-2', 3'-cyclic-nucleotide 3'-phosphodiesterase (CNPase; 1:1,000, Biolegend, Cat# 836402), rat anti-myelin basic protein (MBP; 1:250, Bio-Rad Laboratories, Cat# MCA409S), rabbit anti-C21orf91 (1:200, Bioss, Cat# bs-9983R), rabbit anti-C21orf91 (1:300, Sigma-Aldrich, Cat# HPA049030), mouse anti-CC1 (1:1,000, GeneTex, Cat# GTX16794), mouse anti-Olig2 (1:500, Merck Millipore Cat# MABN50), rabbit anti-Olig2 (1:500, Merck Millipore, Cat# AB9610), mouse anti-myelin oligodendrocyte glycoprotein (MOG; 1:500, Merck Millipore, Cat# MAB5680), goat anti-PDGFR ( $\alpha$ /CD140A, 1:250, Neuromics, Cat# GT15150), mouse anti-astrocyte cell surface antigen-1 (ACSA-1/GLAST; 1:200, Miltenyi, Cat# 130-095-822), rabbit anti-hairy and enhancer of split-1 (HES1; 1:250, Invitrogen, Cat# PA5-28802), mouse anti-NK2 Homeobox 2 (NKX2.2; 1:100, R&D Systems, Cat# 883411), rabbit anti-sex-determining region Y-box 10 (Sox10; 1:100, S1058C002, DCS Immunoline, RRID: AB\_2313583), chicken anti-green fluorescent protein/citrine (GFP; 1:1,000; Aves Labs, Cat#

GFP-1020). Following three washing steps with PBS, secondary antibodies (anti-mouse, anti-rabbit, anti-goat) conjugated with either Alexa Fluor405, Alexa Fluor488, or Alexa Fluor594 (1:500; Thermo Fisher Scientific, Darmstadt, Germany) in PBS supplemented with DAPI (0.02  $\mu$ g/ml; Roche Diagnostic GmbH, Mannheim, Germany) were applied for 90 min at RT. Cells were mounted with Citifluor (Cilifluor, Leicester, United Kingdom). For image acquisition, the Zeiss Axionplan2 microscope (Zeiss, Jena, Germany) was used and the analysis was performed with the ImageJ BioVoxel software (Schindelin et al., 2012). Nine images per coverslip (2 coverslips/condition; mean of 2 coverslips generated from the same animal pool represents  $n = 1$  independent experiment) were captured using 20 $\times$  magnification and the same exposure times throughout each experiment and marker expression strength study. For quantification, the number of marker-positive cells in relation to DAPI-positive- (total number, for non-transfected cells) or GFP expressing cells (for transfected cells) was calculated and shown as a percentage. To assess the degree of morphological maturation, transfected (green fluorescent) OPCs were analyzed by fluorescence microscopy (Zeiss Axioplan, Jena, Germany) as previously described (Kremer et al., 2009; Göttle et al., 2010). Based on morphological cell parameters (processes, branches), cells were distinguished into 3 different categories for morphological maturation starting with a low number of processes in progenitor cells to multiple process-bearing cells (low, medium) up to more mature cells with a high degree of arborization or even sheath building (high). For classification of hybrid cells—cells with oligodendroglial- and astroglial marker coexpression—ubiquitous [indicating astrogenesis (Setoguchi and Kondo, 2004)] as well as nuclear Olig2-, Sox10-, Nkx2.2- and strong CC1 expression was correlated with GFAP- and GLAST expression.

## Western Blotting

Isolated CC and HF tissues were lysed using an Ultra-turrax disperser (IKA®-Werke GmbH and Co. KG, Staufen, Germany) and radioimmunoprecipitation assay buffer (RIPA buffer, Cell Signaling Technology, Danvers, MA, USA) supplemented with HALT™ Protease-/Phosphatase inhibitor cocktail and EDTA (both Thermo Fisher Scientific). Afterward, sonication with an ultrasound homogenizer (SonopulsHD2070, 50% power, pulse 0.5 s on and 0.5 s off) was performed for 10 s and samples were centrifuged (14,000 rpm, 10 min, 4°C) to proceed with supernatants. Protein concentrations were determined using the DC Protein Assay (BioRad). Specimens were subjected to standard sodium dodecyl sulfate (SDS) gel electrophoresis and semi-dry western blotting using Bolt 12% Bis-Tris Plus gels and nitrocellulose membranes (both Thermo Fisher Scientific). Blocking was confirmed by total protein staining using the Pierce™ Reversible Protein Stain Kit (Thermo Fisher Scientific) also used for protein normalization. Afterward, membranes were blocked with Superblock (in TBS, Thermo Fisher Scientific) for 1 h at RT and applying the following primary antibodies: rabbit anti-C21orf91 [1:1,000, Santa Cruz Biotechnology, Cat# sc-83610 (Li et al., 2016)], rabbit anti-C21orf91 (1:300, Sigma-Aldrich, Cat# HPA049030), mouse



anti-GAPDH (1:5,000, Merck Millipore Cat# MAB374) and the secondary antibodies anti-rabbit IgG, HRP-linked (1:2,000, Cell Signaling Technology Cat# 7074,) and anti-mouse IgG (H + L), made in horse (1:5,000, Vector Laboratories, Burlingame, CA, USA Cat# PI-2000). For visualization, Super Signal West Pico Chemiluminescent Substrate (Thermo Fisher Scientific) was applied for 5 min. To ensure reliable quantification, membranes were stripped with 10 ml ReBlot Plus Strong Solution (1×, Merck Millipore) to detect C21orf91 and the housekeeping protein (GAPDH) sequentially on the same membrane. Protein bands were quantified using the Fusion FX software (Vilber Lourmat, Eberhardzell, Germany). The intensity for each band was determined and normalized to the total amount of the loaded protein amount and the intensity of the GAPDH band of the corresponding sample. Quantification was repeated two times for the published C21orf91 antibody (Li et al., 2016) and two times for the C21orf91 antibody from Sigma-Aldrich. Both antibodies marked a protein band of the same size and therefore the mean across all Western blot experiments ( $n = 3$  animals) was calculated.

## Myelinating Co-cultures, OPC Transplantation, and Assessment of Myelination Capacity

Dissociated neuron/oligodendrocyte co-cultures were obtained from E16 rat cerebral cortices (Wistar rats of either sex) as previously described in Göttle et al. (2015) and Göttle et al. (2018) with the only difference that  $9 \times 10^4$  cortical cells were plated per well. After 15 days *in vitro* (DIV15),  $10 \times 10^4$  transfected OPCs per coverslip were plated directly in the center of a co-culture. The medium was exchanged twice a week with freshly prepared myelination medium until DIV25. Then, co-cultures were fixed with 4% paraformaldehyde for 15 min at RT and processed for immunofluorescent staining. Blocking solution contained 2% NGS and 0.5% Triton X-100 in PBS, whereas the following primary antibodies were diluted in 2% NGS and 0.1% Triton X-100: mouse anti-MBP (1:250, Biolegend, San Diego, CA, USA, Cat# 836504), mouse anti-CC1 (1:800, GeneTex, Cat# GTX16794), rabbit anti-GFAP (1:800, DAKO Agilent, Cat# Z0334). After washing with PBS, secondary antibodies (anti-mouse and anti-rabbit) conjugated with either Alexa Fluor405 or Alexa Fluor594 (1:500; Thermo Fisher Scientific, Darmstadt, Germany) in PBS supplemented with DAPI (0.02 µg/ml; Roche Diagnostic GmbH, Mannheim, Germany) were applied for 90 min at RT. To assess the degree of cellular maturation, only transfected (green fluorescent) cells were scored by applying an evaluation tool based on morphological cell parameters (processes, branches). Moreover, expression and distribution of the MBP protein were assessed and led to the categorizations: MBP-positive cells with a high degree of arborization [pos], integrated and myelinating oligodendrocytes displaying T-shape structures (myelin; Göttle et al., 2015), non-organized MBP expressing [NOM] cells, characterized by a rather disorganized MBP accumulation and unusual morphologies as well as MBP-negative cells [neg]. For quantification, the number of protein marker-positive cells in relation to GFP expressing

cells (transfected cells) was calculated and shown as percentage ( $n = 9$  experiments). The generation of rodent myelinating co-cultures was approved by the LANUV (Landesamt für Natur, Umwelt und Verbraucherschutz; Az.81-02.04.2018.A388).

## Statistical Analysis

Data are presented as mean values  $\pm$  standard error of the mean (SEM). Graphs and statistical analysis were performed using Excel and the GraphPad Prism 8.0.2 software (GraphPad Prism, San Diego, CA, USA; RRID: SCR\_002798). Shapiro-Wilk normality test was used to assess the absence of Gaussian distribution of all datasets. To determine statistical significance for normally distributed data sets, the Students *t*-test was applied for comparing two groups and one-way analysis of variance (ANOVA) with Turkey post-test for multiple comparisons was applied to compare three or more groups. For data sets not passing the Shapiro-Wilk normality test, Mann-Whitney U test for comparing two groups, and Kruskal-Wallis test with Dunn's post-test for multiple comparisons of three or more groups was applied. Statistical significance thresholds were set as follows:  $*p \leq 0.05$ ;  $**p \leq 0.01$ ;  $***p \leq 0.001$  and ns = not significant. "*n*" represents the number of independent experiments.

## RESULTS

C21orf91 was previously shown to affect neurogenesis during fetal brain development and suggested to impact neuropathogenesis of HSA21-related disorders such as DS (Li et al., 2016). Interestingly, this study also revealed the highest C21ORF91 mRNA expression levels in the adult corpus callosum (CC) which is considered as the largest white matter structure in the brain. This prompted us to investigate C21orf91's correlations and expression patterns in available databases and to study functional consequences upon forced overexpression in the oligodendroglial lineage.

### The Human C21ORF91 Expression Profile Strongly Correlates With the Oligodendroglial Lineage

According to Genevestigator (Hruz et al., 2008), human C21ORF91 is ubiquitously and highly expressed. Out of 285 human tissues and cells with available RNA sequencing (RNAseq) data, 167 tissues (60%) demonstrated high expression levels ( $\log_2 > 3$  of an average of the mean value of TPM). Based on these RNAseq data, hematopoietic cells and the nervous system including corpus callosum and different regions of the spinal cord belong to the 50 tissues and cells showing the highest expression of C21ORF91 (Figure 1A). Microarray data from this platform, which encompasses a wider panel of brain structures than the RNAseq data, further indicated that within the nervous system; corpus callosum, diencephalon, and cerebral white matter belong to the most C21ORF91 enriched regions (Figure 1B). In agreement with these observations, microarray expression data from 6 human adult donors from the Allen Brain Atlas (Sunkin et al., 2013) confirmed the highest expression levels in the corpus callosum and ventral thalamus and globus pallidus, both part of the diencephalon (Figure 1C). To obtain additional



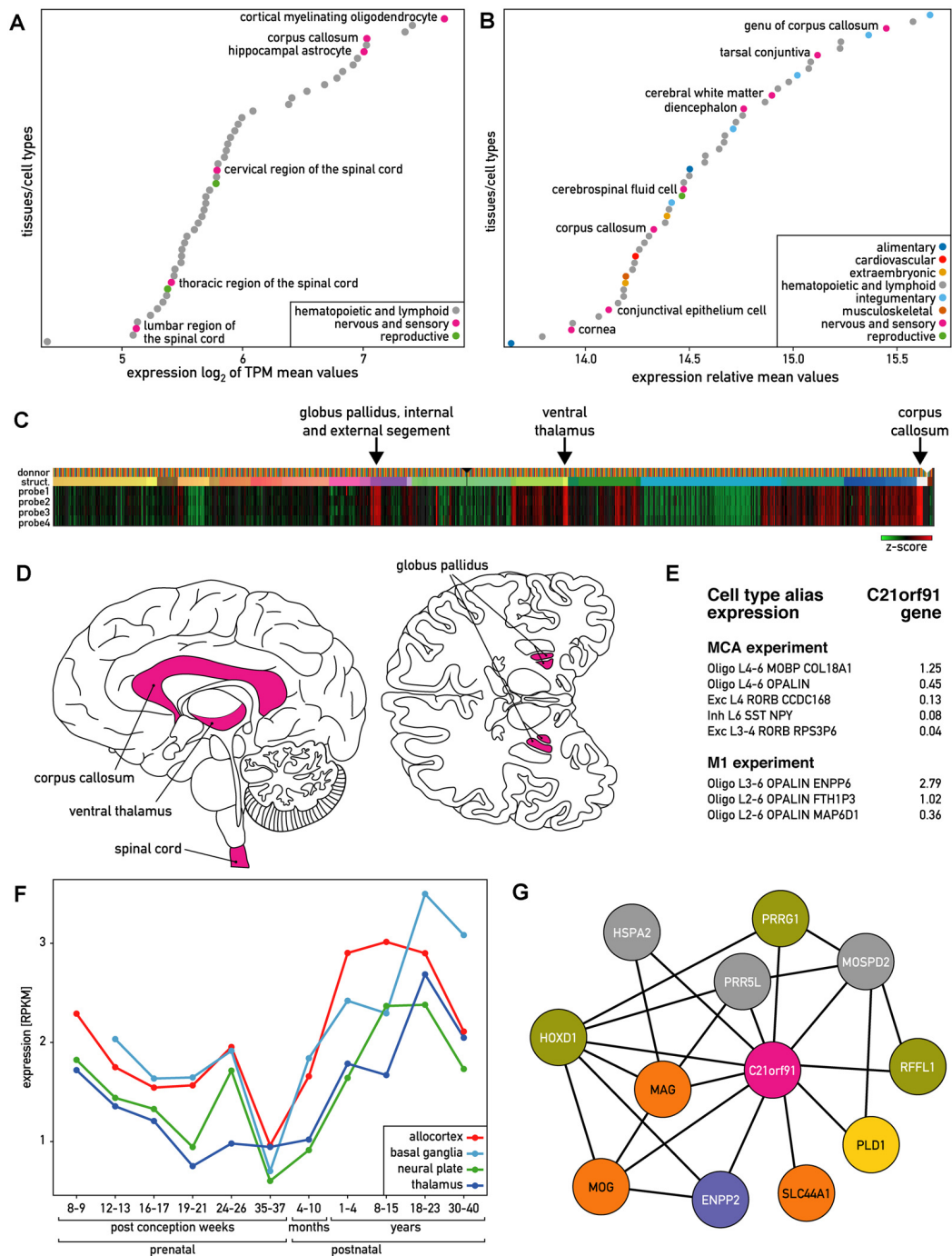


**FIGURE 1 |** Expression of human *C21orf91* gene. **(A)** The 50 tissues and cell types with the highest *C21orf91* expression according to Genevestigator measured with RNAseq and expressed as the  $\log_2$  of TPM (transcripts per kilobase million) mean values. Cortical myelinating oligodendrocytes and hippocampal astrocytes are the cell types, and corpus callosum and spinal cord are the tissues that are most enriched for *C21orf91*. **(B)** The 50 tissues and cell types with the highest *C21orf91* expression according to Genevestigator measured with microarrays and expressed as relative mean expression values. Corpus callosum, diencephalon, and cerebral white matter are the nervous system structures most enriched for *C21orf91*. **(C)** Heat map visualization of microarray expression data from six adult donors for the four available probes for *C21orf91* from the Allen Brain Atlas. Indicated with arrows are the structures with the highest expression. Data is displayed as z-scores. Probe 1–4 correspond to *C21orf91* sequence A\_23\_P211015, A\_24\_P125839, CUST\_5965\_P1416261804 and CUST\_5966\_P1416261804. **(D)** Schematic sagittal and inferior view of the human brain indicating the regions where *C21orf91* gene is expressed according to Genevestigator and Allen Brain Atlas. **(E)** Single-nucleus RNAseq data from Allen Brain Atlas expressed as count per million (cpm) trimmed means.

(Continued)

**FIGURE 1 |** Continued

MCA stands for multiple cortex area set of experiments and M1 for primary motor cortex experiment. L4–6, L6, L3–4, L2–6, L3–6, L4 refer to cortex areas. Oligo stands for oligodendrocytes, Exc for excitatory neuron, and Inh for inhibitory neuron. **(F)** *C21ORF91* expression profile depicts a wave-like pattern, progressively increasing after birth to the age of 23 years. The expression is monitored for different brain structures at different ages. RNAseq data expressed as the mean of RPKM values. Ages vary from prenatal [8–37 post-conception weeks (pcw)] to postnatal stages from 4–10 months and 1–40 years. Brain structures were grouped as follows: *allocortex* (red) = hippocampus; *basal ganglia* (light blue) = striatum; *neural plate* (green) = 19 structures including frontal cortex and cerebellum; *thalamus* (dark blue) = dorsal thalamus, mediodorsal nucleus of thalamus. Data from the *ventricular zone* are not included. **(G)** Coexpression network of genes correlating with *C21ORF91* expression and each other generated from BrainEXP database. Nodes are colored according to protein function: orange: myelination, purple: oligodendrogenesis, yellow: dendrite spine morphogenesis, green: other expression evidence in the nervous system, and gray: other functions.

data on *C21ORF91* expression in the nervous system, we used the Brain EXPression Database (BrainEXP; Jiao et al., 2019). According to this database, *C21ORF91* expression is highest in the spinal cord, a structure that is absent in the panel analyzed by the Allen Brain atlas. The nervous system regions expressing *C21ORF91* (pink) are summarized in **Figure 1D**.

At the cellular level, RNAseq data from Genevestigator showed that *C21ORF91* is enriched in cortical myelinating oligodendrocytes and hippocampal astrocytes (**Figure 1A**). Single nucleus RNAseq data retrieved from the Allen Brain Atlas show that *C21ORF91* is preferentially expressed in oligodendroglial (Oligo) as compared to neuronal populations (Exc, Inh; **Figure 1E**). The oligodendroglial cell population Oligo derived from cortex areas L3–6 (Oligo L3–6 OPALIN ENPP6) which exhibits the highest *C21ORF91* expression also features both, high *OPALIN* transcript levels, encoding a protein involved in oligodendrocyte terminal differentiation (de Faria et al., 2019), as well as *ENPP6* transcripts, encoding a marker of newly forming oligodendrocytes (Xiao et al., 2016). RNAseq expression data from human brain structures at different ages indicate that *C21ORF91* expression is initiated at eight postconceptional weeks (pcw), then decreases until birth and increases progressively until the age of 23 years before it declines again (**Figure 1F**), thus approximately resembling the wave-like myelination process during brain development. Interestingly, the phylogenetic distribution of *C21ORF91*, shown to be conserved in various Gnathostomata (jawed vertebrates)—including mammals, chicken, *Xenopus*, or Zebrafish, but absent in jawless fish (**Supplementary Figure 1**)—closely mirrors the one of myelin (Baumann and Pham-Dinh, 2001).

Both, BrainEXP and the Allen Brain Atlas provide coexpression data. BrainEXP indicates that *C21ORF91* coexpresses with eleven genes (**Figure 1G**). The list includes *MOG*, *SLC44A1* and *MAG*, *HOXD1*, and *ENPP2/autotaxin* of which all were shown to be involved in oligodendrogenesis and myelination (Booth et al., 2007; Wheeler et al., 2015). It also includes *PRRG1* which is uncharacterized but is among the top 50 genes overexpressed in non-activated adult OPCs compared

with activated adult OPCs (Moyon et al., 2015). The other coexpressed genes are *PLD1*, which promotes dendritic spine morphogenesis *via PKD1* activation (Li et al., 2019), *RFFL* which is reported to be expressed in the corpus callosum, brain stem, spinal cord and cerebellar white matter, and *HSPA2* and *PRR5L*, for which we did not find evidence for function in nervous system processes, oligodendrogenesis or myelination.

Additionally, the “Correlate Gene Search” of the Allen Brain Atlas was applied to adult brain microarray data indicating that *C21ORF91* is coexpressed with 51 proteins, including *ENPP2*, *HSPA2*, *MOG*, *PLD1*, *PRR5L*, *PRRG1*, and *SLC44A1* (with a Pearson’s correlation  $\geq 0.85$ ). The analysis of GO terms associated with these 51 proteins revealed an enrichment of the following terms: myelination (GO:0042552), ensheathment of neurons (GO:0007272), axon ensheathment (GO:0008366), glial cell differentiation (GO:0010001), gliogenesis (GO:0042063), and myelin sheath (GO:0043209).

## C21orf91 Ortholog Expression Is Enriched in White Matter Regions and Maturing Oligodendrocytes During Rodent Brain Development

To corroborate human findings, rodent *C21orf91* ortholog expression (*D16Ertd472e* for mouse, *RGD1563888* for rat) was examined using recently generated bulk transcriptomic datasets of numerous purified cell types and workflows for their analysis (Azim et al., 2015, 2018; **Figure 2**). This analysis confirmed the anticipated enrichment of *C21orf91*’s expression in myelinating oligodendrocytes. Note that *C21orf91* subclustered most with known mature oligodendrocyte markers, *MBP*, *Plp1*, and *Myrf*, and forming a larger cluster comprising pan oligodendrocyte or earlier stage lineage markers which include *Olig2*, *Sox10*, *Nkx2.2*, and *Gpr17*. As for a functional assessment we intended to use rat primary OPCs as previously established and published (Kremer et al., 2009; Göttle et al., 2010, 2015, 2018), we additionally examined *C21orf91* expression during rat CNS development. To this end, brains of postnatal day 0 (P0), P7, P25, and 2–3 months old (adult) rats were prepared and transcript and protein expression levels were analyzed in a region-specific way using tissues from the forebrain (FB), corpus callosum (CC), hippocampal formation (HF) and cerebellum (CB; **Figures 3A–C**). Real-time quantitative RT-PCR determination demonstrated that *C21orf91* gene expression was highest in adult CC compared to the other regions and revealed a clear transcript increase over time in all tested brain regions, again most apparent in CC (**Figure 3A**). This could be further verified *via* Western blot analysis, showing that *C21orf91* protein expression was enriched during development in CC and HF (**Figures 3B,C**), peaking at P25 (observed with both tested antibodies, and shown as mean value).

As a next step, immunohistochemical staining of coronal P7 and adult rat CC brain sections was conducted. We assessed the antibody used by Li et al. (2016) as well as several other commercially available antibodies in our immunocytochemistry and confirmed that *C21orf91* expression is correlating with neuronal marker NeuN expression in cortical sections for all of

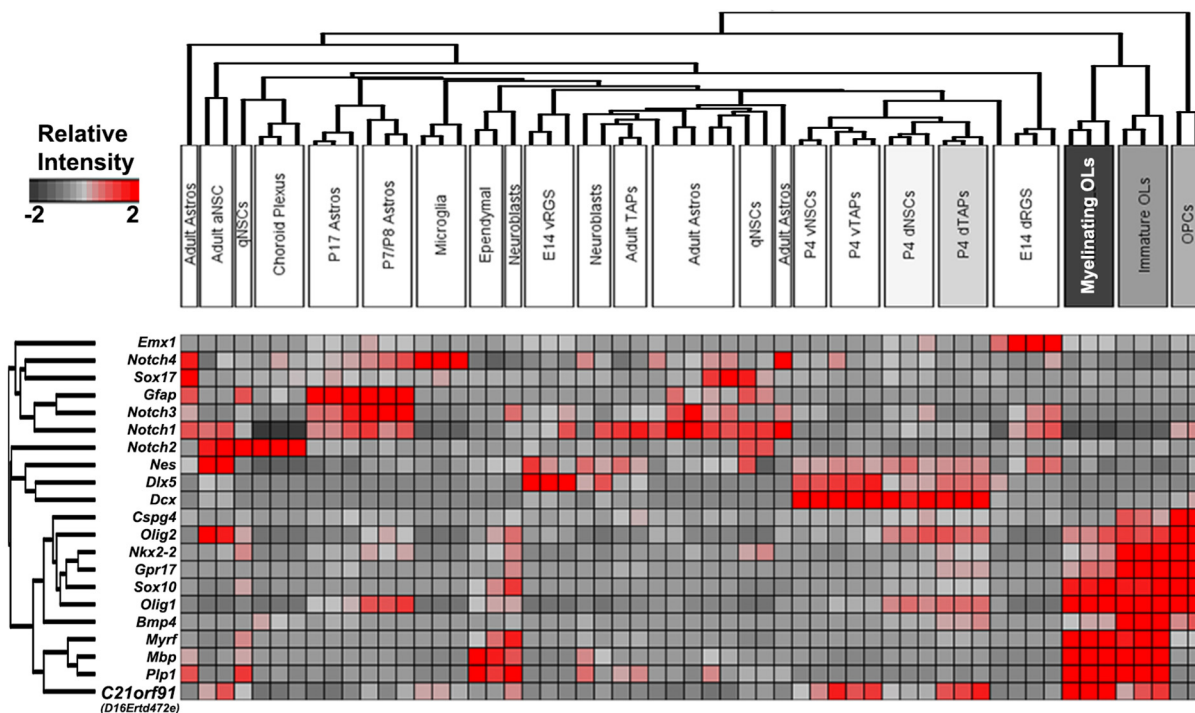


**FIGURE 2 |** Validation of enriched expression of mouse *C21orf91* ortholog in later stage oligodendroglial lineage cells compared to multiple cell types present in the forebrain. Bulk transcriptomic datasets assembled with essential hallmark constructed as a heatmap with known cell-specific hallmark genes and *C21orf91* ortholog (*D16Ert472e*) clusters readily with later stage oligodendroglial markers and is highly expressed in myelinating oligodendrocytes (OL) as well as in transiently amplifying progenitors (TAPs) derived from region-specific early postnatal subventricular zone (SVZ) microdomains. Note: some datasets [e.g., adult astrocytes (Astros)] are not clustered together based on the genes lists for unsupervised clustering. The color legend represents the relative expression strength with red color indicating high values and gray color displaying lower values. Abbreviations: aNSC, activated neural stem cell; qNSC, quiescent NSC; Astros, astrocytes; vRGS/NSCs/TAPs, ventral radial glial cells/NSCs/TAPs; dNSCs/TAPs/RGS, dorsal NSCs/TAPs; OLs, oligodendrocytes; and OPCs, oligodendroglial precursor cells.

them (data not shown). Subsequent staining experiments were then nevertheless conducted using the published antibody (Li et al., 2016), to ensure comparability. Evaluation of staining patterns revealed that the density of *C21orf91* expressing cells per mm<sup>2</sup> was enriched in adult CC compared to the surrounding gray matter (GM; **Figures 3D,D'**). In the next step, the distribution of *C21orf91*-positive cells within lineage-specific marker populations was assessed (**Figure 3E**). PDGFR $\alpha$  hereby represents the OPC population, CC1 accounts for mature oligodendrocytes, and GFAP was used as an astroglial marker. Interestingly, except for small populations in the early developmental stage P7 (see pie area; CC1-positive cells in the GM (gray pie) and GFAP-positive cells in CC (white pie) and GM), between 48–80% of oligodendroglial or astroglial lineage cells expressed *C21orf91* in P7 and adult CC and GM. In a further survey, the distribution of nuclear Olig2- (**Figure 3F**), PDGFR $\alpha$ - (**Figure 3G**), CC1- (**Figure 3H**), and GFAP-positive cells (**Figure 3I**) within the *C21orf91* expressing cell populations were analyzed. In CC, 80% of the *C21orf91* expressing cells in P7 and 60% of the *C21orf91* expressing cells in adult rats were also Olig2-positive (**Figures 3F,F'**). Furthermore, almost 40% of the *C21orf91* expressing cells in P7 CC were PDGFR $\alpha$ -positive, declining in the adult CC along the course of white matter development (**Figures 3G,G'**). In parallel, the

degree of CC1/*C21orf91* expressing cells increased over time (**Figures 3H,H'**), additionally depicted by a proportional increase of *C21orf91*-positive cells within the CC1 population (compare CC1 in P7 and adult; **Figure 3E**). Interestingly, the percentage of *C21orf91* expressing astrocytes also increased in the surrounding GM structures during development, comprising up to 40% of the *C21orf91*-positive cells (**Figures 3I,I'**). Furthermore, the proportional distribution of *C21orf91* expressing cells within the GFAP-positive population doubled during development in both, CC and GM (**Figure 3E**).

### C21orf91 Ortholog Expression Correlates With Differentiation and Maturation of Cultured OPCs

To investigate the role of *C21orf91* in oligodendroglial differentiation, we first examined the expression of differentiation-associated markers and *C21orf91* during spontaneous differentiation of cultured primary rat OPCs. Transcript levels of *C21orf91* (**Figure 4A**) were mildly downregulated at day 3, where *CNPase* expression (**Figure 4B**) is already significantly upregulated, but then upregulated at day 6, similar to the induction of *MBP* and *MOG* expression (**Figures 4C,D**). As oligodendroglial cell differentiation is



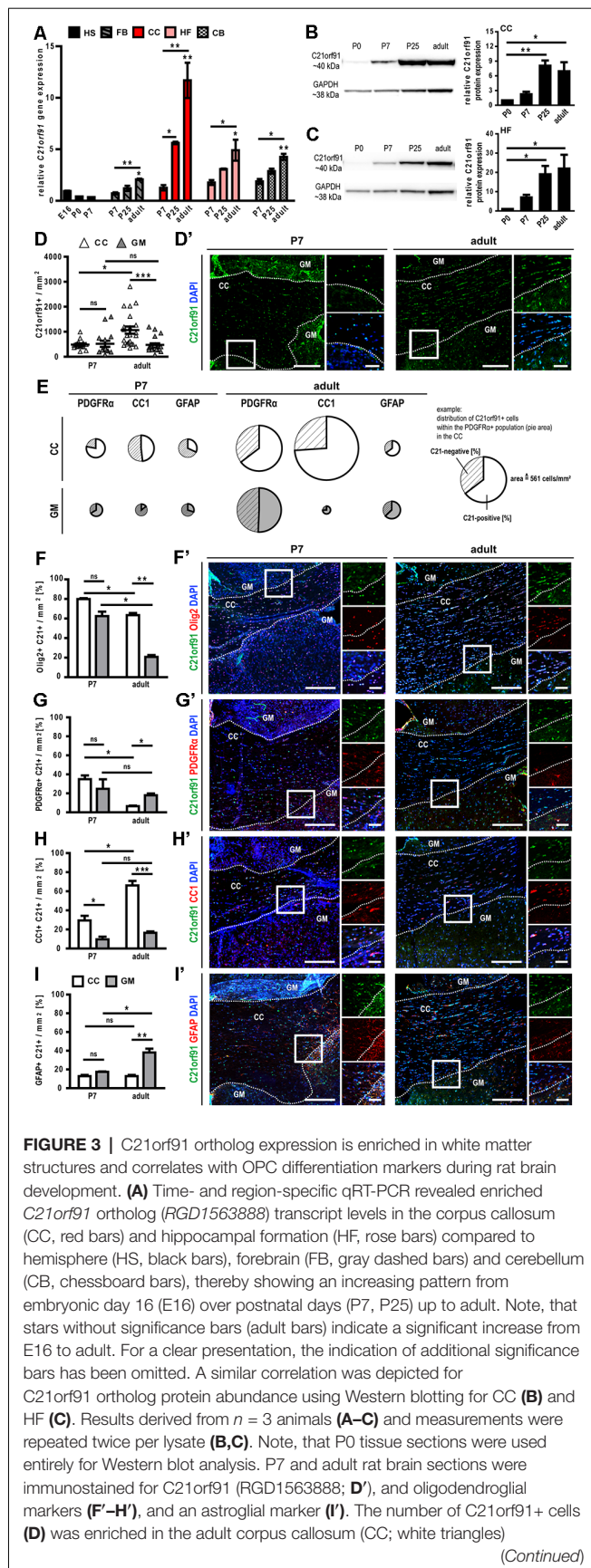


### FIGURE 3 | Continued

compared to the surrounding gray matter (GM; gray triangles) and CC of P7 rats. Panel (D') shows representative tile scans for the analyzed region in P7 and adult rat brain sections stained for C21orf91 (green) with nuclei in blue (DAPI). The average distribution of C21orf91-positive cells within the PDGFR $\alpha$ -, CC1- or GFAP-positive cell population is shown in (E). The marker-related population size/density is depicted by the size (=area) of the pie charts. White pies represent cells of the CC and gray pies refer to GM located cells. The whole circle area of the white PDGFR $\alpha$  pie chart (see example) equals 561 PDGFR $\alpha$ -positive cells/mm<sup>2</sup> and represents the scale for the other pie charts. C21orf91 expression is highly correlated with Olig2 (F), PDGFR $\alpha$  (G) and CC1 (H) expression in the CC and GFAP (I) expression in adult GM. Representative images of tile scans and blow-ups are shown in (F') for Olig2 (red), (G') for PDGFR $\alpha$  (red), (H') for CC1 (red) and (I') for GFAP (red). Nuclei are shown in blue (DAPI). White dashed lines depict the border of CC and surrounding GM. Squares refer to blow-ups. Scale bars for tile scans: 200  $\mu$ m, scale bars for blow-ups: 50  $\mu$ m. Data are shown as mean values ( $\pm$ SEM) deriving from  $n = 4$  animals; Kruskal-Wallis test with Dunn's post-test: \* $p \leq 0.05$ , \*\* $p \leq 0.01$ , \*\*\* $p \leq 0.001$ , ns = not significant.

also reflected by the induction of specific myelin protein expression at particular time points (1d, 3d, 6d), double immunofluorescent staining with antibodies directed against C21orf91, CNPase (Figures 4E,E'), MBP (Figures 4F,F') and MOG (Figures 4G,G') were conducted. Discriminating between different C21orf91 expression strengths (strong: black bars, weak: dashed bars and cells without any positivity), it could be demonstrated that most oligodendroglial cells were expressing C21orf91, with the majority of them featuring strong C21orf91 expression levels (see representative images in Figures 4E–G). Note that especially cells with strong C21orf91 signals (Figures 4E–G) also displayed expression of the stage-specific markers and that none of the myelin-positive cells was negative for C21orf91.

## C21orf91 Ortholog Overexpression Influences Rat OPC Differentiation

Given that the occurrence and strength of differentiation markers correlated with strong C21orf91 ortholog expression levels, it was of interest to find out whether C21orf91 ortholog modulation influences oligodendroglial differentiation, particularly in the context of increased C21orf91 levels in DS. To this end, C21orf91 ortholog (*RGD1563888*) was overexpressed leading to elevated transcript and protein levels (Figures 5A–C). Of note, transfection experiments were conducted with C21orf91 overexpression constructs (black bars) and the corresponding empty control vector (white bars) along with a green fluorescent protein (GFP) expression vector for detection of modulated cells. Morphological assessment of transfected cells was carried out according to our previously published schemes (Kremer et al., 2009; Göttele et al., 2010, 2015) and demonstrated that overexpression of C21orf91 accelerated the maturation process (in terms of process growth and arborization) resulting in a significantly increased number of cells with more mature morphologies (Figures 5B–D).

Although OPCs are generally determined to give rise to oligodendrocytes, they also exert a certain potential to generate astrocytes both *in vitro* (Rao and Mayer-Proschel, 1997; Nishiyama et al., 2009) as well as *in vivo* (Aguirre and Gallo,



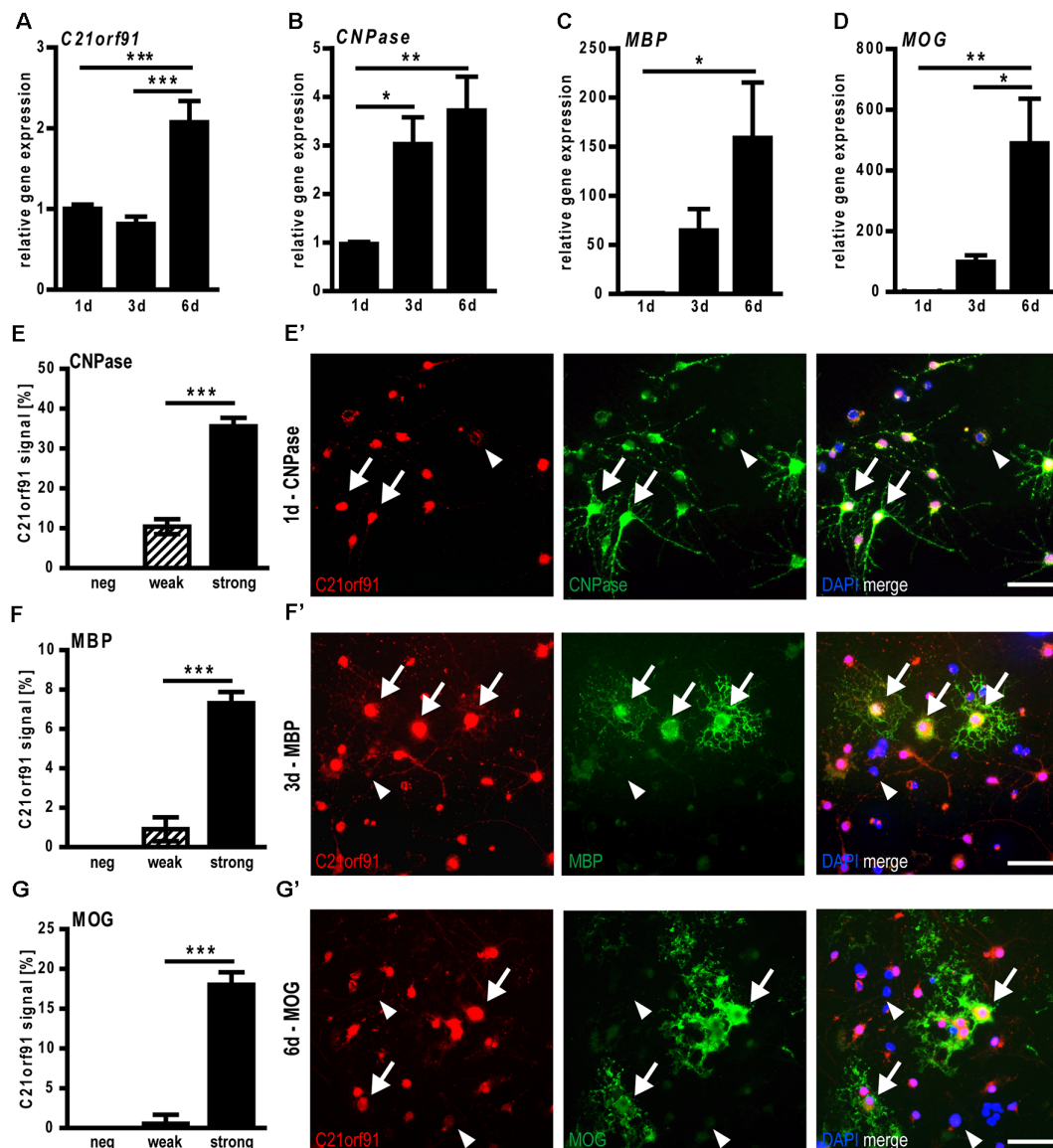


**FIGURE 4 |** C21orf91 ortholog expression correlates with myelin expression during spontaneous differentiation of cultured rat primary oligodendroglial precursor cells (OPCs). Determination of transcript levels using qRT-PCR indicated an upregulation of *C21orf91* ortholog (*RGD1563888*; **A**) concurrent with increased expression of *CNPase* (**B**), *MBP* (**C**), and *MOG* (**D**) for 6 days (1d-6d). Stage-specific analysis of C21orf91 ortholog (*RGD1563888*) protein expression (red, Bioss anti-C21orf91 antibody) via double immunostaining performed for CNPase at 1d (**E,E'**), MBP at 3d (**F,F'**) and MOG at 6d (**G,G'**) revealed that maturation/myelin marker expression during differentiation highly correlates with strong cellular C21orf91 expression levels (black bars). Arrows point to cells with a strong C21orf91 expression that are also myelin-positive, arrowheads point at weak/no expressors that are myelin-negative. Blue nuclei represent DAPI staining. Note, that there are no myelin-positive cells that lack C21orf91 expression. Scale bars: 50  $\mu$ m. Data are shown as mean values ( $\pm$ SEM) deriving from  $n = 8$  experiments (**A-D**) and  $n = 5$  experiments (**E-G**). Statistical significance was calculated using one-way ANOVA with Tukey post-test (**A-D**) and Mann-Whitney  $U$  two-tailed test (**E-G**): \* $p \leq 0.05$ , \*\* $p \leq 0.01$ , \*\*\* $p \leq 0.001$ .

2004; Guo et al., 2009; Tanner et al., 2011; see **Figure 5E**). Interestingly, an increased astrocyte generation (Mito and Becker, 1993; Zdaniuk et al., 2011) along with a diminished myelin formation is observed in DS (Abraham et al., 2012). We, therefore, investigated whether C21orf91 overexpression impacts the lineage fate by depicting the expression changes of several astroglial and oligodendroglial differentiation markers (**Table 1**). This analysis revealed that C21orf91 overexpression resulted in

a distinct reduction of cells exhibiting oligodendroglial features such as nuclear Olig2- and strong Nkx2.2 expression. On the other hand, overexpressing cells increased the expression of PDGFR $\alpha$  compared to control transfected cells. However, CC1 expression appeared to be far less abundant (40% reduction) in modulated cells again. Additionally, Sox10 nuclear localization (Rehberg et al., 2002) appeared to be affected by C21orf91 overexpression as the number of

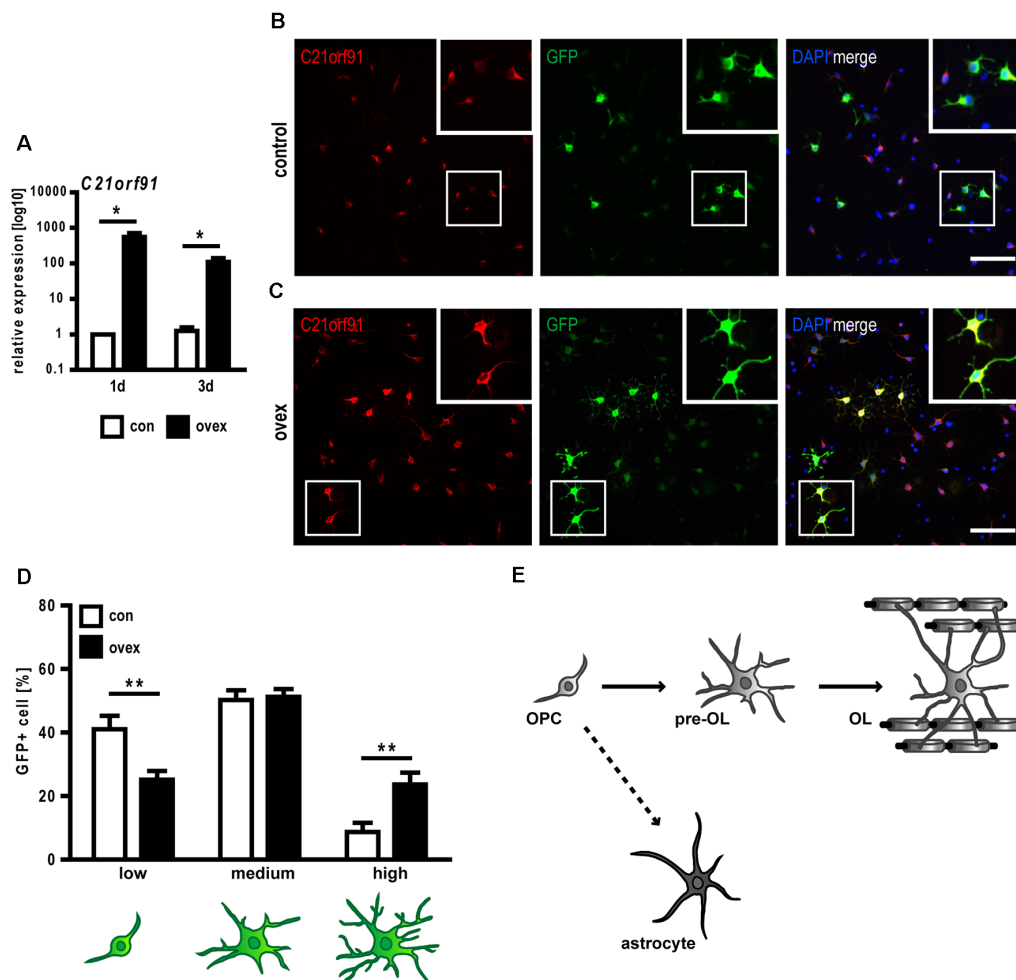


**FIGURE 5 |** C21orf91 ortholog overexpression accelerates morphological maturation of OPCs. OPCs were co-transfected with a GFP expression (for visualization, green) and an empty control vector (con, white bars) or a C21orf91 ortholog (RGD1563888) overexpression construct (ovex, black bars). Overexpression was confirmed using qRT-PCR (**A**) and immunostaining for C21orf91 (red, anti-C21orf91 antibody from Sigma-Aldrich) protein after 2 days of differentiation (**B,C**). Squares show the blow-ups of representative transfected cells which indicate that overexpressing cells in (**C**) exhibited enriched C21orf91 protein abundance. Additionally, their distinct morphological maturation is highlighted (compare cell morphologies in **B,C**) which was further assessed using process- and branch-dependent categories (low-high), indeed revealing an accelerated morphological maturation (**D**). Cell nuclei were labeled by DAPI (blue). Scale bars: 100  $\mu$ m. Data are shown as mean values ( $\pm$ SEM) deriving from  $n = 3$  experiments (**A**) and  $n = 8$  experiments (**D**). Statistical significance was calculated using Mann-Whitney  $U$  two-tailed test (**A**) and Student's two-sided, unpaired  $t$ -test (**B**):  $*p \leq 0.05$ ,  $**p \leq 0.01$ . OPCs, despite their primarily designated development into myelinating oligodendrocytes (OL), can also differentiate into astrocytes (**E**).

cells with exclusively nuclear signals was decreased. On the other hand, an overall induction of astroglial markers was observed. Cytoplasmic translocation of Olig2 is known to account for astroglial differentiation (Setoguchi and Kondo, 2004), and indeed cell numbers with ubiquitous (nuclear and cytoplasmic) Olig2 expression were strongly increased throughout differentiation upon C21orf91 overexpression. Similarly, Hes1-positivity, a transcription factor known to induce astroglial differentiation at the expense of oligodendrogenesis (Wu et al., 2003), was also elevated in cells with forced C21orf91 expression. Moreover, an overall upregulation of GFAP-positive cells at days 2, 3, and 5 of differentiation was observed leading to a 33%-increase in the number of GLAST expressing cells at day 5 (Table 1).

## Overexpression of C21orf91 Ortholog Results in Aberrant Coexpression of Oligodendroglial and Astroglial Differentiation Markers

We next studied to what degree cellular coexpression of astroglial- and oligodendroglial markers could be observed. Immunocytofluorescent staining demonstrated that the forced expression of C21orf91 ortholog initiated aberrant combinations such as (nuclear) Olig2, Sox10, and CC1 expression in combination with GFAP signals at day 2 of differentiation (Figures 6A'–C'). Compared to control transfected cells, the numbers of Olig2/GFAP expressing cells were more than tripled (Figure 6A), whereas Sox10/GFAP expressing (Figure 6B)

**TABLE 1** | C21orf91 ortholog (RGD1563888) overexpression results in a dysbalanced expression profile of glial differentiation markers during OPC differentiation.

Marker		2d		3d		5d	
		Change $\pm$ SEM [%]	p	Change $\pm$ SEM [%]	p	Change $\pm$ SEM [%]	p
Oligodendroglial	Olig2 (nuclear)	−37.64 $\pm$ 2.22	**	−19.64 $\pm$ 2.45	*	−11.31 $\pm$ 1.86	ns
	Sox10 (nuclear)	−34.96 $\pm$ 2.60	**	—	—	−4.50 $\pm$ 7.07	ns
	Nkx2.2	−10.57 $\pm$ 6.60	ns	—	—	−34.45 $\pm$ 4.33	**
	PDGFR $\alpha$	+16.07 $\pm$ 5.36	ns	+14.32 $\pm$ 3.03	*	—	—
	CC1	−10.62 $\pm$ 1.17	*	—	—	−32.34 $\pm$ 9.29	**
	MBP	—	—	+4.17 $\pm$ 1.37	0.07	+3.18 $\pm$ 5.69	ns
Astroglial	Sox10 (ubiquitous/cytoplasmic)	+38.04 $\pm$ 3.56	**	—	—	+16.21 $\pm$ 7.33	*
	Olig2 (ubiquitous)	+44.43 $\pm$ 5.76	**	+26.45 $\pm$ 4.26	*	+18.99 $\pm$ 5.50	*
	Hes1	+21.65 $\pm$ 1.46	**	—	—	—	—
	GFAP	+16.29 $\pm$ 3.88	*	+12.93 $\pm$ 2.15	*	+16.06 $\pm$ 2.44	**
	GLAST	+10.23 $\pm$ 7.15	ns	—	—	+33.10 $\pm$ 1.21	**

Data are shown as mean changes to control transfected cells (%  $\pm$  SEM). Blue color indicates a decreased marker expression, red color relates to increased marker expression. Data derived from  $n = 9$  experiments for GFAP (2d),  $n = 5$  experiments for Olig2 (nuclear and ubiquitous; 2d, 5d), Sox10 (nuclear and ubiquitous / cytoplasmic; 2d), PDGFR $\alpha$  (2d, 3d), CC1 (2d), MBP (3d, 5d) and GFAP (3d, 5d) and  $n = 4$  for Olig2 (nuclear and ubiquitous; 3d), Sox10 (nuclear and ubiquitous / cytoplasmic; 5d), Nkx2.2 (2d, 5d), CC1 (5d), Hes1 (2d) and GLAST (5d). Statistical significance was calculated using Student's two-sided, unpaired t-test and Mann-Whitney U two-tailed test: \* $p \leq 0.05$ , \*\* $p \leq 0.01$ , ns = not significant.

and CC1/GFAP-positive cells (**Figure 6C**) were doubled upon overexpression. In C21orf91 overexpressing cells, this mixed phenotype could occasionally still be found after 5 days in culture (data not shown). Furthermore, also coexpression of Nkx2.2 together with GFAP, as well as a few cells displaying a ubiquitous expression of Olig2 [indicating astrogenesis (Setoguchi and Kondo, 2004)] together with GLAST were found (**Figures 6D,E**).

## Rat Oligodendroglial Cells Display Accelerated Maturation but Diminished Myelination Capacity Upon C21orf91 Ortholog Overexpression

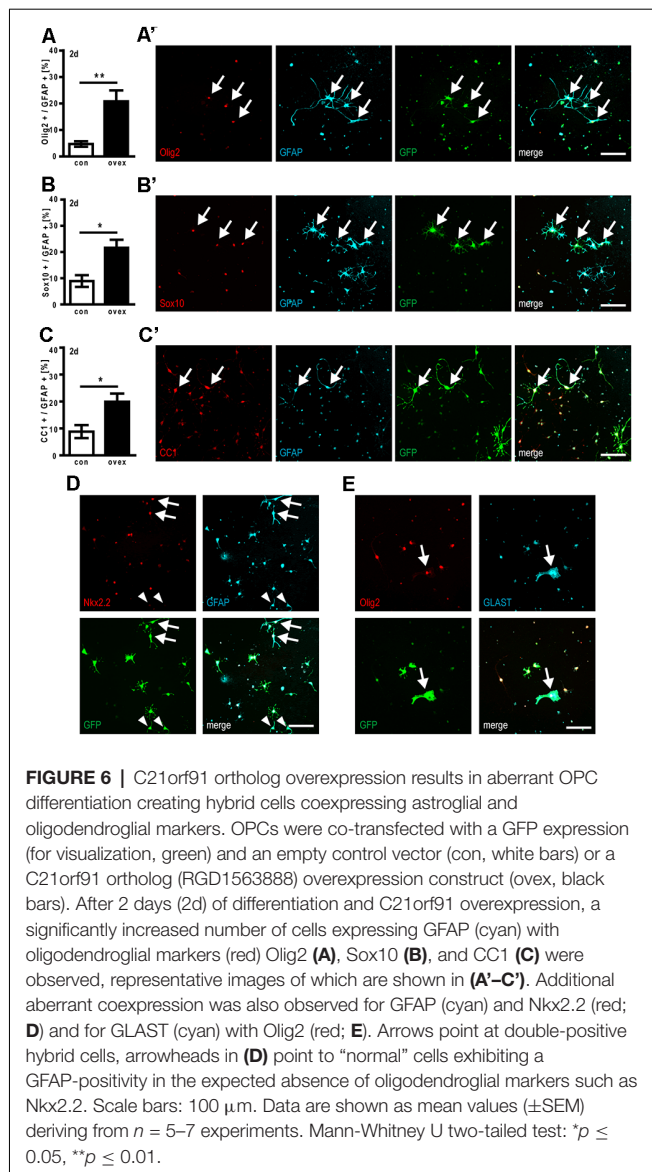
As C21orf91 ortholog overexpression leads to dysregulated OPC differentiation and the acquisition of non-permissive marker combinations, their maturation capacity was evaluated. We first observed, that upon C21orf91 overexpression, cells did not show a significant difference for the positivity of maturation marker MBP (**Table 1**). However, the expression strength of MBP was increased after 3 days of differentiation when compared to control cells (**Figure 7A**). Following the observed accelerated morphological maturation at day 2 of differentiation (**Figure 5D**), C21orf91 overexpressing cells exhibited morphologically elaborated maturation (**Figure 7C**) also at day 3 compared to control transfected cells (**Figure 7B**). Furthermore, control cells displayed vesicle-like MBP signals (**Figure 7B**), indicating MBP expression is still at an earlier stage as compared to C21orf91 overexpressed cells. Next, C21orf91 overexpressing OPCs were evaluated in a more physiological environment allowing axon/oligodendrocyte interactions to occur and we assessed whether the produced MBP protein could contribute to the generation of functional myelin. For this purpose, we used myelinating neuron-oligodendrocyte co-cultures (Göttle et al., 2015, 2018, 2019) onto which transfected primary rat OPCs were applied during the myelination process. Transplanted cells were maintained in co-culture for another 10 days in presence of a myelination-inducing medium and then assessed for their potential to integrate and to

ensheath axons (detectable as T-shaped MBP-positive structures) as previously established for p57kip2 suppressed OPCs in our former studies (Göttle et al., 2015). We distinguished between MBP-negative cells (neg), MBP expressing oligodendrocytes (pos), oligodendrocytes myelinating axons (myelin, T-shapes), and non-organized MBP expressing (NOM) cells. NOM cells were characterized by a rather disorganized MBP accumulation and by a somehow collapsed morphology (**Figures 7D,F**). We found that OPCs with enforced C21orf91 expression failed to ensheath axons when compared to control transfected cells (**Figure 7D**). Also, the number of NOM cells was substantially increased (**Figure 7D**). Of note, GFAP/MBP double staining revealed that some of these NOM cells exhibited non-permissive coexpression of these two proteins (**Figures 7E,F**).

## DISCUSSION

There is an increasing acceptance of the fact that white matter composition and functionality contribute to a healthy and functional CNS and that respective deficiencies are therefore likely implicated in many if not all neurological manifestations (Kremer et al., 2016). And indeed, an unusual, aberrant glial composition has been observed in the CNS of DS patients which has been suggested to contribute to developmental deficiencies and subsequent cognitive impairments and ID (Haydar and Reeves, 2012; Kanaumi et al., 2013; Stagni et al., 2017; Dossi et al., 2018). However, the underlying reasons why the glial compartment is affected by chromosome 21 triplication and which of the dysregulated genes contribute to glial malformation remain to be understood.

The C21ORF91 gene has so far not been investigated in the context of oligodendrogenesis and white matter, although it was listed within the dysregulated gene network M43 in DS which is associated with oligodendroglial development and myelination (Olmos-Serrano et al., 2016). Our here presented studies demonstrate that C21ORF91 correlates with white matter formation and oligodendroglial lineage. Not only being conserved in various jawed vertebrates (**Supplementary Figure 1**), closely mirroring the phylogenetic distribution of



myelin (Baumann and Pham-Dinh, 2001), our bioinformatical analyses independently revealed a coexpression network of genes including *PLD1*, *MOG*, *MAG*, *OPALIN*, *SLC44A1* and *ENPP2/autotaxin* (Figure 1G), all of which are associated with oligodendrogenesis, myelination, glial cell differentiation and axon ensheathment, and also being part of Olmos-Serrano et al.'s (2016) M43 gene cluster. Furthermore, we here confirmed this bioinformatics-based correlation of human expression data for rodents, demonstrating on the one hand that C21orf91 ortholog was indeed enriched in the CC, the largest white matter structure of the CNS while revealing on the other hand, that it was also clearly associated with oligodendroglial differentiation and maturation. Moreover, here we show that slight disturbances in the expression strength as introduced by overexpression, reproducing conditions of the developing CNS in DS (Ait Yahya-Graison et al., 2007; Li et al., 2016) appear to interfere with OPC maturation and the proper establishment of myelin sheaths

while creating cells with aberrant expression profiles. Because forced overexpression led to faster OPC maturation (seen by MBP expression strength; Figure 7), yet defective myelination, complex patterns of hypomyelination in DS could be explained, with myelin markers MBP and MOG depicting non-significant differences in the expression in early periods of life, then being progressively downregulated in DS patients (Abraham et al., 2012; Olmos-Serrano et al., 2016). Based on these observations, we suggest that overexpression of this gene contributes to hypomyelination as described in DS.

In this regard, it is tempting to speculate that the glial disbalance, more precisely the overpopulation of astroglial cells, such as described in the hippocampus of infant and adult DS brains (Mito and Becker, 1993), is related to enriched C21ORF91 expression. We confirmed increased levels of C21orf91 ortholog expression in the hippocampal formation (HF) during rat brain development and showed that in addition to myelinating oligodendrocytes, C21ORF91 is also substantially expressed in hippocampal astrocytes. Furthermore, elevated levels of C21orf91 ortholog augmented the expression of astroglial markers in differentiating OPCs and even resulted in cells displaying both lineage features. To what degree C21orf91-dependent aberrant astrogenesis from OPCs contributes to a DS-related overpopulation of astrocytes and whether also glial precursor cells committed to the astroglial lineage are additionally dysregulated, remains to be addressed in future studies.

Related to the here described significantly increased combinations of astroglial and oligodendroglial markers in OPCs with elevated C21orf91 ortholog expression levels, it is reasonable to assume that such cells are conflicted in their differentiation paths. It remains therefore to be shown in future studies to what extent this is a transient phenomenon with cells exhibiting a possible extension of early glial progenitor virtues. Consequently, whether and when progression into either astroglial or delayed oligodendroglial lineages occurs—possibly inflicting successful distribution, tissue integration, and axon interactions—or whether such cells die or become actively omitted within the developing CNS needs also to be investigated. Moreover, to understand how such aberrant expression patterns arise, it will be necessary to investigate responsible signaling pathways, thus allowing the identification of altered dynamics in DS. As summarized recently (Reiche et al., 2019), several signaling pathways are potentially involved in neural/glial fate decision and differentiation in DS. Of note, in terms of neurogenesis, Li et al. (2016) already demonstrated neural  $\beta$ -catenin upregulation in response to overexpression of C21orf91. Noteworthy, the Wnt/ $\beta$ -catenin signaling is also a key regulator of oligodendrocyte development, as it is transiently activated in OPCs concurrent with the initiation of terminal differentiation (Emery, 2010). It will therefore be of interest to see whether C21orf91-dependent  $\beta$ -catenin regulation also accounts for glial cells and which other suspected molecules are responding to elevated C21orf91 levels in OPCs. In this regard, studies on axin2/catenin are worth mentioning since these molecules are already investigated in the context of white matter lesions in



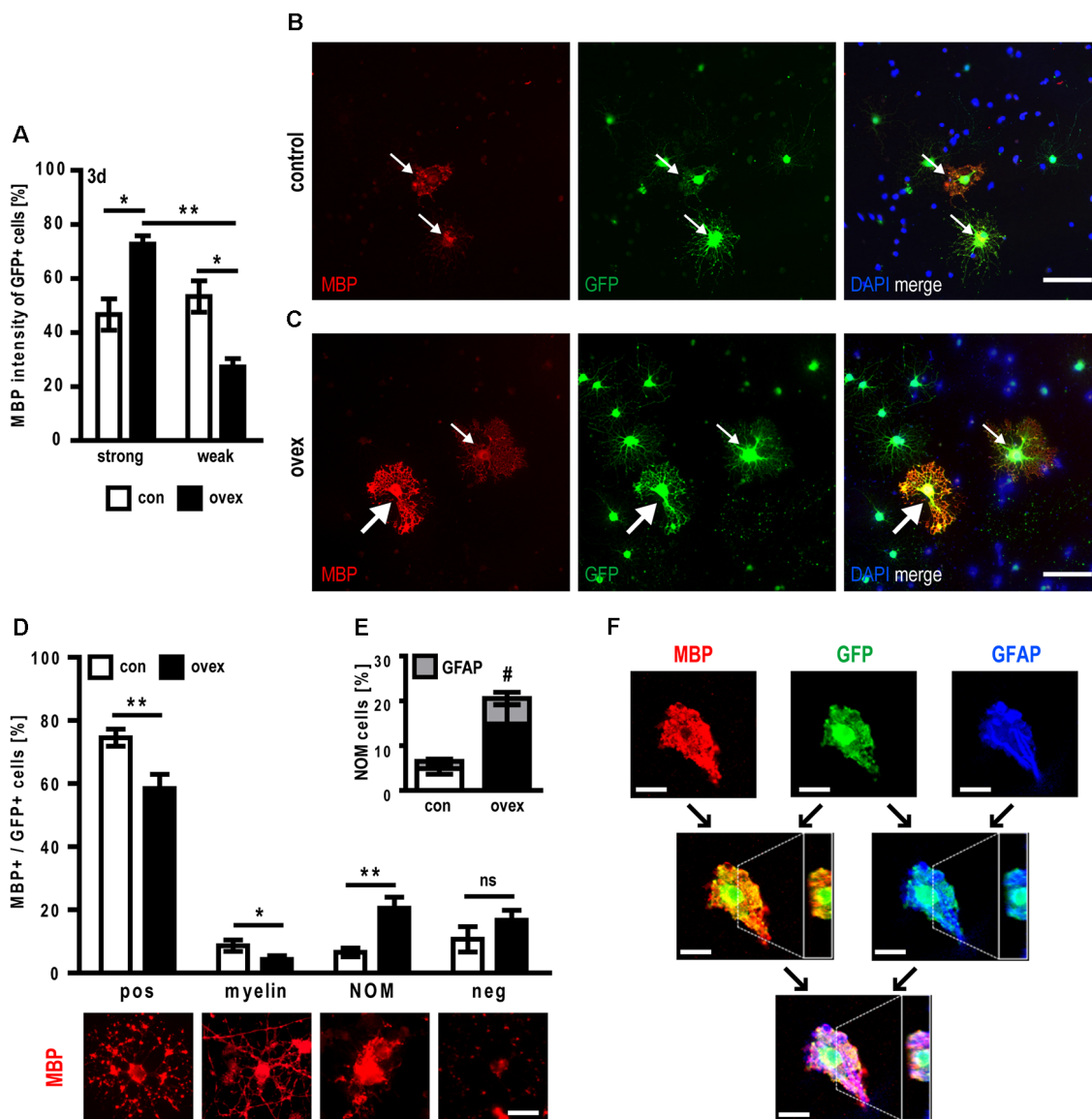


**FIGURE 7 |** C21orf91 ortholog overexpression leads to myelination failures and abnormal GFAP coexpression in myelin-producing oligodendrocytes. Immunofluorescence analysis of co-transfected OPCs with a GFP expression vector (for visualization, green) and an empty control vector (con, white bars) or a C21orf91 ortholog (RGD1563888) overexpression construct (ovex, black bars) revealed that after 3 days (3d) of differentiation the proportion of cells with strong MBP expression was increased upon C21orf91 overexpression (**A**). While control transfected cells exhibited MBP vesicle-like signals (red; **B**) C21orf91 overexpression resulted in stronger MBP signals (bold arrows) and myelin protein presence in cell processes (**C**). Thin arrows point at cells with weak MBP expression. Cell nuclei were labeled by DAPI (blue). To assess whether the observed elevated levels of produced MBP protein correlate with the establishment of functional myelin, transfected OPCs were transplanted onto and cultured for 10 days on dissociated co-cultures. By categorizing GFP-positive cells (green) into different MBP expression- and morphological-related stages (**D**), it was shown that C21orf91 overexpression resulted in fewer MBP expressing (pos) cells and also diminished their capacity to ensheath axons (myelin). They rather exhibited strong but non-organized MBP expression (NOM). Double immunostaining for MBP and GFAP (gray bars, blue stain) exposed NOM cells also to aberrantly coexpress both markers (**E**) which were confirmed via the orthogonal projection of a confocal, z-stacked microscopy image (**F**). Black arrows show which channels were merged; white dashed lines depict the y-axis cut through the z-stack which is shown in the white box on the right side of the images. Scale bars: 50  $\mu$ m (**B,C**); 25  $\mu$ m (**D**) and 20  $\mu$ m (**F**). Data are shown as mean values ( $\pm$ SEM) deriving from  $n = 5$  (**A**) and  $n = 9$  experiments (**D,E**). Statistical significance was calculated using Kruskal-Wallis test with Dunn's post-test (**A**) and Student's two-sided, unpaired *t*-test (**D,E**): \* $p \leq 0.05$ , \*\* $p \leq 0.01$ , ns = not significant; # $p \leq 0.05$  for the statistical analysis of GFAP + /MBP+ cells (gray bars) in (**E**).

human newborns with neonatal ischemic and gliotic brain damage. Axin2 is a target of Wnt and negatively feeds back on this pathway, thereby promoting degradation of  $\beta$ -catenin (Fancy et al., 2011).

Further investigations along this line will be the subject of upcoming studies and could indeed contribute to the identification of therapeutic approaches which would allow to support or protect white matter development in young DS

patients—a so far clinically unmet need. In this regard, it is worth mentioning that myelin repair studies in the context of multiple sclerosis (MS) or after hypoxia-ischemia mediated preterm brain injury have advanced in the last decade and that several modulating pharmacological agents are currently tested in clinical trials (Kremer et al., 2011, 2016; Reiche et al., 2019). Most promising substances emanating from demyelinating disease research should therefore be evaluated for their potential to correct the here described non-permissive cellular phenotype and to promote cells in their process to contact and myelinate axons.

Likewise, when it comes to the misexpression of MBP protein in *C21orf91* ortholog overexpressing cells in a more physiological context, it will also be of interest to study mechanisms of translational control in distal regions of oligodendrocyte processes. Regulated *via* ribonucleoprotein complexes referred to as RNA granules (Maggipinto et al., 2004) and with its mRNA residing in a translationally inactive state, the role of for example ribonucleoprotein types F and A2 (hnRNP\_F, hnRNP\_A2), both involved in post-transcriptional regulation of MBP expression (White et al., 2012) should be examined. Of note, fetal DS brains were found to possess increased protein levels of hnRNP\_A2/B1 which was suggested to lead to impaired MBP expression (Kim et al., 2001). The here observed accumulation of MBP protein around oligodendroglial somata (NOM cells; **Figures 7D,F**) could therefore result from deficits in the transport of the mRNA-packed granules, suggesting that *C21orf91* could be involved in specific transport processes. Such an extended functional role is supported by *C21orf91*'s association with microtubules<sup>3</sup>.

Finally, the here proposed influence of the *C21orf91* protein on the establishment of mainly oligodendrocytes and white matter needs to be confirmed in suitable *in vivo* paradigms. Existing mouse models for DS such as the commonly used strains Ts65Dn and Ts1Cje comprise several HSA21 homologous genes located on mouse chromosome 16 (MMU16; Antonarakis, 2017; Herault et al., 2017) and are therefore likely not to support this strategy as they would not allow focusing exclusively on the functionality of the *C21ORF91* gene. Furthermore, Li et al. (2016) highlighted that this gene is also not represented within the modulated regions of those strains. Likewise, *C21orf91* ortholog knockout animals would also not be suitable, given that our data on oligodendroglia indicate that the observed cellular phenotype is a consequence of non-physiologically elevated gene expression levels. Such a constellation, therefore, needs to be mimicked by a *C21orf91* ortholog transgenic overexpression model, which needs yet to be generated. Here, an inducible expression might be considered to avoid too high protein levels as well as to provide the possibility to apply different time windows of gene induction. Nevertheless, a valuable alternative to such *in vivo* studies would be given by the generation of induced pluripotent stem cell (iPSC) generated neural cells that can be fostered to become oligodendrocytes [as shown by us in Jadasz et al. (2018)]. *C21orf91* overexpression in such cells could be investigated in a tissue environment such as organoids and using DS patient-

derived cells, it could then also be expanded towards humans. Of note, *C21ORF91* was classified as the second most induced gene among 71 genes overexpressed in DS iPSCs (Chou et al., 2012). If such increased levels are maintained in neural/oligodendroglial progeny cells molecular reverting/correcting strategies could be applied to assess the pathophysiological functionality of this gene.

## DATA AVAILABILITY STATEMENT

The datasets presented in this study can be found in online repositories. The names of the repository/repositories and accession number(s) can be found in the article/**Supplementary Material**.

## ETHICS STATEMENT

The animal study was reviewed and approved by LANUV; Landesamt für Natur, Umwelt und Verbraucherschutz.

## AUTHOR CONTRIBUTIONS

LR, PG, and PK contributed to the conception and design of the study. LL, PD, and KA analyzed and presented data from existing databases and websites. LR, MP, JS, and AM performed experiments. LR, MP, LL, PD, KA, JS-H, PG, AM, and PK contributed to data analysis and interpretation. LR, AM, and MP performed the statistical analysis. LR, LL, PD, KA, PG, and PK contributed to the data visualization. LL, PD, and KA contributed written sections of the manuscript. LR and PK wrote the manuscript. LR, PG, and PK contributed to funding acquisition. PK supervised the project. All authors contributed to the article and approved the submitted version.

## FUNDING

LR was supported by the Jürgen Manchot Foundation, Düsseldorf and the iBrain Graduate School, Düsseldorf. This work was also supported by the Stifterverband/Novartisstiftung (to PK).

## ACKNOWLEDGMENTS

We thank Brigida Ziegler and Birgit Blumenkamp for their technical assistance. Furthermore, we thank Hybrigenics SA for providing the *C21orf91* expression vectors.

## SUPPLEMENTARY MATERIAL

The Supplementary Material for this article can be found online at: <https://www.frontiersin.org/articles/10.3389/fncel.2021.653075/full#supplementary-material>.

**SUPPLEMENTARY FIGURE 1 |** Multiple sequence alignment of human *C21ORF91* and model organism orthologs performed with ClustalO and Jalview.

<sup>3</sup><http://www.proteinatlas.org/ENSG00000154642-C21orf91/antibody>

## REFERENCES

- Abraham, H., Vincze, A., Veszpremi, B., Kravjak, A., Gomori, E., Kovacs, G. G., et al. (2012). Impaired myelination of the human hippocampal formation in Down syndrome. *Int. J. Dev. Neurosci.* 30, 147–158. doi: 10.1016/j.ijdevneu.2011.11.005
- Aguirre, A., and Gallo, V. (2004). Postnatal neurogenesis and gliogenesis in the olfactory bulb from NG2-expressing progenitors of the subventricular zone. *J. Neurosci.* 24, 10530–10541. doi: 10.1523/JNEUROSCI.3572-04.2004
- Ait Yahya-Graison, E., Aubert, J., Dauphinot, L., Rivals, I., Prieur, M., Golfier, G., et al. (2007). Classification of human chromosome 21 gene-expression variations in Down syndrome: impact on disease phenotypes. *Am. J. Hum. Genet.* 81, 475–491. doi: 10.1086/520000
- Akkermann, R., Beyer, F., and Küry, P. (2017). Heterogeneous populations of neural stem cells contribute to myelin repair. *Neural Regen. Res.* 12, 509–517. doi: 10.4103/1673-5374.204999
- Antonarakis, S. E. (2017). Down syndrome and the complexity of genome dosage imbalance. *Nat. Rev. Genet.* 18, 147–163. doi: 10.1038/nrg.2016.154
- Azim, K., Akkermann, R., Cantone, M., Vera, J., Jadasz, J. J., and Küry, P. (2018). Transcriptional profiling of ligand expression in cell specific populations of the adult mouse forebrain that regulates neurogenesis. *Front. Neurosci.* 12:220. doi: 10.3389/fnins.2018.00220
- Azim, K., Angonin, D., Marcy, G., Pieropan, F., Rivera, A., Donega, V., et al. (2017). Pharmacogenomic identification of small molecules for lineage specific manipulation of subventricular zone germinal activity. *PLoS Biol.* 15:e2000698. doi: 10.1371/journal.pbio.2000698
- Azim, K., Hurtado-Chong, A., Fischer, B., Kumar, N., Zweifel, S., Taylor, V., et al. (2015). Transcriptional hallmarks of heterogeneous neural stem cell niches of the subventricular zone. *Stem Cells* 33, 2232–2242. doi: 10.1002/stem.2017
- Baburamani, A. A., Patkee, P. A., Arichi, T., and Rutherford, M. A. (2019). New approaches to studying early brain development in Down syndrome. *Dev. Med. Child Neurol.* 61, 867–879. doi: 10.1111/dmnc.14260
- Baumann, N., and Pham-Dinh, D. (2001). Biology of oligodendrocyte and myelin in the mammalian central nervous system. *Physiol. Rev.* 81, 871–927. doi: 10.1152/physrev.2001.81.2.871
- Bercury, K. K., and Macklin, W. B. (2015). Dynamics and mechanisms of CNS myelination. *Dev. Cell* 32, 447–458. doi: 10.1016/j.devcel.2015.01.016
- Beyer, F., Jadasz, J., Samper Agrelo, I., Schira-Heinen, J., Groh, J., Manousi, A., et al. (2020). Heterogeneous fate choice of genetically modulated adult neural stem cells in gray and white matter of the central nervous system. *Glia* 68, 393–406. doi: 10.1002/glia.23724
- Booth, J., Nicolay, D. J., Doucette, J. R., and Nazarali, A. J. (2007). Hoxd1 is expressed by oligodendroglial cells and binds to a region of the human myelin oligodendrocyte glycoprotein promoter *in vitro*. *Cell. Mol. Neurobiol.* 27, 641–650. doi: 10.1007/s10571-007-9150-4
- Cahoy, J. D., Emery, B., Kaushal, A., Foo, L. C., Zamanian, J. L., Christopherson, K. S., et al. (2008). A transcriptome database for astrocytes, neurons, and oligodendrocytes: a new resource for understanding brain development and function. *J. Neurosci.* 28, 264–278. doi: 10.1523/JNEUROSCI.4178-07.2008
- Chou, S. T., Byrka-Bishop, M., Tober, J. M., Yao, Y., Vandorn, D., Opalinska, J. B., et al. (2012). Trisomy 21-associated defects in human primitive hematopoiesis revealed through induced pluripotent stem cells. *Proc. Natl. Acad. Sci. U S A* 109, 17573–17578. doi: 10.1073/pnas.1211175109
- de Faria, O., Jr., Dhaunchak, A. S., Kamen, Y., Roth, A. D., Kuhlmann, T., Colman, D. R., et al. (2019). TMEM10 promotes oligodendrocyte differentiation and is expressed by oligodendrocytes in human remyelinating multiple sclerosis plaques. *Sci. Rep.* 9:3606. doi: 10.1038/s41598-019-40342-x
- Dossi, E., Vasile, F., and Rouach, N. (2018). Human astrocytes in the diseased brain. *Brain Res. Bull.* 136, 139–156. doi: 10.1016/j.brainresbull.2017.02.001
- Emery, B. (2010). Regulation of oligodendrocyte differentiation and myelination. *Science* 330, 779–782. doi: 10.1126/science.1190927
- Fancy, S. P., Harrington, E. P., Yuen, T. J., Silbereis, J. C., Zhao, C., Baranzini, S. E., et al. (2011). Axin2 as regulatory and therapeutic target in newborn brain injury and remyelination. *Nat. Neurosci.* 14, 1009–1016. doi: 10.1038/nn.2855
- Fenoll, R., Pujol, J., Esteba-Castillo, S., de Sola, S., Ribas-Vidal, N., Garcia-Alba, J., et al. (2017). Anomalous white matter structure and the effect of age in down syndrome patients. *J. Alzheimers Dis.* 57, 61–70. doi: 10.3233/JAD-161112
- Göttle, P., Forster, M., Gruchot, J., Kremer, D., Hartung, H. P., Perron, H., et al. (2019). Rescuing the negative impact of human endogenous retrovirus envelope protein on oligodendroglial differentiation and myelination. *Glia* 67, 160–170. doi: 10.1002/glia.23535
- Göttle, P., Kremer, D., Jander, S., Odemis, V., Engele, J., Hartung, H. P., et al. (2010). Activation of CXCR7 receptor promotes oligodendroglial cell maturation. *Ann. Neurol.* 68, 915–924. doi: 10.1002/ana.22214
- Göttle, P., Manousi, A., Kremer, D., Reiche, L., Hartung, H. P., and Küry, P. (2018). Teriflunomide promotes oligodendroglial differentiation and myelination. *J. Neuroinflammation* 15:76. doi: 10.1186/s12974-018-1110-z
- Göttle, P., Sabo, J. K., Heinen, A., Venables, G., Torres, K., Tzekova, N., et al. (2015). Oligodendroglial maturation is dependent on intracellular protein shuttling. *J. Neurosci.* 35, 906–919. doi: 10.1523/JNEUROSCI.1423-14.2015
- Guo, F., Ma, J., McCauley, E., Bannerman, P., and Pleasure, D. (2009). Early postnatal proteolipid promoter-expressing progenitors produce multilineage cells *in vivo*. *J. Neurosci.* 29, 7256–7270. doi: 10.1523/JNEUROSCI.5653-08.2009
- Haydar, T. F., and Reeves, R. H. (2012). Trisomy 21 and early brain development. *Trends Neurosci.* 35, 81–91. doi: 10.1016/j.tins.2011.11.001
- Herauld, Y., Delabar, J. M., Fisher, E. M. C., Tybulewicz, V. L. J., Yu, E., and Braut, V. (2017). Rodent models in Down syndrome research: impact and future opportunities. *Dis. Models Mech.* 10, 1165–1186. doi: 10.1242/dmm.029728
- Hruz, T., Laule, O., Szabo, G., Wessendorp, F., Bleuler, S., Oertle, L., et al. (2008). Genevestigator v3: a reference expression database for the meta-analysis of transcriptomes. *Adv. Bioinformatics* 2008:420747. doi: 10.1155/2008/420747
- Jadasz, J. J., Tepe, L., Beyer, F., Samper Agrelo, I., Akkermann, R., Spitzhorn, L. S., et al. (2018). Human mesenchymal factors induce rat hippocampal- and human neural stem cell dependent oligodendrogenesis. *Glia* 66, 145–160. doi: 10.1002/glia.23233
- Jiao, C., Yan, P., Xia, C., Shen, Z., Tan, Z., Tan, Y., et al. (2019). BrainEXP: a database featuring with spatiotemporal expression variations and co-expression organizations in human brains. *Bioinformatics* 35, 172–174. doi: 10.1093/bioinformatics/bty576
- Kanaumi, T., Milenkovic, I., Adle-Biasette, H., Aronica, E., and Kovacs, G. G. (2013). Non-neuronal cell responses differ between normal and Down syndrome developing brains. *Int. J. Dev. Neurosci.* 31, 796–803. doi: 10.1016/j.ijdevneu.2013.09.011
- Karlsen, A. S., and Pakkenberg, B. (2011). Total numbers of neurons and glial cells in cortex and basal ganglia of aged brains with Down syndrome—a stereological study. *Cereb. Cortex* 21, 2519–2524. doi: 10.1093/cercor/bhr033
- Kim, S. H., Dierssen, M., Ferreres, J. C., Fountoulakis, M., and Lubec, G. (2001). Increased protein levels of heterogeneous nuclear ribonucleoprotein A2/B1 in fetal Down syndrome brains. *J. Neural Transm. Suppl.* 61, 273–280. doi: 10.1007/978-3-7091-6262-0\_22
- Korbel, J. O., Tirosh-Wagner, T., Urban, A. E., Chen, X. N., Kasowski, M., Dai, L., et al. (2009). The genetic architecture of Down syndrome phenotypes revealed by high-resolution analysis of human segmental trisomies. *Proc. Natl. Acad. Sci. U S A* 106, 12031–12036. doi: 10.1073/pnas.0813248106
- Kremer, D., Aktas, O., Hartung, H. P., and Küry, P. (2011). The complex world of oligodendroglial differentiation inhibitors. *Ann. Neurol.* 69, 602–618. doi: 10.1002/ana.22415
- Kremer, D., Göttle, P., Hartung, H.-P., and Küry, P. (2016). Pushing forward: remyelination as the new frontier in CNS diseases. *Trends Neurosci.* 39, 246–263. doi: 10.1016/j.tins.2016.02.004
- Kremer, D., Heinen, A., Jadasz, J., Göttle, P., Zimmermann, K., Zickler, P., et al. (2009). p57kip2 is dynamically regulated in experimental autoimmune encephalomyelitis and interferes with oligodendroglial maturation. *Proc. Natl. Acad. Sci. U S A* 106, 9087–9092. doi: 10.1073/pnas.0900204106
- Lanfranchi, S., Jerman, O., Dal Pont, E., Alberti, A., and Vianello, R. (2010). Executive function in adolescents with Down syndrome. *J. Intellect. Disabil. Res.* 54, 308–319. doi: 10.1111/j.1365-2788.2010.01262.x
- Li, S. S., Qu, Z. D., Haas, M., Ngo, L., Heo, Y. J., Kang, H. J., et al. (2016). The HSA21 gene EURL/C21ORF91 controls neurogenesis within the cerebral

- cortex and is implicated in the pathogenesis of Down syndrome. *Sci. Rep.* 6:29514. doi: 10.1038/srep29514
- Li, W. Q., Luo, L. D., Hu, Z. W., Lyu, T. J., Cen, C., and Wang, Y. (2019). PLD1 promotes dendritic spine morphogenesis via activating PKD1. *Mol. Cell. Neurosci.* 99:103394. doi: 10.1016/j.mcn.2019.103394
- Maggipinto, M., Rabiner, C., Kidd, G. J., Hawkins, A. J., Smith, R., and Barbarese, E. (2004). Increased expression of the MBP mRNA binding protein HnRNP A2 during oligodendrocyte differentiation. *J. Neurosci. Res.* 75, 614–623. doi: 10.1002/jnr.20014
- McCarthy, K. D., and de Vellis, J. (1980). Preparation of separate astroglial and oligodendroglial cell cultures from rat cerebral tissue. *J. Cell Biol.* 85, 890–902. doi: 10.1083/jcb.85.3.890
- Mito, T., and Becker, L. E. (1993). Developmental changes of S-100 protein and glial fibrillary acidic protein in the brain in Down syndrome. *Exp. Neurol.* 120, 170–176. doi: 10.1006/exnr.1993.1052
- Moyon, S., Dubessy, A. L., Aigrot, M. S., Trotter, M., Huang, J. K., Dauphinot, L., et al. (2015). Demyelination causes adult CNS progenitors to revert to an immature state and express immune cues that support their migration. *J. Neurosci.* 35, 4–20. doi: 10.1523/JNEUROSCI.0849-14.2015
- Nave, K. A. (1994). Neurological mouse mutants and the genes of myelin. *J. Neurosci. Res.* 38, 607–612. doi: 10.1002/jnr.490380602
- Nishiyama, A., Komitova, M., Suzuki, R., and Zhu, X. (2009). Polydendrocytes (NG2 cells): multifunctional cells with lineage plasticity. *Nat. Rev. Neurosci.* 10, 9–22. doi: 10.1038/nrn2495
- Olmos-Serrano, J. L., Kang, H. J., Tyler, W. A., Silbereis, J. C., Cheng, F., Zhu, Y., et al. (2016). Down syndrome developmental brain transcriptome reveals defective oligodendrocyte differentiation and myelination. *Neuron* 89, 1208–1222. doi: 10.1016/j.neuron.2016.01.042
- Pennington, B. F., Moon, J., Edgin, J., Stedron, J., and Nadel, L. (2003). The neuropsychology of Down syndrome: evidence for hippocampal dysfunction. *Child Dev.* 74, 75–93. doi: 10.1111/1467-8624.00522
- Powell, D., Caban-Holt, A., Jicha, G., Robertson, W., Davis, R., Gold, B. T., et al. (2014). Frontal white matter integrity in adults with Down syndrome with and without dementia. *Neurobiol. Aging* 35, 1562–1569. doi: 10.1016/j.neurobiolaging.2014.01.137
- Rao, M. S., and Mayer-Proschel, M. (1997). Glial-restricted precursors are derived from multipotent neuroepithelial stem cells. *Dev. Biol.* 188, 48–63. doi: 10.1006/dbio.1997.8597
- Rehberg, S., Lischka, P., Glaser, G., Stamminger, T., Wegner, M., and Rosorius, O. (2002). Sox10 is an active nucleocytoplasmic shuttle protein and shuttling is crucial for Sox10-mediated transactivation. *Mol. Cell. Biol.* 22, 5826–5834. doi: 10.1128/mcb.22.16.5826-5834.2002
- Reiche, L., Küry, P., and Göttle, P. (2019). Aberrant oligodendrogenesis in down syndrome: shift in gliogenesis? *Cells* 8:1591. doi: 10.3390/cells8121591
- Rost, I., Fiegler, H., Fauth, C., Carr, P., Bettecken, T., Kraus, J., et al. (2004). Tetrasomy 21pter-->q21.2 in a male infant without typical Down's syndrome dysmorphic features but moderate mental retardation. *J. Med. Genet.* 41:e26. doi: 10.1136/jmg.2003.011833
- Rowe, J., Lavender, A., and Turk, V. (2006). Cognitive executive function in Down's syndrome. *Br. J. Clin. Psychol.* 45, 5–17. doi: 10.1348/014466505X29594
- Schindelin, J., Arganda-Carreras, I., Frise, E., Kaynig, V., Longair, M., Pietzsch, T., et al. (2012). Fiji: an open-source platform for biological-image analysis. *Nat. Methods* 9, 676–682. doi: 10.1038/nmeth.2019
- Setoguchi, T., and Kondo, T. (2004). Nuclear export of OLIG2 in neural stem cells is essential for ciliary neurotrophic factor-induced astrocyte differentiation. *J. Cell Biol.* 166, 963–968. doi: 10.1083/jcb.200404104
- Simons, M., and Nave, K. A. (2015). Oligodendrocytes: myelination and axonal support. *Cold Spring Harb. Perspect. Biol.* 8:a020479. doi: 10.1101/cshperspect.a020479
- Slavotinek, A. M., Chen, X. N., Jackson, A., Gaunt, L., Campbell, A., Clayton-Smith, J., et al. (2000). Partial tetrasomy 21 in a male infant. *J. Med. Genet.* 37:E30. doi: 10.1136/jmg.37.10.e30
- Snaidero, N., and Simons, M. (2014). Myelination at a glance. *J. Cell Sci.* 127, 2999–3004. doi: 10.1242/jcs.151043
- Stagni, F., Giacomini, A., Emili, M., Guidi, S., and Bartesaghi, R. (2017). Neurogenesis impairment: an early developmental defect in Down syndrome. *Free Radic. Biol. Med.* 114, 15–32. doi: 10.1016/j.freeradbiomed.2017.07.026
- Sunkin, S. M., Ng, L., Lau, C., Dolbeare, T., Gilbert, T. L., Thompson, C. L., et al. (2013). Allen brain atlas: an integrated spatio-temporal portal for exploring the central nervous system. *Nucleic Acids Res.* 41, D996–D1008. doi: 10.1093/nar/gks1042
- Tanner, D. C., Cherry, J. D., and Mayer-Pröschel, M. (2011). Oligodendrocyte progenitors reversibly exit the cell cycle and give rise to astrocytes in response to interferon- $\gamma$ . *J. Neurosci.* 31, 6235–6246. doi: 10.1523/JNEUROSCI.5905-10.2011
- Thomas, P. D., Campbell, M. J., Kejariwal, A., Mi, H., Karlak, B., Daverman, R., et al. (2003). PANTHER: a library of protein families and subfamilies indexed by function. *Genome Res.* 13, 2129–2141. doi: 10.1101/gr.772403
- Thomas, P. D., Kejariwal, A., Guo, N., Mi, H., Campbell, M. J., Muruganujan, A., et al. (2006). Applications for protein sequence-function evolution data: mRNA/protein expression analysis and coding SNP scoring tools. *Nucleic Acids Res.* 34, W645–W650. doi: 10.1093/nar/gkl229
- Waxman, S. G. (1992). Demyelination in spinal cord injury and multiple sclerosis: what can we do to enhance functional recovery? *J. Neurotrauma* 9, S105–S117.
- Wheeler, N. A., Lister, J. A., and Fuss, B. (2015). The autotaxin-lysophosphatidic acid axis modulates histone acetylation and gene expression during oligodendrocyte differentiation. *J. Neurosci.* 35, 11399–11414. doi: 10.1523/JNEUROSCI.0345-15.2015
- White, R., Gonsior, C., Bauer, N. M., Krämer-Albers, E.-M., Luhmann, H. J., and Trotter, J. (2012). Heterogeneous nuclear ribonucleoprotein (hnRNP) F is a novel component of oligodendroglial RNA transport granules contributing to regulation of myelin basic protein (MBP) synthesis. *J. Biol. Chem.* 287, 1742–1754. doi: 10.1074/jbc.M111.235010
- Wilkins, A., Majed, H., Layfield, R., Compston, A., and Chandran, S. (2003). Oligodendrocytes promote neuronal survival and axonal length by distinct intracellular mechanisms: a novel role for oligodendrocyte-derived glial cell line-derived neurotrophic factor. *J. Neurosci.* 23, 4967–4974. doi: 10.1523/JNEUROSCI.23-12-04967.2003
- Wu, Y., Liu, Y., Levine, E. M., and Rao, M. S. (2003). Hes1 but not Hes5 regulates an astrocyte versus oligodendrocyte fate choice in glial restricted precursors. *Dev. Dyn.* 226, 675–689. doi: 10.1002/dvdy.10278
- Xiao, L., Ohayon, D., McKenzie, I. A., Sinclair-Wilson, A., Wright, J. L., Fudge, A. D., et al. (2016). Rapid production of new oligodendrocytes is required in the earliest stages of motor-skill learning. *Nat. Neurosci.* 19, 1210–1217. doi: 10.1038/nn.4351
- Zdaniuk, G., Wierzb-Bobrowicz, T., Szpak, G. M., and Stepień, T. (2011). Astroglia disturbances during development of the central nervous system in fetuses with Down's syndrome. *Folia Neuropathol.* 49, 109–114.

**Conflict of Interest:** The authors declare that the research was conducted in the absence of any commercial or financial relationships that could be construed as a potential conflict of interest.

Copyright © 2021 Reiche, Göttle, Lane, Duek, Park, Azim, Schütte, Manousi, Schira-Heinen and Küery. This is an open-access article distributed under the terms of the Creative Commons Attribution License (CC BY). The use, distribution or reproduction in other forums is permitted, provided the original author(s) and the copyright owner(s) are credited and that the original publication in this journal is cited, in accordance with accepted academic practice. No use, distribution or reproduction is permitted which does not comply with these terms.





# Automated *in vivo* Tracking of Cortical Oligodendrocytes

Yu Kang T. Xu<sup>1,2</sup>, Cody L. Call<sup>1</sup>, Jeremias Sulam<sup>2,3</sup> and Dwight E. Bergles<sup>1,2\*</sup>

<sup>1</sup> The Solomon H. Snyder Department of Neuroscience, Johns Hopkins University, Baltimore, MD, United States, <sup>2</sup> Kavli Neuroscience Discovery Institute, Whiting School of Engineering, Johns Hopkins University, Baltimore, MD, United States, <sup>3</sup> Department of Biomedical Engineering, Johns Hopkins University, Baltimore, MD, United States

## OPEN ACCESS

### Edited by:

Francesca Boscia,  
University of Naples Federico II, Italy

### Reviewed by:

David Lyons,  
University of Edinburgh,  
United Kingdom  
Frank Kirchhoff,  
Saarland University, Germany

### \*Correspondence:

Dwight E. Bergles  
dbergles@jhmi.edu

### Specialty section:

This article was submitted to  
Non-Neuronal Cells,  
a section of the journal  
Frontiers in Cellular Neuroscience

**Received:** 13 February 2021

**Accepted:** 19 March 2021

**Published:** 12 April 2021

### Citation:

Xu YKT, Call CL, Sulam J and  
Bergles DE (2021) Automated *in vivo*  
Tracking of Cortical Oligodendrocytes.  
*Front. Cell. Neurosci.* 15:667595.  
doi: 10.3389/fncel.2021.667595

Oligodendrocytes exert a profound influence on neural circuits by accelerating action potential conduction, altering excitability, and providing metabolic support. As oligodendrogenesis continues in the adult brain and is essential for myelin repair, uncovering the factors that control their dynamics is necessary to understand the consequences of adaptive myelination and develop new strategies to enhance remyelination in diseases such as multiple sclerosis. Unfortunately, few methods exist for analysis of oligodendrocyte dynamics, and even fewer are suitable for *in vivo* investigation. Here, we describe the development of a fully automated cell tracking pipeline using convolutional neural networks (*Oligo-Track*) that provides rapid volumetric segmentation and tracking of thousands of cells over weeks *in vivo*. This system reliably replicated human analysis, outperformed traditional analytic approaches, and extracted injury and repair dynamics at multiple cortical depths, establishing that oligodendrogenesis after cuprizone-mediated demyelination is suppressed in deeper cortical layers. Volumetric data provided by this analysis revealed that oligodendrocyte soma size progressively decreases after their generation, and declines further prior to death, providing a means to predict cell age and eventual cell death from individual time points. This new CNN-based analysis pipeline offers a rapid, robust method to quantitatively analyze oligodendrocyte dynamics *in vivo*, which will aid in understanding how changes in these myelinating cells influence circuit function and recovery from injury and disease.

**Keywords:** oligodendrocyte, *in vivo* cell tracking, automation, deep learning, two photon imaging, injury/repair, cuprizone

## INTRODUCTION

Advances in genetically encoded fluorescent indicators, CRISPR-mediated gene editing and multiphoton microscopy provide unprecedented opportunities for studying cellular dynamics at single-cell resolution in the brains of living animals. While these approaches hold the potential for profound discoveries about brain function, they also come with a host of quantitative challenges. In particular, living brain tissue is unstable; tissue warping disrupts image quality and uneven refractive indices increase noise and produce anisotropic distortions during longitudinal image acquisition (Lecoq et al., 2019). Moreover, large multi-dimensional datasets are cumbersome to quantify, and often require specialized software for 4D visualization and manual curation (Pidhorskyi et al., 2018). As imaging tools become more advanced and enable researchers

to delve deeper into the brain *in vivo* (Horton et al., 2013), the challenges associated with quantification of enormous datasets become more acute. Further advances depend critically on the availability of robust analysis platforms to rapidly extract multi-dimensional observations about cellular dynamics.

Developing rigorous analysis tools for *in vivo* investigation of oligodendrocytes is particularly important. Oligodendrocytes enhance the speed of action potential conduction by ensheathing neuronal axons with concentric wraps of membrane, support neuronal metabolism and control neuronal excitability (Simons and Nave, 2016; Larson et al., 2018). While the population of neurons in the brain remains relatively stable throughout life (Bhardwaj et al., 2006; Ming and Song, 2011), new oligodendrocytes are generated in the adult CNS, allowing for dynamic alteration of myelin patterns in both healthy and pathological conditions (El Waly et al., 2014). This dynamism highlights the need for automated, longitudinal tracking tools to quantify the location, timing and extent of myelin plasticity within defined circuits in response to particular behavioral paradigms, as well as the regeneration of oligodendrocytes after demyelination (Bergles and Richardson, 2015). In this study, we sought to develop fully automated methodologies to overcome the analytic challenges associated with longitudinal tracking of oligodendrocytes *in vivo*.

Currently, most available cell tracking algorithms are designed for *in vitro* analysis and are not readily adaptable to *in vivo* conditions (van Valen et al., 2016; Zhong et al., 2016; Nketia et al., 2017; Lugagne et al., 2020; Wang et al., 2020). The few *in vivo* tracking algorithms that exist are modality specific and cannot be readily adapted to our fluorescent longitudinal datasets (Acton et al., 2002; Nguyen et al., 2011; Wang et al., 2015). The closest *in vivo* tools that can be applied to oligodendrocyte datasets are those developed for analyzing calcium imaging (Pachitariu et al., 2017; Giovannucci et al., 2019). However, calcium imaging tools normally work best with high-frame rate videos taken over seconds, rather than image volumes collected on a weekly basis. Traditional tracking approaches are also often unsuited for the analysis of longitudinal *in vivo* imaging datasets. Many techniques, such as the use of template matching (Brunelli, 2009), optical flow estimation (Horn and Schunck, 1981), or Kalman filters (Kalman, 1960), rely on intensity coherence patterns and unobstructed continuous object motion, which are disrupted by local tissue movements between imaging sessions and challenged by the low sampling frequency typical for imaging myelin dynamics. To provide an improved means of longitudinal volumetric tracking *in vivo*, we opted to use convolutional neural networks (CNN), which are known to find accurate efficient solutions to high-dimensional problems, and have recently demonstrated improvements over traditional tracking methods (Hur and Roth, 2020). Convolutional kernels allow CNNs to adaptively assess local features and global spatial relationships to make tracking decisions that are more perceptual, or human-like, enabling CNNs to find solutions beyond the traditional constraints of intensity coherence and continuous object motion. Moreover, additional techniques such as transfer learning can help trained CNN models generalize to entirely new imaging challenges with minimal

new training data (Zhuang et al., 2020), extending their use to other contexts.

Here, we describe the development of *Oligo-Track*, a fast and reliable cell tracker for *in vivo* semantic segmentation of oligodendrocyte dynamics across cortical layers in longitudinal imaging experiments. We validated our algorithm using the cuprizone model of demyelination *in vivo* and show that *Oligo-Track* outperforms traditional analytic approaches in extracting dynamics of oligodendrogenesis at greater depths than previously available with manual annotation. Moreover, this approach generated volumetric segmentations of tracked cells that were inaccessible to human analysis, due to the considerable time investment required for manual volumetric tracing. This volumetric data revealed that oligodendrocyte soma size varies predictably with age and proximity to death, allowing additional information about the timing of oligodendrogenesis and cell death to be extracted from fixed timepoint imaging experiments.

## MATERIALS AND METHODS

### Animal Care and Use

All animal experiments were performed in strict accordance with protocols approved by the Animal Care and Use Committee at Johns Hopkins University. Female and male adult mice were used for experiments and randomly assigned to experimental groups. All mice were healthy and did not display any overt behavioral phenotypes, and no animals were excluded from the analysis. Generation and genotyping of BAC transgenic lines from *Mobp-EGFP* (GENSAT) have been previously described (Hughes et al., 2018). Mice were maintained on a 12 h light/dark cycle, housed in groups no larger than 5, and food and water were provided *ad libitum* (except during cuprizone-administration, see below).

### Cranial Windows

Cranial windows were prepared as previously described (Holtmaat et al., 2012; Hughes et al., 2018; Orthmann-Murphy et al., 2020). Mice aged 7–10 weeks were deeply anesthetized with isoflurane (5% with 1 L/min O<sub>2</sub> induction; 1.5–2% with 0.5 L/min maintenance), the head shaved, and the scalp removed to expose the skull. The skull was cleaned and dried and a position over somatosensory cortex (−1.5 mm posterior and 3.5 mm lateral from bregma) was marked for drilling. A custom aluminum headplate with a central hole was cemented onto the skull (C and B Metabond) and fixed in place with custom clamping headbars. A 2 mm × 2 mm square or 3 mm × 3 mm circle of skull was removed using a high-speed dental drill. A coverslip (VWR, No. 1) the size of the craniotomy was put in its place and sealed with cyanoacrylate glue (Vetbond and Crazy glue).

### *In vivo* Two Photon Microscopy

*In vivo* imaging was performed as previously described (Orthmann-Murphy et al., 2020). After 2–3 weeks of recovery from cranial window surgery, baseline images of the cortex were acquired with two photon microscopy on a Zeiss LSM 710 microscope (average power at sample <30 mW with 1.58 μs pixel dwell time). Image stacks were 425 μm × 425 μm × 550 μm or

850  $\mu\text{m} \times 850 \mu\text{m} \times 550 \mu\text{m}$  (1024  $\times$  1024 pixels; corresponding to layers I–IV), relative to the pia. Each stack was recorded at 8-bit data depth with four frame averaging. Mice were subsequently imaged weekly for up to 12 weeks.

## Cuprizone Treatment

Directly following baseline two photon image acquisition, mice were switched from regular diet to a diet consisting of milled, irradiated 18% protein chow (Teklad Global) supplemented with 0.2% w/w bis(cyclohexanone) oxalldihydrazone (“cuprizone,” Sigma). Control mice received only the milled chow. After 3 weeks, mice returned to regular pellet diet for the duration of the recovery period (Orthmann-Murphy et al., 2020).

## Analytic Pipeline Overview

Timeseries acquired from our two-photon imaging setup were first registered using ImageJ’s correct 3D drift plugin (Schindelin et al., 2012; Parslow et al., 2014), which accounted for major alignment shifts from week to week. Registered timeseries were then analyzed crop-by-crop, with 50% overlap between adjacent crops, using our segmentation CNN (Seg-CNN) which identified cell somata on a voxel-wise basis. These cell somata were then extracted as individual seeds for our tracking CNN (Track-CNN) that identified the location of each seeded cell soma on a subsequent time point. In parallel, we also developed a cell tracking method based on traditional imaging informatics approaches that used the structural similarity index (SSIM) (Wang et al., 2004) and local tissue movement calculations to track cells. This heuristic model was used as a baseline to assess the improvements of our Track-CNN approach. Cells tracked by either Track-CNN or our heuristic method were also curated by human researchers using syGlass virtual reality software (Pidhorskyi et al., 2018) to assess the accuracy of tracking. Some of these curated traces were also returned to the training pipeline to improve our deep learning approaches in a positive-feedback loop (Figure 2A).

## Training Data Generation

All training data was curated by a human expert using syGlass software to provide point coordinates. To obtain volumetric segmentations, we trained an *ilastik* random forest regressor (Berg et al., 2019) to procure an over-sensitive voxel-wise segmentation model. Then, we excluded every *ilastik* identified object that did not overlap with a ground truth point coordinate to eliminate false positives in our over-sensitive *ilastik* model. Datasets were pooled from 12 animals and multiple treatment conditions. Image scales were standardized to 0.83  $\mu\text{m}/\text{pixel}$  in XY and 3  $\mu\text{m}/\text{pixel}$  in Z. Data was cropped to the appropriate input size for each respective neural network: Seg-CNN 256  $\times$  256  $\times$  64 voxels, and Track-CNN 128  $\times$  128  $\times$  32 voxels. Overall, Seg-CNN was trained with 6,828 training volumes and 759 validation volumes, each containing up to two dozen cells depending on the location of the crop within the larger volume. Track-CNN was trained with 38,696 volumes and a validation set containing 4,300 volumes. Each volume for Track-CNN was associated with one tracked cell across

two timeframes, as indicated by a pair of ground truth point coordinates in the manually curated dataset.

## Segmentation CNN Training and Inference

Segmentation CNN employed a UNet architecture (Ronneberger et al., 2015) with 3D convolutional kernels built in PyTorch 1.6 (Paszke et al., 2017). The neural network took as input a 256  $\times$  256  $\times$  64 voxel volume containing fluorescently labeled oligodendrocytes in a single image channel (Figure 2B). The downsampling branch of the CNN contained five convolutional blocks with 5  $\times$  5  $\times$  5 filters, batch normalization, and max pooling to downsample the data and extract local features. The upsampling branch employed the same blocks in reverse. Max pooling operations were replaced by trilinear upsampling and 1  $\times$  1  $\times$  1 convolutions to resize the image back to the same input size while extracting global spatial features (Supplementary Figure 1). A final 1  $\times$  1  $\times$  1 convolution reduced the output to a two-channel volume which was softmaxed with a threshold of 0.5 to two classes corresponding to background and cell soma. Training was performed using a batch size of 2 for 30 epochs on an RTX 2080 Ti GPU and reached optimal performance after  $\sim 3$  days. Loss was calculated as cross entropy and optimized using an Adam optimizer with weight decay (Loshchilov and Hutter, 2019) set at a learning rate of  $10^{-5}$ . During inference on unseen data, entire timeseries were fed to the neural network one timepoint at a time. Our algorithm then acquired 256  $\times$  256  $\times$  64 voxel crops from these volumes with 50% overlap to ensure all regions were assessed. Each crop was fed to Seg-CNN individually. The output segmentations of individual crops, with 50% overlap, were summed together and binarized before being stitched back into a full volume. The final analyzed timeseries is saved and returned to the user (Figure 2B).

## Track-CNN Training and Inference

Track-CNN employed a similar architecture to Seg-CNN except for a filter size of 7  $\times$  7  $\times$  7 for each convolution and a three channel 128  $\times$  128  $\times$  32 voxel input for our “seed-based” training approach. Seed-based training was employed to draw the attention of our CNN to individual cells in a volume by marking a cell of interest with a binary mask, or “seed” (Figure 3A). The input is thus a three-channel volume where channel 1 contains a raw fluorescence volume cropped from timepoint  $t$  and centered around a cell soma of interest. Channel 2 contains the binary mask/seed to indicate the cell of interest on timepoint  $t$ . All adjacent cells excluding the seed are set to a lower value. Finally, channel 3 contains a raw fluorescence volume cropped from timepoint  $t + 1$  but centered around the same position as in channel 1 (Figure 3A). In summary, this input provides the raw fluorescence from two consecutive timepoints and also indicates which cell we wish to track from timepoint  $t$  to timepoint  $t + 1$  using the binary mask in channel 2. Thus, the ground truth for optimization is a binary volumetric mask indicating the location of the cell of interest on timepoint  $t + 1$  (Figure 3A). Training was performed using a batch size of 4 for 18 epochs on an RTX 2080 Ti GPU and reached optimal performance after  $\sim 5$  days.

Loss was calculated as cross entropy and optimized using Adam optimizer with weight decay (Loshchilov and Hutter, 2019) set at a learning rate of  $10^{-5}$  that was dropped to  $10^{-6}$  at 13 epochs. During inference, volumes were cropped around each cell of interest in timepoint  $t$  along with seed masks and crops from timepoint  $t + 1$  to form a three-channel input for Track-CNN. This is repeated until all cells on timepoint  $t$  are assessed. Unassociated cells on  $t + 1$  are then added as newly formed oligodendrocytes to our list of candidate cells, and the analysis continues until all consecutive timepoints are tested (Figure 3A).

## Post-processing

To prevent misalignment of tracks, we included one major post-processing step in our analytic pipeline. We first noticed that, given a human tracked dataset, we could predict the location of a cell body on a subsequent timepoint within  $\sim 10$  pixels error by using the local directional vector of the tracks of five nearest neighbor cells from timepoint  $t$  to  $t + 1$  (Figures 3B,C). Thus, given that Track-CNN accurately tracks the majority of cells between consecutive timepoints, we can use the average local vector shift of the five nearest neighbors of any cell to correct for tracks that have severely gone off-target ( $> 12$  pixel difference from predicted directional vector endpoint). These gross errors can then be re-evaluated. If an unassociated cell exists at the location of the predicted vector endpoint on  $t + 1$ , then the wrongly associated track now points to this unassociated cell. Otherwise, the track is terminated. We also included minor post-processing steps comprising of: (1) a minimum size threshold of 100 voxels for objects to be considered a cell soma; (2) objects that only exist on a single frame (excluding the first and last frame) are dropped, as they were likely to be debris.

## Heuristic Baseline Method

Since no baseline methods exist for comparison, we developed an approach to assess the extent to which deep learning outperforms traditional imaging informatics methods. We developed a tracking program in MATLAB R2020a (Mathworks) where cells are cropped from timepoint  $t$  and assessed on a pair-wise basis to identify whether its' nearest neighbors on  $t + 1$  correspond to the same cell at timepoint  $t$ . To determine this association, we employed a few simple heuristics and rules: (1) successful tracking required a structural similarity index (SSIM) greater than 0.2 between cropped volumes from different timepoints. SSIM is an indicator of similarity that considers structure, intensity, and contrast-based differences between images. We applied the assumption that if a cell exists at  $t + 1$ , the overall local environment should look rather similar at timepoint  $t$ , thus a correct association would have a moderate to high SSIM. (2) Similar to the post-processing used for Track-CNN, we estimated the average vector of all nearest neighbors to model local tissue movement in a cropped field of view from  $t$  to  $t + 1$ . This allowed us to evaluate if the current track from  $t$  to  $t + 1$  flows in the same direction as the local shift of neighboring tracked cells. If the proposed track does not align with the local shift of neighboring tracked cells, then the track is terminated.

## SNR Calculation

Since there is no standard for defining signal-to-noise ratio (SNR) in fluorescence imaging (Zhu et al., 2012), we adapted a standard logarithmic signal-processing SNR equation for our usage:

$$SNR = 10 * \log \left( \frac{P_{signal}}{P_{noise}} \right)$$

Where we defined  $P_{signal}$  as the average signal (meaningful input) and  $P_{noise}$  as the standard deviation of the background noise. However, since we have no reference image to define what perfect signal is in any raw dataset, we defined our signal to be any pixels above a certain value  $j$  and noise to be any pixels below that value.

$$\widehat{SNR}_j = 10 * \log j \left( \frac{P_{signal \geq j}}{P_{noise < j}} \right)$$

Where,  $P_{signal}$  is defined as the mean of all values above  $j$ , and  $P_{noise}$  is defined as the standard deviation of all values below  $j$ . Since  $j$  would otherwise be arbitrarily determined, we chose to calculate  $j$  from the entire image volume using Otsu threshold for binarization (Otsu, 1979), providing us with a reference free metric of SNR.

## Statistical Analysis

All statistical analysis was performed using Python statsmodels and scipy libraries.  $N$  represents the number of animals used in each experiment, unless otherwise noted. Data are reported as mean  $\pm$  SEM or median  $\pm$  SEM as indicated, and  $p < 0.05$  was considered statistically significant. Level of significance is marked on figures as follows: \* denotes  $p < 0.05$ ; \*\* denotes  $p < 0.01$ ; \*\*\* denotes  $p < 0.001$ .

## Code Availability

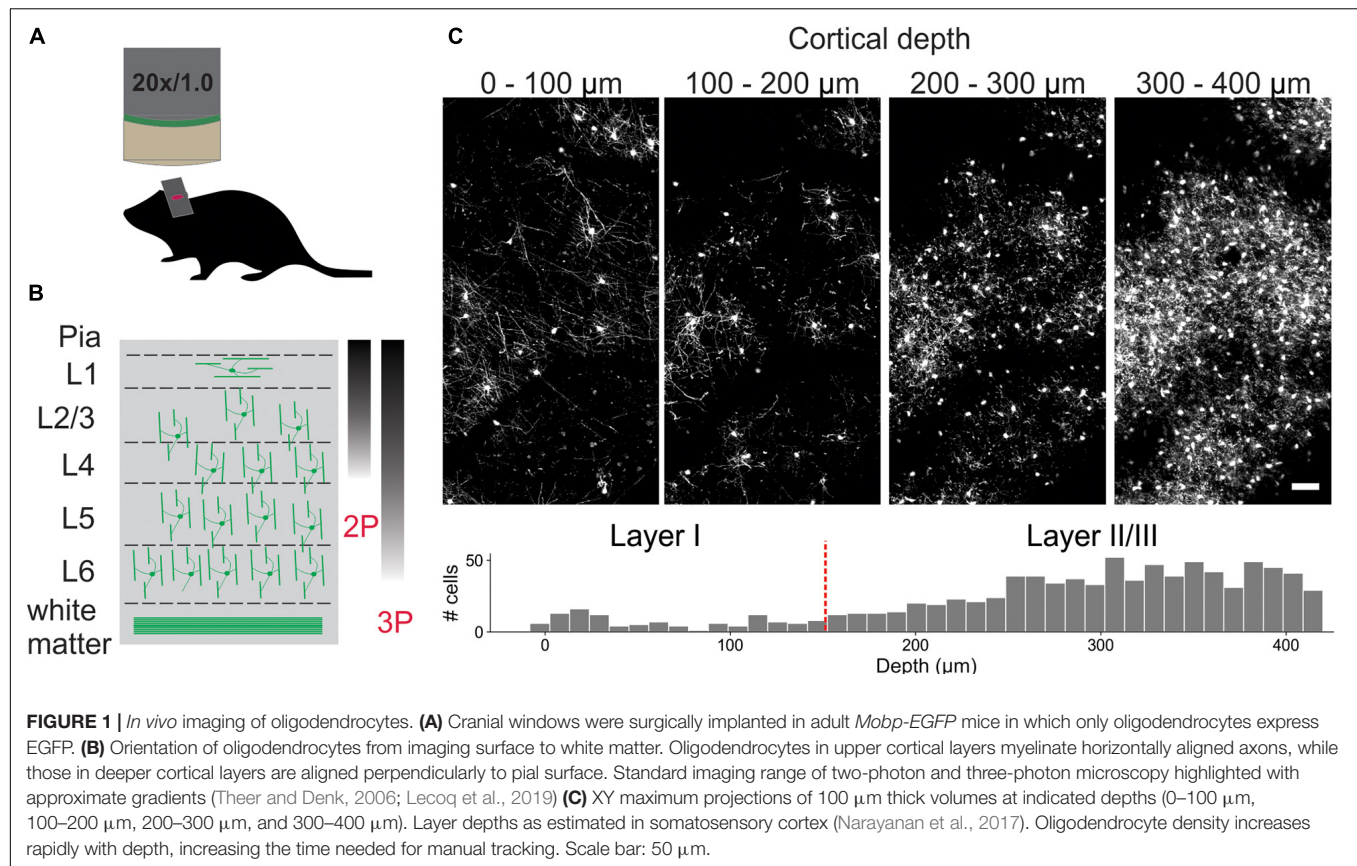
Packaged software code for *Oligo-Track* is readily available at [github.com/Bergles-lab/Xu\\_Bergles\\_2021\\_Oligo\\_Track](https://github.com/Bergles-lab/Xu_Bergles_2021_Oligo_Track) along with instructions for use. The algorithm is prepared to work independent of Linux and Windows operating systems, with minimum Python 3.6.

## RESULTS

### Quantifying Oligodendrocyte Dynamics *in vivo* Using CNN-Assisted Cell Tracking

To visualize individual oligodendrocytes in the cerebral cortex, cranial windows were surgically implanted in mice that express EGFP under control of the *Mobp* promoter/enhancer (Hughes et al., 2018; Orthmann-Murphy et al., 2020; Figure 1A). Using two photon microscopy, the somata and cytosolic processes of oligodendrocytes could be resolved up to a depth of  $\sim 400 \mu\text{m}$  from the pial surface (Figures 1B,C), providing the means to quantify changes in both the number and distribution of oligodendrocytes over weeks to months with repeated imaging. The dramatic increase in density of oligodendrocytes with depth (Figure 1C) presents challenges for unambiguous identification and increases the time necessary to mark and track cell





positions throughout a time series. To overcome this quantitative challenge, we trained two sequential CNNs employing a UNet architecture (**Supplementary Figure 1**), which we termed *Seg-CNN* and *Track-CNN*, to follow oligodendrocytes *in vivo* during repetitive bouts of imaging over many weeks (**Figure 2A**).

Images were first acquired over a  $850 \mu\text{m} \times 850 \mu\text{m} \times 550 \mu\text{m}$  volume and then registered across time using ImageJ's correct 3D drift plugin (Schindelin et al., 2012; Parslow et al., 2014) to adjust for small offsets. Seg-CNN was then used to perform semantic segmentation to identify the position of all oligodendrocyte cell bodies within the imaging volume at each timepoint in the timeseries. This process was completed sequentially on  $256 \times 256 \times 64$  voxel volumes that were adaptively cropped with 50% spatial overlap to reduce the amount of computer memory required to perform the computations (**Figure 2B**). The resulting binary segmentations were then re-stitched to create a stacked timeseries. Image stacks from sequential time points were then analyzed using Track-CNN, which employs a "seed-based" inference approach to determine whether any specific cell of interest exists in a subsequent timepoint. For all comparisons, we defined a tracked cell (or cell track), as a set of locations where a binary object was determined to be the same cell over subsequent timepoints by an algorithm or human researcher. The displacement vector for any cell thus starts at a soma on timepoint  $t$  and ends at the same tracked soma on  $t + n$ . Cell identification in Track-CNN is accomplished by providing a three-channel input to the CNN, which includes (1)

a crop of raw fluorescence from timepoint  $t$  centered around a cell of interest, (2) a binary seed-mask that emphasizes the current cell of interest, and (3) a crop of raw fluorescence from timepoint  $t + 1$  that is centered around the cell on  $t$ . This allows the CNN output to be a volumetric segmentation of the same cell on timepoint  $t + 1$ , given a masked cell of interest on timepoint  $t$  (**Figure 3A**). Additional post-processing was performed using local tissue movement vectors to detect gross errors in tracking between sequential timepoints (**Figures 3B,C**). This post-processing used the observation that the displacement vector for any cell can be predicted within 10-pixel accuracy using the average displacement vectors of the nearest five tracked cells (**Figure 3C**). Thus, any cells with displacement vectors that varied drastically from predicted vectors, calculated from nearest neighbor tracks, could be classified as incorrect associations. Overall, during training, Seg-CNN performance plateaued after  $\sim 30$  epochs, demonstrating accurate segmentation of cell somata relative to ground truth (Jaccard overlap index  $\sim 0.7$ ) and detection of cells across all volumes (95% sensitivity, 91% precision; **Supplementary Figure 2A**). Track-CNN performance plateaued after  $\sim 5$  epochs with highly accurate track associations (98% accuracy, 99% sensitivity, and 99% precision with no post-processing; **Supplementary Figure 2B**).

To determine if this CNN-based method outperforms a heuristic cell tracking method that employs similarity metrics and local tissue movement modeling, similar to the post-processing mentioned above, we tested both algorithms for their ability to

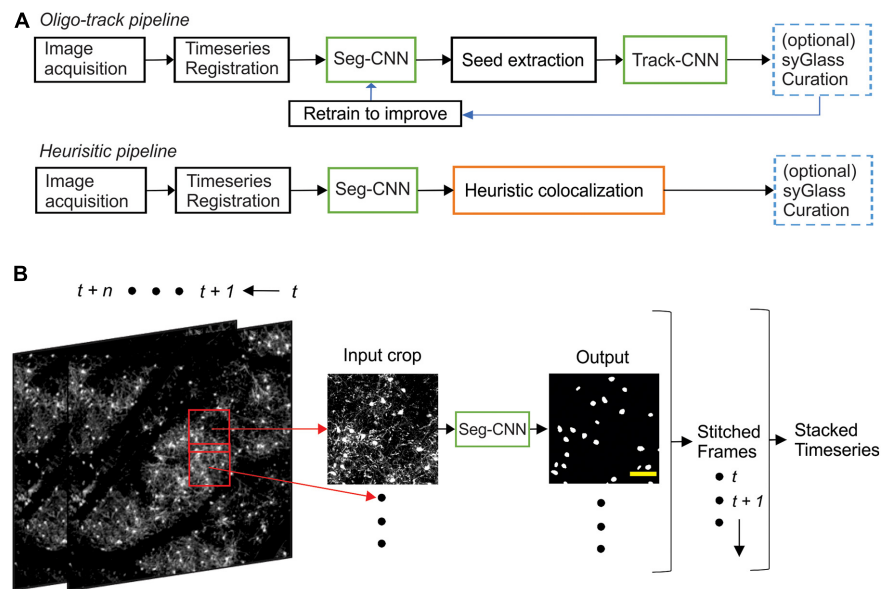


**FIGURE 2 |** Computational neural network analysis pipeline. **(A)** Overview of the sequential CNN multi-object tracking pipeline *Oligo-Track* (top). CNNs marked in green. Overview of heuristic baseline method (orange) for comparison to *Oligo-Track* (bottom). Compatibility with optional syGlass curation provides validation of tracking in both pipelines (blue). Curated tracks can also be reintroduced into training pipeline for refinement of CNNs. **(B)** Seg-CNN pre-processing extracts cropped regions from larger volumes with 50% overlap for computational efficiency at each timepoint  $t$  to  $t+n$ . Cropped regions are restitched to form timeseries. Scale bar: 50  $\mu\text{m}$ .

extract biological trends of spontaneous cell regeneration in the cuprizone model of demyelination (Chang et al., 2012; Baxi et al., 2017; Hughes et al., 2018; Orthmann-Murphy et al., 2020). In this model, mice are fed cuprizone for 3 weeks, resulting in loss of >95% of oligodendrocytes in the upper layers of cortex, which are progressively regenerated as the mice are returned to a normal diet (**Figure 4A**). Both CNN and heuristic models detected the general trend of cell loss during the first 3 weeks of cuprizone treatment and subsequent oligodendrogenesis during recovery, as assessed relative to human counting (**Figure 4B**). However, closer examination revealed that *Oligo-Track* provided a more accurate accounting of cell dynamics. In particular, the heuristic method greatly mis-identified existing cells as being newly formed (**Figure 4C**), suggesting disrupted tracking. This conclusion was further supported by the increased number of wrongly terminated cell tracks by the heuristic algorithm at each timepoint (**Figure 4D**), suggesting that the heuristic approach often failed to identify existing oligodendrocytes in subsequent time points. We also assessed the difference in track length (persistence of cells during the time series) between ground truth and machine outputs (**Figure 4E**). Positive values in this plot indicate under-tracking, where the machine failed to track a cell in subsequent timepoints, while negative values indicate over-tracking, where the machine tracked a cell onto additional timepoints despite cell elimination determined in the ground truth. This graph reveals that Track-CNN markedly reduced the total rate of over-tracked segments errors two-fold from the heuristic algorithm (**Figure 4F**). Moreover, the severe error rate (under or over-tracking for >1 timepoint) decreased almost five-fold. Together, these findings indicate that *Oligo-Track*

provides substantial benefits for following oligodendrocytes in longitudinal 3D imaging datasets.

## CNN-Based Analysis Retains Tracking Ability Despite Changes in Image Quality

Many factors can influence image quality *in vivo*, limiting the ability to accurately assess cell dynamics. Cranial windows can become obscured by local inflammation at later (or earlier) timepoints, resulting in incorrect track associations by both humans and machines. Image scale, cellular debris, and laser power also commonly vary between experiments and impair implementation of standardized analyses. To assess the impact of these factors on our tracking algorithm, we started by first varying image scale, using bilinear interpolation to up- or down-sample raw data before performing Track-CNN analysis. The algorithm struggled with up-sampling beyond two-fold (**Figures 5A,B**) showing that, optimally, input data should be scaled to the same 0.83  $\mu\text{m}/\text{pixel}$  XY and 3  $\mu\text{m}/\text{pixel}$  in Z resolution as the training dataset.

We then assessed the impact of cranial window/image quality on tracking, using a custom reference free signal-to-noise (SNR) metric. We chose two representative imaging volumes, one from a mouse with an optimal cranial window, and one from a mouse with a window that had not yet become optically clear. The obscured window reduced the detection of fluorescence at lower cortical depths. Our average SNR metric clearly delineated the depth-dependent decay of image quality, as the SNR in maximum projections of the obscured volume dropped rapidly after a depth of 200  $\mu\text{m}$  (**Figures 5C,D**). This image quality decay was verified

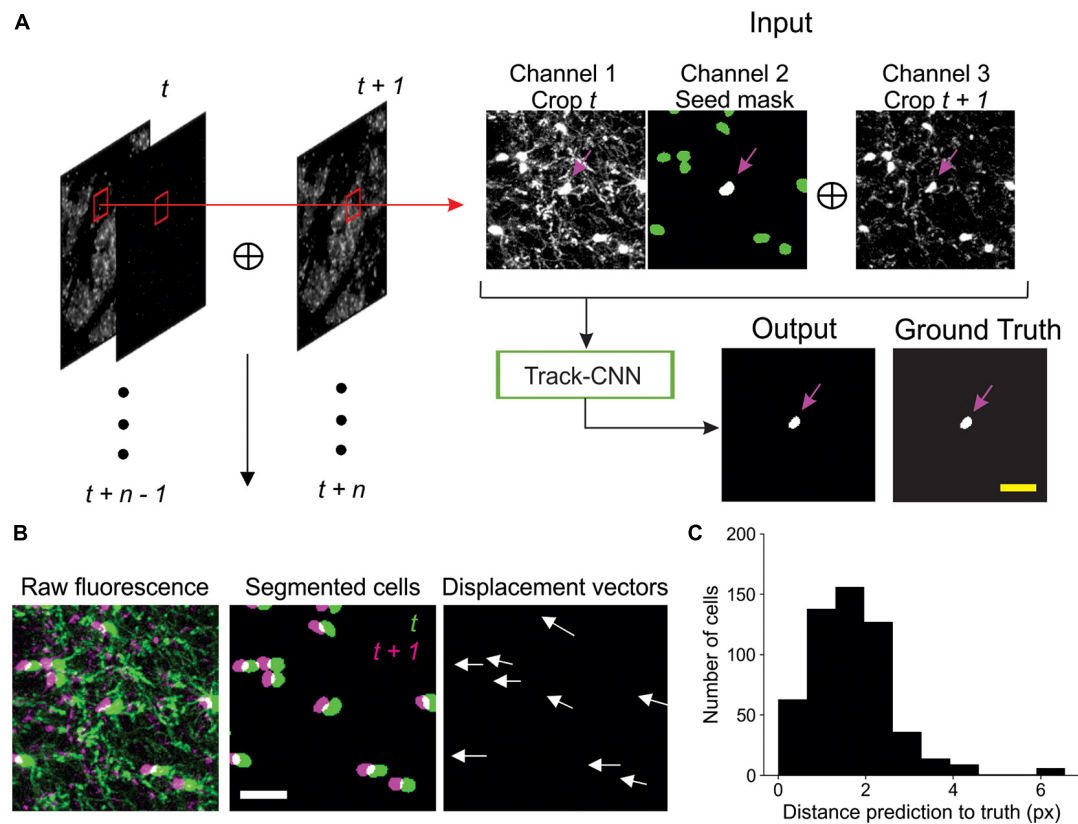


**FIGURE 3 |** Track-CNN processing steps. **(A)** Crops are taken from each pair of timepoints  $t$  and  $t+1$  centered around a cell denoted by magenta arrow on channel 1. Channel 1 contains raw fluorescence from timepoint  $t$ . Channel 2 contains seed mask of cell of interest (magenta arrow). Adjacent segmented cells are set to a lower value (green). Channel 3 contains raw fluorescence from timepoint  $t+1$ . Cropped images are concatenated together to form input to network. The network output is a semantic segmentation indicating the location of the seed masked cell on timepoint  $t+1$ . This procedure is repeated for all cells on all consecutive timepoints. Scale bar: 30  $\mu\text{m}$ . **(B)** Example showing local coherence in how tracked cells in a local region shift between timepoint  $t$  (green) and  $t+1$  (magenta), allowing for predictive post-processing using displacement vectors of each tracked cell from timepoint  $t$  to  $t+1$  (white arrows). Scale bar: 30  $\mu\text{m}$ . **(C)** Distribution of distances from predicted to actual location of cell on timepoint  $t+1$  given any cell on timepoint  $t$ . The prediction is generated by taking the average displacement vector of five nearest neighbor tracks. Differences between predicted and actual location were typically within six pixels.

visually, and while Seg-CNN still generalized and was able to identify oligodendrocyte somata in deeper layers despite the reduction in SNR, it was clear that many cells were obscured from view from both machine and human trackers (Figure 5C). By visual assessment, we set a threshold of SNR  $\sim 1.5$  dB as a limit under which image quality becomes a concern for *Oligo-Track* analysis. Fluctuations in SNR between timepoints can lead to disrupted tracking as cells are arbitrarily obscured and falsely labeled as terminated or newly formed. This threshold was incorporated into our pipeline and offers users a warning during implementation of the algorithm.

Segmentation CNN was also able to avoid some fluorescent, non-cellular components or weak cellular autofluorescence associated with cells other than oligodendrocytes, which can be difficult for non-deep learning approaches (Supplementary Figure 3A). However, the overwhelming density of brightly autofluorescent debris, such as lipofuscin found near the pial surface, were sometimes detected as false positives by Seg-CNN (Supplementary Figure 3B). We suggest that researchers using this software in areas with dense debris or lipofuscin perform manual error correction on the *Oligo-Track* outputs

or employ additional pre-processing techniques to eliminate debris fluorescence. For instance, the broad emission spectrum of lipofuscin enables digital subtraction of debris when using multi-channel imaging (Cornea, 2001), although these pre-processing techniques can still be limited when imaging in aged tissue (Moreno-García et al., 2018; Yakovleva et al., 2020). We also determined that while low imaging power impairs cell detection, *post hoc* adjustments of the intensity histogram toward higher values recovered some undetected cells (Supplementary Figure 3C). Finally, we found that Track-CNN was robust to some variations in noise and motion blur. This was assessed by applying sequentially larger standard deviations of noise (10, 40, and 50) and increasing the rotation range of random motion artifacts (4, 6, and 10 degrees) using the *Torchio* python library (Pérez-García et al., 2021; Supplementary Figures 3D,E). Together, this analysis shows that *Oligo-Track* can maintain performance despite changes in environmental variables that affect the distribution of the data. Moreover, we demonstrated that pre-processing of input data, such as intensity adjustments and the exclusion of regions with high debris or low SNR, can reduce instances of inaccurate tracking.

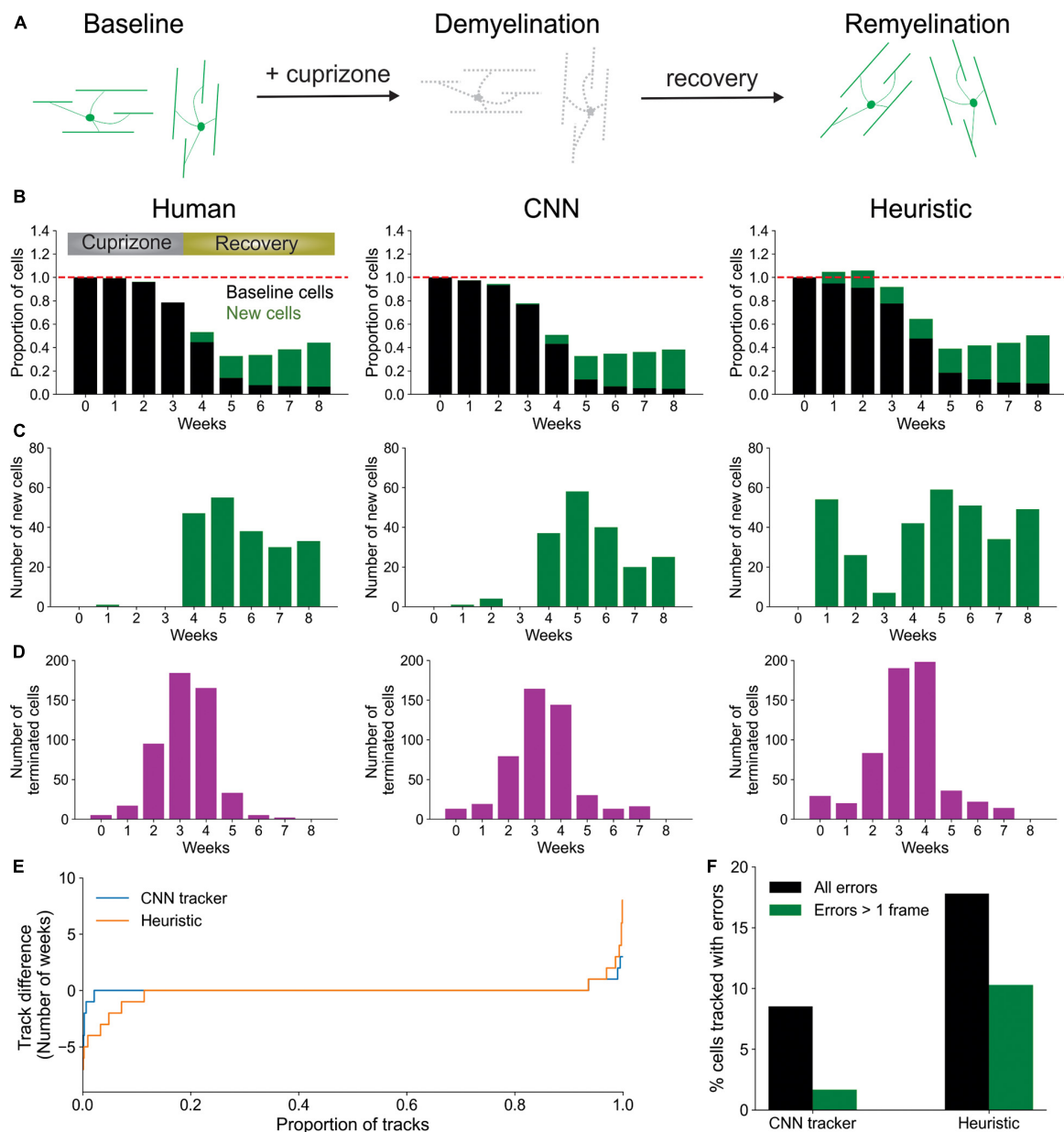


**FIGURE 4 |** CNN-based tracking outperforms heuristic tracking. **(A)** Diagram illustrating cuprizone induced oligodendrocyte loss and recovery during the imaging period. **(B)** Overall normalized trends for human, CNN and heuristic tracking methods on test timeseries withheld from training data. **(C)** Number of new cells detected per timepoint for each method. **(D)** Number of cells terminated per timepoint for each method. **(E)** Track difference (length of track in ground truth – length of track by machine count) comparing ground truth to CNN and heuristic methods, respectively. **(F)** Comparison of major errors, defined as under- or over-tracking for > 1 timepoint, and total errors by CNN and heuristic methods.

## CNN Detects Layer-Specific Suppression of Oligodendrogenesis at Extended Depth

To assess the capacity of our pipeline to extract biological trends, we used the fully automated system to analyze oligodendrocyte dynamics for up to 12 weeks in cuprizone treated and non-treated control mice. As anticipated, cuprizone treatment resulted in a predictable time course of oligodendrocyte degeneration and

subsequent regeneration after mice were no longer exposed to the drug, while control mice gradually added oligodendrocytes over several weeks (Orthmann-Murphy et al., 2020; **Figures 6A,B**; and **Supplementary Videos 1, 2**). Moreover, when cells were segregated into 100  $\mu\text{m}$  thick blocks from the pial surface, greater suppression of oligodendrocyte regeneration was observed in the deeper layers of the cortex (**Figure 6C**), as reported previously (Orthmann-Murphy et al., 2020). The



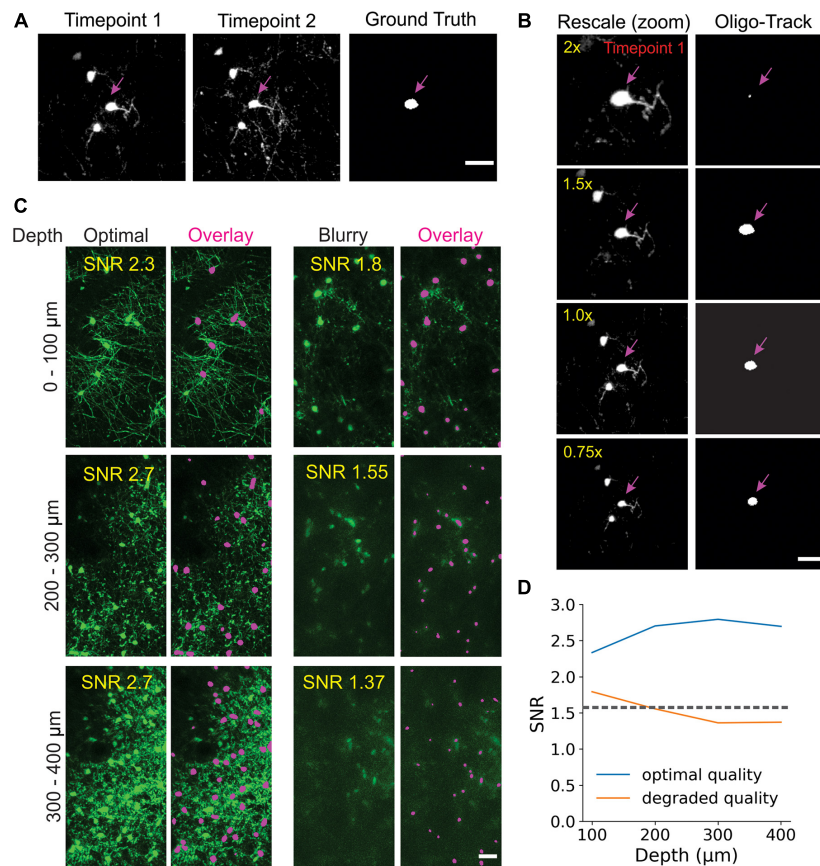


**FIGURE 5 |** Oligo-Track enables robust cell tracking under different experimental conditions. **(A)** Input image for Track-CNN used in **(B)** to assess impact of different rescaling on Track-CNN performance. Cell of interest denoted by magenta arrow. Scale bar: 30 μm. **(C)** Representative XY maximum projections at indicated SNR values and depths in a volume with optimal image quality (left), and a volume with a less transparent cranial window (right). Overlay of cells detected by *Oligo-Track* in Magenta. Scale bar: 30 μm. **(D)** Plotting average SNR across depth of optimal quality and degraded quality volumes. Dashed gray line indicates human perceptual limit for reliably tracing data. Also represents point at which algorithm will provide warning to user.

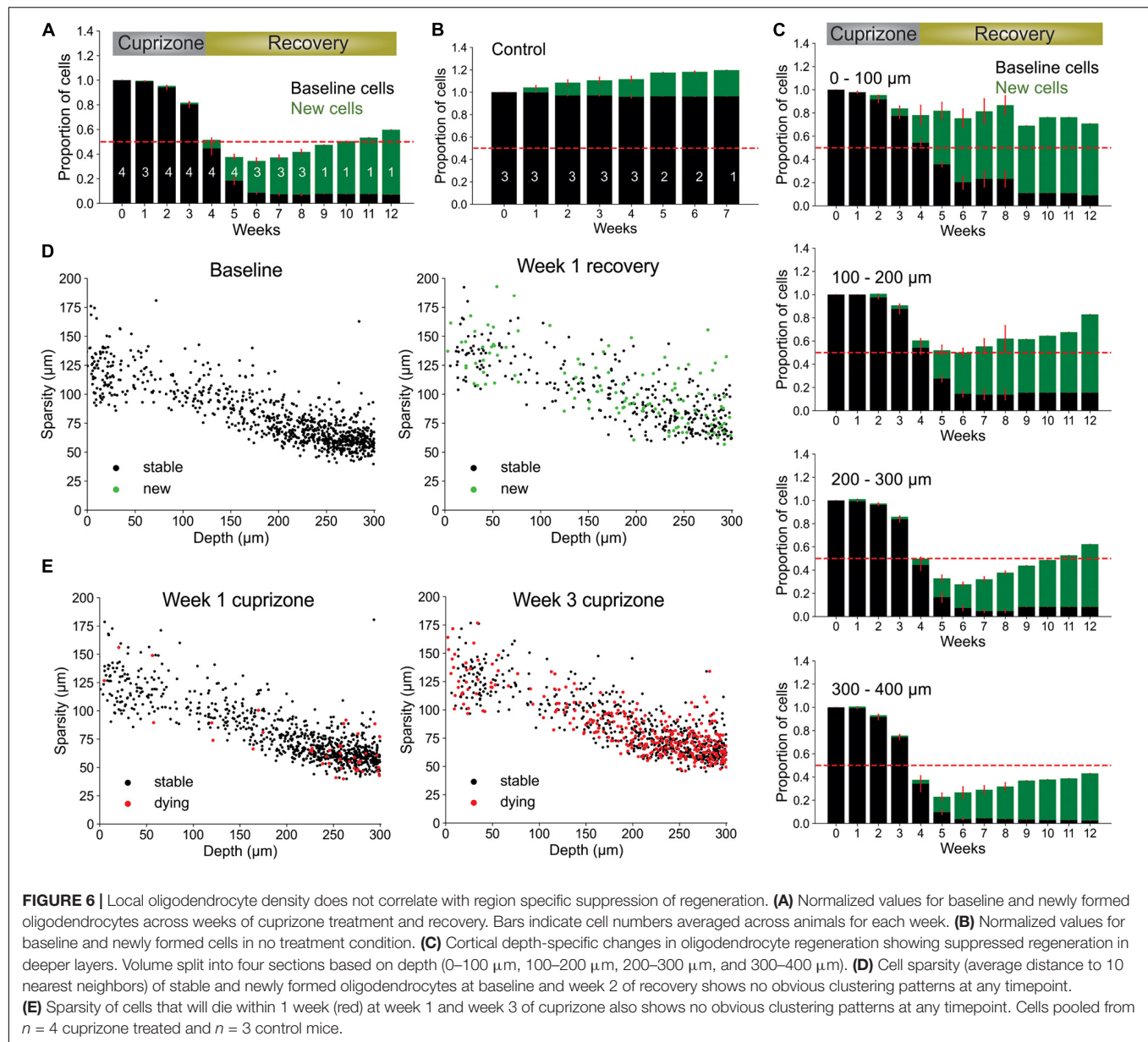
sensitive detection of *Oligo-Track* allowed rapid extension of the analysis by another 100 μm (300–400 μm block), revealing that regeneration was even less efficient than in the area above, providing further evidence of the depth dependent decline in oligodendrocyte regeneration in the somatosensory cortex.

It is possible that the higher demand for oligodendrocyte regeneration in deeper cortical layers outstrips the regenerative capacity of OPCs (Hughes et al., 2013; Streichan et al., 2014). If the extent of oligodendrogenesis is limited by the availability of local cues or accumulation of myelin debris, then newly generated cells should preferentially appear in regions with lower initial oligodendrocyte density (and lower oligodendrocyte death) (Orthmann-Murphy et al., 2020). Our prior studies indicate that new oligodendrocytes do not regenerate in locations where previous cells had died, suggesting possible inhibition of proliferation by myelin debris after cell death (Lampron et al., 2015; Gruchot et al., 2019). As a measure of sparsity, we calculated the average distance from each cell to its ten nearest neighbors. We limited our analysis to the first 300 μm of the cortex to avoid errors in sparsity calculations due to the lack of tracked

nearest-neighbor cells past 400 μm depth. Given this measure, we found that there was no strong correlation between sparsity, cell death or regeneration (Figures 6D,E and Supplementary Video 3), suggesting that cell death and regeneration are not strongly influenced by local oligodendrocyte density at baseline. Rather, global gradients of inhibitory factors such as cytokines released by astrocytes, which become persistently reactive in deeper layers of the cortex after cuprizone mediated demyelination (Orthmann-Murphy et al., 2020), may inhibit oligodendrocyte precursor cell differentiation (Skripuletz et al., 2008; Zhang et al., 2010; Su et al., 2011; Chang et al., 2012; Kirby et al., 2019).

## Volumetric Segmentation Enables Identification of Newly Born Oligodendrocytes

Oligodendrocytes undergo dramatic morphological changes as they transition from progenitors to mature myelinating cells, accompanied by an elaboration of myelin forming processes and changes in soma size (Kuhn et al., 2019). To quantify the



time course of these somatic changes, we analyzed volumetric morphological data provided by *Oligo-Track*, from longitudinal imaging datasets where the birth date of newly formed oligodendrocytes was known. We limited our investigation to the first 300  $\mu\text{m}$  of the cortex, as photon scattering often reduced the brightness of cells in deeper cortical layers, resulting in inaccurate measurement of cell somata volume. Future measurements from deeper layers will require depth-dependent normalization to account for light-scattering. Analysis of the first 300  $\mu\text{m}$  of the cortex revealed that oligodendrocyte soma size was highly correlated with cell age. Most newly formed oligodendrocytes had larger cell bodies than stable cells at any timepoint across all depths (**Figure 7A** and **Supplementary Video 4**). Projecting this across cell age, the soma volume of newly formed oligodendrocytes decayed exponentially over subsequent weeks

from first appearance (**Figures 7B,C**;  $p < 0.001$  at 1 week,  $p = 0.027$  at 2 weeks; Kruskal–Wallis test with Dunn’s *post hoc* analysis). Moreover, the average volume of newly generated cells, post-cuprizone injury, was significantly higher compared to stable mature cells in control animals up to 3 weeks after oligodendrogenesis (**Figure 7D**;  $1.6 \pm 0.04$  fold change  $p < 0.001$  and  $D = 1.29$  at 1 week,  $1.4 \pm 0.04$  fold change  $p < 0.001$  and  $D = 0.85$  at 2 weeks,  $1.2 \pm 0.03$  fold change  $p < 0.001$  and  $D = 0.33$  at 3 weeks,  $1.0 \pm 0.03$  fold change  $p = 0.39$  and  $D = 0.07$  at 4 weeks; Kruskal–Wallis test with Dunn’s *post hoc* analysis and Cohen’s effect size calculation). To confirm that this size difference is not associated with cuprizone induced changes, we also compared the volume of spontaneously generated oligodendrocytes in control animals with their stable counterparts and found that newly formed cells also had significantly larger cell somata (**Figure 7D**;

$1.7 \pm 0.09$  fold change  $p < 0.001$  and  $D = 1.22$  at 1 week,  $1.4 \pm 0.07$  fold change  $p < 0.001$  and  $D = 1.1$  at 2 weeks,  $1.3 \pm 0.06$  fold change  $p < 0.001$  and  $D = 0.54$  at 3 weeks,  $1.0 \pm 0.05$  fold change  $p = 0.28$  and  $D = 0.09$  at 4 weeks; Kruskal–Wallis test with Dunn's *post hoc* analysis and Cohen's effect size calculation). Thus, the increased soma size of newly formed oligodendrocytes is an innate biological phenomenon, rather than a response to cuprizone exposure.

Given the substantially larger cell somata of newly formed oligodendrocytes, we assessed the predictive power of cell soma size as an indicator of cell age. To examine the probability that a cell soma of a certain volume is exactly a certain age or within a range of ages, we plotted the kernel density estimate (KDE) for each distribution of soma volumes at different timepoints (Figure 7E). The KDE offers a normalized estimate of the probability density function such that we can visualize the probability of multiple conditions simultaneously. For example, we observed that a cell with a soma volume greater than  $5,000 \mu\text{m}^3$  has an almost 100% chance of being exactly 1 week old from time of differentiation. Similarly, cell somata between the range of  $3,500\text{--}5,000 \mu\text{m}^3$  are most likely less than 2 weeks old, while somata larger than  $3,000 \mu\text{m}^3$  are likely newly generated cells within the first 3 weeks post-differentiation (Figure 7E). Finally, by comparing the mean soma volume of stable control oligodendrocytes to newly formed cells at multiple timepoints, we also confirmed the statistical significance of the predictive relationship between soma volume and cell age (Figure 7F;  $p < 0.001$  all comparisons; 1-way ANOVA with Tukey's Honest Significant Difference *post hoc* test).

## Oligodendrocyte Death Can Be Predicted From Soma Size

Oligodendrocyte death is typically preceded by nuclear condensation and shrinkage of the soma (Bortner and Cidlowski, 2002; Miller and Zachary, 2017). To determine if the soma size analysis could also be used to predict whether an oligodendrocyte will later degenerate, we plotted the soma volumes of all cells later observed to degenerate. After multiple weeks of cuprizone treatment, the median soma volume of all cells shrank significantly (Figures 8A–C, Supplementary Video 4;  $p < 0.001$  at 1, 2, and 3 weeks), consistent with the high degree of oligodendrocyte degeneration observed in the cortex. When compared to oligodendrocytes at comparable timepoints in control mice, soma size was also significantly smaller after extended cuprizone treatment (Figure 8D;  $0.78 \pm 0.012$  fold change  $p < 0.001$  and  $D = 0.4$  at 1 week,  $0.75 \pm 0.013$  fold change  $p < 0.001$  and  $D = 0.57$  at 2 weeks,  $0.7 \pm 0.017$  fold change  $p < 0.001$  and  $D = 0.69$  at 3 weeks; Kruskal–Wallis test with Dunn's *post hoc* analysis and Cohen's effect size calculation), consistent with progression to apoptosis. A possible confounding factor for this volumetric analysis is that cuprizone treatment itself may reduce EGFP expression over time, which could lead to under-estimations of cell soma volume. To account for possible cuprizone-induced changes, the volumetric measurements in Figure 8D were also normalized to the mean intensity of all oligodendrocytes in each respective cuprizone treated timepoint

(Figure 8D). Given the large statistical power when sampling thousands of cells, we additionally defined a significant difference in soma volume as one having a medium to large effect size ( $>0.5$  Cohen's  $d$ ), which only occurred at 2 and 3 weeks of cuprizone treatment. Assessing the predictive power of soma volume again, we attempted to predict the likelihood that a cell would die within the next subsequent week given that the cell is smaller than a certain soma volume. While not as striking as the predictive power for newly formed oligodendrocytes, the probability that cells with somata below  $500 \mu\text{m}^3$  would disappear within 1 week was over 90% (Figures 8E,F). Together, this analysis reveals that the size of oligodendrocyte somata calculated using deep neural networks can be used to predict, without prior or later longitudinal imaging data, whether a cell was recently generated and whether it is likely to degenerate.

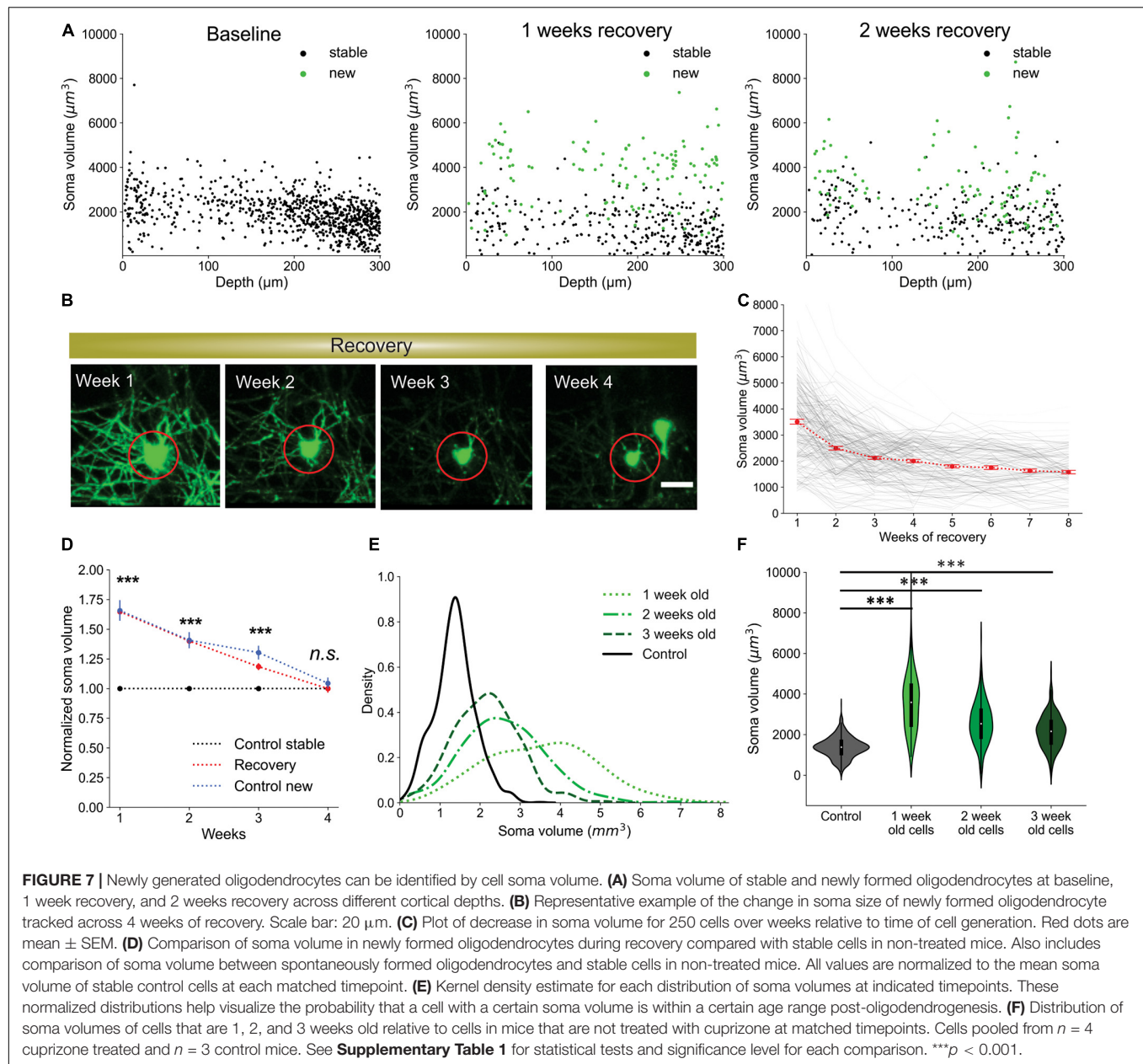
## DISCUSSION

To facilitate analysis of oligodendrocyte dynamics in the adult brain we designed *Oligo-Track*, a deep learning pipeline that uses two sequential CNNs to allow cell tracking in volumetric imaging datasets. This methodology provides a substantial improvement over traditional imaging informatics approaches as it was faster, less subject to user bias and less influenced by factors that commonly deteriorate image quality, allowing reliable automated cell tracking over time series spanning multiple weeks. This automated volumetric analysis enabled us to increase the number of oligodendrocytes analyzed in deeper layers of the mouse cortex and to identify newly formed oligodendrocytes and those that are in the process of degenerating simply based on soma size at a single time point without longitudinal tracking information.

This CNN tracking pipeline follows a two-step approach to optimize multi-object tracking (MOT). We first setup a detection step, where oligodendrocytes are identified in a volume, followed by an association step, to link tracked cells across time frames (Ciaparrone et al., 2020). Unlike other deep learning MOT approaches, which often only use CNNs to generate bounding boxes or extract features (Ciaparrone et al., 2020), we employed two sequential CNNs that both performed semantic segmentation in the MOT detection and association stages (Seg-CNN and Track-CNN, respectively). The output of this pipeline provides not only the location of all tracked cells, but also the volume of each cell soma. This volumetric tracking was made possible by training our association network (Track-CNN) with a seed-based learning approach. Previous studies have shown that, when given input data containing several cells, one can mark cells of interest with a binary mask, or “seed”, to draw the attention of CNNs (Xu et al., 2019). This forces a semantic classifier to not only learn to identify oligodendrocyte somata, but also to identify the somata of individually marked cells of interest across different timepoints.

From a computational standpoint, there are several advantages to this automated approach. Roughly estimating the time for manual analysis with syGlass, a 3D virtual reality based visualization tool, we found that a 10-week, 10-timepoint dataset with a size of  $800 \times 800 \times 300 \mu\text{m}$  per timepoint



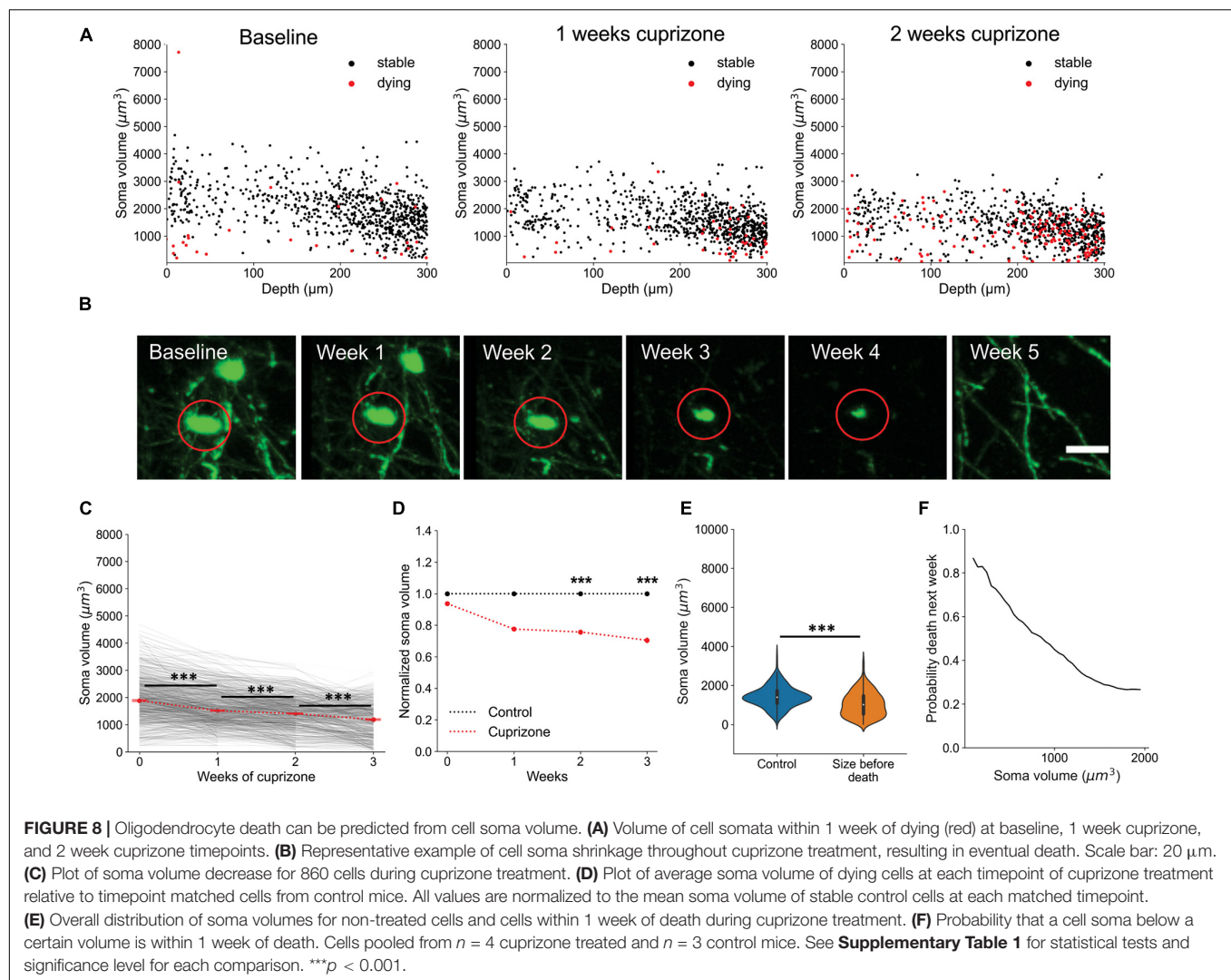


would take a researcher approximately 6 h to identify and track all oligodendrocytes within this volume. This estimate only considers the time to place point coordinates and does not include the considerable additional time it would take to trace every voxel to generate volumetric segmentations. This estimate also does not consider how much longer manual analysis would take without access to specialized VR software (e.g., syGlass). By comparison, *Oligo-Track* requires  $\sim 20$  min for Seg-CNN segmentation ( $\sim 2$  min per timepoint) and  $\sim 25$ – $35$  min for Track-CNN associations for the same volume across 10 timepoints, for a total analysis time of 45–55 min, more than six times faster than achieved with VR-assisted manual tracking, just for cell identification. This processing time is also purely computational, so manual labor time is reduced to almost zero,

and offers fully volumetric segmentations. Total runtime will vary depending on cell density, number of timepoints, the size of volumes during inference and the exact computer configuration.

Standardization of methodology is also an important advantage of the CNN analysis approach. Inter-researcher disagreements on manual tracing methodologies often arise during the quantification of fluorescent data, as fluorescence does not offer as many contextual clues as natural scene images for human decision-making (Xu et al., 2019). Moreover, human inconsistencies may also pervade the use of traditional tracking algorithms, as excessive parameter tuning by researchers may overfit algorithms to specific datasets and prevent accurate cross-experiment comparisons. *Oligo-Track* offers standardization by enabling researchers to apply the same algorithm across





multiple datasets, while relying on the diversity of its training data to provide generalizability rather than having tunable parameters. Finally, as many researchers do not yet have access to 4D visualization/tracking tools, *Oligo-Track* standardizes the approach to longitudinal cell tracking by removing the reliance on specialized proprietary software. Losing dimensionality can be extremely detrimental to manual quantification speed and accuracy, as cells can often lie on top of one another or shift in unpredictable ways that can be missed if viewing 4D data in lower dimensional space. Thus, our open-source quantification algorithm reduces tracking inconsistencies between individual researcher annotations by providing a standardized tracking platform.

Although there are clear technical advantages of using CNNs to track cells over time, the decision to use deep learning as an underlying analytic framework comes with additional considerations. Deep learning is often criticized for its “black box” nature, as researchers are unable to understand the intricate decision-making process of millions of weighted connections in a CNN, resulting in sometimes unpredictable behavior

(Heaven, 2019; Yampolskiy, 2019). For example, as we see in our own network, it was difficult to define the exact level of debris avoidance that the neural network was capable of, and why certain debris were more likely to be identified as false positives. Additionally, we noted that CNN performance was suboptimal when image scaling or intensity of input volumes was beyond the range of values in the training dataset. This variability in performance could be addressed in future work by data augmentation techniques, such as pixel size scaling, random noise injections, and histogram equalization, to improve the generalizability of our current model beyond our standard imaging setup. Moreover, data augmentation could also include the introduction of data containing high levels of real or synthetic debris during CNN training, which could enable improved accuracy in avoiding biological debris. Currently, we partially addressed the unpredictability of deep learning by using VR-based 4D manual curation post-CNN analysis to ensure accuracy in unpredictable scenarios. We also used these *post hoc* manually curated datasets to further improve the CNNs, highlighting a major advantage of deep learning approaches. CNN models are

extraordinarily data hungry and can be continuously improved with new training data that help generalize to new imaging conditions (Klabjan and Zhu, 2020). For instance, while *Oligo-Track* has only been trained on cells up to 400  $\mu\text{m}$  depth in the cortex, it will be possible to further train these networks to imaging conditions in deeper cortical layers. This training advantage is not available for traditional algorithms that may require extensive manual fine-tuning for extrapolation to slight variations in imaging conditions.

While the main limiting factor for developing deep learning technologies is the generation of large ground-truth training datasets to reach optimal performance levels, there are a growing number of methods by which researchers can reduce this high data demand of CNNs. For instance, transfer learning techniques have demonstrated how a network that is pretrained on a large dataset can be rapidly adapted to a new dataset with minimal new training data (Zhuang et al., 2020). Given the large database that our network was trained on, and the relatively similar features of cells that express fluorescent proteins, our pretrained CNN can serve as a basis for additional tool development, in which transfer learning is used to adapt this model to other cell types, where ground truth training data may not be readily available.

Automated quantitative tools will play a growing, critical role in the age of big data that is spurred by advances in biological imaging technologies. Of note for oligodendrocyte biology, three photon imaging promises to take us deeper *in vivo* (Horton et al., 2013; Lecoq et al., 2019), allowing us to examine the dynamics of these myelinating cells in layers 5 and 6 of the cortex and perhaps even into the white matter of the corpus callosum. Additionally, block-face imaging presents us with the opportunity to examine distributions of oligodendrocytes across the entire mouse brain, correlating myelination patterns with neuron type and brain region (Ragan et al., 2012; Amato et al., 2016; Winnubst et al., 2019). To match the scale of these imaging technologies, an important extension of the current work is to extract not only positional information about cells *in vivo*, but also the entire structure of cells. For oligodendrocytes, that means the soma, cytosolic branches, and individual myelin sheaths formed by each cell. As highlighted in this study, gaining quantitative access to even a single parameter, such as soma volume, can greatly extend biological understanding, allowing robust predictions to be made with limited data. Here, the strong correlations we observed between soma size, age, and survival provide us with a tool to infer the regenerative capacity of oligodendrocytes on fixed timepoint experiments acquired from individual tissue sections or from block-face imaging (Ragan et al., 2012). By extension, having access to the complete morphological structures of thousands of oligodendrocytes in the brain would enable us to assess complex region-specific differences in adaptive myelination, regenerative capacity and survival across the brain in mice subjected to different interventions.

Deep learning is well situated to provide us with the adaptable, reliable tools needed for the analysis of enormous new imaging datasets that can no longer be practically annotated using a manual brute force selection approach. Computational power is growing rapidly each year with new GPUs and the development of dozens of new deep learning techniques. Here,

we demonstrate one powerful application of deep learning to resolve a multi-dimensional tracking challenge, which not only facilitates analysis of oligodendrocyte dynamics, but also extends our quantitative limits to extract novel insight into regional differences in regenerative capacity and allows predictions to be made about future behaviors. Having access to more cellular features and dynamics will bring us closer to understanding the events that underlie myelin regeneration that will aid in the discovery of therapeutics for treating demyelinating diseases.

## DATA AVAILABILITY STATEMENT

The raw data supporting the conclusions of this article will be made available by the authors, without undue reservation.

## ETHICS STATEMENT

The animal study was reviewed and approved by the Animal Care and Use Committee at Johns Hopkins University.

## AUTHOR CONTRIBUTIONS

YX: model design, conceptualization, data curation, formal analysis, supervision, validation, investigation, visualization, methodology, writing – original draft, and writing – review and editing. CC: conceptualization, data curation, supervision, methodology, writing – original draft, and writing – review and editing. JS: methodology, supervision, investigation, writing – original draft, and writing – review and editing. DB: conceptualization, resources, supervision, funding acquisition, investigation, methodology, writing – original draft, project administration, and writing – review and editing. All authors contributed to the article and approved the submitted version.

## FUNDING

YX was supported by a fellowship from the Johns Hopkins University Kavli Neuroscience Discovery Institute. CC was supported by a National Science Foundation Graduate Research Fellowship. Funding was provided by NIH BRAIN Initiative grant R01 RF1MH121539, a Collaborative Research Centers Grant from the National Multiple Sclerosis Society, and Dr. Miriam and Sheldon G. Adelson Medical Research Foundation.

## ACKNOWLEDGMENTS

We thank Dr. M. Pucak and N. Ye for technical assistance, T. Shelly for machining expertise, and members of the Bergles Laboratory for discussions.

## SUPPLEMENTARY MATERIAL

The Supplementary Material for this article can be found online at: <https://www.frontiersin.org/articles/10.3389/fncel.2021.667595/full#supplementary-material>

**Supplementary Figure 1** | CNN architecture for Seg-CNN and Track-CNN. UNet architecture used for both Seg- and Track-CNN. Downsampling branch extracts local features, upsampling branch extracts global spatial features.

**Supplementary Figure 2** | Training and validation performance for both CNNs. **(A)** Seg-CNN loss, Jaccard overlap metric (Jaccard, 1912), precision, and sensitivity over 30 epochs. Curves associated with training and validation datasets are indicated. Loss descended stably without overfitting. All other metrics improved as anticipated. **(B)** Track-CNN loss, accuracy, precision, and sensitivity calculated per epoch. Accuracy, precision, and sensitivity only calculated on validation dataset for computational efficiency. Loss decreased stably without overfitting.

**Supplementary Figure 3** | Robustness of CNN-based cellular tracking. **(A)** Example of debris avoidance by Seg-CNN (yellow circles). Arrows indicate debris that was not avoided. Scale bar: 30  $\mu\text{m}$ . **(B)** High intensity, dense debris is more likely to be detected as false positives. Arrows indicate debris that was not avoided. Scale bar: 30  $\mu\text{m}$ . **(C)** Seg-CNN detections in image set with low laser power (left) and after gain adjustment (right). Arrows indicate initially undetected

cells at low laser power. Scale bar: 25  $\mu\text{m}$ . **(D)** Effect of different standard deviations of random noise on Track-CNN performance. **(E)** Effect of changing the rotation range (in degrees) of random motion artifacts on Track-CNN performance. Scale bar: 30  $\mu\text{m}$ .

**Supplementary Video 1** | Cell tracking across two stable timepoints. Timepoint  $t$  (left) and  $t + 1$  (right). Magenta indicates the cell that is currently undergoing assessment by Track-CNN. After assessment, a color is assigned to the cell on  $t$  and  $t + 1$  to represent a tracked cell across timepoints. If the cell is untracked (or dies between timepoints), the cell soma is set to pure white on  $t$ .

**Supplementary Video 2** | Cell tracking across cuprizone injury timepoints. Timepoint  $t$  (left) and  $t + 1$  (right). Magenta indicates the cell that is currently undergoing assessment by Track-CNN. After assessment, a color is assigned to the cell on  $t$  and  $t + 1$  to represent a tracked cell across timepoints. If the cell is untracked (or dies between timepoints), the cell soma is set to pure white on  $t$ .

**Supplementary Video 3** | Cell sparsity over weeks of cuprizone treatment and recovery. Newly formed cells marked in green (left) and cells that will die within a week marked in red (right) starting from baseline followed by 3 weeks of cuprizone treatment and subsequent recovery.

**Supplementary Video 4** | Soma size of dying and newly formed cells over weeks of cuprizone treatment. Newly formed cells marked in green (left) and cells that will die within a week a marked in red (right) starting from baseline followed by 3 weeks of cuprizone treatment and subsequent recovery.

## REFERENCES

- Acton, S. T., Wethmar, K., and Ley, K. (2002). Automatic tracking of rolling leukocytes in vivo. *Microvasc. Res.* 63, 139–148. doi: 10.1006/mvres.2001.2373
- Amato, S. P., Pan, F., Schwartz, J., and Ragan, T. M. (2016). Whole brain imaging with serial two-photon tomography. *Front. Neuroanat.* 10:31. doi: 10.3389/fnana.2016.00031
- Baxi, E. G., DeBruin, J., Jin, J., Strasburger, H. J., Smith, M. D., Orthmann-Murphy, J. L., et al. (2017). Lineage tracing reveals dynamic changes in oligodendrocyte precursor cells following cuprizone-induced demyelination. *Glia* 65, 2087–2098. doi: 10.1002/glia.23229
- Berg, S., Kutra, D., Kroeger, T., Straehle, C. N., Kausler, B. X., Haubold, C., et al. (2019). ilastik: interactive machine learning for (bio)image analysis. *Nat. Methods* 16, 1226–1232. doi: 10.1038/s41592-019-0582-9
- Bergles, D. E., and Richardson, W. D. (2015). Oligodendrocyte development and plasticity. *Cold Spring Harb. Perspect. Biol.* 8:a020453. doi: 10.1101/cshperspect.a020453
- Bhardwaj, R. D., Curtis, M. A., Spalding, K. L., Buchholz, B. A., Fink, D., Björk-Eriksson, T., et al. (2006). Neocortical neurogenesis in humans is restricted to development. *Proc. Natl. Acad. Sci. U.S.A.* 103, 12564–12568. doi: 10.1073/pnas.0605177103
- Bortner, C. D., and Cidlowski, J. A. (2002). Apoptotic volume decrease and the incredible shrinking cell. *Cell Death Differ.* 9, 1307–1310. doi: 10.1038/sj.cdd.4401126
- Brunelli, R. (2009). *Template Matching Techniques in Computer Vision: Theory and Practice*. Chichester: Wiley Publishing.
- Chang, A., Staugaitis, S. M., Dutta, R., Batt, C. E., Easley, K. E., Chomyk, A. M., et al. (2012). Cortical remyelination: a new target for repair therapies in multiple sclerosis. *Ann. Neurol.* 72, 918–926. doi: 10.1002/ana.23693
- Ciarrone, G., Sánchez, F. L., Tabik, S., Troiano, L., Tagliaferri, R., and Herrera, F. (2020). Deep learning in video multi-object tracking: a survey. *Neurocomputing* 381, 61–88. doi: 10.1016/j.neucom.2019.11.023
- Cornea, A. (2001). Digital subtraction of Lipofuscin's fluorescence. *Microsc. Today* 9, 14–15. doi: 10.1017/S1551929500057278
- El Waly, B., Macchi, M., Cayre, M., and Durbec, P. (2014). Oligodendrogenesis in the normal and pathological central nervous system. *Front. Neurosci.* 8:145. doi: 10.3389/fnins.2014.00145
- Giovannucci, A., Friedrich, J., Gunn, P., Kalfon, J., Brown, B. L., Koay, S. A., et al. (2019). CalmAn an open source tool for scalable calcium imaging data analysis. *eLife* 8:e38173. doi: 10.7554/eLife.38173
- Gruchot, J., Weyers, V., Göttle, P., Förster, M., Hartung, H.-P., Küry, P., et al. (2019). The molecular basis for remyelination failure in multiple sclerosis. *Cells* 8:825. doi: 10.3390/cells8080825
- Heaven, D. (2019). Why deep-learning AIs are so easy to fool. *Nature* 574, 163–166. doi: 10.1038/d41586-019-03013-5
- Holtmaat, A., de Paola, V., Wilbrecht, L., Trachtenberg, J. T., Svoboda, K., and Portera-Cailliau, C. (2012). Imaging neocortical neurons through a chronic cranial window. *Cold Spring Harb. Protoc.* 2012, 694–701. doi: 10.1101/pdb.prot069617
- Horn, B. K. P., and Schunck, B. G. (1981). Determining optical flow. *Artif. Intell.* 17, 185–203. doi: 10.1016/0004-3702(81)90024-2
- Horton, N. G., Wang, K., Kobat, D., Clark, C. G., Wise, F. W., Schaffer, C. B., et al. (2013). In vivo three-photon microscopy of subcortical structures within an intact mouse brain. *Nat. Photon.* 7, 205–209. doi: 10.1038/nphoton.2012.336
- Hughes, E. G., Kang, S. H., Fukaya, M., and Bergles, D. E. (2013). Oligodendrocyte progenitors balance growth with self-repulsion to achieve homeostasis in the adult brain. *Nat. Neurosci.* 16, 668–676. doi: 10.1038/nn.3390
- Hughes, E. G., Orthmann-Murphy, J. L., Langseth, A. J., and Bergles, D. E. (2018). Myelin remodeling through experience-dependent oligodendrogenesis in the adult somatosensory cortex. *Nat. Neurosci.* 21, 696–706. doi: 10.1038/s41593-018-0121-5
- Hur, J., and Roth, S. (2020). Optical flow estimation in the deep learning age. *arXiv* [Preprint]. Available online at: <http://arxiv.org/abs/2004.02853> (accessed March 8, 2021).
- Jaccard, P. (1912). The distribution of the flora in the alpine zone.1. *New Phytol.* 11, 37–50. doi: 10.1111/j.1469-8137.1912.tb05611.x
- Kalman, R. E. (1960). A new approach to linear filtering and prediction problems. *J. Basic Eng.* 82, 35–45. doi: 10.1115/1.3662552
- Kirby, L., Jin, J., Cardona, J. G., Smith, M. D., Martin, K. A., Wang, J., et al. (2019). Oligodendrocyte precursor cells present antigen and are cytotoxic targets in inflammatory demyelination. *Nat. Commun.* 10:3887. doi: 10.1038/s41467-019-11638-3
- Klabjan, D., and Zhu, X. (2020). Neural network retraining for model serving. *arXiv* [Preprint]. Available online at: <http://arxiv.org/abs/2004.14203> (accessed October 31, 2020).
- Kuhn, S., Gritti, L., Crooks, D., and Dombrowski, Y. (2019). Oligodendrocytes in development, myelin generation and beyond. *Cells* 8:1424. doi: 10.3390/cells8111424



- Lampron, A., Laroche, A., Laflamme, N., Préfontaine, P., Plante, M.-M., Sánchez, M. G., et al. (2015). Inefficient clearance of myelin debris by microglia impairs remyelinating processes. *J. Exp. Med.* 212, 481–495. doi: 10.1084/jem.20141656
- Larson, V. A., Mironova, Y., Vanderpool, K. G., Waisman, A., Rash, J. E., Agarwal, A., et al. (2018). Oligodendrocytes control potassium accumulation in white matter and seizure susceptibility. *elife* 7:e34829. doi: 10.7554/eLife.34829
- Lecoq, J., Orlova, N., and Grewe, B. F. (2019). Wide. Fast. Deep: recent advances in multiphoton microscopy of in vivo neuronal activity. *J. Neurosci.* 39, 9042–9052. doi: 10.1523/JNEUROSCI.1527-18.2019
- Loshchilov, I., and Hutter, F. (2019). Decoupled weight decay regularization. *arXiv [Preprint]*. Available online at: <http://arxiv.org/abs/1711.05101> (accessed October 30, 2020).
- Lugagne, J.-B., Lin, H., and Dunlop, M. J. (2020). DeLTA: automated cell segmentation, tracking, and lineage reconstruction using deep learning. *PLoS Comput. Biol.* 16:e1007673. doi: 10.1371/journal.pcbi.1007673
- Miller, M. A., and Zachary, J. F. (2017). Mechanisms and morphology of cellular injury, adaptation, and death. *Pathol. Basis Vet. Dis.* 2–43.e19. doi: 10.1016/B978-0-323-35775-3.00001-1
- Ming, G., and Song, H. (2011). Adult neurogenesis in the mammalian brain: significant answers and significant questions. *Neuron* 70, 687–702. doi: 10.1016/j.neuron.2011.05.001
- Moreno-García, A., Kun, A., Calero, O., Medina, M., and Calero, M. (2018). An overview of the role of Lipofuscin in age-related neurodegeneration. *Front. Neurosci.* 12:464. doi: 10.3389/fnins.2018.00464
- Narayanan, R. T., Udvar, D., and Oberlander, M. (2017). Cell type-specific structural organization of the six layers in rat barrel cortex. *Front. Neuroanat.* 11:91. doi: 10.3389/fnana.2017.00091
- Nguyen, N. H., Keller, S., Norris, E., Huynh, T. T., Clemens, M. G., and Shin, M. C. (2011). Tracking colliding cells in vivo microscopy. *IEEE Trans. Biomed. Eng.* 58, 2391–2400. doi: 10.1109/TBME.2011.2158099
- Nketia, T. A., Sailem, H., Rohde, G., Machiraju, R., and Rittscher, J. (2017). Analysis of live cell images: methods, tools and opportunities. *Methods* 115, 65–79. doi: 10.1016/j.ymeth.2017.02.007
- Orthmann-Murphy, J., Call, C. L., Molina-Castro, G. C., Hsieh, Y. C., Rasband, M. N., Calabresi, P. A., et al. (2020). Remyelination alters the pattern of myelin in the cerebral cortex. *eLife* 9:e56621. doi: 10.7554/eLife.56621
- Otsu, N. (1979). A threshold selection method from gray-level histograms. *IEEE Trans. Syst. Man Cybern.* 9, 62–66. doi: 10.1109/TSMC.1979.4310076
- Pachitariu, M., Stringer, C., Dipoppa, M., Schröder, S., Rossi, L. F., Dalgleish, H., et al. (2017). Suite2p: beyond 10,000 neurons with standard two-photon microscopy. *bioRxiv [Preprint]* 061507. doi: 10.1101/061507 bioRxiv:061507,
- Parslow, A., Cardona, A., and Bryson-Richardson, R. J. (2014). Sample drift correction following 4d confocal time-lapse imaging. *J. Vis. Exp.* 51086. doi: 10.3791/51086
- Paszke, A., Gross, S., Chintala, S., Chanan, G., Yang, E., DeVito, Z., et al. (2017). *Automatic Differentiation in PyTorch*. Available online at: <https://openreview.net/forum?id=BJJrmfCZ> (accessed October 30, 2020).
- Pérez-García, F., Sparks, R., and Ourselin, S. (2021). TorchIO: a Python library for efficient loading, preprocessing, augmentation and patch-based sampling of medical images in deep learning. *arXiv [Preprint]*. Available online at: <http://arxiv.org/abs/2003.04696> (accessed January 18, 2021).
- Pidhorsky, S., Morehead, M., Jones, Q., Spirou, G., and Doretto, G. (2018). syGlass: interactive exploration of multidimensional images using virtual reality head-mounted displays. *arXiv [Preprint]*. Available online at: <http://arxiv.org/abs/1804.08197> (accessed October 30, 2020).
- Ragan, T., Kadiri, L. R., Venkataraju, K. U., Bahlmann, K., Sutin, J., Taranda, J., et al. (2012). Serial two-photon tomography: an automated method for ex-vivo mouse brain imaging. *Nat. Methods* 9, 255–258. doi: 10.1038/nmeth.1854
- Ronneberger, O., Fischer, P., and Brox, T. (2015). *U-Net: Convolutional Networks for Biomedical Image Segmentation*. Available online at: <https://arxiv.org/abs/1505.04597v1> (accessed March 7, 2020).
- Schindelin, J., Arganda-Carreras, I., Frise, E., Kaynig, V., Longair, M., Pietzsch, T., et al. (2012). Fiji: an open-source platform for biological-image analysis. *Nat. Methods* 9, 676–682. doi: 10.1038/nmeth.2019
- Simons, M., and Nave, K.-A. (2016). Oligodendrocytes: myelination and axonal support. *Cold Spring Harb. Perspect. Biol.* 8:a020479. doi: 10.1101/cshperspect.a020479
- Skipuletz, T., Lindner, M., Kotsiari, A., Garde, N., Fokuhl, J., Linsmeier, F., et al. (2008). Cortical demyelination is prominent in the murine cuprizone model and is strain-dependent. *Am. J. Pathol.* 172, 1053–1061. doi: 10.2353/ajpath.2008.070850
- Streichan, S. J., Hoerner, C. R., Schneidt, T., Holzer, D., and Hufnagel, L. (2014). Spatial constraints control cell proliferation in tissues. *Proc. Natl. Acad. Sci. U.S.A.* 111, 5586–5591. doi: 10.1073/pnas.1323016111
- Su, Z., Yuan, Y., Chen, J., Zhu, Y., Qiu, Y., Zhu, F., et al. (2011). Reactive astrocytes inhibit the survival and differentiation of oligodendrocyte precursor cells by secreted TNF- $\alpha$ . *J. Neurotrauma* 28, 1089–1100. doi: 10.1089/neu.2010.1597
- Theer, P., and Denk, W. (2006). On the fundamental imaging-depth limit in two-photon microscopy. *J. Opt. Soc. Am. A JOSAA* 23, 3139–3149. doi: 10.1364/JOSAA.23.003139
- van Valen, D. A., Kudo, T., Lane, K. M., Macklin, D. N., Quach, N. T., DeFelice, M. M., et al. (2016). Deep learning automates the quantitative analysis of individual cells in live-cell imaging experiments. *PLoS Comput. Biol.* 12:e1005177. doi: 10.1371/journal.pcbi.1005177
- Wang, J., Su, X., Zhao, L., and Zhang, J. (2020). Deep reinforcement learning for data association in cell tracking. *Front. Bioeng. Biotechnol.* 8:298. doi: 10.3389/fbioe.2020.00298
- Wang, M., Ong, L. S., Dauwels, J., and Asada, H. H. (2015). “Automated tracking of cells from phase contrast images by multiple hypothesis Kalman filters,” in *Proceedings of the 2015 IEEE International Conference on Acoustics, Speech and Signal Processing (ICASSP)*, South Brisbane, QLD, 942–946. doi: 10.1109/ICASSP.2015.7178108
- Wang, Z., Bovik, A. C., Sheikh, H. R., and Simoncelli, E. P. (2004). Image quality assessment: from error visibility to structural similarity. *IEEE Trans. Image Process.* 13, 600–612. doi: 10.1109/TIP.2003.819861
- Winnubst, J., Bas, E., Ferreira, T. A., Wu, Z., Economou, M. N., Edson, P., et al. (2019). Reconstruction of 1,000 projection neurons reveals new cell types and organization of long-range connectivity in the mouse brain. *Cell* 179, 268–281.e13. doi: 10.1016/j.cell.2019.07.042
- Xu, Y. K., Chitsaz, D., Brown, R. A., Cui, Q. L., Dabarno, M. A., Antel, J. P., et al. (2019). Deep learning for high-throughput quantification of oligodendrocyte ensheathment at single-cell resolution. *Commun. Biol.* 2:116. doi: 10.1038/s42003-019-0356-z
- Yakovleva, M. A., Radchenko, A. Sh., Feldman, T. B., Kostyukov, A. A., Arbukhanova, P. M., Borzenok, S. A., et al. (2020). Fluorescence characteristics of lipofuscin fluorophores from human retinal pigment epithelium. *Photochem. Photobiol. Sci.* 19, 920–930. doi: 10.1039/C9PP00406H
- Yampolskiy, R. V. (2019). Unpredictability of AI. *arXiv [Preprint]*. Available online at: <http://arxiv.org/abs/1905.13053> (Accessed October 31, 2020).
- Zhang, Y., Zhang, J., Navrazhina, K., Argaw, A. T., Zameer, A., Gurfein, B. T., et al. (2010). TGF $\beta$ 1 induces Jagged1 expression in astrocytes via ALK5 and Smad3 and regulates the balance between oligodendrocyte progenitor proliferation and differentiation. *Glia* 58, 964–974. doi: 10.1002/glia.20978
- Zhong, B., Pan, S., Wang, C., Wang, T., Du, J., Chen, D., et al. (2016). Robust individual-cell/object tracking via PCANet deep network in biomedicine and computer vision. *Biomed Res. Int.* 2016:8182416. doi: 10.1155/2016/8182416
- Zhu, X., Li, X., Li, Z., and Zhu, B. (2012). “Study on Signal-to-noise ratio algorithms based on no-reference Image quality assessment,” in *Proceedings of the 2012 International Conference on Systems and Informatics (ICSAI2012)*, Yantai, 1755–1759. doi: 10.1109/ICSAI.2012.6223383
- Zhuang, F., Qi, Z., Duan, K., Xi, D., Zhu, Y., Zhu, H., et al. (2020). A comprehensive survey on transfer learning. *arXiv [Preprint]*. Available online at: <http://arxiv.org/abs/1911.02685> (accessed October 30, 2020).

**Conflict of Interest:** The authors declare that the research was conducted in the absence of any commercial or financial relationships that could be construed as a potential conflict of interest.

Copyright © 2021 Xu, Call, Sulam and Bergles. This is an open-access article distributed under the terms of the Creative Commons Attribution License (CC BY). The use, distribution or reproduction in other forums is permitted, provided the original author(s) and the copyright owner(s) are credited and that the original publication in this journal is cited, in accordance with accepted academic practice. No use, distribution or reproduction is permitted which does not comply with these terms.





# Specialized Pro-resolving Lipid Mediators and Glial Cells: Emerging Candidates for Brain Homeostasis and Repair

Marta Tiberi<sup>1</sup> and Valerio Chiurchiù<sup>1,2\*</sup>

<sup>1</sup> Laboratory of Resolution of Neuroinflammation, European Center for Brain Research, IRCCS Santa Lucia Foundation, Rome, Italy, <sup>2</sup> Institute of Translational Pharmacology, National Research Council, Rome, Italy

## OPEN ACCESS

### Edited by:

Enrica Boda,  
University of Turin, Italy

### Reviewed by:

Marta Fumagalli,  
University of Milan, Italy  
Francesca Boscia,  
University of Naples Federico II, Italy

### \*Correspondence:

Valerio Chiurchiù  
v.chiurchiu@ift.cnr.it;  
v.chiurchiu@hsantalucia.it

### Specialty section:

This article was submitted to  
Non-Neuronal Cells,  
a section of the journal  
Frontiers in Cellular Neuroscience

**Received:** 27 February 2021

**Accepted:** 29 March 2021

**Published:** 26 April 2021

### Citation:

Tiberi M and Chiurchiù V (2021)  
Specialized Pro-resolving Lipid  
Mediators and Glial Cells: Emerging  
Candidates for Brain Homeostasis  
and Repair.  
*Front. Cell. Neurosci.* 15:673549.  
doi: 10.3389/fncel.2021.673549

Astrocytes and oligodendrocytes are known to play critical roles in the central nervous system development, homeostasis and response to injury. In addition to their well-defined functions in synaptic signaling, blood-brain barrier control and myelination, it is now becoming clear that both glial cells also actively produce a wide range of immune-regulatory factors and engage in an intricate communication with neurons, microglia or with infiltrated immune cells, thus taking a center stage in both inflammation and resolution processes occurring within the brain. Resolution of inflammation is operated by the superfamily of specialized pro-resolving lipid mediators (SPMs), that include lipoxins, resolvins, protectins and maresins, and that altogether activate a series of cellular and molecular events that lead to spontaneous regression of inflammatory processes and restoration of tissue homeostasis. Here, we review the manifold effects of SPMs on modulation of astrocytes and oligodendrocytes, along with the mechanisms through which they either inhibit inflammatory pathways or induce the activation of protective ones. Furthermore, the possible role of SPMs in modulating the cross-talk between microglia, astrocytes and oligodendrocytes is also summarized. This SPM-mediated mechanism uncovers novel pathways of immune regulation in the brain that could be further exploited to control neuroinflammation and neurodegeneration.

**Keywords:** inflammation, resolution, specialized pro resolving mediators, lipids, microglia, macroglia

## RESOLUTION OF NEUROINFLAMMATION

Inflammation is a self-limited and protective process that usually resolves on its own and restores tissue homeostasis. Occurrence of inflammation within the central nervous system (CNS) is referred to as neuroinflammation, and similar to what happens for the rest of body districts and tissues, when persistent or unresolved is detrimental to neurological functions and leads to neurodegeneration (Nathan and Ding, 2010). Contrary to what has been believed for over a century, the CNS is not an immuno-privileged tissue and neuroinflammatory events occur in the brain parenchyma leading to glial cell activation and recruitment of leukocytes from the periphery to survey for CNS self-antigens or to fight potential pathogens or aggregated proteins (Schwartz and Baruch, 2014). Although the mechanisms that cause neurodegenerative diseases are different, neuroinflammation is a common hallmark and only recently the interactions

between the CNS and circulating immune cells are becoming more fully understood, also thanks to the recently identified neuro-immunological interfaces that serve as gateways to allow immunosurveillance and that, when altered or disrupted, can lead to pathological conditions (Da Mesquita et al., 2018a,b; Rustenhoven et al., 2021).

This evidence not only confirms the “protective autoimmunity” theory that was proposed more than 20 years ago as an essential physiologic mechanism for CNS protection, repair and maintenance in both health and disease (Moalem et al., 1999), but also implies that the concept of resolution of inflammation, together with the underlying temporal lipid mediator class switch and production of the superfamily of specialized pro-resolving lipid mediators (SPMs), holds true also in the CNS for the restoration of full tissue homeostasis and the avoidance of neurodegeneration.

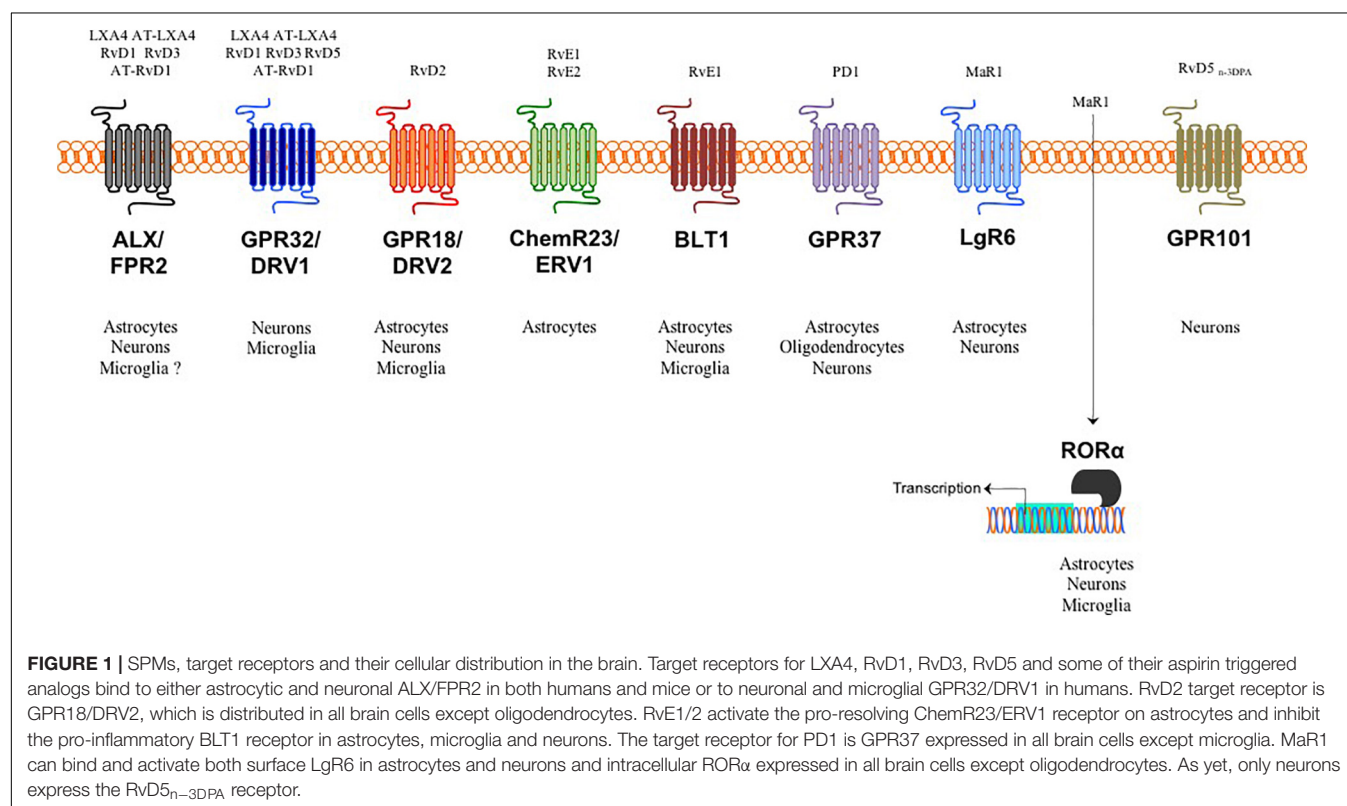
Indeed, during resolution of inflammation, the very same cells that are involved in the first steps of acute inflammation (i.e., vascular endothelial cells and innate immune cells) gradually stop to produce the highly pro-inflammatory classical eicosanoids (prostaglandins, leukotrienes, thromboxanes) from  $\omega$ -6 arachidonic acid (AA) and begin to utilize  $\omega$ -3 eicosapentaenoic acid (EPA) and  $\omega$ -3 docosahexaenoic acid (DHA) to generate over 30 different SPMs (Serhan, 2014; Basil and Levy, 2016; Chiurchiù et al., 2018). These include different families such as resolvins, protectins and maresins and that, although characterized by different biosynthetic pathway and structure, they all share the common feature of activating the signs of resolution: removal, relief, restoration, regeneration,

and remission (Serhan, 2014; Basil and Levy, 2016; Serhan et al., 2020). The recent evidence that different cells of the CNS express several SPM receptors (**Figure 1**) suggest that the activation of pro-resolution pathways are also occurring in the brain and that SPMs might be critical in modulating the crosstalk between glial cells and neurons and thus in affecting the initiation and progression of several neuropathologies.

## AA-Derived Lipoxins

AA is an  $\omega$ -6 PUFA presents in all human tissues and it is esterified to membrane phospholipids at the sn-2 position. Upon inflammation, phospholipase A2 cleaves free AA which is then metabolically converted in a myriad of pro-inflammatory mediators, generally termed eicosanoids or oxylipins. These include mainly prostaglandins, leukotrienes and thromboxanes, which are the classical mediators of inflammation and the responsible of the five cardinal signs of inflammation: redness, heat, swelling, pain, and loss of function.

However, during the peak of inflammation AA can further be metabolized into Lipoxins (LXs), which belong to the superfamily of SPMs and comprise only two isomers: LXA<sub>4</sub> and LXB<sub>4</sub>, which were first described in 1984 by Serhan, Hamberg and the Nobel Laureate Samuelsson (Serhan et al., 1984). The biosynthetic pathway of LXs is a transcellular process that occurs between inflammatory cells (usually eosinophils, macrophages, and dendritic cells) and resident cells in the inflammatory locus (i.e., endothelial cells), and it proceeds through three different biochemical routes, each one characterized by two consecutive oxygenation steps (Bannenberg and Serhan, 2010).



The first biochemical route involves the catalysis of AA by 15 lipoxygenase (15-LOX) in endothelial cells, monocytes or eosinophils, generating the 15-S-HpETE intermediate, which is then converted in 5,6-epoxytetraene by 5-LOX before finally being hydrolyzed into either LXA<sub>4</sub> or LXB<sub>4</sub> (Bennet and Gilroy, 2016). The second synthesis passes through AA oxygenation into leukotriene A<sub>4</sub> (LTA<sub>4</sub>) and proceeds toward LXA<sub>4</sub> and LXB<sub>4</sub> conversion via 12-LOX (Freire and Van Dyke, 2013). Lastly, a third biosynthetic pathway involves administration of aspirin, a commonly used non-steroidal anti-inflammatory drug which triggers irreversible acetylation of cyclooxygenase-2 (COX-2), the enzyme responsible for AA conversion into prostaglandins. Blockage of COX-2 activity allows formation of 15-R-HETE intermediate that is rapidly released and captured by adherent leukocytes or vascular endothelial cells and further metabolized by 5-LOX to form 15-epimeric-LXs or aspirin-triggered LXs (AT-LXs) (Serhan, 2005).

LXA<sub>4</sub>, LXB<sub>4</sub> and AT-LXs are all components of the LXs class of SPMs and they share the same anti-inflammatory and pro-resolving functions, which include to stimulate cellular and tissue responses that trend to reverse the actions of the pro-inflammatory mediators, dampen and reverse the inflammatory response, and initiate tissue repair. These effects include the uptake of apoptotic polymorphonuclear cells by macrophages, the removal of cell debris and pathogen killing (Serhan, 2014; Romano et al., 2015) as well as immunomodulation by targeting innate and adaptive immune cells and the reduction of oxidative stress (Ariel et al., 2006; Leuti et al., 2019; Kooij et al., 2020). The mechanism of action of LXs is exerted by the formyl peptide receptor 2 (FPR2), also known as ALX. This G protein-coupled receptors (GPCR) is bound by LXA<sub>4</sub> but also shared by others SPMs (Chiang et al., 2000, 2005). LXs were the first components of SPMs recognized as endogenous lipid mediators in mediating resolution of inflammation and are often referred to as the initiators of this biological process and the trigger of the metabolic switch (Serhan, 2001). To date, no specific receptor for LXB<sub>4</sub> has been identified yet.

## EPA Derived E-Series Resolvins

During the metabolic switch, occurring at the peak of an inflammatory event, the very same cells that generated the classical eicosanoids or lipoxins, start to utilize the  $\omega$ 3 EPA as a substrate instead of AA. EPA is thus the precursor of the SPM class of E-series resolvins (RvEs). The biosynthesis of RvEs is initiated by vascular endothelial cells that convert EPA into 18-HEPE and proceeds via a transcellular biosynthesis via acetylated COX-2 and cytochrome P450. Subsequently leukocytes through 5-LOX and a series of enzymatic epoxidation and hydrolysis generate RvE1 (Serhan et al., 2000; Arita et al., 2005). During this multi-step biochemical route, also RvE2 can be generated (Tjonahen et al., 2006). Of note, 18-HEPE can directly be transformed into RvE3 through the action of 12/15-LOX by several leukocytes (Isobe et al., 2012). This year, a new member of the EPA-derived E-series resolvins, RvE4, was elucidated and its stereochemistry was assigned; its production is operated in physiologic hypoxia by human neutrophils and macrophages by 5-LOX into 15S-HpEPE, which can undergo a second enzymatic

lipoxygenation to yield a hydroperoxyl group at the carbon C-5 position, which is reduced to form RvE4 (Libreros et al., 2021).

RvE1-E4 are more prominently involved in reducing inflammation by increasing efferocytosis of apoptotic cells by macrophages, blocking leukocyte recruitment into inflamed tissues, to modulate inflammatory responses of key immune cells and also to reduce pain (Vik and Hansen, 2021). The pro-resolving actions of RvE1 and RvE2 are due to their ability to activate ChemR23 and to antagonize BLT1, which usually mediates the proinflammatory actions of LTB<sub>4</sub> (Chiang and Serhan, 2017). Both receptors are widely expressed receptors in several cells in the periphery and in the CNS. To date, the receptors for RvE3 and RvE4 remain to be identified.

## DHA Derived E-Series Resolvins, Protectins, and Maresins

EPA through Elongase 5 is metabolically converted into docosapentanoic acid (DPA), which can also be converted into n-3 DPA series resolvins, protectins, and maresins (Dalli et al., 2013; Hansen et al., 2017) and is also the precursors of 13-series or T-resolvins (RvT1-4) (Dalli et al., 2015). As yet, besides the role of RvD5n-3DPA and its receptor GPR101 in mediating resolution of inflammatory arthritis and pathogen infection (Flak et al., 2020), the biological role of DPA-derived SPMs is yet to be fully elucidated. However, DPA is quickly converted into DHA by means of Elongase 2 and a desaturase (Talamonti et al., 2020) and the majority of SPMs originate from this  $\omega$ -3 fatty acid, which can be converted into D-series Resolvins (RvDs), Protectins (PDs), and Maresins (MaRs) as well as into their more recently identified sulfido-conjugates. Each group is made up of multiple molecules, altogether comprising more than 20 biologically active SPMs.

D-series resolvins synthesis starts off by 15-LOX-mediated conversion of DHA into 17(S)-hydroperoxy DHA (17(S)-HpDHA). From this, the fate of 17(S)-HpDHA depends on 5-LOX action and on which carbon is hydroxylated by its catalytic action. In fact, it can be converted either into 7(S)-hydroperoxy-17(S)-HDHA to generate RvD1, RvD2, and RvD5 or into 4(S)-hydroperoxy-17(S)-HDHA to generate RvD3, RvD4, and RvD6. Alternatively, 17(S)-HpDHA can be converted to a 16,17-epoxydocosatriene intermediate that in turn is converted to protectin D1 (or neuroprotectin D1 when produced in brain tissues) and PDX. Similarly to E-series resolvins, aspirin-acetylated COX-2 can use the D-resolvin precursor, DHA, to generate 17(R)-HpDHA, which is then transformed to epimeric AT-D-resolvins or AT-protectins in a 5-LOX-dependent manner (Serhan, 2014; Serhan et al., 2015). The last family of SPMs belonging to DHA-derived SPMs was discovered in macrophages, therefore named maresins. The biosynthesis of maresins (MaR1 and MaR2) is operated by 12-LOX in humans and by 12/15LOX in mice from 14(S)-HDHA intermediate, which is recognized as marker of maresins (Serhan et al., 2009; Deng et al., 2014).

The bioaction of these 3 classes of DHA-derived SPMs are shared in common with those of the other SPMs because they reduce leukocyte infiltration, induce pathogen killing, promote the clearance of debris and dead cells by the process of efferocytosis and reduce production of pro-inflammatory

mediators and enhance that of anti-inflammatory ones. These biological activities are mediated by several receptors with different affinities to different SPMs of this class. For instance, several D-series resolvins (i.e., RvD1, RvD3, and RvD5) bind to two different GPCRs, FPR2/ALX and GPR32/DRV1, whereas RvD2 engages GPR18/DRV2 receptor (Chiang and Serhan, 2017). In the last couple of years, the molecular targets for PD1 and MaR1 have also been uncovered and these two SPMs, respectively, bind to surface receptors GPR37 (Bang et al., 2018) and LgR6 (Chiang et al., 2019), although the latter SPM can also engage with the nuclear receptor ROR $\alpha$  (Han et al., 2019).

Interestingly, starting from 2014 it was discovered that all these 3 families of DHA-derived SPMs can be biochemically conjugated to glutathione and give rise to a series of novel mediators coined “conjugates in tissue regeneration” and that include mares in conjugates in tissue regeneration (MCTRs), protectin conjugates in tissue regeneration (PCTRs), and resolvins conjugates in tissue regeneration (RCTRs) (Dalli et al., 2016; Serhan et al., 2018). As suggested by their name, their physiological function is to orchestrate host responses and promote tissue regeneration and resolution of infections and has been demonstrated in different model organisms (Serhan et al., 2018).

## SPMS AND GLIAL CELLS

Since the discovery of the different families of SPMs, their role was mostly investigated in peripheral tissues mainly because, to date, their production is carried out by innate immune cells (i.e., granulocytes and macrophages) or vascular endothelial cells. However, in the last decade, on the verge of the revisitation of the concept of the CNS immune privilege and the realization that a network of infiltrated immune cells operates within the brain in a tightly regulated sequence of inflammation/resolution processes, several groups started to investigate whether SPMs are also capable of modulating neuroimmune functions by targeting either neurons or glial cells. Furthermore, recent evidence show that altered SPM metabolism and function is associated to several neuroinflammatory and neurodegenerative diseases, such as Alzheimer's disease, Parkinson's disease, and multiple sclerosis (Chiurchiù et al., 2018; Chamani et al., 2020; Zahoor and Giri, 2020).

### SPMs and Astrocytes

Among all glial cells, astrocytes are probably the cell type that fits the most with the concept of resolution of inflammation due to their vital role in regulating CNS homeostasis. They are by far the most abundant cells in the CNS, where they regulate virtually every physiological process, including: BBB maintenance, neurotrophin secretion, and regulation of neuronal synaptogenesis and elimination, ion buffering, neurotransmitter recycling, synaptic plasticity and modulation of immune functions (Miller, 2018). Recent evidence suggest that these functions are performed in a diverse fashion by different subsets of astroglia. Similarly to macrophages/microglial cells, astrocytes were recently classified into neurotoxic A1 and neuroprotective

A2 cells; however, such nomenclature is to be taken with a grain of salt and it seems that these cells display a high degree of heterogeneity during neuroinflammation. However, only a limited body of literature describes morphological and functional changes of astrocytes along the full spectrum of activation stages and also during the progression of neurodegenerative diseases (Zhang and Barres, 2010). In this context, it's indisputable that immune activation of astrocytes in response to signals released by injured neurons or activated microglia leads to the so-called astrogliosis. Astrogliosis, a hallmark of neuroinflammation, is characterized by a higher production of pro-inflammatory cytokines and reactive species and a lower production of neurotrophic factors, determining glial scars that prevent axonal regeneration and that represents a feature of many neurodegenerative diseases (Jensen et al., 2013; Ding et al., 2021).

Several works reported that astrocytes express high levels of ALX/FPR2 both *in vivo* and *in vitro* and in several brain areas (Svensson et al., 2007; Cattaneo et al., 2010; Bisicchia et al., 2018). Such expression seems to be particularly evident in the spinal cord, with a homogenous distribution in both dorsal and ventral horns (Svensson et al., 2007). This was also confirmed *in vitro* in several astrocytoma cell lines, that expresses a functional receptor both at mRNA and protein level (Le et al., 2000; Decker et al., 2009). In these cells, LXA<sub>4</sub>, one of the SPMs that efficiently binds this receptor, has an inhibitory effect on the expression of the proinflammatory chemokine IL-8 and adhesion molecule ICAM-1 in response to IL-1 $\beta$  and via an NF- $\kappa$ B-dependent mechanism (Decker et al., 2009). Interestingly, ALX/FPR2 was reported to be involved in the internalization and subsequent removal of A $\beta$ 42 in inflamed astrocytes through a physical interaction with the scavenger receptor MARCO (Brandenburg et al., 2010). This receptor has also been linked to MAPK and the inflammatory response in astrogloma U-87 cells, where its activation with its highly potent agonist WKYMVm induces JNK and ERKs phosphorylation and increases the expression of glial fibrillary acidic protein (GFAP) and IL-1 $\beta$ , which are correlated with astrogliosis (Kam et al., 2007). Of note, the involvement of ALX/FPR2 in the regulation of astrogliosis has major biological implications, because reactive astrogliosis and brain inflammation are pathological features of many neuroinflammatory and neurodegenerative diseases.

Indeed, it was reported that LXA<sub>4</sub> and RvD1, the two major SPMs to bind this receptor, reduce astrocyte reactivity by inhibiting their activation and/or pro-inflammatory cytokines production (Svensson et al., 2007; Ren et al., 2020) and by protecting neurons, demonstrating an astrocyte-dependent neuroprotective activity (Ren et al., 2020). Additionally, in a mouse model of postoperative cognitive dysfunction, acute administration of AT-RvD1 prevented neuronal dysfunction and cognitive impairment by regulating long-term potentiation, and astrocyte activation (Terrando et al., 2013). Our group also recently found that peripheral RvD1 administration in a focal brain injury model improved functional recovery, protected neurons from cell death and reduced activation of microglial cells in a mechanism that was dependent on the activation of



an anti-inflammatory ALX/FPR2-regulated microRNA pathway probably induced by astrocytes (Bisicchia et al., 2018).

The finding that ALX/FPR2 is highly expressed in spinal astrocytes is intriguing, since increasing evidence indicates that non-neuronal cells play an important role in spinal facilitation of pain processing. Indeed, not only it has been shown that both nerve injury and peripheral inflammation lead to activation of spinal dorsal horn astrocytes (Sweitzer et al., 1999), but also that spinal delivery of inhibitors or modulators of astrocyte function or administration of lipoxins block initiation and maintenance of persistent pain states (Zhuang et al., 2006; Svensson et al., 2007), supporting an important role for these cells in spinal sensitization and suggesting that the lipoxin/ALX pathway regulates astrocyte-dependent spinal nociception.

Furthermore, astrocytes express also the RvE1 receptors ChemR23/ERV1 in human hippocampus (Wang et al., 2015) and BLT1, the pro-inflammatory receptor that is blocked by RvE1, in both the gray and white matter of several brain regions, including frontal cortex, forebrain, cerebellum and hippocampus (Emre et al., 2020). However, another work reported that BLT1 was mainly expressed in neurons, microglia and endothelial cells but not in astrocytes (Ye et al., 2016).

On account of the fact that ChemR23 might be indeed expressed on astrocytes and it bears a protective role, a recent study performed a chronic and peripheral treatment with RvE1 and LXA<sub>4</sub> alone or in combination in a mouse model of Alzheimer's disease and found that the combined treatment potently reduced astrocyte activation in both hippocampus and cortex and ameliorated AD pathology and the production of several cytokines and chemokines (Kantarci et al., 2018). Of note, all these results were obtained in mice where SPMs were administered peripherally and suggest that resolvins are indeed able to cross the blood-brain barrier and exert their effect in the brain.

Interestingly, cortical astrocytes also express high levels of GPR37 (Galey et al., 2003; Cahoy et al., 2008) and its activation with a potent agonist significantly protected them from oxidative stress-induced death, with these protective effects being attenuated by siRNA-mediated knockdown of endogenous astrocytic GPR37 (Meyer et al., 2013). However, the binding activity of previously used agonists on GPR37 was recently challenged, making this receptor to regain an orphan status until 2018, when it was first confirmed the truthfulness of the initial binding data and its neuroprotective effect from oxidative stress (Liu et al., 2018) and then the identification of PD1 as the endogenous ligand (Bang et al., 2018). However, in the same year another study showed that astrocytes express low levels of GPR37, which was mainly found in oligodendrocytes, but high levels of homologous GPR37-like 1, which played a critical role in protecting neurons during ischemia by modulating astrocyte glutamate transporters and neuronal NMDA receptors (Jolly et al., 2018).

Although GPR32 seems to be completely absent in astrocytes, these cells express also GPR18 (Grabiec et al., 2019) and even the more recently identified LgR6 (Zhang et al., 2014; Miller et al., 2019). In both cases, the role of these two receptors in astrocytes was studied by stimulating them not with their specific SPMs

but with the endocannabinoid N-arachidonoyl glycine for GPR18 and with R-spondin for LgR6 and both showed an astrocyte-dependent protective effects on neurons (Zhang et al., 2014; Miller et al., 2019), highlighting the key role of astrocytes in controlling neuronal functions.

## SPMs and Oligodendrocytes

Oligodendrocytes are the second most abundant population of the CNS and their association with the concept of resolution of inflammation and tissue repair is due to their main role in producing myelin not only in physiological conditions but also in self-resolving situations where myelin loss occurs and is continuously repaired. However, a persistent neuroinflammation often leads to a progressive failure of these cells to restore myelin sheaths (Stadelmann et al., 2019). This is because they are the end product of a cell lineage (i.e., oligodendrocyte precursor cells, OPCs) which has to undergo a complex and spatially and temporally regulated program of proliferation, migration, differentiation, and myelination to finally produce the insulating sheath. Due to this complex differentiation program and their unique metabolism/physiology, oligodendrocytes are considered among the most vulnerable cells of the CNS and put them at a greater risk of damage during neuroinflammation and during pathological conditions (Bradl and Lassmann, 2010). Interestingly, from an immunological point of view, oligodendrocytes were originally thought of as inert and merely representing bystander victims of immune responses. This view has now changed in the light of accumulating evidence that oligodendrocytes actively produce a wide range of immune-regulatory factors (IL-1 $\beta$ , IL-6, IL-8, CCL2) and express immune markers or receptors for such factors (COX-2, MHC-I, CD200, pattern recognition receptors and cytokines/chemokine receptors) (Peferoen et al., 2014), in turn shaping the immune response of other glial cells (Liu and Aguzzi, 2020; Boccazzi et al., 2021). Of note, the presence of COX-2 in these cells and given the contribution of this enzyme to the production of also E-series resolvins, it's likely that oligodendrocytes might also exert immunomodulatory and homeostatic functions on neurons or other glial cells through SPM production.

In keeping with the information collected till now, among all SPM receptors identified so far, oligodendrocytes seem to express only GPR37 both in the brain and spinal cord, where it plays a critical role in the differentiation of these glial cells and in myelin production (Yang et al., 2016). Although Schwann cells of the peripheral nervous system stained positively for ALX/FPR2, oligodendrocytes were negative for this receptor (Cattaneo et al., 2010).

PD1 is considered a ligand for GPR37 because it induced a significant increase in intracellular calcium in HEK293 cells overexpressing GPR37 and in murine macrophages (Bang et al., 2018). Although in this last work the authors report that GPR37 is expressed in macrophages but not microglia, due to its positive colocalization with CD68 and lack of colocalization with CX3CR1 or Iba1, these data need to be better confirmed since all these three markers are expressed by both monocytes/macrophages and microglial cells, therefore they cannot be used to distinguish the two cell types.

Interestingly, GPR37, also known as Parkin-associated endothelin-like receptor (Pael-R) was originally discovered through genomic library screening to find new neuropeptide receptors (Marazziti et al., 1997) and is associated with neurological disorders, such as Parkinson's disease (PD), and autism (Lopes et al., 2015). Mutations within the GPR37 gene affect a variety of autism spectrum disorders (Fujita-Jimbo et al., 2012), dopamine reuptake regulation (Marazziti et al., 2007), oligodendrocyte differentiation (Yang et al., 2016), and demyelination (Smith et al., 2017). Thus, although, so far, no evidence is reported on the potential role of SPM in regulating oligodendroglial functions, this evidence suggests that PD1 might be the ideal candidate to test on these cells and especially on demyelinating diseases and PD.

## SPMs in the Cross-Talk Between Microglia, Other Glial Cells, and Neurons

Differently to astrocytes and oligodendrocytes that establish strict contact with neurons, providing them protection and support (Amaral et al., 2016; Verkhratsky and Nedergaard, 2018), microglia are the immune sentinels of the CNS and are critical for its development and surveillance (Ransohoff and Cardona, 2010; Prinz et al., 2019). To do so, microglial cells are extremely heterogeneous because they can exist in many different forms and activation states, from neuro-protective to neuro-destructive (Nayak et al., 2014). According to this, progression or resolution of neuroinflammation or of CNS disorders is strictly relying on the activity of microglia and, being immune cells, it's no surprise that most of the literature on SPM function in the CNS has been focused on this cell subtype. Indeed, not only they seem to express all the identified SPM receptors but also are highly responsive to the pro-resolving and anti-inflammatory effects of several families of SPMs, from lipoxins, E-series and D-series resolvins to protectins and maresins.

These SPMs have been found to strongly reduce microglial activation, their production of pro-inflammatory mediators and morphology and to increase their ability to phagocytize and remove aggregated proteins such as A $\beta$ , as vastly reported in several comprehensive reviews (Chiurchiù et al., 2018; Dokalis and Prinz, 2019). The importance of their role was also reported in several models of neurodegenerative diseases, such as Alzheimer's disease (Wang et al., 2015), multiple sclerosis (Poisson et al., 2015), and Parkinson's disease (Krashia et al., 2019).

Furthermore, being DHA the most abundant fatty acid in the human brain and although microglia express several enzymes responsible for SPM biosynthesis (i.e., COX-2, 5-LOX, 12-LOX, and 15-LOX), thus having what it takes to be the main cellular source of SPMs within the CNS, so far, only few studies have analyzed the cellular origin of SPMs in the brain. For instance, *in vitro* studies demonstrated production of PD1 in mixed human neuron-glia cell cultures (Lukiw et al., 2005) and on the human microglia cell line CHME-3 showed LXA<sub>4</sub> and RvD1 in the conditioned medium (Zhu et al., 2015). Furthermore, immunohistochemical studies on human and murine brains have shown the occurrence of the biosynthetic enzymes 5-LOX and 15-LOX in neurons and glia (Ohtsuki et al., 1995; Lammers

et al., 1996; Pratico et al., 2004; Ikonovic et al., 2008; Haynes and van Leyen, 2013). However, despite lack of evidence on SPM production from neurons or oligodendrocytes, a recent study performed a metabolomic screening on retinal astrocytes and, using liquid chromatography–tandem mass spectrometry, detected pathways markers for DHA-derived resolvins and protectins as well as the two SPMs LXA<sub>4</sub> and LXB<sub>4</sub> and that their levels are reduced following injury. This suggests that the lipoxin circuit, comprising biosynthetic enzymes and the ALX/FPR2 receptor, is present in astrocytes and that its functional activity is compromised in response to injury (Livne-Bar et al., 2017). In this study it was also reported that such astrocyte-derived lipoxins promoted neuroprotection in a chronic model of glaucoma, identifying a potential paracrine mechanism that coordinates neuronal homeostasis and inflammation in the CNS.

These evidences account for the existence of a crosstalk between glial cells and neurons that is not only limited to the synapses or to the release of inflammatory mediators or neurotrophic factors but also on the activation of pro-resolution pathways that involve the production of SPMs, most likely from microglia and astrocytes, that exert autocrine or paracrine activity on the resolution of inflammatory events or injury occurring to the neurons or to oligodendrocytes, in order to maintain CNS homeostasis and to sustain reparative processes (Figure 2).

## SPMs AS NOVEL TOOLS TO MODULATE NEURO-GLIAL COMMUNICATIONS

In addition to classical means of cell-to-cell communication, the transfer of extracellular vesicles (EVs) from microglia, astrocytes or oligodendrocytes to surrounding cells has been recently proposed to be an efficient mechanism by which these cells may contribute to sustain brain homeostasis, immune functions and tissue regeneration. Indeed, not only glia and neurons can secrete EVs exerting a profound impact in CNS pathophysiology, but brain-derived EVs can also travel further through the body via the CSF and blood and thus impact also peripheral districts (Prada et al., 2013; Lizarraga-Valderrama and Sheridan, 2021). Independently of their cell origin and in comparison with their originating cells, EVs are enriched in membrane phospholipids containing saturated and unsaturated fatty acids.

Since SPMs are indeed originated from such membrane phospholipids, EVs may also represent sources of these lipid mediators either already formed or partially synthesized by their biosynthesizing enzymes packaged within vesicles. Conveying SPMs via EVs represents a mean to protect these mediators from degradation and exchange these molecules between different cell types (Sagini et al., 2018). Indeed, through a systematic lipidomic profiling of EVs isolated from inflammatory exudates during the time course of a self-resolving inflammation, several SPM precursors such as 14-HDHA and 17-HDHA were identified. The level of these precursors was high during the initial phase of acute inflammatory response, decreased during the peak of inflammation, and accumulated in resolution. Based on these results, nanoparticles containing RvD1 or LXA<sub>4</sub> analogs were constructed and were shown to reduce the influx of granulocytes

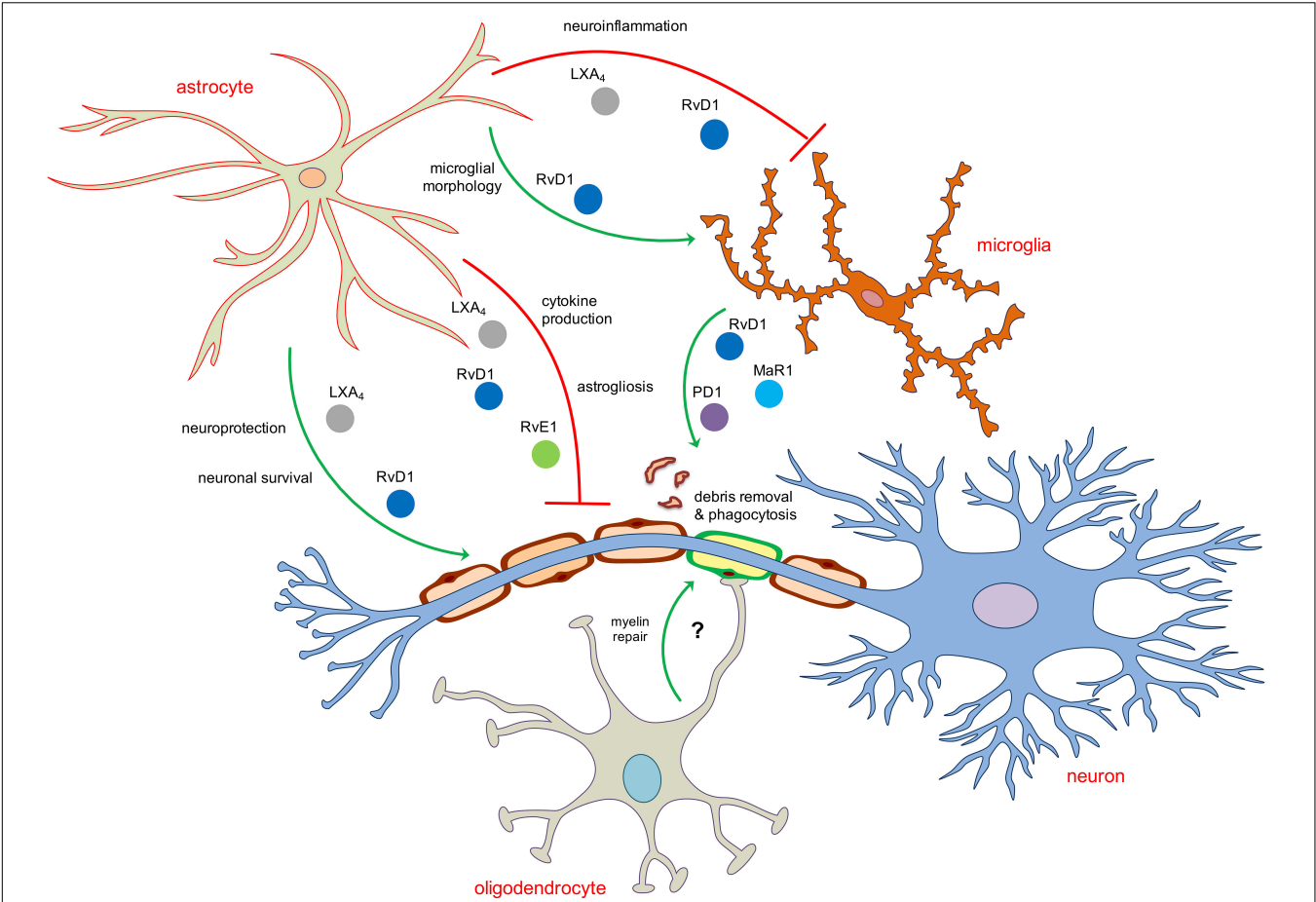


**FIGURE 2 |** Schematic representation of the main role of SPMs in modulating neuroinflammatory and pro-resolving functions of astroglia and oligodendroglia. Astrocytes and microglia are the two main direct targets of SPMs. LXA<sub>4</sub>, RvD1 and RvE1 inhibit astrocytic and microglial reactivity mainly by reducing pro-inflammatory cytokines or shaping their morphology as well as induce neuroprotection and neuronal survival acting indirectly on astrocytes. The removal of debris, dead cells or aggregated proteins in the brain is operated mainly by RvD1, MaR1 and PD1 by enhancing the phagocytic activity of microglial cells. No direct role of SPMs on oligodendrocytes has been reported yet.

**TABLE 1 |** Main role of SPMs in astrocytes and oligodendrocytes.

SPM	Receptor	Target cell	Function	References
LXA4	ALX/FPR2	Astrocytes	Inhibition of IL-8 and ICAM-I Reduction of astrocyte reactivity	Decker et al., 2009; Svensson et al., 2007; Kantarci et al., 2018; Ren et al., 2020
RvD1	ALX/FPR2	Astrocytes	Reduction of astrocyte reactivity Protection of astrocytic mitochondria	Terrando et al., 2013; Bisiocchia et al., 2018; Krashia et al., 2019; Ren et al., 2020
RvD2	GPR18/DRV2	Astrocytes	Not reported	–
RvE1	ChemR23/ERV1	Astrocytes	Reduction of astrocyte reactivity	Kantarci et al., 2018
PD1	GPR37	Astrocytes	Not reported	–
		Oligodendrocytes	Not reported	–
MaR1	LgR6	Astrocytes	Not reported	–

and to shorten resolution intervals in a mouse model of peritonitis (Norling et al., 2011).

Accumulating evidence account for a role for EVs in the pathogenesis of several neurodegenerative diseases including AD and PD; however, the role of EVs in neuronal communication under normal physiological conditions remains under investigated. Deciphering the role of EVs under

physiological conditions is crucial for developing therapies to cure or alleviate neurological diseases. For instance, a lipidomic analysis of the composition of brain-derived EVs from patients affected by the different neurodegenerative diseases would be instrumental to identify potential resolution defects associated to a specific pathology and such information could be used to design personalized nanomedicines loaded with specific SPMs

(either obtained from EVs extracted from young healthy humans and/or bioengineered) and administrated to patients. However, more information on the specific mechanisms of cell recognition and internalization of EVs by recipient cells as well as how cargoes are unloaded and processed by the recipient cells is required to develop such targeted treatments.

## CONCLUDING REMARKS

For a long time it was believed that the acute response to inflammation both in the periphery and in the CNS passively dissipated over time due to a reduced production of inflammatory mediators from either resident non-neuronal cells or infiltrated leukocytes; however, it has been more recently appreciated that also in the brain termination of neuroinflammation is kept in homeostatic balance by the active process of resolution, orchestrated by several families of SPMs, and that ultimately results in the maintenance of brain homeostasis and avoidance of neurodegeneration and subsequent development of neurodegenerative diseases.

Although the biochemical and physiological processes governing the production and biological activities of such pro-resolving mediators and pathways have been largely investigated in peripheral tissues, knowledge on how resolution of inflammation operates in the brain is still at infancy due to many reasons. Firstly, the biggest unresolved issue is to identify the anatomical and cellular source of SPMs within the CNS. Indeed, despite few evidences suggest a local production of SPMs in the brain, probably operated by microglia and astrocytes, as yet it's not clear which cell type is their actual source, due to the use of mixed cultures, of immortalized cell lines or methods of SPM detection by commercial EIA kits instead of the gold standard liquid chromatography mass spectrometry. As happens in the periphery, where the vascular endothelium is actively involved in the recruitment of leukocytes and in the initial steps of SPM biosynthesis, it is possible that other cells from the brain parenchyma, such as ependymal cells of brain ventricles or choroid plexus, might be involved in SPM production. This is also complicated by their very short half-life and rapid metabolic inactivation, making their endogenous levels challenging to detect in brain cells that are already difficult to culture. The additional difficulty to culture isolated and viable brain-derived cells from mice models or from fresh human biopsies in order to study SPM metabolism and functions make the research in this field even more challenging.

## REFERENCES

- Amaral, A. I., Tavares, J. M., Sonnewald, U., and Kotter, M. R. (2016). Oligodendrocytes: development. *Physiol. Glucose Metab. Adv. Neurobiol.* 13, 275–294. doi: 10.1007/978-3-319-45096-4\_10
- Ariel, A., Fredman, G., Sun, Y. P., Kantarci, A., Van Dyke, T. E., Luster, A. D., et al. (2006). Apoptotic neutrophils and T cells sequester chemokines during immune response resolution through modulation of CCR5 expression. *Nat. Immunol.* 7, 1209–1216. doi: 10.1038/ni1392
- Since astrocytes are natural neuroprotectors and they are the brain cells that express the highest levels of all SPM biosynthesizing enzymes and their target receptors, it is likely that brain resilience can be enhanced by mobilizing the protective potential of these cells through the activation of pro-resolving pathways that indirectly affect neuronal or non-neuronal cells. For instance, the majority of the SPM-mediated potent anti-inflammatory effects observed in microglial cells are likely to be mediated by astrocytes because microglia bear low levels or do not express key SPM receptors such ALX/FPR2, ChemR23, and GPR37. Furthermore, even the SPM-induced protective effects on neurons or oligodendrocytes seem to be indirectly resolved by either astrocytes or microglia, possibly due to the role of SPM in shifting their phenotype toward a pro-resolving and anti-inflammatory one (Table 1 and Figure 2).
- This not only suggests that a crosstalk between glial cells and neurons occurs also during the process of resolution of inflammation, where cells support and help each other to instate resolute and protective pathways, but also that dysregulations and defects in resolving inflammation affecting such crosstalk can be involved in the onset and progression of several neuropathologies. In this context, much less is known so far on the exact role of these processes in the different diseases of the CNS. Addressing these questions and how the different brain cells establishing interactions during a resolution process will be a major challenge for the near future and will be helpful to also understand their pathophysiological role and to design better therapeutic strategies aimed at boosting pro-resolving cellular networks rather than breaking off pro-inflammatory ones. This could be achieved by inducing SPM biosynthesis, inhibiting their metabolic inactivation or by synthesizing stable analogs that could be used to treat pathological conditions characterized by exacerbated chronic inflammation and neuroinflammatory diseases.

## AUTHOR CONTRIBUTIONS

MT and VC designed and wrote the manuscript. Both authors contributed to the article and approved the submitted version.

## FUNDING

This work was supported by Italian Foundation of Multiple Sclerosis (FISM 2017/R/08) and the Italian Ministry of Health grant (GR-2016-02362380) to VC.

- Arita, M., Bianchini, F., Aliberti, J., Sher, A., Chiang, N., Hong, S., et al. (2005). Stereochemical assignment, antiinflammatory properties, and receptor for the omega-3 lipid mediator resolvin E1. *J. Exp. Med.* 201, 713–722. doi: 10.1084/jem.20042031
- Bang, S., Xie, Y. K., Zhang, Z. J., Wang, Z., Xu, Z. Z., and Ji, R. R. (2018). GPR37 regulates macrophage phagocytosis and resolution of inflammatory pain. *J. Clin. Invest.* 128, 3568–3582. doi: 10.1172/JCI99888
- Bannenberg, G., and Serhan, C. N. (2010). Specialized pro-resolving lipid mediators in the inflammatory response: an update.



- Biochim. Biophys. Acta* 1801, 1260–1273. doi: 10.1016/j.bbali.2010.08.002
- Basil, M. C., and Levy, B. D. (2016). Specialized pro-resolving mediators: endogenous regulators of infection and inflammation. *Nat. Rev. Immunol.* 16, 51–67. doi: 10.1038/nri.2015.4
- Bennet, M., and Gilroy, D. W. (2016). Lipid mediators in inflammation. *Microbiol. Spec.* 4:MCHD-0035-2016. doi: 10.1128/microbiolspec.MCHD-0035-2016
- Bisicchia, E., Sasso, V., Catanzaro, G., Leuti, A., Besharat, Z. M., Chiacchiarini, M., et al. (2018). Resolvin D1 halts remote neuroinflammation and improves functional recovery after focal brain damage via ALX/FPR2 receptor-regulated MicroRNAs. *Mol. Neurobiol.* 55, 6894–6905. doi: 10.1007/s12035-018-0889-z
- Bocazzi, M., Van Steenwinkel, J., Schang, A. L., Faivre, V., Le Charpentier, T., Bokobza, C., et al. (2021). The immune-inflammatory response of oligodendrocytes in a murine model of preterm white matter injury: the role of TLR3 activation. *Cell Death Dis.* 12:166. doi: 10.1038/s41419-021-03446-3449
- Bradl, M., and Lassmann, H. (2010). Oligodendrocytes: biology and pathology. *Acta Neuropathol.* 119, 37–53. doi: 10.1007/s00401-009-0601-605
- Brandenburg, L. O., Konrad, M., Wruck, C. J., Koch, T., Lucius, R., and Pufe, T. (2010). Functional and physical interactions between formyl-peptide-receptors and scavenger receptor MARCO and their involvement in amyloid beta 1-42-induced signal transduction in glial cells. *J. Neurochem.* 113, 749–760. doi: 10.1111/j.1471-4159.2010.06637.x
- Cahoy, J. D., Emery, B., Kaushal, A., Foo, L. C., Zamanian, J. L., Christopherson, K. S., et al. (2008). A transcriptome database for astrocytes, neurons, and oligodendrocytes: a new resource for understanding brain development and function. *J. Neurosci.* 28, 264–278. doi: 10.1523/JNEUROSCI.4178-07.2008
- Cattaneo, F., Guerra, G., and Ammendola, R. (2010). Expression and signaling of formyl-peptide receptors in the brain. *Neurochem* 35, 2018–2026. doi: 10.1007/s11064-010-0301-305
- Chamani, S., Bianconi, V., Tasbandi, A., Pirro, M., Barreto, G. E., Jamialahmadi, T., et al. (2020). Resolution of inflammation in neurodegenerative diseases: the role of resolvins. *Med. Inflamm.* 2020:3267172. doi: 10.1155/2020/3267172
- Chiang, N., Arita, M., and Serhan, C. N. (2005). Anti-inflammatory circuitry: lipoxin, aspirin-triggered lipoxins and their receptor ALX. *Prostaglandins Leukot. Essent. Fatty Acids* 73, 163–177. doi: 10.1016/j.plefa.2005.05.003
- Chiang, N., Fierro, I. M., Gronert, K., and Serhan, C. N. (2000). Activation of lipoxin A(4) receptors by aspirin-triggered lipoxins and select peptides evokes ligand-specific responses in inflammation. *J. Exp. Med.* 191, 1197–1208. doi: 10.1084/jem.191.7.1197
- Chiang, N., Libreros, S., Norris, P. C., de la Rosa, X., and Serhan, C. N. (2019). Maresin 1 activates LGR6 receptor promoting phagocyte immunoresolvent functions. *J. Clin. Invest.* 129, 5294–5311. doi: 10.1172/JCI129448
- Chiang, N., and Serhan, C. N. (2017). Structural elucidation and physiologic functions of specialized pro-resolving mediators and their receptors. *Mol. Aspects. Med.* 58, 114–129. doi: 10.1016/j.mam.2017.03.005
- Chiurchiù, V., Leuti, A., and Maccarrone, M. (2018). Bioactive lipids and chronic inflammation: managing the fire within. *Front. Immunol.* 9:38. doi: 10.3389/fimmu.2018.00038
- Da Mesquita, S., Fu, Z., and Kipnis, J. (2018a). The meningeal lymphatic system: a new player in neurophysiology. *Neuron* 100, 375–388. doi: 10.1016/j.neuron.2018.09.022
- Da Mesquita, S., Louveau, A., Vaccari, A., Smirnov, I., Cornelison, R. C., Kingsmore, K. M., et al. (2018b). Functional aspects of meningeal lymphatics in ageing and Alzheimer's disease. *Nature* 560, 185–191. doi: 10.1038/s41586-018-0368-368
- Dalli, J., Chiang, N., and Serhan, C. N. (2015). Elucidation of novel 13-series resolvins that increase with atorvastatin and clear infections. *Nat. Med.* 21, 1071–1075. doi: 10.1038/nm.3911
- Dalli, J., Colas, R. A., and Serhan, C. N. (2013). Novel n-3 immunoresolvents: structures and actions. *Sci. Rep.* 3:1940. doi: 10.1038/srep01940
- Dalli, J., Vlasakov, I., Riley, I. R., Rodriguez, A. R., Spur, B. W., Petasis, N. A., et al. (2016). Maresin conjugates in tissue regeneration biosynthesis enzymes in human macrophages. *Proc. Natl. Acad. Sci. U S A.* 113, 12232–12237. doi: 10.1073/pnas.1607003113
- Decker, Y., McBean, G., and Godson, C. (2009). Lipoxin A4 inhibits IL-1beta-induced IL-8 and ICAM-1 expression in 1321N1 human astrocytoma cells. *Am. J. Physiol. Cell Physiol.* 296, C1420–C1427. doi: 10.1152/ajpcell.00380.2008
- Deng, B., Wang, C. W., Arnardottir, H. H., Li, Y., Cheng, C. Y., Dalli, J., et al. (2014). Maresin biosynthesis and identification of maresin 2, a new anti-inflammatory and pro-resolving mediator from human macrophages. *PLoS One* 9:e102362. doi: 10.1371/journal.pone.0102362
- Ding, Z. B., Song, L. J., Wang, Q., Kumar, G., Yan, Y. Q., and Ma, C. G. (2021). Astrocytes: a double-edged sword in neurodegenerative diseases. *Neural Regen. Res.* 16, 1702–1710. doi: 10.4103/1673-5374.306064
- Dokalis, N., and Prinz, M. (2019). Resolution of neuroinflammation: mechanisms and potential therapeutic option. *Semin. Immunopathol.* 41, 699–709. doi: 10.1007/s00281-019-00764-761
- Emre, C., Hjorth, E., Bharani, K., Carroll, S., Granholm, A. C., and Schultzberg, M. (2020). Receptors for pro-resolving mediators are increased in Alzheimer's disease brain. *Brain Pathol.* 30, 614–640. doi: 10.1111/bpa.12812
- Flak, M. B., Koenis, D. S., Sobrino, A., Smith, J., Pistorius, K., Palmas, F., et al. (2020). GPR101 mediates the pro-resolving actions of RvD5n-3 DPA in arthritis and infections. *J. Clin. Invest.* 130, 359–373. doi: 10.1172/JCI131609
- Freire, M. O., and Van Dyke, T. E. (2013). Natural resolution of inflammation. *Periodontol* 2000 63, 149–164. doi: 10.1111/prd.12034
- Fujita-Jimbo, E., Yu, Z. L., Li, H., Yamagata, T., Mori, M., Momoi, T., et al. (2012). Mutation in Parkinson disease-associated, G-protein-coupled receptor 37 (GPR37/PaelR) is related to autism spectrum disorder. *PLoS One* 7:e51155. doi: 10.1371/journal.pone.0051155
- Galey, D., Becker, K., Haughey, N., Kolehua, A., Taub, D., Woodward, J., et al. (2003). Differential transcriptional regulation by human immunodeficiency virus type 1 and gp120 in human astrocytes. *J. Neurovirol.* 9, 358–371. doi: 10.1080/13550280390201119
- Grabiec, U., Hohmann, T., Ghadban, C., Rothgänger, C., Wong, D., Antonietti, A., et al. (2019). Protective effect of N-Arachidonoyl Glycine-GPR18 signaling after excitotoxic lesion in murine organotypic hippocampal slice cultures. *Int. J. Mol. Sci.* 20:1266. doi: 10.3390/ijms20061266
- Han, Y. H., Shin, K. O., Kim, J. Y., Khadka, D. B., Kim, H. J., Lee, Y. M., et al. (2019). A maresin 1/ROR $\alpha$ /12-lipoxygenase autoregulatory circuit prevents inflammation and progression of nonalcoholic steatohepatitis. *J. Clin. Invest.* 129, 1684–1698. doi: 10.1172/JCI124219
- Hansen, T. V., Dalli, J., and Serhan, C. N. (2017). The novel lipid mediator PD1n-3 DPA: an overview of the structural elucidation, synthesis, biosynthesis and bioactions. *Prostaglandins Other Lipid Mediat.* 133, 103–110. doi: 10.1016/j.prostaglandins.2017.06.003
- Haynes, R. L., and van Leyen, K. (2013). 12/15-lipoxygenase expression is increased in oligodendrocytes and microglia of periventricular leukomalacia. *Dev. Neurosci.* 35, 140–154. doi: 10.1159/000350230
- Ikonomic, M. D., Abrahamson, E. E., Uz, T., Manev, H., and Dekosky, S. T. (2008). Increased 5-lipoxygenase immunoreactivity in the hippocampus of patients with Alzheimer's disease. *J. Histochem. Cytochem.* 56, 1065–1073. doi: 10.1369/jhc.2008.951855
- Isobe, Y., Arita, M., Matsueda, S., Iwamoto, R., Fujihara, T., Nakanishi, H., et al. (2012). Identification and structure determination of novel anti-inflammatory mediator resolvin E3, 17,18-dihydroxyicosapentaenoic acid. *J. Biol. Chem.* 287, 10525–10534. doi: 10.1074/jbc.M112.340612
- Jensen, C. J., Massie, A., and De Keyser, J. (2013). Immune players in the CNS: the astrocyte. *J. Neuroimmune Pharmacol.* 8, 824–839. doi: 10.1007/s11481-013-9480-9486
- Jolly, S., Bazargani, N., Quiroga, A. C., Pringle, N. P., Attwell, D., Richardson, W. D., et al. (2018). G protein-coupled receptor 37-like 1 modulates astrocyte glutamate transporters and neuronal NMDA receptors and is neuroprotective in ischemia. *Glia* 66, 47–61. doi: 10.1002/glia.23198
- Kam, A. Y., Tse, T. T., Kwan, D. H., and Wong, Y. H. (2007). Formyl peptide receptor like 1 differentially requires mitogen-activated protein kinases for the induction of glial fibrillary acidic protein and interleukin-1alpha in human U87 astrocytoma cells. *Cell. Signal.* 19, 2106–2117. doi: 10.1016/j.cellsig.2007.06.005
- Kantarci, A., Aytan, N., Palaska, I., Stephens, D., Crabtree, L., Benincasa, C., et al. (2018). Combined administration of resolvin E1 and lipoxin A4 resolves inflammation in a murine model of Alzheimer's disease. *Exp. Neurol.* 300, 111–120. doi: 10.1016/j.expneurol.2017.11.005
- Kooij, G., Troletti, C. D., Leuti, A., Norris, P. C., Riley, I., and Albanese, M. (2020). Specialized pro-resolving lipid mediators are differentially altered in peripheral blood of patients with multiple sclerosis and attenuate monocyte and

- blood-brain barrier dysfunction. *Haematologica* 105, 2056–2070. doi: 10.3324/haematol.2019.219519
- Krashia, P., Cordella, A., Nobili, A., La Barbera, L., Federici, M., Leuti, A., et al. (2019). Blunting neuroinflammation with resolvin D1 prevents early pathology in a rat model of Parkinson's disease. *Nat. Commun.* 10:3945. doi: 10.1038/s41467-019-11928-w
- Lammers, C. H., Schweitzer, P., Facchinetti, P., Arrang, J. M., Madamba, S. G., Siggins, G. R., et al. (1996). Arachidonate 5-lipoxygenase and its activating protein: prominent hippocampal expression and role in somatostatin signaling. *J. Neurochem.* 66, 147–152. doi: 10.1046/j.1471-4159.1996.66010147.x
- Le, Y., Hu, J., Gong, W., Shen, W., Li, B., Dunlop, N. M., et al. (2000). Expression of functional formyl peptide receptors by human astrocytoma cell lines. *J. Neuroimmunol.* 111, 102–108. doi: 10.1016/s0165-5728(00)00373-378
- Leuti, A., Maccarrone, M., and Chiurchiù, V. (2019). Proresolving lipid mediators: endogenous modulators of oxidative stress. *Oxid. Med. Cell. Longev.* 2019:8107265. doi: 10.1155/2019/8107265
- Libreros, S., Shay, A. E., Nshimiyimana, R., Fichtner, D., Martin, M. J., Wourms, N., et al. (2021). A new e-series resolvin: RvE4 stereochemistry and function in efferocytosis of inflammation-resolution. *Front. Immunol.* 11:631319. doi: 10.3389/fimmu.2020.631319
- Liu, B., Mosienko, V., Vaccari Cardoso, B., Prokudina, D., Huentelman, M., Teschemacher, A. G., et al. (2018). Glio- and neuro-protection by prosaposin is mediated by orphan G-protein coupled receptors GPR37L1 and GPR37. *Glia* 66, 2414–2426. doi: 10.1002/glia.23480
- Liu, Y., and Aguzzi, A. (2020). NG2 glia are required for maintaining microglia homeostatic state. *Glia* 68, 345–355. doi: 10.1002/glia.23721
- Livne-Bar, I., Wei, J., Liu, H. H., Alqawlaq, S., Won, G. J., Tuccitto, A., et al. (2017). Astrocyte-derived lipoxins A4 and B4 promote neuroprotection from acute and chronic injury. *J. Clin. Invest.* 127, 4403–4414. doi: 10.1172/JCI77398
- Lizarraga-Valderrama, L. R., and Sheridan, G. K. (2021). Extracellular vesicles and intercellular communication in the central nervous system. *FEBS Lett* doi: 10.1002/1873-3468.14074 [Epub ahead of print].
- Lopes, J. P., Morató, X., Souza, C., Pinhal, C., Machado, N. J., Canas, P. M., et al. (2015). The role of parkinson's disease-associated receptor GPR37 in the hippocampus: functional interplay with the adenosinergic system. *J. Neurochem.* 134, 135–146. doi: 10.1111/jnc.13109
- Lukiw, W. J., Cui, J. G., Marcheselli, V. L., Bodker, M., Botkjaer, A., Gotlinger, K., et al. (2005). A role for docosahexaenoic acid-derived neuroprotectin D1 in neural cell survival and Alzheimer disease. *J. Clin. Invest.* 115, 2774–2783. doi: 10.1172/JCI25420
- Marazziti, D., Golini, E., Gallo, A., Lombardi, M. S., Matteoni, R., and Tocchini-Valentini, G. P. (1997). Cloning of GPR37, a gene located on chromosome 7 encoding a putative G-protein-coupled peptide receptor, from a human frontal brain EST library. *Genomics* 45, 68–77. doi: 10.1006/geno.1997.4900
- Marazziti, D., Mandillo, S., Di Pietro, C., Golini, E., Matteoni, R., and Tocchini-Valentini, G. P. (2007). GPR37 associates with the dopamine transporter to modulate dopamine uptake and behavioral responses to dopaminergic drugs. *Proc. Natl. Acad. Sci. U S A* 104, 9846–9851. doi: 10.1073/pnas.0703368104
- Meyer, R. C., Giddens, M. M., Schaefer, S. A., and Hall, R. A. (2013). Hall GPR37 and GPR37L1 are receptors for the neuroprotective and glioprotective factors prosaptide and prosaposin. *Proc. Natl. Acad. Sci. U S A* 110, 9529–9534. doi: 10.1073/pnas.1219004110
- Miller, S. J. (2018). Astrocyte heterogeneity in the adult central nervous system. *Front. Cell Neurosci.* 12:401. doi: 10.3389/fncel.2018.00401
- Miller, S. J., Philips, T., Kim, N., Dastgheyb, R., Chen, Z., Hsieh, Y. C., et al. (2019). Molecularly defined cortical astroglia subpopulation modulates neurons via secretion of Norrin. *Nat. Neurosci.* 22, 741–752. doi: 10.1038/s41593-019-0366-367
- Moalem, G., Leibowitz-Amit, R., Yoles, E., Mor, F., Cohen, I. R., and Schwartz, M. (1999). Autoimmune T cells protect neurons from secondary degeneration after central nervous system axotomy. *Nat. Med.* 5, 49–55. doi: 10.1038/4734
- Nathan, C., and Ding, A. (2010). Nonresolving inflammation. *Cell* 140, 871–882. doi: 10.1016/j.cell.2010.02.029
- Nayak, D., Roth, T. L., and McGavern, D. B. (2014). Microglia development and function. *Annu. Rev. Immunol.* 32, 367–402. doi: 10.1146/annurev-immunol-032713-120240
- Norling, L. V., Spite, M., Yang, R., Flower, R. J., Perretti, M., and Serhan, C. N. (2011). Cutting edge: humanized nano-proresolving medicines mimic inflammation-resolution, and enhance wound healing. *J. Immunol.* 186, 5543–5547. doi: 10.4049/jimmunol.1003865
- Ohtsuki, T., Matsumoto, M., Hayashi, Y., Yamamoto, K., Kitagawa, K., Ogawa, S., et al. (1995). Reperfusion induces 5-lipoxygenase translocation and leukotriene C4 production in ischemic brain. *Am. J. Physiol.* 268(3 Pt 2), H1249–H1257. doi: 10.1152/ajpheart.1995.268.3.H1249
- Peferoen, L., Kipp, M., van der Valk, P., van Noort, J. M., and Amor, S. (2014). Oligodendrocyte-microglia cross-talk in the central nervous system. *Immunology* 141, 302–313. doi: 10.1111/imm.12163
- Poisson, L. M., Suhail, H., Singh, J., Datta, I., Denic, A., Labuzek, K., et al. (2015). Untargeted plasma metabolomics identifies endogenous metabolite with drug-like properties in chronic animal model of multiple sclerosis. *J. Biol. Chem.* 290, 30697–30712. doi: 10.1074/jbc.M115.679068
- Prada, I., Furlan, R., Matteoli, M., and Verderio, C. (2013). Classical and unconventional pathways of vesicular release in microglia. *Glia* 61, 1003–1017. doi: 10.1002/glia.22497
- Pratico, D., Zhukareva, V., Yao, Y., Uryu, K., Funk, C. D., Lawson, J. A., et al. (2004). 12/15-lipoxygenase is increased in Alzheimer's disease: possible involvement in brain oxidative stress. *Am. J. Pathol.* 164, 1655–1662. doi: 10.1016/S0002-9440(10)63724-63728
- Prinz, M., Jung, S., and Priller, J. (2019). Microglia biology: one century of evolving concepts. *Cell* 179, 292–311. doi: 10.1016/j.cell.2019.08.053
- Ransohoff, R. M., and Cardona, A. E. (2010). The myeloid cells of the central nervous system parenchyma. *Nature* 468, 253–262. doi: 10.1038/nature09615
- Ren, Y. Z., Zhang, B. Z., Zhao, X. J., and Zhang, Z. Y. (2020). Resolvin D1 ameliorates cognitive impairment following traumatic brain injury via protecting astrocytic mitochondria. *J. Neurochem.* 154, 530–546. doi: 10.1111/jnc.14962
- Romano, M., Cianci, E., Simiele, F., and Recchiuti, A. (2015). Lipoxins and aspirin-triggered lipoxins in resolution of inflammation. *Eur. J. Pharmacol.* 760, 49–63. doi: 10.1016/j.ejphar.2015.03.083
- Rustenhoven, J., Drieu, A., Mamuladze, T., de Lima, K. A., Dykstra, T., Wall, M., et al. (2021). Functional characterization of the dural sinuses as a neuroimmune interface. *Cell* 184, 1000–1016.e27. doi: 10.1016/j.cell.2020.12.040
- Sagini, K., Costanzi, E., Emiliani, C., Buratta, S., and Urbanelli, L. (2018). Extracellular vesicles as conveyors of membrane-derived bioactive lipids in immune system. *Int. J. Mol. Sci.* 19:1227. doi: 10.3390/ijms19041227
- Schwartz, M., and Baruch, K. (2014). The resolution of neuroinflammation in neurodegeneration: leukocyte recruitment via the choroid plexus. *EMBO J.* 33, 7–22. doi: 10.1002/embj.201386609
- Serhan, C. N. (2001). Lipoxins and aspirin-triggered 15-epi-lipoxins are endogenous components of antiinflammation: emergence of the counterregulatory side. *Arch. Immunol. Ther. Exp. (Warsz)*. 49, 177–188.
- Serhan, C. N. (2005). Lipoxins and aspirin-triggered 15-epi-lipoxins are the first lipid mediators of endogenous anti-inflammation and resolution. *Prostaglandins Leukot. Essent. Fatty Acids* 73, 141–162. doi: 10.1016/j.plefa.2005.05.002
- Serhan, C. N. (2014). Pro-resolving lipid mediators are leads for resolution physiology. *Nature* 510, 92–101. doi: 10.1038/nature13479
- Serhan, C. N., Chiang, N., and Dalli, J. (2018). New pro-resolving n-3 mediators bridge resolution of infectious inflammation to tissue regeneration. *Mol. Aspects. Med.* 64, 1–17. doi: 10.1016/j.mam.2017.08.002
- Serhan, C. N., Clish, C. B., Brannon, J., Colgan, S. P., Chiang, N., and Gronert, K. (2000). Novel functional sets of lipid-derived mediators with antiinflammatory actions generated from omega-3 fatty acids via cyclooxygenase 2-nonsteroidal antiinflammatory drugs and transcellular processing. *J. Exp. Med.* 192, 1197–1204. doi: 10.1084/jem.192.8.1197
- Serhan, C. N., Dalli, J., Colas, R. A., Winkler, J. W., and Chiang, N. (2015). Protectins and maresins: new pro-resolving families of mediators in acute inflammation and resolution bioactive metabolome. *Biochim. Biophys. Acta.* 1851, 397–413. doi: 10.1016/j.bbalip.2014.08.006
- Serhan, C. N., Gupta, S. K., Perretti, M., Godson, C., Brennan, E., Li, Y., et al. (2020). The Atlas of Inflammation Resolution (AIR). *Mol Aspects Med.* 74:100894. doi: 10.1016/j.mam.2020.100894
- Serhan, C. N., Hamberg, M., and Samuelsson, B. (1984). Trihydroxytetraenes: a novel series of compounds formed from arachidonic acid in human leukocytes. *Biochem. Biophys. Res. Commun.* 118, 943–949. doi: 10.1016/0006-291x(84)91486-91484

- Serhan, C. N., Yang, R., Martinod, K., Kasuga, K., Pillai, P. S., Porter, T. F., et al. (2009). Maresins: novel macrophage mediators with potent antiinflammatory and proresolving actions. *J. Exp. Med.* 206, 15–23. doi: 10.1084/jem.20081880
- Smith, B. M., Giddens, M. M., Neil, J., Owino, S., Nguyen, T. T., Duong, D., et al. (2017). Mice lacking Gpr37 exhibit decreased expression of the myelin-associated glycoprotein MAG and increased susceptibility to demyelination. *Neuroscience* 358, 49–57. doi: 10.1016/j.neuroscience.2017.06.006
- Stadelmann, C., Timmler, S., Barrantes-Freer, A., and Simons, M. (2019). Myelin in the central nervous system: structure, function, and pathology. *Physiol. Rev.* 99, 1381–1431. doi: 10.1152/physrev.00031.2018
- Svensson, C. I., Zattoni, M., and Serhan, C. N. (2007). Lipoxins and aspirin-triggered lipoxin inhibit inflammatory pain processing. *J. Exp. Med.* 204, 245–252. doi: 10.1084/jem.20061826
- Sweitzer, S. M., Colburn, R. W., Rutkowski, M., and DeLeo, J. A. (1999). Acute peripheral inflammation induces moderate glial activation and spinal IL-1 $\beta$  expression that correlates with pain behavior in the rat. *Brain Res.* 829, 209–221. doi: 10.1016/s0006-8993(99)01326-1328
- Talamonti, E., Sasso, V., To, H., Haslam, R. P., Napier, J. A., Ulfhake, B., et al. (2020). Impairment of DHA synthesis alters the expression of neuronal plasticity markers and the brain inflammatory status in mice. *FASEB J.* 34, 2024–2040. doi: 10.1096/fj.201901890RR
- Terrando, N., Gómez-Galán, M., Yang, T., Carlström, M., Gustavsson, D., Harding, R. E., et al. (2013). Aspirin-triggered resolvin D1 prevents surgery-induced cognitive decline. *FASEB J.* 27, 3564–3571. doi: 10.1096/fj.13-230276
- Tjonahen, E., Oh, S. F., Siegelman, J., Elangovan, S., Percarpio, K. B., Hong, S., et al. (2006). Resolvin E2: identification and anti-inflammatory actions: pivotal role of human 5-lipoxygenase in resolvin E series biosynthesis. *Chem. Biol.* 13, 1193–1202. doi: 10.1016/j.chembiol.2006.09.011
- Verkhatsky, A., and Nedergaard, M. (2018). Physiology of Astroglia. *Physiol. Rev.* 98, 239–389. doi: 10.1152/physrev.00042.2016
- Vik, A., and Hansen, T. V. (2021). Stereoselective syntheses and biological activities of E-series resolvins. *Org. Biomol. Chem.* 19, 705–721. doi: 10.1039/d0ob02218g
- Wang, X., Zhu, M., Hjorth, E., Cortés-Toro, V., Eyjolfsson, H., Graff, C., et al. (2015). Resolution of inflammation is altered in Alzheimer's disease. *Alzheimers Dement.* 11, 40–50.e2. doi: 10.1016/j.jalz.2013.12.024
- Yang, H. J., Vainshtein, A., Maik-Rachline, G., and Peles, E. (2016). G protein-coupled receptor 37 is a negative regulator of oligodendrocyte differentiation and myelination. *Nat. Commun.* 7:10884. doi: 10.1038/ncomms10884
- Ye, Z. N., Zhuang, Z., Wu, L. Y., Liu, J. P., Chen, Q., Zhang, X. S., et al. (2016). Expression and cell distribution of leukotriene B4 receptor 1 in the rat brain cortex after experimental subarachnoid hemorrhage. *Brain Res.* 1652, 127–134. doi: 10.1016/j.brainres.2016.10.006
- Zahoor, I., and Giri, S. (2020). Specialized pro-resolving lipid mediators: emerging therapeutic candidates for multiple sclerosis. *Clin. Rev. Allergy Immunol.* 60, 147–163. doi: 10.1007/s12016-020-08796-8794
- Zhang, Y., and Barres, B. A. (2010). Astrocyte heterogeneity: an underappreciated topic in neurobiology. *Curr. Opin. Neurobiol.* 20, 588–594. doi: 10.1016/j.conb.2010.06.005
- Zhang, Y., Chen, K., Sloan, S. A., Bennett, M. L., Scholze, A. R., O'Keefe, S., et al. (2014). An RNA-sequencing transcriptome and splicing database of glia, neurons, and vascular cells of the cerebral cortex. *J. Neurosci.* 34, 11929–11947. doi: 10.1523/JNEUROSCI.1860-14.2014
- Zhu, M., Wang, X., Hjorth, E., and Schultzberg, M. (2015). Differential regulation of resolution in inflammation induced by A $\beta$ 42 and LPS in human microglia. *J. Alzheimers Dis.* 43, 1237–1250. doi: 10.3233/JAD-141233
- Zhuang, Z. Y., Wen, Y. R., Zhang, D. R., Borsello, T., Bonny, C., Strichartz, G. R., et al. (2006). A peptide c-Jun N-terminal kinase (JNK) inhibitor blocks mechanical allodynia after spinal nerve ligation: respective roles of JNK activation in primary sensory neurons and spinal astrocytes for neuropathic pain development and maintenance. *J. Neurosci.* 26, 3551–3560. doi: 10.1523/JNEUROSCI.5290-05.2006

**Conflict of Interest:** The authors declare that the research was conducted in the absence of any commercial or financial relationships that could be construed as a potential conflict of interest.

Copyright © 2021 Tiberi and Chiurchiù. This is an open-access article distributed under the terms of the Creative Commons Attribution License (CC BY). The use, distribution or reproduction in other forums is permitted, provided the original author(s) and the copyright owner(s) are credited and that the original publication in this journal is cited, in accordance with accepted academic practice. No use, distribution or reproduction is permitted which does not comply with these terms.



# Novel Tools and Investigative Approaches for the Study of Oligodendrocyte Precursor Cells (NG2-Glia) in CNS Development and Disease

Christophe Galichet\*, Richard W. Clayton and Robin Lovell-Badge

Laboratory of Stem Cell Biology and Developmental Genetics, The Francis Crick Institute, London, United Kingdom

## OPEN ACCESS

### Edited by:

Francesca Boscia,  
University of Naples Federico II, Italy

### Reviewed by:

Moritz Rossner,  
Ludwig Maximilian University of  
Munich, Germany

Davide Lecca,  
University of Milan, Italy

Akiko Nishiyama,  
University of Connecticut,  
United States

### \*Correspondence:

Christophe Galichet  
christophe.galichet@crick.ac.uk  
<https://orcid.org/0000-0002-2497-2942>

### Specialty section:

This article was submitted to  
Non-Neuronal Cells,  
a section of the journal  
Frontiers in Cellular Neuroscience

**Received:** 26 February 2021

**Accepted:** 07 April 2021

**Published:** 29 April 2021

### Citation:

Galichet C, Clayton RW and  
Lovell-Badge R (2021) Novel Tools  
and Investigative Approaches for the  
Study of Oligodendrocyte Precursor  
Cells (NG2-Glia) in CNS Development  
and Disease.  
*Front. Cell. Neurosci.* 15:673132.  
doi: 10.3389/fncel.2021.673132

Oligodendrocyte progenitor cells (OPCs), also referred to as NG2-glia, are the most proliferative cell type in the adult central nervous system. While the primary role of OPCs is to serve as progenitors for oligodendrocytes, in recent years, it has become increasingly clear that OPCs fulfil a number of other functions. Indeed, independent of their role as stem cells, it is evident that OPCs can regulate the metabolic environment, directly interact with and modulate neuronal function, maintain the blood brain barrier (BBB) and regulate inflammation. In this review article, we discuss the state-of-the-art tools and investigative approaches being used to characterize the biology and function of OPCs. From functional genetic investigation to single cell sequencing and from lineage tracing to functional imaging, we discuss the important discoveries uncovered by these techniques, such as functional and spatial OPC heterogeneity, novel OPC marker genes, the interaction of OPCs with other cells types, and how OPCs integrate and respond to signals from neighboring cells. Finally, we review the use of *in vitro* assay to assess OPC functions. These methodologies promise to lead to ever greater understanding of this enigmatic cell type, which in turn will shed light on the pathogenesis and potential treatment strategies for a number of diseases, such as multiple sclerosis (MS) and gliomas.

**Keywords:** oligodendrocyte precursor cells, NG2-glia, heterogeneity, imaging, sequencing, genetic alteration

## INTRODUCTION

Oligodendrocytes (OLs) are the myelin-producing cells of the central nervous system (CNS) and play an essential role in facilitating neuronal signal conduction. OLs are the most numerous of the various types of glial cell in the adult mouse brain, representing approximately 20% of all brain cells (Valério-Gomes et al., 2018), and while OLs can be found throughout the entire CNS, they are most abundant in white matter tracts (Valério-Gomes et al., 2018). OLs are derived from precursor cells that can be defined by expression of the proteoglycan NG2, *neuron-glia antigen 2* (also known as CSPG4, *Chondroitin Sulfate Proteoglycan 4*; **Figure 1**). These progenitor cells are therefore frequently referred to as “NG2-glia,” but this term is often used interchangeably with that of “oligodendrocyte precursor cells” (OPCs), which we will use throughout this review article.



The process of oligodendrocyte lineage differentiation from OPCs, to pre-OLs, maturing OLs, and finally, fully mature OLs, has been well delineated, with many underlying transcription factors and signaling pathways having been shown to play a role (**Figure 1**; for review: Elbaz and Popko, 2019; Kuhn et al., 2019). In mice, the majority of OLs are generated within the first 4 weeks of post-natal life. However, generation of new OLs continues throughout adulthood (Rivers et al., 2008; Kang et al., 2010; Zhu et al., 2011), although this process declines with age, and is influenced by environmental factors such as daylight or physical exercise (for review: Wang and Young, 2014). Many excellent reviews have already extensively covered the subject of OL development (Bergles and Richardson, 2015; Traiffort et al., 2016; Elbaz and Popko, 2019; Kuhn et al., 2019; Boshans et al., 2020).

Similar to OLs, OPCs are located throughout the CNS. In the adult brain, OPCs represent approximately 5–10% of all brain cells, and are the most proliferative cell type (Dawson et al., 2000, 2003). This proliferative behavior makes OPCs especially sensitive to experimental manipulations of the cell cycle (Djogo et al., 2016). Subtypes of OPCs have been described according to various parameters, such as their spatial relation to the brain's vasculature: e.g., perivascular, parenchymal, and intermediate (Seo et al., 2014; Maki et al., 2015; Kishida et al., 2019), whether they are located in white or gray matter, or according to the differential expression of receptors and ion channels (Spitzer et al., 2019). Morphologically, OPCs have small, rounded cell bodies (10–15  $\mu\text{m}$ ) and exhibit extensive branching processes. In gray matter, these processes spread out from the OPC cell body in a radial manner, whereas in white matter, they are more longitudinally orientated, following the path of axons in tracts of white matter (Levine et al., 2001). The full extent of the potential morphological, functional and molecular heterogeneity of OPCs remains unclear, as does the importance of different subsets of OPCs to brain function and disease (Zong et al., 2015; Duncan and Radcliff, 2016).

Outside of their role as progenitor cells for OLs, recent evidence has demonstrated that OPCs may have additional functions, such as interacting with other cell types and modulating their function. For example, not only do OPCs receive synaptic input from both excitatory and inhibitory neurons (Bergles et al., 2000; Lin and Bergles, 2004; Vélez-Fort et al., 2010; Nagy et al., 2017), they also synthesize neuro-modulatory factors such as prostaglandins D2 synthetase and neuronal pentrazin 2 (Sakry et al., 2015). NG2 proteoglycan, the stereotypical marker of OPCs, has itself been shown to modulate NMDA-dependent long-term potentiation and AMPA receptor sub-unit composition in excitatory neurons (Sakry et al., 2014). Moreover, targeted ablation of OPCs results in deficits in glutamatergic neurotransmission (Birey et al., 2015).

OPCs also receive inhibitory neuronal input (Lin and Bergles, 2004; Kukley et al., 2008), which, at least in the mouse cerebellum, is mediated through GABA<sub>A</sub> receptors (Labrada-Moncada et al., 2020); however the functional consequence of this interaction remains unclear.

OPCs also interact with other non-neuronal cell types including astrocytes, which themselves have many roles, such

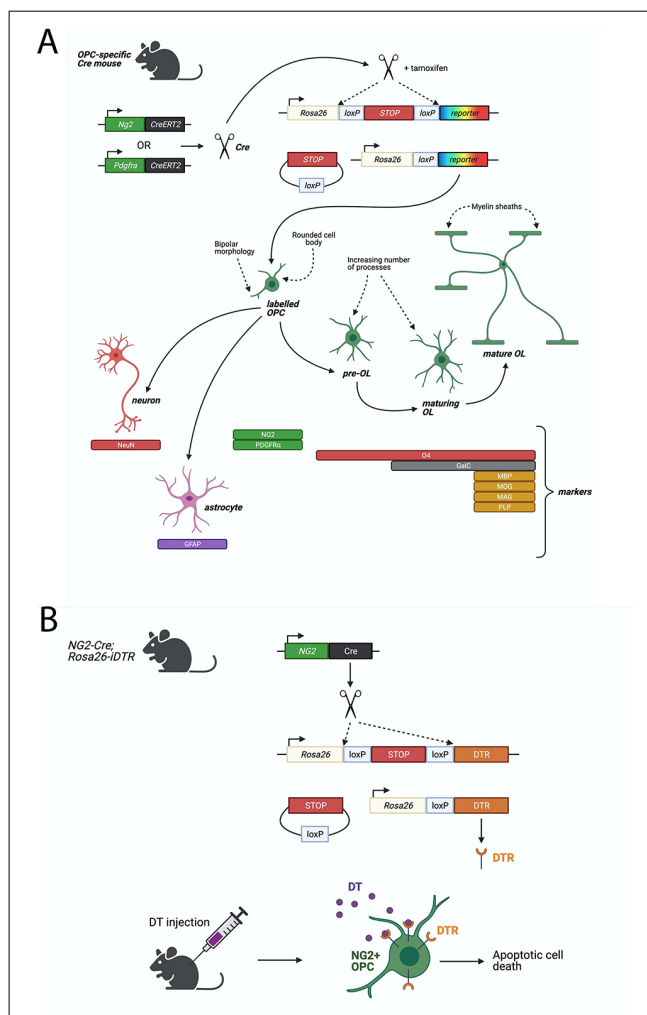


**FIGURE 1 |** Cre-LoxP based systems to study Oligodendrocyte progenitor cell (OPC) functions. **(A)** Fluorescent proteins can be specifically expressed in OPCs in a Cre-LoxP system where Cre-recombinase or Cre-ERT2 (Cre fused to a mutant estrogen ligand-binding domain) is expressed downstream of an OPC-specific marker, such as NG2 or PDGFR $\alpha$ . Upon Tamoxifen administration (for Cre-ERT2), Cre-recombinase excises a floxed stop signal, which then permits expression of fluorescent protein under the ubiquitous Rosa26 promoter. Fluorescently-labeled OPCs will transmit the excised allele to their progeny. Lineage tracing of labeled-NG2-glia showed that OPCs give rise primarily to MBP<sup>+</sup>, MAG<sup>+</sup>, MOG<sup>+</sup>, PLP<sup>+</sup> oligodendrocytes, but could also generate GFAP<sup>+</sup> astrocytes or NeuN<sup>+</sup> neurons. **(B)** Diphtheria toxin receptor (DTR) can be specifically expressed in OPCs by the Cre-LoxP system described above. Cre-recombinase excises a floxed stop signal, which then permits expression of DTR under the ubiquitous Rosa26 promoter. Injection of diphtheria toxin (DT) then elicits apoptotic cell death in DTR-expressing cells. In a non-inducible system, such as the one depicted, DTR will be expressed in NG2<sup>+</sup> cells and their progeny which (in the case of OPCs) will result in cell death of OPCs but also any derived progeny, including oligodendrocytes. Such models must be validated for specificity of expression of DTR in the desired cell type, such as *via* immunostaining for DTR and OPC-specific markers, or by quantifying loss of OPCs and other cell types following DT-administration.

as supporting and modulating neuronal function, or from regulating cerebral blood flow to maintaining the blood brain barrier (BBB; for review: Nutma et al., 2020) and microglia, which

can be considered the immune cells of the CNS (for review: Domingues et al., 2016). Altogether, these findings indicate the existence and functional importance of bi-directional crosstalk between OPCs, neurons, and other cell types, and have shed light on the extent to which normal function of the adult brain may be dependent on OPCs.

It is becoming increasingly clear that OPCs are of great clinical importance, and understanding their biology and function is a prerequisite to understanding their potential role in various diseases. For example, many conditions are associated with defective myelination, such as multiple sclerosis (MS) (MS, an auto-immune disease that results in the destruction of myelin), Devic's disease (where inflammation results in subsequent demyelination of the CNS) or exposure to chemical toxins that directly affect myelin and/or OLs (for review: Duncan and Radcliff, 2016). The formation of gliomas, including oligodendrogliomas, implicates OPCs as they represent a potential cell type from which these tumors can originate (for review: Zong et al., 2015), and the functional interaction of OPCs with neurons and other cell types may indicate their relevance for a wide range of other conditions, for example, hypopituitarism or depression (Birey et al., 2015; Djogo et al., 2016).

In recent years, our understanding of different OPC functions and characteristics has greatly expanded, and several excellent reviews have highlighted this (Dawson et al., 2000; Levine et al., 2001; Dimou and Gallo, 2015; Domingues et al., 2016; Eugenin-Von Bernhardt and Dimou, 2016; Foerster et al., 2019; Kuhn et al., 2019; Hirbec et al., 2020). In this review article, we focus our discussion on both established and novel tools and approaches that can be used to investigate the roles of OPCs in the developing and adult brain. We cover functional approaches, including use of various transgenic mice and experimental treatments, transcriptomic techniques, available imaging methodologies and physiological approaches such as electrophysiology and optogenetics, and we also discuss the multitude of culture systems used to generate and maintain OPCs *in vitro*, including 2D and 3D techniques, using primary animal or human cell lines or OPCs derived from induced pluripotent stem cells.

## GENETIC TECHNOLOGIES

### Functional Genetics

The use of genetically altered animals offers several advantages compared to *in vitro* experiments, such as being able to study the functions of genes in an endogenous environment, with full interplay between different organ systems. Nevertheless, *in vitro* methods, which are described later in the review, bring invaluable data that often cannot be achieved using animal models. Functional genetic approaches, have revealed both intrinsic and extrinsic factors associated with different stages of OPC development; from initiation, proliferation, and maintenance to differentiation into pre-myelinating OLs and subsequently myelinating OLs (Bergles and Richardson, 2015; Elbaz and Popko, 2019; Boshans et al., 2020). For example, the

use of transgenes expressing extrinsic factors have shown how several secreted factors regulate this process, including platelet-derived growth factor (PDGF; Woodruff et al., 2004), and thyroid hormone (Ahlgren et al., 1997). More recently, progesterone has been shown to up-regulate expression of *NG2*, *PDGFR $\alpha$*  and *Sox9* (González-Orozco et al., 2020). OPC-derived interleukin-33 (IL-33) has also been shown to regulate the differentiation of OLs to mature OLs *in vitro*, by lentivirus-mediated knock-down experiments resulting in a down-regulation of OL differentiation genes, and *in vivo*, by analyzing *IL-33* null mice which revealed defective myelination in the corpus callosum (Sung et al., 2019). Cells of the OPC lineage are also influenced by other systemic or environmental changes (ageing, inflammation or hypoxia; for review: Baydyuk et al., 2020). Extrinsic factors also include different cell types with which cells of the OPC lineage are in contact (neurons, astrocytes, blood vessels and microglia), some of which were manipulated by genetic alteration while other evidence came from co-culture *in vitro* experiments (for review: Baydyuk et al., 2020).

An especially informative genetic approach involves conditional expression of diphtheria toxin (DT) receptor (iDTR), enabling targeted ablation of OPCs in the adult mouse brain. Expression of Cre-inducible iDTR in NG2-expressing cells has allowed for the targeted induction of cell death in OPCs following DT administration (Figure 1; Birey et al., 2015; Zhang S.-Z. et al., 2019; Liu and Aguzzi, 2020). By this method, tissue-specific ablation of OPCs in the mouse prefrontal cortex was achieved by delivering DT *via* a cannula implanted into the targeted brain region, with the result of causing depressive-like behaviors, indicated by reduced open field activity (Birey et al., 2015). It was subsequently found that this loss of OPCs leads to deficits in glutamatergic neurotransmission as well as in extracellular glutamate uptake by astrocytes (Birey et al., 2015).

Similar studies, again using DT-mediated ablation of NG2-expressing cells, have provided the first indications of a role of OPCs in the maintenance of brain immune homeostasis and, while it has been known for some time that microglia can regulate the behavior and differentiation of OPCs (reviewed by Domingues et al., 2016), these studies have shown that OPCs can, in turn, modulate microglia (Zhang S.-Z. et al., 2019; Liu and Aguzzi, 2020; Marsters et al., 2020; Mecha et al., 2020). In the absence of NG2-positive OPCs, microglia become hypersensitive to lipopolysaccharide (LPS) injection, resulting in microglial activation and neuroinflammation (Zhang S.-Z. et al., 2019). OPC-derived TGF- $\beta$ 2 was subsequently shown to suppress microglial activation *in vitro* (Zhang S.-Z. et al., 2019). Building on this work, a more recent study has shown that, following ablation of OPCs *in vivo*, using the described DT methods in *Pdgfra<sup>CreERT</sup>* mice (Liu and Aguzzi, 2020), there is a whole-brain reduction in the expression of genes associated with microglial homeostasis (such as *Tmem119* and *Olfml3*). Similar effects on microglial gene expression can be observed using Crenolanib (a PDGFR inhibitor) in mouse brain slice cultures, which has the effect of depleting OPCs (Liu and Aguzzi, 2020). Finally, this role of microglial-OPC crosstalk has also been highlighted in the development of the hypothalamus (Marsters et al., 2020).

Depletion of microglia, achieved by administering PLX5622, an antagonist of the receptor for the microglia-stimulating CSF1, results in decreased OPC migration to the mantle zone in the embryonic hypothalamus; a result which likely arises due to the lack of microglia-secreted cytokines (Marsters et al., 2020). Intriguingly, it is also possible that OPCs directly fulfill immune cell-associated functions, such as tissue remodeling and regulating blood vessel permeability. For example, in a mouse model of prolonged cerebral hypoperfusion, OPCs are the first cell type to produce matrix metalloproteinase 9 (MMP-9), an enzyme which degrades the extracellular matrix. Expression of MMP9 was shown to facilitate infiltration of neutrophils beyond the blood brain barrier (BBB), suggesting that OPCs may contribute to pathological neuroinflammation (Seo et al., 2013). Moreover, under certain conditions, OPCs express inflammatory cytokines such as IL-1 $\beta$  or CCL-2, which are implicated in recruiting monocytes (Deshmane et al., 2009; Moyon et al., 2015). Some studies have also indicated that OPCs may be the cell of origin in gliomas/glioblastomas (Zong et al., 2015). While adult mouse OPCs were transformed by mutation of *p53* and *NF1* *in vivo* using *NG2-CreER*, which led to formation of malignant gliomas (Galvao et al., 2014), much of the molecular mechanism remains unknown.

More conventional gene mutation studies have also been instrumental in dissecting out components of OPC biology. For example, building on the potential role of OPCs in regulating the status of the BBB, tissue-specific ablation of TGF- $\beta$ 1 in mice (*Pdgfra-Cre; Tgfb1<sup>fllox</sup>*) resulted in loss of BBB function and cerebral hemorrhage (Seo et al., 2014). Other work has further refined the function of OPC-neuronal crosstalk, as previously discussed (Birey et al., 2015; Labrada-Moncada et al., 2020). From such studies, we know that OPCs express ion-channels and neurotransmitter receptors which allow them to detect neuronal activity (Larson et al., 2016) and, in turn, modulate neuronal behavior (Wang and Young, 2014; Douglas Fields, 2015; Purger et al., 2016). To give an example, the voltage-gated calcium channel (CaV1.2; Haberlandt et al., 2011) has been shown to be a major channel for depolarization-induced calcium entry in OPCs (Cheli et al., 2015, 2016). Conditional deletion of CaV1.2 within OPCs results in impaired myelination during postnatal mouse development (Cheli et al., 2016), as well as reduced reactive remyelination in a mouse model of chemically-induced demyelination (Santiago González et al., 2017). Interestingly, while studies with genetically altered mice have shown that CaV1.2 is essential for OPC survival in the adult mouse corpus callosum, it is dispensable in the motor cortex or spinal cord (Pitman et al., 2020) indicating regional heterogeneity, at least in the case of a reliance of OPCs on specific ion channels. Other conditional mutation studies have, for example, demonstrated the importance of iron storage proteins for OPC development and differentiation (Wan et al., 2020), as well as shown that Golgi proteins (derivatives of the myelin basic protein gene complex) facilitate OPC migration during development by promoting Ca<sup>2+</sup> transient currents in OPCs (Paez et al., 2009).

Finally, instigation of local disturbances in OPC function, through virus-mediated gene expression, has further illuminated

the functional nature of neuronal-OPC crosstalk. Depending on the type of viruses used, these offer distinct approaches from affecting only dividing cells, to integrating the genetic information into the host genome, or only allowing for transient expression (Kamimura et al., 2011). For example, it is known that OPCs express AMPA receptors, activation of which by neuronal glutamate leads to OPC depolarization (Bergles et al., 2000). Retroviral delivery of various forms of modified AMPA-R GluA2 subunit to early postnatal animals (when the rate of OPC proliferation is highest; Moshrefi-Ravadsjani et al., 2017) reveals that both ionotropic and non-ionotropic properties of AMPA-R are essential for regulating the balance between OPC proliferation and differentiation (Chen et al., 2018). For example, forcible expression of a Ca<sup>2+</sup>-permeable AMPA-Rs in OPCs results in increased proliferation at the expense of differentiation into myelinating OLs (Chen et al., 2018). Non-virus mediated gene expression methods can also be used, such as transfection with cationic polymer or magnetofection, however, these methods currently only show low expression efficiencies (Kamimura et al., 2011).

## Lineage Tracing and Fate Mapping

Genetically-inducible fate mapping (lineage tracing allowing to follow labeled cell and their progeny) techniques have been used to study OPCs and their subsequent lineages for decades, and have made it possible to characterize and fate-map OPCs and their progeny. In embryonic mouse brains, lineage tracing experiments have demonstrated that the generation of OPCs follows a ventral-to-dorsal “Mexican wave” (Kessaris et al., 2006). While the majority of OPCs will generate OLs, recent studies have also indicated that OPCs may be capable of forming neurons and astrocytes (Rivers et al., 2008; Zhu et al., 2008a,b; Guo et al., 2010; Robins et al., 2013). Using *NG2-Cre* transgenic animals, *NG2*-positive OPCs were shown to generate a subpopulation of protoplasmic astrocytes in the gray matter of both the ventrolateral forebrain and spinal cord, but they did not form white matter astrocytes (Zhu et al., 2008a,b). More recent studies have demonstrated that OPCs are able to generate neurons in the adult hypothalamus, using *NG2-CreER* transgenic mice (Robins et al., 2013), and in the cortex, using *PLP-Cre<sup>ERT</sup>* (Guo et al., 2010) or *Pdgfra-Cre<sup>ERT2</sup>* mice (Rivers et al., 2008). The latter is still subject to debate, because subsequent work has indicated that OPCs do not generate cortical neurons (Kang et al., 2010; Zhu et al., 2011; Clarke et al., 2012). However, using *NG2<sup>CreERT2</sup>* mice, it has been shown that postnatal OPCs can generate at least some cortical neurons (Huang et al., 2014), while embryonic OPCs are exclusively gliogenic, with derivatives restricted mainly to the OL lineage, apart from a small amount of astrocyte production in the ventral forebrain (Huang et al., 2019). Tools have also been generated to study the organization and development of the OPC lineage network at single-cell resolution, notably using *PLP-CreERT2* combined with the Brainbow system (Dumas et al., 2015). This method makes it possible to distinguish individual cells from their neighbors using multiple fluorescent proteins activated at random *via* the *Cre/LoxP* system, and further allows studies into the clonal dynamics of OPC development.



In order to characterize which neurons make direct connections to OPCs, monosynaptic tracing methods can be employed. For example, *PDGFR $\alpha$ -CreER* mice have been used to conditionally express the rabies virus glycoprotein 4 (gp4) and the avian TVA receptor, the receptor for subgroup A avian leukosis viruses, in OPCs. Following tamoxifen administration, gp4-deleted rabies viruses encoding GFP are stereotactically administered to different brain regions (corpus callosum, premotor cortex). As they express the missing viral component for infection, only OPCs are infected by gp4-deleted virus allowing a monosynaptic transmission of OPC inputs to first, but not higher orders of connected cells. This revealed that corpus callosum OPCs receive brain-wide synaptic inputs both from excitatory and inhibitory neurons (Mount et al., 2019).

An important technical consideration regarding NG2- or Pdgfr $\alpha$ -based lineage tracing of OPCs (and indeed, of any functional genetic approaches using the same gene drivers), is that NG2 and Pdgfr $\alpha$  are also expressed by certain other cell types. These include pericytes, cells which enwrap the vasculature of the brain (Ozerdem et al., 2001), or a sub-population of adult sub-ependymal zone (SEZ) B cells and non-vascular meningeal cells (Jackson et al., 2006; Andrae et al., 2016) respectively. Lineage tracing experiments using NG2-CreBAC and NG2<sup>CreERT2</sup> mice may therefore encompass pericytes and any cell that is derived from them. Of course, consideration must also be given to the fact that transgenic animals may not necessarily fully reflect endogenous gene expression and/or may have ectopic expression (for review: Bouabe and Okkenhaug, 2013). One study has used a dual-promoter approach to more selectively target pericytes rather than OPCs, by requiring both expression of *Pdgfrb* and NG2 for induction of Cre-mediated recombination (Nikolakopoulou et al., 2019). A similar approach could conceivably be used to better target and label OPCs based on the expression of multiple markers, especially given the recent studies characterizing the OPC transcriptome, which could be further interrogated to reveal novel OPC marker genes (Marques et al., 2018; Elbaz and Popko, 2019).

## Irradiation and Cell-Cycle Disruption

As mentioned above, OPCs are the most proliferative cell type in the brain (Dawson et al., 2000, 2003). OPCs are therefore especially susceptible to cell cycle disruption, and to cell death induced as a result of DNA damage checkpoints during the cell cycle (Borges et al., 2008). Consequently, inducing DNA damage through external factors [e.g., by irradiation or administration of the mitotic blocker cytosine- $\beta$ -D-arabinofuranoside (Ara-C)] or genetically in the brain has the effect of predominantly affecting OPCs (Chari and Blakemore, 2002; Irvine and Blakemore, 2007; Robins et al., 2013; Djogo et al., 2016). Used concomitantly with tissue specific gene drivers, such experiments can achieve very specific ablation of OPCs. For example, Djogo et al. (2016) employed such methods to ablate NG2-glia within the hypothalamus, including AraC administration *via* the third ventricle, X-irradiation, and genetic ablation using *Sox10-iCreERT2* to delete *Esco2* (a necessary cell cycle gene). Together, these techniques demonstrated the importance of OPCs in maintaining leptin receptor-expressing neuronal processes and

regulating feeding behaviors in mice. Another approach has been the use of the suicide gene herpes simplex virus thymidine kinase (*HSVtk*), expressed under the control of the NG2 promoter in rats. Upon ganciclovir administration, dividing *HSVtk*-expressing OPCs are selectively ablated leading to impaired hippocampal neuronal functions and increased inflammation (Nakano et al., 2017). Similarly, NG2-*tk* mice have been generated to ablate NG2-positive pericytes and OPCs in the context of spinal cord injury, leading to altered astrocytic responses and recovery (Hesp et al., 2018).

The genetic techniques discussed above have been instrumental in building our current understanding of OPC biology. However, in order to further advance the boundaries of the field, more recent techniques seeking to examine OPC transcriptomes and metabolomes have begun to uncover the extent of OPC heterogeneity, and to identify novel OPC markers and potential genes for further mechanistic investigation.

## TRANSCRIPTOMIC TECHNOLOGIES

The different potential functions of OPCs have begun to be revealed by mutation studies and by using techniques for genetic ablation and lineage tracing, as described. However, such advances are greatly supplemented by genome-wide transcriptomic analyses, which have become powerful investigative tools in their own right (Hwang et al., 2018). Indeed, the generation of global gene expression/regulatory networks through bulk RNA sequencing (RNA-seq) or single cell approaches has greatly refined our understanding of the biology of OPCs and OLs (Figure 2). Techniques such as single cell or single nucleus RNA sequencing (scRNA-seq and snRNA-seq respectively), where the latter allows profiling from frozen tissues or when fresh tissue dissociation is unsuccessful, while the former gives higher amounts of mRNA (Habib et al., 2017), as well as sequencing of open chromatin, which generally reflects areas of active gene expression or active enhancer regions, by Assay for Transposase-Accessible Chromatin (ATAC-seq), have been crucial in uncovering marker profiles of OPCs (Marques et al., 2018), identifying important regulatory genes and gene networks in OPC differentiation (for review: Elbaz and Popko, 2019). These sequencing methodologies have also delineated heterogeneity amongst OPC and OL populations in both spatial and temporal contexts (Marques et al., 2016, 2018; Beiter et al., 2020).

Indeed, a prevailing question that these transcriptomic techniques has begun to answer is whether OPCs and OLs represent homogenous populations, or whether they exist in functionally and transcriptomically distinct subgroups. Pioneering work, using microarray systems and bulk RNA-seq, has revealed the molecular signatures of many different cell types in the brain, including OPCs and oligodendrocytes (Cahoy et al., 2008; Zhang et al., 2014). The first study to focus exclusively on gene expression in OPCs was conducted in a mouse model of demyelination (Moyon et al., 2015). In this study, OPCs were purified through FACS, using brains from Pdgfr $\alpha$ -GFP mice at either the neonatal stage, in 2-month old adults, or adult mice that had been treated with cuprizone for 5 weeks.



Transcriptomic differences were then analyzed by microarray, and early neonatal and adult OPCs were found to differ in the expression of markers of OL differentiation, with adult OPCs having a transcriptome more akin to that of OLs than that of neonatal OPCs (Moyon et al., 2015). Interestingly, in demyelination conditions elicited by cuprizone treatment, adult OPCs reverted to a more neonatal and relatively undifferentiated state (Moyon et al., 2015).

Subsequent work has confirmed the existence of this temporal heterogeneity between OPCs in the juvenile and adult mouse brain, and further indicated that transcriptional homogeneity in the juvenile brain gives way to transcriptional divergence in the adult, which may or may not reflect regional differences (Marques et al., 2016, 2018; Beiter et al., 2020). By using flow cytometry to isolate OPCs in *Pdgfra*-H2B-GFP or *Pdgfra*-CreERT mice, followed by bulk RNA-seq and scRNA-seq, different embryonic stages were associated with distinct gene expression profiles that reflect the regional and temporal patterns of OPC generation. Interestingly, there appears to be a convergence of gene expression in early postnatal OPCs (Marques et al., 2018), while in the different clusters identified in adult mice, some were not specific to the OL lineage, such as fibroblasts, endothelial cells, pericytes, and leptomeningeal cells (Marques et al., 2016; Beiter et al., 2020). In the adult, OPC-specific clusters, on further investigation, were also found to be heterogeneous, with genes like *Gpr17* and *Clusterin* representing novel markers of different OPC populations (Beiter et al., 2020). Furthermore, sex-specific differences in the composition of heterogeneous OPC populations within specific brain regions has been recently noted, although the varieties of OPCs present throughout the brain do not appear to be different between sexes (Beiter et al., 2020). Finally, a recent study has translated these findings to humans, where scRNA-seq revealed in humans that fetal, pediatric and adult OPCs have distinct transcriptomes (Perlman et al., 2020). Furthermore, OPC diversity seems to become more pronounced over time, at least in mice (Spitzer et al., 2019).

While these data provide a valuable insight into OPC heterogeneity in the adult brain, it remains unclear whether there is a correlation between regional and functional differences in OPCs, in other words, asking whether OPCs from distinct brain regions function differently. Previous studies that targeted their scRNA-seq characterization to specific brain regions have not so far described any heterogeneity in OPCs, although it is worth noting that these studies did not focus on OPCs exclusively (Zeisel et al., 2015; Habib et al., 2016; Tasic et al., 2016; Chen et al., 2017). More recently, bulk RNA-seq of magnetic activated cell sorted (MACS) OPCs revealed that OPCs become regionally diverse with age, with respect to their expression of particular ion channels and sensitivity to neuronal activity (Spitzer et al., 2019). Since then, two molecularly distinct OPC populations have been described in the adult suprachiasmatic nucleus, but no further characterization has yet been undertaken (Wen et al., 2020). In the embryonic zebrafish spinal cord, at least two spatially and functionally distinct OPC subgroups have been described: one population that migrates laterally and generates myelinating OLs, and another that regulates neuronal excitability (Marisca

et al., 2020). Furthermore, novel transcriptomic methods such as spatial transcriptomics could be used to perform scRNA-seq in tissue sections, potentially leading to the identification of uncharacterized OPC sub-groups in different anatomical regions (Figure 2; Ståhl et al., 2016).

OPC heterogeneity has also been demonstrated regarding their responses to growth factors and cytokines. For example, gray and white matter-derived OPCs respond differently to INF $\gamma$  in terms of their proliferation, differentiation and process arborization (Lentferink et al., 2018), and to PDGF in terms of their proliferation (Hill et al., 2013). Furthermore, subpopulations of adult white matter OPCs differentially respond to growth factor (PDGF-AA, IGF-1 and FGF-2) and display differential gene expression patterns (Mason and Goldman, 2002; Lin et al., 2009). In summary, RNA sequencing of adult OPCs have revealed that they are a heterogeneous population of many different cells whose individual functions remain unknown.

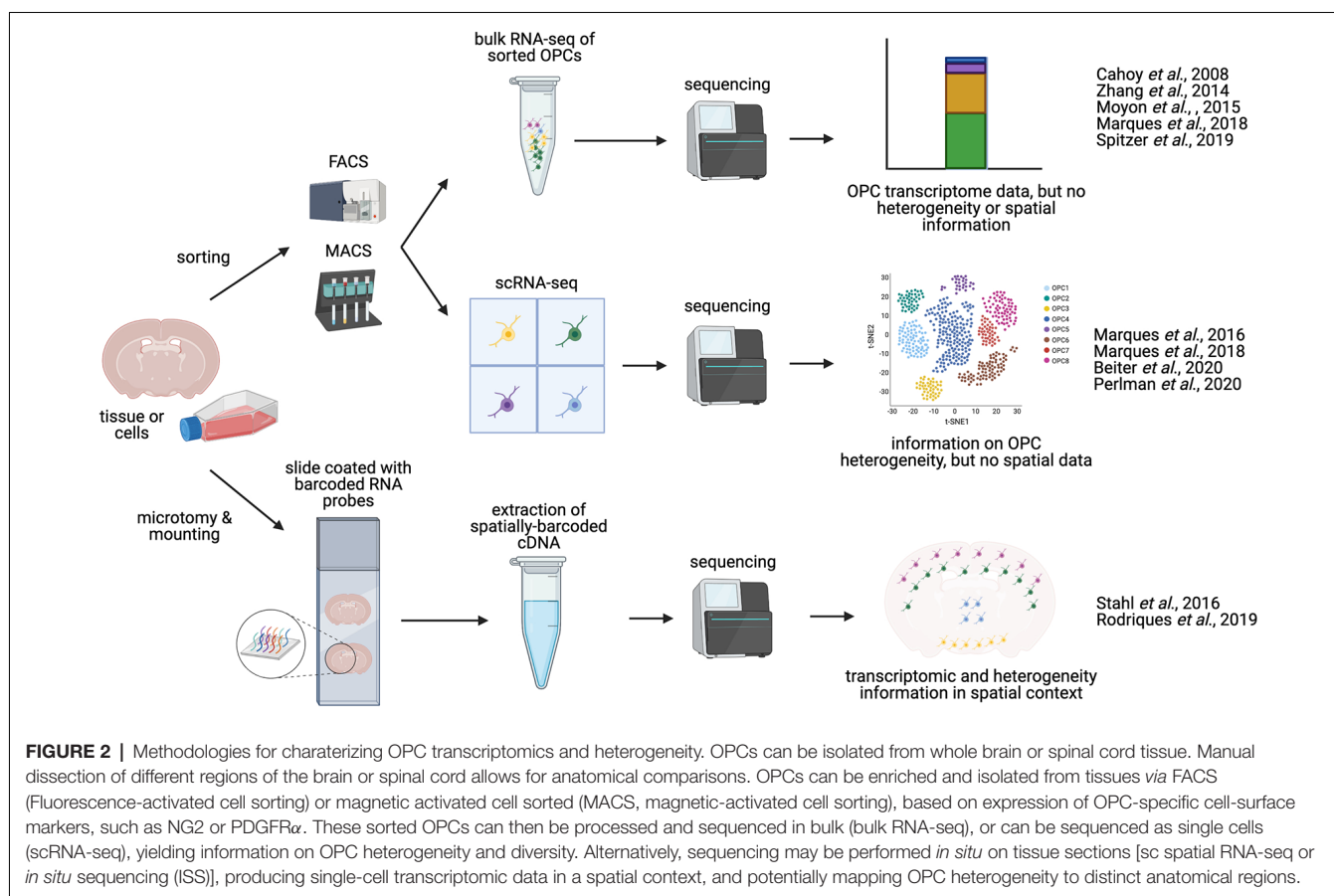
The changing chromatin landscape has also been analyzed during OPC differentiation (Castelo-Branco and Liu, 2020) and mutations in chromatin modifiers, such as CHD7 and CHD8, have a profound effect on the formation of OLs from OPCs (Marie et al., 2018). Given the now widespread appreciation of the relationship between chromatin status and differentiation in multiple tissues (for example in skeletal muscle; Hernández-Hernández et al., 2020), this is not a surprising finding, but it nevertheless underscores epigenetic regulation as another field of ongoing research regarding OPCs (Gregath and Lu, 2018).

Finally, while transcriptomic studies yield invaluable information about the RNA contents of specific cells, proteomics are essential in correlating transcription with actual protein expression (Vidova and Spacil, 2017). In one study, large numbers of rat OPCs were cultured and differentiated *in vitro*. The proteomic profile of these cells was then analyzed at different time points throughout differentiation. Quantitative expression data was subsequently obtained for 5,259 proteins, revealing distinct patterns of regulation. Such techniques could also be used for novel candidate protein identification (Schoor et al., 2019).

Altogether, these studies indicate that, by global or local functional genetic approaches and transcriptional analysis, valuable information arises about the crosstalk between OPCs and their neighboring cells. Such information should be put in the context in which the cells are found, namely their physical interactions with their neighbors and their anatomical location. Furthermore, as OPCs are precursor cells, understanding their fate in relation to their heterogeneity will be crucial, for example, it may be that one subpopulation of OPCs is more likely to differentiate than others. Imaging techniques, including lineage tracing, are powerful tools to begin tackling these questions.

## IMAGING AND MICROSCOPIC TECHNIQUES

Oligodendrocytes and OPCs, like many of the different cell types in the brain, have a complex, branched morphology and reside in a substantial three-dimensional volume (Ono et al., 2001).



Efforts towards understanding OPC morphology and the precise contacts they make with their neighboring cells promises to shed light on their potential functions. Conventional histological techniques, such as immunohistochemistry have highlighted important morphological differences between gray and white matter OPCs such as, as mentioned above, the former having radially orientated processes while in the latter, the processes are aligned parallel with neuronal axons (Levine et al., 2001). Of course, histological sectioning results in the loss of important volumetric information, which can otherwise more accurately inform on important parameters such as cell size, polarity, branch number, branch length, and the number of synapses and interacting cells (Hillman, 2000). Additionally, the categorization and measurement of relevant OPC parameters could be further enhanced by the use of computational techniques, such as “deep learning” which, in the case of studies concerning astrocytes, have already been used to characterize morphological parameters in a relatively unbiased manner (Kayasandik et al., 2020). It follows that investigations regarding OPC morphology may benefit from such computational techniques (Kayasandik et al., 2020), possibly highlighting previously unseen characteristics of OPCs which may provide functional insights.

Confocal microscopy has of course been essential in demonstrating the entire morphology of OPCs and

oligodendrocytes (Eftekharpour et al., 2007; Robins et al., 2013), while recent advances have facilitated imaging of whole cells in their *in vivo* context, such as light sheet fluorescence microscopy (Adams et al., 2015), two-photon or multiphoton microscopy (Table 1; Christensen and Nedergaard, 2011; Eugenin von Bernhardt and Dimou, 2019), and expansion microscopy (Wassie et al., 2019), with optical clearing allowing visualization of ever larger samples (Yu et al., 2018; Zhu et al., 2019). Zebrafish and *Xenopus* are especially useful for live imaging studies of OPCs and their lineage by light sheet fluorescence microscopy (LSFM; Bin and Lyons, 2016) or spinning disk confocal microscopy (Wang et al., 2018) due to the transparency of their embryos (Table 1). However with advances in optical clearing (Yu et al., 2018), brain tissues for larger animals (such as mice and rats) could be analyzed by two-photon or light sheet microscopy. OPC and OLs visualization could also be performed *ex vivo* (brain slice culture; Zhou et al., 2007; Gadea et al., 2009). At least with trans-cranial two-photon microscopy, *in vivo* visualization of OPCs and their lineage descendants can also be performed (Eugenin von Bernhardt and Dimou, 2019).

Furthermore, volumetric electron microscopy (such as ion beam-scanning electron microscopy; FIB-SEM) promise to more extensively reveal OPC/oligodendrocyte ultrastructure as already documented in the mouse optic nerve (Schertel et al., 2013)

**TABLE 1** | Imaging techniques.

Technique	Type of imaging	Applications	Major benefits	Drawbacks	Notable uses	Reference(s)
(SBF-SEM) Serial block face—scanning electron microscopy	Destructive scanning electron microscopy (serial ultramicrotome sectioning)	Studying sub-cellular structures and cell-cell interactions in 3D	High resolution (5–10 nm) through 3D volume	Destroys the sample, feasible only for a relatively small total volume (slow acquisition and large data sets)	Characterization of axon diameter and myelination status in transected mouse optic nerve [5 nm (X–Y), 50 nm (Z), total volume = 50 $\mu\text{m}$ (X–Y), 100 $\mu\text{m}$ (Z)]; 3D-reconstruction of normal and cuprizone-demyelinated axons in mouse corpus callosum [1 nm (X–Y), 80 nm (Z), area per “slice” = 204.54 $\mu\text{m} \times 61.36 \mu\text{m}$ ]	Giacci et al. (2018) and Fischbach et al. (2019)
(FIB-SEM) Focussed ion beam—scanning electron microscopy	Destructive scanning electron microscopy (focussed ion beam ablation of block face)	Studying sub-cellular structures and cell-cell interactions in 3D	Better Z-resolution than SBF-SEM (<10 nm) due to different surface ablation method	Destroys the sample, typically smaller total volumes can be imaged than for SBF-SEM	3D reconstruction of organelles in a myelinating oligodendrocyte within mouse optic nerve [7.5 nm resolution (X–Y), 30 nm (Z), total volume = 7.72 $\mu\text{m}$ (X), 5.79 $\mu\text{m}$ (Y), 3.81 $\mu\text{m}$ (Z)].	Schertel et al. (2013)
(CLEM) Correlative light and electron microscopy	Correlated light and electron microscopy on the same samples	EM-resolution of samples (cells and sub-cellular structures) with wider contextual information	Places nm-scale EM resolution within the wider context of cells and tissues, allows for easier localization of nano-scale structures by first identifying them through fluorescent microscopy	Requires multiple types of imaging and careful alignment of separate imaging data sets of the same sample	Combined <i>in vivo</i> multiphoton microscopy, confocal microscopy, and FIB-SEM on the same samples of mouse brain (using myelinated axons as landmarks)	Luckner et al. (2018)
(LSFM) Lightsheet fluorescence microscopy	Volumetric fluorescent microscopy (sheet of illuminating light)	Whole organism/organ imaging and tissue architecture	Non-destructive fluorescent imaging of whole animals, organs or tissues	Relatively low resolution (microns)	Mapping expansion and migration of grafted human neural progenitor cells in mouse (whole mouse brain); identification of functionally, morphologically and spatially distinct subtypes of OPC in zebrafish spinal cord (entire zebrafish larvae)	Vogel et al. (2019) and Marisca et al. (2020)
Expansion microscopy	Fluorescent imaging of artificially expanded samples to increase resolution	Imaging organelles, synapses, synaptic vesicles and cell-cell interactions	High resolution beyond capabilities of typical light microscopy objectives, due to expansion of sample (effectively tens of nm)	Lengthy expansion procedure; possible distortion of tissue architecture	Super-resolution visualization of myelinated axons in mouse hippocampus (150- $\mu\text{m}$ thick slices of mouse brain)	Min et al. (2020)

(Continued)

**TABLE 1 |** Continued

Technique	Type of imaging	Applications	Major benefits	Drawbacks	Notable uses	Reference(s)
Super-resolution microscopy (e.g., STED—Stimulated Emission Depletion Microscopy)	Super-resolution microscopy	Imaging organelles, synapses, synaptic vesicles and cell-cell interactions	High resolution light microscopy, achieved by limiting or negating the inherent diffraction of light	Limited volumetric information, most super-resolution techniques require post-processing of images (although not STED)	Demonstration of preferential interaction of OPCs with the nodes of Ranvier of large diameter axons in mouse CNS	Serwanski et al. (2017)
Synchrotron X-ray microtomography	Non-destructive volumetric imaging	3D imaging organs and tissues	Better resolution and contrast compared to conventional $\mu$ CT	High energy X-rays means cannot image live specimens, feasible only for smaller total volumes of dissected tissue (mm-scale)	Visualization of myelinated axons and other structures in a subvolume of mouse neocortex (voxel size of approx. $1 \mu\text{m}^3$ , mm-sized piece of tissue)	Dyer et al. (2017)
Multiphoton	Non-invasive, <i>in vivo</i> fluorescent imaging	Longitudinal or time-lapse studies in live animals or cultured organs/tissues	Live imaging and ability to image cells and structures at depth within tissues, limited photobleaching, can perform optical sectioning	Relatively slow acquisition, resolution is not superior to conventional confocal microscopy	Imaging of OPC migration from SVZ to cortex in postnatal mouse brain slices	Gadea et al. (2009)

and in the lamprey nervous system (Weil et al., 2018). Such destructive electron microscopy techniques use scanning electron microscopy (SEM) to image the surface of a specimen sample, combined with an ablation method that serially eliminates the surface layer resulting in a three-dimensional stack with nm-scale resolution. Major techniques of this variety include FIB-SEM where a particle beam is used to ablate the sample surface (Schertel et al., 2013), and SBF-SEM (serial block face—SEM), where the sample is sectioned *via* microtome between images (Giacci et al., 2018; Fischbach et al., 2019; Table 1). These techniques are especially valuable when the research question requires careful identification of discrete organelles or other cellular structures that exist in a complicated 3D space. For example, FIB-SEM has been recently used to reconstruct the shape of abnormal unfolded myelin structures in mice lacking the *Anilin* gene in oligodendrocytes (Erwig et al., 2019). Physical interactions between OPCs and neurons could also be more effectively identified, classified and mapped in 3D by volumetric EM techniques, as has already been done for astrocyte-OPC interactions (Schertel et al., 2013) and more recently for synapses between astrocytes and neurons (Kikuchi et al., 2020).

Finally, imaging techniques that are based on the spin density of protons in water, notably magnetic resonance imaging (MRI) can also be used, given that the physical properties of myelin allow for it to be well contrasted against other brain tissues by virtue of its water content (40% compared to 80% respectively) (Alonso-Ortiz et al., 2015; Watanabe et al., 2016), and of course, MRI has the bonus of being non-invasive. However, the resolution given by MRI is not sufficient to allow for visualization of cells. CRISPR/Cas9 can also be used to facilitate a

variety of imaging applications (reviewed by Galichet and Lovell-Badge, 2021). CRISPR/Cas9-mediated gene editing techniques that result in the epitope tagging of proteins have been developed to target neurons, and could be adapted to analyze OPCs in greater depth (Willems et al., 2020). In the next section, we discuss how the merging of functional and imaging approaches, in which light is used to modify gene expression, can be used to refine our understanding of OPC functions.

## FUNCTIONAL PHYSIOLOGICAL APPROACHES

### Electrophysiology

A recent study has used whole-cell patch clamp recordings in brain slice cultures to investigate the electrophysiological properties of NG2 positive OPCs through development and adulthood. It was observed that OPCs acquire electrophysiological heterogeneity with age, and that differences in excitability and ion channel expression are associated with distinct functional OPC states, including naïve, proliferative, primed and quiescent (Spitzer et al., 2019). While electrophysiological recordings are informative regarding ion channel expression, synapse formation and interaction with neurons and other cells, they can also provide helpful inferences regarding OPC morphology. Capacitance, a measure of stored charge, is dependent on cellular surface area, and can therefore be measured to indicate OPC size and morphology. Using this method, it was demonstrated that OPC capacitance is greatest during the active myelination phase of murine brain development (Spitzer et al., 2019). We have discussed above data showing that functional



genetic approaches have revealed that OPC behavior and crosstalk with neighboring cells is region-specific. Therefore, future experiments that manage to achieve region-specific alterations, such as ablation of OPCs or their neighboring cells, would help understand the functional implications of this spatial heterogeneity.

## Functional Imaging and Optogenetics

Novel techniques of improving our understanding of OPC functions include optogenetic, intra cellular ion signaling activity and imaging (Friess et al., 2016; Ortolani et al., 2018; Zhang M. et al., 2019; Heredia et al., 2020; Marisca et al., 2020). Optogenetics involves the use of light to modulate cells expressing a light-sensitive ion channel, and has historically been used primarily to modulate neuronal activity (Lee et al., 2020). Typically, a photo-sensitive variant of channel-rhodopsin 2 (ChR2) is used. Activation of ChR2 leads to the depolarization of the cell membrane which, in neurons, could trigger an action potential (Ernst et al., 2008). To study the importance of the transient early postnatal synaptic input from GABAergic interneurons to OPCs (Vélez-Fort et al., 2010), optogenetic methods have been used (Ortolani et al., 2018). Using *Nkx2.1-Cre* and *Parvalbumin<sup>Cre</sup>*, ChR2 was expressed in a subpopulation of interneurons. Upon light activation on 10-days old pups, cortical OPC proliferation and density was analyzed. However, neither were affected by the increased interneuron activity, thus supporting previous findings indicating that postnatal GABAergic activity does not affect cortical oligodendroglia (Balía et al., 2017; Ortolani et al., 2018). Optogenetics also allows the control of gene expression *via* light exposure (Yamada et al., 2020) and modulation of gene expression in OPCs *in vivo* by shining light in a region-specific manner is an approach that could be used in the future.

Calcium signaling is often involved in intracellular communication (but also in some other processes), however, this may subsequently lead to release of molecules that can affect adjacent cells. Upon entry into the cytosol, calcium ions often exert an allosteric effects on a plethora of enzymes and proteins to regulate their activity and function (Clapham, 2007). In terms of the properties or behavior of a cell, the effects of  $\text{Ca}^{2+}$  can be relatively rapid (e.g., release of a signaling molecule) or more long-term and global, e.g., *via* calmodulin or calcineurin to trigger nuclear entry of a transcription factor or phosphatase activity. As  $\text{Ca}^{2+}$  ions chelate with many chemicals, methods have been developed to measure calcium variation intra-cellularly. Typically, a fluorescent molecule is fused to a chelating agent to which  $\text{Ca}^{2+}$  can bind. Upon calcium binding, the quantum-yield of fluorescence is increased resulting in higher intensity signals where  $\text{Ca}^{2+}$  concentrations are elevated (Tsien, 1980; Grynkiewicz et al., 1985; Tsien, 1989; Dean et al., 2012). Calcium imaging and calcium signaling have been used in many contexts including the study of Schwann cells (Heredia et al., 2020) and oligodendrocytes (Zhang M. et al., 2019; Rui et al., 2020). Furthermore, using calcium imaging together with lineage tracing, single-cell transcriptomics and neuronal activity manipulation, Marisca et al. (2020) have dissected the functionality of different OPC subgroups in

zebrafish spinal cord, where, as described earlier, the OPC population is heterogenous, both in spatial arrangement and in functionality (Marques et al., 2016, 2018; Foerster et al., 2019; Spitzer et al., 2019). In the zebrafish spinal cord, OPC subgroups have different degrees of calcium signaling activity, visualized using the calcium indicator GcaMP6m. Calcium imaging has revealed that, in embryonic zebrafish spinal cord, OPCs showing a higher rate of calcium signaling activity are less likely to differentiate directly (Marisca et al., 2020). Furthermore, *in vitro* and *ex vivo* studies have demonstrated that intracellular calcium, alongside intracellular sodium and potassium, influence myelin basic protein synthesis in OPCs (Friess et al., 2016).

## CULTURE SYSTEMS

Several approaches can be taken to grow and manipulate OPCs *in vitro*, where the primary advantages are more precisely defined conditions and greater experimental tractability. Methods such as these also allow for rapid and efficient generation of OPCs and OLs, which can then be used for therapeutic purposes as part of regenerative medicine (Egawa et al., 2016; Morales Pantoja et al., 2020), or used for further experiments, such as in drug screens to identify treatments for demyelinating diseases, glioma or CNS injuries (Badr et al., 2011; Lariosa-Willingham et al., 2016). In particular, the generation of patient-derived OPCs and OLs *via* human induced pluripotent stem cells (hiPSCs) allows for the study of cell and molecular processes underlying human disease (for review: Chanoumidou et al., 2020). Furthermore, adoption of three-dimensional culture systems has enabled the study of OPCs in contexts that better recapitulate the *in vivo* environment (Chiaradia and Lancaster, 2020).

OPCs can be obtained and differentiated from mouse epiblast stem cells (Najm et al., 2011; Lager et al., 2018), from human embryonic stem cells (hESCs) or hiPSCs (Wang et al., 2013; Kim et al., 2017; Biswas et al., 2019) or by trans-differentiation of other cell types (e.g., fibroblasts) by CRISPR/Cas9-mediated gene activation (Matjusaitis et al., 2019). OPCs can also be derived from different post-natal brain regions in mice (Yang et al., 2016) by manually dissecting the region of interest and using the “shake-off” technique to discard dead or terminally differentiated cells and cells that have different adhesion properties, namely astrocytes and microglia, thereby leaving only proliferative, adherent progenitor cells (Chen et al., 2007; O’Meara et al., 2011; Medina-Rodríguez et al., 2013). Spheres of oligodendrocyte lineage cells, also known as “oligospheres” can also be obtained from multipotent mouse or rat cortical progenitor cells (Chen et al., 2007; Pedraza et al., 2008). The composition of such cultures usually requires validation by immunocytochemistry to determine the proportions of different cell types (Vitry et al., 1999; Chen et al., 2007). In comparison, purified OPC cultures can also be derived by dissociating cells from tissues and sorting for OPC-specific markers by FACS or MACS (Barateiro and Fernandes, 2014). Furthermore, zebrafish-derived OPC cultures may be ideally suited for studying fundamental processes and for small molecule screens, and can also be co-cultured with human cells (Kroehne et al., 2017).

Differentiation of OPCs and subsequently OLs from hiPSCs or hESCs can be achieved by recapitulating the signaling processes associated with differentiation (Goldman and Kuypers, 2015), either pharmacologically by timely addition of agonist and antagonists during the differentiation process (Douvaras and Fossati, 2015), or by driving expression of key regulatory genes, such as SOX10 and OLIG2 in ESCs (Pawlowski et al., 2017), or SOX10, OLIG2 and NKX6.2 (Ehrlich et al., 2017) and SOX9 in hiPSCs (Ng et al., 2020). A combination of both pharmacological and genetic differentiation methodologies can also be used to great synergistic effect (García-León et al., 2020). As mentioned, these protocols enable the production of relatively large amounts of OPCs and OLs, which can be used therapeutically (Egawa et al., 2016; Morales Pantoja et al., 2020) or for experimentation. Xenograft experiments have shown that hiPSC-derived OPCs/OLs survive and can influence disease processes in model animals (Wang et al., 2013b; Kawabata et al., 2016; Feng et al., 2020; Ng et al., 2020). Finally, and perhaps most illuminating are studies where patient-derived iPSCs are used to make OPCs/OLs, which are then used to study disease processes (for review: Chanoumidou et al., 2020).

For example, Palizaues-Merzbacher disease (PMD) is a rare pediatric monogenic condition affecting myelin in the CNS, which is linked to a variety of mutations in proteolipid protein 1 (PLP1). Using hiPSCs derived from different patients, a screen was developed that linked particular mutations in PLP1 with specific phenotypes, such as regarding ability to develop OPCs and form OLs, cellular morphology, and myelination capacity (Nevin et al., 2017). More recently, OLs derived from MS patient iPSCs have shed light on the importance of the extracellular milieu, indicating that OPCs in the context of MS are more sensitive to inflammatory environments, which impairs their ability to differentiate (Morales Pantoja et al., 2020). The use of hiPSC or hESC-derived OPCs/OLs, in combination with “omic” methodologies described above, provide a deeper understanding of differences in gene expression between OPCs in health and disease (Lopez-Caraballo et al., 2020; Ng et al., 2020; Chamling et al., 2021). Bulk RNA-seq of hiPSC-derived OPCs for example, has indicated transcriptomic differences between OPCs in healthy donors and MS patients. Further proteomic characterization of OPC-condition media revealed that MS-associated OPCs are likely less able to promote migration of other OPCs, which was subsequently confirmed *via in vitro* migration assays (Lopez-Caraballo et al., 2020).

The utility of iPSC cultures for understanding OPCs in disease is, of course, not limited to the generation of OL-lineage cells. For example, it has been shown that neural progenitor cells, differentiated from hiPSCs of MS patients, were unable to promote maturation of OPCs compared to healthy neural progenitor cells, and this was linked to expression of cellular senescence genes in MS-derived neural progenitors (Nicaise et al., 2019). Another study has shown that astrocytes derived from patient iPSCs suffering from Alexander disease, which is a rare genetic leukodystrophy that features demyelination, inhibit proliferation and differentiation of OPCs in co-culture (Li et al., 2018).

Furthermore, the culture of iPSC-derived OPCs as well as from other sources, has been advanced by the incorporation of 3D culture systems. Such methods not only increase the efficiency of generation of OPCs and OLs, but also better recapitulate the *in vivo* environment, allowing for more accurate and translational studies of their biology (Rodrigues et al., 2017). Here, we will refer to both spheroids and organoids, where spheroids are small “balls” of cells of usually one or two cell types (Birey et al., 2017), and organoids being larger accumulations of cells comprised of heterogeneous cell types which more closely resemble actual tissues (Chiaradia and Lancaster, 2020). For example, 3D cultures have been made by aggregation of hiPSCs, which through timely addition of signaling pathway modifiers, generate oligodendrocyte spheroids. These 3D spheroids contain cells of the OPC lineage and myelinated neurons and thus can be used for OL development and interaction with other cells (Marton et al., 2019). One limitation of cerebral organoids has been that the emergence of myelinating OLs within cerebral organoids can take a long time; between 103 and 210 days (Madhavan et al., 2018; Marton et al., 2019). However, in a recent study, hiPSCs were simultaneously differentiated into organoids containing both neurons and OL-lineage cells through a combination of differentiation media and induction of expression of cell autonomously-acting transcription factors (Ng et al., 2020). This method resulted in rapid formation of myelinating-oligodendrocytes and production of myelinated neuronal axons at a density comparable to that of healthy human brains (Ng et al., 2020). Such neuronal/OL co-cultures also allow for direct study of the process of axonal myelination in both healthy and diseased contexts using patient-derived cells (Pang et al., 2018; Assetta et al., 2020). 3D culture systems are of course also useful in glial tumor research, where gliomas and glioblastomas cultured as either tumor-spheres or as organoids permit maintenance of 3D tumor architecture (Ogawa et al., 2018; Azzarelli, 2020) and tumor heterogeneity (Jacob et al., 2020) compared to 2D culture systems (Melissaridou et al., 2019; Ruiz-Garcia et al., 2020). Brain slice cultures are also of importance in this context. For example, time-lapse imaging of brain slices could shed light on the invasiveness and evolution of gliomas as well as the cell of origin (Fayzullin et al., 2016).

Finally, the utility of conventional 2D culture systems should not be discounted, as they are nonetheless invaluable and eminently tractable methods of examining more specific aspects of OPC biology. Indeed, many of the iPSC studies described above were conducted in monolayer cultures (Wang et al., 2013; Kim et al., 2017; Yamashita et al., 2017; Biswas et al., 2019; Assetta et al., 2020). To give some further examples, treatment of *in vitro* cultured OPCs with various endocannabinoid ligands and antagonists has highlighted the potential regulatory role of the endocannabinoid system in regulating OPCs in both health and disease (for review: Ilyasov et al., 2018). Incubation of immortalized rat cerebral endothelial cells with media conditioned with primary rat OPCs resulted in increased expression of tight junction proteins and decreased transwell permeability, indicating a role of OPCs in maintaining the BBB (Seo et al., 2014). Lastly, culture of hiPSC-derived OPCs on substrates of varying stiffness has demonstrated that

OPC migration is both mechanosensitive and donor-dependent (Espinosa-Hoyos et al., 2020).

## CONCLUSIONS

Oligodendrocytes, arising from oligodendrocyte progenitor cells (OPCs) or NG2-glia, are crucial cells in the nervous system facilitating rapid electrical conductance in neurons. While originally OPCs were thought of only as the precursors of oligodendrocytes, they are also able to generate other cell types including neurons and astrocytes (Figure 1), and that they have functions of their own (Rivers et al., 2008; Zhu et al., 2008a,b; Guo et al., 2010). OPCs are fully integrated in the CNS, receiving inputs from and affecting the behavior of neighboring cells including neurons, astrocytes and microglia (Domingues et al., 2016; Nutma et al., 2020). It is important to note that the appearance of OPCs from ESCs in humans follow some similar conserved transcriptional networks but also respond differently to certain factors, such as FGF2 (Hu et al., 2009; Bribián et al., 2019). It is therefore essential to understand these differences before comparing OPCs and other OL-lineage cells between species.

While OPCs share core markers, it has become increasingly clear that adult OPCs are heterogenous in their transcriptomes (Marques et al., 2016, 2018; Beiter et al., 2020). However, it is not currently fully understood how this transcriptomic heterogeneity translates into functional heterogeneity. Furthermore, OPC location may also reflect differences in OPC functions, such as illustrated with perivascular OPCs promoting angiogenesis as described under cerebral ischemia conditions (Kishida et al., 2019). With advances in transcriptomic analysis and discovery of markers specific to sub-populations of OPCs, these cells could now be sorted according to their location and/or transcriptomic profile and ATAC-seq, bisulfite-seq or proteomic studies could be performed at a single-cell level (Kashima et al., 2020). Such methods could also be applied to analyze OPCs in disease conditions.

Advances in imaging and functional imaging have allowed a better understanding of OPC localization, differentiation and relationship with other cell types. While the neuronal connectome is fundamental to understanding information processing (Oh et al., 2014), one could think of determining the OPC-specific connectome to refine our understanding of OPC integration within the CNS. With functional imaging techniques, OPCs could be ablated or have their gene expression altered in a position specific manner; this would permit further understanding of the link between OPC location and function.

## REFERENCES

- Adams, M. W., Loftus, A. F., Dunn, S. E., Joens, M. S., and Fitzpatrick, J. A. J. (2015). Light sheet fluorescence microscopy (LSFM). *Curr. Protoc. Cytom.* 71, 12.37.1–12.37.15. doi: 10.1002/0471142956.cy1237s1
- Ahlgren, S. C., Wallace, H., Bishop, J., Neophytou, C., and Raff, M. C. (1997). Effects of thyroid hormone on embryonic oligodendrocyte precursor cell development *in vivo* and *in vitro*. *Mol. Cell. Neurosci.* 9, 420–432. doi: 10.1006/mcne.1997.0631

Conditions affecting the function of myelin, as well as gliomas, have profound health consequences in which OPCs most likely have an etiological role to play and could be target cells for drug discovery experiments. Indeed, in specific cases of gliomas, OPCs seem to be the cell of origin (Zong et al., 2015). A greater understanding of the heterogeneity of OPCs would permit studies to determine whether gliomas that arise from NG2-glia involve a specific sub-type(s). Such information would permit a more targeted approach to treatments. In diseases affecting myelin function, such as MS or Devic's disease (Duncan and Raddcliff, 2016), it is crucial to direct OPCs to promote regeneration and remyelination. It is also important to investigate whether, for these conditions, OPCs are not themselves contributing to disease processes. For example, multiple sclerosis is an auto-immune disease affecting myelin, and OPCs contribute to brain immunity (Domingues et al., 2016) and may act as immune responder cells (Seo et al., 2013); hence a better understanding of the potential different OPC functions may help to tackle disease response and evolution. Furthermore, as OPCs are the most proliferative cells within the CNS, one could think of directing their fate in response to specific injuries (for example, generation of neurons after stroke).

It is therefore crucial to fully understand populations of OPCs; their diversity and the different functions they may have. Increased knowledge would permit the use and/or the manipulation of these cells in different neurological contexts, including those involving aging, inflammation, cancer, or degeneration.

## AUTHOR CONTRIBUTIONS

CG and RC wrote the initial review. CG, RC and RL-B contributed to the critical reading of the review. All authors contributed to the article and approved the submitted version.

## FUNDING

This review article was supported by the Francis Crick Institute which receives its core funding from Cancer Research UK (FC001107), the UK Medical Research Council (FC001107) and the Wellcome Trust (FC001107). This work was also supported by an additional UK Medical Research Council grant (reference MR/T000759/1).

## ACKNOWLEDGMENTS

All figures were created with BioRender.com.

- Alonso-Ortiz, E., Levesque, I. R., and Pike, G. B. (2015). MRI-based myelin water imaging: a technical review. *Magn. Reson. Med.* 73, 70–81. doi: 10.1002/mrm.25198
- Andrae, J., Gouveia, L., Gallini, R., He, L., Fredriksson, L., Nilsson, I., et al. (2016). A role for PDGF-C/PDGFR $\alpha$  signaling in the formation of the meningeal basement membranes surrounding the cerebral cortex. *Biol. Open* 5, 461–474. doi: 10.1242/bio.017368
- Assetta, B., Tang, C., Bian, J., O'rourke, R., Connolly, K., Brickler, T., et al. (2020). Generation of human neurons and oligodendrocytes from pluripotent



- stem cells for modeling neuron-oligodendrocyte interactions. *J. Vis. Exp.* 9:165. doi: 10.3791/61778
- Azzarelli, R. (2020). Organoid models of glioblastoma to study brain tumor stem cells. *Front. Cell Dev. Biol.* 8:220. doi: 10.3389/fcell.2020.00220
- Badr, C. E., Wurdinger, T., and Tannous, B. A. (2011). Functional drug screening assay reveals potential glioma therapeutics. *Assay Drug Dev. Technol.* 9, 281–289. doi: 10.1089/adt.2010.0324
- Balia, M., Benamer, N., and Angulo, M. C. (2017). A specific GABAergic synapse onto oligodendrocyte precursors does not regulate cortical oligodendrogenesis. *Glia* 65, 1821–1832. doi: 10.1002/glia.23197
- Barateiro, A., and Fernandes, A. (2014). Temporal oligodendrocyte lineage progression: *in vitro* models of proliferation, differentiation and myelination. *Biochim. Biophys. Acta* 1843, 1917–1929. doi: 10.1016/j.bbamcr.2014.04.018
- Baydyuk, M., Morrison, V. E., Gross, P. S., and Huang, J. K. (2020). Extrinsic factors driving oligodendrocyte lineage cell progression in CNS development and injury. *Neurochem. Res.* 45, 630–642. doi: 10.1007/s11064-020-02967-7
- Beiter, R. M., Fernández-Castañeda, A., Rivet-Noor, C., Merchak, A., Bai, R., Slogar, E., et al. (2020). Evidence for oligodendrocyte progenitor cell heterogeneity in the adult mouse brain. *bioRxiv* [Preprint]. doi: 10.1101/2020.03.06.981373
- Bergles, D. E., and Richardson, W. D. (2015). Oligodendrocyte development and plasticity. *Cold Spring Harb. Perspect. Biol.* 8:a020453. doi: 10.1101/cshperspect.a020453
- Bergles, D. E., Roberts, J. D., Somogyi, P., and Jahr, C. E. (2000). Glutamatergic synapses on oligodendrocyte precursor cells in the hippocampus. *Nature* 405, 187–191. doi: 10.1038/35012083
- Bin, J. M., and Lyons, D. A. (2016). Imaging myelination *in vivo* using transparent animal models. *Brain Plast.* 2, 3–29. doi: 10.3233/BPL-160029
- Birey, F., Andersen, J., Makinson, C. D., Islam, S., Wei, W., Huber, N., et al. (2017). Assembly of functionally integrated human forebrain spheroids. *Nature* 545, 54–59. doi: 10.1038/nature22330
- Birey, F., Kloc, M., Chavali, M., Hussein, I., Wilson, M., Christoffel, D. J., et al. (2015). Genetic and stress-induced loss of NG2 glia triggers emergence of depressive-like behaviors through reduced secretion of FGF2. *Neuron* 88, 941–956. doi: 10.1016/j.neuron.2015.10.046
- Biswas, S., Chung, S. H., Jiang, P., Dehghan, S., and Deng, W. (2019). Development of glial restricted human neural stem cells for oligodendrocyte differentiation *in vitro* and *in vivo*. *Sci. Rep.* 9:9013. doi: 10.1038/s41598-019-45247-3
- Borges, H. L., Linden, R., and Wang, J. Y. J. (2008). DNA damage-induced cell death: lessons from the central nervous system. *Cell Res.* 18, 17–26. doi: 10.1038/cr.2007.110
- Boshans, L. L., Sherfat, A., and Nishiyama, A. (2020). The effects of developmental and current niches on oligodendrocyte precursor dynamics and fate. *Neurosci. Lett.* 715:134593. doi: 10.1016/j.neulet.2019.134593
- Bouabe, H., and Okkenhaug, K. (2013). Gene targeting in mice: a review. *Methods Mol. Biol.* 1064, 315–336. doi: 10.1007/978-1-62703-601-6\_23
- Bribián, A., Medina-Rodríguez, E., Josa-Prado, F., García-Álvarez, I., Machín-Díaz, I., Murcia-Belmonte, V., et al. (2019). Age-linked heterogeneity among oligodendrocyte precursor cells in the cerebral cortex of mice and human. *bioRxiv* [Preprint]. doi: 10.1101/799544
- Cahoy, J. D., Emery, B., Kaushal, A., Foo, L. C., Zamanian, J. L., Christopherson, K. S., et al. (2008). A transcriptome database for astrocytes, neurons and oligodendrocytes: a new resource for understanding brain development and function. *J. Neurosci.* 28, 264–278. doi: 10.1523/JNEUROSCI.4178-07.2008
- Chamling, X., Kallman, A., Fang, W., Berlinicke, C. A., Mertz, J. L., Devkota, P., et al. (2021). Single-cell transcriptomic reveals molecular diversity and developmental heterogeneity of human stem cell-derived oligodendrocyte lineage cells. *Nat. Commun.* 12:652. doi: 10.1038/s41467-021-20892-3
- Chanoumidou, K., Mozafari, S., Baron-Van Evercooren, A., and Kuhlmann, T. (2020). Stem cell derived oligodendrocytes to study myelin diseases. *Glia* 68, 705–720. doi: 10.1002/glia.23733
- Chari, D. M., and Blakemore, W. F. (2002). Efficient recolonisation of progenitor-depleted areas of the CNS by adult oligodendrocyte progenitor cells. *Glia* 37, 307–313. doi: 10.1002/glia.10038
- Cheli, V. T., Santiago Gonzalez, D. A., Namgyal Lama, T., Spreuer, V., Handley, V., Murphy, G. G., et al. (2016). Conditional deletion of the L-type calcium channel Cav1.2 in oligodendrocyte progenitor cells affects postnatal myelination in mice. *J. Neurosci.* 36, 10853–10869. doi: 10.1523/JNEUROSCI.1770-16.2016
- Cheli, V. T., Santiago Gonzalez, D. A., Spreuer, V., and Paez, P. M. (2015). Voltage-gated Ca<sup>2+</sup> entry promotes oligodendrocyte progenitor cell maturation and myelination *in vitro*. *Exp. Neurol.* 265, 69–83. doi: 10.1016/j.expneurol.2014.12.012
- Chen, Y., Balasubramanian, V., Peng, J., Hurlock, E. C., Tallquist, M., Li, J., et al. (2007). Isolation and culture of rat and mouse oligodendrocyte precursor cells. *Nat. Protoc.* 2, 1044–1051. doi: 10.1038/nprot.2007.149
- Chen, T. J., Kula, B., Nagy, B., Barzan, R., Gall, A., Ehrlich, I., et al. (2018). *In vivo* regulation of oligodendrocyte precursor cell proliferation and differentiation by the AMPA-receptor subunit GluA2. *Cell Rep.* 25, 852–861. doi: 10.1016/j.celrep.2018.09.066
- Chen, R., Wu, X., Jiang, L., and Zhang, Y. (2017). Single-cell RNA-seq reveals hypothalamic cell diversity. *Cell Rep.* 18, 3227–3241. doi: 10.1016/j.celrep.2017.03.004
- Chiaradia, I., and Lancaster, M. A. (2020). Brain organoids for the study of human neurobiology at the interface of *in vitro* and *in vivo*. *Nat. Neurosci.* 23, 1496–1508. doi: 10.1038/s41593-020-00730-3
- Christensen, D. J., and Nedergaard, M. (2011). Two-photon *in vivo* imaging of cells. *Pediatr. Nephrol.* 26, 1483–1489. doi: 10.1007/s00467-011-1818-9
- Clapham, D. E. (2007). Calcium signaling. *Cell* 131, 1047–1058. doi: 10.1016/j.cell.2007.11.028
- Clarke, L. E., Young, K. M., Hamilton, N. B., Li, H., Richardson, W. D., and Attwell, D. (2012). Properties and fate of oligodendrocyte progenitor cells in the corpus callosum, motor cortex and piriform cortex of the mouse. *J. Neurosci.* 32, 8173–8185. doi: 10.1523/JNEUROSCI.0928-12.2012
- Dawson, M. R., Levine, J. M., and Reynolds, R. (2000). NG2-expressing cells in the central nervous system: are they oligodendroglial progenitors? *J. Neurosci. Res.* 61, 471–479. doi: 10.1002/1097-4547(20000901)61:5<471::AID-JNR1>3.0.CO;2-N
- Dawson, M. R., Polito, A., Levine, J. M., and Reynolds, R. (2003). NG2-expressing glial progenitor cells: an abundant and widespread population of cycling cells in the adult rat CNS. *Mol. Cell. Neurosci.* 24, 476–488. doi: 10.1016/s1044-7431(03)00210-0
- Dean, K. M., Qin, Y., and Palmer, A. E. (2012). Visualizing metal ions in cells: an overview of analytical techniques, approaches, and probes. *Biochim. Biophys. Acta* 1823, 1406–1415. doi: 10.1016/j.bbamcr.2012.04.001
- Deshmane, S. L., Kremlev, S., Amini, S., and Sawaya, B. E. (2009). Monocyte chemoattractant protein-1 (MCP-1): an overview. *J. Interferon Cytokine Res.* 29, 313–326. doi: 10.1089/jir.2008.0027
- Dimou, L., and Gallo, V. (2015). NG2-glia and their functions in the central nervous system. *Glia* 63, 1429–1451. doi: 10.1002/glia.22859
- Djogo, T., Robins, S. C., Schneider, S., Kryzskaya, D., Liu, X., Mingay, A., et al. (2016). Adult NG2-glia are required for median eminence-mediated leptin sensing and body weight control. *Cell Metab.* 23, 797–810. doi: 10.1016/j.cmet.2016.04.013
- Domingues, H. S., Portugal, C. C., Socodato, R., and Relvas, J. B. (2016). Oligodendrocyte, astrocyte and microglia crosstalk in myelin development, damage and repair. *Front. Cell Dev. Biol.* 4:71. doi: 10.3389/fcell.2016.00071
- Douglas Fields, R. (2015). A new mechanism of nervous system plasticity: activity-dependent myelination. *Nat. Rev. Neurosci.* 16, 756–767. doi: 10.1038/nrn4023
- Douvaras, P., and Fossati, V. (2015). Generation and isolation of oligodendrocyte progenitor cells from human pluripotent stem cells. *Nat. Protoc.* 10, 1143–1154. doi: 10.1038/nprot.2015.075
- Dumas, L., Heitz-Marchaland, C., Fouquet, S., Suter, U., Livet, J., Moreau-Fauvarque, C., et al. (2015). Multicolor analysis of oligodendrocyte morphology, interactions and development with Brainbow. *Glia* 63, 699–717. doi: 10.1002/glia.22779
- Duncan, I. D., and Radcliff, A. B. (2016). Inherited and acquired disorders of myelin: the underlying myelin pathology. *Exp. Neurol.* 283, 452–475. doi: 10.1016/j.expneurol.2016.04.002
- Dyer, E. L., Gray Roncal, W., Prasad, J. A., Fernandes, H. L., Gürsoy, D., De Andrade, V., et al. (2017). Quantifying mesoscale neuroanatomy using X-ray microtomography. *eNeuro* 4:ENEURO.0195–0117.2017. doi: 10.1523/ENEURO.0195-17.2017



- Eftekkharpour, E., Karimi-Abdolrezaee, S., Wang, J., El-Beheiry, H., Morshead, C., and Fehlings, M. (2007). Myelination of congenitally dysmyelinated spinal cord axons by adult neural precursor cells results in formation of nodes of ranvier and improved axonal conduction. *J. Neurosci.* 27, 3416–3428. doi: 10.1523/JNEUROSCI.0273-07.2007
- Egawa, N., Takase, H., Josephine, L., Takahashi, R., and Arai, K. (2016). Clinical application of oligodendrocyte precursor cells for cell-based therapy. *Brain Circ.* 2, 121–125. doi: 10.4103/2394-8108.192515
- Ehrlich, M., Mozafari, S., Glatz, M., Starost, L., Velychko, S., Hallmann, A. L., et al. (2017). Rapid and efficient generation of oligodendrocytes from human induced pluripotent stem cells using transcription factors. *Proc. Natl. Acad. Sci. U S A* 114, E2243–E2252. doi: 10.1073/pnas.1614412114
- Elbaz, B., and Popko, B. (2019). Molecular control of oligodendrocyte development. *Trends Neurosci.* 42, 263–277. doi: 10.1016/j.tins.2019.01.002
- Ernst, O. P., Sánchez Murcia, P. A., Daldrop, P., Tsunoda, S. P., Kateriya, S., and Hegemann, P. (2008). Photoactivation of channelrhodopsin. *J. Biol. Chem.* 283, 1637–1643. doi: 10.1074/jbc.M708039200
- Erwig, M. S., Patzig, J., Steyer, A. M., Dibaj, P., Heilmann, M., Heilmann, I., et al. (2019). Anillin facilitates septin assembly to prevent pathological outfoldings of central nervous system myelin. *eLife* 8:e43888. doi: 10.7554/eLife.43888
- Espinosa-Hoyos, D., Burstein, S. R., Cha, J., Jain, T., Nijsure, M., Jagielska, A., et al. (2020). Mechanosensitivity of human oligodendrocytes. *Front. Cell. Neurosci.* 14:222. doi: 10.3389/fncel.2020.00222
- Eugenín-Von Bernhardt, J., and Dimou, L. (2016). NG2-glia, more than progenitor cells. *Adv. Exp. Med. Biol.* 949, 27–45. doi: 10.1007/978-3-319-40764-7\_2
- Eugenin von Bernhardt, J., and Dimou, L. (2019). Recent advances in live imaging of cells of the oligodendrocyte lineage. *Methods Mol. Biol.* 1936, 275–294. doi: 10.1007/978-1-4939-9072-6\_16
- Fayzullin, A., Tuvnes, F. A., Skjelleggrind, H. K., Behnan, J., Mughal, A. A., Langmoen, I. A., et al. (2016). Time-lapse phenotyping of invasive glioma cells ex vivo reveals subtype-specific movement patterns guided by tumor core signaling. *Exp. Cell Res.* 349, 199–213. doi: 10.1016/j.yexcr.2016.08.001
- Feng, L., Chao, J., Tian, E., Li, L., Ye, P., Zhang, M., et al. (2020). Cell-based therapy for canavan disease using human iPSC-derived NPCs and OPCs. *Adv. Sci.* 7:2002155. doi: 10.1002/advs.202002155
- Fischbach, F., Nedelcu, J., Leopold, P., Zhan, J., Clarner, T., Nellesen, L., et al. (2019). Cuprizone-induced graded oligodendrocyte vulnerability is regulated by the transcription factor DNA damage-inducible transcript 3. *Glia* 67, 263–276. doi: 10.1002/glia.23538
- Foerster, S., Hill, M. F. E., and Franklin, R. J. M. (2019). Diversity in the oligodendrocyte lineage: plasticity or heterogeneity? *Glia* 67, 1797–1805. doi: 10.1002/glia.23607
- Friess, M., Hammann, J., Unichenko, P., Luhmann, H. J., White, R., and Kirischuk, S. (2016). Intracellular ion signaling influences myelin basic protein synthesis in oligodendrocyte precursor cells. *Cell Calcium* 60, 322–330. doi: 10.1016/j.ceca.2016.06.009
- Gadea, A., Aguirre, A., Haydar, T. F., and Gallo, V. (2009). Endothelin-1 regulates oligodendrocyte development. *J. Neurosci.* 29, 10047–10062. doi: 10.1523/JNEUROSCI.0822-09.2009
- Galichet, C., and Lovell-Badge, R. (2021). Applications of genome editing on laboratory animals. *Lab. Anim.* doi: 10.1177/0023677221993141. [Epub ahead of print].
- Galvao, R. P., Kasina, A., McNeill, R. S., Harbin, J. E., Foreman, O., Verhaak, R. G. W., et al. (2014). Transformation of quiescent adult oligodendrocyte precursor cells into malignant glioma through a multistep reactivation process. *Proc. Natl. Acad. Sci. U S A* 111, E4214–E4223. doi: 10.1073/pnas.1414389111
- García-León, J. A., García-Díaz, B., Eggermont, K., Cáceres-Palomo, L., Neyrinck, K., Madeiro Da Costa, R., et al. (2020). Generation of oligodendrocytes and establishment of an all-human myelinating platform from human pluripotent stem cells. *Nat. Protoc.* 15, 3716–3744. doi: 10.1038/s41596-020-0395-4
- Giacci, M. K., Bartlett, C. A., Huynh, M., Kilburn, M. R., Dunlop, S. A., and Fitzgerald, M. (2018). Three dimensional electron microscopy reveals changing axonal and myelin morphology along normal and partially injured optic nerves. *Sci. Rep.* 8:3979. doi: 10.1038/s41598-018-22361-2
- Goldman, S. A., and Kuypers, N. J. (2015). How to make an oligodendrocyte. *Development* 142, 3983–3995. doi: 10.1242/dev.126409
- González-Orozco, J. C., Moral-Morales, A. D., and Camacho-Arroyo, I. (2020). Progesterone through progesterone receptor b isoform promotes rodent embryonic oligodendrogenesis. *Cells* 9:960. doi: 10.3390/cells9040960
- Gregath, A., and Lu, Q. R. (2018). Epigenetic modifications-insight into oligodendrocyte lineage progression, regeneration, and disease. *FEBS Lett.* 592, 1063–1078. doi: 10.1002/1873-3468.12999
- Gryniewicz, G., Poenie, M., and Tsien, R. Y. (1985). A new generation of Ca<sup>2+</sup> indicators with greatly improved fluorescence properties. *J. Biol. Chem.* 260, 3440–3450. doi: 10.1016/s0021-9258(19)83641-4
- Guo, F., Maeda, Y., Ma, J., Xu, J., Horiuchi, M., Miers, L., et al. (2010). Pyramidal neurons are generated from oligodendroglial progenitor cells in adult piriform cortex. *J. Neurosci.* 30, 12036–12049. doi: 10.1523/JNEUROSCI.1360-10.2010
- Haberlandt, C., Derouiche, A., Wyczynski, A., Haseleu, J., Pohle, J., Karam, K., et al. (2011). Gray matter NG2 cells display multiple Ca<sup>2+</sup>-signaling pathways and highly motile processes. *PLoS One* 6:e17575. doi: 10.1371/journal.pone.0017575
- Habib, N., Avraham-David, I., Basu, A., Burks, T., Shekhar, K., Hofree, M., et al. (2017). Massively parallel single-nucleus RNA-seq with DroNc-seq. *Nat. Methods* 14, 955–958. doi: 10.1038/nmeth.4407
- Habib, N., Li, Y., Heidenreich, M., Swiech, L., Avraham-David, I., Trombetta, J. J., et al. (2016). Div-Seq: single-nucleus RNA-Seq reveals dynamics of rare adult newborn neurons. *Science* 353, 925–928. doi: 10.1126/science.aad7038
- Heredia, D. J., De Angeli, C., Fedi, C., and Gould, T. W. (2020). Calcium signaling in schwann cells. *Neurosci. Lett.* 729:134959. doi: 10.1016/j.neulet.2020.134959
- Hernández-Hernández, O., Ávila-Avilés, R. D., and Hernández-Hernández, J. M. (2020). Chromatin landscape during skeletal muscle differentiation. *Front. Genet.* 11:578712. doi: 10.3389/fgene.2020.578712
- Hesp, Z. C., Yoseph, R. Y., Suzuki, R., Jukkola, P., Wilson, C., Nishiyama, A., et al. (2018). Proliferating NG2-cell-dependent angiogenesis and scar formation alter axon growth and functional recovery after spinal cord injury in mice. *J. Neurosci.* 38, 1366–1382. doi: 10.1523/JNEUROSCI.3953-16.2017
- Hill, R. A., Patel, K. D., Medved, J., Reiss, A. M., and Nishiyama, A. (2013). NG2 cells in white matter but not gray matter proliferate in response to PDGF. *J. Neurosci.* 33, 14558–14566. doi: 10.1523/JNEUROSCI.2001-12.2013
- Hillman, H. (2000). Limitations of clinical and biological histology. *Med. Hypotheses* 54, 553–564. doi: 10.1054/mehy.1999.0894
- Hirbec, H., Déglon, N., Foo, L. C., Goshen, I., Grutzendler, J., Hangen, E., et al. (2020). Emerging technologies to study glial cells. *Glia* 68, 1692–1728. doi: 10.1002/glia.23780
- Hu, B.-Y., Du, Z.-W., Li, X.-J., Ayala, M., and Zhang, S.-C. (2009). Human oligodendrocytes from embryonic stem cells: conserved SHH signaling networks and divergent FGF effects. *Development* 136, 1443–1452. doi: 10.1242/dev.029447
- Huang, W., Guo, Q., Bai, X., Scheller, A., and Kirchhoff, F. (2019). Early embryonic NG2 glia are exclusively gliogenic and do not generate neurons in the brain. *Glia* 67, 1094–1103. doi: 10.1002/glia.23590
- Huang, W., Zhao, N., Bai, X., Karam, K., Trotter, J., Goebbels, S., et al. (2014). Novel NG2-CreERT2 knock-in mice demonstrate heterogeneous differentiation potential of NG2 glia during development. *Glia* 62, 896–913. doi: 10.1002/glia.22648
- Hwang, B., Lee, J. H., and Bang, D. (2018). Single-cell RNA sequencing technologies and bioinformatics pipelines. *Exp. Mol. Med.* 50, 1–4. doi: 10.1038/s12276-018-0071-8
- Ilyasov, A. A., Milligan, C. E., Pharr, E. P., and Howlett, A. C. (2018). The endocannabinoid system and oligodendrocytes in health and disease. *Front. Neurosci.* 12:733. doi: 10.3389/fnins.2018.00733
- Irvine, K. A., and Blakemore, W. F. (2007). A different regional response by mouse oligodendrocyte progenitor cells (OPCs) to high-dose X-irradiation has consequences for repopulating OPC-depleted normal tissue. *Eur. J. Neurosci.* 25, 417–424. doi: 10.1111/j.1460-9568.2007.05313.x
- Jackson, E. L., Garcia-Verdugo, J. M., Gil-Perotin, S., Roy, M., Quinones-Hinojosa, A., Vandenberg, S., et al. (2006). PDGFR  $\alpha$ -positive B cells are neural stem cells in the adult SVZ that form glioma-like growths in response to increased PDGF signaling. *Neuron* 51, 187–199. doi: 10.1016/j.neuron.2006.06.012

- Jacob, F., Salinas, R. D., Zhang, D. Y., Nguyen, P. T. T., Schnoll, J. G., Wong, S. Z. H., et al. (2020). A patient-derived glioblastoma organoid model and biobank recapitulates inter- and intra-tumoral heterogeneity. *Cell* 180, 188.e22–204.e22. doi: 10.1016/j.cell.2019.11.036
- Kamimura, K., Suda, T., Zhang, G., and Liu, D. (2011). Advances in gene delivery systems. *Pharmaceut. Med.* 25, 293–306. doi: 10.2165/11594020-000000000-00000
- Kang, S. H., Fukaya, M., Yang, J. K., Rothstein, J. D., and Bergles, D. E. (2010). NG2<sup>+</sup> CNS glial progenitors remain committed to the oligodendrocyte lineage in postnatal life and following neurodegeneration. *Neuron* 68, 668–681. doi: 10.1016/j.neuron.2010.09.009
- Kashima, Y., Sakamoto, Y., Kaneko, K., Seki, M., Suzuki, Y., and Suzuki, A. (2020). Single-cell sequencing techniques from individual to multiomics analyses. *Exp. Mol. Med.* 52, 1419–1427. doi: 10.1038/s12276-020-00499-2
- Kawabata, S., Takano, M., Numasawa-Kuroiwa, Y., Itakura, G., Kobayashi, Y., Nishiyama, Y., et al. (2016). Grafted human iPS cell-derived oligodendrocyte precursor cells contribute to robust remyelination of demyelinated axons after spinal cord injury. *Stem Cell Rep.* 6, 1–8. doi: 10.1016/j.stemcr.2015.11.013
- Kayasandik, C. B., Ru, W., and Labate, D. (2020). A multistep deep learning framework for the automated detection and segmentation of astrocytes in fluorescent images of brain tissue. *Sci. Rep.* 10:5137. doi: 10.1038/s41598-020-61953-9
- Kessaris, N., Fogarty, M., Iannarelli, P., Grist, M., Wegner, M., and Richardson, W. D. (2006). Competing waves of oligodendrocytes in the forebrain and postnatal elimination of an embryonic lineage. *Nat. Neurosci.* 9, 173–179. doi: 10.1038/nn1620
- Kikuchi, T., Gonzalez-Soriano, J., Kastanauskaitė, A., Benavides-Piccione, R., Merchan-Perez, A., Defelipe, J., et al. (2020). Volume electron microscopy study of the relationship between synapses and astrocytes in the developing rat somatosensory cortex. *Cereb. Cortex* 30, 3800–3819. doi: 10.1093/cercor/bhz343
- Kim, D.-S., Jung, S. J., Lee, J. S., Lim, B. Y., Kim, H. A., Yoo, J.-E., et al. (2017). Rapid generation of OPC-like cells from human pluripotent stem cells for treating spinal cord injury. *Exp. Mol. Med.* 49:e361. doi: 10.1038/emmm.2017.106
- Kishida, N., Maki, T., Takagi, Y., Yasuda, K., Kinoshita, H., Ayaki, T., et al. (2019). Role of perivascular oligodendrocyte precursor cells in angiogenesis after brain ischemia. *J. Am. Heart Assoc.* 8:e011824. doi: 10.1161/JAHA.118.011824
- Kroehne, V., Tsata, V., Marrone, L., Froeb, C., Reinhardt, S., Gompf, A., et al. (2017). Primary spinal OPC culture system from adult zebrafish to study oligodendrocyte differentiation *in vitro*. *Front. Cell. Neurosci.* 11:284. doi: 10.3389/fncel.2017.00284
- Kuhn, S., Gritti, L., Crooks, D., and Dombrowski, Y. (2019). Oligodendrocytes in development, myelin generation and beyond. *Cells* 8:1424. doi: 10.3390/cells8111424
- Kukley, M., Kiladze, M., Tognatta, R., Hans, M., Swandulla, D., Schramm, J., et al. (2008). Glial cells are born with synapses. *FASEB J.* 22, 2957–2969. doi: 10.1096/fj.07-090985
- Labrada-Moncada, F. E., Martínez-Torres, A., and Reyes-Haro, D. (2020). GABAA receptors are selectively expressed in NG2 glia of the cerebellar white matter. *Neuroscience* 433, 132–143. doi: 10.1016/j.neuroscience.2020.03.003
- Lager, A. M., Corradin, O. G., Cregg, J. M., Elitt, M. S., Shick, H. E., Clayton, B. L. L., et al. (2018). Rapid functional genetics of the oligodendrocyte lineage using pluripotent stem cells. *Nat. Commun.* 9:3708. doi: 10.1038/s41467-018-06102-7
- Lariosa-Willingham, K. D., Rosler, E. S., Tung, J. S., Dugas, J. C., Collins, T. L., and Leonoudakis, D. (2016). A high throughput drug screening assay to identify compounds that promote oligodendrocyte differentiation using acutely dissociated and purified oligodendrocyte precursor cells. *BMC Res. Notes* 9:419. doi: 10.1186/s13104-016-2220-2
- Larson, V. A., Zhang, Y., and Bergles, D. E. (2016). Electrophysiological properties of NG2<sup>+</sup> cells: matching physiological studies with gene expression profiles. *Brain Res.* 1638, 138–160. doi: 10.1016/j.brainres.2015.09.010
- Lee, C., Lavoie, A., Liu, J., Chen, S. X., and Liu, B. H. (2020). Light up the brain: the application of optogenetics in cell-type specific dissection of mouse brain circuits. *Front. Neural Circuits* 14:18. doi: 10.3389/fncir.2020.00018
- Lentferink, D. H., Jongsma, J. M., Werkman, I., and Baron, W. (2018). Grey matter OPCs are less mature and less sensitive to IFN $\gamma$  than white matter OPCs: consequences for remyelination. *Sci. Rep.* 8:2113. doi: 10.1038/s41598-018-19934-6
- Levine, J. M., Reynolds, R., and Fawcett, J. W. (2001). The oligodendrocyte precursor cell in health and disease. *Trends Neurosci.* 24, 39–47. doi: 10.1016/s0166-2236(00)01691-x
- Li, L., Tian, E., Chen, X., Chao, J., Klein, J., Qu, Q., et al. (2018). GFAP mutations in astrocytes impair oligodendrocyte progenitor proliferation and myelination in an hiPSC model of alexander disease. *Cell Stem Cell* 23, 239.e6–251.e6. doi: 10.1016/j.stem.2018.07.009
- Lin, S.-C., and Bergles, D. E. (2004). Synaptic signaling between GABAergic interneurons and oligodendrocyte precursor cells in the hippocampus. *Nat. Neurosci.* 7, 24–32. doi: 10.1038/nn1162
- Lin, G., Mela, A., Guilfoyle, E. M., and Goldman, J. E. (2009). Neonatal and adult O4<sup>+</sup> oligodendrocyte lineage cells display different growth factor responses and different gene expression patterns. *J. Neurosci. Res.* 87, 3390–3402. doi: 10.1002/jnr.22065
- Liu, Y., and Aguzzi, A. (2020). NG2 glia are required for maintaining microglia homeostatic state. *Glia* 68, 345–355. doi: 10.1002/glia.23721
- Lopez-Caraballo, L., Martorell-Marugan, J., Carmona-Sáez, P., and Gonzalez-Munoz, E. (2020). iPS-derived early oligodendrocyte progenitor cells from SPMS patients reveal deficient *in vitro* cell migration stimulation. *Cells* 9:1803. doi: 10.3390/cells9081803
- Luckner, M., Burgold, S., Filser, S., Scheungrab, M., Niyaz, Y., Hummel, E., et al. (2018). Label-free 3D-CLEM using endogenous tissue landmarks. *iScience* 6, 92–101. doi: 10.1016/j.isci.2018.07.012
- Madhavan, M., Nevin, Z. S., Shick, H. E., Garrison, E., Clarkson-Paredes, C., Karl, M., et al. (2018). Induction of myelinating oligodendrocytes in human cortical spheroids. *Nat. Methods* 15, 700–706. doi: 10.1038/s41592-018-0081-4
- Maki, T., Maeda, M., Uemura, M., Lo, E. K., Terasaki, Y., Liang, A. C., et al. (2015). Potential interactions between pericytes and oligodendrocyte precursor cells in perivascular regions of cerebral white matter. *Neurosci. Lett.* 597, 164–169. doi: 10.1016/j.neulet.2015.04.047
- Marie, C., Clavairol, A., Frah, M., Hmidan, H., Yan, J., Zhao, C., et al. (2018). Oligodendrocyte precursor survival and differentiation requires chromatin remodeling by Chd7 and Chd8. *Proc. Natl. Acad. Sci. U S A* 115:E8246. doi: 10.1073/pnas.1802620115
- Marasca, R., Hoche, T., Agirre, E., Hoodless, L. J., Barkey, W., Auer, F., et al. (2020). Functionally distinct subgroups of oligodendrocyte precursor cells integrate neural activity and execute myelin formation. *Nat. Neurosci.* 23, 363–374. doi: 10.1038/s41593-019-0581-2
- Marques, S., Van Bruggen, D., Vanichkina, D. P., Floriddia, E. M., Munguba, H., Varem, L., et al. (2018). Transcriptional convergence of oligodendrocyte lineage progenitors during development. *Dev. Cell* 46, 504.e7–517.e7. doi: 10.1016/j.devcel.2018.07.005
- Marques, S., Zeisel, A., Codeluppi, S., van Bruggen, D., Mendanha Falcao, A., Xiao, L., et al. (2016). Oligodendrocyte heterogeneity in the mouse juvenile and adult central nervous system. *Science* 352, 1326–1329. doi: 10.1126/science.aaf6463
- Marsters, C. M., Nesan, D., Far, R., Klenin, N., Pittman, Q. J., and Kurrasch, D. M. (2020). Embryonic microglia influence developing hypothalamic glial populations. *J. Neuroinflammation* 17:146. doi: 10.1186/s12974-020-01811-7
- Marton, R. M., Miura, Y., Sloan, S. A., Li, Q., Revah, O., Levy, R. J., et al. (2019). Differentiation and maturation of oligodendrocytes in human three-dimensional neural cultures. *Nat. Neurosci.* 22, 484–491. doi: 10.1038/s41593-018-0316-9
- Mason, J. L., and Goldman, J. E. (2002). A2B5<sup>+</sup> and O4<sup>+</sup> Cycling progenitors in the adult forebrain white matter respond differentially to PDGF-AA, FGF-2, and IGF-1. *Mol. Cell. Neurosci.* 20, 30–42. doi: 10.1006/mcne.2002.1114
- Matjusaitis, M., Wagstaff, L. J., Martella, A., Baranowski, B., Blin, C., Gogolok, S., et al. (2019). Reprogramming of fibroblasts to oligodendrocyte progenitor-like cells using CRISPR/Cas9-based synthetic transcription factors. *Stem Cell Rep.* 13, 1053–1067. doi: 10.1016/j.stemcr.2019.10.010
- Mecha, M., Yanguas-Casés, N., Feliú, A., Mestre, L., Carrillo-Salinas, F. J., Riecken, K., et al. (2020). Involvement of Wnt7a in the role of M2c microglia in neural stem cell oligodendrogenesis. *J. Neuroinflammation* 17:88. doi: 10.1186/s12974-020-01734-3

- Medina-Rodríguez, E. M., Arenzana, F. J., Bribián, A., and De Castro, F. (2013). Protocol to isolate a large amount of functional oligodendrocyte precursor cells from the cerebral cortex of adult mice and humans. *PLoS One* 8:e81620. doi: 10.1371/journal.pone.0081620
- Melissaridou, S., Wiech, E., Magan, M., Jain, M. V., Chung, M. K., Farnebo, L., et al. (2019). The effect of 2D and 3D cell cultures on treatment response, EMT profile and stem cell features in head and neck cancer. *Cancer Cell Int.* 19:16. doi: 10.1186/s12935-019-0733-1
- Min, K., Cho, I., Choi, M., and Chang, J.-B. (2020). Multiplexed expansion microscopy of the brain through fluorophore screening. *Methods* 174, 3–10. doi: 10.1016/j.ymeth.2019.07.017
- Morales Pantoja, I. E., Smith, M. D., Rajbhandari, L., Cheng, L., Gao, Y., Mahairaki, V., et al. (2020). iPSCs from people with MS can differentiate into oligodendrocytes in a homeostatic but not an inflammatory milieu. *PLoS One* 15:e0233980. doi: 10.1371/journal.pone.0233980
- Moshrefi-Ravassdani, B., Dublin, P., Seifert, G., Jennissen, K., Steinhäuser, C., Kafitz, K. W., et al. (2017). Changes in the proliferative capacity of NG2 cell subpopulations during postnatal development of the mouse hippocampus. *Brain Struct. Funct.* 222, 831–847. doi: 10.1007/s00429-016-1249-2
- Mount, C. W., Yalçın, B., Cunliffe-Koehler, K., Sundaresh, S., and Monje, M. (2019). Monosynaptic tracing maps brain-wide afferent oligodendrocyte precursor cell connectivity. *eLife* 8:e49291. doi: 10.7554/eLife.49291
- Moyon, S., Dubessy, A. L., Agriot, M. S., Trotter, M., Huang, J. K., Dauphinot, L., et al. (2015). Demyelination causes adult CNS progenitors to revert to an immature state and express immune cues that support their migration. *J. Neurosci.* 35, 4–20. doi: 10.1523/JNEUROSCI.0849-14.2015
- Nagy, B., Hovhannissyan, A., Barzan, R., Chen, T. J., and Kukley, M. (2017). Different patterns of neuronal activity trigger distinct responses of oligodendrocyte precursor cells in the corpus callosum. *PLoS Biol.* 15:e2001993. doi: 10.1371/journal.pbio.2001993
- Najm, F. J., Zaremba, A., Caprariello, A. V., Nayak, S., Freundt, E. C., Scacheri, P. C., et al. (2011). Rapid and robust generation of functional oligodendrocyte progenitor cells from epiblast stem cells. *Nat. Methods* 8, 957–962. doi: 10.1038/nmeth.1712
- Nakano, M., Tamura, Y., Yamato, M., Kume, S., Eguchi, A., Takata, K., et al. (2017). NG2 glial cells regulate neuroimmunological responses to maintain neuronal function and survival. *Sci. Rep.* 7:42041. doi: 10.1038/srep42041
- Nevin, Z. S., Factor, D. C., Karl, R. T., Douvaras, P., Laukka, J., Windrem, M. S., et al. (2017). Modeling the mutational and phenotypic landscapes of pelizaeus-merzbacher disease with human iPSC-derived oligodendrocytes. *Am. J. Hum. Genet.* 100, 617–634. doi: 10.1016/j.ajhg.2017.03.005
- Ng, A. H. M., Khoshakhlagh, P., Rojo Arias, J. E., Pasquini, G., Wang, K., Swiersy, A., et al. (2020). A comprehensive library of human transcription factors for cell fate engineering. *Nat. Biotechnol.* doi: 10.1038/s41587-020-0742-6 [Epub ahead of print].
- Nicaise, A. M., Wagstaff, L. J., Willis, C. M., Paisie, C., Chandok, H., Robson, P., et al. (2019). Cellular senescence in progenitor cells contributes to diminished remyelination potential in progressive multiple sclerosis. *Proc. Natl. Acad. Sci. U S A* 116, 9030–9039. doi: 10.1073/pnas.1818348116
- Nikolakopoulou, A. M., Montagne, A., Kisler, K., Dai, Z., Wang, Y., Huuskonen, M. T., et al. (2019). Pericyte loss leads to circulatory failure and pleiotrophin depletion causing neuron loss. *Nat. Neurosci.* 22, 1089–1098. doi: 10.1038/s41593-019-0434-z
- Nutma, E., van Gent, D., Amor, S., and Peferoen, L. A. N. (2020). Astrocyte and oligodendrocyte cross-talk in the central nervous system. *Cells* 9:600. doi: 10.3390/cells9030600
- Ogawa, J., Pao, G. M., Shokhirev, M. N., and Verma, I. M. (2018). Glioblastoma model using human cerebral organoids. *Cell Rep.* 23, 1220–1229. doi: 10.1016/j.celrep.2018.03.105
- Oh, S. W., Harris, J. A., Ng, L., Winslow, B., Cain, N., Mihalas, S., et al. (2014). A mesoscale connectome of the mouse brain. *Nature* 508, 207–214. doi: 10.1038/nature13186
- O'Meara, R. W., Ryan, S. D., Colognato, H., and Kothary, R. (2011). Derivation of enriched oligodendrocyte cultures and oligodendrocyte/neuron myelinating co-cultures from post-natal murine tissues. *J. Vis. Exp.* 54:3324. doi: 10.3791/3324
- Ono, K., Kagawa, T., Tsumori, T., Yokota, S., and Yasui, Y. (2001). Morphological changes and cellular dynamics of oligodendrocyte lineage cells in the developing vertebrate central nervous system. *Dev. Neurosci.* 23, 346–355. doi: 10.1159/000048718
- Ortolani, D., Manot-Saillet, B., Orduz, D., Ortiz, F. C., and Angulo, M. C. (2018). *in vivo* optogenetic approach to study neuron-oligodendroglia interactions in mouse pups. *Front. Cell. Neurosci.* 12:477. doi: 10.3389/fncel.2018.00477
- Ozerdem, U., Grako, K. A., Dahlin-Huppe, K., Monosov, E., and Stallcup, W. B. (2001). NG2 proteoglycan is expressed exclusively by mural cells during vascular morphogenesis. *Dev. Dyn.* 222, 218–227. doi: 10.1002/dvdy.1200
- Paez, P. M., Fulton, D. J., Spreuer, V., Handley, V., Campagnoni, C. W., Macklin, W. B., et al. (2009). Golli myelin basic proteins regulate oligodendroglial progenitor cell migration through voltage-gated  $Ca^{2+}$  influx. *J. Neurosci.* 29, 6663–6676. doi: 10.1523/JNEUROSCI.5806-08.2009
- Pang, Y., Simpson, K., Miguel-Hidalgo, J. J., and Savich, R. (2018). Neuron/oligodendrocyte myelination coculture. *Methods Mol. Biol.* 1791, 131–144. doi: 10.1007/978-1-4939-7862-5\_10
- Pawlowski, M., Ortmann, D., Bertero, A., Tavares, J. M., Pedersen, R. A., Vallier, L., et al. (2017). Inducible and deterministic forward programming of human pluripotent stem cells into neurons, skeletal myocytes, and oligodendrocytes. *Stem Cell Rep.* 8, 803–812. doi: 10.1016/j.stemcr.2017.02.016
- Pedraza, C. E., Monk, R., Lei, J., Hao, Q., and Macklin, W. B. (2008). Production, characterization, and efficient transfection of highly pure oligodendrocyte precursor cultures from mouse embryonic neural progenitors. *Glia* 56, 1339–1352. doi: 10.1002/glia.20702
- Perlman, K., Couturier, C. P., Yaqubi, M., Tanti, A., Cui, Q. L., Pernin, F., et al. (2020). Developmental trajectory of oligodendrocyte progenitor cells in the human brain revealed by single cell RNA sequencing. *Glia* 68, 1291–1303. doi: 10.1002/glia.23777
- Pitman, K. A., Ricci, R., Gasperini, R., Beasley, S., Pavez, M., Charlesworth, J., et al. (2020). The voltage-gated calcium channel  $Ca_v1.2$  promotes adult oligodendrocyte progenitor cell survival in the mouse corpus callosum but not motor cortex. *Glia* 68, 376–392. doi: 10.1002/glia.23723
- Purger, D., Gibson, E. M., and Monje, M. (2016). Myelin plasticity in the central nervous system. *Neuropharmacology* 110, 563–573. doi: 10.1016/j.neuropharm.2015.08.001
- Rivers, L. E., Young, K. M., Rizzi, M., Jamen, F., Psachoulia, K., Wade, A., et al. (2008). PDGFRA/NG2 glia generate myelinating oligodendrocytes and piriform projection neurons in adult mice. *Nat. Neurosci.* 11, 1392–1401. doi: 10.1038/nn.2220
- Robins, S. C., Trudel, E., Rotondi, O., Liu, X., Djogo, T., Kryzskaya, D., et al. (2013). Evidence for NG2-glia derived, adult-born functional neurons in the hypothalamus. *PLoS One* 8:e78236. doi: 10.1371/journal.pone.0078236
- Rodrigues, G. M. C., Gaj, T., Adil, M. M., Wahba, J., Rao, A. T., Lorbeer, F. K., et al. (2017). Defined and scalable differentiation of human oligodendrocyte precursors from pluripotent stem cells in a 3D culture system. *Stem Cell Rep.* 8, 1770–1783. doi: 10.1016/j.stemcr.2017.04.027
- Rui, Y., Pollitt, S. L., Myers, K. R., Feng, Y., and Zheng, J. Q. (2020). Spontaneous local calcium transients regulate oligodendrocyte development in culture through store operated  $Ca^{2+}$  entry and release. *eNeuro* 4:ENEURO.0347-19.2020. doi: 10.1523/ENEURO.0347-19.2020
- Ruiz-Garcia, H., Alvarado-Estrada, K., Schiapparelli, P., Quinones-Hinojosa, A., and Trifiletti, D. M. (2020). Engineering three-dimensional tumor models to study glioma cancer stem cells and tumor microenvironment. *Front. Cell. Neurosci.* 14:558381. doi: 10.3389/fncel.2020.558381
- Sakry, D., Neitz, A., Singh, J., Frischknecht, R., Marongiu, D., Biname, F., et al. (2014). Oligodendrocyte precursor cells modulate the neuronal network by activity-dependent ectodomain cleavage of glial NG2. *PLoS Biol.* 12:e1001993. doi: 10.1371/journal.pbio.1001993
- Sakry, D., Yigit, H., Dimou, L., and Trotter, J. (2015). Oligodendrocyte precursor cells synthesize neuromodulatory factors. *PLoS One* 10:e0127222. doi: 10.1371/journal.pone.0127222
- Samudiyata, Castelo-Branco, G., and Liu, J. (2020). Epigenetic regulation of oligodendrocyte differentiation: from development to demyelinating disorders. *Glia* 68, 1619–1630. doi: 10.1002/glia.23820



- Santiago González, D. A., Cheli, V. T., Zamora, N. N., Lama, T. N., Spreuer, V., Murphy, G. G., et al. (2017). Conditional deletion of the L-type calcium channel Cav1.2 in NG2-positive cells impairs remyelination in mice. *J. Neurosci.* 37, 10038–10051. doi: 10.1523/JNEUROSCI.1787-17.2017
- Schertel, A., Snaidro, N., Han, H.-M., Ruhwedel, T., Laue, M., Grabenbauer, M., et al. (2013). Cryo FIB-SEM: Volume imaging of cellular ultrastructure in native frozen specimens. *J. Struct. Biol.* 184, 355–360. doi: 10.1016/j.jsb.2013.09.024
- Schoor, C., Brocke-Ahmadinejad, N., Gieselmann, V., and Winter, D. (2019). Investigation of oligodendrocyte precursor cell differentiation by quantitative proteomics. *Proteomics* 19:e1900057. doi: 10.1002/pmic.201900057
- Seo, J. H., Maki, T., Maeda, M., Miyamoto, N., Liang, A. C., Hayakawa, K., et al. (2014). Oligodendrocyte precursor cells support blood-brain barrier integrity via TGF- $\beta$  signaling. *PLoS One* 9:e103174. doi: 10.1371/journal.pone.0103174
- Seo, J. H., Miyamoto, N., Hayakawa, K., Pham, L. D., Maki, T., Ayata, C., et al. (2013). Oligodendrocyte precursors induce early blood-brain barrier opening after white matter injury. *J. Clin. Invest.* 123, 782–786. doi: 10.1172/JCI65863
- Serwanski, D. R., Jukkola, P., and Nishiyama, A. (2017). Heterogeneity of astrocyte and NG2 cell insertion at the node of ranvier. *J. Comp. Neurol.* 525, 535–552. doi: 10.1002/cne.24083
- Spitzer, S. O., Sitnikov, S., Kamen, Y., Evans, K. A., Kronenberg-Versteeg, D., Dietmann, S., et al. (2019). Oligodendrocyte progenitor cells become regionally diverse and heterogeneous with age. *Neuron* 101, 459.e5–471.e5. doi: 10.1016/j.neuron.2018.12.020
- Ståhl, P. L., Salmén, F., Vickovic, S., Lundmark, A., Navarro, J. F., Magnusson, J., et al. (2016). Visualization and analysis of gene expression in tissue sections by spatial transcriptomics. *Science* 353, 78–82. doi: 10.1126/science.aaf2403
- Sung, H.-Y., Chen, W.-Y., Huang, H.-T., Wang, C.-Y., Chang, S.-B., and Tzeng, S.-F. (2019). Down-regulation of interleukin-33 expression in oligodendrocyte precursor cells impairs oligodendrocyte lineage progression. *J. Neurochem.* 150, 691–708. doi: 10.1111/jnc.14788
- Tasic, B., Menon, V., Nguyen, T. N., Kim, T. K., Jarsky, T., Yao, Z., et al. (2016). Adult mouse cortical cell taxonomy revealed by single cell transcriptomics. *Nat. Neurosci.* 19, 335–346. doi: 10.1038/nn.4216
- Traiffort, E., Zakaria, M., Laouare, Y., and Ferent, J. (2016). Hedgehog: a key signaling in the development of the oligodendrocyte lineage. *J. Dev. Biol.* 4:28. doi: 10.3390/jdb4030028
- Tsien, R. Y. (1980). New calcium indicators and buffers with high selectivity against magnesium and protons: design, synthesis, and properties of prototype structures. *Biochemistry* 19, 2396–2404. doi: 10.1021/bi00552a018
- Tsien, R. Y. (1989). Fluorescent indicators of ion concentrations. *Methods Cell Biol.* 30, 127–156. doi: 10.1016/s0091-679x(08)60978-4
- Valério-Gomes, B., Guimarães, D. M., Szczupak, D., and Lent, R. (2018). The absolute number of oligodendrocytes in the adult mouse brain. *Front. Neuroanat.* 12:90. doi: 10.3389/fnana.2018.00090
- Vélez-Fort, M., Maldonado, P. P., Butt, A. M., Audinat, E., and Angulo, M. C. (2010). Postnatal switch from synaptic to extrasynaptic transmission between interneurons and NG2 cells. *J. Neurosci.* 30, 6921–6929. doi: 10.1523/JNEUROSCI.0238-10.2010
- Vidova, V., and Spacil, Z. (2017). A review on mass spectrometry-based quantitative proteomics: targeted and data independent acquisition. *Anal. Chim. Acta* 964, 7–23. doi: 10.1016/j.aca.2017.01.059
- Vitry, S., Avellana-Adalid, V., Hardy, R., Lachapelle, F., and Baron-Van Evercooren, A. (1999). Mouse oligospheres: from pre-progenitors to functional oligodendrocytes. *J. Neurosci. Res.* 58, 735–751. doi: 10.1002/(sici)1097-4547(19991215)58:6<735::aid-jnr2>3.0.co;2-9
- Vogel, S., Schäfer, C., Hess, S., Folz-Donahue, K., Nelles, M., Minassian, A., et al. (2019). The *in vivo* timeline of differentiation of engrafted human neural progenitor cells. *Stem Cell Res.* 37:101429. doi: 10.1016/j.scr.2019.101429
- Wan, R., Cheli, V. T., Santiago-Gonzalez, D. A., Rosenblum, S. L., Wan, Q., and Paez, P. M. (2020). Impaired postnatal myelination in a conditional knockout mouse for the ferritin heavy chain in oligodendroglial cells. *J. Neurosci.* 40, 7609–7624. doi: 10.1523/JNEUROSCI.1281-20.2020
- Wang, Y., Ali, M., Wang, Y., Kucenas, S., and Yu, G. (2018). Detection and tracking of migrating oligodendrocyte progenitor cells from *in vivo* fluorescence time-lapse imaging data. *Proc. IEEE Int. Symp. Biomed. Imaging* 2018, 961–964. doi: 10.1109/ISBI.2018.8363730
- Wang, S., Bates, J., Li, X., Schanz, S., Chandler-Militello, D., Levine, C., et al. (2013). Human iPSC-derived oligodendrocyte progenitor cells can myelinate and rescue a mouse model of congenital hypomyelination. *Cell Stem Cell* 12, 252–264. doi: 10.1016/j.stem.2012.12.002
- Wang, S., and Young, K. M. (2014). White matter plasticity in adulthood. *Neuroscience* 276, 148–160. doi: 10.1016/j.neuroscience.2013.10.018
- Wassie, A. T., Zhao, Y., and Boyden, E. S. (2019). Expansion microscopy: principles and uses in biological research. *Nat. Methods* 16, 33–41. doi: 10.1038/s41592-018-0219-4
- Watanabe, T., Frahm, J., and Michaelis, T. (2016). *In vivo* brain MR imaging at subnanoliter resolution: contrast and histology. *Magn. Reson. Med. Sci.* 15, 11–25. doi: 10.2463/mrms.2015-0048
- Weil, M.-T., Heibeck, S., Töpperwien, M., Tom Dieck, S., Ruhwedel, T., Salditt, T., et al. (2018). Axonal ensheathment in the nervous system of lamprey: implications for the evolution of myelinating glia. *J. Neurosci.* 38, 6586–6596. doi: 10.1523/JNEUROSCI.1034-18.2018
- Wen, S., Ma, D., Zhao, M., Xie, L., Wu, Q., Gou, L., et al. (2020). Spatiotemporal single-cell analysis of gene expression in the mouse suprachiasmatic nucleus. *Nat. Neurosci.* 23, 456–467. doi: 10.1038/s41593-020-0586-x
- Willems, J., de Jong, A. P. H., Scheefhals, N., Mertens, E., Catsburg, L. A. E., Poorthuis, R. B., et al. (2020). ORANGE: a CRISPR/Cas9-based genome editing toolbox for epitope tagging of endogenous proteins in neurons. *PLoS Biol.* 18:e3000665. doi: 10.1371/journal.pbio.3000665
- Woodruff, R. H., Fruttiger, M., Richardson, W. D., and Franklin, R. J. (2004). Platelet-derived growth factor regulates oligodendrocyte progenitor numbers in adult CNS and their response following CNS demyelination. *Mol. Cell. Neurosci.* 25, 252–262. doi: 10.1016/j.mcn.2003.10.014
- Yamada, M., Nagasaki, S. C., Ozawa, T., and Imayoshi, I. (2020). Light-mediated control of Gene expression in mammalian cells. *Neurosci. Res.* 152, 66–77. doi: 10.1016/j.neures.2019.12.018
- Yamashita, T., Miyamoto, Y., Bando, Y., Ono, T., Kobayashi, S., Doi, A., et al. (2017). Differentiation of oligodendrocyte progenitor cells from dissociated monolayer and feeder-free cultured pluripotent stem cells. *PLoS One* 12, e0171947–e0171947. doi: 10.1371/journal.pone.0171947
- Yang, J., Cheng, X., Shen, J., Xie, B., Zhao, X., Zhang, Z., et al. (2016). A novel approach for amplification and purification of mouse oligodendrocyte progenitor cells. *Front. Cell. Neurosci.* 10:203. doi: 10.3389/fncel.2016.00203
- Yu, T., Qi, Y., Gong, H., Luo, Q., and Zhu, D. (2018). Optical clearing for multiscale biological tissues. *J. Biophotonics* 11:e201700187. doi: 10.1002/jbio.201700187
- Zeisel, A., Muñoz-Manchado, A. B., Codeluppi, S., Lönnerberg, P., La Manno, G., Jureus, A., et al. (2015). Brain structure. Cell types in the mouse cortex and hippocampus revealed by single-cell RNA-seq. *Science* 347, 1138–1142. doi: 10.1126/science.aaa1934
- Zhang, Y., Chen, K., Sloan, S. A., Bennett, M. L., Scholze, A. R., O’Keefe, S., et al. (2014). An RNA-sequencing transcriptome and splicing database of glia, neurons and vascular cells of the cerebral cortex. *J. Neurosci.* 34, 11929–11947. doi: 10.1523/JNEUROSCI.1860-14.2014
- Zhang, M., Liu, Y., Wu, S., and Zhao, X. (2019). Ca<sup>2+</sup> signaling in oligodendrocyte development. *Cell. Mol. Neurobiol.* 39, 1071–1080. doi: 10.1007/s10571-019-00705-4
- Zhang, S.-Z., Wang, Q.-Q., Yang, Q.-Q., Gu, H.-Y., Yin, Y.-Q., Li, Y.-D., et al. (2019). NG2 glia regulate brain innate immunity via TGF- $\beta$ 2/TGFB2 axis. *BMC Med.* 17:204. doi: 10.1186/s12916-019-1439-x
- Zhou, W., Ge, W.-P., Zeng, S., Duan, S., and Luo, Q. (2007). Identification and two-photon imaging of oligodendrocyte in CA1 region of hippocampal slices. *Biochem. Biophys. Res. Commun.* 352, 598–602. doi: 10.1016/j.bbrc.2006.11.048
- Zhu, X., Bergles, D. E., and Nishiyama, A. (2008a). NG2 cells generate both oligodendrocytes and gray matter astrocytes. *Development* 135, 145–157. doi: 10.1242/dev.004895
- Zhu, X., Hill, R. A., and Nishiyama, A. (2008b). NG2 cells generate oligodendrocytes and gray matter astrocytes in the spinal cord. *Neuron Glia Biol.* 4, 19–26. doi: 10.1017/S1740925X09000015



- Zhu, X., Hill, R. A., Dietrich, D., Komitova, M., Suzuki, R., and Nishiyama, A. (2011). Age-dependent fate and lineage restriction of single NG2 cells. *Development* 138, 745–753. doi: 10.1242/dev.047951
- Zhu, X., Huang, L., Zheng, Y., Song, Y., Xu, Q., Wang, J., et al. (2019). Ultrafast optical clearing method for three-dimensional imaging with cellular resolution. *Proc. Natl. Acad. Sci. U S A* 116, 11480–11489. doi: 10.1073/pnas.1819583116
- Zong, H., Parada, L. F., and Baker, S. J. (2015). Cell of origin for malignant gliomas and its implication in therapeutic development. *Cold Spring Harb. Perspect. Biol.* 7:a020610. doi: 10.1101/cshperspect.a020610

**Conflict of Interest:** The authors declare that the research was conducted in the absence of any commercial or financial relationships that could be construed as a potential conflict of interest.

Copyright © 2021 Galichet, Clayton and Lovell-Badge. This is an open-access article distributed under the terms of the Creative Commons Attribution License (CC BY). The use, distribution or reproduction in other forums is permitted, provided the original author(s) and the copyright owner(s) are credited and that the original publication in this journal is cited, in accordance with accepted academic practice. No use, distribution or reproduction is permitted which does not comply with these terms.



# Heterogeneity and Development of Fine Astrocyte Morphology Captured by Diffraction-Limited Microscopy

Daniel Minge<sup>1</sup>, Cátia Domingos<sup>1</sup>, Petr Unichenko<sup>1</sup>, Charlotte Behringer<sup>1</sup>, Alberto Pauletti<sup>1</sup>, Stefanie Anders<sup>1</sup>, Michel K. Herde<sup>1</sup>, Andrea Delekate<sup>2</sup>, Polina Gulakova<sup>3</sup>, Susanne Schoch<sup>3</sup>, Gabor C. Petzold<sup>2,4</sup> and Christian Henneberger<sup>1,2,5\*</sup>

<sup>1</sup>Institute of Cellular Neurosciences, Medical Faculty, University of Bonn, Bonn, Germany, <sup>2</sup>German Center for Neurodegenerative Diseases (DZNE), Bonn, Germany, <sup>3</sup>Department of Neuropathology, University Hospital Bonn, Bonn, Germany, <sup>4</sup>Division of Vascular Neurology, University Hospital Bonn, Bonn, Germany, <sup>5</sup>Institute of Neurology, University College London, London, United Kingdom

## OPEN ACCESS

### Edited by:

Christian Lohr,  
University of Hamburg, Germany

### Reviewed by:

Mutsuo Nuriya  
Keio University School of Medicine,  
Japan  
João Filipe Oliveira,  
University of Minho, Portugal

### \*Correspondence:

Christian Henneberger  
christian.henneberger@uni-bonn.de

### Specialty section:

This article was submitted to  
Non-Neuronal Cells,  
a section of the journal  
Frontiers in Cellular Neuroscience

**Received:** 18 February 2021

**Accepted:** 06 May 2021

**Published:** 04 June 2021

### Citation:

Minge D, Domingos C, Unichenko P, Behringer C, Pauletti A, Anders S, Herde MK, Delekate A, Gulakova P, Schoch S, Petzold GC and Henneberger C (2021) Heterogeneity and Development of Fine Astrocyte Morphology Captured by Diffraction-Limited Microscopy. *Front. Cell. Neurosci.* 15:669280. doi: 10.3389/fncel.2021.669280

The fine processes of single astrocytes can contact many thousands of synapses whose function they can modulate through bi-directional signaling. The spatial arrangement of astrocytic processes and neuronal structures is relevant for such interactions and for the support of neuronal signaling by astrocytes. At the same time, the geometry of perisynaptic astrocyte processes is variable and dynamically regulated. Studying these fine astrocyte processes represents a technical challenge, because many of them cannot be fully resolved by diffraction-limited microscopy. Therefore, we have established two indirect parameters of astrocyte morphology, which, while not fully resolving local geometry by design, provide statistical measures of astrocyte morphology: the fraction of tissue volume that astrocytes occupy and the density of resolvable astrocytic processes. Both are straightforward to obtain using widely available microscopy techniques. We here present the approach and demonstrate its robustness across various experimental conditions using mainly two-photon excitation fluorescence microscopy in acute slices and *in vivo* as well as modeling. Using these indirect measures allowed us to analyze the morphology of relatively large populations of astrocytes. Doing so we captured the heterogeneity of astrocytes within and between the layers of the hippocampal CA1 region and the developmental profile of astrocyte morphology. This demonstrates that volume fraction (VF) and segment density are useful parameters for describing the structure of astrocytes. They are also suitable for online monitoring of astrocyte morphology with widely available microscopy techniques.

**Keywords:** astrocytes, morphology, perisynaptic processes of astrocytes, microscopy, analysis, development, heterogeneity

## INTRODUCTION

Astrocytes have several distinct morphological features that set them apart from other brain cells. For instance, individual astrocytes and their processes occupy territories that largely do not overlap between neighbors (Bushong et al., 2002). Within those territories, their processes branch out extensively forming the so-called gliapil, into which many thousand synapses can be embedded. The processes that approach synapses are called perisynaptic astrocyte processes, which can be very thin (~100–200 nm; Ventura and Harris, 1999; Witcher et al., 2007). Because of their proximity to synapses, they are believed to be important sites for neuron-astrocyte interactions.

However, not all synapses are necessarily approached by fine astrocytic processes and, if they are, the contact area can be highly variable. In the hippocampus, for instance, only ~40–60% of synapses are directly apposed by astrocyte processes (Ventura and Harris, 1999; Witcher et al., 2007). This variability has functional consequences for synapse function. In the supraoptic nucleus, for example, a reduction of the astrocytic coverage of neurons leads to a decreased uptake of synaptically released glutamate, which increases the activation of presynaptic glutamate receptors (Oliet et al., 2001). In the hippocampus, we could recently demonstrate that the relative coverage of spines by astrocytes depends on the spine size and sets the local efficacy of glutamate uptake (Herde et al., 2020). Importantly, the spatial arrangement of astrocyte processes and synapses is not static. For instance, astrocytic processes have been demonstrated to be motile in the brainstem and hippocampus (Hirrlinger et al., 2004; Haber et al., 2006), and especially plasticity-inducing stimuli are potent triggers of changes of perisynaptic process morphology (Genoud et al., 2006; Lushnikova et al., 2009; Bernardinelli et al., 2014; Henneberger et al., 2020), which can alter synapse stability and the spatial precision of synaptic transmission (Bernardinelli et al., 2014; Henneberger et al., 2020). In addition, it is well-established that pathophysiological conditions can lead to strong astrocyte morphology changes. Therefore, revealing how the morphology of these small astrocyte processes and their dynamic changes shape synapse behavior is important for understanding brain function.

However, this remains technically challenging because a substantial proportion of astrocytic processes are too small to be fully resolved by widely available diffraction-limited microscopy, for review see Heller and Rusakov (2017). There are of course techniques that have the necessary higher spatial resolution (Heller and Rusakov, 2017), but each has its specific advantages and disadvantages. Electron microscopy, for instance, has provided many important insights into astrocyte morphology, into structural synapse-astrocyte relationships and their potential functional implications (Ventura and Harris, 1999; Genoud et al., 2006; Witcher et al., 2007; Lushnikova et al., 2009; Patrushev et al., 2013; Medvedev et al., 2014). One caveat of electron microscopy and many other suitable super-resolution techniques is that they require chemical tissue fixation or have been used successfully mostly in fixed tissue, for review see (Heller and Rusakov, 2017). There are two disadvantages of using fixed tissue. First, fixation can potentially lead to artifacts depending on the fixation protocol as demonstrated for astrocytes (Korogod et al., 2015). Second, it is incompatible with real-time monitoring of astrocytic morphology changes. These obstacles can be overcome by stimulated-emission depletion (STED) imaging, which has been successfully used to visualize astrocytes at the necessary resolution in living brain tissue (Tønnesen et al., 2018; Arizono et al., 2020, 2021; Henneberger et al., 2020). However, three-dimensional STED imaging typically requires high illumination powers, which can limit the number of image acquisitions, and is at least currently not widely available.

Therefore, we previously started to investigate whether information about small astrocytic processes can be extracted from data obtained by diffraction-limited microscopy from

organized tissue, i.e., from tissue in which the three-dimensional structure of astrocytes is preserved. We have previously demonstrated that measuring the fraction of tissue volume occupied by astrocytes can be used to obtain information about the local astrocyte structure (Medvedev et al., 2014; King et al., 2020) and to detect changes of perisynaptic astrocyte processes (Henneberger et al., 2020). Here, we present an additional indirect measure of astrocyte structure, the segment density, and support the usefulness of both parameters with simulations and experiments. Since both parameters are easily computed, they allowed us to study relatively large populations of astrocytes *in situ*. Analyzing several hundred astrocytes, we found that the fraction of tissue volume occupied by astrocytes varies between regions of the hippocampus but is surprisingly constant during a rodent's life. In contrast, the complexity of the branching pattern, captured by the segment density, depended on the hippocampal subregion and developmental stage.

## MATERIALS AND METHODS

### Animals

Transgenic mice expressing EGFP under a GFAP promoter (Nolte et al., 2001) of either gender were used throughout this study (FVB background). Their age ranged from 7 to 570 days and is indicated for individual experiments. Animals were housed under 12 h light/dark conditions with food and water *ad libitum*. All animal procedures were conducted in accordance with the regulations of the European Commission and all relevant national and institutional guidelines and requirements. All procedures have been approved by the Landesamt für Natur, Umwelt und Verbraucherschutz Nordrhein-Westfalen (LANUV, Germany) where required.

### Virus Injections

In a subset of experiments, tdTomato was expressed in hippocampal astrocytes using recombinant adeno-associated viruses (rAAV). tdTomato expression was achieved by replacing iGluSnFR (Marvin et al., 2013) from pAAV1.GFAP.iGluSnFR.WPRE.SV40 (plasmid obtained from PennCore, addgene #98930) with tdTomato (addgene #62726) *via* BamHI/HindIII restriction sites. The resulting plasmid, pAAV1.GFAP.tdTomato.WPRE.SV40, was verified by sequencing. AAV1.GFAP.tdTomato.WPRE.SV40 viruses (serotype 1/2) were produced in HEK293T cells, harvested and purified as described before (Woittecki et al., 2016). Briefly, the AAV1.GFAP.tdTomato.WPRE.SV40 plasmid was co-expressed with the helper plasmids pRV1, pH21 and pFΔ6 in HEK283T cells and harvested ~48 h later. Next, cells were lysed, virus particles were purified by HiTrapTN heparin columns and concentrated with Amicon Ultra Centrifuge Filters to a final stock of 500 µl. Intrahippocampal virus injections were administered as described before (Herde et al., 2020). Briefly, 4–5-week-old mice were anesthetized through intraperitoneal (i.p.) injection of Fentanyl/Midazolam/Medetomidin (0.05/5.0/0.5 mg/kg body weight) and stereotactically injected (coordinates for the dorsal hippocampus, relative to bregma: anterior –1.8 mm, lateral +/– 1.6 mm, ventral –1.6 mm)

with 1  $\mu$ L of virus AAV1/2.GFAP.tdTomato (virus titer:  $\sim 10^9$  viral particles per  $\mu$ L, injection speed: 100 nl/min). anesthesia was terminated by Naloxon/Flumazenil/Atipamezol (1.2/0.5/2.5 mg/kg body weight, i.p. injection). Animals were sacrificed 2–4 weeks after virus injection.

## Preparation of Acute Hippocampal Slices

Acute slices were prepared from mice as previously described (Anders et al., 2014; Minge et al., 2017). Briefly, mice between postnatal day 7 and 570 were anesthetized with isoflurane and decapitated. 300  $\mu$ m thick slices from the dorsal hippocampus (coronal), ventral hippocampus (horizontal) or somatosensory cortex (horizontal, layer 2/3) were obtained using a vibratome (Campden Instruments, UK) in an ice-cold slicing solution containing (in mM): NaCl 60, sucrose 105, KCl 2.5,  $MgCl_2$  7,  $NaH_2PO_4$  1.25, ascorbic acid 1.3, sodium pyruvate 3,  $NaHCO_3$  26,  $CaCl_2$  0.5, and glucose 10 (osmolality 300–310 mOsm/kg), and kept in the slicing solution at 34°C for 15 min before being stored at room temperature in an extracellular solution containing (in mM): NaCl 126, KCl 2.5,  $MgSO_4$  1.3,  $NaH_2PO_4$  1.25,  $NaHCO_3$  26,  $CaCl_2$  2, and glucose 10 (osmolality 297–303 mOsm/kg). Slices were allowed to rest for at least 45 min before the experiments, which were performed at 33–34°C in a submerged recording chamber. All solutions were constantly bubbled with 95%  $O_2$ /5%  $CO_2$ . In some experiments, the osmolality of the extracellular solution was rapidly changed to  $\sim 200$  mOsm/kg or  $\sim 400$  mOsm/kg. This was achieved by switching to an extracellular solution with a reduced concentration of NaCl (61 mM) or one to which sucrose had been added (100 mM). In these experiments, a baseline image of an EGFP-expressing astrocyte was taken (see below) before the solution exchange and then another one 10 min after the solution exchange had begun.

## Two-Photon Excitation (2PE) Fluorescence Microscopy in Acute Slices

Astrocytes expressing fluorescent proteins or filled with fluorescent dyes were visualized using a Scientifica 2PE fluorescence microscope with a 40 $\times$  /0.8 NA objective (Olympus) or an Olympus FV10MP 2PE fluorescence microscope with a 25 $\times$  /1.05 NA objective and a pulsed infrared laser (Vision S, Coherent,  $\lambda$  = 800 nm unless stated otherwise). Laser power was adjusted for depth to obtain a fluorescence intensity equivalent to that recorded with a laser power of 2–3 mW at the slice surface. In a subset of experiments, EGFP-expressing astrocytes were dialyzed for 20 min with the gap junction impermeable red fluorescent dye Texas Red dextran 3 kDa (300  $\mu$ M; Thermo Fisher Scientific, USA) *via* standard patch-pipettes (3.5–4.5 M $\Omega$ ) filled with an intracellular solution containing (in mM):  $KCH_3O_3S$  135, HEPES 10, di-Tris-Phosphocreatine 10,  $MgCl_2$  4,  $Na_2$ -ATP 4, Na-GTP 0.4 (pH adjusted to 7.2 using KOH, osmolality 290–295 mOsm/kg). For further details see Henneberger et al. (2010) and Henneberger and Rusakov (2012). The access resistance was continuously monitored, and recordings were rejected if they exceeded 30 M $\Omega$  at the beginning of the recording or changed by more than 30% during dye-loading

(20 min). Images and image stacks of astrocytes were routinely acquired with a nominal resolution of 0.04–0.09  $\mu$ m/pixel in the x-y plane (512  $\times$  512–2048  $\times$  2048 pixels) and in 1  $\mu$ m steps in the z-direction. The cell bodies of all studied astrocytes were  $>80$   $\mu$ m below the tissue surface.

## *In vivo* Two-Photon Excitation (2PE) Fluorescence Microscopy

Acute *in vivo* imaging experiments were performed in 8–12-week-old animals as described previously (Monai et al., 2016; King et al., 2020) using isoflurane inhalation anesthesia (3% for induction, 1.3–1.5% for maintenance) and additional buprenorphine analgesia (0.1 mg/kg). Briefly, the mouse head was fixed in a stereotaxic apparatus, the skull was exposed and a small craniotomy (about 3 mm diameter, 1.5 mm posterior to bregma and 3.5 mm lateral from the midline) above the right barrel cortex was performed using a dental drill. The skull, but not the dura mater, was carefully removed. The cortex was covered with a 1.2% low-melting agarose. A glass coverslip (4 mm in diameter, Warner Instruments, Hamden, USA) was placed on top and secured by dental cement (Temdent Classic, Schütz Dental GmbH, Rosbach, Germany). A custom-made metal frame was attached to the skull using dental cement. Eyes were covered with bepanthen (Bayer Vital GmbH, Leverkusen, Germany) during the whole surgical and imaging procedure. Recordings were then performed under continued isoflurane inhalation anesthesia (1.2–1.5%), for which mice were head-fixed to another stereotaxic frame and placed under a 2PE microscope (COSYS Ltd, East Sussex, UK) equipped with a femtosecond infrared pulsed Mai Tai HP laser (Spectra-Physics, wavelength set to 800 nm) and a 16 $\times$  water-immersion objective lens (Nikon LWD, NA 0.8). To avoid brain tissue damage, the laser power did not exceed 30 mW at the front lens of the objective. Images (1024  $\times$  1024 pixels) were acquired at a depth of 100–150  $\mu$ m from the pia with a nominal resolution of  $\sim 0.100$   $\mu$ m/pixel using ScanImage 5.6. Animals were kept at a constant temperature of 37°C throughout surgery and the experiment by placing them on a heating blanket. Data were analyzed offline as explained below.

## Expansion Microscopy (ExM)

Expansion Microscopy (ExM; Chen et al., 2015; Chozinski et al., 2016) of EGFP-expressing astrocytes was performed as previously described (Deshpande et al., 2017; Bürgers et al., 2019; Herde et al., 2020). Briefly, 4–10-week-old animals were deeply anesthetized and transcardially perfused with 4% paraformaldehyde (PFA) in phosphate-buffered saline (PBS, pH 7.4). Their brains were removed and fixed at 4°C either overnight (ON) or for 1–2 h. Coronal sections of 70  $\mu$ m thickness were cut on a vibratome and incubated in permeabilization buffer (0.5% Triton X-100 in PBS pH 7.4, ON, 4°C). Slices were incubated with a chicken anti GFP (1:5,000; Abcam ab13970, lot GR89472–16) primary antibody (24 or 48 h, 4°C). After 3  $\times$  20 min washing in permeabilization buffer, slices were incubated with a secondary antibody (anti-chicken Alexa Fluor 488, 1:200; ThermoFisher A11039, 4°C, 24 h). After washing in PBS, slices were incubated with Hoechst 33342 (1:2,000, Invitrogen H3570, lot 1874027) in



distilled water for 10 min at RT. After washing again, slices were imaged in PBS containing 0.05% p-phenylenediamine before expansion with a  $20\times$  /0.75 NA or a  $40\times$  /1.1 NA objective in a Leica SP8 confocal microscope. Further treatment was adopted from Chen et al. (2015), Chozinski et al. (2016) and similar to Herde et al. (2020). In short, slices were incubated in 1 mM methylacrylic acid-NHS (Sigma Aldrich #730300, RT, 1 h). After  $3 \times 20$  min washing in PBS, slices were incubated for 45 min in monomer solution (in g/100 ml PBS: 8.6 sodium acrylate, 2.5 acrylamide, 0.15 N,N'-methylenebisacrylamide, 11.7 NaCl,  $4^{\circ}\text{C}$ ). Slices were then incubated with gelling solution (monomer solution supplemented with % (w/v): 0.01 4-hydroxy-TEMPO, 0.2 TEMED, 0.2 APS) at  $4^{\circ}\text{C}$  for 5 min before being transferred to a chamber sandwiched between two coverslips at  $37^{\circ}\text{C}$  for 2 h. Coverslips were removed and proteins were digested in digestion buffer (50 mM Tris pH 8, 1 mM EDTA, 0.5% Triton X-100, 0.8 M guanidine, 16 U/ml proteinase K) at  $37^{\circ}\text{C}$  for 12–14 h. For expansion, slices were incubated for 2.5 h in distilled water at RT and water was exchanged every 15–20 min. Finally, slices were mounted on poly-lysine coated m-Slide 2 well Ibidi-chambers and sealed with a poly-lysine coated coverslip on top, adding a drop of water to prevent the gel from drying. All imaging was performed on a Leica SP8 confocal microscope using a  $40\times$  /1.1 NA objective and hybrid detectors. For each sample, the expansion factor ( $\sim 4$ –5 over all experiments) was determined by identifying the same cells labeled with Hoechst 33342 in the dentate gyrus before and after expansion and then measuring their sizes pre- and post-expansion. For analysis, image stacks of EGFP-expressing astrocytes were acquired (x-y-z, typically  $\sim 2,500 \times 2,500 \times 15$  voxels, voxel dimensions  $\sim 0.1 \mu\text{m} \times 0.1 \mu\text{m} \times 0.4 \mu\text{m}$ , corresponding to pre-expansion dimensions of  $\sim 0.025 \mu\text{m} \times 0.025 \mu\text{m} \times 0.10 \mu\text{m}$ ). Images were then processed using Huygens Essential and analyzed as explained below.

## Image Analysis and Quantification of Volume Fraction and Segment Density

Image data were processed using in-house written scripts in MATLAB (Mathworks). All images of astrocytes had a nominal resolution of at least  $0.1 \mu\text{m}/\text{pixel}$  and contained a single optical section through the center of the astrocyte soma. Before further analysis, the background intensity was determined in a region without any labeled structures and subtracted from all pixels. All images were then processed using a median filter ( $0.3 \mu\text{m} \times 0.3 \mu\text{m}$ ). For experimental data, a circular region of interest (ROI) was placed at the center of the soma for obtaining the fluorescence intensity corresponding to a volume fraction (VF) of 100% (reference ROI, see for instance Figure 3). A second analysis ROI was then defined, in which the astrocytic VF was determined by taking the average fluorescence intensity in this ROI and dividing it by the value corresponding to 100%. For analyzing the distribution of the astrocytic VF (Figure 3D), the analysis ROI was cut into quadratic subregions and the VF for each subregion was determined. Please see the next section for simulated data and their analysis.

To obtain a measure related to the number of astrocytic processes in the analysis ROI, the image was then binarized using

the fluorescence intensity corresponding to the VF as a threshold. All continuous objects in the binarized image with a size of more than one pixel were considered to be astrocytic segments and counted. For experimental data, the number of segments was normalized to the area of the analysis ROI (segment density in  $\mu\text{m}^{-2}$ ), which is more useful for comparison between astrocytes with varying territory sizes.

In a subset of experiments (Figure 4), image stacks of astrocytes were analyzed to compare measurements of astrocytic VF and segment density along image planes in x-y, x-z and y-z orientations. Here, the image stacks were resliced as indicated in Figure 4 and each section was analyzed as described above.

For the analysis of data obtained from ExM (see above) for Figure 1, the astrocytic VF and segment density were first determined from the central slice of the original data stack, as explained above. The ExM image stack was then convolved with a point spread function [PSF, full width at half-maximum (FWHM) of  $0.45 \mu\text{m}$  in x-y and of  $0.90 \mu\text{m}$  in z] to emulate diffraction-limited microscopy. The astrocytic VF and segment density were then determined a second time from the same central slice of the convolved image stack with identical reference and analysis ROIs. For the comparison of VF and segment densities measured before expansion with ExM data (Figure 2), images of astrocytes taken before and after expansion (pre-ExM and ExM respectively) were aligned and divided into identical rectangular ROIs. For each cell, all ROIs except somatic ROIs and ROIs without astrocyte structures were analyzed separately. For pre-ExM images, the VF and segment number were determined for each ROI as explained above. For ExM images, the number and average size of astrocyte segments in each ROI were determined from images that had been binarized as explained above.

## Simulations of Diffraction-Limited Microscopy of Astroglial Processes

An optical section through an astrocyte contains cross-sections of astrocyte processes with sizes that are typically close to or below the diffraction limit of 2PE fluorescence microscopy. We established the relationship between the number and size of astrocyte processes and astrocyte volume fraction and segment density (see above) by mimicking a typical experiment. Non-overlapping virtual astrocyte processes were approximated by rectangular cuboids and placed randomly in a 3D tissue block (matrix of  $2,000 \times 2,000 \times 31$  voxels corresponding to  $40.0 \mu\text{m} \times 40.0 \mu\text{m} \times 3.1 \mu\text{m}$ , all voxels initialized to 0) by setting all voxels within all cuboids to a value of 255. A set of these 3D tissue blocks filled with astrocyte processes was generated by randomly varying the numbers and sizes of simulated astrocyte processes (Visual Studio C++ and OpenCV image processing library). The generated tissue blocks were then convolved with a three-dimensional Gaussian PSF with an FWHM of  $0.45 \mu\text{m}$  in the x-y plane and  $0.90 \mu\text{m}$  in the z-direction to simulate diffraction-limited imaging (MATLAB, Mathworks). The central x-y plane of the convolved matrix is equivalent to a single focal section using diffraction-limited imaging and was further analyzed. First, the volume fraction was calculated by taking the average voxel intensity and normalizing it to the value

corresponding to 100% (255, see above). Second, the number of segments was determined as described above. Both were then correlated with the number of astrocyte processes that were initially placed in the simulated 3D tissue block and the known fraction of volume occupied by virtual astrocyte processes in the 3D tissue block.

## Quantification and Statistical Analysis

Image analysis was performed in FIJI/ImageJ (NIH) and MATLAB (Mathworks). Numerical and statistical analyses were performed in Excel (Microsoft), Origin Pro (OriginLab Corporation) and MATLAB (Mathworks). In the text, results are given as mean  $\pm$  s.e.m. unless stated otherwise.  $n$  denotes the number of experiments. In graphs, statistical significance is indicated by asterisks. \* for  $p < 0.05$ , \*\* for  $p < 0.01$  and \*\*\* for  $p < 0.001$ . Statistical tests such as Student's  $t$ -tests, ANOVA, Kruskal-Wallis test and Spearman's rank correlations were always two-tailed and used as appropriate and as indicated in the text and figure legends. The Shapiro-Wilk test was used to establish if data followed a normal distribution.

## RESULTS

### Parameters of Fine Astrocyte Morphology in Diffraction-Limited Microscopy

Diffraction-limited microscopy cannot fully resolve the complex morphology of the fine peripheral processes of astrocytes (see "Introduction" section) and how these processes are precisely arranged around synapses, for instance. Nonetheless, it captures the distribution of labeled astrocyte structures. A typical example of an astrocyte expressing EGFP in its cytosol (**Figure 1A**) illustrates how large structures with high volume such as the soma or big branches are represented by a high fluorescence intensity whereas the fine branches in the periphery are relatively dim and blurry. To illustrate how the latter arises from astrocytic structures we re-investigated electron microscopic sections in which astrocytic structures had been identified, published data from Medvedev et al. (2014) and Henneberger et al. (2020) (**Figure 1B**, left panel). Looking only at the cross-sections of astrocytic processes in this example, called segments in the following (**Figure 1B**, middle panel), this tissue section can be characterized by the number of astrocytic segments ( $n_{\text{segments}}$ ) and their average size ( $s_{\text{segments}}$ ). The product of both divided by the total area of the tissue section is equal to the area fraction, i.e., the fraction of area occupied by astrocytic segments. When the thickness of the tissue section is also considered, the corresponding measure is the astrocyte volume fraction, i.e., the fraction of volume of the tissue section occupied by astrocyte processes. Importantly, the area fraction is a consistent estimate of the volume fraction, which is known as the Delesse principle, also see Chayes (1953). Thus, the astrocyte volume fraction is an indirect measure of astrocyte process number and their average size in a tissue section. It is also an indicator of dynamic changes because it increases when astrocyte processes become more abundant or bigger, for instance. When diffraction-limited microscopy of the same section is simulated by convolving the image with a typical

point spread function (PSF), a blurry image reminiscent of the periphery of the astrocyte in **Figure 1A** is obtained and astrocyte segments cannot be clearly identified any longer (**Figure 1B**, right panel). Therefore, the volume fraction needs to be extracted by different means. If all astrocyte processes in a tissue section are equally filled with a dye/label, then the fraction of volume they occupy is given by the cumulative intensity of that label divided by the value corresponding to the tissue section being entirely filled by astrocytic structures. When divided by the number of pixels/voxels of the tissue sections, this corresponds to the average label intensity  $I_{\text{average}}$  divided by  $I_{100\%}$ . One area, for which 100% occupancy by astrocytes can be safely assumed, is the somatic region because the soma is much larger than a typical PSF (Medvedev et al., 2014; Savtchenko et al., 2018; Henneberger et al., 2020). This procedure requires that pixels/voxels devoid of astrocyte processes have a fluorescence intensity of zero. Therefore, background fluorescence and other offsets need to be carefully subtracted before analysis. Thus, the astrocytic volume fraction VF can be calculated from diffraction-limited microscopy as a measure of both the number and size of astrocytic processes in a region of interest. Importantly, we have previously shown that this VF measure from diffraction-limited microscopy matches that obtained by electron microscopy (Medvedev et al., 2014).

In addition, we established a second measure of astrocyte morphology that is correlated with the number of astrocytic processes in the analyzed tissue section. It is obtained by binarizing the image using a fluorescence intensity threshold. This threshold is set to the fluorescence intensity that is equivalent to the volume fraction in the analyzed ROI, which is  $I_{\text{average}}$  (**Figure 1B**, right panel). This threshold was chosen because it does not require any manual adjustments by the investigator and is instead fully determined by the analyzed image itself. Then the number of confluent supra-threshold areas is determined (number of segments, also see "Material and Methods" section). It should be noted that this approach links the threshold for segment detection to the volume fraction. Alternatively, the threshold could be set to a fixed percentage of the somatic fluorescence intensity.

We next quantified the extent to which the astrocyte VF and the number of segments reveal details of astrocyte morphology using simulations. Diffraction-limited imaging of astrocytic processes was emulated by randomly placing cuboids of varying geometry and number into simulated three-dimensional tissue sections, which were then convolved by a PSF typical for our imaging conditions (**Figures 1C,D**). For each simulated tissue section, the VF and number of segments were determined as described above and correlated with the fraction of simulated voxels filled by cuboids and the number of simulated cuboids, respectively (**Figures 1E,F**). As expected, diffraction-limited microscopy does not affect the value of the VF (**Figure 1E**). The number of detected segments also displayed a highly significant but weaker correlation (**Figure 1F**). This number of detected segments in simulated diffraction-limited microscopy is lower than the simulated astrocytic cuboids (by a factor of two to three in these simulations), which is expected because of the limited spatial resolution of diffraction-limited microscopy.

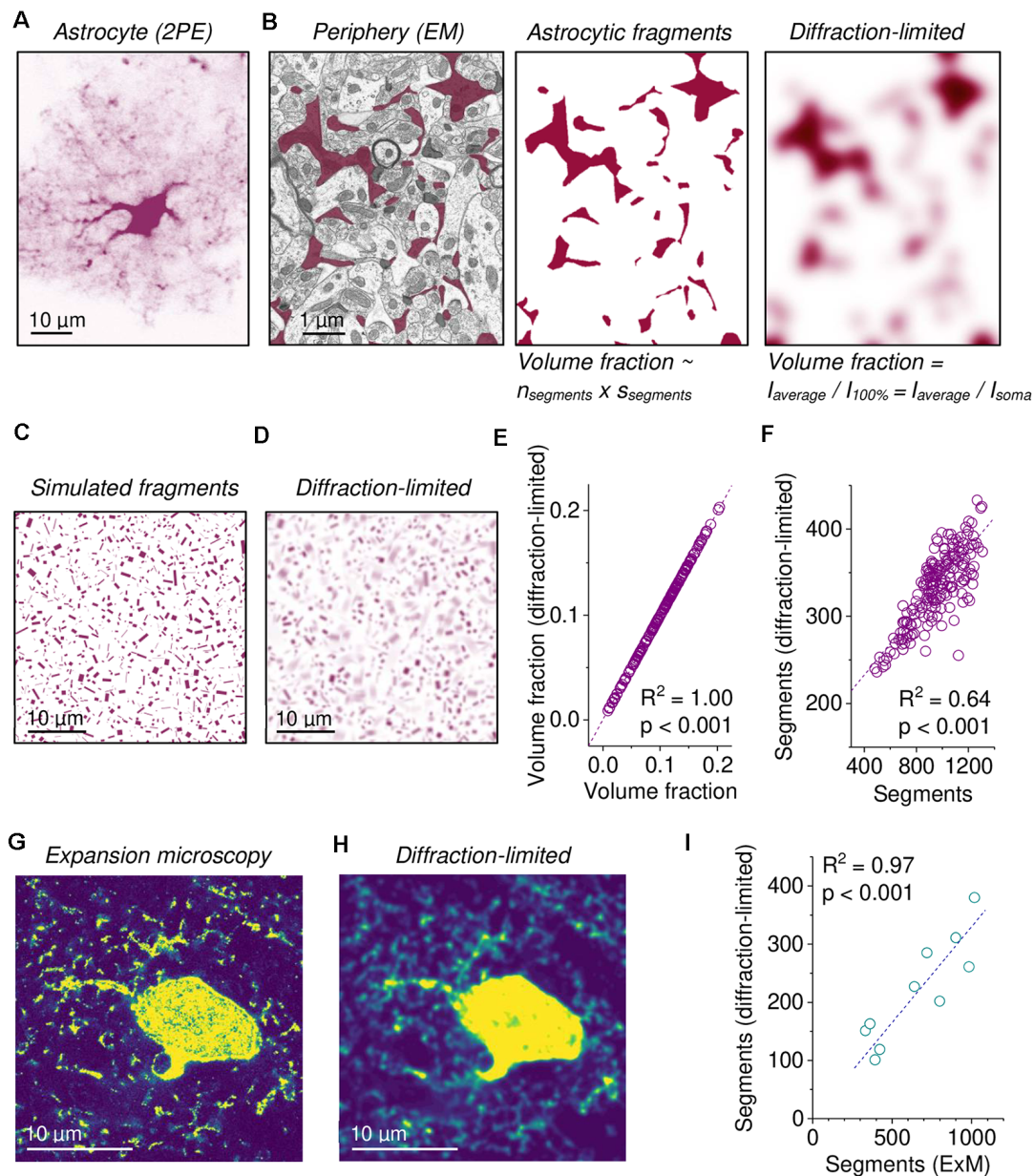


**FIGURE 1 |** Assessing fine astroglial morphology in diffraction-limited microscopy by measuring astroglial volume fraction (VF) and segment density. **(A)** Example of a single EGFP-expressing astrocyte imaged using diffraction-limited two-photon excitation (2PE) fluorescence microscopy (single focal plane through the soma). Note the blurry periphery representing small astroglial processes. **(B)** Left panel: example of an electron micrograph of the hippocampal neuropil with clearly delineated astrocyte fragments highlighted in purple (left panel). For further experimental details see Medvedev et al. (2014). Middle panel: same section only showing astrocyte fragments. The fraction of the section that is occupied by astroglial segments is the product of their number ( $n_{\text{segments}}$ ) and average size ( $S_{\text{segments}}$ ) divided by the total area. The fraction of occupied area/volume can be calculated by normalizing the average intensity ( $I_{\text{average}}$ ) to the value corresponding to 100% ( $I_{100\%}$ ). **(C)** An example of a single section at full resolution cutting through simulated astrocyte processes of various sizes and orientations in a simulated image stack (see text and methods). **(D)** Emulation of diffraction-limited fluorescence imaging of the image stack from **(C)**. Note that this is not a smoothed version of **(C)** but instead representative of diffraction-limited imaging of the entire stack. Also, note the now blurry and overlapping astrocyte processes. **(E)** The VF obtained from simulated diffraction-limited microscopy ( $I_{\text{average}}/I_{100\%}$ ) strongly depends on the original fraction of volume occupied by astrocyte processes (linear fit,  $n = 190$  separate sets of astrocyte processes). **(F)** The number of detectable astrocyte segments was determined (see text and methods) in simulations of diffraction-limited microscopy **(D)**. The number of detected segments was smaller than the number of simulated astrocyte processes but showed a highly significant positive correlation (linear fit, same data set as in **(E)**). **(G)** Example of super-resolution expansion microscopy (ExM) of an EGFP-expressing astrocyte (single focal plane from a stack). Note the high level of detail. **(H)** Simulation of diffraction-limited microscopy of ExM data (same cell as in **G**). Note the appearance of out-of-focus structures and blurring. **(I)** The number of astrocyte segments determined in ExM was lower after simulation of diffraction-limited imaging but strongly correlated with the number obtained directly from ExM data (linear fit,  $n = 10$  independent experiments).



To test this relationship on real astrocytes, we re-analyzed previously published superresolution fluorescence microscopy data obtained by expansion microscopy (ExM) of astrocytes expressing EGFP (Herde et al., 2020; **Figure 1G**). The spatial resolution of ExM in these experiments is increased by a factor of four to five compared to standard confocal microscopy. Similar to the simulated data above, we emulated diffraction-limited microscopy by convolving ExM image stacks with a typical PSF (**Figure 1H**). We then compared the number of detectable segments in ExM and in convolved ExM data using the procedure explained above (**Figure 1I**). Again, the number of segments was highly correlated, and emulating diffraction-limited microscopy reduced the number of detectable astrocyte processes in the image.

Next, we further explored how local characteristics of astrocyte structure are captured by the VF and segment number by re-analyzing a subset of experiments from Herde et al. (2020), in which we had managed to obtain confocal images of an EGFP-expressing astrocyte before expansion and after expansion of the tissue sample (pre-ExM and ExM, respectively; **Figure 2A**). The higher spatial resolution of ExM allowed us to obtain more precise measurements of the number of astrocyte segments and their average size in for each ROI (illustrated by the grid in **Figure 2A**), which we then compared to the VF and segment number measured from diffraction-limited fluorescence imaging (pre-ExM) in the same ROI as explained above. The prediction was that if a ROI contained a high number of astrocyte segments in ExM, then the VF and number of segments obtained in that ROI in diffraction-limited microscopy should both be high too. In addition, if the average size of astrocyte segments in ExM is high in an ROI, then the VF in the ROI in the pre-ExM data should be high too. Indeed, this was observed for the example cell (**Figures 2A,B**) and across a total of five astrocytes (**Figure 2C**). In contrast, the size of astrocyte segments in ExM and the number of detected segments before the expansion was only weakly correlated in one out of five cells (**Figure 2C**, left panel).

Overall, these experiments demonstrate that the volume fraction and the number of segments can be easily extracted from imaging data and that both are indirect but reliable measures of the number and size of fine astrocyte processes.

## Probing the Reliability of Volume Fraction Measurements

Volume fraction (VF) measurements need to be consistent across experimental conditions to be widely applicable. We, therefore, tested the robustness of VF using several approaches. First, we reasoned that if fluorescent dyes fulfil the important requirement of having a constant concentration throughout the astrocyte cytosol then they should report the same VF regardless of the specific properties of the dye. This was tested in acute hippocampal slices with astrocytes expressing EGFP. In a first set of experiments, single EGFP-expressing cells were selected, and an image was taken (**Figure 3A**, left panel). Cells were then filled with dextran conjugated Texas Red (3 kDa), which cannot pass through gap junctions because of its molecular weight (**Figure 3A**, middle panel), and another image was taken. A

somatic reference ROI and an analysis ROI covering the astrocyte territory (sparing the soma and the perisomatic region) were defined and the VF was determined from both images with identical ROIs. The analysis revealed that both VFs were highly correlated (**Figure 3A**, right panel, linear fit through the origin) and on average not statistically different (unpaired Student's *t*-test,  $p = 0.998$ ,  $n = 13$ ). In a second experiment, EGFP-expressing cells were virally transduced to express tdTomato (**Figure 3B**). Images of astrocytes expressing both EGFP and tdTomato were taken, and the VFs of astrocytes were measured from both channels using identical ROIs. Again, the VFs obtained from both channels were almost identical (**Figure 3B**). These experiments demonstrate that VF measurements from astrocytes are independent of the used dye, the method for dye delivery and of the dye concentration because expression levels of tdTomato and EGFP can vary considerably between cells. We next compared VFs of astrocytes from acute slices to VFs recorded from *in vivo* data, because astrocytes in acute slices had been suggested to rapidly show a reactive phenotype accompanied by a significant loss of small astrocyte processes (Takano et al., 2014). We compared VFs of EGFP-expressing astrocytes in the somatosensory cortex (layer 2/3) in acute horizontal slices and in anesthetized mice (**Figure 3C**, left and middle panel, respectively). No statistically significant difference between the VFs in the two preparations was detected (**Figure 3C**, right panel). Note that in these experiments the analysis ROI included the soma and the perisomatic region. This indicates that there is no major loss of astrocyte volume across the astrocyte territory in this slice preparation and that VF measurements can be comparable between microscopes and preparations. Finally, VF measurements do not need to cover the entire astrocyte. Instead, it might be of interest how specific subregions of the astrocyte change or how the astrocyte volume is distributed across the cell's territory. An example of such a refined analysis is shown in **Figure 3D**. Here, the entire astrocyte is divided into a grid of quadratic ROIs (**Figure 3D**, left panel), for each the VF is determined and the probability distribution of VFs across the astrocyte territories is calculated (**Figure 3D**, middle panel). As expected, low local VFs below  $\sim 0.2$ , which represent parts of the astrocyte territory dominated by small astrocytic processes, are most frequent. Across all cells, 96% of all ROIs have a local VF of less than 20%. In contrast, high local VFs, i.e., ROIs being more extensively filled by larger branches, are far less often encountered. This type of analysis can be useful to reveal, for instance, in which part of the astrocyte morphology is changing (Henneberger et al., 2020), and to correlate subcellular structures with properties of astrocytic  $\text{Ca}^{2+}$  signals (King et al., 2020). In addition, we performed a Sholl-like analysis and plotted the average VF and the coefficient of variation of the VF against the distance from the soma center (**Figure 3D**, right panel). The VF drops sharply at 3–5  $\mu\text{m}$  from the soma center to average values below 10%, illustrating that even at short distances from the soma the territory of the astrocyte is predominantly filled by small astrocyte processes. At the transition zone, the coefficient of variation is highest because ROIs with high VF, i.e., ROIs covering major branches are mixed with low VF ROIs.



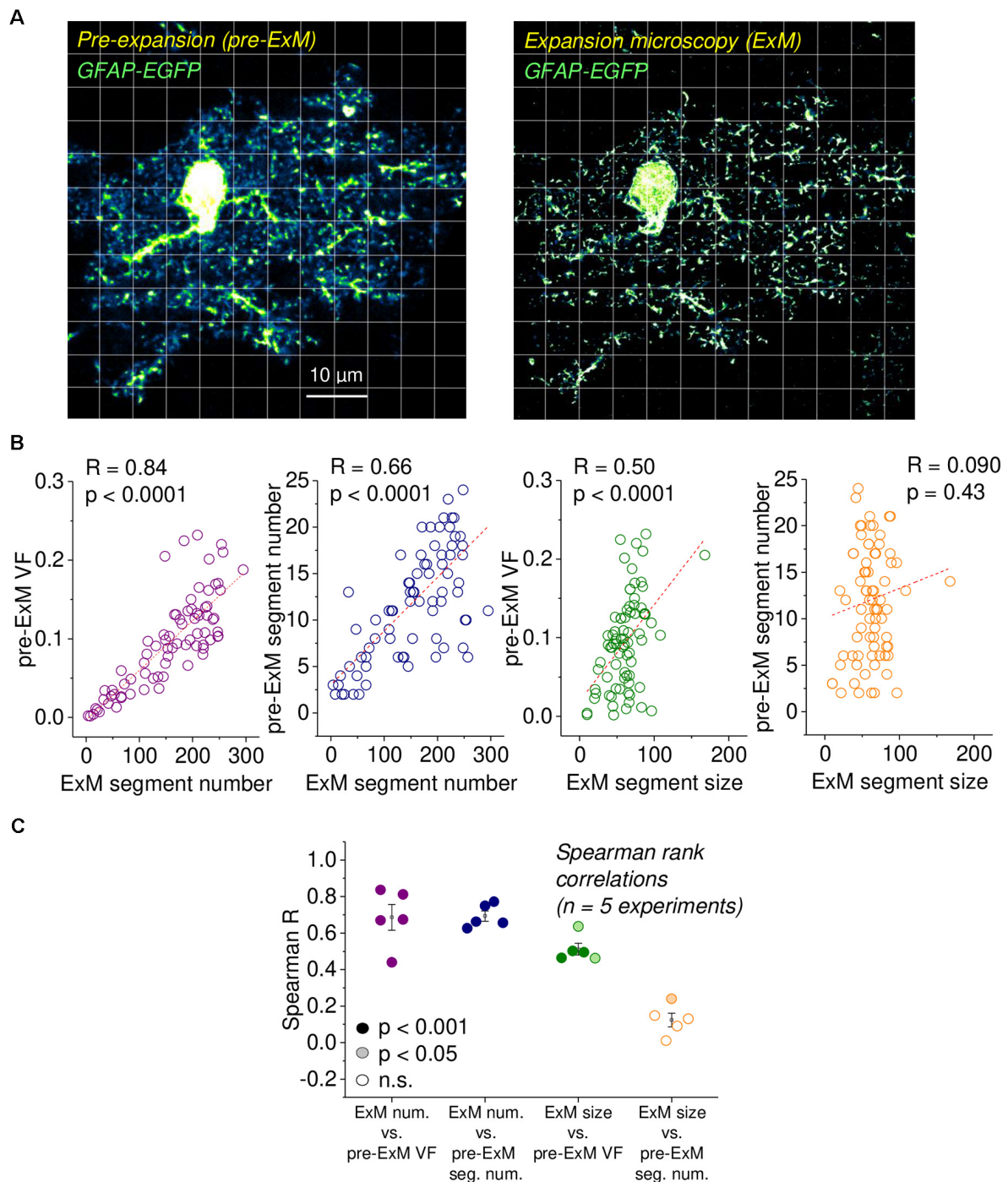


**FIGURE 2 |** Validation of astrocytic volume fraction (VF) and segment density using expansion microscopy (ExM). **(A)** Example of an EGFP-expressing astrocyte before expansion (left panel, pre-ExM) and after expansion (right panel, ExM), both obtained using confocal microscopy. The ExM image was rescaled to the original size of the tissue. The scale bar applies to both panels and refers to the pre-ExM dimension. Note the highly resolved small astrocyte processes and the disappearance of out-of-focus structures in ExM. The grid illustrates the regions of interest (ROIs) for both images. The soma and areas without astrocyte structures were excluded from the analysis. Experimental data from Herde et al. (2020). **(B)** For each ROI in **(A)**, the VF and segment number were determined from the pre-ExM image and compared with the average segment size and number of segments measured in the ExM image in the same ROI. Strong correlations were found between the astrocyte segment number after expansion with the pre-expansion VF and segment number (1st and 2nd panel from the left) and between the astrocytic segment size after ExM and the pre-expansion VF (3rd panel from the left) but not between the astrocytic segment size after ExM and the pre-expansion segment number. Spearman rank correlations throughout ( $n = 77$  ROIs). Dashed lines are linear fits, only for illustration. **(C)** Spearman's rank correlation coefficients for five independent experiments, as illustrated in **(A,B)**. Filling represents statistical significance (dark for  $p < 0.001$ , light for  $p < 0.05$  and white for  $p > 0.20$ ).

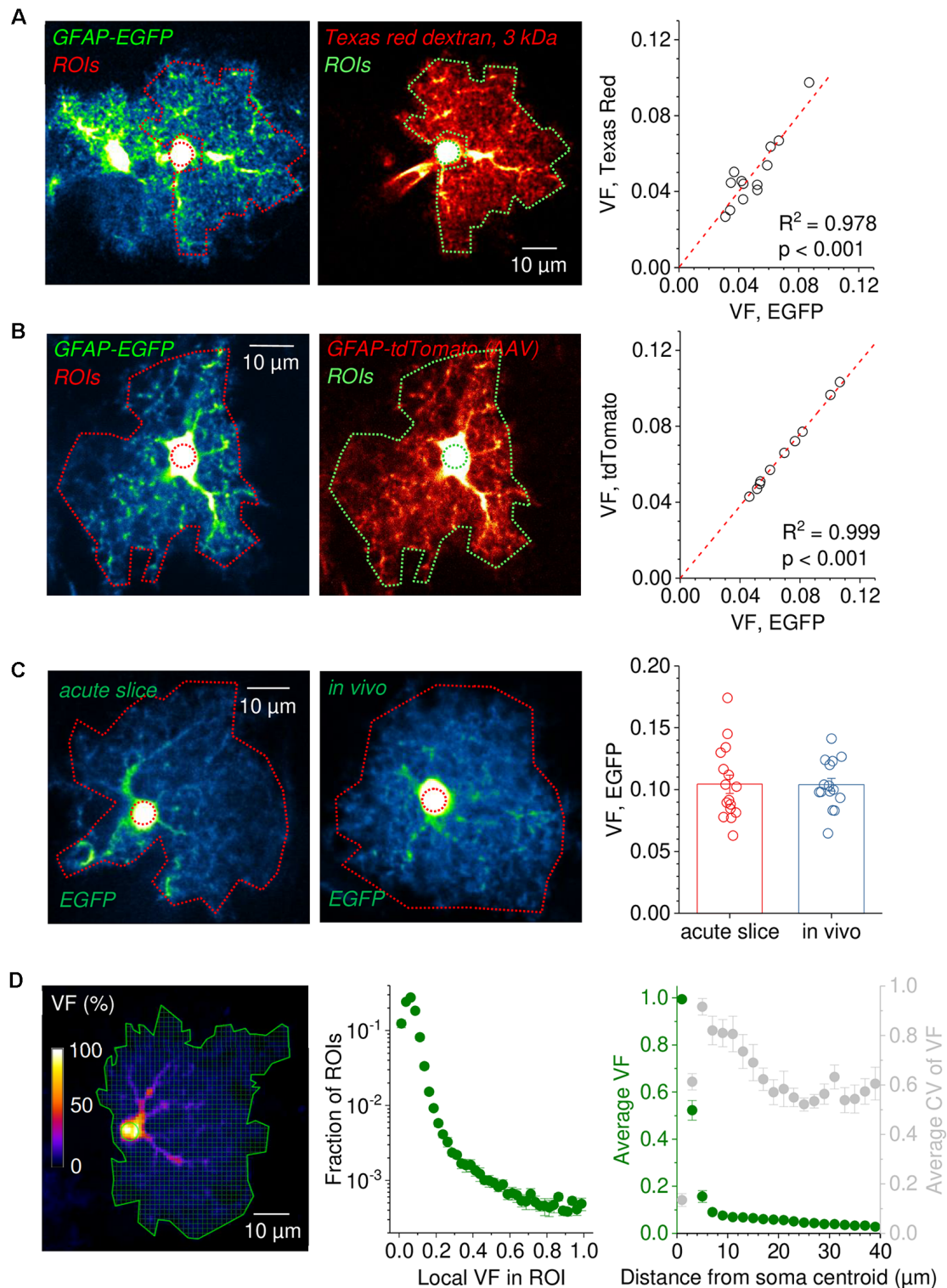


**FIGURE 3 |** Robustness of astrocytic volume fraction (VF) measurements across experimental conditions. **(A)** Example of an EGFP-expressing astrocyte before (left panel) and after patching and filling with the gap junction impermeable dye Texas Red dextran 3 kDa for 20 min (middle panel, patch pipette visible left of the soma). Note the similar appearance of the patched cell and the previous EGFP fluorescence). The somatic reference regions of interest (ROIs) are illustrated by a circular dotted line. ROIs for analysis sparing the soma and perisomatic region are also delineated by dotted lines. Pseudo color images for revealing low-intensity details. Right panel: Comparison of volume fractions (VF) obtained by normalizing the average fluorescence in the analysis ROI to that in the somatic reference ROI.

(Continued)

**FIGURE 3 | Continued**

The VFs of EGFP-expressing cells are tightly correlated with the VFs obtained after filling the same cells with Texas Red dextran 3 kDa (linear regression through origin,  $n = 13$ ). **(B)** Analysis of astrocytes simultaneously expressing the two fluorescent proteins EGFP and tdTomato. An example of an astrocyte expressing both EGFP and tdTomato is shown in the left (EGFP) and middle panel (tdTomato). Dotted lines represent the analysis and somatic reference ROIs. VF values obtained from analysis of the EGFP and tdTomato fluorescence using the same ROIs were virtually identical (linear regression through origin,  $n = 10$ , right panel). **(C)** Comparison of VFs of EGFP-expressing astrocytes in the somatosensory cortex (layer 2/3) between horizontal slice preparations and in anesthetized mice *in vivo*. Example images of EGFP-expressing astrocytes in an acute slice (left) and *in vivo* (middle). Dotted lines delineate the ROI for analysis including the soma (outer) and the somatic reference ROI (inner, circular). On average, VFs from both preparations were nearly identical (unpaired Student's *t*-test:  $p = 0.966$ ,  $n = 16$  astrocytes in slices from two independent preparations,  $n = 15$  astrocytes *in vivo* from three different animals). **(D)** Analysis of VF distribution within the territory of a single astrocyte. The entire territory (solid green line) of a sample EGFP-expressing astrocyte is divided into ROIs of  $\sim 1 \times 1 \mu\text{m}^2$  (left panel). The fluorescence intensity of each ROI is normalized to the somatic reference ROI (solid green circle) and the VF distribution across ROIs is calculated. Middle panel: average VFs distribution of hippocampal astrocytes [CA1, stratum radiatum (SR),  $n = 10$ ]. Right panel: the dependence of the VF on the distance from the soma was calculated by averaging the VF of all ROIs at the given distances in each cell and then averaging the obtained data across all cells (same data set, green, left axis). The average coefficient of variation of VF is also plotted against distance from the soma (gray, right axis). In panels **(A–C)**, the contrast of example images has been enhanced for display purposes and the scale bars apply to both panels.

## Astrocytic Volume Fraction and Segment Measurements in Three Dimensions

All analyses above were performed on single optical sections through the soma of astrocytes. However, astrocytes display a complex three-dimensional morphology. We, therefore, tested to what extent single-plane volume fractions and segment counts are representative of the entire cell. This was done by recording imaging stacks of single astrocytes and then obtaining three two-dimensional optical sections through the soma from each stack (X-Y, X-Z, Y-Z). See **Figure 4A** for an example. First, we calculated the VF in each set of optical sections as described above and correlated the results between the three orientations. As displayed in **Figure 4B**, the VFs are highly correlated between the different orientations. Second, we determined how many astrocytic segments can be detected in the three corresponding optical sections. In this analysis, the number of detected astrocytic segments were divided by the area of the analysis ROI to obtain the segment density (**Figure 4C**). This was done for comparisons because the sizes of analysis ROIs vary between orientations. The segment density was also highly correlated between planes although it is noteworthy that the segment density in sections along the Z-axis is generally lower when compared to the X-Y plane. This is expected because both the nominal resolution in our experiments and, more importantly, the optical resolution is significantly lower in the Z-direction compared to X-Y (Helmchen and Denk, 2005; Yang and Yuste, 2017), which can be easily spotted by comparing the middle and right panel of **Figure 4A** with the left panel. For all statistical details

please see the legend of **Figure 4**. There are two important conclusions that can be drawn from these observations. On one hand, it is convenient for the experimenter that a single focal plane is representative of the entire astrocyte. On the other hand, our data reveal that volume fraction and segment density are set to some extent on the level of individual cells, because they are similar across different sections through the same cell, even though they vary considerably between cells.

## Heterogeneity and Development of Astrocyte Morphology

The rapidness and relative ease with which the information about fine astrocyte processes can be captured using VF and segment density measurements allows the experimenter to study larger populations of astrocytes. We first investigated the heterogeneity among 158 astrocytes in the stratum radiatum of the hippocampus (CA1) and found that both the astrocyte VF and segment density are highly variable with coefficients of variation of 0.26 and 0.39, respectively (**Figure 5A**). Interestingly, there is no correlation between the VF and segment density of individual astrocytes (Spearman's rank correlation,  $R = 0.013$ ,  $p = 0.878$ ). Also, see **Supplementary Figure 1**. Building on this observation we next studied a total of 437 astrocytes (including the 158 astrocytes from above) in acute hippocampal slices prepared from animals with postnatal ages of 1 week to 80 (**Figure 5B**). When the VF and segment density of these astrocytes were analyzed, we observed that the average VF was surprisingly constant throughout the life of mice whereas the segment density increased during the first three postnatal weeks and then remained stable overall. The gradual appearance of a higher astrocytic segment density, i.e., of a more strongly ramified astrocyte morphology and a stable VF suggests that the astrocyte process undergo a developmental transition during which finer astrocyte processes are being generated at the expense of their volume. Finally, we compared the VF and segment density of astrocytes between different layers of the hippocampal CA1 region (**Figure 5C**). While the VF of astrocytes in the *stratum radiatum* (SR) was higher than in *stratum lacunosum-moleculare* (SLM) and *stratum oriens* (SO), the segment density of astrocytes in the SLM was higher when compared to the SR and SO. This suggests that astrocytes in the SLM have a more ramified morphology with more fine processes, which overall have a smaller volume compared to SO and SR astrocytes.

In a final set of experiments, we tested how measurements of VF and segment density change in response to rapid volume changes of peripheral astrocytic processes. The latter were induced by acutely reducing or increasing the osmolarity of the extracellular solution. The prediction is that the expected volume increase in hypoosmolar solution would increase the VF and the volume decrease in hyperosmolar solution would decrease the VF, respectively. This was indeed observed for the VF (**Figure 6**) whereas no statistically significant effect on the segment density was detected (see figure legend for statistical details).



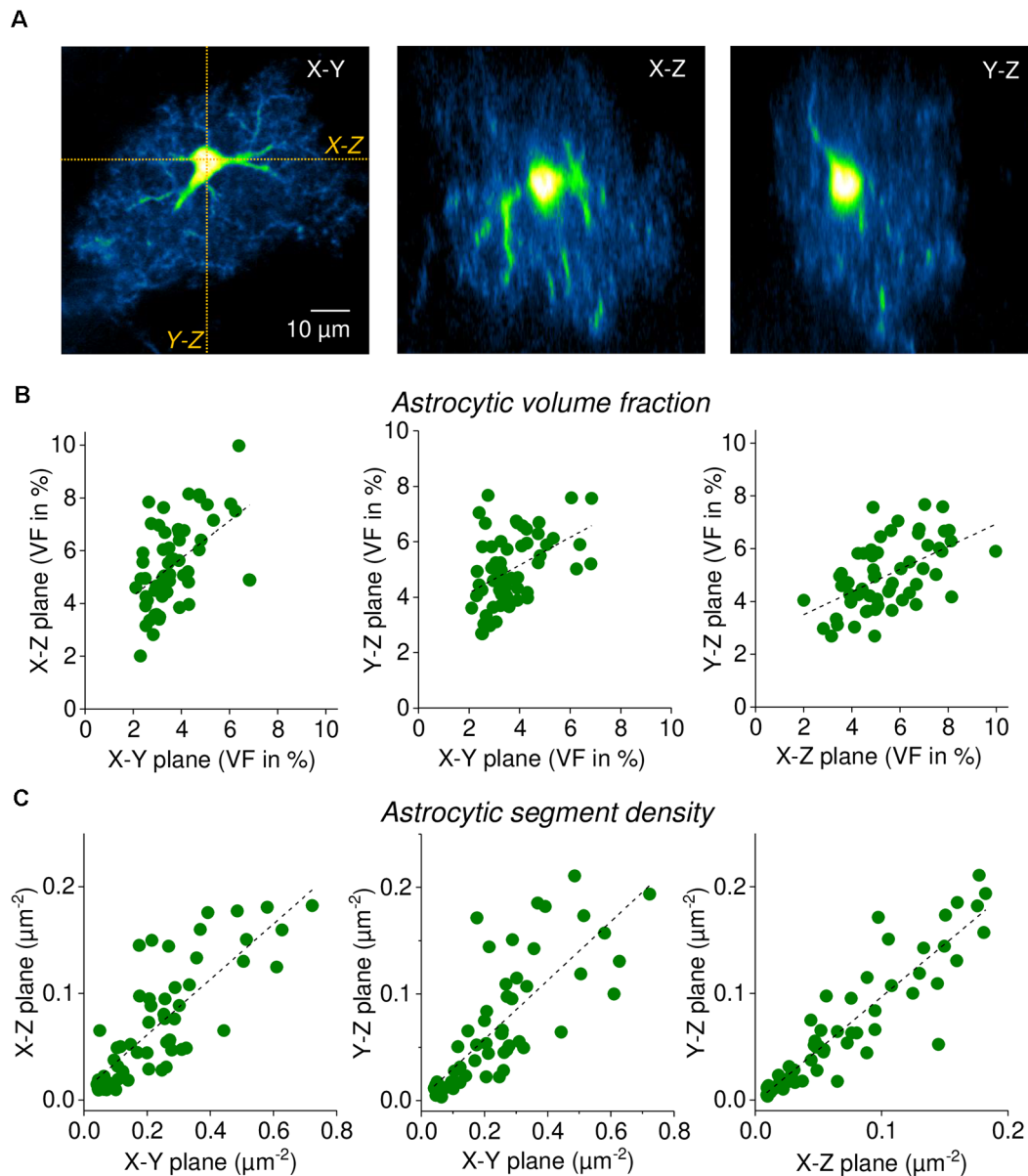


**FIGURE 4 |** Single focal plane measurements of astrocytic volume fraction (VF) and segment density are representative of three-dimensional morphology. **(A)** Sample EGFP-expressing astrocyte (CA1 stratum radiatum, acute slice). Left panel: single horizontal focal plane (X-Y) through the soma from an image stack (2PE fluorescence microscopy, nominal x-y resolution of  $0.09 \mu\text{m}/\text{pixel}$ , z-steps of  $1 \mu\text{m}$ ). X-Z and Y-Z sections through the stack were taken as indicated (orange dotted lines) and labeled. Middle panel: X-Z section (same scale as in left panel). Right panel: Y-Z section (same scale as in left panel). Note the reduced resolution along the Z-axis. In all three planes, the astrocytic volume fraction and segment density was determined ( $n = 58$  astrocytes). **(B)** Correlation of astrocytic volume fractions (in %) between planes. Spearman's rank correlations from left to right:  $R = 0.520$ ,  $p < 0.0001$ ;  $R = 0.422$ ,  $p = 0.000976$ ;  $R = 0.552$ ,  $p < 0.0001$ . Linear fits as a visual guide (dashed black lines). **(C)** Correlation of astrocytic segment densities (in segments per  $\mu\text{m}^2$ ) between planes. Spearman's rank correlations from left to right:  $R = 0.812$ ,  $p < 0.0001$ ;  $R = 0.931$ ,  $p < 0.0001$ ;  $R = 0.859$ ,  $p < 0.0001$ . Linear fits as a visual guide (dashed black lines). Note that segment densities are generally lower in planes along the Z-axis because of the reduced resolution (see text). In these analyses, large processes were excluded from the analysis to focus on fine astrocyte processes.

## DISCUSSION

The morphology of astrocytes and its changes can be characterized on many levels: from the volume of their territory and number of main branches to the precise geometry of their

small perisynaptic processes. Here, we describe two measures of astrocyte morphology, the astrocytic volume fraction and the segment density, that can be rapidly extracted from a single optical section through an astrocyte and its cells body. While the volume fraction is directly related to the number of astrocytic



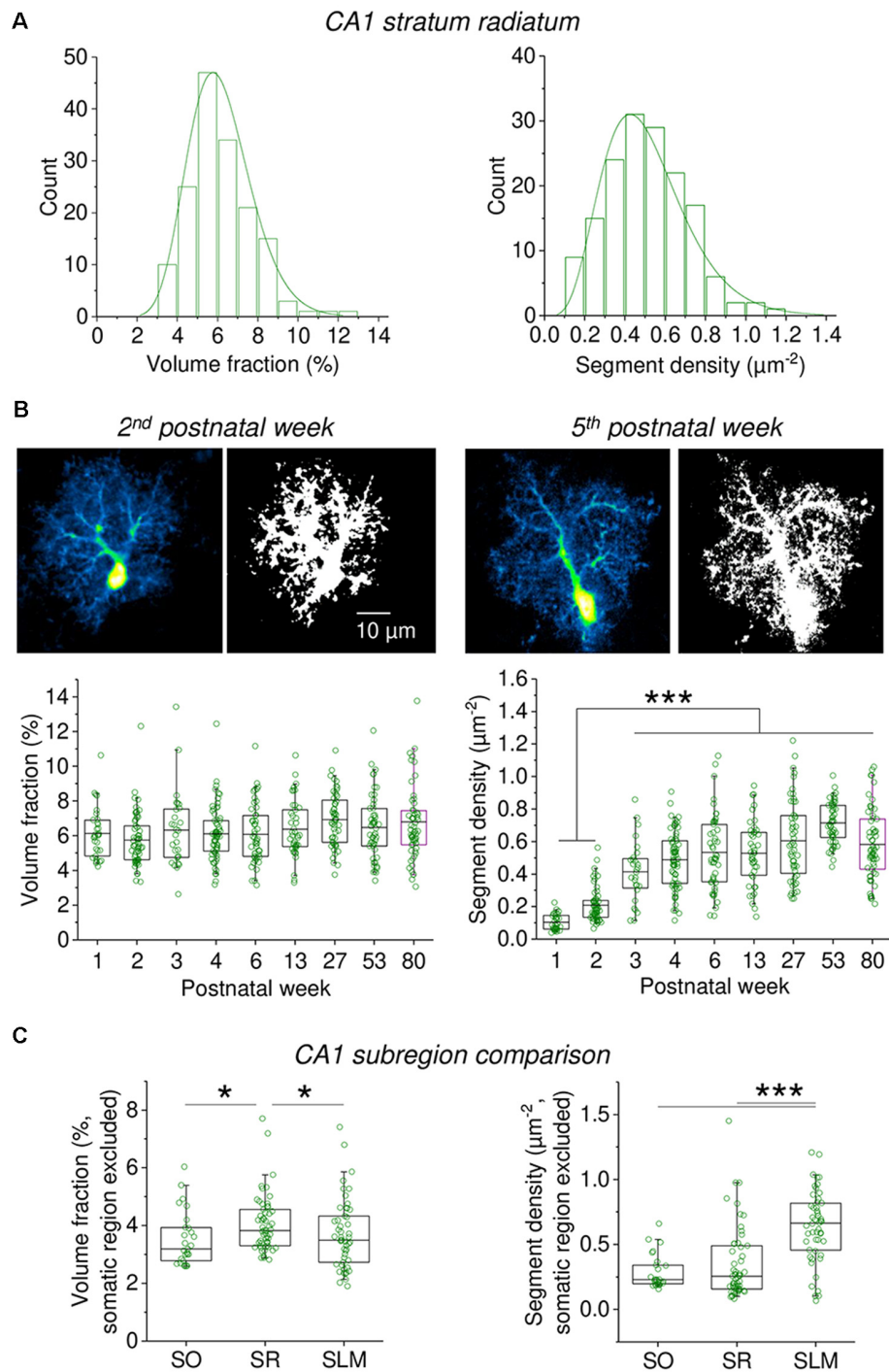


**FIGURE 5 |** Capturing the heterogeneity and developmental profile of astrocyte morphology using measurements of volume fraction and segment density. **(A)** The volume fraction and segment density of EGFP-expressing astrocytes in the CA1 stratum radiatum was analyzed in acute slices ( $n = 158$ ). Somatic reference region as before. Entire cross-sections including the soma were analyzed (see **Figure 3**). A significant heterogeneity of both parameters was observed (coefficient of variation of volume fraction = 0.26; of segment density = 0.39). **(B)** Developmental changes of volume fraction and segment density ( $n = 437$  astrocytes). Time windows in postnatal weeks and number of astrocytes from left to right: 1st  $n = 31$ , 2nd  $n = 59$ , 3rd  $n = 28$ , 4th  $n = 67$ , 5th–7th  $n = 49$ , 12th–14th  $n = 42$ , 26th–28th  $n = 52$ , 52nd–54th  $n = 50$ , 79th–81st  $n = 59$ . Like in **(A)**, entire cross-sections of astrocytes including the soma were analyzed (somatic reference region). Examples of astrocytes from the 2nd and 5th postnatal week are shown (top panel pairs, scale bar applies to all panels). Each image pair is a representative astrocyte shown before (left) and after (right) binarization for quantifying astrocyte segment density. Note the more granular binarized image for the astrocyte from a 5-week-old animal. See **Supplementary Figure 2** for further examples. Lower panels illustrate the developmental profile. Left: volume fraction (one-way ANOVA  $p = 0.01846$ ;

(Continued)

**FIGURE 5 |** Continued

Tukey *post hoc*  $p < 0.05$  for week 2 vs. 27 and week 2 vs. 80). Right: segment density (one ANOVA  $p < 0.0001$ ; Tukey *post hoc*  $p < 0.0001$  for all combinations of weeks 2 and 3 vs. weeks 3–80). Individual circles represent measurements from single astrocytes. Box represents mean and 25th and 75th percentile. Whiskers represent 5th and 95th percentiles. **(C)** The volume fraction and segment density were measured in cross-sections of astrocytes from the *stratum oriens* (SO,  $n = 27$ ), *stratum radiatum* (SR,  $n = 55$ ) and *stratum lacunosum-moleculare* (SLM,  $n = 50$ ). A total of six mice 6–8-week-old were used. Both parameters were analyzed in regions of interest sparing the somatic region (see **Figure 2A**). Somatic reference region as elsewhere. Left panel: volume fraction comparison (Kruskal Wallis  $p = 0.0110$ , Dunn *post hoc*  $p < 0.05$  for SR vs. SO and SLM). Right panel: segment density comparison (Kruskal Wallis  $p < 0.0001$ ; Dunn *post hoc*  $p < 0.0001$  for SLM vs. SO and SR). \* $p < 0.05$  and \*\*\* $p < 0.001$ .

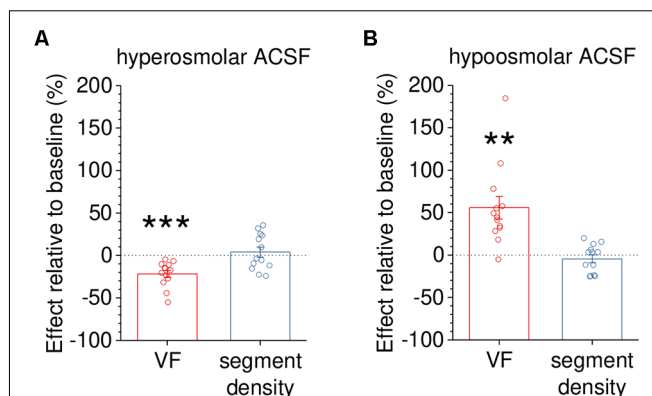


**FIGURE 6 |** Capturing dynamic changes of astrocyte volume in response to altered extracellular osmolarity. To demonstrate that volume fraction (VF) measurements are a sensitive indicator of volume changes of small astrocyte processes, astrocytes were acutely exposed to hyper- or hypoosmolar extracellular solution (see “Materials and Methods” section). The morphology of EGFP-expressing astrocytes (not illustrated) was analyzed before (baseline) and 10 min after changing the extracellular solution. Changes in VF and segment density were expressed as per cent change relative to the baseline recording. **(A)** The VF was significantly reduced by application of hyperosmolar solution ( $\sim 400$  mOsm/kg,  $-21.8 \pm 4.1\%$ ,  $p < 0.001$ ) whereas the segment density was not ( $+4.0 \pm 5.8\%$ ,  $p = 0.510$ ,  $n = 13$  and paired Student's *t*-test for both tests). **(B)** In a second set of experiments, the VF of astrocyte processes was increased by exposure to hypoosmolar extracellular solution ( $\sim 200$  mOsm/kg,  $+55.8 \pm 13.2\%$ ,  $p = 0.00117$ ) whereas the segment density was not affected ( $-4.5 \pm 4.6\%$ ,  $p = 0.351$ ,  $n = 13$  and paired Student's *t*-test for both tests). Overall, changes of VF and segment density did not display a statistically significant correlation (Spearman's rank correlation,  $R = -0.246$ ,  $p = 0.226$ ,  $n = 26$ ). Also, see **Supplementary Figure 1C**. \*\* $p < 0.01$  and \*\*\* $p < 0.001$ .

processes and their average volume in the optical section/region of interest, the segment density is representative of but not equal to the number of astrocyte processes (also see below). For the interpretation of both parameters, there are several important points to consider. Also, the entire approach was designed with three-dimensional astrocytes in organized tissue such as brain slices or *in vivo* experiments in mind and requires modification for flat preparations.

## Volume Fraction

Determining the volume fraction requires a reference, where 100% of the optical section is filled by the astrocyte. This is the case for the astrocyte soma with diameters of  $\sim 5$ – $10 \mu\text{m}$  and the typical point spread function (PSF) of the two-photon excitation microscopes used in this study (full width at half-maximum,  $0.35$ – $0.50 \mu\text{m}$  in x-y and  $1.5$ – $2.5 \mu\text{m}$  in z), because the PSF is fully within the cell at the somatic region (Savtchenko et al., 2018; Henneberger et al., 2020). This would need to be verified for other microscopes or techniques. In addition, the z-positions of optical sections through the soma need to be carefully set and maintained, e.g., for time-lapse imaging. The second assumption of VF measurements is that the cytosolic concentration of the dye is the same throughout the cell. Aggregation of fluorescent proteins, their accumulation in cellular sub-compartments, or rapid dye bleaching can be incompatible with reliably measuring the volume fraction. Special care needs to be taken when astrocytes are acutely filled with a dye, for instance *via* a patch pipette. In this case, sufficient access to the cell and stable filling needs to be ensured. Filling astrocytes with dyes with a low molecular weight represents the additional challenge that these dyes can escape from the patched cell through gap junction and hemichannels, which could lead to intracellular concentration gradients. Sufficiently large dextran-conjugated dyes can be used as an alternative (**Figure 3A**; Breithausen et al., 2020) or appropriate control experiments need to be performed (Henneberger et al., 2020). However, larger dyes re-equilibrate more slowly across the cytosol after a morphology change and therefore report these changes less rapidly (Henneberger et al., 2020). Finally, basic requirements of quantitative microscopy need to be met, i.e., imaging settings must be such that there is no clipping of the fluorescence intensity distribution (e.g., no saturation) and that there is a linear relationship between dye concentration in an imaged volume and fluorescence intensity. For interpreting the volume fraction and its changes, it needs to be kept in mind that it is the product of the number of processes and their average size, and therefore cannot distinguish between the two factors on its own. Also, it captures the cytosolic volume and may therefore be insensitive to changes or redistribution of intracellular organelles. Despite these potential drawbacks, our current study demonstrates that the astrocytic volume fraction can be easily and reliably obtained across various experimental approaches. In addition, we have verified it previously using electron microscopy (Medvedev et al., 2014), and successfully used astrocytic volume fraction measurements to constrain the morphology of realistic *in silico* models of astrocytes (Savtchenko et al., 2018), to correlate astrocyte morphology and  $\text{Ca}^{2+}$  signaling (King et al., 2020) and to demonstrate astrocyte process withdrawal from synapses after induction of synaptic long-term potentiation (Henneberger et al., 2020).

## Segment Density

To complement volume fraction measurements, we have established the segment density as a second parameter for describing the abundance of small astrocyte processes. Because diffraction-limited microscopy does not fully resolve individual

processes, the calculated segment density is not the true density of astrocyte cross-sections in an optical section. However, our simulations, emulations of diffraction-limited microscopy on super-resolved ExM data and analysis of pre- and post-expansion data showed that the detected segment density is lower but strongly correlated with the true value. It is intuitive that the quantified segment density depends on the dimensions of the microscope's PSF. Therefore, absolute values of segment density may not be comparable between microscopes. Indeed, it is our experience that all imaging settings (e.g., objective, excitation wavelength, fluorescence detection) should be kept as constant as possible to compare individual recordings of segment density. Such considerations play a lesser role in experiments with online monitoring of astrocyte morphology and acute manipulations, where it is usually easier to keep imaging conditions constant. Increases or decreases of the segment density, or differences between two experimental groups, indicate a different number of astrocytic process cross-sections in the optical sections. For example, an increase in the astrocytic segment density could reflect the outgrowth/appearance of new astrocytic processes. Such observations can be easier to interpret when combined with volume fraction measurements. For instance, the appearance of new astrocyte processes with comparable size should also increase the volume fraction. Similarly, the disappearance of astrocyte processes or a less ramified morphology can reduce the segment density and the volume fraction. In contrast, a change of volume fraction but not the segment density would indicate that primarily the volume of astrocyte processes is affected. It should be noted, however, that an isolated change of process volume could also affect the detection of astrocytic processes. For example, swollen processes could be more difficult to separate in diffraction-limited microscopy leading to fewer detected segments and thus a lower segment density (but see **Figure 6**). Whether such effects play a role depends on the optical resolution of the used microscope.

Interestingly, we found no correlation between the volume fraction and segment density of individual astrocytes when we studied sufficiently large populations (**Supplementary Figure 1**). This indicates, for example, that an astrocyte with a high density of small processes does not simply arise from an astrocyte with a low density of processes by the addition of new processes of the same volume, because that would also increase the volume fraction. Instead, our data imply that an increase in process density affects the average size of astrocytic processes. The development of astrocyte morphology could be an example of such a process (see below). Studying such relationships in further detail will require isolated manipulation of either astrocyte process volume or density.

## Selecting the Region of Analysis

In this study, we mostly selected the region for analysis manually. Naturally, the calculated volume fraction and segment density will depend on how this region was chosen. If it includes the soma, for instance, the volume fraction across the region of analysis will be higher compared to an analysis region

sparing the soma. Similarly, volume fraction and segment density will change if blood vessels are not excluded or endfeet are included in the analysis. Many alternatives to manual selection are possible. For instance, multiple regions of interest covering the entire astrocyte can be defined automatically (**Figure 2**; King et al., 2020), a standardized region of interest in the periphery of astrocytes can be defined (Henneberger et al., 2020) or individual spot-like regions of analysis can be placed at a site of experimental manipulations, e.g., glutamate uncaging (Henneberger et al., 2020). Automated detection of astrocyte boundaries would be helpful for the analysis of large populations of astrocytes. This will require images in which the outer boundaries of single astrocytes can be reliably traced automatically, which could be the case for animal models with consistently sparse or combinatorial expression of fluorescent reporters in astrocytes (Livet et al., 2007; García-Marqués and López-Mascaraque, 2013).

## Capturing Heterogeneity and Developmental Changes of Astrocyte Morphology

After testing the robustness of volume fraction and segment density measurements in various experimental approaches in acute slices and *in vivo*, we used both parameters to explore the heterogeneity and development of astrocyte morphology. Interestingly, we observed that within their territories the astrocyte volume fraction remained constant while the segment density increased over the first three postnatal weeks. This indicates that astrocyte ramification increases over this period of development and that small astrocyte processes become more abundant but also thinner, which is similar to a previous qualitative assessment of astrocyte development (Bushong et al., 2004). The advantage of easily obtainable measures of morphology over a qualitative assessment is that it can enable the experimenter to quantify the contribution of specific signaling molecules, such as GTPases of the Rho family (Zeug et al., 2018; Müller et al., 2021) or BDNF (Holt et al., 2019), to the development and heterogeneity of astrocyte morphology. Because the astrocyte volume fraction and segment density can be quickly extracted from a single optical section through a dye-filled astrocyte and its soma, and because this is representative of the entire astrocyte, this approach allowed us to analyze hundreds of astrocytes using two-photon excitation fluorescence microscopy in acute slices and *in vivo*. This approach should also be useful in other preparations, in fixed tissue and for microscopy methods such as confocal microscopy, if the aforementioned conditions are met. Despite these advantages, our approach cannot replace the methods that accurately quantify the geometry and branching patterns of large astrocyte processes, see for instance Tavares et al. (2017), or that resolve the fine geometric details of astrocyte structure such as electron (Ventura and Harris, 1999), STED (Arizono et al., 2020, 2021) or expansion microscopy (Herde et al., 2020), among other techniques as recently reviewed (Heller and Rusakov, 2017). However, the approach can be used to efficiently screen for

biologically relevant scenarios by comparing large populations of astrocytes in different conditions or by online monitoring of astrocyte morphology changes, their triggers and functional consequences. Interesting scenarios can then be explored using the more complex methods mentioned above. Our recent study on synaptic plasticity is one example (Henneberger et al., 2020), in which results from volume fraction measurements were then further investigated using STED and electron microscopy. Other options are techniques for locating neuron-astrocyte interaction sites using proximity assays (Oceau et al., 2018) and for identifying the proteins enriched at such contact sites (Takano et al., 2020).

## DATA AVAILABILITY STATEMENT

The raw data supporting the conclusions of this article will be made available by the authors, without undue reservation.

## ETHICS STATEMENT

The animal study was reviewed and approved and all animal procedures were conducted in accordance with the regulations of the European Commission and all relevant national and institutional guidelines and requirements. All procedures have been approved by the Landesamt für Natur, Umwelt und Verbraucherschutz Nordrhein-Westfalen (LANUV, Germany) where required.

## AUTHOR CONTRIBUTIONS

DM, CD, PU, AP, SA, MH, CB, and CH performed and analyzed experiments in acute slices and expansion microscopy. PU, AD,

GP, and CH performed and analyzed *in vivo* experiments. PG and SS designed and produced AAVs. CH conceived the study, performed the modeling, and wrote the manuscript. All authors contributed to the article and approved the submitted version.

## FUNDING

Research was supported by the NRW-Rückkehrerprogramm (CH; Ministerium für Klimaschutz, Umwelt, Landwirtschaft, Natur- und Verbraucherschutz des Landes Nordrhein-Westfalen) and the German Research Foundation [Deutsche Forschungsgemeinschaft (DFG); SFB1089 B03, SPP1757 HE6949/1, FOR2795 HE6949/4, and HE6949/3 to CH; SFB1089 A06 and P02, SCHO 820/4-1, SCHO 820/6-1, SPP1757 SCHO 820/7-2, SCHO 820/5-2, SCHO 820/8-1 to SS; SPP1757 Young Investigator Award to MH]. GP was supported by the DFG (FOR2795 PE1193/6-1) and the European Union (EU) Joint Program Neurodegenerative Disease Research program (JPND; Horizon 2020 Framework Programme, grant agreement 643417/DACAPO-AD).

## ACKNOWLEDGMENTS

We thank Dr. Nikolai Medvedev and Dr. Michael G. Stewart for providing the example electron micrograph (Figure 1), for details see Medvedev et al. (2014).

## SUPPLEMENTARY MATERIAL

The Supplementary Material for this article can be found online at: <https://www.frontiersin.org/articles/10.3389/fncel.2021.669280/full#supplementary-material>.

## REFERENCES

- Anders, S., Minge, D., Griemsmann, S., Herde, M. K., Steinhäuser, C., and Henneberger, C. (2014). Spatial properties of astrocyte gap junction coupling in the rat hippocampus. *Philos. Trans. R. Soc. B.* 369:20130600. doi: 10.1098/rstb.2013.0600
- Arizono, M., Inavalli, V. V. G. K., Bancelin, S., Fernández-Monreal, M., and Nägerl, U. V. (2021). Super-resolution shadow imaging reveals local remodeling of astrocytic microstructures and brain extracellular space after osmotic challenge. *Glia* 69, 1605–1613. doi: 10.1002/glia.23995
- Arizono, M., Inavalli, V. V. G. K., Panatier, A., Pfeiffer, T., Angibaud, J., Levot, F., et al. (2020). Structural basis of astrocytic Ca<sup>2+</sup> signals at tripartite synapses. *Nat. Commun.* 11, 1–15. doi: 10.1038/s41467-020-15648-4
- Bernardinelli, Y., Randall, J., Janett, E., Nikonenko, I., König, S., Jones, E. V., et al. (2014). Activity-dependent structural plasticity of perisynaptic astrocytic domains promotes excitatory synapse stability. *Curr. Biol.* 24, 1679–1688. doi: 10.1016/j.cub.2014.06.025
- Breithausen, B., Kautzmann, S., Boehlen, A., Steinhäuser, C., and Henneberger, C. (2020). Limited contribution of astroglial gap junction coupling to buffering of extracellular K<sup>+</sup> in CA1 stratum radiatum. *Glia* 68, 918–931. doi: 10.1002/glia.23751
- Bürgers, J., Pavlova, I., Rodriguez-Gatica, J. E., Henneberger, C., Oeller, M., Ruland, J. A., et al. (2019). Light-sheet fluorescence expansion microscopy: fast mapping of neural circuits at super resolution. *Neurophotonics* 6:015005. doi: 10.1117/1.NPh.6.1.015005
- Bushong, E. A., Martone, M. E., and Ellisman, M. H. (2004). Maturation of astrocyte morphology and the establishment of astrocyte domains during postnatal hippocampal development. *Int. J. Dev. Neurosci.* 22, 73–86. doi: 10.1016/j.jdevneu.2003.12.008
- Bushong, E. A., Martone, M. E., Jones, Y. Z., and Ellisman, M. H. (2002). Protoplasmic astrocytes in CA1 stratum radiatum occupy separate anatomical domains. *J. Neurosci.* 22, 183–192. doi: 10.1523/JNEUROSCI.22-01-00183.2002
- Chayes, F. (1953). The relation between area and volume in micrometric analysis. *Mineralogical Magazine and Journal of the Mineralogical Society* 30, 147–149. doi: 10.1180/minmag.1953.030.221.08
- Chen, F., Tillberg, P. W., and Boyden, E. S. (2015). Expansion microscopy. *Science* 347, 543–548. doi: 10.1126/science.1260088
- Chozinski, T. J., Halpern, A. R., Okawa, H., Kim, H.-J., Tremel, G. J., Wong, R. O. L., et al. (2016). Expansion microscopy with conventional antibodies and fluorescent proteins. *Nat. Methods* 13, 485–488. doi: 10.1038/nmeth.3833
- Deshpande, T., Li, T., Herde, M. K., Becker, A., Vatter, H., Schwarz, M. K., et al. (2017). Subcellular reorganization and altered phosphorylation of the astrocytic gap junction protein connexin43 in human and experimental temporal lobe epilepsy. *Glia* 65, 1809–1820. doi: 10.1002/glia.23196
- García-Marqués, J., and López-Mascaraque, L. (2013). Clonal identity determines astrocyte cortical heterogeneity. *Cereb. Cortex* 23, 1463–1472. doi: 10.1371/journal.pntd.0008948
- Genoud, C., Quairiaux, C., Steiner, P., Hirling, H., Welker, E., and Knott, G. W. (2006). Plasticity of astrocytic coverage and glutamate transporter expression in adult mouse cortex. *PLoS Biol.* 4:e343. doi: 10.1371/journal.pbio.0040343



- Haber, M., Zhou, L., and Murai, K. K. (2006). Cooperative astrocyte and dendritic spine dynamics at hippocampal excitatory synapses. *J. Neurosci.* 26, 8881–8891. doi: 10.1523/JNEUROSCI.1302-06.2006
- Heller, J. P., and Rusakov, D. A. (2017). The nanoworld of the tripartite synapse: insights from super-resolution microscopy. *Front. Cell. Neurosci.* 11:374. doi: 10.3389/fncel.2017.00374
- Helmchen, F., and Denk, W. (2005). Deep tissue two-photon microscopy. *Nat. Methods* 2, 932–940. doi: 10.1038/nmeth818
- Henneberger, C., Bard, L., Panatier, A., Reynolds, J. P., Kopach, O., Medvedev, N. I., et al. (2020). LTP induction boosts glutamate spillover by driving withdrawal of perisynaptic astroglia. *Neuron* 108, 919–936.e11. doi: 10.1016/j.neuron.2020.08.030
- Henneberger, C., Papouin, T., Oliet, S. H. R., and Rusakov, D. A. (2010). Long-term potentiation depends on release of d-serine from astrocytes. *Nature* 463, 232–236. doi: 10.1038/nature08673
- Henneberger, C., and Rusakov, D. A. (2012). Monitoring local synaptic activity with astrocytic patch pipettes. *Nat. Protoc.* 7, 2171–2179. doi: 10.1038/nprot.2012.140
- Herde, M. K., Bohmbach, K., Domingos, C., Vana, N., Komorowska-Müller, J. A., Passlick, S., et al. (2020). Local efficacy of glutamate uptake decreases with synapse size. *Cell Rep.* 32:108182. doi: 10.1016/j.celrep.2020.108182
- Hirrlinger, J., Hülsmann, S., and Kirchhoff, F. (2004). Astroglial processes show spontaneous motility at active synaptic terminals *in situ*. *Eur. J. Neurosci.* 20, 2235–2239. doi: 10.1111/j.1460-9568.2004.03689.x
- Holt, L. M., Hernandez, R. D., Pacheco, N. L., Torres Ceja, B., Hossain, M., and Olsen, M. L. (2019). Astrocyte morphogenesis is dependent on BDNF signaling via astrocytic TrkB.T1. *eLife* 8:e44667. doi: 10.7554/eLife.44667
- King, C. M., Bohmbach, K., Minge, D., Delekate, A., Zheng, K., Reynolds, J., et al. (2020). Local resting Ca<sup>2+</sup> controls the scale of astroglial Ca<sup>2+</sup> signals. *Cell Rep.* 30, 3466–3477. doi: 10.1016/j.celrep.2020.02.043
- Korogod, N., Petersen, C. C., and Knott, G. W. (2015). Ultrastructural analysis of adult mouse neocortex comparing aldehyde perfusion with cryo fixation. *eLife* 4:e05793. doi: 10.7554/eLife.05793
- Livet, J., Weissman, T. A., Kang, H., Draft, R. W., Lu, J., Bennis, R. A., et al. (2007). Transgenic strategies for combinatorial expression of fluorescent proteins in the nervous system. *Nature* 450, 56–62. doi: 10.1038/nature06293
- Lushnikova, I., Skibo, G., Muller, D., and Nikonenko, I. (2009). Synaptic potentiation induces increased glial coverage of excitatory synapses in CA1 hippocampus. *Hippocampus* 19, 753–762. doi: 10.1002/hipo.20551
- Marvin, J. S., Borghuis, B. G., Tian, L., Cichon, J., Harnett, M. T., Akerboom, J., et al. (2013). An optimized fluorescent probe for visualizing glutamate neurotransmission. *Nat. Methods* 10, 162–170. doi: 10.1038/nmeth.2333
- Medvedev, N., Popov, V., Henneberger, C., Kraev, I., Rusakov, D. A., and Stewart, M. G. (2014). Glia selectively approach synapses on thin dendritic spines. *Philos. Trans. R. Soc. Lond. B Biol. Sci.* 369:20140047. doi: 10.1098/rstb.2014.0047
- Minge, D., Senkov, O., Kaushik, R., Herde, M. K., Tikhobrazova, O., Wulff, A. B., et al. (2017). Heparan sulfates support pyramidal cell excitability, synaptic plasticity and context discrimination. *Cereb. Cortex* 27, 903–918. doi: 10.1093/cercor/bhx003
- Monai, H., Ohkura, M., Tanaka, M., Oe, Y., Konno, A., Hirai, H., et al. (2016). Calcium imaging reveals glial involvement in transcranial direct current stimulation-induced plasticity in mouse brain. *Nat. Commun.* 7:11100. doi: 10.1038/ncomms11100
- Müller, F. E., Schade, S. K., Cherkas, V., Stopper, L., Breithausen, B., Minge, D., et al. (2021). Serotonin receptor 4 regulates hippocampal astrocyte morphology and function. *Glia* 69, 872–889. doi: 10.1002/glia.23933
- Nolte, C., Matyash, M., Pivneva, T., Schipke, C. G., Ohlemeyer, C., Hanisch, U. K., et al. (2001). GFAP promoter-controlled EGFP-expressing transgenic mice: a tool to visualize astrocytes and astrogliosis in living brain tissue. *Glia* 33, 72–86. doi: 10.1002/1098-1136(20010101)33:1%3C72::AID-GLIA1007%3E3.0.CO;2-A
- Octeau, J. C., Chai, H., Jiang, R., Bonanno, S. L., Martin, K. C., and Khakh, B. S. (2018). An optical neuron-astrocyte proximity assay at synaptic distance scales. *Neuron* 98, 49–66.e9. doi: 10.1016/j.neuron.2018.03.003
- Oliet, S. H., Piet, R., and Poulain, D. A. (2001). Control of glutamate clearance and synaptic efficacy by glial coverage of neurons. *Science* 292, 923–926. doi: 10.1126/science.1059162
- Patrushev, I., Gavrillov, N., Turlapov, V., and Semyanov, A. (2013). Subcellular location of astrocytic calcium stores favors extrasynaptic neuron-astrocyte communication. *Cell Calcium* 54, 343–349. doi: 10.1016/j.ceca.2013.08.003
- Savchenko, L. P., Bard, L., Jensen, T. P., Reynolds, J. P., Kraev, I., Medvedev, N., et al. (2018). Disentangling astroglial physiology with a realistic cell model *in silico*. *Nat. Commun.* 9:3554. doi: 10.1016/j.ceca.2013.08.003
- Takano, T., He, W., Han, X., Wang, F., Xu, Q., Wang, X., et al. (2014). Rapid manifestation of reactive astrogliosis in acute hippocampal brain slices. *Glia* 62, 78–95. doi: 10.1002/glia.22588
- Takano, T., Wallace, J. T., Baldwin, K. T., Purkey, A. M., Uezu, A., Courtland, J. L., et al. (2020). Chemico-genetic discovery of astrocytic control of inhibition *in vivo*. *Nature* 588, 296–302. doi: 10.1038/s41586-020-2926-0
- Tavares, G., Martins, M., Correia, J. S., Sardinha, V. M., Guerra-Gomes, S., das Neves, S. P., et al. (2017). Employing an open-source tool to assess astrocyte tridimensional structure. *Brain Struct. Funct.* 222, 1989–1999. doi: 10.1007/s00429-016-1316-8
- Tønnesen, J., Inavalli, V. V. G. K., and Nägerl, U. V. (2018). Super-resolution imaging of the extracellular space in living brain tissue. *Cell* 172, 1108.e15–1121.e15. doi: 10.1016/j.cell.2018.02.007
- Ventura, R., and Harris, K. M. (1999). Three-dimensional relationships between hippocampal synapses and astrocytes. *J. Neurosci.* 19, 6897–6906. doi: 10.1523/JNEUROSCI.19-16-06897.1999
- Witcher, M. R., Kirov, S. A., and Harris, K. M. (2007). Plasticity of perisynaptic astroglia during synaptogenesis in the mature rat hippocampus. *Glia* 55, 13–23. doi: 10.1002/glia.20415
- Woitecki, A. M. H., Müller, J. A., Loo, K. M. J., van Sowade, R. F., Becker, A. J., and Schoch, S. (2016). Identification of synaptotagmin 10 as effector of NPAS4-mediated protection from excitotoxic neurodegeneration. *J. Neurosci.* 36, 2561–2570. doi: 10.1523/JNEUROSCI.2027-15.2016
- Yang, W., and Yuste, R. (2017). *in vivo* imaging of neural activity. *Nat. Methods* 14, 349–359. doi: 10.1038/nmeth.4230
- Zeug, A., Müller, F. E., Anders, S., Herde, M. K., Minge, D., Ponimaskin, E., et al. (2018). Control of astrocyte morphology by Rho GTPases. *Brain Res. Bull.* 136, 44–53. doi: 10.1016/j.brainresbull.2017.05.003

**Conflict of Interest:** The authors declare that the research was conducted in the absence of any commercial or financial relationships that could be construed as a potential conflict of interest.

Copyright © 2021 Minge, Domingos, Unichenko, Behringer, Pauletti, Anders, Herde, Delekate, Gulakova, Schoch, Petzold and Henneberger. This is an open-access article distributed under the terms of the Creative Commons Attribution License (CC BY). The use, distribution or reproduction in other forums is permitted, provided the original author(s) and the copyright owner(s) are credited and that the original publication in this journal is cited, in accordance with accepted academic practice. No use, distribution or reproduction is permitted which does not comply with these terms.



# Calcium Signals in Astrocyte Microdomains, a Decade of Great Advances

Annamaria Lia<sup>1,2†</sup>, Vanessa Jorge Henriques<sup>1,2†</sup>, Micaela Zonta<sup>1,2</sup>, Angela Chiavegato<sup>2</sup>, Giorgio Carmignoto<sup>1,2</sup>, Marta Gómez-Gonzalo<sup>1,2\*</sup> and Gabriele Losi<sup>1,2\*</sup>

<sup>1</sup> Neuroscience Institute, National Research Council (IN-CNR), Padua, Italy, <sup>2</sup> Department of Biomedical Sciences, University of Padua, Padua, Italy

## OPEN ACCESS

### Edited by:

Christian Lohr,  
University of Hamburg, Germany

### Reviewed by:

Christian Henneberger,  
University of Bonn, Germany  
Valentin Nägerl,  
UMR 5297 Institut Interdisciplinaire  
de Neurosciences (IINS), France

### \*Correspondence:

Marta Gómez-Gonzalo  
marta.gomezgonzalo@cnr.it  
Gabriele Losi  
gabriele.losi@bio.unipd.it

<sup>†</sup> These authors have contributed  
equally to this work

### Specialty section:

This article was submitted to  
Non-Neuronal Cells,  
a section of the journal  
Frontiers in Cellular Neuroscience

**Received:** 27 February 2021

**Accepted:** 23 April 2021

**Published:** 07 June 2021

### Citation:

Lia A, Henriques VJ, Zonta M,  
Chiavegato A, Carmignoto G,  
Gómez-Gonzalo M and Losi G (2021)  
Calcium Signals in Astrocyte  
Microdomains, a Decade of Great  
Advances.  
Front. Cell. Neurosci. 15:673433.  
doi: 10.3389/fncel.2021.673433

The glial cells astrocytes have long been recognized as important neuron-supporting elements in brain development, homeostasis, and metabolism. After the discovery that the reciprocal communication between astrocytes and neurons is a fundamental mechanism in the modulation of neuronal synaptic communication, over the last two decades astrocytes became a hot topic in neuroscience research. Crucial to their functional interactions with neurons are the cytosolic  $\text{Ca}^{2+}$  elevations that mediate gliotransmission. Large attention has been posed to the so-called  $\text{Ca}^{2+}$  microdomains, dynamic  $\text{Ca}^{2+}$  changes spatially restricted to fine astrocytic processes including perisynaptic astrocytic processes (PAPs). With presynaptic terminals and postsynaptic neuronal membranes, PAPs compose the tripartite synapse. The distinct spatial-temporal features and functional roles of astrocyte microdomain  $\text{Ca}^{2+}$  activity remain poorly defined. However, thanks to the development of genetically encoded  $\text{Ca}^{2+}$  indicators (GECIs), advanced microscopy techniques, and innovative analytical approaches,  $\text{Ca}^{2+}$  transients in astrocyte microdomains were recently studied in unprecedented detail. These events have been observed to occur much more frequently ( $\sim 50$ – $100$ -fold) and dynamically than somatic  $\text{Ca}^{2+}$  elevations with mechanisms that likely involve both  $\text{IP}_3$ -dependent and -independent pathways. Further progress aimed to clarify the complex, dynamic machinery responsible for astrocytic  $\text{Ca}^{2+}$  activity at microdomains is a crucial step in our understanding of the astrocyte role in brain function and may also reveal astrocytes as novel therapeutic targets for different brain diseases. Here, we review the most recent studies that improve our mechanistic understanding of the essential features of astrocyte  $\text{Ca}^{2+}$  microdomains.

**Keywords:** astrocytes, calcium, tripartite synapses, microdomains, gliotransmission

## INTRODUCTION

Studies performed over the last two decades have revealed that astrocytes are intrinsic elements in brain circuits that through reciprocal signaling with neurons contribute to fundamental phenomena in brain function (Araque et al., 2014). Intracellular  $\text{Ca}^{2+}$  transients, which are evoked by different neurotransmitters, are fundamental for astrocyte signaling, releasing gliotransmitters (Bezzi and Volterra, 2001) that differently modulate synaptic transmission (Di Castro et al., 2011; Panatier et al., 2011), long-term synaptic plasticity (Henneberger et al., 2010;

Gómez-Gonzalo et al., 2015; Vignoli et al., 2016; Papouin et al., 2017; Robin et al., 2018), cognitive functions, and behavior (Santello et al., 2019; Kofuji and Araque, 2021; Nagai et al., 2021).

Initially centered on astrocytic soma or main processes (Cornell-Bell et al., 1990; Parpura et al., 1994), early investigations then focused on small processes, revealing that  $\text{Ca}^{2+}$  elevations can either remain restricted locally or eventually propagate to the main processes and soma (Pasti et al., 1997). Localized  $\text{Ca}^{2+}$  events were first described as microdomains in Bergmann glia processes (Grosche et al., 1999). Then, microdomains were observed in different *ex vivo* and *in vivo* brain preparations, becoming the focus of several recent studies and reviews (Volterra et al., 2014; Bazargani and Attwell, 2016; Semyanov et al., 2020). A strict and shared definition of microdomains is currently missing because of the lack of knowledge of these events. Like others, we use the term microdomains to describe  $\text{Ca}^{2+}$  events that are restricted to small portions of individual astrocyte territories that can be assigned to astrocytic thin processes with high-resolution imaging techniques.

While the molecular mechanisms and physiological roles of astrocyte  $\text{Ca}^{2+}$  microdomains remain poorly defined, the development of GECIs and advanced microscopy techniques revealed a high complexity of microdomain spatial and temporal profiles (Shigetomi et al., 2013a; Srinivasan et al., 2015; Agarwal et al., 2017; Bindocci et al., 2017). Although generally much slower than neuronal  $\text{Ca}^{2+}$  events,  $\text{Ca}^{2+}$  microdomains in astrocytes may exhibit fast kinetics on a timescale similar to neurons (Stobart et al., 2018). Notably, most studies on microdomains have to face technical limitations due to the nanoscopic size and the intrinsic remarkable dynamics of these structures (Semyanov et al., 2020). These limitations include: (i) the resolution of optical microscopy, which should be ideally paralleled by super-resolution microscopy; (ii) the type and concentration of the  $\text{Ca}^{2+}$  indicator used that buffers intracellular  $\text{Ca}^{2+}$  transients; (iii) the possible photostimulation or photodamage; (iv) the use of 2D scanning as opposed to ideal 3D acquisition; (v) the type of analysis that has to consider the highly dynamic spatial-temporal profile of these events. Despite these limitations, several recent studies revealed that the intracellular  $\text{Ca}^{2+}$  activity occurring in ultra-small processes (i.e., microdomains), where “the most important calcium transients occur,” is crucial for the dynamic cooperation with neurons (Bazargani and Attwell, 2016). In this review, we highlight the most recent advances in the different aspects that characterize astrocyte  $\text{Ca}^{2+}$  microdomains.

## THE LOCUS OF $\text{Ca}^{2+}$ MICRODOMAINS

Elucidating the fine anatomy of astrocytic processes is crucial for understanding how PAPs contact synapses and affect neuronal functions. Astrocyte complex morphology is mainly composed of nanoscopic irregular protrusions that are highly fluid and plastic (Bernardinelli et al., 2014; Rusakov, 2015) and account for the majority of astrocyte volume (75–85%) (Bushong et al., 2002; Bindocci et al., 2017). These structures are below the resolution of optical microscopy with smaller processes 30–50 nm in size

(Rusakov, 2015). A shared nomenclature for these structures is missing, with different terms being used, including terms such as leaflets (Gavrilov et al., 2018), nodes, and shafts (Arizono et al., 2020), or more generically gliapil, in analogy with neuropil (Bindocci et al., 2017). Serial electron microscopy (EM) with 3D reconstruction (Ventura and Harris, 1999; Calì et al., 2019) revealed the intracellular organization of astrocytic organelles, while EM imaging of astrocytes after fluorescence dye-loading through a patch pipette has revealed the fine details of PAPs (Bushong et al., 2002).

The nanoscopic size of these structures is an obstacle for functional imaging of  $\text{Ca}^{2+}$  activity and innovative imaging approaches are needed (Heller and Rusakov, 2017). A recent study using 3D-super resolution microscopy combined with  $\text{Ca}^{2+}$  imaging revealed that astrocyte processes form a spongiform domain composed of a meshwork of fine structures with nodes and shafts that may form loops of reconnecting processes (Arizono et al., 2020). In line with a previous study (Shigetomi et al., 2013a), Arizono et al. (2020) found that nodes and shafts are equally present in the entire astrocyte territory irrespective of the distance from the soma. Astrocyte morphology is thus like a sponge with the meshwork of ultrathin small processes that cover the surrounding territory (Rusakov, 2015; Arizono et al., 2020), in contrast with the classic view of star shaped cells. Analysis of the spatial relationship with excitatory synapses revealed that most PAPs are nodes, i.e., compartmentalized structures ( $0.07\text{--}0.7\ \mu\text{m}^2$ ), where the majority of localized  $\text{Ca}^{2+}$  transients occur and may or may not propagate to nearby shafts. A strict correlation was reported between node and spine size, and also between  $\text{Ca}^{2+}$  transients and spine size (Arizono et al., 2020), suggesting that PAPs are morphologically and functionally correlated with their synaptic partners. Accordingly, nodes would be the “primary site” of  $\text{Ca}^{2+}$  signaling in excitatory tripartite synapses and may represent specialized compartments endowed with all the machinery needed for governing astrocyte-neuron dynamic interactions. Of note, a significant portion of spines is in contact with shafts (35% compared to 55% contacting nodes), which could differ in terms of  $\text{Ca}^{2+}$  sources and handling from nodes.

## THE GENESIS OF $\text{Ca}^{2+}$ MICRODOMAINS

Calcium transients at astrocyte soma and main processes have been studied by conventional bulk-loading with  $\text{Ca}^{2+}$ -sensitive membrane-permeable chemical dyes. This approach is, however, inadequate for revealing  $\text{Ca}^{2+}$  changes at fine PAPs. The only available, though invasive, tool to study  $\text{Ca}^{2+}$  signaling at PAPs was the microinjection of chemical dyes into individual astrocytes through glass pipettes (Rungta et al., 2016). However, GECIs recently emerged as a powerful tool to study  $\text{Ca}^{2+}$  dynamics also in astrocytic microdomains (Shigetomi et al., 2013a; Kanemaru et al., 2014). The release of  $\text{Ca}^{2+}$  from the endoplasmic reticulum (ER) into the cytosol can be initiated by stimulation of metabotropic  $G_q$  G-protein-coupled receptors (GPCRs) through activation of PLC, production of  $\text{IP}_3$ , and activation of  $\text{IP}_3$  receptors ( $\text{IP}_3\text{Rs}$ ) on ER membranes (Perea et al., 2009). Notably,

G<sub>i</sub> coupled GPCRs, such as GABA<sub>B</sub> receptors, can induce Ca<sup>2+</sup> transients in astrocytes through an intracellular pathway that seems to converge also on IP<sub>3</sub>Rs signaling (Mariotti et al., 2016, 2018; Durkee et al., 2019; Caudal et al., 2020).

Historically, PAPs have been considered structures without organelles. However, through the use of serial block-face scanning EM, one or more subcellular organelles, including ER and mitochondria, were detected in about 40% of cortical PAPs (Aboufars El Alaoui et al., 2021). Consistent with the presence of ER in PAPs, deletion of the IP<sub>3</sub>R type 2 (IP<sub>3</sub>R2), which is known to be enriched in astrocytes, partially reduces the number or amplitude (~60–70% of reduction) of spontaneous Ca<sup>2+</sup> microdomains (Kanemaru et al., 2014; Srinivasan et al., 2015; Stobart et al., 2016; Agarwal et al., 2017, but see Rungta et al., 2016). In these mice, the level of impairment of Ca<sup>2+</sup> microdomain responses to different GPCR agonists or electrical stimuli is, instead, variable among different studies (Kanemaru et al., 2014; Srinivasan et al., 2015; Stobart et al., 2016; Agarwal et al., 2017). However, the IP<sub>3</sub>R2 seems not to be the only astrocytic receptor mediating Ca<sup>2+</sup> release from the ER. Okubo et al. recently used the ER luminal Ca<sup>2+</sup> indicator G-CEPIA1er to visualize spontaneous and evoked ER Ca<sup>2+</sup> release in astrocytes. While in fine processes of wild-type (WT) mice they observed spontaneous Ca<sup>2+</sup> elevations with cytosolic GCaMP6f and spontaneous ER Ca<sup>2+</sup> release with G-CEPIA1er, in IP<sub>3</sub>R2<sup>-/-</sup> mice they could detect spontaneous cytosolic Ca<sup>2+</sup> elevations without decreases in ER Ca<sup>2+</sup> levels. In contrast, in fine processes of IP<sub>3</sub>R2<sup>-/-</sup> mice, Gq receptor activation evoked a significant Ca<sup>2+</sup> release from ER, although attenuated with respect to WT. Interestingly, this IP<sub>3</sub>R2-independent Ca<sup>2+</sup> release induced low cytosolic Ca<sup>2+</sup> elevations but robust Ca<sup>2+</sup> transients in mitochondria (Okubo et al., 2019). Accordingly, in IP<sub>3</sub>R2<sup>-/-</sup> mice, IP<sub>3</sub>R1/3 and/or ryanodine receptors (Parpura et al., 2011; Sherwood et al., 2017) possibly account for residual IP<sub>3</sub>R2-independent Ca<sup>2+</sup> release. Because evidence of ER cisternae is present in only ~45% of PAPs, other ER-independent mechanisms must occur to allow Ca<sup>2+</sup> dynamics in ER-free PAPs (Aboufars El Alaoui et al., 2021). For instance, Bergles's laboratory has recently described that mitochondria are important players in astrocytic Ca<sup>2+</sup> microdomains, in WT and IP<sub>3</sub>R2<sup>-/-</sup> mice. The authors demonstrated that Ca<sup>2+</sup> microdomains can arise through Ca<sup>2+</sup> efflux from mitochondria after transient openings of the mitochondrial permeability transition pore (mPTP). The opening of mPTP is facilitated by the production of reactive oxygen species owing to a rise in the metabolic demand after increased neuronal activity, suggesting a direct link between metabolic rate and Ca<sup>2+</sup> microdomains (Agarwal et al., 2017). Although Ca<sup>2+</sup> microdomains rely in part on Ca<sup>2+</sup> release from intracellular stores, they may depend also on transmembrane Ca<sup>2+</sup> influxes (Rungta et al., 2016). The substantial contribution of Ca<sup>2+</sup> influxes from the extracellular space to spontaneous Ca<sup>2+</sup> transients in PAPs has been established with Ca<sup>2+</sup>-free buffers (Srinivasan et al., 2015; Rungta et al., 2016; Gómez-Gonzalo et al., 2018).

Plasma membrane channels and transporters have been proposed to contribute to Ca<sup>2+</sup> microdomain activity. Among

these, the involvement of the TRPA1 channel has been described (Shigetomi et al., 2012, 2013b), though a clear role of this channel has not been conclusively established (Rungta et al., 2016). A promising candidate to directly link neuronal activity with Ca<sup>2+</sup> microdomains is the Na<sup>+</sup>/Ca<sup>2+</sup> exchanger (NCX). Na<sup>+</sup>-dependent neurotransmitter transporters localized in PAPs, such as the GABA transporter GAT3 (Minelli et al., 1996) or the glutamate transporter GLT-1 (Danbolt et al., 1992; Sakers et al., 2017), can generate Na<sup>+</sup> microdomains (Felix et al., 2020) which in turn can trigger Ca<sup>2+</sup> elevations in PAPs through the reverse function of the NCX, as recently described in the hippocampus after exogenous GABA applications (Boddum et al., 2016). However, the role of this mechanism in Ca<sup>2+</sup> microdomains, both spontaneous and evoked, has been poorly investigated (Matos et al., 2018).

Although Ca<sup>2+</sup> microdomains can have a pure intracellular or extracellular Ca<sup>2+</sup> source, a cooperativity that finely shapes Ca<sup>2+</sup> transients may occur among different sources. The release of Ca<sup>2+</sup> from the ER typically triggers activation of store-operated Ca<sup>2+</sup> entry (SOCE). During SOCE, depletion of ER Ca<sup>2+</sup> stores activates the Ca<sup>2+</sup> sensor stromal interaction molecules (STIMs) to translocate to the junctional ER-plasmatic membranes, where STIMs interact with and activate the store-operated Ca<sup>2+</sup>-release-activated Ca<sup>2+</sup> channels (CRAC channels) formed by Orai proteins. Recently, Toth et al. (2019) observed that the frequency and amplitude of Ca<sup>2+</sup> transients evoked by thrombin in PAPs from Orai1<sup>-/-</sup> mice were substantially attenuated, suggesting that Ca<sup>2+</sup> microdomains rely on coordinated Ca<sup>2+</sup> release from intracellular stores and transmembrane Ca<sup>2+</sup> influxes from the extracellular space.

Even though knowledge is rapidly increasing (**Figure 1**), a complete picture of the Ca<sup>2+</sup> microdomain essential features is lacking. Key questions remain unsolved. For example, which proteins are involved in Ca<sup>2+</sup> influxes shaping microdomains? Astrocytes are mechanosensitive cells and the high motility of astrocyte processes (Bernardinelli et al., 2014) may expose them to physical forces that, in turn, may activate Ca<sup>2+</sup>-permeable mechanosensitive channels. Some plausible candidates that mediate mechanically induced Ca<sup>2+</sup> microdomains have been described in astrocyte cultures and include TRPC1 (Reyes et al., 2013), TRPV4 (Turovsky et al., 2020), and Piezo1 (Velasco-Estevez et al., 2020) channels. Furthermore, are Ca<sup>2+</sup> influxes modulated by activation of GPCRs? In addition to the IP<sub>3</sub>R-dependent signaling, GPCRs trigger different second messenger pathways, such as DAG-PKC and cAMP-PKA, that may regulate proteins mediating Ca<sup>2+</sup> events.

The intracellular signaling mechanism that links activation of GPCRs to an increase in Ca<sup>2+</sup> microdomains in IP<sub>3</sub>R2<sup>-/-</sup> mice is also undefined. A partially unaltered neuronal function and the lack of somatic Ca<sup>2+</sup> elevations in IP<sub>3</sub>R2<sup>-/-</sup> mice have been used to cast doubts about the role of astrocytic Ca<sup>2+</sup> signaling in brain function (Fiacco and McCarthy, 2018). The observation of a richer Ca<sup>2+</sup> activity at microdomains than at soma and the relative preservation of evoked Ca<sup>2+</sup> microdomains in IP<sub>3</sub>R2<sup>-/-</sup> mice have turned attention to the relevance of astrocytic Ca<sup>2+</sup> signaling in the modulation of neuronal function (Bazargani and Attwell, 2016; Savtchouk and Volterra, 2018). However, further



evidence on the mechanisms of evoked  $\text{Ca}^{2+}$  microdomains in  $\text{IP}_3\text{R}^{-/-}$  mice is necessary to unambiguously support a role for  $\text{IP}_3$ -independent astrocytic  $\text{Ca}^{2+}$  signaling in neuronal function. The development of new tools to impair astrocytic  $\text{Ca}^{2+}$  signaling in an  $\text{IP}_3\text{R}$ -independent manner (Yu et al., 2018) will help to better understand the molecular mechanism of  $\text{Ca}^{2+}$  microdomain generation.

## THE ANALYSIS OF $\text{Ca}^{2+}$ SIGNALS IN ASTROCYTIC MICRODOMAINS

Many experimental and analytical approaches have been developed to properly dissect the features of  $\text{Ca}^{2+}$  signals at the level of astrocytic microdomains. The measurement of  $\text{Ca}^{2+}$  fluctuations in astrocytic soma is relatively simple, owing to the easy identification of the somatic area. Analysis of  $\text{Ca}^{2+}$  signals in astrocytic microdomains, instead, is complex because their morphological features cannot be accurately defined under routinely used confocal or 2-photon microscopy techniques. For this reason, their identification has been handled based on the detection of  $\text{Ca}^{2+}$  changes rather than on morphological criteria. We can, indeed, gather information on microdomain  $\text{Ca}^{2+}$  signaling by imaging the fluorescent  $\text{Ca}^{2+}$  signal without, however, obtaining indications of fine process morphological details. The fluorophores of choice for this purpose have been the cytosolic or sub-membrane GECIs of the GCaMP family which revealed unexpectedly a high number of localized  $\text{Ca}^{2+}$  events throughout astrocyte distal territories (Shigetomi et al., 2013b) albeit without an estimate of the actual  $\text{Ca}^{2+}$  concentration. The increased complexity of  $\text{Ca}^{2+}$  signals revealed by GECIs, however, demanded a corresponding breakthrough in the analytical approach to properly evaluate the  $\text{Ca}^{2+}$  events. In this context, Khakh's laboratory performed pioneering work in the decoding of astrocytic  $\text{Ca}^{2+}$  activity at the level of microdomains. Published in 2015, GECIquant represents the first software written to specifically analyze  $\text{Ca}^{2+}$  transients in GCaMP expressing astrocytes. Using a threshold-based criterion for signal amplitude, GECIquant obtains a semi-automated detection of the regions of interest (ROIs) containing  $\text{Ca}^{2+}$  fluctuations (Srinivasan et al., 2015). The software works at single cell level allowing us to distinguish between somatic  $\text{Ca}^{2+}$  fluctuations, waves involving principal processes, and sparkly signals at microdomains, providing as principal output, the raw fluorescence data along time from each region. Traces obtained through GECIquant can be further processed to obtain additional features, such as the amplitude and frequency of the  $\text{Ca}^{2+}$  events for each ROI, as performed in Mariotti et al. (2018), where a MATLAB script was used to identify significant peaks, based on additional amplitude thresholds along global and local baselines (Mariotti et al., 2018).

In 2017, CaSCaDe software was developed, overcoming the need for two scripts (Agarwal et al., 2017). CaSCaDe, like GECIquant, performs a semi-automated analysis, in this case using a machine-learning-based algorithm to identify  $\text{Ca}^{2+}$  microdomains. Time-series images are processed to remove background noise and binarized using an amplitude threshold.

Microdomains are selected based on additional criteria of amplitude and duration. Besides producing a spatial map of active regions, the software provides information about the number, frequency, amplitude, and time course of events.

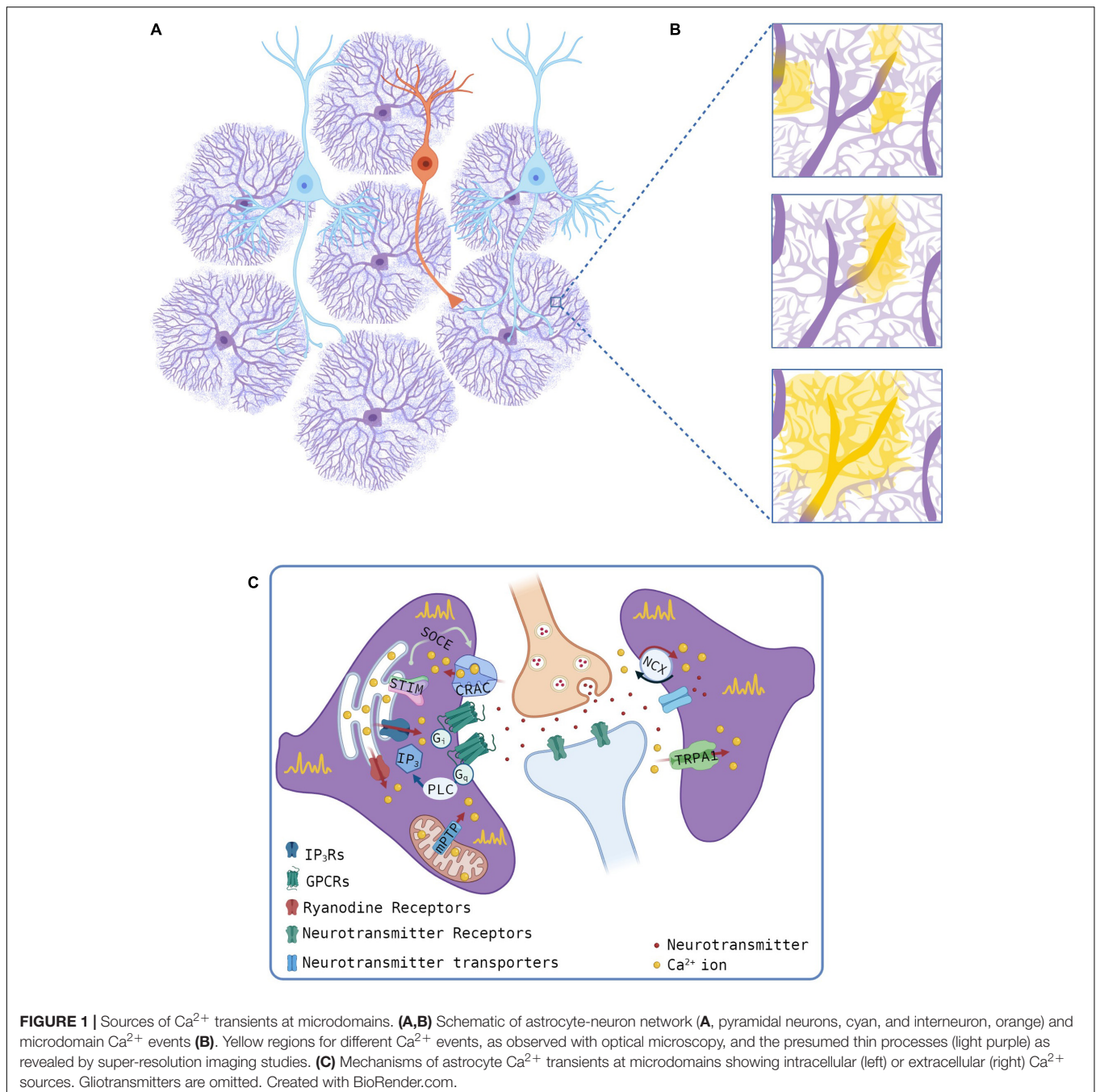
Weber's laboratory worked to develop a processing suite aimed at simplifying the analysis workflows. This is the main purpose of CHIPS, a MATLAB based open-source toolbox that gathers different algorithms and provides the user with options for a number of analysis types. CHIPS offers helpful pre-processing functions, such as motion correction and denoising. Different algorithms can then be applied to analyze data and plot the resulting outputs (Barrett et al., 2018).

All the analytical procedures described so far rely on the concept of ROIs applied to microdomains, defined by spatial coordinates and measurable along different time series. However, constraining microdomains in defined boundaries may result in signal detection inaccuracy. Regions involved in  $\text{Ca}^{2+}$  variations may become larger than the defined ROI, leading the signal to invade other territories, finally resulting in signal fragmentation among adjacent ROIs. Conversely, larger ROIs may fail to faithfully capture the signal amplitude if  $\text{Ca}^{2+}$  increases only in a portion of the ROI.

The turning point in this concern was represented by AQuA software (Wang et al., 2019), which reverses the logic at the basis of ROI detection by adopting an event-based analytical approach, as already suggested in Wu et al. (2014). Calcium events are thus captured in their dynamic changes along space and time, revealing signals that can propagate and modify their size or shape, expressing different tracts of the same, composite fingerprint.

AQuA software does not include pre-processing functions but offers suggestions about pre-processing steps to be considered. A valuable feature is the possibility to choose between different data type pre-sets, depending on the  $\text{Ca}^{2+}$  indicator used and on the acquisition signal to noise ratio, with optimized but user-adjustable parameters. AQuA can work also on a single cell level and isolate events in astrocytic processes, but without distinction between principal branches and thin processes. The identification of events is achieved through different image processing steps, including thresholding and smoothing, and the application of a number of algorithms that aim to define the temporal limits and spatial propagation features of individual events. The user proceeds step-by-step and can inspect traces and spatial boundaries of the events along time, as training which is recommended to achieve the best parameters to apply to the specific experimental datasets. AQuA outputs a broad and rich collection of features for detected events, such as area, amplitude, duration, frequency, and propagation features, revealing itself as a valuable tool for astrocytic  $\text{Ca}^{2+}$  analysis.

While the approaches described so far refer to 2D imaging, it is worth mentioning that a study from Volterra's group focused on the analysis of astrocytic  $\text{Ca}^{2+}$  activity recorded through 3D imaging. This approach captures the entire extension of individual astrocytes, adding a significant step of complexity to the comprehension of  $\text{Ca}^{2+}$  signal dynamics (Bindocci et al., 2017).



All in all, the development of different analytical approaches confirms the important role acquired by astrocytes in the studies of brain function. In the near future, analytical and experimental advances will enable us to unveil new types of modulation exerted by astrocytes.

## DISCUSSION

Over the last decade, the combined use of innovative tools has provided compelling evidence that astrocyte dynamic

interactions with neurons have fundamental roles in brain function. The different players involved in this interplay are beginning to be elucidated, particularly regarding  $\text{Ca}^{2+}$  activities at microdomains. In this restricted and elusive subcellular region, an unexpected complexity has emerged. Here, the stage of  $\text{Ca}^{2+}$  activity has been populated by new actors but many questions remain unanswered. For example, how these players interact? How  $\text{Ca}^{2+}$  events propagate from fine to major processes? What is the role of spontaneous microdomain  $\text{Ca}^{2+}$  activity in brain functions? The use of different types of preparations,  $\text{Ca}^{2+}$  detection techniques, and analytical tools in different

brain regions has provided invaluable results that, however, cannot always be easily compared. New shared techniques and analytical tools are thus needed. Elucidating all the mechanisms of neuron-astrocyte interplay at tripartite synapses is crucial to understanding brain functions and dysfunctions (Pekny et al., 2016), and will possibly unveil new therapeutic targets. We believe that a new decade of great discoveries has just begun.

## AUTHOR CONTRIBUTIONS

AL wrote the introduction with GL and the chapter on the Analysis of  $\text{Ca}^{2+}$  events with MZ. VH created the figure. AC wrote the chapter on the locus of  $\text{Ca}^{2+}$  with GL. MZ wrote chapter on the Analysis of  $\text{Ca}^{2+}$  events with AL. GC contributed to the manuscript. MG-G wrote the chapter on the genesis of  $\text{Ca}^{2+}$  events. GL wrote the abstract,

introduction, the chapter on the site of  $\text{Ca}^{2+}$  events with AC, and the discussion with the help of all other authors. All authors contributed to the article and approved the submitted version.

## FUNDING

The work was supported by the Marie Skłodowska-Curie ITN, EU-Glia Ph.D. to GC and VH, Cariparo Foundation Excellence 2018 to GC, PRIN 2018 to GC.

## ACKNOWLEDGMENTS

We thank Gian Michele Ratto for helpful discussion on analytical approaches to  $\text{Ca}^{2+}$  transients in astrocyte microdomains.

## REFERENCES

- Aboufars El Alaoui, A., Jackson, M., Fabri, M., de Vivo, L., and Bellesi, M. (2021). Characterization of subcellular organelles in cortical perisynaptic astrocytes. *Front. Cell. Neurosci.* 14:573944. doi: 10.3389/fncel.2020.573944
- Agarwal, A., Wu, P. H., Hughes, E. G., Fukaya, M., Tischfield, M. A., Langseth, A. J., et al. (2017). Transient opening of the mitochondrial permeability transition pore induces microdomain calcium transients in astrocyte processes. *Neuron* 93, 587.e–605.e. doi: 10.1016/j.neuron.2016.12.034
- Araque, A., Carmignoto, G., Haydon, P. G., Oliet, S. H. R., Robitaille, R., and Volterra, A. (2014). Gliotransmitters travel in time and space. *Neuron* 81, 728–739. doi: 10.1016/j.neuron.2014.02.007
- Arizono, M., Inavalli, V. V. G. K., Panatier, A., Pfeiffer, T., Angibaud, J., Levet, F., et al. (2020). Structural basis of astrocytic  $\text{Ca}^{2+}$  signals at tripartite synapses. *Nat. Commun.* 11:1906. doi: 10.1038/s41467-020-15648-4
- Barrett, M. J. P., Ferrari, K. D., Stobart, J. L., Holub, M., and Weber, B. (2018). CHIPS: an extensible toolbox for cellular and hemodynamic two-photon image analysis. *Neuroinformatics* 16, 145–147. doi: 10.1007/s12021-017-9344-y
- Bazargani, N., and Attwell, D. (2016). Astrocyte calcium signaling: the third wave. *Nat. Neurosci.* 19, 182–189. doi: 10.1038/nn.4201
- Bernardinelli, Y., Muller, D., and Nikonenko, I. (2014). Astrocyte-synapse structural plasticity. *Neural Plast.* 2014:232105. doi: 10.1155/2014/232105
- Bezzi, P., and Volterra, A. (2001). A neuron–glia signalling network in the active brain. *Curr. Opin. Neurobiol.* 11, 387–394. doi: 10.1016/S0959-4388(00)00223-3
- Bindocci, E., Savtchouk, I., Liaudet, N., Becker, D., Carriero, G., and Volterra, A. (2017). Three-dimensional  $\text{Ca}^{2+}$  imaging advances understanding of astrocyte biology. *Science* 356:eaai8185. doi: 10.1126/science.aai8185
- Boddum, K., Jensen, T. P., Magloire, V., Kristiansen, U., Rusakov, D. A., Pavlov, I., et al. (2016). Astrocytic GABA transporter activity modulates excitatory neurotransmission. *Nat. Commun.* 7:13572. doi: 10.1038/ncomms13572
- Bushong, E. A., Martone, M. E., Jones, Y. Z., and Ellisman, M. H. (2002). Protoplasmic astrocytes in CA1 stratum radiatum occupy separate anatomical domains. *J. Neurosci.* 22, 183–192. doi: 10.1523/jneurosci.22-01-00183.2002
- Cali, C., Agus, M., Kare, K., Boges, D. J., Lehtälä, H., Hadwiger, M., et al. (2019). 3D cellular reconstruction of cortical glia and parenchymal morphometric analysis from serial block-face electron microscopy of juvenile rat. *Prog. Neurobiol.* 183:101696. doi: 10.1016/j.pneurobio.2019.101696
- Caudal, L. C., Gobbo, D., Scheller, A., and Kirchhoff, F. (2020). The paradox of astroglial  $\text{Ca}^{2+}$  signals at the interface of excitation and inhibition. *Front. Cell. Neurosci.* 14:609947. doi: 10.3389/fncel.2020.609947
- Cornell-Bell, A. H., Finkbeiner, S. M., Cooper, M. S., and Smith, S. J. (1990). Glutamate induces calcium waves in cultured astrocytes: long-range glial signaling. *Science* 247, 470–473. doi: 10.1126/science.1967852
- Danbolt, N. C., Storm-Mathisen, J., and Kanner, B. I. (1992). An  $[\text{Na}^{+} + \text{K}^{+}]$ -coupled glutamate transporter purified from rat brain is located in glial cell processes. *Neuroscience* 51, 295–310. doi: 10.1016/0306-4522(92)90316-T
- Di Castro, M. A., Chuquet, J., Liaudet, N., Bhaukaurally, K., Santello, M., Bouvier, D., et al. (2011). Local  $\text{Ca}^{2+}$  detection and modulation of synaptic release by astrocytes. *Nat. Neurosci.* 14, 1276–1284. doi: 10.1038/nn.2929
- Durkee, C. A., Covelo, A., Lines, J., Kofuji, P., Aguilar, J., and Araque, A. (2019). G i/o protein-coupled receptors inhibit neurons but activate astrocytes and stimulate gliotransmission. *Glia* 67, 1076–1093. doi: 10.1002/glia.23589
- Felix, L., Delekate, A., Petzold, G. C., and Rose, C. R. (2020). Sodium fluctuations in astroglia and their potential impact on astrocyte function. *Front. Physiol.* 11:871. doi: 10.3389/fphys.2020.00871
- Fiacco, T. A., and McCarthy, K. D. (2018). Multiple lines of evidence indicate that gliotransmission does not occur under physiological conditions. *J. Neurosci.* 38, 3–13. doi: 10.1523/JNEUROSCI.0016-17.2017
- Gavrilov, N., Golyagina, I., Brazhe, A., Scimemi, A., Turlapov, V., and Semyanov, A. (2018). Astrocytic coverage of dendritic spines, dendritic shafts, and axonal boutons in hippocampal neuropil. *Front. Cell. Neurosci.* 12:248. doi: 10.3389/fncel.2018.00248
- Gómez-Gonzalo, M., Navarrete, M., Perea, G., Covelo, A., Martín-Fernández, M., Shigemoto, R., et al. (2015). Endocannabinoids induce lateral long-term potentiation of transmitter release by stimulation of gliotransmission. *Cereb. Cortex* 25, 3699–3712. doi: 10.1093/cercor/bhu231
- Gómez-Gonzalo, M., Zehnder, T., Reque, L. M., Bezzi, P., and Carmignoto, G. (2018). Insights into the release mechanism of astrocytic glutamate evoking in neurons NMDA receptor-mediated slow depolarizing inward currents. *Glia* 66, 2188–2199. doi: 10.1002/glia.23473
- Grosche, J., Matyash, V., Möller, T., Verkhratsky, A., Reichenbach, A., and Kettenmann, H. (1999). Microdomains for neuron–glia interaction: parallel fiber signaling to Bergmann glial cells. *Nat. Neurosci.* 2, 139–143. doi: 10.1038/5692
- Heller, J. P., and Rusakov, D. A. (2017). The nanoworld of the tripartite synapse: insights from super-resolution microscopy. *Front. Cell. Neurosci.* 11:374. doi: 10.3389/fncel.2017.00374
- Henneberger, C., Papouin, T., Oliet, S. H. R., and Rusakov, D. A. (2010). Long-term potentiation depends on release of d-serine from astrocytes. *Nature* 463, 232–236. doi: 10.1038/nature08673
- Kanamaru, K., Sekiya, H., Xu, M., Satoh, K., Kitajima, N., Yoshida, K., et al. (2014). In Vivo visualization of subtle, transient, and local activity of astrocytes using an ultrasensitive  $\text{Ca}^{2+}$  indicator. *Cell Rep.* 8, 311–318. doi: 10.1016/j.celrep.2014.05.056
- Kofuji, P., and Araque, A. (2021). Astrocytes and behavior. *Annu. Rev. Neurosci.* 44, 49–67. doi: 10.1146/annurev-neuro-101920-112225



- Mariotti, L., Losi, G., Lia, A., Melone, M., Chiavegato, A., Gómez-Gonzalo, M., et al. (2018). Interneuron-specific signaling evokes distinctive somatostatin-mediated responses in adult cortical astrocytes. *Nat. Commun.* 9:82. doi: 10.1038/s41467-017-02642-6
- Mariotti, L., Losi, G., Sessolo, M., Marcon, I., and Carmignoto, G. (2016). The inhibitory neurotransmitter GABA evokes long-lasting Ca<sup>2+</sup> oscillations in cortical astrocytes. *Glia* 64, 363–373. doi: 10.1002/glia.22933
- Matos, M., Bosson, A., Riebe, I., Reynell, C., Vallée, J., Laplante, I., et al. (2018). Astrocytes detect and upregulate transmission at inhibitory synapses of somatostatin interneurons onto pyramidal cells. *Nat. Commun.* 9:4254. doi: 10.1038/s41467-018-06731-y
- Minelli, A., DeBiasi, S., Brecha, N. C., Zuccarello, L. V., and Conti, F. (1996). GAT-3, a high-affinity GABA plasma membrane transporter, is localized to astrocytic processes, and it is not confined to the vicinity of GABAergic synapses in the cerebral cortex. *J. Neurosci.* 16, 6255–6264. doi: 10.1523/jneurosci.16-19-06255.1996
- Nagai, J., Yu, X., Papouin, T., Cheong, E., Freeman, M. R., Monk, K. R., et al. (2021). Behaviorally consequential astrocytic regulation of neural circuits. *Neuron* 109, 576–596. doi: 10.1016/j.neuron.2020.12.008
- Okubo, Y., Kanemaru, K., Suzuki, J., Kobayashi, K., Hirose, K., and Iino, M. (2019). Inositol 1,4,5-trisphosphate receptor type 2-independent Ca<sup>2+</sup> release from the endoplasmic reticulum in astrocytes. *Glia* 67, 113–124. doi: 10.1002/glia.23531
- Panati, A., Vallée, J., Haber, M., Murai, K. K., Lacaille, J. C., and Robitaille, R. (2011). Astrocytes are endogenous regulators of basal transmission at central synapses. *Cell* 146, 785–798. doi: 10.1016/j.cell.2011.07.022
- Papouin, T., Dunphy, J., Tolman, M., Foley, J. C., and Haydon, P. G. (2017). Astrocytic control of synaptic function. *Philos. Trans. R. Soc. B Biol. Sci.* 372:20160154. doi: 10.1098/rstb.2016.0154
- Parpura, V., Basarsky, T. A., Liu, F., Jętrinić, S., and Haydon, P. G. (1994). Glutamate-mediated astrocyte–neuron signalling. *Nature* 369, 744–747. doi: 10.1038/369744a0
- Parpura, V., Grubišić, V., and Verkhratsky, A. (2011). Ca<sup>2+</sup> sources for the exocytotic release of glutamate from astrocytes. *Biochim. Biophys. Acta Mol. Cell Res.* 1813, 984–991. doi: 10.1016/j.bbamcr.2010.11.006
- Pasti, L., Volterra, A., Pozzan, T., and Carmignoto, G. (1997). Intracellular calcium oscillations in astrocytes: a highly plastic, bidirectional form of communication between neurons and astrocytes in situ. *J. Neurosci.* 17, 7817–7830. doi: 10.1523/jneurosci.17-20-07817.1997
- Pekny, M., Pekna, M., Messing, A., Steinhäuser, C., Lee, J.-M., Parpura, V., et al. (2016). Astrocytes: a central element in neurological diseases. *Acta Neuropathol.* 131, 323–345. doi: 10.1007/s00401-015-1513-1
- Perea, G., Navarrete, M., and Araque, A. (2009). Tripartite synapses: astrocytes process and control synaptic information. *Trends Neurosci.* 32, 421–431.
- Reyes, R. C., Verkhratsky, A., and Parpura, V. (2013). TRPC1-mediated Ca<sup>2+</sup> and Na<sup>+</sup> signalling in astroglia: differential filtering of extracellular cations. *Cell Calcium* 54, 120–125. doi: 10.1016/j.ceca.2013.05.005
- Robin, L. M., Oliveira da Cruz, J. F., Langlais, V. C., Martin-Fernandez, M., Metna-Laurent, M., Busquets-Garcia, A., et al. (2018). Astroglial CB1 receptors determine synaptic D-serine availability to enable recognition memory. *Neuron* 98, 935.e–944.e. doi: 10.1016/j.neuron.2018.04.034
- Rungta, R. L., Bernier, L. P., Dissing-Olesen, L., Groten, C. J., LeDue, J. M., Ko, R., et al. (2016). Ca<sup>2+</sup> transients in astrocyte fine processes occur via Ca<sup>2+</sup> influx in the adult mouse hippocampus. *Glia* 64, 2093–2103. doi: 10.1002/glia.23042
- Rusakov, D. A. (2015). Disentangling calcium-driven astrocyte physiology. *Nat. Rev. Neurosci.* 16, 226–233. doi: 10.1038/nrn3878
- Sakers, K., Lake, A. M., Khazanchi, R., Ouwenga, R., Vasek, M. J., Dani, A., et al. (2017). Astrocytes locally translate transcripts in their peripheral processes. *Proc. Natl. Acad. Sci. U.S.A.* 114, E3830–E3838. doi: 10.1073/pnas.1617782114
- Santello, M., Toni, N., and Volterra, A. (2019). Astrocyte function from information processing to cognition and cognitive impairment. *Nat. Neurosci.* 22, 154–166. doi: 10.1038/s41593-018-0325-8
- Savtchouk, I., and Volterra, A. (2018). Gliotransmission: beyond black-and-white. *J. Neurosci.* 38, 14–25. doi: 10.1523/JNEUROSCI.0017-17.2017
- Semyanov, A., Henneberger, C., and Agarwal, A. (2020). Making sense of astrocytic calcium signals from acquisition to interpretation. *Nat. Rev. Neurosci.* 21, 551–564. doi: 10.1038/s41583-020-0361-8
- Sherwood, M. W., Arizono, M., Hisatsune, C., Bannai, H., Ebisui, E., Sherwood, J. L., et al. (2017). Astrocytic IP3Rs: contribution to Ca<sup>2+</sup> signalling and hippocampal LTP. *Glia* 65, 502–513. doi: 10.1002/glia.23107
- Shigetomi, E., Bushong, E. A., Hausteiner, M. D., Tong, X., Jackson-Weaver, O., Kracun, S., et al. (2013a). Imaging calcium microdomains within entire astrocyte territories and endfeet with GCaMPs expressed using adeno-associated viruses. *J. Gen. Physiol.* 141, 633–647. doi: 10.1085/jgp.201210949
- Shigetomi, E., Jackson-Weaver, O., Huckstepp, R. T., O'Dell, T. J., and Khakh, B. S. (2013b). TRPA1 channels are regulators of astrocyte basal calcium levels and long-term potentiation via constitutive d-serine release. *J. Neurosci.* 33, 10143–10153. doi: 10.1523/JNEUROSCI.5779-12.2013
- Shigetomi, E., Tong, X., Kwan, K. Y., Corey, D. P., and Khakh, B. S. (2012). TRPA1 channels regulate astrocyte resting calcium and inhibitory synapse efficacy through GAT-3. *Nat. Neurosci.* 15, 70–80. doi: 10.1038/nn.3000
- Srinivasan, R., Huang, B. S., Venugopal, S., Johnston, A. D., Chai, H., Zeng, H., et al. (2015). Ca<sup>2+</sup> signaling in astrocytes from *Ip3r2* <sup>-/-</sup> mice in brain slices and during startle responses in vivo. *Nat. Neurosci.* 18, 708–717. doi: 10.1038/nn.4001
- Stobart, J. L., Ferrari, K. D., Barrett, M. J. P., Glück, C., Stobart, M. J., Zuend, M., et al. (2018). Cortical circuit activity evokes rapid astrocyte calcium signals on a similar timescale to neurons. *Neuron* 98, 726.e–735.e. doi: 10.1016/j.neuron.2018.03.050
- Stobart, J. L., Ferrari, K. D., Barrett, M. J. P., Stobart, M. J., Looser, Z. J., Saab, A. S., et al. (2016). Long-term in vivo calcium imaging of astrocytes reveals distinct cellular compartment responses to sensory stimulation. *Cereb. Cortex* 28, 184–198. doi: 10.1093/cercor/bhw366
- Toth, A. B., Hori, K., Novakovic, M. M., Bernstein, N. G., Lambot, L., and Prakriya, M. (2019). CRAC channels regulate astrocyte Ca<sup>2+</sup> signaling and gliotransmitter release to modulate hippocampal GABAergic transmission. *Sci. Signal.* 12:eaw5450. doi: 10.1126/scisignal.aaw5450
- Turovsky, E. A., Braga, A., Yu, Y., Esteras, N., Korsak, A., Theparambil, S. M., et al. (2020). Mechanosensory signaling in astrocytes. *J. Neurosci.* 40, 9364–9371. doi: 10.1523/JNEUROSCI.1249-20.2020
- Velasco-Estevez, M., Rolle, S. O., Mampay, M., Dev, K. K., and Sheridan, G. K. (2020). Piezo1 regulates calcium oscillations and cytokine release from astrocytes. *Glia* 68, 145–160. doi: 10.1002/glia.23709
- Ventura, R., and Harris, K. M. (1999). Three-dimensional relationships between hippocampal synapses and astrocytes. *J. Neurosci.* 19, 6897–6906. doi: 10.1523/jneurosci.19-16-06897.1999
- Vignoli, B., Battistini, G., Melani, R., Blum, R., Santi, S., Berardi, N., et al. (2016). Peri-synaptic glia recycles brain-derived neurotrophic factor for LTP stabilization and memory retention. *Neuron* 92, 873–887. doi: 10.1016/j.neuron.2016.09.031
- Volterra, A., Liaudet, N., and Savtchouk, I. (2014). Astrocyte Ca<sup>2+</sup> signalling: an unexpected complexity. *Nat. Rev. Neurosci.* 15, 327–335. doi: 10.1038/nrn3725
- Wang, Y., DelRosso, N. V., Vaidyanathan, T. V., Cahill, M. K., Reitman, M. E., Pittolo, S., et al. (2019). Accurate quantification of astrocyte and neurotransmitter fluorescence dynamics for single-cell and population-level physiology. *Nat. Neurosci.* 22, 1936–1944. doi: 10.1038/s41593-019-0492-2
- Wu, Y., Tang, X., Arizono, M., Bannai, H., Shih, P., Dembitskaya, Y., et al. (2014). Cell calcium spatiotemporal calcium dynamics in single astrocytes and its modulation by neuronal activity. *Cell Calcium* 55, 119–129. doi: 10.1016/j.ceca.2013.12.006
- Yu, X., Taylor, A. M. W., Nagai, J., Golshani, P., Evans, C. J., Coppola, G., et al. (2018). Reducing astrocyte calcium signaling in vivo alters striatal microcircuits and causes repetitive behavior. *Neuron* 99, 1170.e–1187.e. doi: 10.1016/j.neuron.2018.08.015

**Conflict of Interest:** The authors declare that the research was conducted in the absence of any commercial or financial relationships that could be construed as a potential conflict of interest.

Copyright © 2021 Lia, Henriques, Zonta, Chiavegato, Carmignoto, Gómez-Gonzalo and Losi. This is an open-access article distributed under the terms of the Creative Commons Attribution License (CC BY). The use, distribution or reproduction in other forums is permitted, provided the original author(s) and the copyright owner(s) are credited and that the original publication in this journal is cited, in accordance with accepted academic practice. No use, distribution or reproduction is permitted which does not comply with these terms.





# Auxiliary Subunits Control Function and Subcellular Distribution of AMPA Receptor Complexes in NG2 Glia of the Developing Hippocampus

Stefan Hardt, Dario Tascio, Stefan Passlick, Aline Timmermann, Ronald Jabs, Christian Steinhäuser\* and Gerald Seifert\*

*Institute of Cellular Neurosciences, Medical Faculty, University of Bonn, Bonn, Germany*

## OPEN ACCESS

### Edited by:

Christian Lohr,  
University of Hamburg, Germany

### Reviewed by:

Arthur Morgan Butt,  
University of Portsmouth,  
United Kingdom  
Yuriy Pankratov,  
University of Warwick,  
United Kingdom  
Jakob von Engelhardt,  
Johannes Gutenberg University  
Mainz, Germany

### \*Correspondence:

Christian Steinhäuser  
cste@uni-bonn.de  
Gerald Seifert  
Gerald.Seifert@ukbonn.de

### Specialty section:

This article was submitted to  
Non-Neuronal Cells,  
a section of the journal  
Frontiers in Cellular Neuroscience

**Received:** 19 February 2021

**Accepted:** 18 May 2021

**Published:** 10 June 2021

### Citation:

Hardt S, Tascio D, Passlick S,  
Timmermann A, Jabs R,  
Steinhäuser C and Seifert G (2021)  
Auxiliary Subunits Control Function  
and Subcellular Distribution of AMPA  
Receptor Complexes in NG2 Glia  
of the Developing Hippocampus.  
*Front. Cell. Neurosci.* 15:669717.  
doi: 10.3389/fncel.2021.669717

Synaptic and axonal glutamatergic signaling to NG2 glia in white matter is critical for the cells' differentiation and activity dependent myelination. However, in gray matter the impact of neuron-to-NG2 glia signaling is still elusive, because most of these cells keep their non-myelinating phenotype throughout life. Early in postnatal development, hippocampal NG2 glia express AMPA receptors with a significant  $\text{Ca}^{2+}$  permeability allowing for plasticity of the neuron-glia synapses, but whether this property changes by adulthood is not known. Moreover, it is unclear whether NG2 glia express auxiliary transmembrane AMPA receptor related proteins (TARPs), which modify AMPA receptor properties, including their  $\text{Ca}^{2+}$  permeability. Through combined molecular and functional analyses, here we show that hippocampal NG2 glia abundantly express TARPs  $\gamma 4$ ,  $\gamma 7$ , and  $\gamma 8$  as well as cornichon (CNIH)-2. TARP  $\gamma 8$  undergoes profound downregulation during development. Receptors of adult NG2 glia showed an increased sensitivity to blockers of  $\text{Ca}^{2+}$  permeable AMPA receptors, but this increase mainly concerned receptors located close to the soma. Evoked synaptic currents of NG2 glia were also sensitive to blockers of  $\text{Ca}^{2+}$  permeable AMPA receptors. The presence of AMPA receptors with varying  $\text{Ca}^{2+}$  permeability during postnatal maturation may be important for the cells' ability to sense and respond to local glutamatergic activity and for regulating process motility, differentiation, and proliferation.

**Keywords:** NG2 glia, hippocampus, AMPA receptor, TARP,  $\text{Ca}^{2+}$  permeability, developmental regulation

## HIGHLIGHTS

- The  $\text{Ca}^{2+}$  permeability of AMPA receptors in NG2 glia of the hippocampus increases during postnatal maturation.
- This increase was proven by applying solutions with  $\text{Ca}^{2+}$  as the sole permeant ion as well as receptor inhibition by polyamines.
- The AMPA receptor complexes are associated with various auxiliary subunits, particularly TARPs  $\gamma 4$ ,  $\gamma 7$ ,  $\gamma 8$ , and CNIH-2.
- The developmental increase of  $\text{Ca}^{2+}$  permeability of the receptors accompanies downregulation of TARP  $\gamma 8$ .

## INTRODUCTION

AMPA receptors co-assemble with auxiliary subunits, called transmembrane AMPA receptor regulatory protein (TARP), which modulates receptor function. The subunit TARP  $\gamma 2$ , also called stargazin, is necessary for surface translocation and synaptic expression of AMPA receptors as demonstrated in cerebellar granule cells (Chen et al., 2000; Tomita et al., 2005). Meanwhile a whole family of TARPs has been identified, which show region specificity in their expression and interact with AMPA receptors in various cell types (Mauric et al., 2013). Thus, in the hippocampus TARP  $\gamma 4$  was specifically identified in glial cells but not in neurons (Tomita et al., 2003). TARPs do not only affect translocation of the receptor channels but also influence its function such as binding affinity and efficacy, receptor desensitization and deactivation, and sensitivity to intracellular polyamine block [reviewed by Jackson and Nicoll (2011)]. In heterologous expression systems and cerebellar stellate cells, TARP expression may affect polyamine block and enhance channel conductance (Soto et al., 2007; Jackson et al., 2011). Furthermore it was suggested that TARPs may influence the  $\text{Ca}^{2+}$  permeability of AMPA receptors (Kott et al., 2009). Specifically, co-assembly with distinct TARPs determines the  $\text{Ca}^{2+}$  permeability of the receptors. In stellate cells of the cerebellum, TARP  $\gamma 2$  promotes synaptic expression of  $\text{Ca}^{2+}$  impermeable AMPA receptors while its deletion increased the proportion of extrasynaptic  $\text{Ca}^{2+}$  permeable AMPA receptors associated with TARP  $\gamma 7$  (Bats et al., 2012). In granule cells, however, synaptic localization of  $\text{Ca}^{2+}$  permeable AMPA receptors requires TARP  $\gamma 7$ , while  $\gamma 2$  promotes expression of  $\text{Ca}^{2+}$  impermeable AMPA receptors at postsynapses (Studniarczyk et al., 2013). TARP  $\gamma 8$  is predominantly expressed in the hippocampus, striatum and amygdala, but not in the cerebellum (Tomita et al., 2003; Fukaya et al., 2005). Genetic deletion of TARP  $\gamma 8$  led to mislocation of AMPA receptors and impaired synaptic plasticity in hippocampal neurons (Rouach et al., 2005). The preferred expression of TARP  $\gamma 8$  in the hippocampus initiated the search for inhibitors of this subunit to prevent hyperexcitation as observed in temporal lobe epilepsy or anxiety disorders (Maher et al., 2017). Another family of AMPA receptor-associated proteins is formed by the cornichons (CNIHs), among which CNIH-2 and CNIH-3 are abundantly expressed in the brain and assemble with GluA subunits (Schwenk et al., 2009). CNIHs increase surface expression of AMPA receptors in neural cells and slow deactivation and desensitization of glutamate-evoked responses (Schwenk et al., 2009). CNIH-2 has been shown to modulate receptor gating and pharmacology of AMPA receptor-TARP complexes (Kato et al., 2010; Gill et al., 2011).

NG2 glial cells express functional AMPA receptors and receive direct synaptic input from glutamatergic neurons (Bergles et al., 2000; Jabs et al., 2005; Haberlandt et al., 2011). In cultured oligodendrocyte precursor cells (OPCs) from optic nerve as well as in CG4 cells, concomitant activation of metabotropic glutamate receptors (mGluRs) increases expression of  $\text{Ca}^{2+}$  permeable AMPA receptors, while activation of P2Y receptors led to a decrease (Zonouzi et al., 2011). The latter study also

suggested that AMPA receptors in OPCs co-assemble with TARPs to influence expression of  $\text{Ca}^{2+}$  permeable AMPA receptors at climbing fiber-NG2 glia synapses of the cerebellum. RT-PCR data from optic nerve OPCs identified TARP subunits  $\gamma 2$ ,  $\gamma 3$ ,  $\gamma 4$ ,  $\gamma 5$ , and  $\gamma 6$ . Microarray analysis in PDGFR $\alpha$ -positive NG2 glia (OPCs) from mouse forebrain revealed abundant expression of TARP  $\gamma 4$ ,  $\gamma 8$  and, to a lower extent,  $\gamma 5$  (Cahoy et al., 2008). Expression of  $\text{Ca}^{2+}$  permeable AMPA receptors requires full length TARPs, which interact with the postsynaptic scaffold protein PSD-95 (Zonouzi et al., 2011). Bergmann glia express  $\text{Ca}^{2+}$  permeable AMPA receptors lacking GluA2 (Saab et al., 2012), which are associated with TARP  $\gamma 5$  to modify rectification properties and influence surface expression of the receptors (Soto et al., 2009).

NG2 glial cells in the hippocampus express AMPA receptors with an intermediate  $\text{Ca}^{2+}$  permeability (Seifert and Steinhäuser, 1995; Seifert et al., 1997b). In newborn mice, the receptors of these cells are  $\text{Ca}^{2+}$  permeable (Seifert et al., 2003). Their activation provokes intracellular  $\text{Ca}^{2+}$  elevations (Jabs et al., 1994; Haberlandt et al., 2011; Barron and Kim, 2019), which constitute the basis for plasticity of neuron-glia synapses (Ge et al., 2006). During maturation,  $\text{Ca}^{2+}$  permeability and sensitivity to intracellular polyamine block of the receptor channels decrease (Seifert et al., 2003; Ge et al., 2006). In hilar NG2 glia, amplitude and frequency of receptor-mediated synaptic currents increase (Mangin et al., 2008) while in the hippocampus, synaptic connectivity decreases in older mice (Passlick et al., 2016) and AMPA receptors are downregulated (Kukley et al., 2010).

Expression and functional consequences of TARPs in NG2 glia of the hippocampus have not yet been studied during development. Here we report that these cells abundantly express TARPs  $\gamma 4$ ,  $\gamma 7$ , and to a lower extent  $\gamma 8$ . In addition, the auxiliary subunit CNIH-2 was found in almost all cells analyzed. During postnatal development, expression of most TARPs and CNIH-2 was downregulated. Our functional analyses revealed that the sensitivity to polyamine block of  $\text{Ca}^{2+}$  permeable receptors increases in maturing NG2 glia. Moreover, the proportion of  $\text{Ca}^{2+}$  permeable AMPA receptors at the soma increases during development, which is accompanied by downregulation of TARP  $\gamma 8$ .

## MATERIALS AND METHODS

### Preparation of Brain Slices and Acutely Isolated Cells

Transgenic mice [NG2ki-EYFP (Karram et al., 2008)] of postnatal days (p) 6–12 (referred to as p10) and p40–76 (p60) were anaesthetized, sacrificed by decapitation and their brains were dissected, washed, and the hemispheres were cut into 300  $\mu\text{m}$  thick slices in frontal or horizontal orientation using a vibratome (Leica Microsystems VT 1200S, Wetzlar, Germany). Slice preparation was performed at 6°C in ACSF supplemented with sucrose (preparation solution). Subsequently, slices were stored for at least 30 min in preparation solution at 35°C and afterward in ACSF at room temperature. ACSF was gassed with

carbogen. Preparation solution contained (in mM): 87 NaCl, 2.5 KCl, 1.25  $\text{NaH}_2\text{PO}_4$ , 7  $\text{MgSO}_4$ , 0.5  $\text{CaCl}_2$ , 25 glucose, 25  $\text{NaHCO}_3$ , and 105 sucrose (325 mOsm, pH 7.4). For acute cell isolation, slices were stored in HEPES-buffered solution lacking nominal  $\text{Ca}^{2+}$  (pH 7.4; 6°C).

### Patch Clamp-Recordings *in situ*

Membrane currents were measured with the patch-clamp technique in the whole-cell configuration. Current signals were amplified (EPC-7 or EPC 800, HEKA elektronik, Lambrecht, Germany), filtered at 3 and 10 kHz and sampled at 10 and 100 kHz by an interface connected to a computer system, which also served as a stimulus generator. The resistance of the patch pipettes was 2–4 M $\Omega$  (borosilicate glass; Hilgenberg). Capacitance compensation was used to improve voltage clamp control. The input resistance was determined by stepping the membrane from –70 to –60 mV. To block  $\text{K}^+$  channels,  $\text{Na}^+$  channels and GABA<sub>A</sub> receptors,  $\text{Ba}^{2+}$  (100  $\mu\text{M}$ ), quinine (200  $\mu\text{M}$ ), TTX (0.5  $\mu\text{M}$ ) and picrotoxin (100  $\mu\text{M}$ ) was added to the bath solution. AMPA receptor agonists, modulators and blockers were applied *via* the bath solution. The artificial cerebrospinal fluid (aCSF) contained (in mM): 126 NaCl, 3 KCl, 1.25  $\text{NaH}_2\text{PO}_4$ , 2  $\text{MgCl}_2$ , 2  $\text{CaCl}_2$ , 10 glucose, 26  $\text{NaHCO}_3$  (gassed with carbogen, pH 7.4, 310 mOsm). The pipette solution was composed of (in mM): 130 KCl, 0.5  $\text{CaCl}_2$ , 2  $\text{MgCl}_2$ , 5 BAPTA, 10 HEPES, and 3  $\text{Na}_2\text{-ATP}$  (pH 7.28). Recordings were obtained at room temperature.

For analysis of postsynaptic currents, a CsCl-based pipette solution was used (in mM): 120 CsCl, 2  $\text{MgCl}_2$ , 0.5  $\text{CaCl}_2$ , 5 BAPTA, 10 Hepes, 3  $\text{Na}_2\text{-ATP}$ , 10 TEA. Stimulation of Schaffer collaterals was performed through a chlorinated silver electrode inserted in a low resistance (<1 M $\Omega$ ), aCSF-filled glass capillary which served as a monopolar stimulation electrode. Pulse sequences were generated with an AM-Systems isolation pulse stimulator (model 2100, Jerusalem, Israel). The stimulation electrode was positioned close to the patch electrode (distance ~60  $\mu\text{m}$ , pulse duration 100  $\mu\text{s}$ ). Responses were analyzed with custom-written macros in Igor Pro 8 software (Wavemetrics). Stimulus artifacts were offline compensated by subtracting averaged failures. Recordings were obtained at 35°C.

### Recordings From Freshly Isolated Cells

Freshly isolated cells were obtained from slices after protease treatment as described (Matthias et al., 2003).  $\text{K}^+$  channel blockers (100  $\mu\text{M}$   $\text{Ba}^{2+}$ , 100  $\mu\text{M}$  quinine) as well as AMPA receptor agonists, blockers and modulators were applied by transferring the cells with a tube electrode to the different solutions (Seifert and Steinhäuser, 1995). Membrane currents were measured in the whole-cell configuration as described above. The resistance of the patch pipettes was 4 M $\Omega$ , the input resistance was determined as described above. The bath solution contained (in mM): 150 NaCl, 5 KCl, 2  $\text{MgCl}_2$ , 2  $\text{CaCl}_2$ , 10 HEPES, and 10 glucose (pH 7.4). The pipette solution was the same as for slice recordings. For recordings in high  $\text{Ca}^{2+}$  solution, 150 mM NaCl was replaced by 50 mM  $\text{CaCl}_2$  and adjusted with *N*-methyl-D-glucamine (NMDG) to an osmolarity of 320 mOsm (pH 7.4). As for recording synaptic currents (cf.

above), CsCl-based pipette solution was used. Recordings were obtained at room temperature. Salts and buffers were purchased from AppliChem (Darmstadt, Germany), kainate and CTZ were received from Abcam (Milton, United Kingdom), Naspmm from Alomone Labs (Israel), and IEM-1460, JNJ 55511118 and GYKI53655 from Tocris (Bristol, United Kingdom).

### Single-Cell RT-PCR

Single-cell transcript analysis was performed as previously reported (Seifert et al., 1997a; Matthias et al., 2003). Briefly, after slice recording the cell at the tip of the pipette was lifted above the slice and aspirated into the recording pipette under microscopic control. The cell content and ~3  $\mu\text{l}$  of the pipette solution were expelled into a reaction tube containing 3  $\mu\text{l}$  of DEPC-treated water. Only single cells without any adherent tissue debris were selected for the analysis. The reaction tube was frozen and stored at –80°C until reverse transcription (RT). The RT mastermix contained first strand buffer (Invitrogen, Karlsruhe, Germany), dithiothreitol (DTT, 10 mM), dNTPs (4  $\mu\text{M}$   $\times$  250  $\mu\text{M}$ ; Applied Biosystems, Darmstadt, Germany), RNasin<sup>TM</sup> (20 U; Promega, Mannheim, Germany), random hexamer primers (50  $\mu\text{M}$ ; Roche, Mannheim, Germany), and reverse transcriptase (SuperscriptIII, 100 U, Invitrogen). The reaction mix was added to the harvested cell content, final volume was 10  $\mu\text{l}$ , and the reaction mix was incubated at 37°C for 1 h. A multiplex two-round single-cell PCR was performed with primers for TARPs, CNH-2 and the housekeeping gene PDGFR $\alpha$ . The first PCR was performed after adding PCR buffer,  $\text{MgCl}_2$  (2.5 mM), dNTP (4  $\mu\text{M}$   $\times$  50  $\mu\text{M}$ ), primer (200 nM each), and 5 U *Taq* polymerase (Invitrogen) to the RT product (final volume 50  $\mu\text{l}$ ). Thirty-five cycles were performed (denaturation at 94°C, 25 s; annealing at 51°C, 2 min for the first five cycles, and 45 s for the remaining cycles; extension at 72°C, 25 s; final elongation at 72°C, 7 min). An aliquot (2  $\mu\text{l}$ ) of the PCR product was used as a template for the second PCR (35 cycles; annealing at 54°C, first five cycles: 2 min, remaining cycles: 45 s) using nested primers (**Supplementary Table 1**). The conditions were the same as described for the first round, but Platinum *Taq* polymerase (2.5 U; Invitrogen) was added. Products were identified with gel electrophoresis. As a positive control, total RNA from mouse brain was run in parallel. Negative controls were performed using distilled water or bath solution for RT-PCR.

### FACS Sorting and RT-qPCR

NG2ki-EYFP mice (p10 and p60, male and female) were sacrificed and their brains were dissected and the hippocampus was isolated under microscopic control (Stereo microscope, Zeiss, Germany). A cell suspension was prepared by mincing the tissue, digesting in papain (37°C, 15 min) and incubating with DNaseI [10 min; Neural Dissociation Kit (P), Miltenyi, Germany]. Fluorescent NG2 glial cells were identified by their EYFP fluorescence (emission at 527 nm) and sorted by a FACSAriaIII flow cytometer (70  $\mu\text{m}$  nozzle, BD Biosciences, Heidelberg, Germany) into tubes containing Hanks' balanced salt solution (HBSS,  $\text{Ca}^{2+}$ - and  $\text{Mg}^{2+}$ -free). After centrifugation (2,000 g, 10 min) the supernatant was discarded and the cells were suspended in 200  $\mu\text{l}$  lysis/binding buffer (Invitrogen, Darmstadt,

Germany), frozen in liquid nitrogen and stored at  $-80^{\circ}\text{C}$ . Messenger RNA was isolated from isolated cells by cell lysis in the lysis/binding buffer and by using oligo(dT)25-linked Dynabeads (Invitrogen). The beads with adherent mRNA were suspended in DEPC-treated water (20  $\mu\text{l}$ ). For first strand synthesis, RT was performed using oligo-dT<sub>24</sub>-primer (5  $\mu\text{M}$ , Eurogentec). The reaction mix was incubated for 1 h at  $50^{\circ}\text{C}$  (final volume 40  $\mu\text{l}$ ).

The reaction mixture for real-time PCR contained Takyon real-time PCR mastermix (Eurogentec, Seraing, Belgium) and Taqman primer/probe mix (Thermo Fisher Scientific, Darmstadt, Germany). One  $\mu\text{l}$  of the RT product was added, the reaction volume was 12.5  $\mu\text{l}$ . PCRs for the respective target genes and  $\beta$ -actin, as a housekeeping gene, were run in parallel wells for each sample (triplicates for each sample). Water served as a negative control in each run. After denaturation ( $95^{\circ}\text{C}$ , 10 min), 50 cycles were performed (denaturation at  $95^{\circ}\text{C}$ , 15 s; primer annealing and extension at  $60^{\circ}\text{C}$ , 60 s; thermocycler CFX 384, Biorad, Munich, Germany). Fluorescence intensity was read out during each annealing/extension step. Target gene/ $\beta$ -actin expression ratios were determined by comparing  $C_T$  values of the target gene with those of the reference gene,  $\beta$ -actin. Relative quantification of different genes was determined according to the  $2^{\Delta\Delta C_T}$  method:

$$X_{\text{target}}/X_{\beta\text{-actin}} = E^{\text{CT}\beta\text{-actin}}/E^{\text{CTtarget}}, \quad (1)$$

yielding a gene ratio with  $X$  being the input copy number and  $C_T$  the cycle number at threshold. The amplification efficiency for TARP  $\gamma 2$  was 1.89, for  $\gamma 4$  1.90, for  $\gamma 7$  1.92, for  $\gamma 8$  1.96, for CNH-2 1.98, and for  $\beta$ -actin 1.94. For the AMPA receptor subunits the amplification efficiencies were 1.95 (GluA1, GluA3) and 1.96 (GluA2, GluA4).

## Data Analysis

The rectification index (RI) of receptor currents was determined by comparing the chord conductance of agonist/blocker-sensitive currents at  $-70$  and  $+70$  mV or  $+40$  mV according to:

$$\text{RI} = [I_{+70\text{mV}}/(+70\text{mV} - E_{\text{rev}})]/[I_{-70\text{mV}}/(-70\text{mV} - E_{\text{rev}})], \quad (2a)$$

$$\text{RI} = [I_{+40\text{mV}}/(+40\text{mV} - E_{\text{rev}})]/[I_{-70\text{mV}}/(-70\text{mV} - E_{\text{rev}})], \quad (2b)$$

where  $I$  is the amplitude of the currents at  $+70$ ,  $+40$ , and  $-70$  mV, respectively, and  $E_{\text{rev}}$  its extrapolated reversal potential.

Data were tested for Gaussian distribution by the Shapiro-Wilk tests and for homogeneity of variance with Levene's test, followed by a two sample  $t$ -test or Mann-Whitney- $U$ -test with or without Welch correction for equal or diverse variance. In case of paired data, a paired  $t$ -test or Wilcoxon signed rank test was performed. For group analyses, we used two-way ANOVA followed by Tukey or Holm's *post hoc* test, in case of non-parametric data, aligned rank transformed ANOVA

followed by Mann-Whitney- $U$ -Test or Wilcoxon signed rank test with Holm's correction for multiple comparisons. Tests were performed with the software R (R Development Core Team<sup>1</sup>). Non-Gaussian distributed data are displayed in box plots showing median (central line), quartiles (25 and 75%; box) and whiskers ( $\pm 1.5$  times the interquartile range). Statistical significance of gene expression by single-cell RT-PCR was analyzed by  $\chi^2$  test. Significance level was set to  $P < 0.05$ . Except box plots, data are given as mean  $\pm$  SD.  $n$  and  $N$  refer to the number of cells and mice, respectively.

## RESULTS

### Pharmacological Characterization of $\text{Ca}^{2+}$ Permeable AMPA Receptors in Brain Slices From Juvenile and Adult Mice

The NG2ki-EYFP mouse line has been extensively characterized and allows for identification of NG2 glia prior to electrophysiological recordings and cell identification for flow cytometry (Karram et al., 2008). NG2<sup>+</sup> cells located next to blood vessels were excluded from this study to avoid mix up with NG2<sup>+</sup> pericytes (Figure 1A). NG2 glial cells were identified by their EYFP fluorescence, characteristic morphology and current pattern (small  $\text{Na}^+$  inward currents, prominent A-type  $\text{K}^+$  currents, inwardly rectifying  $\text{K}^+$  currents with the latter increasing with age; e.g. (Moshrefi-Ravasdjani et al., 2017; Seifert and Steinhäuser, 2018; Figure 1B).

At p10, adding the  $\text{K}^+$  channel blockers quinine (200  $\mu\text{M}$ ) and  $\text{Ba}^{2+}$  (100  $\mu\text{M}$ ) to the bath shifted the resting potential of the NG2 glial cells from  $-85$  mV (median; quartiles:  $-75$ – $-90$  mV) to  $-50$  mV ( $-55$  to  $-44$  mV) and increased the input resistance from 225 M $\Omega$  (165–320 M $\Omega$ ) to 1,000 M $\Omega$  (833–2,000 M $\Omega$ ,  $n = 26$  cells,  $N = 6$  mice). Subsequent application of kainate (250  $\mu\text{M}$ ) induced inward currents of  $-5.85$  pA/pF ( $-5.14$  to  $-7.93$  pA/pF) ( $V = -70$  mV;  $n = 20$ ,  $N = 6$ ) (Figures 2A,C). Although spermine was added to the pipette solution (50  $\mu\text{M}$ ) to block outward currents through  $\text{Ca}^{2+}$  permeable receptors, we still observed significant outward rectification (RI = 1.77, 1.60–1.94) (Figures 2B,D). The reversal potential of the responses was  $-0.1$  mV ( $-1.2$  to  $7.0$  mV; Figure 2B). Increasing the spermine concentration to 100  $\mu\text{M}$  did not change rectification (1.58, 1.44–1.86,  $n = 6$ ,  $N = 2$ ,  $p = 0.298$ ). Next we co-applied kainate (250  $\mu\text{M}$ ) with 1-naphthyl-acetyl-spermine (Naspm; 100  $\mu\text{M}$ ) to detect putative currents through  $\text{Ca}^{2+}$  permeable AMPA receptors (Koike et al., 1997). While the reversal potential slightly increased in the presence of Naspm (from  $-0.1$  mV,  $-1.2$ – $7.0$  mV to  $4.8$  mV,  $0.1$ – $12.8$  mV;  $n = 20$ ,  $p < 0.001$ ), RI did not change (1.69, 1.59–1.96,  $n = 20$ ,  $N = 5$ ) (Figure 2D). Naspm reduced the kainate-induced currents by  $8.1 \pm 12.1\%$  ( $V = -100$  mV; Figure 2A, left).

At p60, the  $\text{K}^+$  channel blockers induced a depolarization from  $-87$  mV ( $-84$  to  $-90$  mV) to  $-65$  mV ( $-70$  to  $-52$  mV)

<sup>1</sup><http://www.R-project.org>



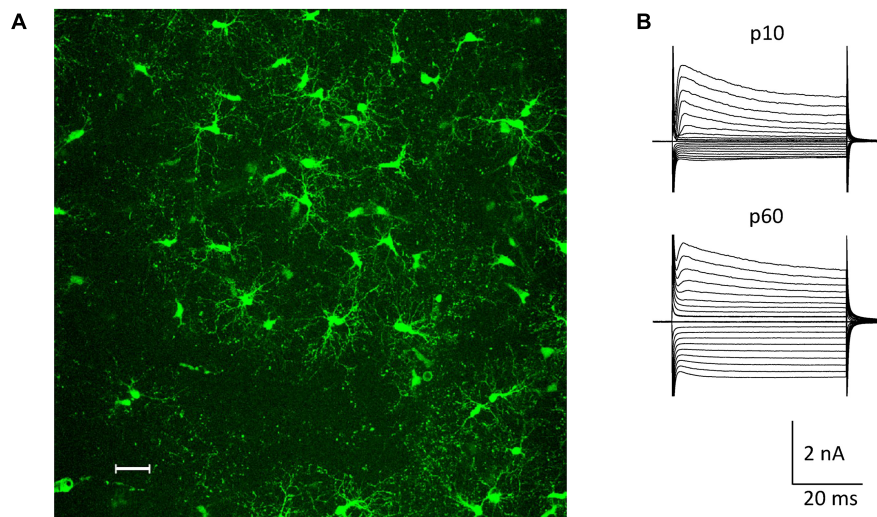


**FIGURE 1 |** NG2 glia in the hippocampal CA1 region *in situ*. **(A)** Fluorescent NG2 glia in the stratum radiatum of a NG2ki-EYFP mouse at p78. Maximum intensity projection of 200 optical sections obtained by 2-photon-laser-scanning microscopy (950 nm excitation; Leica TSM, Leica Microsystems, Pulheim, Germany). Scale bar 30 μm. **(B)** Current patterns of NG2 glial cells obtained from the CA1 stratum radiatum of acute slices at p10 and p60 (de- and hyperpolarization from -160 to +20 mV; 10 mV increment, holding potential -70 mV).

while the input resistance increased from 80 MΩ (66–104 MΩ) to 714 MΩ (625–1,000 MΩ,  $n = 41$ ,  $N = 9$ ;  $p < 0.001$ ). The lower input resistance in these older mice reflected the cells' increased Kir conductance (Seifert and Steinhäuser, 2018). Application of kainate (250 μM, with 50 μM spermine in the pipette) induced inward currents of -7.86 pA/pF (-70 mV; -4.20 to -11.7 pA/pF), which reversed current direction at -0.2 mV (-3.2–7.3 mV), showed an RI of 1.24 (1.12–1.38,  $n = 41$ ,  $N = 9$ ) and were completely blocked by NBQX (10 μM) (**Figures 2A–D**). This stronger rectification compared to the juvenile stage ( $p < 0.001$ ) might have indicated a more efficient spermine block and hence an elevated  $\text{Ca}^{2+}$  permeability in NG2 glia from the older mice. In the presence of Naspmm, RI was 1.36 (1.28–1.46,  $n = 8$ ;  $N = 3$ ), i.e., lower than at juvenile stage (**Figure 2D**), but the efficiency of Naspmm-dependent inhibition of kainate-induced currents (by  $15.5 \pm 16.8\%$  at  $V = -100$  mV) did not change during maturation.

Recently it was reported that intracellular application of Naspmm completely blocks outward currents through GluA2-lacking,  $\text{Ca}^{2+}$  permeable AMPA receptors and that this block, in contrast to intracellular spermine block, does not depend on TARP expression (Coombs et al., 2021). Indeed, with Naspmm (100 μM) in the pipette solution (**Figures 2E,F**), we observed stronger rectification of kainate-induced responses (p10: RI =  $1.44 \pm 0.30$ ,  $n = 18$ ,  $N = 3$ ,  $p < 0.01$ ; p60: RI =  $1.03 \pm 0.17$ ,  $n = 18$ ,  $N = 3$ ,  $p < 0.01$ ). At p60, the blocking effect of intracellular Naspmm was also stronger than at p10 ( $p < 0.01$ ) (**Figures 2F,G**).

Intracellular polyamines block outward currents through  $\text{Ca}^{2+}$  permeable, GluA2-lacking AMPA receptors (Bowie and Mayer, 1995; Donevan and Rogawski, 1995; Kamboj et al., 1995), which reduces rectification (Koh et al., 1995; Toth and McBain, 1998; Soto et al., 2007). Thus, in line with previous findings

(Seifert and Steinhäuser, 1995; Seifert et al., 2003), our data confirm a low  $\text{Ca}^{2+}$  permeability of AMPA receptors in juvenile NG2 glia which, judged by the lower RI, increased by adulthood.

## Developmental Regulation of TARPs and CNIHs in Hippocampal NG2 Glia

Since TARPs and CNIHs affect the intracellular polyamine block and may accompany  $\text{Ca}^{2+}$  permeable AMPA receptor subunits, we analyzed their expression by NG2 glial cells. First, multiplex single cell RT-PCR was performed after electrophysiological characterization of the cells in acute slices, using PDGFRα mRNA as a NG2 glia-specific marker. This marker was found in all cells harvested (p10,  $n = 64$ ; p60,  $n = 43$ ). We found heterogeneous expression of auxiliary subunits in NG2 glia. At p10, a majority of cells expressed TARP γ4 (80%,  $n = 43$ ), TARP γ7 (100%,  $n = 24$ ), TARP γ8 (67%,  $n = 43$ ), and CNIH-2 (100%,  $n = 19$ ) while TARP γ2 and TARP γ5 were less frequent (37%,  $n = 38$  and 29%,  $n = 24$ , respectively) (**Figures 3A,B**). At p60, a similar expression pattern was observed: TARP γ4 (95%,  $n = 21$ ), TARP γ7 (86%,  $n = 20$ ) and CNIH-2 (71%,  $n = 20$ ) were most abundant while TARPs γ2 and γ5 were less frequent (36%,  $n = 21$  and 29%,  $n = 20$ ). However, the expression of TARP γ8 differed, declining to 23% at p60 ( $n = 21$ ,  $p = 0.0005$ ), and CNIH-2 was also less abundant than at p10 ( $n = 20$ ,  $p = 0.02$ ) (**Figure 3C**).

To receive quantitative information as to the expression of the auxiliary subunits, real-time PCR was performed with cDNA from FAC sorted NG2 glial cells isolated from the hippocampus of EYFP mice, using β-actin as a housekeeping gene. At p10, TARP γ4 was most abundant (expression ratio  $0.864 \pm 0.166$ ,  $n = 8$ ), followed by TARP γ7 ( $0.064 \pm 0.014$ ,  $n = 8$ ) and CNIH-2 ( $0.05 \pm 0.011$ ,  $n = 8$ ). Expression of the hippocampus-specific subunit γ8 was low in NG2 glia ( $0.014 \pm 0.004$ ,

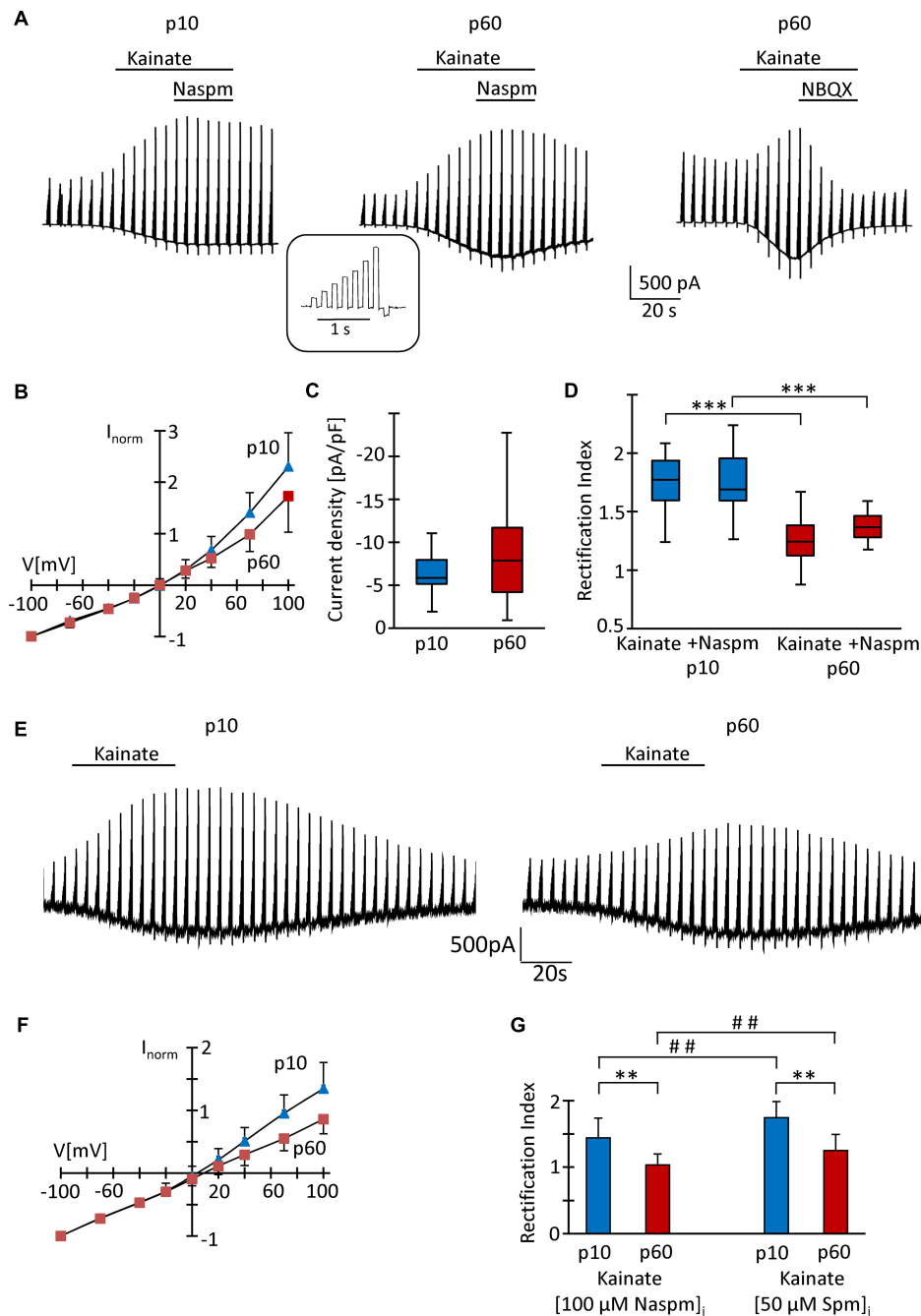


**FIGURE 2 |** Analysis of AMPA receptors in hippocampal NG2 glia *in situ*. **(A)** After incubation in blockers of  $K^+$ - and  $Na^+$ -channels (200  $\mu$ M quinine, 100  $\mu$ M  $Ba^{2+}$ , 0.5  $\mu$ M TTX) and GABA $_A$  receptors (100  $\mu$ M picrotoxin), kainate (250  $\mu$ M) and Naspm (100  $\mu$ M) were applied to slices as indicated while the membrane of the patched cell was de- and hyperpolarized (-70, -40, -20, 0, 20, 40, 70 100, and -100 mV; duration 100 ms, separated by 100 ms, every 4.5 s; see inset). The pipette solution contained spermine (50  $\mu$ M). Representative responses are shown from cells at p10 (left) and p60 (middle, right). NBQX (10  $\mu$ M) almost completely (by 97%) blocked kainate-induced currents (right). **(B)** To obtain I/V relations of kainate-induced responses, currents before and during agonist application were subtracted at corresponding voltages. Responses were normalized to maximum inward currents and averaged (p10, blue,  $n = 20$ ; p60, red,  $n = 41$ ). **(C)** Current density of AMPA receptor currents at -70 mV did not differ between p10 (-5.85 pA/pF,  $n = 20$ ) and p60 (-7.86 pA/pF,  $n = 41$ ). **(D)** Rectification of the I/V curves significantly differed between p10 (kainate: RI = 1.77; kainate + Naspm: RI = 1.69,  $n = 20$ ) and p60 (kainate: RI = 1.24,  $n = 41$ ; kainate + Naspm: RI = 1.37,  $n = 8$ ). Within individual age groups, application of Naspm did not affect RI. Significant differences are indicated by asterisks ( $p < 0.001$ ). **(E)** Same conditions as described in panel **(A)**, but with Naspm (100  $\mu$ M) instead of spermine in the pipette solution. **(F)** Kainate responses were determined as described in panel **(B)** (p10, blue,  $n = 18$ ; p60, red,  $n = 18$ ). **(G)** Rectification of I/V curves at p10 (RI = 1.44,  $n = 18$ ) and p60 (RI = 1.03,  $n = 18$ ). Significant differences are indicated [between ages: \*\* $p < 0.01$ , \*\*\* $p < 0.001$ ; between (Naspm) $_i$  and (spermine) $_i$ : ## $p < 0.01$ ].

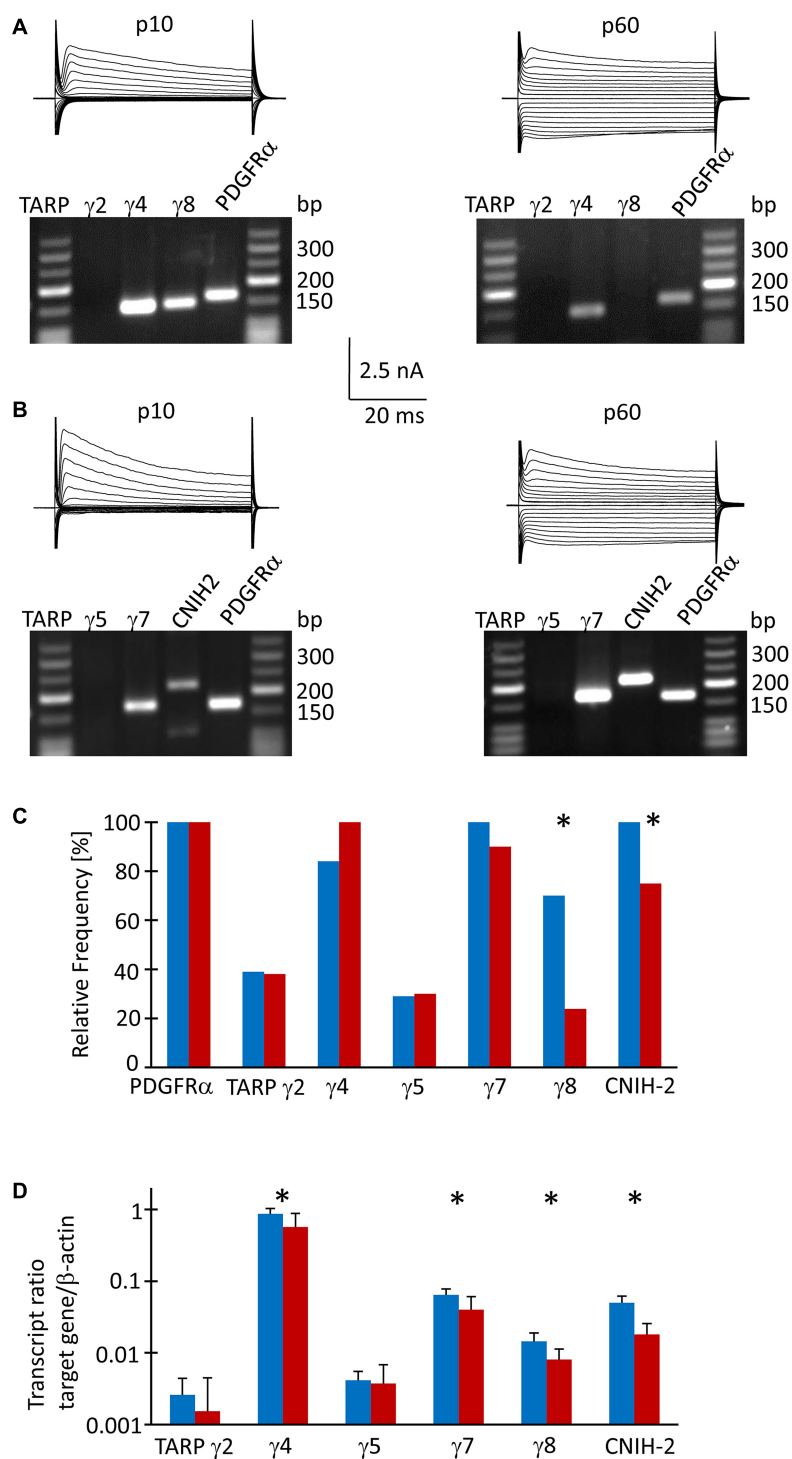


**FIGURE 3 |** TARP/CNIH expression in individual und FAC sorted NG2 glia. **(A,B)** Membrane currents were evoked through de- and hyperpolarization of the cell membrane (−160 to 20 mV, 10 mV increments, duration 50 ms, holding potential −70 mV). After recording *in situ*, the cell content was harvested and RT-PCR was performed. The agarose gels show the respective transcript patterns. PDGFR $\alpha$  receptor mRNA served as a positive control. The PCR products matched the predicted lengths (**Supplementary Table 1**). **(C)** Relative frequencies of TARP- and CNIH-2 expression by individual cells (p10:  $\gamma 2$ ,  $n = 38$  cells;  $\gamma 4$  and  $\gamma 8$ ,  $n = 43$ ;  $\gamma 5$  and  $\gamma 7$ ,  $n = 24$ ; CNIH-2,  $n = 19$ . p60:  $\gamma 2$ ,  $\gamma 4$  and  $\gamma 8$ ,  $n = 20$ ;  $\gamma 5$ ,  $\gamma 7$  and CNIH-2,  $n = 21$ ). **(D)** qPCR was performed with FAC sorted NG2 glial cells. Expression ratios were determined according to equation (1). Mean and SD were determined at p10 ( $n = 8$ ) and p60 ( $n = 12$ ). Significant differences are indicated by asterisks ( $p < 0.05$ ).

$n = 8$ ). TARP  $\gamma 2$  and  $\gamma 5$ , which are abundantly present in the cerebellum, were expressed at a low level while TARP  $\gamma 3$  was absent (Figure 3D). At p60, the relation between the individual auxiliary subunits remained similar, although expression was generally lower (TARP  $\gamma 4$ ,  $0.570 \pm 0.313$ ,  $n = 12$ ; TARP  $\gamma 7$ ,  $0.040 \pm 0.021$ ,  $n = 12$ ; CNH-2,  $0.018 \pm 0.008$ ,  $n = 12$ ; TARP  $\gamma 8$ ,  $0.008 \pm 0.003$ ,  $n = 12$ ) (Figure 3D). Expression of TARP  $\gamma 2$  and TARP  $\gamma 5$  was close to the detection threshold and showed no developmental regulation.

Next, we compared expression of mRNA for the subunits GluA1-4 in FAC-sorted NG2 glia from mice at both ages, using again  $\beta$ -actin as a housekeeping gene. At p10, GluA2 was most abundant (expression ratio  $0.102 \pm 0.059$ ), followed by GluA3 ( $0.050 \pm 0.023$ ), GluA4 ( $0.030 \pm 0.014$ ) and GluA1 ( $0.017 \pm 0.008$ ,  $n = 10$  for all) (Supplementary Figure 1). A similar expression pattern was found at p60 (GluA2,  $0.098 \pm 0.066$ ; GluA3,  $0.035 \pm 0.025$ ; GluA4,  $0.025 \pm 0.018$ ; GluA1,  $0.013 \pm 0.018$ ;  $n = 10$  for all) (Supplementary Figure 1).

## Pharmacological Characterization of $\text{Ca}^{2+}$ Permeable AMPA Receptors in NG2 Glia Freshly Isolated From p10 Mice

Because the slow application of the receptor blockers, diffusion barriers and putative indirect effects of drug application in slices might have compromised the results, we characterized properties of AMPA receptors also in acutely isolated NG2 glial cells. The developmental differences in TARP  $\gamma 8$  expression also led us to test the effect of a TARP  $\gamma 8$  antagonist, JNJ55511118 (further on called JNJ; Maher et al., 2016), in addition to the more global blockers of  $\text{Ca}^{2+}$  permeable AMPA receptors, Naspmm and IEM-1460 (Magazanik et al., 1997).

After fresh isolation, NG2 glia was identified by their intrinsic fluorescence. At p10, addition of quinine and  $\text{Ba}^{2+}$  (100  $\mu\text{M}$  both) to the bath depolarized the cells from  $-28.2 \pm 15.8$  mV to  $-16.2 \pm 8.0$  mV and increased their input resistance from  $1,285 \pm 847$  M $\Omega$  to  $2,152 \pm 2,044$  M $\Omega$  ( $n = 35$ ,  $N = 13$ ) (Figure 4A). With spermine (50  $\mu\text{M}$ ) in the pipette, kainate (250  $\mu\text{M}$ ) together with the AMPA receptor modulator cyclothiazide (100  $\mu\text{M}$ ) induced inward currents of  $161.4 \pm 124.4$  pA/pF ( $n = 35$ ,  $N = 13$ ,  $V = -70$  mV) (Figure 4B). The I/V relations of the kainate-induced responses revealed a reversal potential ( $V_{\text{rev}}$ ) of  $-1.5 \pm 8.9$  mV and RI =  $1.26 \pm 0.27$  ( $n = 35$ ,  $N = 13$ ), confirming previous findings (Figure 4C; Seifert et al., 2003). GYKI53655 reduced the AMPA receptor currents by  $97 \pm 4\%$  ( $n = 11$ ,  $N = 9$ ) (Figure 4D), with the RI of GYKI-sensitive currents being  $1.44 \pm 0.46$  ( $V_{\text{rev}} = -2.8 \pm 10.2$  mV).

To further characterize expression of  $\text{Ca}^{2+}$  permeable AMPA receptors and putative involvement of TARP  $\gamma 8$  in kainate-induced responses of NG2 glia, JNJ was applied subsequent to Naspmm or IEM-1460. Naspmm (50  $\mu\text{M}$ ) decreased the inward currents (by  $53.1 \pm 18.3\%$ ,  $V = -70$  mV,  $n = 15$ ,  $N = 11$ ) while the subsequent application of JNJ (10  $\mu\text{M}$ ) led to a further block of the kainate-induced currents (by  $19.8 \pm 14.7\%$ ,  $n = 6$ ,  $N = 5$ ) (Figure 4B). With the blockers in reverse order, JNJ at 10  $\mu\text{M}$  reduced currents by  $30.5 \pm 6.9\%$  ( $n = 8$ ,  $N = 5$ ) while addition of Naspmm led to a further reduction by  $30.2 \pm 11.8\%$  ( $n = 7$ ;

$N = 4$ ) (Figure 4B). To avoid putative non-specific effects, we reduced the JNJ concentration to 1  $\mu\text{M}$ . Under these conditions, JNJ reduced the currents by  $15.1 \pm 5.3\%$  ( $n = 10$ ,  $N = 4$ ,  $V = -70$  mV), which was less compared to block by 10  $\mu\text{M}$  JNJ ( $p < 0.001$ ; Supplementary Figure 2C). The Naspmm (50  $\mu\text{M}$ )-mediated block of JNJ (1  $\mu\text{M}$ )-insensitive currents was not different from the values obtained with 10  $\mu\text{M}$  JNJ ( $36.8 \pm 11.4\%$ ,  $n = 9$ ;  $N = 4$ ) (Supplementary Figures 2A,C). These data demonstrated that despite the inefficacy of intracellular spermine, extracellularly applied spermine analogs profoundly affected the receptor currents in juvenile hippocampal NG2 glia. Naspmm and JNJ showed an additive inhibition. The reversal potential of the Naspmm-sensitive responses was  $0.2 \pm 8.9$  mV, with RI =  $0.55 \pm 0.27$  mV ( $n = 21$ ,  $N = 11$ ) (Figure 4C), indicating that these currents were indeed mediated by  $\text{Ca}^{2+}$  permeable receptors. The corresponding I/V relations of JNJ-sensitive currents is outward rectifying ( $V_{\text{rev}} = -7.2 \pm 14.1$  mV, RI =  $1.28 \pm 0.36$ ,  $n = 12$ ,  $N = 6$ ) (Figure 4E). Notably, a significant proportion of the responses remained in the presence of both blockers (10  $\mu\text{M}$  JNJ:  $38.3 \pm 19.2\%$ ,  $n = 13$ ,  $N = 6$ ; 1  $\mu\text{M}$  JNJ:  $45.9 \pm 11.1\%$ ,  $n = 11$ ,  $N = 4$ ) (Figures 4F,G; Supplementary Figure 2C).

To confirm the above findings another, structurally related blocker of  $\text{Ca}^{2+}$  permeable AMPA receptors was used, IEM-1460. IEM-1460 (100  $\mu\text{M}$ ) blocked  $38.8 \pm 10.8\%$  of the kainate responses ( $V = -70$  mV,  $n = 11$ ,  $N = 4$ ). Compared to Naspmm, this blocking efficacy was lower ( $p = 0.03$ ). Subsequent application of JNJ further reduced the receptor currents (by  $20.6 \pm 9.2\%$ ,  $n = 10$ ,  $N = 4$ ) (Figure 4D). Vice versa, if JNJ was applied first, the responses were reduced by  $34.7 \pm 6.7\%$  ( $n = 7$ ;  $N = 4$ ) and additionally by  $28.2 \pm 10\%$  through IEM-1460 ( $n = 6$ ,  $N = 4$ ). Again,  $40.5 \pm 9.4\%$  ( $n = 16$ ,  $N = 4$ ) of the responses were insensitive to both inhibitors (Figure 4G). IEM-sensitive currents reversed at  $-3.9 \pm 6.1$  mV and showed inward rectification (RI =  $0.4 \pm 0.32$ ,  $n = 17$ ,  $N = 4$ ) (Figure 4E). In contrast, JNJ-sensitive currents were again outward rectifying (RI =  $1.31 \pm 0.55$ ,  $V_{\text{rev}} = -3.9 \pm 8.2$ ,  $n = 16$ ,  $N = 4$ ) (Figure 4E).

JNJ still blocked part of the Naspmm- or IEM-1460-insensitive currents. Vice versa, after initial application of JNJ, Naspmm and IEM-1460 still blocked  $\text{Ca}^{2+}$  permeable receptors. Thus, TARP  $\gamma 8$  is mainly associated with  $\text{Ca}^{2+}$ -impermeable AMPA receptors.

## Pharmacological Characterization of $\text{Ca}^{2+}$ Permeable AMPA Receptors in NG2 Glia Freshly Isolated From Mice at p60

At p60, quinine and  $\text{Ba}^{2+}$  depolarized the cells (from  $-23.6 \pm 11.5$  mV to  $-15.9 \pm 8.1$  mV) and increased the input resistance (from  $877 \pm 418$  M $\Omega$  to  $1,958 \pm 1,416$  M $\Omega$ ;  $n = 20$ ,  $N = 10$ ) (Figure 5A). Co-application of kainate and cyclothiazide induced similar inward currents as at p10 ( $191.1 \pm 182.8$  pA/pF,  $V = -70$  mV,  $n = 20$ ,  $N = 10$ ). With spermine (50  $\mu\text{M}$ ) in the pipette solution, the kainate-induced currents reversed at  $-0.5 \pm 6.0$  mV. RI was  $0.98 \pm 0.26$  ( $n = 20$ ) indicating linear I/V relationships, which differed from the outward rectifying responses seen in juvenile NG2 glia (Figures 5B,C;



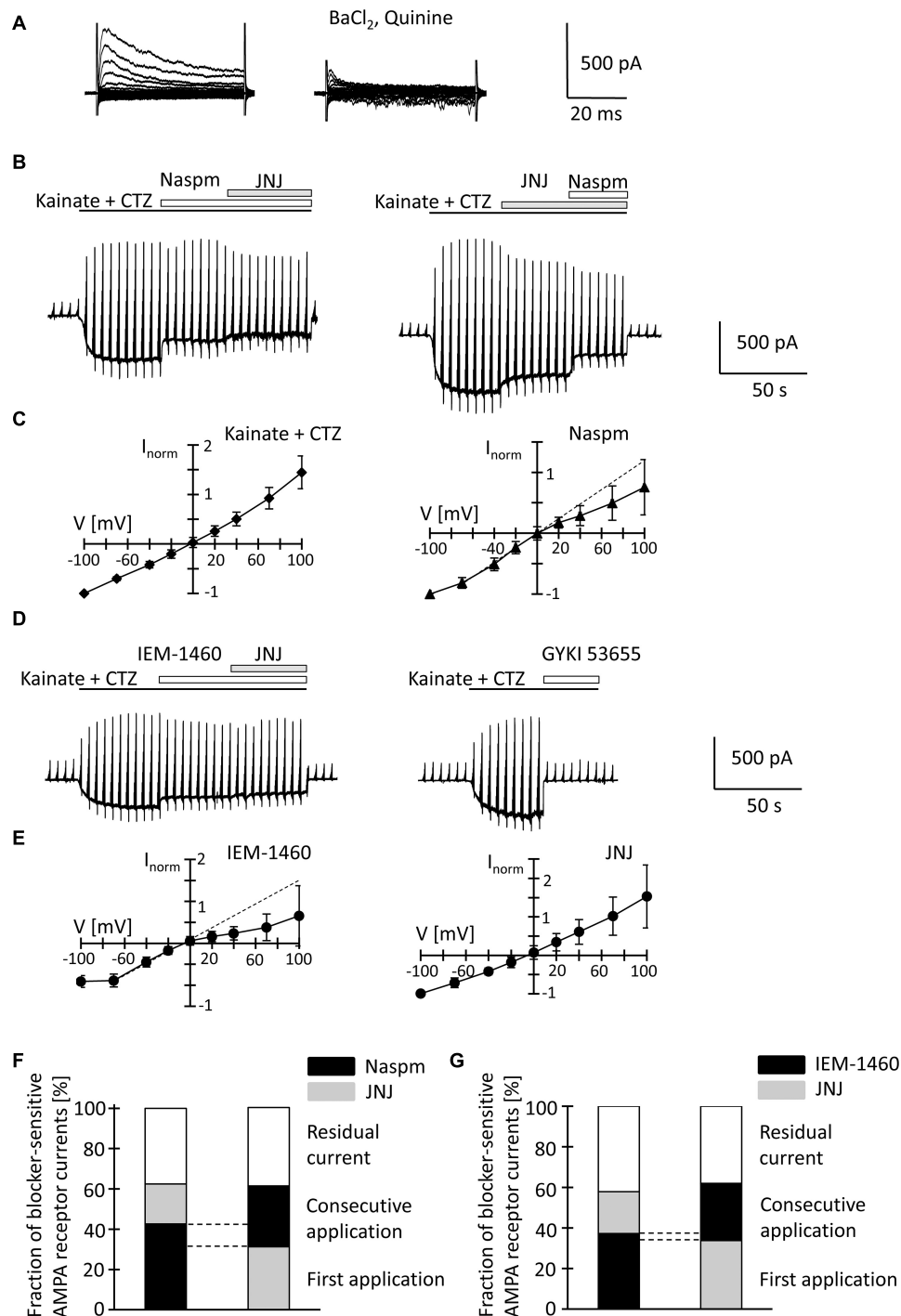


**FIGURE 4 |** Inhibition of AMPA receptor currents by blockers of Ca<sup>2+</sup> permeable receptors and a TARP  $\gamma$ 8 inhibitor in freshly isolated NG2 glia at p10.

**(A)** Membrane currents were elicited as described in **Figure 2** (left, normal bath solution; right, after adding 100  $\mu$ M quinine and 10  $\mu$ M BaCl<sub>2</sub>). **(B)** The membrane was de- and hyperpolarized as explained in **Figure 2A** and kainate (250  $\mu$ M), CTZ (100  $\mu$ M), Naspm (50  $\mu$ M) and the TARP  $\gamma$ 8 inhibitor, JNJ 55511118 (10  $\mu$ M), were applied as indicated. **(C)** shows mean I/V relations of kainate-induced current ( $n = 35$ ; left) and the Naspm-sensitive component ( $n = 21$ ; right). Currents were normalized to maximal inward currents in each cell. The blocker-sensitive currents were determined by successively calculating the difference between the current amplitude in the presence of the blocker and the amplitude in the presence of the preceding substance. **(D)** Using the protocols explained in panel **(B)**, AMPA receptor currents were elicited and blocked by adding IEM-1460 (100  $\mu$ M), JNJ (10  $\mu$ M), and GYKI 53655 (100  $\mu$ M). **(E)** Mean I/V relations of IEM-1460- ( $n = 17$ ; left) and JNJ-sensitive currents ( $n = 19$ ; right). **(F,G)** Relative fractions of AMPA receptor currents sensitive to Naspm, IEM-1460 and JNJ. The order of consecutive applications has been reversed. Overlapping sensitivity to both blockers is indicated by dashed lines. The relative respective inhibition was averaged [**(F)**  $n = 6$  and 7; **(G)**  $n = 10$  and 6, respectively]. Only those cells are shown in which both blockers could be successfully applied consecutively.

$p = 0.0005$ ). GYKI53655 almost completely blocked the responses (by  $97 \pm 5\%$ ,  $n = 6$ ,  $N = 4$ ). RI of GYKI-sensitive currents was  $1.00 \pm 0.13$  ( $V_{rev} = -2.8 \pm 8.3$  mV) (**Figure 5D**).

Naspm (50  $\mu$ M) exerted a much stronger inhibition than at p10 (by  $77.4 \pm 15.2\%$ ,  $-70$  mV,  $n = 10$ ,  $N = 6$ ,  $p = 0.002$ ). Subsequent co-application of JNJ (10  $\mu$ M) led to further reduction of the responses (by  $5.6 \pm 5.7\%$ ,  $n = 4$ ,  $N = 3$ ) (**Figure 5B**). With the blockers applied in reverse order, 10  $\mu$ M JNJ reduced currents by  $50.5 \pm 20.0\%$  ( $n = 6$ ,  $N = 3$ ) while subsequent co-application of Naspm further reduced the currents by  $44.0 \pm 24.0\%$  ( $n = 5$ ,  $N = 3$ ) (**Figure 5B**). At a concentration of 1  $\mu$ M, JNJ-induced inhibition (by  $24.4 \pm 8.7\%$ ;  $n = 10$ ,  $N = 4$ ) was weaker ( $p < 0.05$ ) (**Supplementary Figures 2B,C**), but more efficient than at p10 ( $p < 0.05$ ). Subsequent block by Naspm (50  $\mu$ M) was as efficient as after application of JNJ at the higher concentration (by  $53.8 \pm 9.7\%$ ,  $n = 9$ ,  $N = 4$ ), but stronger than at p10 ( $p = 0.01$ ). The reversal potential of Naspm-sensitive currents was  $-1.3 \pm 9.0$  mV, with RI =  $0.74 \pm 0.39$  mV ( $n = 15$ ;  $N = 7$ ), indicating that the current were partially mediated by  $\text{Ca}^{2+}$  permeable receptors. JNJ-blocked currents reversed at  $-1.4 \pm 7.1$  mV and showed outward rectification (RI =  $1.20 \pm 0.51$ ,  $n = 8$ ;  $N = 3$ ) (**Figures 5C,D**). The proportion of blocker-insensitive receptor currents was much smaller than at p10 ( $5.8 \pm 10.1\%$ ,  $n = 9$ ,  $N = 3$ ,  $p = 0.0001$ ) (**Figure 5F**). In 6/9 cells, inhibition of the responses was even virtually complete. These results indicate that AMPA receptors in NG2 glia at p60 show a higher  $\text{Ca}^{2+}$  permeability, and that JNJ may also inhibit part of the Naspm-sensitive currents.

IEM-1460 (100  $\mu$ M) inhibited  $63.1 \pm 6.4\%$  ( $V = -70$  mV,  $n = 6$ ,  $N = 3$ ) of the receptor currents, thus being more efficient than at p10 ( $p < 0.001$ ) but less efficient than Naspm at p60 ( $p = 0.028$ ). IEM-sensitive currents showed strong inward rectification (RI =  $0.30 \pm 0.31$ ,  $V_{rev} = -2.9 \pm 7.6$  mV,  $n = 12$ ,  $N = 3$ ) (**Figures 5D,E**). Subsequent co-application of JNJ exerted additional inhibition (by  $19.3 \pm 7.3\%$ ) and the JNJ-sensitive currents were again outwardly rectifying (RI =  $1.46 \pm 0.91$ ,  $V_{rev} = -1.3 \pm 7.1$ ,  $n = 12$ ) (**Figures 5D,E**). When JNJ was applied before adding IEM-1460, inhibition was  $54.7 \pm 5.4$  and  $27.2 \pm 6.1\%$  ( $n = 6$ ,  $N = 3$ ). Inhibition by JNJ was more effective than at cells at p10 ( $p = 0.00007$ ), and the proportion of currents insensitive to the co-applied blockers was lower than at the early stage (10  $\mu$ M JNJ:  $17.8 \pm 8.2\%$ ,  $n = 12$ ,  $N = 3$ ,  $p < 0.001$ ; 1  $\mu$ M JNJ:  $21.8 \pm 8.0\%$ ,  $n = 12$ ,  $N = 4$ ,  $p < 0.001$ ) (**Figure 5G** and **Supplementary Figure 2C**). In contrast to Naspm, consecutive application of IEM-1460 and JNJ showed only a small overlap (**Figures 5D,G**).

Together, the data demonstrate that extracellularly applied spermine analogs inhibit AMPA receptors in hippocampal NG2 glia. The efficiency of inhibition by Naspm and IEM-1460 was higher in NG2 glia from adult mice. Naspm and JNJ showed a partly overlapping block. Since there was almost no overlap of IEM-1460- and JNJ-mediated inhibition, it seems that Naspm also blocked some  $\text{Ca}^{2+}$  impermeable receptors. In line with the observations at p10, the data suggested that JNJ blocked  $\text{Ca}^{2+}$  impermeable receptors. Although molecular analysis revealed developmental downregulation of TARP  $\gamma 8$ , the modulatory effect of JNJ was stronger in adult NG2 glia.

## $\text{Ca}^{2+}$ Permeability of Glial AMPA Receptors

To quantify the  $\text{Ca}^{2+}$  permeability of NG2 glia AMPA receptors,  $\text{Na}^+$ -free extracellular solution with  $\text{Ca}^{2+}$  (50 mM) as the sole charge carrier was used. Kainate/CTZ induced currents in high  $\text{Ca}^{2+}$  solution, indicating  $\text{Ca}^{2+}$  permeability of the glial AMPA receptors. The permeability coefficient  $P_{\text{Ca}}/P_{\text{Cs}}$  was calculated according to the constant field equation (Mayer and Westbrook, 1987; Seifert and Steinhäuser, 1995). In juvenile mice, the ratio  $I_{\text{Ca}}/I_{\text{Na}}$  of kainate-evoked responses was  $4.1 \pm 1.2\%$  (**Figure 6A**). The I/V relations changed from a linear shape in  $\text{Na}^+$  solution to strong outward rectification in high  $\text{Ca}^{2+}$  solution (**Figure 6B**). The reversal potential of kainate/CTZ-evoked responses in high  $\text{Ca}^{2+}$  solution was  $-34.7 \pm 10.0$  mV, and the permeability ratio  $P_{\text{Ca}}/P_{\text{Cs}}$  amounted to  $0.25 \pm 0.18$  ( $n = 6$ ;  $N = 4$ ) (**Figures 6C,D**).

Since the inhibitory effects of Naspm and IEM-1460 were stronger at p60, we performed the same analysis at the older stage. Here, we found  $I_{\text{Ca}}/I_{\text{Na}} = 5.5 \pm 1.6\%$ , a reversal potential in high  $\text{Ca}^{2+}$  solution at  $-35.1 \pm 10.7$  mV, and  $P_{\text{Ca}}/P_{\text{Cs}} = 0.24 \pm 0.13$  ( $n = 6$ ;  $N = 5$ ) (**Figures 6A,C,D**). None of those parameters differed from the juvenile stage and they were in accordance with previous data (Seifert et al., 1997b). Thus, the overall  $\text{Ca}^{2+}$  permeability of the receptors was similar at both stages. However, in NG2 glia from older mice, the higher blocking efficacy of Naspm and IEM-1460 and the enhanced polyamine block indicated expression of a mosaic of  $\text{Ca}^{2+}$  permeable and impermeable receptors.

## Characterization of Postsynaptic Responses in NG2 Glia of the Hippocampal CA1 Region

Acute isolation of cells from the tissue shears off many of the fine processes. Thus, the properties reported above should have largely represented receptors located close to the soma, while previous work found them mostly at postsynapses on the processes (Haberlandt et al., 2011). Therefore, we tested the sensitivity of postsynaptic currents of NG2 glia to Naspm and IEM-1460. Stimulation of Schaffer collaterals was performed in the presence of cyclothiazide (100  $\mu$ M) and picrotoxin (100  $\mu$ M). Naspm (50  $\mu$ M) and IEM-1460 (100  $\mu$ M) similarly reduced synaptic currents (p10, by  $31.2 \pm 14.4\%$ ,  $n = 6$ ,  $N = 4$  and  $41.1 \pm 16.8\%$ ,  $n = 5$ ,  $N = 3$ ; p60, by  $31.5 \pm 10.8\%$ ,  $n = 7$ ,  $N = 4$  and  $32.8 \pm 4.8\%$ ,  $n = 6$ ,  $N = 5$ ) (**Figures 7A–D**). The efficiency of inhibition was similar for IEM-1460 and Naspm and for both developmental stages. Thus, after minimal stimulation at a frequency 0.1 Hz, both blockers of  $\text{Ca}^{2+}$  permeable receptors inhibited evoked synaptic AMPA receptor responses.

## DISCUSSION

Previous functional analyses showed that early after birth, NG2 glia express  $\text{Ca}^{2+}$  permeable AMPA receptors (Seifert et al., 2003), although further details, particularly the expression of auxiliary subunits were not known. Here we addressed the question whether NG2 glial cells in the hippocampus express

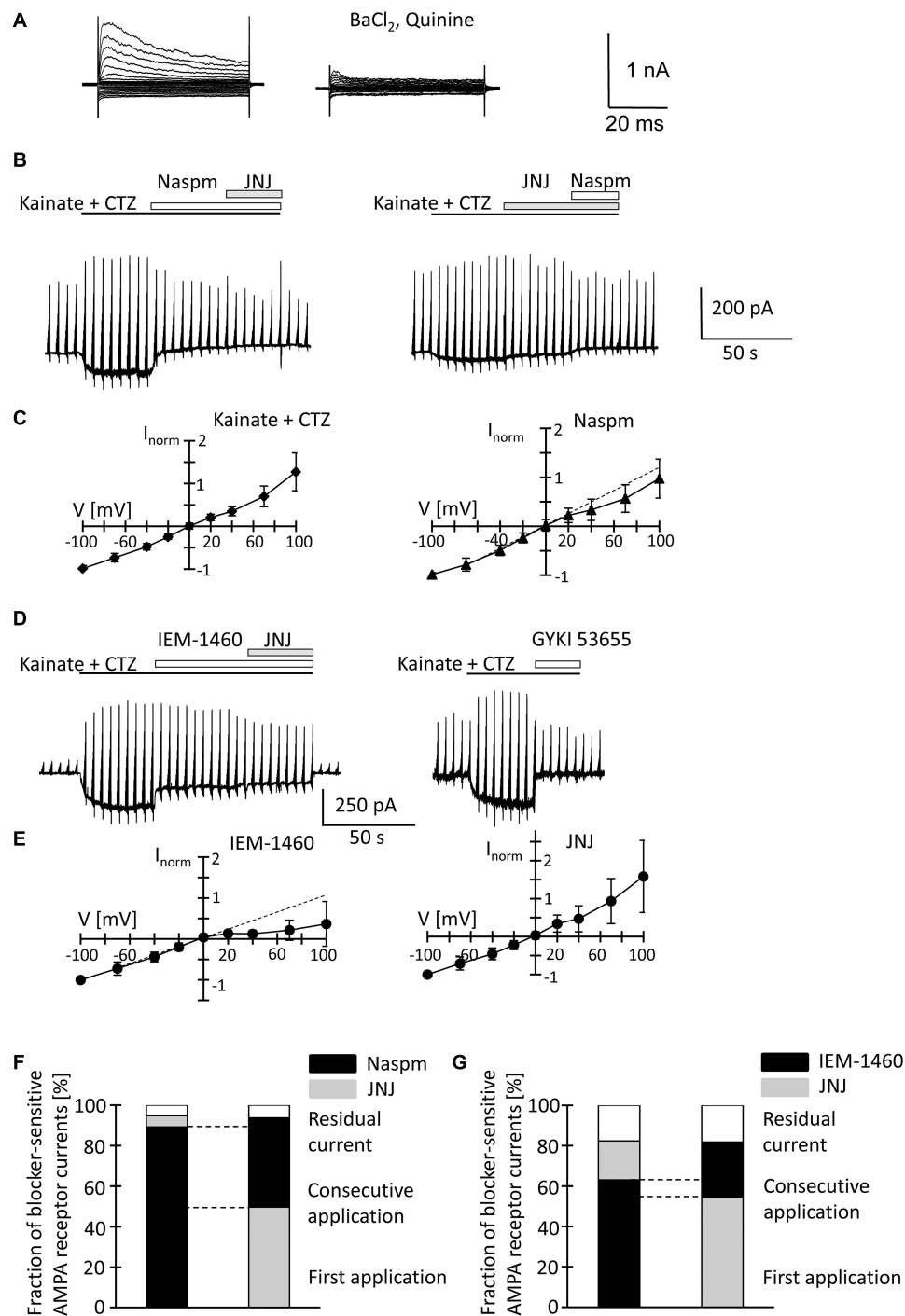


**FIGURE 5 |** Inhibition of AMPA receptor currents by blockers of Ca<sup>2+</sup> permeable receptors and a TARP  $\gamma$ 8 inhibitor in freshly isolated NG2 glia at p60. **(A,B,D)** Stimulation and drug application were as described for p10 (**Figure 4**). **(C,E)** I/V relations for responses evoked by kainate + CTZ ( $n = 20$ , left), Naspm- ( $n = 15$ ), IEM-1460- ( $n = 12$ ), and JNJ-sensitive currents ( $n = 8$ ). **(F,G)** Relative current inhibition was only compared for those cells in which both blockers could be successfully applied consecutively [**F**]  $n = 4$  and 5; [**G**]  $n = 6$  and 6].

TARP and CNIH subunits and whether expression changes during postnatal maturation. The data demonstrate abundant expression of TARPs  $\gamma$ 4,  $\gamma$ 7,  $\gamma$ 8, and CNIH-2, which declined by

maturity. Functional analyses using spermine analogs suggested enhanced expression of Ca<sup>2+</sup> permeable receptors in NG2 glia of the adult hippocampus.

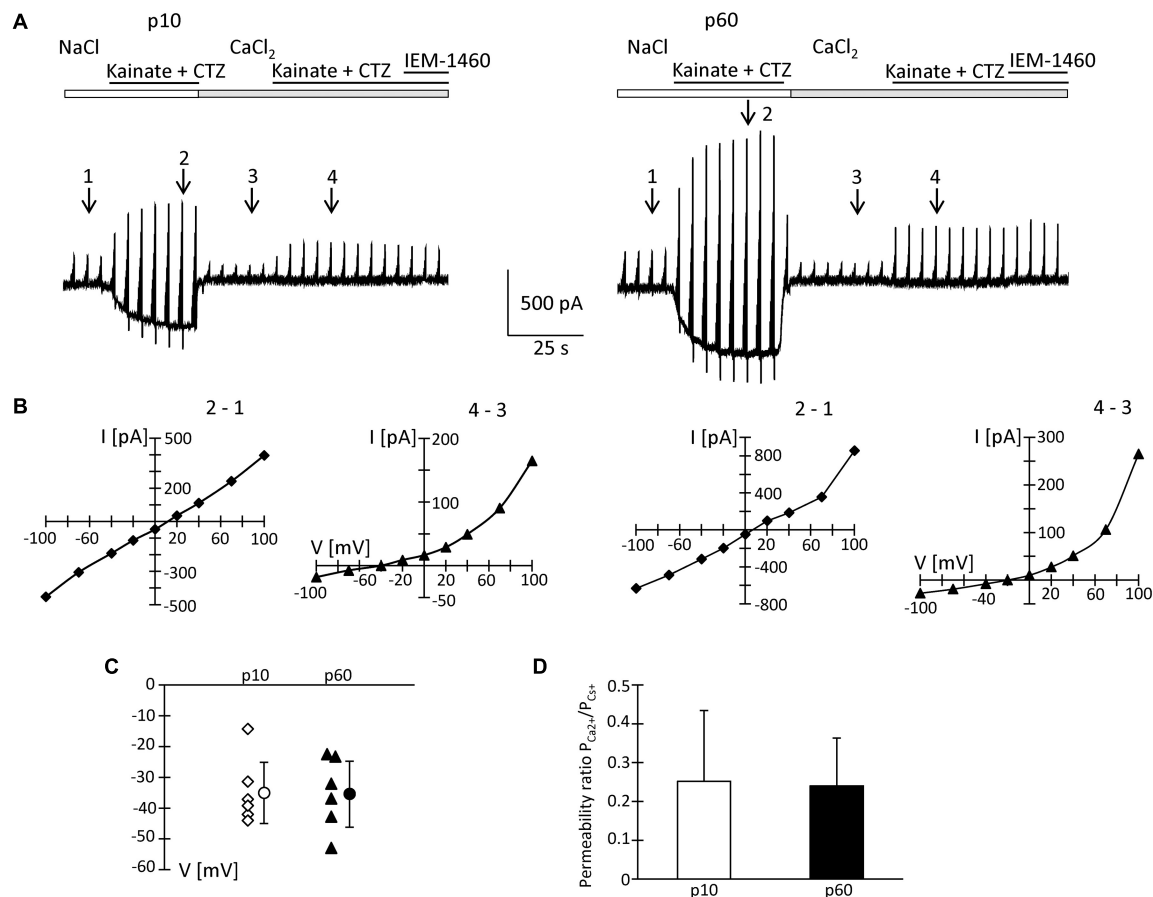


**FIGURE 6 |**  $Ca^{2+}$  permeability of kainate-activated membrane currents. **(A)** Receptor currents were elicited by co-applying kainate (250  $\mu$ M) and CTZ (100  $\mu$ M) to NG2 glia freshly isolated at p10 and p60 (cf. **Figures 2, 4** for stimulation protocols). After initial recording in standard bath solution, high  $CaCl_2$  (50 mM) solution was applied. At holding potential, kainate/CTZ induced inward currents of 325 and 500 pA (standard solution) or 15 and 20 pA (high  $Ca^{2+}$  solution) at p10 and p60, respectively. **(B)** I/V relations of the cells shown in panel **(A)** were determined by subtracting the current amplitudes at corresponding voltages at the indicated time points (in standard solution: 2–1; in  $Ca^{2+}$  solution: 4–3). **(C)** Reversal potentials (V) of receptor currents obtained in high  $CaCl_2$  solution were plotted as a function of postnatal age. Bars indicate mean  $\pm$  SD ( $n = 6$  for each age group). **(D)** Bar graph give the ratio  $P_{Ca^{2+}}/P_{Cs^{+}}$  with mean  $\pm$  SD of AMPA receptor currents elicited in high  $Ca^{2+}$  solution. In these experiments, intracellular  $K^+$  was replaced by  $Cs^+$  and TEA.

## TARP and CNIH Expression in Glial Cells

The first auxiliary transmembrane protein described to interact with AMPA receptors was stargazin, later termed TARP  $\gamma 2$ , which is responsible for surface expression of AMPA receptors in cerebellar granule cells (Chen et al., 2000). TARP  $\gamma 2$  has a PDZ-binding site, which interacts with PSD-95 and also accounts for synaptic clustering (Schnell et al., 2002). While TARP  $\gamma 2$  is abundantly expressed by cerebellar granule and Purkinje cells, it is less present in other brain regions. Meanwhile, a whole gene family of TARPs was identified (Tomita et al., 2003). Because NG2 glia receives synaptic input from neurons through their AMPA receptors the question of glial TARP expression emerged. TARP  $\gamma 4$  was found in glial cells of cerebellum, hippocampus, and neocortex (Tomita et al., 2003; Fukaya et al., 2005). Our molecular analysis extended these findings by revealing that in the hippocampus, NG2 glia express TARPs, with TARP  $\gamma 4$  being most abundant, followed by TARPs  $\gamma 7$ ,  $\gamma 8$ , and CNIH-2. Predominant expression of TARPs  $\gamma 4$  and  $\gamma 7$  was also found with

RNA-Seq analysis (Larson et al., 2016). A characteristic feature of  $\gamma 4$  is its strong expression in the embryonic and early postnatal brain and subsequent down-regulation. Expression of CNIH-2 similarly decreased during development, both on the single cell level and in FAC-sorted NG2 glia.

## Consequences of TARP/CNIH Expression for AMPA Receptor Function

In our previous work we have reported molecular and functional properties of AMPA receptors in NG2 glia of the juvenile hippocampus, including  $Ca^{2+}$  permeability, splicing, and desensitization kinetics (Seifert and Steinhäuser, 1995; Seifert et al., 1997a,b; Matthias et al., 2003). Some of the earlier data appeared contradictory, e.g., the finding that enhanced expression of GluA2 flip did not entail changes in receptor desensitization (Seifert et al., 2003). The heterogeneous expression of auxiliary subunits identified in the present



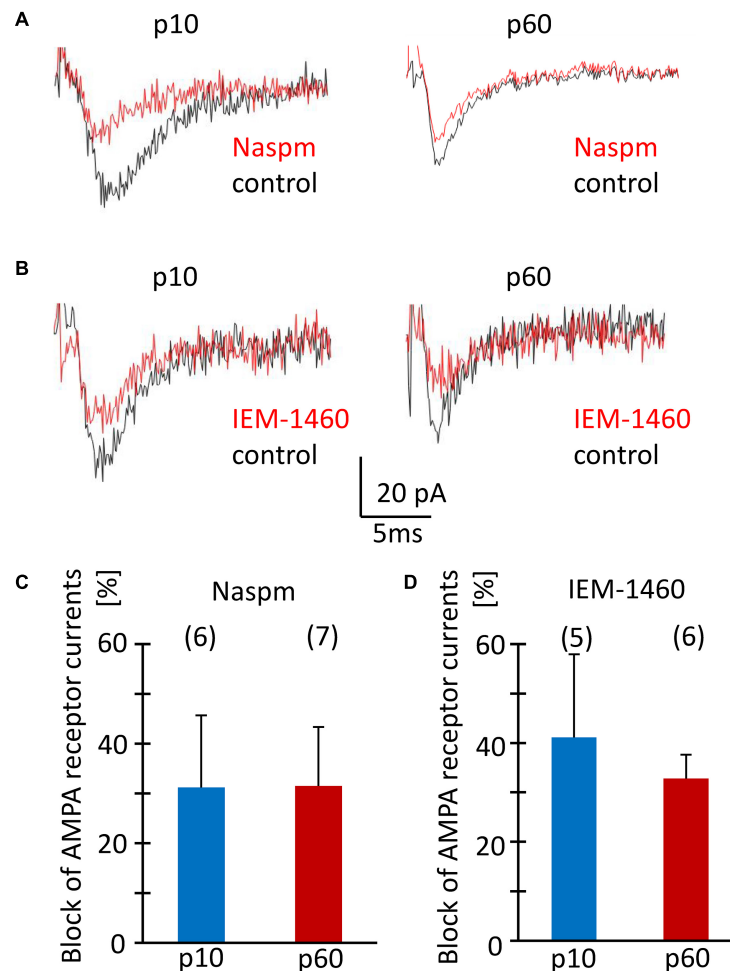


**FIGURE 7 |** Sensitivity to Naspm and IEM-1460 of synaptic AMPA receptor currents in NG2 glia *in situ*. **(A,B)** Stimulation of Schaffer collaterals in the stratum radiatum of the CA1 region elicited ePSCs in NG2 glial cells (holding potential  $-70$  mV). Bath solution contained picrotoxin ( $100 \mu\text{M}$ ) to inhibit  $\text{GABA}_A$  receptors, and CTZ ( $100 \mu\text{M}$ ) to increase AMPA receptor responses. Bath application of Naspm ( $50 \mu\text{M}$ ) or IEM-1460 ( $100 \mu\text{M}$ ) reduced ePSCs. **(C,D)** Mean and SD of peak ePSC inhibition by Naspm and IEM-1460 in NG2 glia of slices from mice at p10 and p60. Number of cells is given in parentheses. The pipette solution contained CsCl to block  $\text{K}^+$  channels. The sensitivity to Naspm and IEM-1460 did not change during development (two-tailed *t*-test).

study might explain this apparent discrepancy, because they profoundly affect receptor function.

In heterologous expression systems, co-expression of TARP  $\gamma 4$  with GluA2 conferred high kainate efficacy to the receptor complex, slowed its desensitization and favored incomplete desensitization while rectification of the I/V relations was not altered (Korber et al., 2007). TARP  $\gamma 7$  is highly expressed in the cerebellum where it binds to the scaffold protein PSD-95 and supports synaptic targeting of AMPA receptors (Kato et al., 2007). It is tempting to speculate that TARP  $\gamma 7$  has a similar role in NG2 glia where it is abundantly expressed according to our data. TARP  $\gamma 8$  is highly expressed in the hippocampus, both at asymmetrical postsynaptic and extrasynaptic sites. Deletion of this subunit reduced AMPA receptor density, synaptic localization and impaired the induction of long term potentiation (LTP) (Rouach et al., 2005; Fukaya et al., 2006). Both TARP  $\gamma 7$  and  $\gamma 8$  interact with AMPA receptors to increase their CTZ

potentiation and kainate efficacy (Gill et al., 2011). TARP  $\gamma 7$  modulates GluA2 containing receptors in a subunit composition specific manner (Kato et al., 2008). In contrast to hippocampal neurons, expression of TARP  $\gamma 8$  in NG2 glia was lower than TARP  $\gamma 4$  and  $\gamma 7$ , and strongly downregulated until adulthood.

While CNIH-2 is expressed in astrocytes of the hippocampus (Schwenk et al., 2009) we found it also in the vast majority of NG2 glial cells. This subunit regulates trafficking of the receptors, slows channel gating and increases CTZ potency in cells co-expressing TARP  $\gamma 8$  (Schwenk et al., 2009; Shi et al., 2010; Gill et al., 2012). Expression of TARPs and CNIH-2 can decrease the polyamine block (Coombs et al., 2012). The latter study has also found CNIH-2 protein in cultured optic nerve oligodendroglial precursor cells. In heterologous expression systems, TARPs  $\gamma 4$ ,  $\gamma 7$ , and  $\gamma 8$  mediate a recovery from desensitization called resensitization, which is abrogated by CNIH-2 (Kato et al., 2010). The lack of resensitization in NG2 glia

(Seifert and Steinhäuser, 1995; Seifert et al., 1997b) might thus be due to abundant expression of CNIH-2 as demonstrated in the present study.

## Pharmacological Determination of $\text{Ca}^{2+}$ Permeability of Glial AMPA Receptors

To further characterize the  $\text{Ca}^{2+}$  permeability of AMPA receptors in NG2 glia, polyamine analogs were used, which recognize binding sites within the pore. Transcript expression of GluA1-4 did not change during postnatal development, with GluA2 being the most abundant subunit. GluA2 limits the  $\text{Ca}^{2+}$  permeability of the receptors and prevents polyamine binding (Bowie and Mayer, 1995; Washburn et al., 1997). TARPs and CNIH2 also attenuate polyamine block of  $\text{Ca}^{2+}$  permeable receptors (Coombs et al., 2012; Soto et al., 2014). Expression of the latter might have prevented the polyamine block in our experiments.

In NG2 glia of mice early after birth (up to p5), we observed inward rectifying receptor currents in the presence of intracellular spermine, indicating expression of  $\text{Ca}^{2+}$  permeable receptors, which disappeared by p10 (Seifert et al., 2003). In rat, however, spermine sensitivity was still observed 2 weeks postnatally (Bergles et al., 2000). Naspmm and intracellular spermine also inhibited EPSCs in NG2 glia of rat hippocampus, and the efficiency of inhibition declined with increasing age (Ge et al., 2006) while in mice, we observed no developmental changes. This species difference might be due to different contributions of TARPs/CNIHs to the glial AMPA receptor complexes. The latter study also revealed a physiological significance of AMPA-receptor-mediated  $\text{Ca}^{2+}$  influx, by demonstrating long-term potentiation at neuron-NG2 glia synapses at early developmental stages.

A  $\text{Ca}^{2+}$  permeability of AMPA receptors in juvenile NG2 glia has already been demonstrated with  $\text{Ca}^{2+}$  imaging (Jabs et al., 1994). In the present study, the inward rectifying I/V relations of Naspmm- and IEM-1460-sensitive currents and analyses in solutions with  $\text{Ca}^{2+}$  as the sole charge carrier confirmed functional expression of  $\text{Ca}^{2+}$  permeable receptors. Masking of intracellular spermine block of outward currents through  $\text{Ca}^{2+}$  permeable AMPA receptors, as observed here, was previously demonstrated in heterologous expression systems and cultured cortical glial cells (Meucci and Miller, 1998), and might hint at variable contributions of GluA2 to the tetrameric channels [reviewed by Bowie (2012)]. The increased extracellular polyamine block of receptor currents at negative voltages, we have observed at p60, indicated enhanced expression of  $\text{Ca}^{2+}$  permeable AMPA receptors in mature NG2 glia. A recent publication demonstrated that intracellular Naspmm confers complete and TARP-independent block to  $\text{Ca}^{2+}$  permeable, GluA2-lacking AMPA receptors (Coombs et al., 2021). In our study, intracellular Naspmm led to inwardly rectifying I/V relations of AMPA receptor responses in 8/18 NG2 glia at p60 while at p10, 17/18 cells showed outward rectification. The inhibitory effect of Naspmm and IEM-1460 on synaptic currents did not change during development. Block of evoked synaptic responses may have indicated that  $\text{Ca}^{2+}$  permeable AMPA receptors were located on postsynaptic glial membranes (Lujan et al., 2019).

Some anti-epileptic drugs, for example perampanel (Chappell et al., 2002; French et al., 2012), target AMPA receptors. However, AMPA receptor blockers harbor many undesired side effects, because of their unspecific dampening of excitation throughout the brain. The relative brain region- and/or cell type-specific expression of TARPs, for example TARP  $\gamma 2$  in the cerebellum, TARP  $\gamma 8$  in the hippocampus, TARP  $\gamma 4$  in glial cells, might allow for the development of new drugs with better specificity. To modulate excitatory transmission in the hippocampus, the TARP  $\gamma 8$  specific antagonists LY3130481 and JNJ-55511118 were developed, which leave AMPA receptor complexes lacking this auxiliary subunit unaffected (Gardinier et al., 2016; Maher et al., 2016). These antagonists inhibit excitation in the cortex and hippocampus, dampen cortical EEG activity and have anticonvulsant effects, with only mild motor and learning deficits (Kato et al., 2016; Maher et al., 2016). In our study, TARP  $\gamma 8$  was downregulated during maturation, as evidenced by its lower incidence in both single cells and after bulk isolation. Unexpectedly, however, modulation by JNJ was more pronounced in NG2 glia from older mice. This result might be explained by interactions of different TARPs/CNIH-2 with the receptor complex (Schober et al., 2011).

## CONCLUSION

NG2 cells in hippocampus primarily express the TARP subunits  $\gamma 4$ ,  $\gamma 7$ , and  $\gamma 8$  as well as CNIH-2. These auxiliary subunits may slow receptor desensitization, increase kainate efficacy and reduce the sensitivity of  $\text{Ca}^{2+}$  permeable AMPA receptors to endogenous polyamines.  $\text{Ca}^{2+}$  influx through somatic AMPA receptors may regulate proliferation and differentiation (Chen et al., 2018), and deletion of AMPA receptors in NG2 glia reduces the survival of oligodendrocytes (Kougioumtzidou et al., 2017). Systematic analysis of mice with deletions of AMPA receptor subunits in NG2 glia may help to decipher its specific role in neural signaling.

## DATA AVAILABILITY STATEMENT

The original contributions presented in the study are included in the article/**Supplementary Material**, further inquiries can be directed to the corresponding author/s.

## ETHICS STATEMENT

Ethical review and approval was not required for the animal study because we only performed organ harvesting after anesthesia.

## AUTHOR CONTRIBUTIONS

CS and GS designed and supervised the experiments. SH, DT, SP, AT, RJ, and GS performed and/or analyzed the experiments. SH, GS, and CS wrote the manuscript. All authors contributed to the article and approved the submitted version.

## FUNDING

This work was supported by grants from the Deutsche Forschungsgemeinschaft (STE 552/5, SE 774/6).

## SUPPLEMENTARY MATERIAL

The Supplementary Material for this article can be found online at: <https://www.frontiersin.org/articles/10.3389/fncel.2021.669717/full#supplementary-material>

## REFERENCES

- Barron, T., and Kim, J. H. (2019). Neuronal input triggers Ca(2+) influx through AMPA receptors and voltage-gated Ca(2+) channels in oligodendrocytes. *Glia* 10, 1922–1932. doi: 10.1002/glia.23670
- Bats, C., Soto, D., Studniarczyk, D., Farrant, M., and Cull-Candy, S. G. (2012). Channel properties reveal differential expression of TARPed and TARPless AMPARs in stargazer neurons. *Nat. Neurosci.* 6, 853–861. doi: 10.1038/nn.3107
- Bergles, D. E., Roberts, J. D., Somogyi, P., and Jahr, C. E. (2000). Glutamatergic synapses on oligodendrocyte precursor cells in the hippocampus. *Nature* 6783, 187–191. doi: 10.1038/35012083
- Bowie, D. (2012). Redefining the classification of AMPA-selective ionotropic glutamate receptors. *J. Physiol.* 590, 49–61. doi: 10.1113/jphysiol.2011.221689
- Bowie, D., and Mayer, M. L. (1995). Inward rectification of both AMPA and kainate subtype glutamate receptors generated by polyamine-mediated ion channel block. *Neuron* 15, 453–462. doi: 10.1016/0896-6273(95)90049-7
- Cahoy, J. D., Emery, B., Kaushal, A., Foo, L. C., Zamanian, J. L., Christopherson, K. S., et al. (2008). A transcriptome database for astrocytes, neurons, and oligodendrocytes: a new resource for understanding brain development and function. *J. Neurosci.* 1, 264–278. doi: 10.1523/jneurosci.4178-07.2008
- Chappell, A. S., Sander, J. W., Brodie, M. J., Chadwick, D., Lledo, A., Zhang, D., et al. (2002). A crossover, add-on trial of talampanel in patients with refractory partial seizures. *Neurology* 11, 1680–1682. doi: 10.1212/wnl.58.11.1680
- Chen, L., Chetkovich, D. M., Petralia, R. S., Sweeney, N. T., Kawasaki, Y., Wenthold, R. J., et al. (2000). Stargazin regulates synaptic targeting of AMPA receptors by two distinct mechanisms. *Nature* 6815, 936–943. doi: 10.1038/35050030
- Chen, T. J., Kula, B., Nagy, B., Barzan, R., Gall, A., Ehrlich, I., et al. (2018). In vivo regulation of oligodendrocyte precursor cell proliferation and differentiation by the AMPA-receptor subunit GluA2. *Cell Rep.* 4, 852–861. doi: 10.1016/j.celrep.2018.09.066
- Coombs, I. D., Bats, C., Sexton, C. A., Cull-Candy, S. G., and Farrant, M. (2021). Intracellular NASPM allows an unambiguous functional measure of GluA2-lacking calcium-permeable AMPA receptor prevalence. *bioRxiv [preprint]*. doi: 10.1101/2021.02.18.431828
- Coombs, I. D., Soto, D., Zonouzi, M., Renzi, M., Shelley, C., Farrant, M., et al. (2012). Cornichons modify channel properties of recombinant and glial AMPA receptors. *J. Neurosci.* 29, 9796–9804. doi: 10.1523/jneurosci.0345-12.2012
- Donevan, S. D., and Rogawski, M. A. (1995). Intracellular polyamines mediate inward rectification of Ca2+-permeable  $\alpha$ -amino-3-hydroxy-5-methyl-4-isoxazolepropionic acid receptors. *Proc. Natl. Acad. Sci. USA.* 96, 9298–9302. doi: 10.1073/pnas.92.20.9298
- French, J. A., Krauss, G. L., Biton, V., Squillacote, D., Yang, H., Laurenza, A., et al. (2012). Adjunctive perampanel for refractory partial-onset seizures: randomized phase III study 304. *Neurology* 6, 589–596. doi: 10.1212/wnl.0b013e3182635735
- Fukaya, M., Tsujita, M., Yamazaki, M., Kushiya, E., Abe, M., Akashi, K., et al. (2006). Abundant distribution of TARP gamma-8 in synaptic and extrasynaptic surface of hippocampal neurons and its major role in AMPA receptor expression on spines and dendrites. *Eur. J. Neurosci.* 8, 2177–2190. doi: 10.1111/j.1460-9568.2006.05081.x
- Fukaya, M., Yamazaki, M., Sakimura, K., and Watanabe, M. (2005). Spatial diversity in gene expression for VDCCgamma subunit family in developing and adult mouse brains. *Neurosci. Res.* 4, 376–383. doi: 10.1016/j.neures.2005.08.009
- Gardinier, K. M., Gernert, D. L., Porter, W. J., Reel, J. K., Ornstein, P. L., Spinazze, P., et al. (2016). Discovery of the First  $\alpha$ -Amino-3-hydroxy-5-methyl-4-isoxazolepropionic acid (AMPA) receptor antagonist dependent upon transmembrane AMPA receptor regulatory protein (TARP) gamma-8. *J. Med. Chem.* 10, 4753–4768.
- Ge, W. P., Yang, X. J., Zhang, Z., Wang, H. K., Shen, W., Deng, Q. D., et al. (2006). Long-term potentiation of neuron-glia synapses mediated by Ca2+-permeable AMPA receptors. *Science* 5779, 1533–1537. doi: 10.1126/science.1124669
- Gill, M. B., Kato, A. S., Roberts, M. F., Yu, H., Wang, H., Tomita, S., et al. (2011). Cornichon-2 modulates AMPA receptor-transmembrane AMPA receptor regulatory protein assembly to dictate gating and pharmacology. *J. Neurosci.* 18, 6928–6938. doi: 10.1523/jneurosci.6271-10.2011
- Gill, M. B., Kato, A. S., Wang, H., and Bredt, D. S. (2012). AMPA receptor modulation by cornichon-2 dictated by transmembrane AMPA receptor regulatory protein isoform. *Eur. J. Neurosci.* 2, 182–194. doi: 10.1111/j.1460-9568.2011.07948.x
- Haberlandt, C., Derouiche, A., Wyczynski, A., Haseleu, J., Pohle, J., Karram, K., et al. (2011). Gray matter NG2 cells display multiple Ca-signaling pathways and highly motile processes. *PLoS One* 3:e17575. doi: 10.1371/journal.pone.0017575
- Jabs, R., Kirchhoff, F., Kettenmann, H., and Steinhäuser, C. (1994). Kainate activates Ca2+-permeable glutamate receptors and blocks voltage-gated K+ currents in glial cells of mouse hippocampal slices. *Pflügers Arch.* 42, 310–319. doi: 10.1007/bf00374787
- Jabs, R., Pivneva, T., Hüttmann, K., Wyczynski, A., Nolte, C., Kettenmann, H., et al. (2005). Synaptic transmission onto hippocampal glial cells with hGFAP promoter activity. *J. Cell Sci.* 16, 3791–3803. doi: 10.1242/jcs.02515
- Jackson, A. C., and Nicoll, R. A. (2011). The expanding social network of ionotropic glutamate receptors: TARPs and other transmembrane auxiliary subunits. *Neuron* 2, 178–199. doi: 10.1016/j.neuron.2011.04.007
- Jackson, A. C., Milstein, A. D., Soto, D., Farrant, M., Cull-Candy, S. G., and Nicoll, R. A. (2011). Probing TARP modulation of AMPA receptor conductance with polyamine toxins. *J. Neurosci.* 20, 7511–7520. doi: 10.1523/jneurosci.6688-10.2011
- Kamboj, S. K., Swanson, G. T., and Cull-Candy, S. G. (1995). Intracellular spermine confers rectification on rat calcium-permeable AMPA and kainate receptors. *J. Physiol.* 486, 297–303. doi: 10.1113/jphysiol.1995.sp020812
- Karram, K., Goebels, S., Schwab, M., Jennissen, K., Seifert, G., Steinhäuser, C., et al. (2008). NG2-expressing cells in the nervous system revealed by the NG2-EYFP-knockin mouse. *Genesis* 12, 743–757. doi: 10.1002/dvg.20440
- Kato, A. S., Burris, K. D., Gardinier, K. M., Gernert, D. L., Porter, W. J., Reel, J., et al. (2016). Forebrain-selective AMPA-receptor antagonism guided by TARP

- gamma-8 as an antiepileptic mechanism. *Nat. Med.* 12, 1496–1501. doi: 10.1038/nm.4221
- Kato, A. S., Gill, M. B., Ho, M. T., Yu, H., Tu, Y., Siuda, E. R., et al. (2010). Hippocampal AMPA receptor gating controlled by both TARP and cornichon proteins. *Neuron* 6, 1082–1096. doi: 10.1016/j.neuron.2010.11.026
- Kato, A. S., Siuda, E. R., Nisenbaum, E. S., and Bredt, D. S. (2008). AMPA receptor subunit-specific regulation by a distinct family of type II TARPs. *Neuron* 6, 986–996. doi: 10.1016/j.neuron.2008.07.034
- Kato, A. S., Zhou, W., Milstein, A. D., Knierman, M. D., Siuda, E. R., Dotzla, J. E., et al. (2007). New transmembrane AMPA receptor regulatory protein isoform, gamma-7, differentially regulates AMPA receptors. *J. Neurosci.* 18, 4969–4977. doi: 10.1523/jneurosci.5561-06.2007
- Koh, D.-S., Burnashev, N., and Jonas, P. (1995). Block of native Ca<sup>2+</sup>-permeable AMPA receptors in rat brain by intracellular polyamines generates double rectification. *J. Physiol.* 486, 305–312. doi: 10.1113/jphysiol.1995.sp020813
- Koike, M., Iino, M., and Ozawa, S. (1997). Blocking effect of 1-naphthyl acetyl spermine on Ca<sup>2+</sup>-permeable AMPA receptors in cultured rat hippocampal neurons. *Neurosci. Res.* 1, 27–36. doi: 10.1016/s0168-0102(97)00067-9
- Korber, C., Werner, M., Kott, S., Ma, Z. L., and Hollmann, M. (2007). The transmembrane AMPA receptor regulatory protein gamma 4 is a more effective modulator of AMPA receptor function than stargazin (gamma 2). *J. Neurosci.* 31, 8442–8447. doi: 10.1523/jneurosci.0424-07.2007
- Kott, S., Sager, C., Tapken, D., Werner, M., and Hollmann, M. (2009). Comparative analysis of the pharmacology of GluR1 in complex with transmembrane AMPA receptor regulatory proteins gamma2, gamma3, gamma4, and gamma8. *Neuroscience* 1, 78–88. doi: 10.1016/j.neuroscience.2007.12.047
- Kougioumtzidou, E., Shimizu, T., Hamilton, N. B., Tohyama, K., Sprengel, R., Monyer, H., et al. (2017). Signalling through AMPA receptors on oligodendrocyte precursors promotes myelination by enhancing oligodendrocyte survival. *Elife* 6:e28080.
- Kukley, M., Nishiyama, A., and Dietrich, D. (2010). The fate of synaptic input to NG2 glial cells: neurons specifically downregulate transmitter release onto differentiating oligodendroglial cells. *J. Neurosci.* 24, 8320–8331. doi: 10.1523/jneurosci.0854-10.2010
- Larson, V. A., Zhang, Y., and Bergles, D. E. (2016). Electrophysiological properties of NG2(+) cells: matching physiological studies with gene expression profiles. *Brain Res.* 638, 138–160. doi: 10.1016/j.brainres.2015.09.010
- Lujan, B., Dagostin, A., and von, G. H. (2019). Presynaptic diversity revealed by Ca(2+)-Permeable AMPA receptors at the calyx of held synapse. *J. Neurosci.* 16, 2981–2994. doi: 10.1523/jneurosci.2565-18.2019
- Magazani, L. G., Buldakova, S. L., Samoilova, M. V., Gmiro, V. E., Mellor, I. R., Usherwood, P. N. (1997). Block of open channels of recombinant AMPA receptors and native AMPA/kainate receptors by adamantane derivatives. *J. Physiol.* 505, 655–663. doi: 10.1111/j.1469-7793.1997.655ba.x
- Maher, M. P., Matta, J. A., Gu, S., Seierstad, M., and Bredt, D. S. (2017). Getting a handle on neuropharmacology by targeting receptor-associated proteins. *Neuron* 5, 989–1001. doi: 10.1016/j.neuron.2017.10.001
- Maher, M. P., Wu, N., Ravula, S., Ameriks, M. K., Savall, B. M., Liu, C., et al. (2016). Discovery and characterization of AMPA receptor modulators selective for TARP-gamma8. *J. Pharmacol. Exp. Ther.* 2, 394–414.
- Mangin, J. M., Kunze, A., Chittajallu, R., and Gallo, V. (2008). Satellite NG2 progenitor cells share common glutamatergic inputs with associated interneurons in the mouse dentate gyrus. *J. Neurosci.* 30, 7610–7623. doi: 10.1523/jneurosci.1355-08.2008
- Matthias, K., Kirchhoff, F., Seifert, G., Hüttmann, K., Matyash, M., Kettenmann, H., et al. (2003). Segregated expression of AMPA-type glutamate receptors and glutamate transporters defines distinct astrocyte populations in the mouse hippocampus. *J. Neurosci.* 5, 1750–1758. doi: 10.1523/jneurosci.23-05-01750.2003
- Mauric, V., Molders, A., Harmel, N., Heimrich, B., Sergeeva, O. A., and Klocker, N. (2013). Ontogeny repeats the phylogenetic recruitment of the cargo exporter cornichon into AMPA receptor signaling complexes. *Mol. Cell Neurosci.* 56, 10–17. doi: 10.1016/j.mcn.2013.02.001
- Mayer, M. L., and Westbrook, G. L. (1987). Permeation and block of NMDA acid receptor channels by divalent cations in mouse cultured central neurones. *J. Physiol.* 394, 501–527. doi: 10.1113/jphysiol.1987.sp016883
- Meucci, O., and Miller, R. J. (1998). Dissociation between the Joro spider toxin sensitivity of recombinant  $\alpha$ -amino-3-hydroxy-5-methyl-4-isoxazolepropionic acid receptors and their ability to increase intracellular calcium. *Neuropharmacology* 37, 1431–1443. doi: 10.1016/s0028-3908(98)00147-6
- Moshrefi-Ravasdjani, B., Dublin, P., Seifert, G., Jennissen, K., Steinhäuser, C., Kafitz, K. W., et al. (2017). Changes in the proliferative capacity of NG2 cell subpopulations during postnatal development of the mouse hippocampus. *Brain Struct. Funct.* 2, 831–847. doi: 10.1007/s00429-016-1249-2
- Passlick, S., Trotter, J., Seifert, G., Steinhäuser, C., and Jabs, R. (2016). The NG2 protein is not required for glutamatergic Neuron-NG2 cell synaptic signaling. *Cereb. Cortex* 1, 51–57. doi: 10.1093/cercor/bhu171
- Rouach, N., Byrd, K., Petralia, R. S., Elias, G. M., Adesnik, H., Tomita, S., et al. (2005). TARP gamma-8 controls hippocampal AMPA receptor number, distribution and synaptic plasticity. *Nat. Neurosci.* 11, 1525–1533. doi: 10.1038/nn1551
- Saab, A. S., Neumeyer, A., Jahn, H. M., Cupido, A., Simek, A. A., Boele, H. J., et al. (2012). Bergmann glial AMPA receptors are required for fine motor coordination. *Science* 6095, 749–753. doi: 10.1126/science.1221140
- Schnell, E., Sizemore, M., Karimzadegan, S., Chen, L., Bredt, D. S., and Nicoll, R. A. (2002). Direct interactions between PSD-95 and stargazin control synaptic AMPA receptor number. *Proc. Natl. Acad. Sci. U. S. A.* 21, 13902–13907. doi: 10.1073/pnas.172511199
- Schober, D. A., Gill, M. B., Yu, H., Gernert, D. L., Jeffries, M. W., Ornstein, P. L., et al. (2011). Transmembrane AMPA receptor regulatory proteins and cornichon-2 allosterically regulate AMPA receptor antagonists and potentiators. *J. Biol. Chem.* 15, 13134–13142. doi: 10.1074/jbc.m110.212522
- Schwenk, J., Harmel, N., Zolles, G., Bildl, W., Kulik, A., Heimrich, B., et al. (2009). Functional proteomics identify cornichon proteins as auxiliary subunits of AMPA receptors. *Science* 5919, 1313–1319. doi: 10.1126/science.1167852
- Seifert, G., and Steinhäuser, C. (1995). Glial cells in the mouse hippocampus express AMPA receptors with an intermediate Ca<sup>2+</sup> permeability. *Eur. J. Neurosci.* 7, 1872–1881. doi: 10.1111/j.1460-9568.1995.tb00708.x
- Seifert, G., and Steinhäuser, C. (2018). Heterogeneity and function of hippocampal macroglia. *Cell Tissue Res.* 3, 653–670. doi: 10.1007/s00441-017-2746-1
- Seifert, G., Rehn, L., Weber, M., and Steinhäuser, C. (1997a). AMPA receptor subunits expressed by single astrocytes in the juvenile mouse hippocampus. *Mol. Brain Res.* 4, 286–294. doi: 10.1016/s0169-328x(97)00059-4
- Seifert, G., Weber, M., Schramm, J., and Steinhäuser, C. (2003). Changes in splice variant expression and subunit assembly of AMPA receptors during maturation of hippocampal astrocytes. *Mol. Cell Neurosci.* 2, 248–258. doi: 10.1016/s1044-7431(03)00039-3
- Seifert, G., Zhou, M., and Steinhäuser, C. (1997b). Analysis of AMPA receptor properties during postnatal development of mouse hippocampal astrocytes. *J. Neurophysiol.* 6, 2916–2923. doi: 10.1152/jn.1997.78.6.2916
- Shi, Y., Suh, Y. H., Milstein, A. D., Isozaki, K., Schmid, S. M., Roche, K. W., et al. (2010). Functional comparison of the effects of TARPs and cornichons on AMPA receptor trafficking and gating. *Proc. Natl. Acad. Sci. U. S. A.* 37, 16315–16319. doi: 10.1073/pnas.1011706107
- Soto, D., Coombs, I. D., Gratacos-Battle, E., Farrant, M., and Cull-Candy, S. G. (2014). Molecular mechanisms contributing to TARP regulation of channel conductance and polyamine block of calcium-permeable AMPA receptors. *J. Neurosci.* 35, 11673–11683. doi: 10.1523/jneurosci.0383-14.2014
- Soto, D., Coombs, I. D., Kelly, L., Farrant, M., and Cull-Candy, S. G. (2007). Stargazin attenuates intracellular polyamine block of calcium-permeable AMPA receptors. *Nat. Neurosci.* 10, 1260–1267. doi: 10.1038/nn1966
- Soto, D., Coombs, I. D., Renzi, M., Zonouzi, M., Farrant, M., and Cull-Candy, S. G. (2009). Selective regulation of long-form calcium-permeable AMPA receptors by an atypical TARP, gamma-5. *Nat. Neurosci.* 3, 277–285. doi: 10.1038/nn.2266
- Studniarczyk, D., Coombs, I., Cull-Candy, S. G., and Farrant, M. (2013). TARP gamma-7 selectively enhances synaptic expression of calcium-permeable AMPARs. *Nat. Neurosci.* 9, 1266–1274. doi: 10.1038/nn.3473



- Tomita, S., Adesnik, H., Sekiguchi, M., Zhang, W., Wada, K., Howe, J. R., et al. (2005). Stargazin modulates AMPA receptor gating and trafficking by distinct domains. *Nature* 7045, 1052–1058. doi: 10.1038/nature03624
- Tomita, S., Chen, L., Kawasaki, Y., Petralia, R. S., Wenthold, R. J., Nicoll, R. A., et al. (2003). Functional studies and distribution define a family of transmembrane AMPA receptor regulatory proteins. *J. Cell Biol.* 4, 805–816. doi: 10.1083/jcb.200212116
- Toth, K., and McBain, C. J. (1998). Afferent-specific innervation of two distinct AMPA receptor subtypes on single hippocampal interneurons. *Nat. Neurosci.* 7, 572–578. doi: 10.1038/2807
- Washburn, M. S., Numberger, M., Zhang, S., and Dingledine, R. (1997). Differential dependence on GluR2 expression of three characteristic features of AMPA receptors. *J. Neurosci.* 24, 9393–9406. doi: 10.1523/jneurosci.17-24-09393.1997
- Zonouzi, M., Renzi, M., Farrant, M., and Cull-Candy, S. G. (2011). Bidirectional plasticity of calcium-permeable AMPA receptors in oligodendrocyte lineage cells. *Nat. Neurosci.* 11, 1430–1438. doi: 10.1038/nn.2942
- Conflict of Interest:** The authors declare that the research was conducted in the absence of any commercial or financial relationships that could be construed as a potential conflict of interest.

Copyright © 2021 Hardt, Tascio, Passlick, Timmermann, Jabs, Steinhäuser and Seifert. This is an open-access article distributed under the terms of the Creative Commons Attribution License (CC BY). The use, distribution or reproduction in other forums is permitted, provided the original author(s) and the copyright owner(s) are credited and that the original publication in this journal is cited, in accordance with accepted academic practice. No use, distribution or reproduction is permitted which does not comply with these terms.



# Using Genetically Encoded Calcium Indicators to Study Astrocyte Physiology: A Field Guide

Christian Lohr<sup>1\*</sup>, Antonia Beiersdorfer<sup>1</sup>, Timo Fischer<sup>1</sup>, Daniela Hirnet<sup>1</sup>, Natalie Rotermund<sup>1</sup>, Jessica Sauer<sup>1</sup>, Kristina Schulz<sup>1</sup> and Christine E. Gee<sup>2</sup>

<sup>1</sup>Division of Neurophysiology, University of Hamburg, Hamburg, Germany, <sup>2</sup>Institute of Synaptic Physiology, University Medical Center Hamburg-Eppendorf, Hamburg, Germany

## OPEN ACCESS

### Edited by:

Hajime Hirase,  
University of Copenhagen, Denmark

### Reviewed by:

Jillian L. Stobart,  
University of Manitoba, Canada

Martin Paukert,  
Johns Hopkins University,  
United States

### \*Correspondence:

Christian Lohr  
christian.lohr@uni-hamburg.de

### Specialty section:

This article was submitted to  
Non-Neuronal Cells,  
a section of the journal  
Frontiers in Cellular Neuroscience

**Received:** 02 April 2021

**Accepted:** 06 May 2021

**Published:** 11 June 2021

### Citation:

Lohr C, Beiersdorfer A, Fischer T, Hirnet D, Rotermund N, Sauer J, Schulz K and Gee CE (2021) Using Genetically Encoded Calcium Indicators to Study Astrocyte Physiology: A Field Guide. *Front. Cell. Neurosci.* 15:690147. doi: 10.3389/fncel.2021.690147

Ca<sup>2+</sup> imaging is the most frequently used technique to study glial cell physiology. While chemical Ca<sup>2+</sup> indicators served to visualize and measure changes in glial cell cytosolic Ca<sup>2+</sup> concentration for several decades, genetically encoded Ca<sup>2+</sup> indicators (GECIs) have become state of the art in recent years. Great improvements have been made since the development of the first GECI and a large number of GECIs with different physical properties exist, rendering it difficult to select the optimal Ca<sup>2+</sup> indicator. This review discusses some of the most frequently used GECIs and their suitability for glial cell research.

**Keywords:** glial cells, astrocyte, calcium imaging, genetically encoded calcium indicator, GCaMP, calcium sensor

## INTRODUCTION

Astrocytes have long been considered as passive cells, merely supporting neurons and maintaining nervous tissue homeostasis. Physiological studies during the past two decades have fundamentally changed this view. Not only are astrocytes responsive to neuronally derived neurotransmitters, they also release signaling molecules named “gliotransmitters” to affect neuronal development and synaptic transmission (Clarke and Barres, 2013; Khakh and Sofroniew, 2015; Verkhratsky and Nedergaard, 2018; Kofuji and Araque, 2021a). Ca<sup>2+</sup> signaling plays a pivotal role in both the physiology and function of astrocytes (Khakh and McCarthy, 2015; Semyanov et al., 2020). Therefore, it is not surprising that Ca<sup>2+</sup> imaging is the main technique used to study astrocyte physiology (Lohr and Deitmer, 2010). While chemical Ca<sup>2+</sup> indicators were employed in the early years to visualize Ca<sup>2+</sup> signals in astrocytes, genetically encoded Ca<sup>2+</sup> indicators (GECIs) have become the method of choice in state-of-the-art experimentation (Okubo and Iino, 2020; Yu et al., 2020). This review provides an overview of available Ca<sup>2+</sup> indicators and compares their advantages and drawbacks to aid scientists in selecting the optimal GECI for glial cell research.

## CHEMICAL Ca<sup>2+</sup> INDICATORS

Since glial cells such as astrocytes are electrically non-excitabile cells, electrophysiological techniques revealed only limited insights into astrocyte properties. Rather than changes in membrane potential, most astrocytic transmitter receptors cause a rise in cytosolic Ca<sup>2+</sup> concentration (Deitmer et al., 1998; Kofuji and Araque, 2021b). The development of chemical fluorescent Ca<sup>2+</sup> indicators, with a major contribution of Nobel laureate Roger Tsien, was a breakthrough for glial cell research (Tsien, 1989). Chemical Ca<sup>2+</sup> indicators are fluorescent dyes that change their spectral properties

upon binding of  $\text{Ca}^{2+}$  and therefore indicate changes in cytosolic  $\text{Ca}^{2+}$ . As a keyword, Fura-2, the most popular chemical  $\text{Ca}^{2+}$  indicator, yields more than 12,000 hits in a Pubmed search, and its original publication (Grynkiewicz et al., 1985) has been cited over 21,000 times. The development of membrane-permeant acetoxymethyl ester (AM) derivatives of Fura-2 and other chemical  $\text{Ca}^{2+}$  indicators such as Fluo-3, Indo-1, and Calcium Green-1 coincided with the increasing availability of confocal fluorescence microscopy. This combination of circumstances resulted in a rapidly increasing number of studies of intracellular  $\text{Ca}^{2+}$  signaling in non-excitable cells, including astrocytes. Indicators with increased response amplitude, different spectral properties, and  $\text{Ca}^{2+}$  binding affinities, and the ability to be attached to membranes or accumulate in intracellular organelles were developed (Eberhard and Erne, 1991; Gee et al., 2000; Paredes et al., 2008). However, using chemical indicators to study astrocytes also has some drawbacks, in particular when applied in tissue such as brain slices. Although astrocytes are particularly efficient at taking up some AM dyes (Mulligan and MacVicar, 2004; Covelo and Araque, 2018; Tran et al., 2018), depending on brain region bulk-loading astrocytes with membrane-permeant  $\text{Ca}^{2+}$  indicators is not entirely cell-specific, hence neurons and other cells may also be loaded with the indicator (Singaravelu et al., 2006; Doengi et al., 2008; Lind et al., 2013; Otsu et al., 2015; Beiersdorfer et al., 2019). Consequently, astrocytes may need to be identified and distinguished from neurons. In many rodent brain areas, sulforhodamine 101 (SR101) is selectively taken up by astrocytes and can be used as a morphological marker of astrocytes (Nimmerjahn et al., 2004). In some brain regions, however, astrocytes fail to accumulate significant amounts of SR101 (Schnell et al., 2015) and SR101 has been reported to induce epileptic activity, limiting the applicability of SR101 (Kang et al., 2010). Other ways that can be employed to distinguish neuronal and astrocytic  $\text{Ca}^{2+}$  transients are to withdraw  $\text{K}^+$ , which increases cytosolic  $\text{Ca}^{2+}$  in astrocytes but not neurons, as shown for brain stem, olfactory bulb, and cerebellum (Singaravelu et al., 2006; Härtel et al., 2007; Doengi et al., 2009; Fischer et al., 2020). In addition, we observed in the olfactory bulb that ATP induces  $\text{Ca}^{2+}$  transients in astrocytes and not in Fluo-4-loaded neurons (Doengi et al., 2008; Fischer et al., 2020, 2021). Hence, “physiological” markers can be used to distinguish between astrocytes and neurons when genetic or chemical markers cannot be applied. Somatic  $\text{Ca}^{2+}$  transients in astrocytes occur on a distinctively slower timescale than those in neurons, but this is not the case for transients in fine astrocytic processes and microdomains, which rise and fall on subsecond time scales. Recently, AM  $\text{Ca}^{2+}$  indicators and BAPTA AM have been shown to inhibit the  $\text{Na}^+/\text{K}^+$  ATPase, compromising cellular metabolism and increasing extracellular  $\text{K}^+$ , thus raising additional concerns about their use (Smith et al., 2018). Another disadvantage of bulk-loading astrocytes in brain slices with  $\text{Ca}^{2+}$  indicator dyes is a lack of contrast. If not only astrocytes but also other cells contain the dye, the surrounding tissue is bright and the very fine astrocyte processes do not stand out from the background. These problems are circumvented by loading a single astrocyte, e.g., by including the chemical  $\text{Ca}^{2+}$  indicator in a patch pipette used to record the astrocyte

(Grosche et al., 1999; Henneberger et al., 2010). However, this procedure is time-consuming, requires additional equipment, and results in only a single dye-loaded astrocyte. First studies of single dye-loaded astrocytes revealed a hitherto unknown complexity of  $\text{Ca}^{2+}$  signaling in glial cells, including localized  $\text{Ca}^{2+}$  signals that occurred independently in very small microdomains (Grosche et al., 1999; Lohr and Deitmer, 1999; Di Castro et al., 2011). These results highlighted the need for improved methods to study astrocytic  $\text{Ca}^{2+}$  signaling in brain slices and *in vivo*.

## GENETICALLY ENCODED $\text{Ca}^{2+}$ INDICATORS (GECIs)

The discovery that the gene encoding the green fluorescent protein (GFP) from *Aequoria victoria* can render other cells fluorescent heralded a new era in life science that included glial cell research (Prasher et al., 1992; Chalfie et al., 1994; Heim et al., 1995; Heim and Tsien, 1996). Protein engineering efforts produced fluorescent protein-based  $\text{Ca}^{2+}$  indicators by attaching the  $\text{Ca}^{2+}$  binding domains of calmodulin and the myosin light chain kinase peptides M13 and RS20, respectively, or troponin-C to the fluorescent proteins (Nakai et al., 2001; Heim and Griesbeck, 2004). The binding of  $\text{Ca}^{2+}$  to the  $\text{Ca}^{2+}$  binding domain then changes the conformation and spectral properties of the attached fluorescent protein(s), yielding a genetically encoded  $\text{Ca}^{2+}$  indicator (GECI) that can be expressed in genetically defined cells. GECIs have been employed to study glial  $\text{Ca}^{2+}$  signaling and proven superior compared to chemical  $\text{Ca}^{2+}$  indicators (Shigetomi et al., 2013).

Two principally different types of GECIs exist. Single wavelength GECIs consist of a  $\text{Ca}^{2+}$  sensing domain and a single fluorescent protein, whose fluorescence intensity changes when shifting between  $\text{Ca}^{2+}$ -free and  $\text{Ca}^{2+}$ -bound states, whereas FRET (Förster or fluorescence resonance energy transfer) GECIs consist of two fluorescent proteins linked by the  $\text{Ca}^{2+}$  binding domain (Mollinedo-Gajate et al., 2019; Inoue, 2020; Shen et al., 2020). Both types of GECIs have advantages and drawbacks and within each are many indicators with different properties. Selecting an indicator with appropriate spectral properties,  $\text{Ca}^{2+}$  binding affinity and dynamic range for the application can save a great deal of time and money. If it is important to quantify  $\text{Ca}^{2+}$  concentration, rather than  $\text{Ca}^{2+}$  dynamics, then FRET sensors, in which the energy transfer from donor to acceptor fluorophores change upon  $\text{Ca}^{2+}$  binding, are the option of choice. As the donor and acceptor fluorophores are expressed in a single protein, the ratio between the fluorescence intensity of the acceptor and the fluorescence intensity of the donor solely depends on  $\text{Ca}^{2+}$  concentration and is independent of expression levels. Stimulated emission/intensity FRET measurements may be affected, however, if fluorophore maturation or bleaching rates are very different, or when imaging deep in tissue because different wavelengths scatter differently. If using 2-photon excitation with wide-field detection, an additional problem arises: The dichroic mirrors in the detection pathway are sensitive to the angle of incident light and will split the light at

different wavelengths, creating color gradients across the image. The resulting variations in red/green or cyan/yellow ratio across the field of view must be corrected for. Fluorescence lifetime imaging FRET (FLIM-FRET) of donor fluorescence is largely devoid of these artifacts but image acquisition is much slower and costly hybrid detectors and photon-counting boards are required. For quantification of  $\text{Ca}^{2+}$  signals with FRET sensors, the  $\text{Ca}^{2+}$  binding domain used to construct the GECI must also be considered. The  $\text{Ca}^{2+}$  binding domain of calmodulin, e.g., binds four calcium ions with positive cooperativity with a Hill coefficient in the range of 2, leading to a non-linear representation of the ambient  $\text{Ca}^{2+}$  concentration by the FRET ratio (Mank and Griesbeck, 2008). Recent FRET sensors of the Twitch family use a minimal  $\text{Ca}^{2+}$  binding motif of troponin C, which lacks cooperativity and therefore exhibits much better linearity of the  $\text{Ca}^{2+}$ /FRET relationship (Thestrup et al., 2014; Wilms and Häusser, 2014).

The reason single wavelength GECIs are unsuitable for determining  $\text{Ca}^{2+}$  concentration is that intensity is not only  $\text{Ca}^{2+}$ -dependent but depends critically on protein expression levels and imaging conditions. Single wavelength GECIs are, however, the option of choice for studying  $\text{Ca}^{2+}$  dynamics. Indeed, non-ratiometric GECIs such as GFP-based GCaMPs are the most popular  $\text{Ca}^{2+}$  indicators for studying glial cell physiology (Nakai et al., 2001; Ohkura et al., 2012b; Chen et al., 2013; Srinivasan et al., 2016; Droste et al., 2017; Stobart et al., 2018). Firstly, GCaMPs of the latest generations exhibit an enormous dynamic range, displaying a several 100 percent increase in fluorescence upon binding of  $\text{Ca}^{2+}$  (Figure 1). In addition, non-ratiometric GECIs require only one detector channel of the microscope to visualize  $\text{Ca}^{2+}$ -dependent changes in fluorescence, leaving additional channels for other reporter proteins, fluorescent probes, and GECIs with different spectral properties to image  $\text{Ca}^{2+}$  changes, e.g., in a second cell type or multiple intracellular compartments. For instance, this method has been used to record  $\text{Ca}^{2+}$  signals in astrocytes and neurons with two spectrally different  $\text{Ca}^{2+}$  indicators or  $\text{Ca}^{2+}$  and cAMP simultaneously in cortical astrocytes using green fluorescent G-CaMP7 and red fluorescent Pink Flamindo, respectively (Stobart et al., 2018; Bojarskaite et al., 2020; Oe et al., 2020; Ung et al., 2020). FRET indicators, in contrast, occupy two detector channels. Since most FRET indicators comprise CFP and YFP (or their derivatives) as donor and acceptor proteins, light sources for excitation of around 430–450 nm (for CFP) and 515 nm (for YFP) are necessary and, hence, the configuration of the available microscopes needs to be checked before selecting such indicators. Whereas for the actual FRET measurement only the donor fluorophore needs to be excited, the ability to directly excite the acceptor is needed as well for setting up the experiments. One additional drawback of most FRET GECIs is their incompatibility with channelrhodopsin-2 (ChR2), the most frequently used optogenetic tool to stimulate neurons (Nagel et al., 2003; Boyden et al., 2005). ChR2 has a broad excitation spectrum, peaking at 450 nm. Thus, excitation of the FRET donor protein will inevitably activate ChR2 during the imaging process. This problem also occurs with green fluorescent non-ratiometric GECIs that are excited at 488 nm,

however, several red fluorescent non-ratiometric GECIs with excitation peaks not interfering with ChR2 excitation are available.

Not only the properties of the fluorescent proteins determine the usefulness of the  $\text{Ca}^{2+}$  indicator, but also the second component, the  $\text{Ca}^{2+}$  binding domain. Mainly two different proteins provided  $\text{Ca}^{2+}$  binding domains for GECIs: Calmodulin and troponin C (Nakai et al., 2001; Heim and Griesbeck, 2004). In both cases, GECIs with fast kinetics and good dynamic range could be developed. However, GCaMPs using calmodulin have the drawback that many proteins interacting with calmodulin exist in glial cells and neurons and, hence, high expression of the GECI might interfere with calmodulin-dependent pathways in the cells unless modified (Yang et al., 2018). Troponin C, in contrast, is a protein only found in muscle cells and has no function in neural cells, avoiding undesirable effects of the  $\text{Ca}^{2+}$  indicator on cell physiology (Direnberger et al., 2012). Nevertheless, the troponin C-based  $\text{Ca}^{2+}$  indicator TN-XXL has also been shown to have detrimental side-effects leading to impaired neural development (Gasterstädt et al., 2020). Other  $\text{Ca}^{2+}$  binding proteins have been employed to construct GECIs that do not interfere with the biochemical environment in mammalian cells, including calmodulin derived from *Aspergillus* fungi in the FGCaMPs (Barykina et al., 2020). In addition to the biological activity of the  $\text{Ca}^{2+}$  binding domain,  $\text{Ca}^{2+}$  binding itself affects biological processes because the  $\text{Ca}^{2+}$  binding domains act as  $\text{Ca}^{2+}$  buffers that can significantly add to the endogenous  $\text{Ca}^{2+}$  buffer capacity. This is particularly perturbing using GECIs with high  $\text{Ca}^{2+}$  affinity (low  $K_d$ ) and multiple  $\text{Ca}^{2+}$  binding sites (four for most of the GECIs) and a key reason why expression levels must be kept low.

## A FIELD GUIDE TO GECIs FOR USE IN GLIAL CELLS

As outlined above, there are many factors to consider when selecting the appropriate GECI. There are numerous available GECIs. Alone the derivatives descending from the first GCaMP developed by Nakai et al. (2001) comprise more than 50 members (Kerruth et al., 2019). In the following, we highlight the most popular GECIs currently used for glial cell research or related fields, their key properties, and for which applications they are best suited. Figure 1 contains single wavelength GECIs (Ohkura et al., 2012a; Chen et al., 2013; Dana et al., 2018, 2019) and Figure 2 GECIs suitable for ratiometric FRET and FLIM-FRET imaging (Nagai et al., 2004; Mank et al., 2008; Horikawa et al., 2010; Trigo-Mourino et al., 2019). While recently published GECIs are included, there are others not yet tested in astrocytes that will eventually prove superior. We, therefore, compare and discuss the properties that make particular GECIs useful for particular applications, which should help in selecting from yet newer GECIs and not only from those in Figures 1, 2. In the figurative summaries, we have highlighted those references in which GECIs have been published in astrocytes (Atkin et al., 2009; Hausteine et al., 2014; Kanemaru et al., 2014; Monai et al., 2016; Nakayama et al., 2016; Srinivasan et al., 2016; Stobart et al., 2018; Woo et al., 2020).



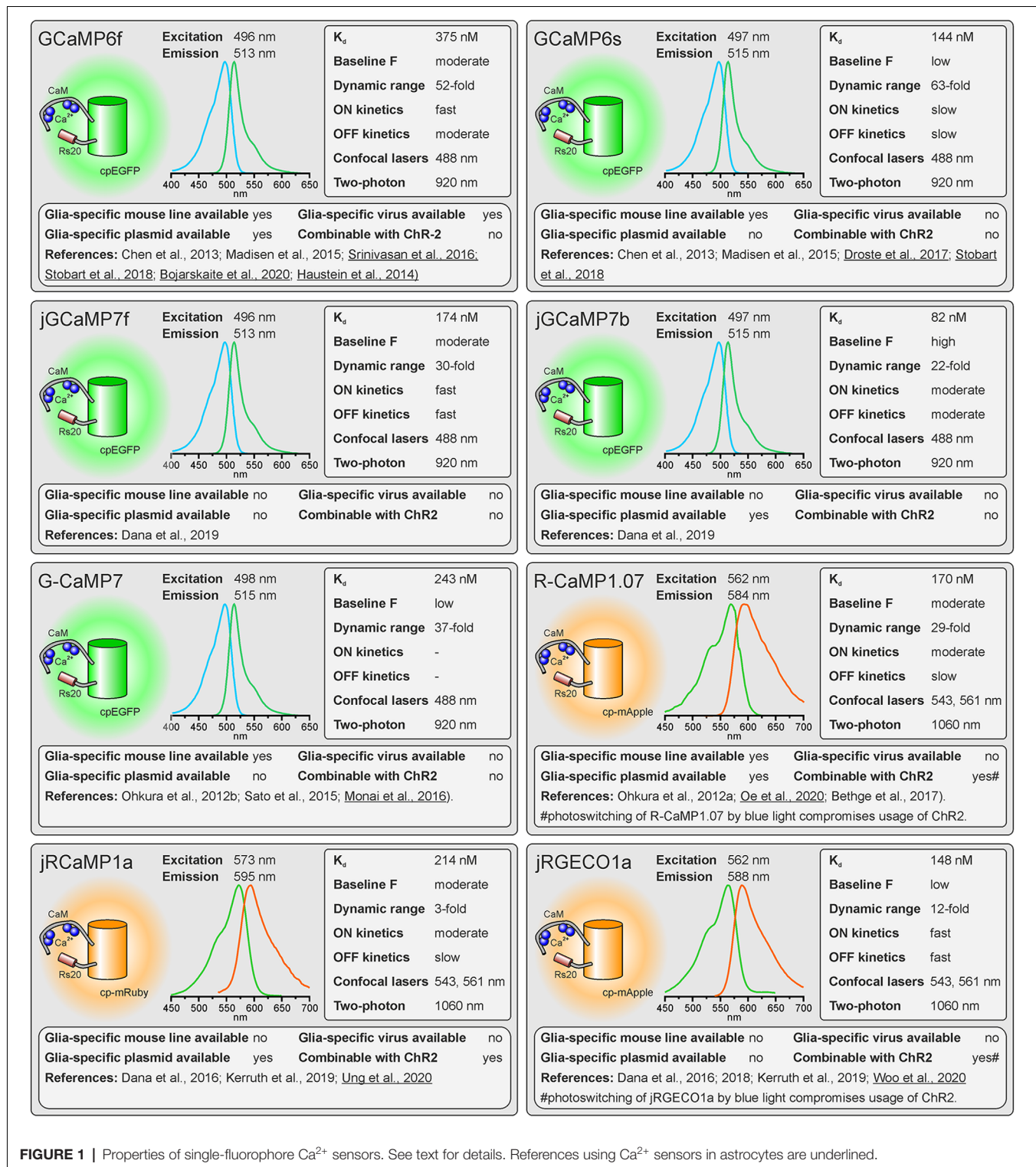
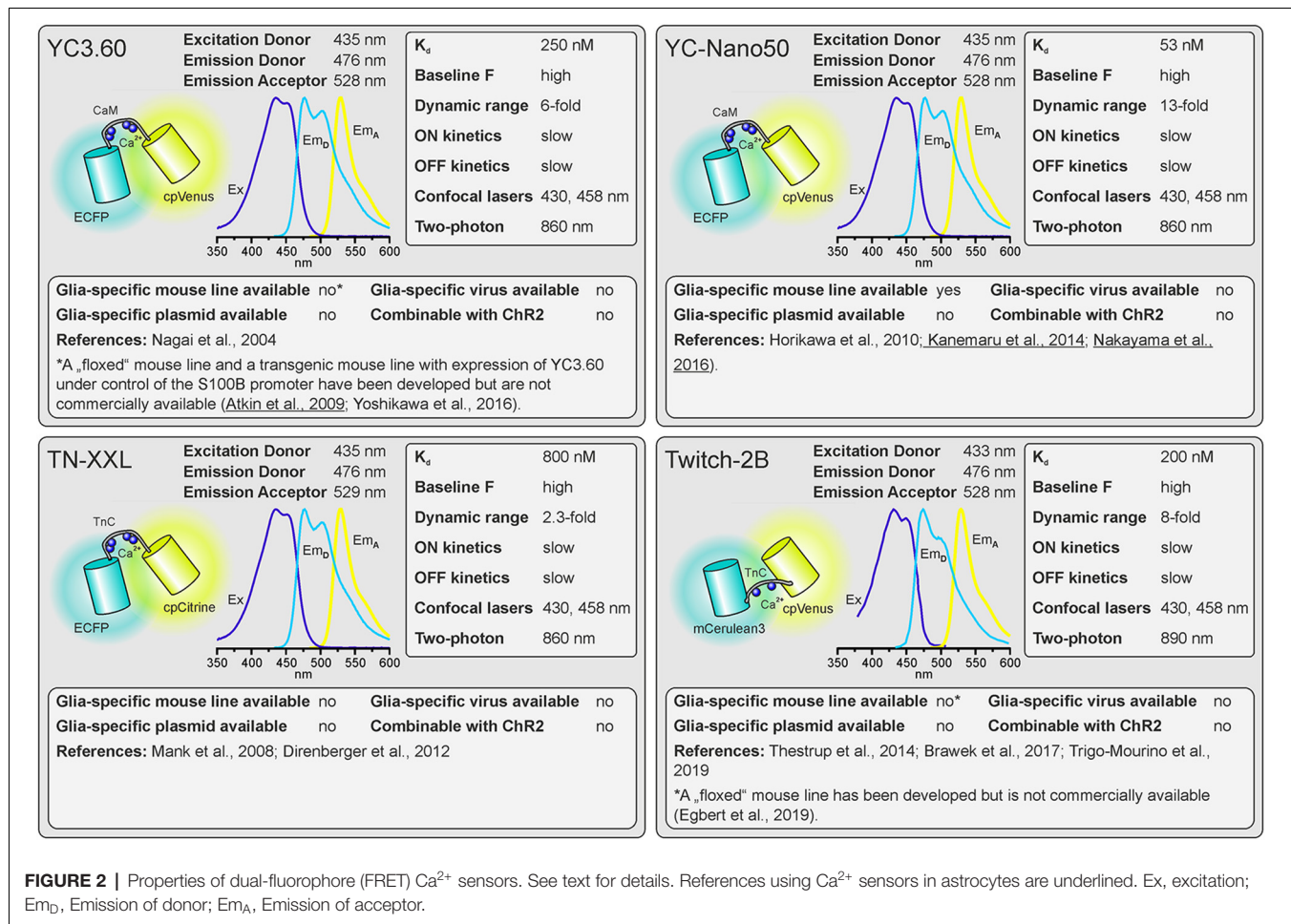


**FIGURE 1 |** Properties of single-fluorophore  $\text{Ca}^{2+}$  sensors. See text for details. References using  $\text{Ca}^{2+}$  sensors in astrocytes are underlined.

## Spectral Properties

The first considerations are the excitation and emission spectra of the  $\text{Ca}^{2+}$  indicators. These must be matched to the light source, detectors, and filter sets available or new optical elements must be purchased. The excitation and emission

maxima are listed for the various indicators. Since only the donor fluorophore is excited when using dual fluorophore (FRET) sensors, the excitation spectrum and maximum of the acceptor fluorophore are not quoted but it is highly advisable to also have the ability to directly excite the acceptor to



visualize the cells, e.g., in order to select the optimal field of view.

## Dissociation Constant $K_d$

The  $K_d$  reflects the  $\text{Ca}^{2+}$  concentration at which half of the  $\text{Ca}^{2+}$  indicator molecules are bound by  $\text{Ca}^{2+}$ , while the other half is dissociated (Paredes et al., 2008). This also defines the point at which the relationship between an increase in the  $\text{Ca}^{2+}$  concentration and the resulting change in fluorescence is close to linear. The resting  $\text{Ca}^{2+}$  concentration in astrocytes is in the range of 80–100 nM (Deitmer et al., 1998), hence GECIs with  $K_d$  values close to this concentration will record  $\text{Ca}^{2+}$  changes reliably. However, if very large  $\text{Ca}^{2+}$  signals are expected with a peak concentration of 1  $\mu\text{M}$  and above, the  $\text{Ca}^{2+}$  indicators might saturate and the amplitude of the  $\text{Ca}^{2+}$  signal might be underestimated.  $\text{Ca}^{2+}$  indicators with higher  $K_d$  values are more appropriate for these measurements.

## Baseline Fluorescence

The GECIs with the highest dynamic range often achieve this by extremely low fluorescence in the apo state, i.e., when no  $\text{Ca}^{2+}$  is bound. While at first glance this seems like an excellent feature, in practice it becomes almost impossible to visualize and focus on astrocytes expressing for instance the indicator GCaMP6s unless

they are pre-stimulated. For astrocyte imaging, particularly when one wants to examine signals in the fine processes, it is, therefore, advantageous to choose single wavelength GECIs that are already fairly bright at baseline  $\text{Ca}^{2+}$  concentrations (100 nM). This is much less important for FRET sensors as one can always excite the acceptor directly to visualize and focus before switching to excite the donor for the actual ratiometric measurements.

## Dynamic Range

For single-fluorophore indicators, the dynamic range is calculated by the difference between the fluorescence intensity when  $\text{Ca}^{2+}$ -saturated ( $F_{\max}$ ) and the fluorescence intensity in  $\text{Ca}^{2+}$ -free conditions ( $F_{\min}$ ) divided by the fluorescence value in  $\text{Ca}^{2+}$ -free conditions:  $(F_{\max} - F_{\min})/F_{\min}$ . For FRET sensors, it is similarly calculated by using the FRET ratio values instead of the fluorescence values. As mentioned above, while a high dynamic range is always desirable for single-wavelength GECIs it often reflects very low baseline fluorescence rather than very bright  $\text{Ca}^{2+}$ -bound fluorescence. It is therefore important to consider not only the dynamic range but also how bright the sensor is at baseline. Whereas the best single wavelength sensors now have dynamic ranges of several hundred percent, the FRET sensors always appear inferior in this regard at first glance. In fact, a dynamic range of 40% is excellent for a FRET sensor.

## On and Off Kinetics

The rate of binding and unbinding of  $\text{Ca}^{2+}$  by the indicator molecule is reflected by values such as the half rise time ( $t_{1/2}$  rise) and half decay time ( $t_{1/2}$  decay). If binding and unbinding of  $\text{Ca}^{2+}$  occurs much slower than the actual increase and decrease in the  $\text{Ca}^{2+}$  concentration, the time course of the  $\text{Ca}^{2+}$  signal is distorted. Although it was believed for many years that  $\text{Ca}^{2+}$  transients in astrocytes rise and decay at slow rates and hence can readily be recorded with  $\text{Ca}^{2+}$  indicators with slow on and off kinetics, more recent studies showed that fast  $\text{Ca}^{2+}$  signals in astrocyte microdomains can occur at a time scale of tens of ms (Di Castro et al., 2011; Stobart et al., 2018). A direct comparison between GCaMP3 and GCaMP6f revealed a much faster and more reliable detection of  $\text{Ca}^{2+}$  transients in astrocyte microdomains by GCaMP6f, while global  $\text{Ca}^{2+}$  transients were equally well recorded by both indicators, illustrating the need for fast  $\text{Ca}^{2+}$  binding kinetics of the  $\text{Ca}^{2+}$  indicator for measurements in microdomains (Ye et al., 2017). Therefore, GECIs with fast on and off kinetics should be selected when recording fast and local  $\text{Ca}^{2+}$  transients. In addition, low expression levels of the GECI are necessary to minimize the effect of the  $\text{Ca}^{2+}$  buffer capacity that is added by the  $\text{Ca}^{2+}$  sensors on  $\text{Ca}^{2+}$  signal kinetics.

## Suitability for Standard Confocal and Two-Photon Microscopy

Confocal microscopy is the standard technique when imaging glial  $\text{Ca}^{2+}$  signaling in brain slices. While confocal microscopes, as available in virtually any life science institution, are typically equipped with a 488-nm laser (cyan excitation), a 543-nm or 568-nm laser (green excitation), deep blue lasers (430 nm, 458 nm), which are necessary for optimal excitation of cyan fluorophores such as CFP, cerulean or turquoise, are much less common. Therefore, we list lasers suitable for ideal (one-photon) excitation in the figurative summaries. In addition to confocal microscopy, an increasing number of laboratories use two-photon microscopy, in particular, to study glial  $\text{Ca}^{2+}$  signaling *in vivo* (Srinivasan et al., 2015; Brawek et al., 2017; Stobart et al., 2018; Tran et al., 2018; Lines et al., 2020; Oe et al., 2020). Most of the GECIs are efficiently excited using a Ti:Sapphire laser in the range of 840 nm (e.g., TN-XXL) to 1,060 nm (e.g., jRGECO1a), although longer wavelengths up to 1,300 nm are preferred for 2-photon excitation of most “red” GECIs (Mohr et al., 2020).

## Glia-Specific Expression of GECIs

Before imaging  $\text{Ca}^{2+}$  one also has to have the GECI of choice expressed in astrocytes or glial cells of choice. Using viral vectors to express the GECI is highly effective. Recombinant AAV vectors are convenient and can be used at biosafety level 1 with the appropriate permissions. Many of the GECIs listed are available as plasmids with glial-specific promoters such as GFAP and gfaABC1D or GLAST that can be packaged into rAAVs with appropriate serotypes such as AAV8 or AAV9. Alternatively, breeding transgenic mice with GECIs encoded in their genome is a convenient and effective way to express GECIs in astrocytes for *in situ* and *in vivo* studies (Madisen et al., 2015; Sato et al., 2015; Bethge et al.,

2017). Additional advantages of using transgenic mice are: (I) expression is non-invasive; (II) protein expression levels are usually more uniform; and (III) expression is usually lower than following rAAV transduction and hence the effect of additional  $\text{Ca}^{2+}$  buffering capacity is less severe. The disadvantage is the limited choice of GECI mouse lines. Members of the GCaMP6 family of GECIs, e.g., are commercially available as “floxed” mouse lines and can be cross-bred with mice that express Cre recombinase in astrocytes to achieve astrocyte-specific expression of GECIs (Madisen et al., 2015). Several astrocyte-specific Cre driver lines are available, which might differ in expression rate and specificity for certain brain regions. Cell-type specificity is achieved by using astrocyte-specific promoters to drive Cre expressions, such as Aldh1L1, GFAP, and GLAST (Yu et al., 2020). However, neuronal and oligodendroglial precursor cells may also express these astrocyte-typical proteins and hence Cre recombinase when using constitutively active promoters, resulting in GECI expression in cells derived from these precursors. This fate mapping effect can be circumvented by induction of GECI expression after neuronal and oligodendroglial maturation in inducible Cre driver mouse lines (tamoxifen or tetracycline/doxycycline). For some GECIs, transgenic mouse lines to allow for glia-specific  $\text{Ca}^{2+}$  imaging have been published, but are not commercially available (Yoshikawa et al., 2016; Egbert et al., 2019). According to our knowledge, we indicate whether transgenic mice, rAAVs, or plasmids ready-to-use for astrocytic expression are available and listed those in **Supplementary Table 1**.

## Combinability With Channelrhodopsins

Channelrhodopsins are light-activated ion channels used to control neuronal excitability (Nagel et al., 2003; Boyden et al., 2005). ChR2 is still the most commonly used optogenetic tool to excite neurons and hence is frequently employed to drive neuron-to-glia communication (Bernardinelli et al., 2011; Losi et al., 2017; Mariotti et al., 2018; Nikolic et al., 2018). As ChR2 is activated by blue light, it cannot be used together with GFP-based or CFP-based GECIs in widefield or confocal  $\text{Ca}^{2+}$  imaging experiments. However, they can be combined in two-photon  $\text{Ca}^{2+}$  imaging, since the spatially restricted stimulation of ChR2 is insufficient to significantly stimulate neurons (Losi et al., 2019). In widefield and confocal microscopy, violet-light-activated channels such as eTsChR (*Tetraselmis striata* channelrhodopsin) are better options (Farhi et al., 2019) or using ChR2 together with a red fluorescent GECI that is activated by green/yellow light. Some of these red fluorescent GECIs, however, use mApple as fluorophore, which photoswitches from a dim to a bright state upon illumination with blue light as used to stimulate ChR2, resulting in a  $\text{Ca}^{2+}$ -independent fluorescence increase that interferes with the  $\text{Ca}^{2+}$  measurement (Akerboom et al., 2013; Dana et al., 2016).

## RECENT ADDITIONS TO THE $\text{Ca}^{2+}$ INDICATOR PORTFOLIO

While we have limited the indicators presented in **Figures 1, 2** to published calcium indicators tested in glial cells, there



are some very interesting indicators published in the last few years that we think warrant mentioning. The blue to red X-CaMP series is interesting for multi-color imaging (Inoue et al., 2019). Still unpublished but already available on Addgene is the jGCaMP8 series from Janelia farms<sup>1</sup>. The  $K_d$  range from 46 nM (jGCaMP8s, “s” for sensitive) to 334 nM (jGCaMP8f, “f” for fast), and the slowest of these is as fast as GCaMP6f. None rival the apo brightness of jGCaMP7b, although resting brightness will also depend on resting  $Ca^{2+}$  concentration. Also of interest are jYCaMP1 and jYCaMP1s ( $K_d$  79 and 70 nM) and XCaMP-Y, which are particularly suitable for 2-photon excitation using inexpensive pulsed lasers with a fixed wavelength around 1,030 nm (Inoue et al., 2019; Mohr et al., 2020). K-GECO is the first of a new series of bright red  $Ca^{2+}$  indicators designed to retain the excellent responsiveness of the R-GECO series and reduce photoswitching, which limits the usefulness of i.e., jRGECO1a (Shen et al., 2018). Ideal for confocal or widefield camera-based imaging, particularly in tissue, may be the near-infrared indicators NIR-GECO2 and NIR-GECO2G excited at 640 nm, although photobleaching remains problematic with long exposures (Qian et al., 2020). Very fast green and red indicators have also been developed but signals are smaller and to our knowledge, these have not been tested in astrocytes (Kerruth et al., 2019).

## CONCLUDING STATEMENT

There is not a single GECI that provides optimal characteristics for all applications. For quantification of changes in cytosolic  $Ca^{2+}$ , FRET sensors are the method of choice, however, transgenic mouse models and ready-to-use viruses are not commercially available. Among the FRET sensors, Twitch-2B is a good choice and has been reported to work in non-excitable cells such as microglial cells (Brawek et al., 2017). Compared to FRET sensors, recent single-fluorophore sensors have a larger dynamic range and faster kinetics. Hence, they are more often used in

glial cell research. Both transgenic mice and plasmids/viruses are available for the GCaMP6 family of GECIs, making them the first choice when a straightforward approach is pursued. The high dynamic range of GCaMP6s comes at the cost of very dim fluorescence at resting  $Ca^{2+}$  concentrations, hence GCaMP6f is favored as it allows visualization of astrocytes at rest. We have recently found that the single-wavelength sensor jGCaMP7b possesses an excellent combination of properties for use in astrocytes, including large dynamic range, fast kinetics, and high resting fluorescence and therefore included it in **Figure 1**. However, studies using jGCaMP7b in astrocytes have not been published yet and transgenic mice are not available to date.

## AUTHOR CONTRIBUTIONS

All authors contributed to the research that is the base for this review as well as to the writing and editing of the manuscript. All authors contributed to the article and approved the submitted version.

## FUNDING

This work was funded by the Deutsche Forschungsgemeinschaft (German Research Foundation)—project numbers: 278170285; 279354007; 350733686; 335447717.

## ACKNOWLEDGMENTS

We thank A. C. Rakete and M. Fink for excellent technical assistance.

## SUPPLEMENTARY MATERIAL

The Supplementary Material for this article can be found online at: <https://www.frontiersin.org/articles/10.3389/fncel.72021.690147/full#supplementary-material>.

<sup>1</sup><https://www.janelia.org/jgcam8-calcium-indicators>

## REFERENCES

- Akerboom, J., Carreras Calderon, N., Tian, L., Wabnig, S., Prigge, M., Tolo, J., et al. (2013). Genetically encoded calcium indicators for multi-color neural activity imaging and combination with optogenetics. *Front. Mol. Neurosci.* 6:2. doi: 10.3389/fnmol.2013.00002
- Atkin, S. D., Patel, S., Kocharyan, A., Holtzclaw, L. A., Weerth, S. H., Schram, V., et al. (2009). Transgenic mice expressing a cameleon fluorescent  $Ca^{2+}$  indicator in astrocytes and Schwann cells allow study of glial cell  $Ca^{2+}$  signals *in situ* and *in vivo*. *J. Neurosci. Methods* 181, 212–226. doi: 10.1016/j.jneumeth.2009.05.006
- Barykina, N. V., Sotskov, V. P., Gruzdeva, A. M., Wu, Y. K., Portugues, R., Subach, O. M., et al. (2020). FGCAMP7, an improved version of fungi-based ratiometric calcium indicator for *in vivo* visualization of neuronal activity. *Int. J. Mol. Sci.* 21:3012. doi: 10.3390/ijms21083012
- Beiersdorfer, A., Scheller, A., Kirchhoff, F., and Lohr, C. (2019). Panglial gap junctions between astrocytes and olfactory ensheathing cells mediate transmission of  $Ca^{2+}$  transients and neurovascular coupling. *Glia* 67, 1385–1400. doi: 10.1002/glia.23613
- Bernardinelli, Y., Salmon, C., Jones, E. V., Farmer, W. T., Stellwagen, D., Murai, K. K., et al. (2011). Astrocytes display complex and localized calcium responses to single-neuron stimulation in the hippocampus. *J. Neurosci.* 31, 8905–8919. doi: 10.1523/JNEUROSCI.6341-10.2011
- Bethge, P., Carta, S., Lorenzo, D. A., Ego, L., Goniotaki, D., Madisen, L., et al. (2017). An R-CaMP1.07 reporter mouse for cell-type-specific expression of a sensitive red fluorescent calcium indicator. *PLoS One* 12:e0179460. doi: 10.1371/journal.pone.0179460
- Bojarskaite, L., Bjørnstad, D. M., Pettersen, K. H., Cunen, C., Hermansen, G. H., Åbjørnsbråten, K. S., et al. (2020). Astrocytic  $Ca^{2+}$  signaling is reduced during sleep and is involved in the regulation of slow wave sleep. *Nat. Commun.* 11:3240. doi: 10.1038/s41467-020-17062-2
- Boyden, E. S., Zhang, F., Bamberg, E., Nagel, G., and Deisseroth, K. (2005). Millisecond-timescale, genetically targeted optical control of neural activity. *Nat. Neurosci.* 8, 1263–1268. doi: 10.1038/nn1525
- Brawek, B., Liang, Y., Savitska, D., Li, K., Fomin-Thunemann, N., Kovalchuk, Y., et al. (2017). A new approach for ratiometric *in vivo* calcium imaging of microglia. *Sci. Rep.* 7:6030. doi: 10.1038/s41598-017-05952-3
- Chalfie, M., Tu, Y., Euskirchen, G., Ward, W. W., and Prasher, D. C. (1994). Green fluorescent protein as a marker for gene expression. *Science* 263, 802–805. doi: 10.1126/science.8303295



- Chen, T. W., Wardill, T. J., Sun, Y., Pulver, S. R., Renninger, S. L., Baohan, A., et al. (2013). Ultrasensitive fluorescent proteins for imaging neuronal activity. *Nature* 499, 295–300. doi: 10.1038/nature12354
- Clarke, L. E., and Barres, B. A. (2013). Emerging roles of astrocytes in neural circuit development. *Nat. Rev. Neurosci.* 14, 311–321. doi: 10.1038/nrn3484
- Covelo, A., and Araque, A. (2018). Neuronal activity determines distinct gliotransmitter release from a single astrocyte. *eLife* 7:e32237. doi: 10.7554/eLife.32237
- Dana, H., Mohar, B., Sun, Y., Narayan, S., Gordus, A., Hasseman, J. P., et al. (2016). Sensitive red protein calcium indicators for imaging neural activity. *eLife* 5:e12727. doi: 10.7554/eLife.12727
- Dana, H., Novak, O., Guardado-Montesino, M., Fransen, J. W., Hu, A., Borghuis, B. G., et al. (2018). Thy1 transgenic mice expressing the red fluorescent calcium indicator jRGECO1a for neuronal population imaging *in vivo*. *PLoS One* 13:e0205444. doi: 10.1371/journal.pone.0205444
- Dana, H., Sun, Y., Mohar, B., Hulse, B. K., Kerlin, A. M., Hasseman, J. P., et al. (2019). High-performance calcium sensors for imaging activity in neuronal populations and microcompartments. *Nat. Methods* 16, 649–657. doi: 10.1038/s41592-019-0435-6
- Deitmer, J. W., Verkhratsky, A. J., and Lohr, C. (1998). Calcium signaling in glial cells. *Cell Calcium* 24, 405–416. doi: 10.1016/s0143-4160(98)90063-x
- Di Castro, M. A., Chuquet, J., Liaudet, N., Bhaukaurally, K., Santello, M., Bouvier, D., et al. (2011). Local Ca<sup>2+</sup> detection and modulation of synaptic release by astrocytes. *Nat. Neurosci.* 14, 1276–1284. doi: 10.1038/nn.2929
- Direnberger, S., Mues, M., Micale, V., Wotjak, C. T., Dietzel, S., Schubert, M., et al. (2012). Biocompatibility of a genetically encoded calcium indicator in a transgenic mouse model. *Nat. Commun.* 3:1031. doi: 10.1038/ncomms2035
- Doengi, M., Deitmer, J. W., and Lohr, C. (2008). New evidence for purinergic signaling in the olfactory bulb: A2A and P2Y1 receptors mediate intracellular calcium release in astrocytes. *FASEB J.* 22, 2368–2378. doi: 10.1096/fj.07-101782
- Doengi, M., Hirnet, D., Coulon, P., Pape, H. C., Deitmer, J. W., and Lohr, C. (2009). GABA uptake-dependent Ca<sup>2+</sup> signaling in developing olfactory bulb astrocytes. *Proc. Natl. Acad. Sci. U S A* 106, 17570–17575. doi: 10.1073/pnas.0809513106
- Droste, D., Seifert, G., Seddar, L., Jadtke, O., Steinhäuser, C., and Lohr, C. (2017). Ca<sup>2+</sup>-permeable AMPA receptors in mouse olfactory bulb astrocytes. *Sci. Rep.* 7:44817. doi: 10.1038/srep44817
- Eberhard, M., and Erne, P. (1991). Calcium binding to fluorescent calcium indicators: calcium green, calcium orange and calcium crimson. *Biochem. Biophys. Res. Commun.* 180, 209–215. doi: 10.1016/s0006-291x(05)81278-1
- Egbert, J. R., Fahey, P. G., Reimer, J., Owen, C. M., Eysikov, A. V., Nikolaev, V. O., et al. (2019). Follicle-stimulating hormone and luteinizing hormone increase Ca<sup>2+</sup> in the granulosa cells of mouse ovarian follicles. *Biol. Reprod.* 101, 433–444. doi: 10.1093/biolre/iz085
- Farhi, S. L., Parot, V. J., Grama, A., Yamagata, M., Abdelfattah, A. S., Adam, Y., et al. (2019). Wide-area all-optical neurophysiology in acute brain slices. *J. Neurosci.* 39, 4889–4908. doi: 10.1523/JNEUROSCI.0168-19.2019
- Fischer, T., Prey, J., Eschholz, L., Rotermund, N., and Lohr, C. (2021). Norepinephrine-induced calcium signaling and store-operated calcium entry in olfactory bulb astrocytes. *Front. Cell. Neurosci.* 15:639754. doi: 10.3389/fncel.2021.639754
- Fischer, T., Scheffler, P., and Lohr, C. (2020). Dopamine-induced calcium signaling in olfactory bulb astrocytes. *Sci. Rep.* 10:631. doi: 10.1038/s41598-020-57462-4
- Gasterstädt, I., Jack, A., Stahlhut, T., Rennau, L. M., Gonda, S., and Wahle, P. (2020). Genetically encoded calcium indicators can impair dendrite growth of cortical neurons. *Front. Cell. Neurosci.* 14:570596. doi: 10.3389/fncel.2020.570596
- Gee, K. R., Brown, K. A., Chen, W. N., Bishop-Stewart, J., Gray, D., Johnson, I., et al. (2000). Chemical and physiological characterization of fluo-4 Ca<sup>2+</sup>-indicator dyes. *Cell Calcium* 27, 97–106. doi: 10.1054/ceca.1999.0095
- Grosche, J., Matyash, V., Moller, T., Verkhratsky, A., Reichenbach, A., and Kettenmann, H. (1999). Microdomains for neuron-glia interaction: parallel fiber signaling to Bergmann glial cells. *Nat. Neurosci.* 2, 139–143. doi: 10.1038/5692
- Gryniewicz, G., Poenie, M., and Tsien, R. Y. (1985). A new generation of Ca<sup>2+</sup> indicators with greatly improved fluorescence properties. *J. Biol. Chem.* 260, 3440–3450.
- Härtel, K., Singaravelu, K., Kaiser, M., Neusch, C., Hülsmann, S., and Deitmer, J. W. (2007). Calcium influx mediated by the inwardly rectifying K<sup>+</sup> channel Kir4.1 (KCNJ10) at low external K<sup>+</sup> concentration. *Cell Calcium* 42, 271–280. doi: 10.1016/j.ceca.2006.12.004
- Haustein, M. D., Kracun, S., Lu, X. H., Shih, T., Jackson-Weaver, O., Tong, X., et al. (2014). Conditions and constraints for astrocyte calcium signaling in the hippocampal mossy fiber pathway. *Neuron* 82, 413–429. doi: 10.1016/j.neuron.2014.02.041
- Heim, R., Cubitt, A. B., and Tsien, R. Y. (1995). Improved green fluorescence. *Nature* 373, 663–664. doi: 10.1038/373663b0
- Heim, N., and Griesbeck, O. (2004). Genetically encoded indicators of cellular calcium dynamics based on troponin C and green fluorescent protein. *J. Biol. Chem.* 279, 14280–14286. doi: 10.1074/jbc.M312751200
- Heim, R., and Tsien, R. Y. (1996). Engineering green fluorescent protein for improved brightness, longer wavelengths and fluorescence resonance energy transfer. *Curr. Biol.* 6, 178–182. doi: 10.1016/s0960-9822(02)00450-5
- Henneberger, C., Papouin, T., Oliet, S. H., and Rusakov, D. A. (2010). Long-term potentiation depends on release of D-serine from astrocytes. *Nature* 463, 232–236. doi: 10.1038/nature08673
- Horikawa, K., Yamada, Y., Matsuda, T., Kobayashi, K., Hashimoto, M., Matsu-ura, T., et al. (2010). Spontaneous network activity visualized by ultrasensitive Ca<sup>2+</sup> indicators, yellow Cameleon-Nano. *Nat. Methods* 7, 729–732. doi: 10.1038/nmeth.1488
- Inoue, M. (2020). Genetically encoded calcium indicators to probe complex brain circuit dynamics *in vivo*. *Neurosci. Res.* 9:S0168-0102(20)30230-3. doi: 10.1016/j.neures.2020.05.013
- Inoue, M., Takeuchi, A., Manita, S., Horigane, S. I., Sakamoto, M., Kawakami, R., et al. (2019). Rational engineering of XCaMPs, a multicolor GECI suite for *in vivo* imaging of complex brain circuit dynamics. *Cell* 177, 1346–1360.e1324. doi: 10.1016/j.cell.2019.04.007
- Kanemaru, K., Sekiya, H., Xu, M., Satoh, K., Kitajima, N., Yoshida, K., et al. (2014). *In vivo* visualization of subtle, transient and local activity of astrocytes using an ultrasensitive Ca<sup>2+</sup> indicator. *Cell Rep.* 8, 311–318. doi: 10.1016/j.celrep.2014.05.056
- Kang, J., Kang, N., Yu, Y., Zhang, J., Petersen, N., Tian, G. F., et al. (2010). Sulforhodamine 101 induces long-term potentiation of intrinsic excitability and synaptic efficacy in hippocampal CA1 pyramidal neurons. *Neuroscience* 169, 1601–1609. doi: 10.1016/j.neuroscience.2010.06.020
- Kerruth, S., Coates, C., Durst, C. D., Oertner, T. G., and Torok, K. (2019). The kinetic mechanisms of fast-decay red-fluorescent genetically encoded calcium indicators. *J. Biol. Chem.* 294, 3934–3946. doi: 10.1074/jbc.RA118.004543
- Khakh, B. S., and McCarthy, K. D. (2015). Astrocyte calcium signaling: from observations to functions and the challenges therein. *Cold. Spring Harb. Perspect. Biol.* 7:a020404. doi: 10.1101/cshperspect.a020404
- Khakh, B. S., and Sofroniew, M. V. (2015). Diversity of astrocyte functions and phenotypes in neural circuits. *Nat. Neurosci.* 18, 942–952. doi: 10.1038/nn.4043
- Kofuji, P., and Araque, A. (2021a). Astrocytes and Behavior. *Annu. Rev. Neurosci.* 44:2021. doi: 10.1146/annurev-neuro-101920-112225
- Kofuji, P., and Araque, A. (2021b). G-protein-coupled receptors in astrocyte-neuron communication. *Neuroscience* 456, 71–84. doi: 10.1016/j.neuroscience.2020.03.025
- Lind, B. L., Brazhe, A. R., Jessen, S. B., Tan, F. C., and Lauritzen, M. J. (2013). Rapid stimulus-evoked astrocyte Ca<sup>2+</sup> elevations and hemodynamic responses in mouse somatosensory cortex *in vivo*. *Proc. Natl. Acad. Sci. U S A* 110, E4678–E4687. doi: 10.1073/pnas.1310065110
- Lines, J., Martin, E. D., Kofuji, P., Aguilar, J., and Araque, A. (2020). Astrocytes modulate sensory-evoked neuronal network activity. *Nat. Commun.* 11:3689. doi: 10.1038/s41467-020-17536-3
- Lohr, C., and Deitmer, J. W. (1999). Dendritic calcium transients in the leech giant glial cell *in situ*. *Glia* 26, 109–118.
- Lohr, C., and Deitmer, J. W. (2010). “Ca<sup>2+</sup> Imaging of g,” in *Calcium Measurement Methods*, eds A. Verkhratsky, and O. H. Petersen (Totowa, NJ: Humana Press), 221–249.

- Losi, G., Lia, A. M., Gomez-Gonzalo, M., Zonta, M., and Carmignoto, G. (2019). Optogenetic interneuron stimulation and calcium imaging in astrocytes. *Methods Mol. Biol.* 1925, 173–182. doi: 10.1007/978-1-4939-9018-4\_16
- Losi, G., Mariotti, L., Sessolo, M., and Carmignoto, G. (2017). New tools to study astrocyte  $\text{Ca}^{2+}$  signal dynamics in brain networks *in vivo*. *Front. Cell. Neurosci.* 11:134. doi: 10.3389/fncel.2017.00134
- Madisen, L., Garner, A. R., Shimaoka, D., Chuong, A. S., Klapoetke, N. C., Li, L., et al. (2015). Transgenic mice for intersectional targeting of neural sensors and effectors with high specificity and performance. *Neuron* 85, 942–958. doi: 10.1016/j.neuron.2015.02.022
- Mank, M., and Griesbeck, O. (2008). Genetically encoded calcium indicators. *Chem. Rev.* 108, 1550–1564. doi: 10.1021/cr078213v
- Mank, M., Santos, A. F., Drenth, S., Mrcic-Flogel, T. D., Hofer, S. B., Stein, V., et al. (2008). A genetically encoded calcium indicator for chronic *in vivo* two-photon imaging. *Nat. Methods* 5, 805–811. doi: 10.1038/nmeth.1243
- Mariotti, L., Losi, G., Lia, A., Melone, M., Chiavegato, A., Gómez-Gonzalo, M., et al. (2018). Interneuron-specific signaling evokes distinctive somatostatin-mediated responses in adult cortical astrocytes. *Nat. Commun.* 9:82. doi: 10.1038/s41467-017-02642-6
- Mohr, M. A., Bushey, D., Aggarwal, A., Marvin, J. S., Kim, J. J., Marquez, E. J., et al. (2020). jYCaMP: an optimized calcium indicator for two-photon imaging at fiber laser wavelengths. *Nat. Methods* 17, 694–697. doi: 10.1038/s41592-020-0835-7
- Mollinedo-Gajate, I., Song, C., and Knöpfel, T. (2019). Genetically encoded fluorescent calcium and voltage indicators. *Handb. Exp. Pharmacol.* 260, 209–229. doi: 10.1007/164\_2019\_299
- Monai, H., Ohkura, M., Tanaka, M., Oe, Y., Konno, A., Hirai, H., et al. (2016). Calcium imaging reveals glial involvement in transcranial direct current stimulation-induced plasticity in mouse brain. *Nat. Commun.* 7:11100. doi: 10.1038/ncomms11100
- Mulligan, S. J., and MacVicar, B. A. (2004). Calcium transients in astrocyte endfeet cause cerebrovascular constrictions. *Nature* 431, 195–199. doi: 10.1038/nature02827
- Nagai, T., Yamada, S., Tominaga, T., Ichikawa, M., and Miyawaki, A. (2004). Expanded dynamic range of fluorescent indicators for  $\text{Ca}^{2+}$  by circularly permuted yellow fluorescent proteins. *Proc. Natl. Acad. Sci. U S A* 101, 10554–10559. doi: 10.1073/pnas.0400417101
- Nagel, G., Szellas, T., Huhn, W., Kateriya, S., Adeishvili, N., Berthold, P., et al. (2003). Channelrhodopsin-2, a directly light-gated cation-selective membrane channel. *Proc. Natl. Acad. Sci. U S A* 100, 13940–13945. doi: 10.1073/pnas.1936192100
- Nakai, J., Ohkura, M., and Imoto, K. (2001). A high signal-to-noise  $\text{Ca}^{2+}$  probe composed of a single green fluorescent protein. *Nat. Biotechnol.* 19, 137–141. doi: 10.1038/84397
- Nakayama, R., Sasaki, T., Tanaka, K. F., and Ikegaya, Y. (2016). Subcellular calcium dynamics during juvenile development in mouse hippocampal astrocytes. *Eur. J. Neurosci.* 43, 923–932. doi: 10.1111/ejn.13188
- Nikolic, L., Shen, W., Nobili, P., Virenque, A., Ulmann, L., and Audinat, E. (2018). Blocking TNF $\alpha$ -driven astrocyte purinergic signaling restores normal synaptic activity during epileptogenesis. *Glia* 66, 2673–2683. doi: 10.1002/glia.23519
- Nimmerjahn, A., Kirchhoff, F., Kerr, J. N., and Helmchen, F. (2004). Sulforhodamine 101 as a specific marker of astroglia in the neocortex *in vivo*. *Nat. Methods* 1, 31–37. doi: 10.1038/nmeth706
- Oe, Y., Wang, X., Patriarchi, T., Konno, A., Ozawa, K., Yahagi, K., et al. (2020). Distinct temporal integration of noradrenergic signaling by astrocytic second messengers during vigilance. *Nat. Commun.* 11:471. doi: 10.1038/s41467-020-14378-x
- Ohkura, M., Sasaki, T., Kobayashi, C., Ikegaya, Y., and Nakai, J. (2012a). An improved genetically encoded red fluorescent  $\text{Ca}^{2+}$  indicator for detecting optically evoked action potentials. *PLoS One* 7:e39933. doi: 10.1371/journal.pone.0039933
- Ohkura, M., Sasaki, T., Sadakari, J., Gengyo-Ando, K., Kagawa-Nagamura, Y., Kobayashi, C., et al. (2012b). Genetically encoded green fluorescent  $\text{Ca}^{2+}$  indicators with improved detectability for neuronal  $\text{Ca}^{2+}$  signals. *PLoS One* 7:e51286. doi: 10.1371/journal.pone.0051286
- Okubo, Y., and Iino, M. (2020). Visualization of astrocytic intracellular  $\text{Ca}^{2+}$  mobilization. *J. Physiol.* 598, 1671–1681. doi: 10.1113/JP277609
- Otsu, Y., Couchman, K., Lyons, D. G., Collot, M., Agarwal, A., Mallet, J. M., et al. (2015). Calcium dynamics in astrocyte processes during neurovascular coupling. *Nat. Neurosci.* 18, 210–218. doi: 10.1038/nn.3906
- Paredes, R. M., Etzler, J. C., Watts, L. T., Zheng, W., and Lechleiter, J. D. (2008). Chemical calcium indicators. *Methods* 46, 143–151. doi: 10.1016/j.ymeth.2008.09.025
- Prasher, D. C., Eckenrode, V. K., Ward, W. W., Prendergast, F. G., and Cormier, M. J. (1992). Primary structure of the Aequorea victoria green-fluorescent protein. *Gene* 111, 229–233. doi: 10.1016/0378-1119(92)90691-h
- Qian, Y., Cosio, D. M. O., Piatkevich, K. D., Aufmkolk, S., Su, W. C., Celiker, O. T., et al. (2020). Improved genetically encoded near-infrared fluorescent calcium ion indicators for *in vivo* imaging. *PLoS Biol.* 18:e3000965. doi: 10.1371/journal.pbio.3000965
- Sato, M., Kawano, M., Ohkura, M., Gengyo-Ando, K., Nakai, J., Hayashi, Y., et al. (2015). Generation and imaging of transgenic mice that express G-CaMP7 under a tetracycline response element. *PLoS One* 10:e0125354. doi: 10.1371/journal.pone.0125354
- Schnell, C., Shahmoradi, A., Wichert, S. P., Mayerl, S., Hagos, Y., Heuer, H., et al. (2015). The multispecific thyroid hormone transporter OATP1C1 mediates cell-specific sulforhodamine 101-labeling of hippocampal astrocytes. *Brain Struct. Funct.* 220, 193–203. doi: 10.1007/s00429-013-0645-0
- Semyanov, A., Henneberger, C., and Agarwal, A. (2020). Making sense of astrocytic calcium signals—from acquisition to interpretation. *Nat. Rev. Neurosci.* 21, 551–564. doi: 10.1038/s41583-020-0361-8
- Shen, Y., Dana, H., Abdelfattah, A. S., Patel, R., Shea, J., Molina, R. S., et al. (2018). A genetically encoded  $\text{Ca}^{2+}$  indicator based on circularly permuted sea anemone red fluorescent protein eqFP578. *BMC Biol.* 16:9. doi: 10.1186/s12915-018-0480-0
- Shen, Y., Nasu, Y., Shkolnikov, I., Kim, A., and Campbell, R. E. (2020). Engineering genetically encoded fluorescent indicators for imaging of neuronal activity: progress and prospects. *Neurosci. Res.* 152, 3–14. doi: 10.1016/j.neures.2020.01.011
- Shigetomi, E., Bushong, E. A., Hausteine, M. D., Tong, X., Jackson-Weaver, O., Kracun, S., et al. (2013). Imaging calcium microdomains within entire astrocyte territories and endfeet with GCaMPs expressed using adeno-associated viruses. *J. Gen. Physiol.* 141, 633–647. doi: 10.1085/jgp.201210949
- Singarvelu, K., Lohr, C., and Deitmer, J. W. (2006). Regulation of store-operated calcium entry by calcium-independent phospholipase A2 in rat cerebellar astrocytes. *J. Neurosci.* 26, 9579–9592. doi: 10.1523/JNEUROSCI.2604-06.2006
- Smith, N. A., Kress, B. T., Lu, Y., Chandler-Militello, D., Benraiss, A., and Nedergaard, M. (2018). Fluorescent  $\text{Ca}^{2+}$  indicators directly inhibit the Na,K-ATPase and disrupt cellular functions. *Sci. Signal.* 11:eaa12039. doi: 10.1126/scisignal.aal2039
- Srinivasan, R., Huang, B. S., Venugopal, S., Johnston, A. D., Chai, H., Zeng, H., et al. (2015).  $\text{Ca}^{2+}$  signaling in astrocytes from  $\text{Ip3r2}^{-/-}$  mice in brain slices and during startle responses *in vivo*. *Nat. Neurosci.* 18, 708–717. doi: 10.1038/nn.4001
- Srinivasan, R., Lu, T. Y., Chai, H., Xu, J., Huang, B. S., Golshani, P., et al. (2016). New transgenic mouse lines for selectively targeting astrocytes and studying calcium signals in astrocyte processes *in situ* and *in vivo*. *Neuron* 92, 1181–1195. doi: 10.1016/j.neuron.2016.11.030
- Stobart, J. L., Ferrari, K. D., Barrett, M. J. P., Gluck, C., Stobart, M. J., Zuend, M., et al. (2018). Cortical circuit activity evokes rapid astrocyte calcium signals on a similar timescale to neurons. *Neuron* 98, 726–735.e724. doi: 10.1016/j.neuron.2018.03.050
- Thestrup, T., Litzlbauer, J., Bartholomäus, I., Mues, M., Russo, L., Dana, H., et al. (2014). Optimized ratiometric calcium sensors for functional *in vivo* imaging of neurons and T lymphocytes. *Nat. Methods* 11, 175–182. doi: 10.1038/nmeth.2773
- Tran, C. H. T., Perinod, G., and Gordon, G. R. (2018). Astrocytes integrate behavioral state and vascular signals during functional hyperemia. *Neuron* 100, 1133–1148.e1133. doi: 10.1016/j.neuron.2018.09.045
- Trigo-Mourino, P., Thestrup, T., Griesbeck, O., Griesinger, C., and Becker, S. (2019). Dynamic tuning of FRET in a green fluorescent protein biosensor. *Sci. Adv.* 5:eaa4988. doi: 10.1126/sciadv.aaw4988

- Tsien, R. Y. (1989). Fluorescent indicators of ion concentrations. *Methods Cell Biol.* 30, 127–156. doi: 10.1016/s0091-679x(08)60978-4
- Ung, K., Tepe, B., Pekarek, B., Arenkiel, B. R., and Deneen, B. (2020). Parallel astrocyte calcium signaling modulates olfactory bulb responses. *J. Neurosci. Res.* 98, 1605–1618. doi: 10.1002/jnr.24634
- Verkhratsky, A., and Nedergaard, M. (2018). Physiology of astroglia. *Physiol. Rev.* 98, 239–389. doi: 10.1152/physrev.00042.2016
- Wilms, C. D., and Häusser, M. (2014). Twitching towards the ideal calcium sensor. *Nat. Methods* 11, 139–140. doi: 10.1038/nmeth.2814
- Woo, J., Jang, M. W., Lee, J., Koh, W., Mikoshiba, K., and Lee, C. J. (2020). The molecular mechanism of synaptic activity-induced astrocytic volume transient. *J. Physiol.* 598, 4555–4572. doi: 10.1113/jp279741
- Yang, Y., Liu, N., He, Y., Liu, Y., Ge, L., Zou, L., et al. (2018). Improved calcium sensor GCaMP-X overcomes the calcium channel perturbations induced by the calmodulin in GCaMP. *Nat. Commun.* 9:1504. doi: 10.1038/s41467-018-03719-6
- Ye, L., Haroon, M. A., Salinas, A., and Paukert, M. (2017). Comparison of GCaMP3 and GCaMP6f for studying astrocyte Ca<sup>2+</sup> dynamics in the awake mouse brain. *PLoS One* 12:e0181113. doi: 10.1371/journal.pone.0181113
- Yoshikawa, S., Usami, T., Kikuta, J., Ishii, M., Sasano, T., Sugiyama, K., et al. (2016). Intravital imaging of Ca<sup>2+</sup> signals in lymphocytes of Ca<sup>2+</sup> biosensor transgenic mice: indication of autoimmune diseases before the pathological onset. *Sci. Rep.* 6:18738. doi: 10.1038/srep18738
- Yu, X., Nagai, J., and Khakh, B. S. (2020). Improved tools to study astrocytes. *Nat. Rev. Neurosci.* 21, 121–138. doi: 10.1038/s41583-020-0264-8

**Conflict of Interest:** The authors declare that the research was conducted in the absence of any commercial or financial relationships that could be construed as a potential conflict of interest.

Copyright © 2021 Lohr, Beiersdorfer, Fischer, Hirnet, Rotermund, Sauer, Schulz and Gee. This is an open-access article distributed under the terms of the Creative Commons Attribution License (CC BY). The use, distribution or reproduction in other forums is permitted, provided the original author(s) and the copyright owner(s) are credited and that the original publication in this journal is cited, in accordance with accepted academic practice. No use, distribution or reproduction is permitted which does not comply with these terms.



# Versatile Surface Electrodes for Combined Electrophysiology and Two-Photon Imaging of the Mouse Central Nervous System

Michael Schweigmann<sup>1,2†</sup>, Laura C. Caudal<sup>1†</sup>, Gebhard Stopper<sup>1</sup>, Anja Scheller<sup>1</sup>, Klaus P. Koch<sup>2</sup> and Frank Kirchhoff<sup>1\*</sup>

<sup>1</sup>Molecular Physiology, Center for Integrative Physiology and Molecular Medicine (CIPMM), University of Saarland, Homburg, Germany, <sup>2</sup>Department of Electrical Engineering, Trier University of Applied Sciences, Trier, Germany

## OPEN ACCESS

### Edited by:

Francesca Boscia,  
University of Naples Federico II, Italy

### Reviewed by:

Bernd Kuhn,  
Okinawa Institute of Science and  
Technology Graduate University,  
Japan

Yu-Feng Wang,  
Harbin Medical University, China

### \*Correspondence:

Frank Kirchhoff  
frank.kirchhoff@uks.eu

<sup>†</sup>These authors have contributed  
equally to this work

### Specialty section:

This article was submitted to  
Non-Neuronal Cells,  
a section of the journal  
Frontiers in Cellular Neuroscience

**Received:** 04 June 2021

**Accepted:** 19 July 2021

**Published:** 10 August 2021

### Citation:

Schweigmann M, Caudal LC, Stopper G, Scheller A, Koch KP and Kirchhoff F (2021) Versatile Surface Electrodes for Combined Electrophysiology and Two-Photon Imaging of the Mouse Central Nervous System. *Front. Cell. Neurosci.* 15:720675. doi: 10.3389/fncel.2021.720675

Understanding and modulating CNS function in physiological as well as pathophysiological contexts remains a significant ambition in research and clinical applications. The investigation of the multifaceted CNS cell types including their interactions and contributions to neural function requires a combination of the state-of-the-art *in vivo* electrophysiology and imaging techniques. We developed a novel type of liquid crystal polymer (LCP) surface micro-electrode manufactured in three customized designs with up to 16 channels for recording and stimulation of brain activity. All designs include spare central spaces for simultaneous 2P-imaging. Nanoporous platinum-plated contact sites ensure a low impedance and high current transfer. The epidural implantation of the LCP micro-electrodes could be combined with standard cranial window surgery. The epidurally positioned electrodes did not only display long-term biocompatibility, but we also observed an additional stabilization of the underlying CNS tissue. We demonstrate the electrode's versatility in combination with *in vivo* 2P-imaging by monitoring anesthesia-awake cycles of transgenic mice with GCaMP3 expression in neurons or astrocytes. Cortical stimulation and simultaneous 2P  $\text{Ca}^{2+}$  imaging in neurons or astrocytes highlighted the astrocytes' integrative character in neuronal activity processing. Furthermore, we confirmed that spontaneous astroglial  $\text{Ca}^{2+}$  signals are dampened under anesthesia, while evoked signals in neurons and astrocytes showed stronger dependency on stimulation intensity rather than on various levels of anesthesia. Finally, we show that the electrodes provide recordings of the electrocorticogram (ECoG)

**Abbreviations:** 2P-LSM, two-photon laser scanning microscopy; CNS, central nervous system; Cre, Cre DNA recombinase; CreERT2, Cre DNA recombinase fused to mutated human estrogen receptor ligand-binding domain; CSCc, cathodic charge storage capacity; DAPI, 4',6-diamidino-2-phenylindole; ECoG, electrocorticogram; FI, fluorescence intensity; GFAP, glial fibrillary acidic protein; GFP, green fluorescent protein; GLAST, glutamate/aspartate transporter; Iba1, ionized calcium binding adaptor molecule 1; LCP, liquid crystal polymer; loxP, locus of crossover of the bacteriophage P1; NCX,  $\text{Na}^+/\text{Ca}^{2+}$  exchanger; Nex, NeuroD6, subfamily of neuronal basic helix-loop-helix transcription factors; NMDA receptor, N-methyl-D-aspartate receptor; pCAGGS, cytomegalovirus immediate early enhancer/chicken beta-actin/rabbit beta-globin hybrid promoter; PMCA, plasma membrane  $\text{Ca}^{2+}$  ATPase; ROI, region of interest; SD, standard deviation; SERCA, sarcoplasmic/endoplasmic reticulum  $\text{Ca}^{2+}$  ATPase; Th, Threshold; WPRE, Woodchuck hepatitis virus posttranscriptional regulatory element; Z, impedance.



with a high signal-to noise ratio and spatial signal differences which help to decipher brain activity states during experimental procedures. Summarizing, the novel LCP surface micro-electrode is a versatile, convenient, and reliable tool to investigate brain function *in vivo*.

**Keywords:** liquid crystal polymer electrodes, cortical stimulation, electrocorticogram, *in vivo* two-photon laser-scanning microscopy, neuron-glia interaction, astrocytes

## INTRODUCTION

The perpetuate quest of understanding and modulating brain function continuously confronts the scientific community with a multitude of technical challenges (Rusakov, 2015; Chen et al., 2021). Neurons and their electrophysiological characteristics were the long-standing focus of brain research, promoting the development of various electrophysiological probes to record and/or stimulate brain activity. Applications ranged from single cell experiments, over *ex vivo* slice measurements, to *in vivo* recording and stimulation from the surface or within the tissue. Electrical stimulation of the CNS is used in clinical routines to treat disorders such as Parkinson's disease by deep brain stimulation or depression by transcranial electrical stimulation (Kirsch and Nichols, 2013; Beudel and Brown, 2016; Beckner, 2020). The interaction of the electrical field and the excitable tissue is the base for artificial stimulation. When artificially triggering action potentials with electrical stimulation, the voltage-dependent conductivity of the cell membrane for Na<sup>+</sup> (and K<sup>+</sup>) is exploited. The neuronal excitation depends on the applied field and cell orientation, neuronal subtype, cellular structure, as well as the resulting field distribution generated by the anisotropy of the neural tissue (Rattay, 1998; Basser and Roth, 2000; Radman et al., 2009; Ye and Steiger, 2015). However, advances in neuroscience established the essential contribution of glial cells to brain function in health and disease. Glial cells not only crucially maintain brain homeostasis, but actively participate in neurotransmission, shape neural circuits (Parpura et al., 1994; Araque et al., 1999; Verkhratsky and Nedergaard, 2018; Durkee and Araque, 2019; Caudal et al., 2020), act as resident immune-competent cells (Nimmerjahn et al., 2005; Prinz et al., 2019) and provide myelin sheaths, thereby ensuring fast and reliable neuronal communication (Simons and Nave, 2015; Swire and Ffrench-Constant, 2018). Moreover, glial cell (dys-) function has been implicated in a variety of CNS disorders including Alzheimer's (Gómez-Gonzalo et al., 2017; Arranz and De Strooper, 2019), Parkinson's (Yun et al., 2018; Guo et al., 2020), multiple sclerosis (International Multiple Sclerosis Genetics Consortium, 2019; Yeung et al., 2019; Traiffort et al., 2020) and epilepsy (Heuser et al., 2018; Nikolic et al., 2018; Deshpande et al., 2020). Importantly, glial cells such as astrocytes, primarily display activation through intracellular Ca<sup>2+</sup> rises coupled to the release of neuroactive substances, modulating network function (Bazargani and Attwell, 2016; Covelo and Araque, 2018). In contrast, neurons are primarily characterized by their electrical activity but nonetheless exhibit extensive Ca<sup>2+</sup> signaling relevant in physiology and pathology (Brini et al., 2014). In addition, neuron-glia interactions are governed by second

messengers other than Ca<sup>2+</sup>, e.g., Na<sup>+</sup> (Ross et al., 2013; Karus et al., 2015; Ziemens et al., 2019) and cyclic AMP (Harada et al., 2017; Bernier et al., 2019). Investigation of those second messenger dynamics *in vivo* requires the use of fluorescent indicators and sensors, thus endorsing the refinement and novel development of neuroscientific tools to study neuron-glia interactions by combining electrophysiological and 2P-imaging techniques.

Considering combined electrophysiology and 2P-imaging *in vivo* (Figure 1A), the requirements for microelectrodes are ample (Chen et al., 2021). First and foremost, the electrode material must be biocompatible for chronic use, without mechanically damaging the tissue or eliciting inflammatory responses from glial cells. Along the same lines, the electrode array application should be minimally invasive and preferentially keep the dura mater intact (surface electrodes) without entailing major compromises on spatial resolution. Next, the electrode array should be either highly transparent (Park et al., 2014) or provide an optical window to perform imaging (multiphoton, coherent anti-stokes Raman spectroscopic microscopy etc.), potentially coupled to optogenetic approaches (Park et al., 2014; Xie et al., 2020). However, the biomaterial should be stable yet flexible for optimal tissue contact and withstand the impact of laser radiation during 2P-imaging without excessive heat generation. From an electrochemical point of view, the electrodes should be optimized, providing low impedance and high current transfer capability (Cogan, 2008). Finally, the fully assembled microelectrode should allow a safe, fast, and reproducible application in common (rodent) model organisms and come at an affordable cost.

Polyimide (PI) and LCP are the most common flexible carrier materials of industrial large-scale production. Their electrical properties in combination with their chemical and mechanical strength make both materials good candidates for microelectrode assemblies, with LCP electrodes being significantly less expensive than PI electrodes (Woods et al., 2018). Here, we developed LCP electrodes of a stacked support structure formed by Ultralam 3850 sheets and Ultralam 3908 bonding film (Rogers Corporation; Woods et al., 2018). Such LCP material has also been used to record acute neuronal activity in humans (Chiang et al., 2021), indicating its high biocompatibility.

## MATERIALS AND METHODS

### Electrode Technology

The electrodes were designed based on triple LCP layers (Dyconex AG, Switzerland) allowing flexibility, yet maintaining stability, while the electrical circuit structure was made of a

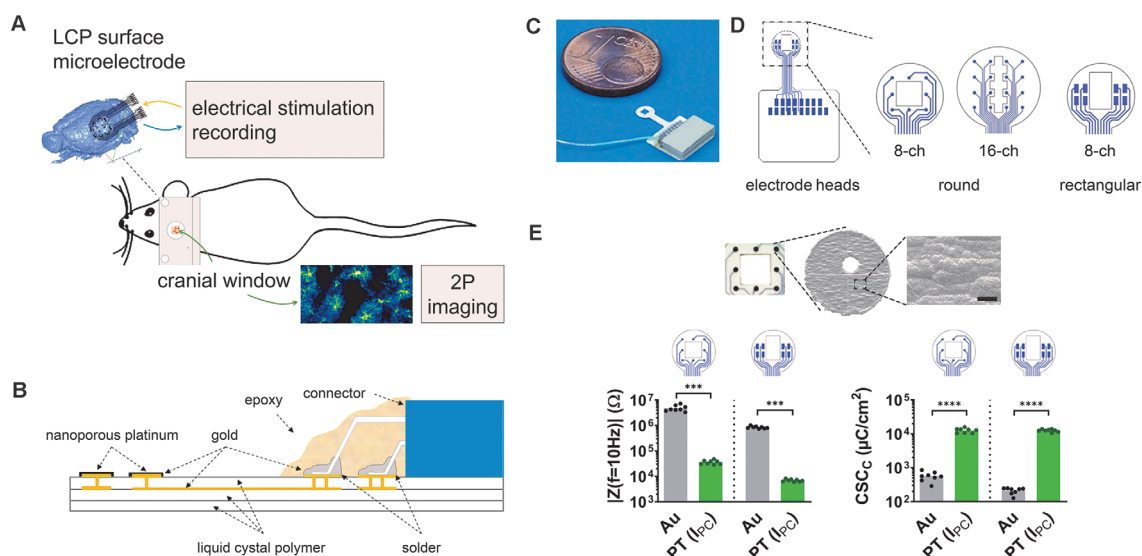


**FIGURE 1** | Development of liquid crystal polymer (LCP) surface electrodes for *in vivo* studies combining electrophysiology and imaging. **(A)** Flexible yet robust surface microelectrodes, applicable for *in vivo* investigation of electrical brain stimulation, electrocorticographic recording of brain activity, and 2P-imaging of  $\text{Ca}^{2+}$  signals. **(B)** Electrode structure with an LCP base including golden electrical structure and superficial gold electrodes, electroplated with nanoporous platinum. The nano-connector is soldered to the terminal pads and secured with epoxy resin. **(C)** Fully assembled LCP surface microelectrode. **(D)** Three different electrode arrays with eight or 16 circular electrodes (3 mm or 4 mm in diameter) for ECoG recording or eight rectangular electrodes for stimulation. Circular electrode sites are 150  $\mu\text{m}$  in diameter; the size of rectangular-shaped sites is 400  $\mu\text{m}$   $\times$  200  $\mu\text{m}$ . The two 8-channel electrode configurations have a spare square in the center (1 mm  $\times$  1 mm or 1 mm  $\times$  1.5 mm), the 16-channel electrode has a polygon (length 2.8 mm; small width: 400  $\mu\text{m}$ ; large width: 800  $\mu\text{m}$ ), allowing 2P-imaging. **(E)** Top: scanning electron micrograph of a single electrode site showing the surface structure, scale bar = 5  $\mu\text{m}$ . Bottom: typical magnitude of electrode impedance at a frequency of 10 Hz ( $|Z(f = 10 \text{ Hz})|$ ) and typical cathodic charge storage capacity ( $\text{CSC}_c$ ). Compared with the gold electrode sites, platinum-coated sites display a lower impedance enabling recordings with less noise and a higher  $\text{CSC}_c$  allowing for higher stimulation currents. Statistics:  $|Z(f = 10 \text{ Hz})|$ : Mann-Whitney test and  $\text{CSC}_c$ : unpaired *t*-test \*\*\* $p < 0.001$ , \*\*\*\* $p < 0.0001$ .  $N = 8$  measurements per condition.

double gold layer (**Figure 1B**). The LCP structure had a thickness of about 75  $\mu\text{m}$ , a limitation in the minimum electrode site size of about 100  $\mu\text{m}$ , and an interconnection width of about 30  $\mu\text{m}$ . The PCB layout program EAGLE (version 7.5.0 Light; CadSoft) was used to generate the electrode geometry and electrical layout, which was sent to the manufacturer for large-volume industrial production. Epoxy resin (TC-EP05-24, TOOLCRAFT) was used to cover the connector (NPD-18-18AA-GS, Omnetics Connector Corp.) and pads. The gold electrode sites were coated with galvanized nanoporous platinum (5 g hexachloroplatinic acid dissolved in 375 ml distilled water; pulse electroplating at 0.3  $\text{kA}/\text{m}^2$ , 90 pulses) and electrochemically characterized by determining the electrode impedance and the cathodic charge storage capacity ( $\text{CSC}_c$ ; Cogan, 2008) with the multi-chemistry device Gamry Interface 1000 (Gamry Instruments).

## Epidural Electrode Implantation and Cranial Window Surgery

Animals were anesthetized with a mixture of 2% Isoflurane with  $\text{O}_2$  (0.6 L/min) and  $\text{N}_2\text{O}$  (0.4 L/min) and kept on a heating plate. A standard craniotomy (3–4 mm in diameter; Cupido et al., 2014; Kislin et al., 2014) was performed over the somatosensory cortex and the surface electrode was placed on the dura mater before applying the glass coverslip. A ground electrode (platinum wire) was superficially inserted into the cerebellar vermis and fixed to the skull surface with dental cement. Electrodes, glass

coverslips, and platinum wire were disinfected and cleaned with alcohol (70% ethanol) and distilled water. Finally, a 3D-printed custom-made holder for head restraining was applied and all components were fixed with dental cement.

## *In vivo* Two-Photon Laser Scanning Microscopy (2P-LSM)

Images were acquired on a custom-made 2P-LSM setup with a mode-locked Ti:Sapphire laser (Vision II, Coherent) using ScanImage software (Pologruto et al., 2003). 2P-LSM settings: laser power 30–50 mW; frame rate of 1.9 Hz [field of view (FOV) size 256  $\mu\text{m}$   $\times$  256  $\mu\text{m}$ ] or 3.3 Hz (FOV size 256  $\mu\text{m}$   $\times$  256  $\mu\text{m}$ ); pixel size: 0.5  $\mu\text{m}$   $\times$  0.5  $\mu\text{m}$ ; astroglial  $\text{Ca}^{2+}$ -transients were acquired in cortical layer I (40  $\mu\text{m}$ –90  $\mu\text{m}$ ) and neuronal activity in layer II/III (180  $\mu\text{m}$ –210  $\mu\text{m}$ ). Prior to  $\text{Ca}^{2+}$  imaging, animals were habituated according to adapted protocols without water restriction (Guo et al., 2014; Kislin et al., 2014). During imaging, the animals were head-fixed and anesthesia was delivered *via* a breathing mask [0–2.5% isoflurane with  $\text{O}_2$  (0.6 L/min) and  $\text{N}_2\text{O}$  (0.4 L/min)].

## Automated Detection of Spontaneous $\text{Ca}^{2+}$ Events

$\text{Ca}^{2+}$ -event analysis was performed using a custom-made analysis software based on MATLAB (MSparkles, unpublished). First, the fluorescence range of each pixel along the temporal

axes of the image stack was computed. Next, local maxima within the range projection were used as seed points for simultaneous, correlation-based region growing. Thereby, the temporal correlation of a candidate pixel with the corresponding seed point was computed using Pearson's linear correlation coefficient. A user-definable correlation threshold was set as the stopping criterion of the region growing process in case the temporal evolution of a candidate pixel deviated too strongly from its respective seed point. A pixel-based correlation coefficient maximization algorithm was employed for image registration (Evangelidis and Psarakis, 2008) and to reduce small motion artifacts of the acquired time series. Upon ROI integration (computing the mean fluorescence per ROI per image), properties of  $\text{Ca}^{2+}$  transients were obtained using the MATLAB function *findpeaks()*.

## Electrocorticographical Recording

A 16-channel biosignal amplifier (g.USBamp, g.Tec medical engineering) with a preamplifier (g.HEADstage, g.Tec medical engineering) and a custom made control software based on MATLAB/Simulink (Englert et al., 2017) was used to acquire the electrical biosignals at a channel sampling rate of 1.2 kHz. Filtering was chosen with a band pass filter of 0.5 Hz to 250 Hz and a notch filter of 50 Hz. Signal processing was performed by calculating the short-time Fourier transform (rectangular sliding window of 2 s shifted in steps of 1 s) and by calculating the correlation coefficient between all single recording channels with customized MATLAB scripts using the main functions *spectrogram()* and *corr()*, respectively. ECoG sections of 30 s from awake and anesthetized mice were used to calculate channel correlation and analyzed as a function of electrode distances. In addition, the channel correlation was calculated with a rectangular sliding window of 2 s in steps of 1 s.

## Electrical Stimulation

A single channel stimulator (ISO-STIM 01D, NPI electronic) connected via a digital-to-analog output card (NI PCI-6723, National Instruments) was controlled by a customized control software (LabView, National Instruments). A second output channel of the analog output card was used for synchronization with the 2P-microscope. The output sampling rate was set to 100 kHz. Threshold (Th) definition was performed in anesthetized animals (isoflurane concentration 1.5%) at 50 Hz stimulation frequency by increasing stimulation current intensities in steps of 25  $\mu\text{A}$  (starting at 100  $\mu\text{A}$ ) for 300 frames (approximately 90 s). Threshold values typically ranged from 125–200  $\mu\text{A}$ . Subsequently, we applied two stimulations at Th, Th + 50  $\mu\text{A}$ , Th + 100  $\mu\text{A}$  to quantify the  $\text{Ca}^{2+}$ -responses. For signal analysis, the mean value per statistical parameter of both stimulation per current strength was calculated. The stimulation series was applied to anesthetized (isoflurane concentrations: 1.5%, 1%, 0.5%) and awake (isoflurane concentrations: 0%) mice.

## Detection of Electrically Evoked $\text{Ca}^{2+}$ Events

Custom-made MATLAB scripts were used to analyze the  $\text{Ca}^{2+}$  events in neurons and astrocytes. A pixel-based correlation

algorithm to align individual images was employed for stack registration (Evangelidis and Psarakis, 2008) followed by the calculation of the mean fluorescence intensity of the whole individual gray-scale images [MATLAB function *mean()*]. Peak amplitude ( $F - F_0/F_0$ ), delay to peak, given as time from 10% of peak amplitude (rising signal) to peak amplitude, and signal duration, given as time from 10% to 10% of peak amplitude, were determined as parameters of the transient signals. Only  $\text{Ca}^{2+}$  events that followed from electrical stimulation were considered.

## Immunohistochemistry

Animals were perfused intracardially with PBS and 4% formaldehyde. Dissected brains were subsequently post-fixed overnight at 4°C. Free-floating coronal vibratome slices (40  $\mu\text{m}$ ) were generated (VT1000S, Leica, Biosystems, Wetzlar, Germany) and sections were collected, blocked, and permeabilized (blocking solution, 0.5% Triton X-100 and 5% horse serum in PBS) for 1 h at RT. The slices were incubated with primary antibodies diluted in blocking solution overnight, at 4°C. After washing with PBS, the slices were incubated with fluorescent secondary antibodies diluted in blocking solution for 2 h at RT. DAPI (0.025  $\mu\text{g}/\text{ml}$  final concentration) was added to the secondary antibody solutions to stain nuclei. The primary antibodies were used as follows: goat anti-GFP (1:1,000, Rockland, Limerick, PA, USA), mouse anti-GFAP (1:500, Novocastra, Leica Biosystems, Wetzlar, Germany) and rabbit anti-Iba1 (1:500, Wako, Osaka, Japan). Stained slices were scanned with the fully automated epifluorescence slide scanner microscope AxioScan.Z1 (Zeiss, Oberkochen, Germany) and analyzed with the ZEN imaging software (Zeiss). Cortical areas ( $3.92 \pm 0.32 \text{ mm}^2$ ) on both hemispheres of the slices were selected for analysis of the fluorescence intensities. The same area size was used for all stainings of one slice.

## Statistics

Statistical analysis was performed with GraphPad Prism 8. Data distributions were assessed with the Shapiro-Wilk normality test. In the case of normal distribution, single comparisons were computed with parametric unpaired *t*-tests and multiple comparisons with two-way ANOVA (mixed model) followed by Tukey's *post hoc* test. When data were not normally distributed, we applied a non-parametric Mann-Whitney test for single comparisons and Kruskal-Wallis test followed by Dunn's *post hoc* test for multiple comparisons.

## Animals

Mice were maintained in the animal facilities of the Centre for Integrative Physiology and Molecular Medicine (CIPMM, University of Saarland). Mice received food *ad libitum*. Knockin GLAST-Cre<sup>ERT2</sup> mice (Slc1a3<sup>tm1(cre/ERT2)Mgoe</sup>, MGI:3830051; Mori et al., 2006) and knockin Nex-Cre mice (Neurod6<sup>tm1(cre)Kan</sup>, MGI: 2668659) were crossbred to mice with Rosa26 reporter mice (Gt(ROSA)26Sor<sup>tm1(CAG-GCaMP3)Dbe</sup>, MGI: 5659933 (Paukert et al., 2014). For *in vivo* 2P-LSM, ECoG recording, stimulation experiments, and IHC, 12–17 week old mice were studied. To induce reporter expression in 8 week old transgenic GLAST-Cre<sup>ERT2</sup> mice, animals received tamoxifen



intraperitoneally (10  $\mu\text{g/ml}$ , 100  $\mu\text{l}/10\text{ g}$  body weight) once per day for five consecutive days (Jahn et al., 2018).

## Ethics Statement

Animal experiments were carried out at the University of Saarland according to European and German guidelines and approved by “Landesamt für Gesundheit und Verbraucherschutz” of Saarland state (license numbers: 71/2013, 36/2016).

## RESULTS

### Surface Electrode Arrays for Electrical Stimulation and ECoG Recording Enclosing an Optical Window

Our aim was to develop microelectrodes, applicable for *in vivo* measurements of electrical brain stimulation as well as the electrocorticographic recording of brain activity coupled to 2P-imaging in the region of interest (Figure 1A). Thereby, minimizing electrode effects on the tissue is pivotal for the functional assessment of complex network interactions. To avoid cellular responses associated with penetrating electrodes (Burda et al., 2016; Sohal et al., 2016; Donat et al., 2017), three different LCP surface electrodes were developed to be placed on the dura, enabling stimulation and recording of the brains' electrical activity (Figure 1A). The electrode base consists of a triple layer of white LCP, accommodating the two-layered golden electrical structure. The inner gold layer served as an interconnection plane, the outer layer harbors the electrode sites and solder pads. Electrode sites were electroplated with nanoporous platinum. An 18-pin nano-connector was soldered to the terminal pads and fixed by epoxy resin (Figure 1B).

Each electrode can potentially be used for stimulation and recording. Here, we used preferentially an eight-channel model with circular electrode sites (diameter = 150  $\mu\text{m}$ ) arranged in a three-by-three matrix (center-center distance: 750  $\mu\text{m}$ ) with sparing the center, for recordings (Figures 1C,D, rec) and an eight-channel model with rectangular electrodes sites (400  $\mu\text{m} \times 200\text{ }\mu\text{m}$ ) arranged in two groups of four for stimulation (Figure 1D, stim). The round electrode diameter was 3 mm and both electrodes contained a central window for 2P-LSM (size: 1 mm  $\times$  1 mm or 1 mm  $\times$  1.5 mm respectively; Figures 1C,D). In addition, a 16-channel electrode with round-shaped sites (diameter = 150  $\mu\text{m}$ ; center-center distance = 750  $\mu\text{m}$ ; arranged in a four-by-four matrix) was developed for the acquisition of electrocorticograms (ECoGs) over a larger cortical region. The optical window of the electrode has a polygonal shape (length 2.8 mm; small width: 400  $\mu\text{m}$ ; large width: 800  $\mu\text{m}$ ; Figure 1D). The distance between electrode sites and optical window, as well as the sizes of round electrode sites were chosen in accordance with the manufacturer's minimum recommendations. The catwalk of each electrode array had a length of 3 mm and a width of 1.1 mm and allowed the placement of the electrode within the craniotomy. The pad area accommodating the connector was 8.2 mm  $\times$  7.4 mm. Prior to covering the connector with epoxy resin, an additional wire

was soldered to the electrode connector enabling the use of an additional ground electrode (Figure 1C).

After platinum electroplating of the electrode sites (Figure 1E), the impedance magnitude at a frequency of 10 Hz was reduced from 3.3 M $\Omega$ –7.2 M $\Omega$  to 29 k $\Omega$ –48 k $\Omega$  for the round-shaped sites and 740 k $\Omega$ –1 M $\Omega$  to 6 k $\Omega$ –8.2 k $\Omega$  for the rectangular-shaped sites. This resulted in lower noise (Obien et al., 2014) and a lower voltage drop during stimulation. The cathodic charge storage capacities, as a comparable measure of stimulation current drive capability, were increased from 420  $\mu\text{C}/\text{m}^2$  to 550  $\mu\text{C}/\text{m}^2$  to 10,500  $\mu\text{C}/\text{cm}^2$  to 15,800  $\mu\text{C}/\text{cm}^2$  (round electrode sites) and from 130  $\mu\text{C}/\text{m}^2$  to 250  $\mu\text{C}/\text{m}^2$  to 10,500  $\mu\text{C}/\text{m}^2$  to 14,000  $\mu\text{C}/\text{m}^2$  (Figure 1E). The rectangular electrode sites can either be used in single electrode configuration for a higher stimulation selectivity or connected together for generating a broader and more uniform current distribution.

### LCP Surface Electrodes Are Highly Biocompatible and Even Stabilize the Tissue After Cranial Window Surgery

Reactive astrocytes and microglia are primary and reliable indicators of CNS inflammation at different time scales. While microglia respond rapidly, within minutes to hours, astrocytes are activated after a couple of days. After an acute insult of sufficient magnitude or continuous inflammatory processes, both cell types contribute to the development of gliosis (glial scar; Burda and Sofroniew, 2014). Considering that chronic *in vivo* experiments usually start after several days of recovery, we investigated the biocompatibility of the LCP surface electrodes in transgenic mice with astroglial GCaMP3 expression (Figure 2A) 3 days (for acute responses) and 28 days (for chronic responses) post-implantation (Figure 2B). LCP surface electrodes were implanted after a standard craniotomy, covered with a glass coverslip, and histological outcomes were compared to sham-treated mice that only underwent cranial window surgery (Figure 2B).

Cortical cell responses were assessed by fluorescence intensity (FI) analysis of immunohistochemical markers for microglia (Iba1) and reactive astrocytes (GFAP; Figure 2C). The density of recombined astrocytes was assessed by immunodetection of GCaMP3 using GFP antibodies. The general cell density was visualized by nuclear DAPI staining. No alterations of cortical layer structures were detected in either group at any time point (Figure 2C). Ipsilateral FI values normalized to the contralateral side showed that neither the surgery nor the electrode itself changed expression levels of DAPI, GFP, or Iba1 at three or 28 days post-surgery (FI normalized to contra  $\approx$  1, Figures 2C,D). In contrast, GFAP levels in sham operated animals tripled compared to the contralateral side as well as compared to electrode-implanted animals at both three (FI normalized to contra = 3.4) and 28 days post-surgery (FI normalized to contra = 3.2,  $p = 0.031$ ; Figures 2C,D). Animals carrying the LCP surface electrode displayed a slight GFAP increase 3 days post-surgery (FI normalized to contra = 1.4) that was negligible 28 days post-surgery (FI normalized to contra = 1.2; Figure 2D). We concluded that the LCP surface



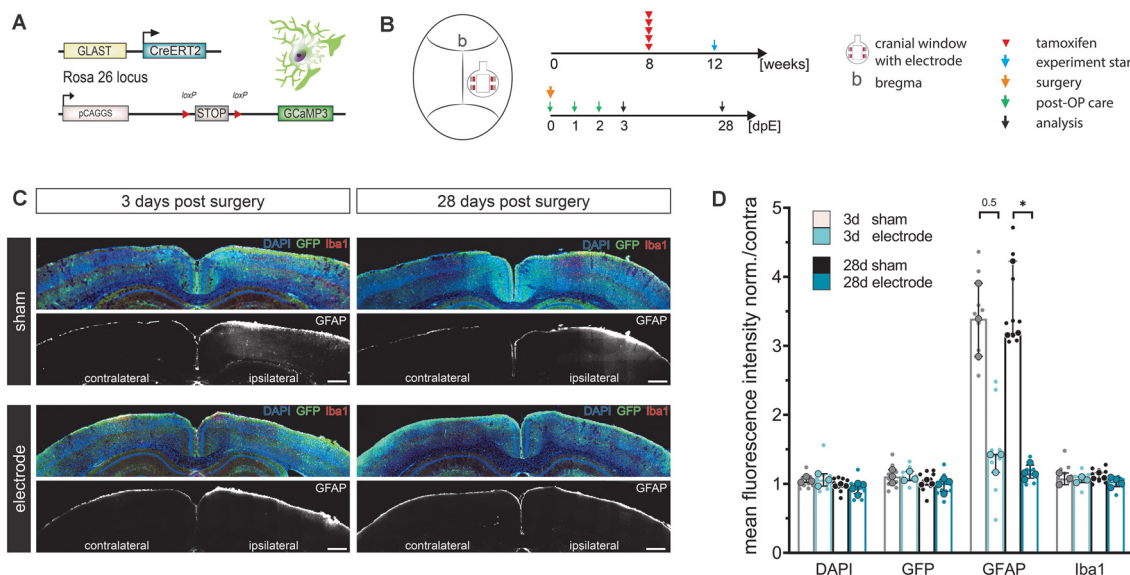


**FIGURE 2 |** LCP surface electrodes are long-term biocompatible and favorable for *in vivo* studies. **(A)** The biocompatibility study was carried out on transgenic mice with tamoxifen-induced, astrocyte-specific GCaMP3 expression. **(B)** Eight-week-old animals were administered five consecutive i.p. injections of tamoxifen to induce GCaMP3 expression in astrocytes. At 12 weeks of age, animals underwent cranial window surgery with or without (sham) surface electrode implantation. An immunohistochemical analysis was carried out 3 or 28 days post-surgery. **(C)** Activation of microglia (Iba1) and astrocytes (GFAP) was assessed by immunohistochemical staining of coronal slices. GCaMP3 expression was revealed by GFP immunostaining. Ipsilateral: surgery side, contralateral: control side. Scale bars indicate 500  $\mu$ m. **(D)** Astroglial GFAP reactivity was increased in sham groups compared to electrode implanted groups both 3 and 28 days post-surgery, while the astrocyte activation of the electrode implanted groups was only minimally increased, indicating high biocompatibility and an additional stabilizing effect of the LCP cortical surface electrode. Ipsilateral fluorescence intensity values were normalized to the contralateral side. Statistics: Kruskal–Wallis test followed by Dunn’s multiples comparisons test  $*p < 0.05$ . Data are displayed as median with IQR. Larger data points correspond to the average of slices from the same animal, smaller data points indicate individual slices. 3 d sham  $N$  (animal) = 3,  $n$  (slice) = 9; 3 d electrode  $N$  = 3,  $n$  = 9; 28 d sham  $N$  = 3,  $n$  = 9; 28 d electrode  $N$  = 4,  $n$  = 12.

electrode did not elicit significant activation of microglia or astrocytes at an acute or chronic time scale. In fact, the electrode had an alleviating effect on cortical glia activation compared to the simple cranial window surgery, suggesting an additional stabilizing effect.

## Electrical Stimulation Synchronized With *In vivo* 2P- $\text{Ca}^{2+}$ Imaging Reveals Stimulation Intensity and Anesthesia-Dependent Biphasic Neuronal $\text{Ca}^{2+}$ -Signal Signature

Electrical stimulations were performed in Nex-Cre  $\times$  GCaMP3 mice (Figure 3A) at different isoflurane concentrations to investigate how anesthesia could affect the  $\text{Ca}^{2+}$  response of neuronal networks. The surface electrode with rectangular-shaped sites was used (Figure 3A, stim). The influence of the imaging position with reference to the electrode sites was minimized by simultaneously using the two inner electrode sites left and right of the observation window to apply an electrical current. Layer II/III of the cortex were recorded by 2P-LSM at a depth of 180  $\mu$ m–210  $\mu$ m. Threshold (Th) definition was performed in anesthetized animals at 50 Hz stimulation until a large  $\text{Ca}^{2+}$  wave was induced. Subsequently, two 50 Hz stimulations at Th, Th + 50  $\mu$ A, Th +100  $\mu$ A were applied to study the elicited  $\text{Ca}^{2+}$  responses.

The stereotypical neuronal  $\text{Ca}^{2+}$  waves could be elicited across all levels of anesthesia (Figures 3B,C). Under lower anesthesia ( $\leq 0.5\%$ ), two peaks became apparent in the  $\text{Ca}^{2+}$  transients, after extracting the image brightness (Figure 3C). The sources of these peaks were estimated from the short image series of every second 2P-LSM image (Figure 3B). The image at time 0 s was set as the image directly at stimulation onset. Two frames later (1.17 s), the activation of the neuropil was clearly visible (first peak in the  $\text{Ca}^{2+}$  transients in Figure 3C①), before the somata were activated (second peak, Figure 3C②). The response of the neuropil did not show any dependence on the anesthesia level or stimulation amplitude (Figure 3D). In contrast, the somatic  $\text{Ca}^{2+}$  transient amplitude varied with isoflurane and strongly depended on the stimulation intensity (Figure 3E). The delay times (mean  $\pm$  SD) from stimulation onset to maximum image intensities (peak) were rather constant for all measurements (delay peak I: 0.86 s  $\pm$  0.13 s; delay peak II: 2.34 s  $\pm$  0.16 s; Figures 3F,G). The duration of the  $\text{Ca}^{2+}$  signal including neuropil and somata was 3.63 s  $\pm$  0.24 s and did not respond to the variations of isoflurane or stimulation amplitude (Figure 3H). After each stimulation, an undershoot of fluorescence intensity occurred (Figure 3C③). The undershoot duration decreased from 57.4 s  $\pm$  5.5 s to 33.5 s  $\pm$  3.0 s with decreasing anesthesia level, but was independent of the stimulation strength (Figure 3I).

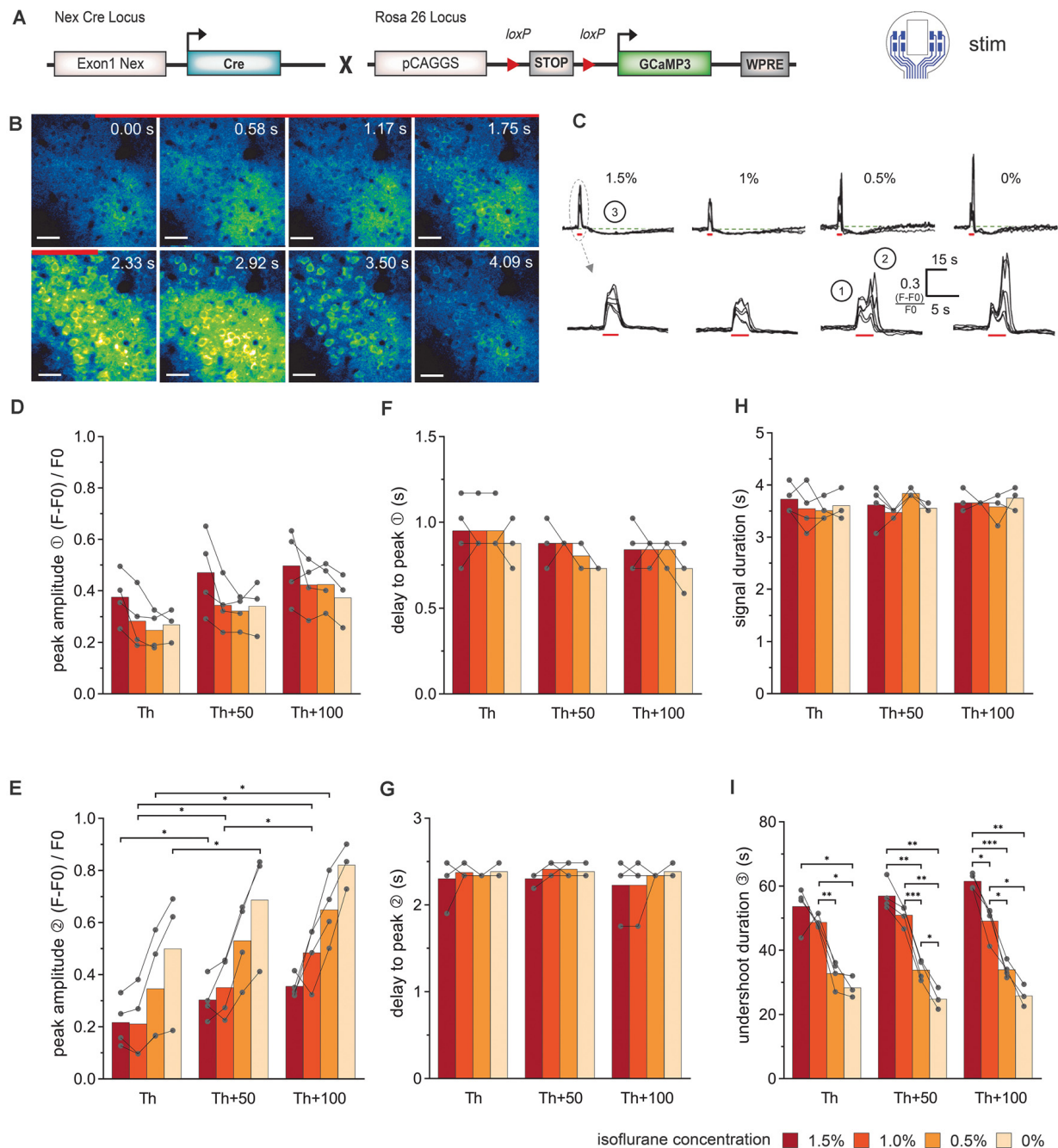


**FIGURE 3 |** Simultaneous electrical stimulation and *in vivo* 2P-Ca<sup>2+</sup> imaging reveals the stimulation intensity- and anesthesia-dependent neuronal Ca<sup>2+</sup>-signal signature. **(A)** Transgenic mice expressing the Ca<sup>2+</sup> sensor GCaMP3 in cortical neurons were used for stimulations with the 8-channel stimulation electrode. **(B)** 2P-Ca<sup>2+</sup> imaging sequence during electrical stimulation (red bar). The first Ca<sup>2+</sup> response originates from the neuropil (0–1.17 s) and was followed by transient somatic signals (1.75–3.5 s), scale bar = 40 μm. **(C)** Top row: neuronal Ca<sup>2+</sup> peaks in response to electric stimulation (red bar) are systematically followed by an undershoot (3) at all isoflurane concentrations (1.5–0%), scale bar = 15 s. Bottom row: at higher temporal magnification, a biphasic peak (1, 2) was reliably observed at isoflurane concentrations ≤0.5%. **(D)** The amplitude of the first neuronal Ca<sup>2+</sup> peak component was independent of stimulation intensity and anesthesia level. **(E)** The amplitude of the second peak component was potentiated with increasing stimulation intensities. **(F)** The delay between the stimulation onset and the local maximum of the first peak component did not change with stimulation intensity or anesthesia level. **(G)** The delay between the stimulation and the local maximum of the second peak component remained unchanged with varying stimulation intensity or anesthesia level. **(H)** Ca<sup>2+</sup> peak duration did not vary with stimulation intensities and isoflurane concentrations. **(I)** Duration of the undershoot following the biphasic peak was strongly dependent on the level of anesthesia, with approximately 50% shorter durations in awake animals compared to 1.5% isoflurane anesthesia, across stimulation protocols. Statistics: Two-Way ANOVA (mixed model) followed by Tukey's multiple comparisons test \**p* < 0.05, \*\**p* < 0.01, \*\*\**p* < 0.001, for isoflurane 1.5–0.5% *N* = 4 and isoflurane 0% *N* = 3 measurements per stimulation intensity. Th: threshold.

## Evoked Astroglial $\text{Ca}^{2+}$ Signals Display Stimulation Intensity-Dependent Characteristics

Electrical stimulations were also performed in GLAST-Cre<sup>ERT2</sup>  $\times$  GCaMP3 mice to study the response of astrocytes (Figure 4A). The stimulation procedure was chosen as described above (different levels of isoflurane concentration: 1.5%, 1.0%, 0.5%, and 0%; electrode with rectangular-shaped sites (Figure 4A, stim), the inner electrode sites were electrically connected; 50 Hz stimulation; 100 pulses). 2P-LSM recordings were performed in layer I of the cortex at a depth of 40  $\mu\text{m}$ –90  $\mu\text{m}$ . Threshold (Th) definition was performed in anesthetized animals at 50 Hz stimulation until a  $\text{Ca}^{2+}$  wave was visible. Subsequently, we applied 50 Hz stimulations at Th, Th + 50  $\mu\text{A}$ , Th + 100  $\mu\text{A}$  to study the elicited  $\text{Ca}^{2+}$  responses.

$\text{Ca}^{2+}$  transients in cortical astrocytes (somata and processes) could be provoked by electrical stimulation at all levels of anesthesia (Figures 4B,C). In general, astrocytes responded stronger to the stimulation amplitude rather than isoflurane concentration. The astroglial peak amplitudes (Figure 4D) showed an increase from Th to Th + 50  $\mu\text{A}$ , while the  $\text{Ca}^{2+}$  signal amplitude was rather constant from Th + 50  $\mu\text{A}$  to Th + 100  $\mu\text{A}$ . However, the amplitude values showed high variability. The peak of the astrocytic  $\text{Ca}^{2+}$  related signals was detected after the end of the stimulation (Figure 4E). There was a slight reduction in the delay time from stimulation onset until the maximum was reached with increasing stimulation intensity. For the highest stimulation current, the delay time was approximately within 3.5 s to 5 s and for the lowest stimulation current approximately 3.5 s to 5.5 s. The delay time from stimulation onset to the  $\text{Ca}^{2+}$  transient rise (10% of maximum) was decreased by the duration of 1 to 2 imaging frames (300 ms to 600 ms) with increasing stimulation strength (Figure 4F). No significant difference in the duration of the  $\text{Ca}^{2+}$  transient was visible, neither with the stimulation amplitude nor with the depth of anesthesia (Figure 4G).

## Recordings With the LCP Electrode Arrays Showed a High Signal-to-Noise Ratio and Spatial Signal Differences Reflecting the Brains' Activity States

The 16-channel electrode was used to evaluate the recording quality and to assess the spatial distribution of signal events. The depth of anesthesia was modulated (isoflurane 1.5% to 0%) to vary the pattern of the bioelectrical activity (Land et al., 2012). The recordings showed a typical synchronous burst activation of neurons when the mice were anesthetized (Figure 5A). With decreasing anesthesia, the time between the bursts became shorter and the signal amplitude lower, indicating a loss of synchrony. When the mouse was awake, the burst pattern was no longer visible. The difference in neuronal activity was also visible in the spectrograms of the signals (Figure 5B). In the anesthetized mouse, the highest signal intensities were at frequencies below 10 Hz, and frequencies higher than 30 Hz were temporarily visible when the neurons fired synchronously. Since there was no evidence of signal components with a

broad frequency range during the burst suppression phases, we concluded that there was no detectable noise affecting the signal quality. In the awake state, the highest signal intensity was also below 10 Hz, but the higher frequencies were always present due to the continuous spiking activity (Figure 5B).

The individual time of signal traces showed a high similarity between the individual channels (Figure 5A). To characterize the channel similarity, the correlation between the recorded signals was calculated. A stepwise calculation (sliding window of 2 s, step time 0.5 s) demonstrated the dependency on the synchrony of cortical electrical activity (Figure 5C). The channel similarity was lower if there was high spike activity (bursts and neuronal activity in the awake state). In addition, the correlation decreased with channel distance. Correlations were calculated for 30 s traces in relation to the distance of the electrode sites (Figure 5D). The distances of the electrode sites are given as normalized geometric distances (value of 1 means the electrode center-center distance of 750  $\mu\text{m}$ , 1.41 means 1057.5  $\mu\text{m}$ , etc.). This diagram confirms the results from the stepwise calculation. The correlation coefficient was high for electrode sites nearby and decreased with increasing distance. For awake mice, the correlation was constantly lower than for mice under anesthesia. The variation within one electrode distance resulted from the different signals in the single recordings and from the various channel pairs. At electrode distance 0, the result of the correlation of the channels with themselves is given.

## Stable Long-Term Recordings of Electrophysiological and Spontaneous Astroglial $\text{Ca}^{2+}$ Signals in the Mouse Cortex

To demonstrate the functionality of the combination of *in vivo* ECoG recording and  $\text{Ca}^{2+}$  events by 2P-LSM, an eight-channel electrode was implanted in a GLAST-Cre<sup>ERT2</sup>  $\times$  GCaMP3 mouse (Figure 6A). The depth of anesthesia was varied in an arbitrarily selected variation of isoflurane from 2.5% to 0% (orange stars in Figure 6E) to change the activity state, and thus the activity of neurons and astrocytes. We could achieve high-quality 2P-LSM and ECoG recordings over a long recording period (>30 min) and up to 35 days after electrode implantation. The cranial window quality allowed clear visibility of astroglial somata, processes, and  $\text{Ca}^{2+}$  transients (Figure 6B). The 2P-LSM images were processed with the MATLAB based tool MSparkles to find activity-based regions of interest (ROIs; Figure 6C), calculating the signal amplitudes  $[(F - F_0)/F_0]$ ; Figure 6D and to classify the  $\text{Ca}^{2+}$  events in small (1 SD  $\leq$  signal amplitude < 2 SD), medium (2 SD  $\leq$  signal amplitude < 3 SD), and large signals (3 SD  $\leq$  signal amplitude; Figure 6E). The standard deviation (SD) referred to the base fluorescence  $F_0$ . The activity of the astrocytes increased with decreasing anesthesia which is in line with previous reports of other groups (Thrane et al., 2012; Bojarskaite et al., 2020).

To obtain a more comprehensive overview of the responses in a given field-of-view, the signal classification from the different ROIs was summed up within a time step of 30 s and the normalized FI, as well as the correlation of subsequent images, was calculated (Figure 6E). Under high anesthesia (2.5%)



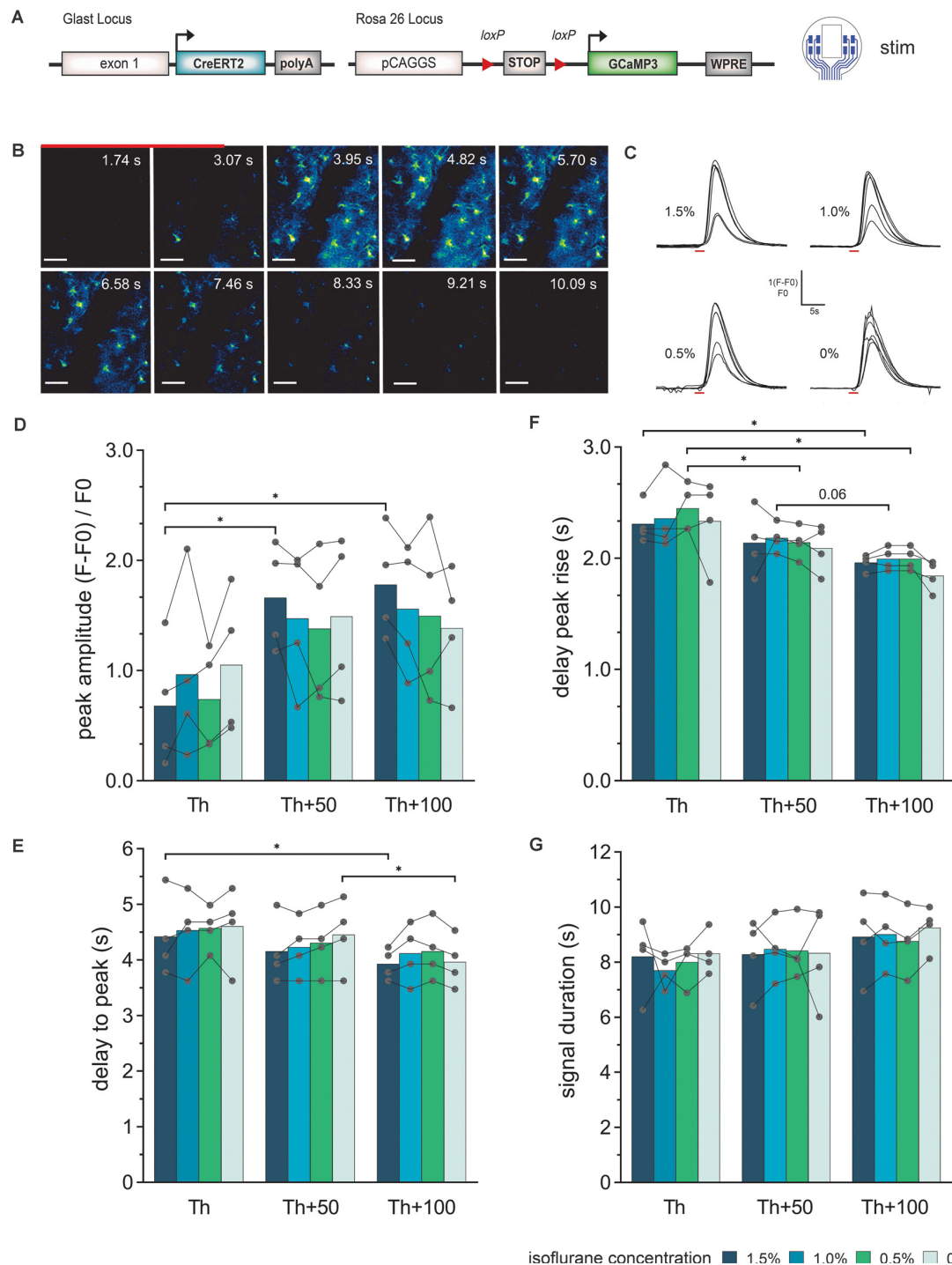


**FIGURE 4 |** Astroglial Ca<sup>2+</sup>-signal elicited by electrical stimulation *via* the LCP surface electrodes and recorded by *in vivo* 2P imaging. **(A)** The experiment was performed in transgenic mice expressing the Ca<sup>2+</sup> sensor GCaMP3 in astrocytes and cortical stimulations were applied with the 8-channel stimulation electrode. **(B)** 2P-Ca<sup>2+</sup> imaging sequence during electrical stimulation (red bar), scale bar = 50 μm. **(C)** Astroglial Ca<sup>2+</sup> transients in response to electric stimulation (red bar) display a single, uniform peak at all tested isoflurane concentrations (1.5–0%). **(D)** The Ca<sup>2+</sup> peak amplitude increases with increasing stimulation intensity, especially at high isoflurane concentrations (1.5%), while no significant effect of changing anesthesia levels at the same stimulation intensity could be detected. **(E)** The delay from stimulation onset to Ca<sup>2+</sup> peak decreases with increasing stimulation intensities but is independent of isoflurane levels. **(F)** Rise of the Ca<sup>2+</sup> transient to 10% of its maximum was reduced by increasing the stimulation current without changing at varying anesthesia levels of the same current intensity. **(G)** The astroglial Ca<sup>2+</sup> signal duration was independent of stimulation intensity and anesthesia. Statistics: Two-Way ANOVA followed by Tukey's multiple comparisons test \**p* < 0.05, *N* = 4 measurements per stimulation intensity. Th, threshold.



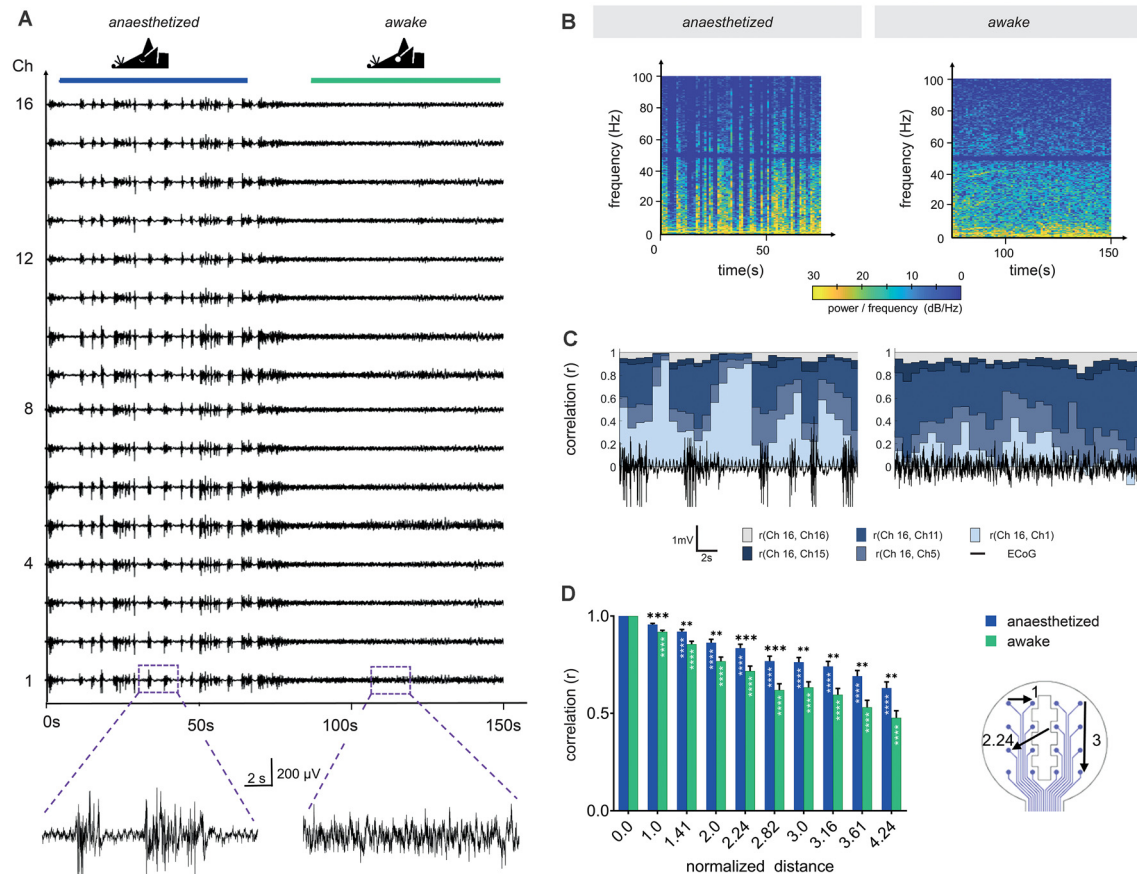


**FIGURE 5 |** Channel correlation analysis detects differences in brain activity between the anesthetized and the awake state. **(A)** Sixteen-channel ECoG recording displays the pattern change from the anesthetized state (1.5% isoflurane) to the awake state. **(B)** Spectrograms in anesthetized and awake conditions represent the power spectral densities of individual frequencies over time. In the anesthetized animal, frequencies below 10 Hz display the highest power with intermittent synchronous activity bursts, raising the power of frequencies up to approximately 100 Hz. Similarly, frequencies below 10 Hz dominated in the awake state, however, higher frequencies were continuously represented. We applied a Notch filter at 50 Hz, represented by the dark band in this frequency range. **(C)** Channel similarity revealed by correlation analysis between the different electrode sites (channels) and under anesthetized and awake conditions. The similarity of the most distant recording sites [ $r(\text{Ch16}, \text{Ch1})$ ] increased substantially after synchronous burst activity under anesthesia. **(D)** Channel similarity (correlation) decreases with increasing distance between electrode sites (channels). In awake animals, the channel correlation is systematically lower than under anesthesia. Statistics: Two-Way ANOVA followed by Dunnett's multiple comparisons test for different distances compared to distance 0.0 of the respective anesthesia group (white stars inside bars) and Fisher's LSD for comparisons between awake and anesthetized (black stars above). Data are shown as mean  $\pm$  SEM,  $**p < 0.01$ ,  $***p < 0.001$ ,  $****p < 0.0001$ ,  $N$  (anesthetized) = 21 and  $N$  (awake) = 23 measurements per distance value.

0–0.2 events ( $\text{Ca}^{2+}$  counts) per second were detected, increasing up to 3.9 events (all classified signal types) per second in the awake mouse. This was paralleled by the normalized FI, which increased and decreased according to the inversely varying isoflurane concentration. The image correlation demonstrated fast  $\text{Ca}^{2+}$  signal changes (fast changing correlation result) during the awake state. Due to the image noise (which is different from image to image) the correlation coefficient is never exactly equal to 1. The average signal of the eight ECoG channels was calculated (Figure 6F). This signal allows for an exact determination of the actual depth of anesthesia during the 2P-imaging experiment or similar experimental procedures. Overall, the animal recovers rapidly from the anesthetized state but it lasts longer returning to the anesthetized condition after an awake episode.

## DISCUSSION

Three different LCP surface micro-electrodes for electrical stimulation and ECoG recordings were developed and electrochemically optimized with platinum coating. Several application examples in anesthetized and awake mice demonstrated the versatility, convenience, and reliability of the novel LCP micro-electrodes to investigate brain function *in vivo*. Quality assurance (impedance measurements, microscopic control) was performed to sort out electrodes with production defects. In the animal studies, surface electrodes were easy to handle and showed excellent robustness. The investigations were not disrupted by electrode damages of any kind. The possibility of combined electrical stimulation or ECoG recording with 2P-imaging *in vivo* opens various opportunities to study neural

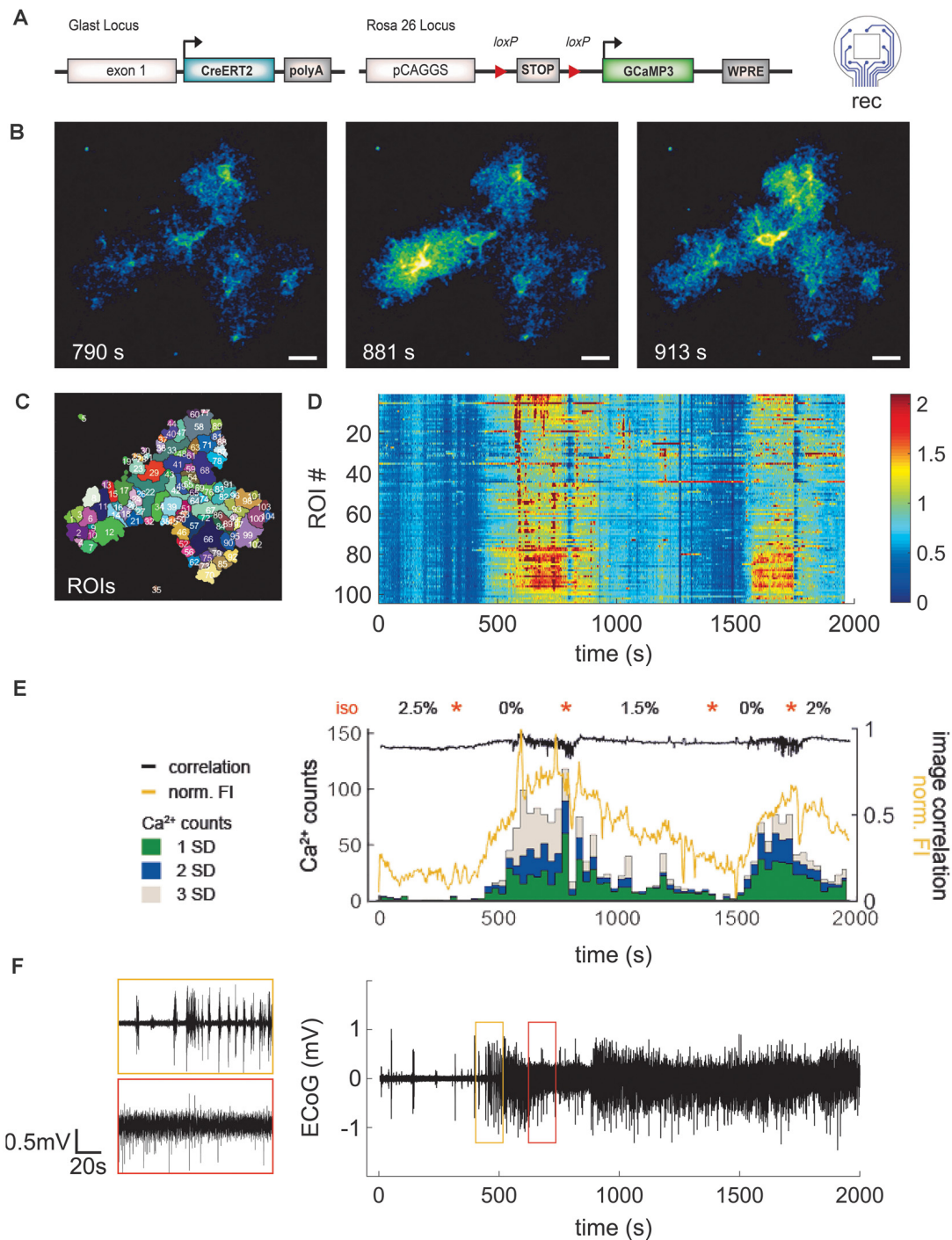


**FIGURE 6 |** Application of LCP electrode for ECoG recording combined with 2P-  $\text{Ca}^{2+}$  imaging substantiates reduction of spontaneous astroglial  $\text{Ca}^{2+}$  signals under anesthesia. **(A)** Eight-channel ECoG recording and simultaneous 2P- $\text{Ca}^{2+}$  imaging in transgenic mice with GCaMP3 expression in astrocytes. **(B)** 2P-LSM sequence displaying good cranial window quality with implanted LCP electrode 35 days post-surgery, scale bar = 20  $\mu$ m. **(C)** Regions of interest (ROI) map computed by activity-dependent analysis using custom-made Matlab routines. **(D)** Heatmap illustrating normalized  $\text{Ca}^{2+}$  signal amplitudes  $[(F - F_0)/F_0]$  per ROI over time. Graphs **(D–F)** have the same time scale and isoflurane variations (orange stars). In contrast to the anesthetized state, awake mice display higher  $\text{Ca}^{2+}$  signal amplitudes. **(E)**  $\text{Ca}^{2+}$  events (counts) were grouped into small (1 SD), medium (2 SD), and large (3 SD) signals and merged with corresponding normalized fluorescence intensity of the image (FI, yellow trace) and image correlation (black trace). Anesthesia reduced particularly the frequency of medium and large  $\text{Ca}^{2+}$  signals which were highly abundant in awake animals. Increases of  $\text{Ca}^{2+}$  events were accompanied by rises in fluorescence amplitude and variation of image correlation. Orange stars indicate transitions between isoflurane concentrations. **(F)** ECoG trace displayed as average over all channels shows clear transitions in brain activity depending on the anesthesia level.

function, e.g., to investigate neuron-glia interactions in the CNS.

## LCP Surface Electrodes Are Highly Biocompatible for Long-Term *In vivo* Observations

Biocompatibility of neural implants is a major concern in clinical application as well as research (Polikov et al., 2005). In contrast to the reported tissue response in rodents to intracortical electrodes (Minnikanti et al., 2010; Potter et al., 2012; Salatino et al., 2017), little information was obtained about the tissue response to epidural electrodes (Schendel et al., 2013; Shokoueiinejad et al., 2019). Consequently, in this work, the macroscopic and cellular biocompatibility was tested under acute (3 days post-implantation) as well as chronic conditions (28 days post-implantation). Since the LCP electrodes were used in combination with cranial windows for 2P-imaging, we assessed the inflammatory response of glial cells by comparing animals with cranial window and electrode implant to simple cranial window surgery (sham). Neither astrocytes nor microglia displayed significant acute or chronic activation in LCP electrode carrying animals. In fact, sham animals showed an increased astroglial reactivity reflected by increased GFAP immunoreactivity, especially in the chronic application. Thus, the LCP surface electrode appears to display an even beneficial effect after cranial window surgery, likely due to the thickness of the electrodes (approx. 75  $\mu\text{m}$ ) filling the gap between the cortex and the glass coverslip. Thereby, the tissue may be stabilized and hemorrhages, as well as edema, may be reduced. In addition, no impact on the expression of the genetically encoded  $\text{Ca}^{2+}$  sensor GCaMP3 was detected, providing optimal conditions for 2P-  $\text{Ca}^{2+}$  imaging. An additional advantage of the LCP surface electrodes is the convenient use of their inner edges as a reference system for repetitive imaging of the same ROIs in chronic imaging experiments.

## Cortical Stimulation Activated Local and Global Network Activity

For *in vivo* stimulation of cortical tissue, the electrode arrays with the rectangular-shaped electrode sites were implanted in mice with GCaMP3 expression by principal neurons of the neocortex. The stimulation-evoked  $\text{Ca}^{2+}$  signals were dependent on stimulation amplitude and anesthesia level. With lower anesthesia, biphasic  $\text{Ca}^{2+}$  transients were observed, representing the consecutive activation of neuropil and somata. The direct effect of electrical stimulation mainly targets neuronal structures in cortical layer I with depolarizations further propagating to the somata in layer II/III. Simultaneously, the  $\text{Ca}^{2+}$  signal spreads intracellularly. The fluorescence intensity of the neuropil region (peak 1) did not show a significant relation to stimulation strength and anesthesia. The amplitude of the second peak involving the somata was mainly dependent on the stimulation intensity, and less on the anesthesia level. A stronger stimulation would elicit a stronger depolarization, leading to increased intracellular  $\text{Ca}^{2+}$  mobilization. A volatile anesthetic such as isoflurane acts on multiple targets. It reduces  $\text{Na}^+$  currents while inducing  $\text{K}^+$  currents, lowers resting

membrane potential, depresses NMDA receptor-dependent excitatory transmission, and increases GABA<sub>A</sub> receptor-mediated inhibitory transmission (Franks and Lieb, 1988; Rudolph and Antkowiak, 2004; Westphalen and Hemmings, 2006; Lissek et al., 2016; Zhao et al., 2019). Thus, neuronal excitability is considerably reduced, leading to the decreased opening probability of voltage-gated  $\text{Ca}^{2+}$  channels for example (Study, 1994; Koyanagi et al., 2019; Timic Stamenic et al., 2019). Hence, higher peak amplitudes are observed at lower isoflurane levels. The signal drop between activation of neuropil and soma was probably a local effect of activated  $\text{Ca}^{2+}$  pumps restoring the intracellular  $\text{Ca}^{2+}$  homeostasis, counteracting the active stimulation. In a recent study (Michelson et al., 2019), a  $\text{Ca}^{2+}$  signal decrease in neuronal soma and neuropil is described, supporting the finding of this study.

A signal undershoot after evoked  $\text{Ca}^{2+}$  transients has been previously reported (Majewska et al., 2000; Collins and Thomas, 2001). This phenomenon could reflect a state of depression after strong stimulation and depletion of intracellular  $\text{Ca}^{2+}$  stores. Reports of volatile anesthetics' effect on ER and plasma membrane  $\text{Ca}^{2+}$  transport are controversial and less described in neurons than in myocytes for example (Blanck and Thompson, 1982; Collins and Thomas, 2001; Hannon and Cody, 2002). However, it is possible that the prolonged undershoot in anesthetized animals is caused by hyperactivity of the sarcoplasmic reticulum  $\text{Ca}^{2+}$  ATPase to refill the ER stores and delayed compensation by replenishing mechanisms. No significant changes were seen in the delay to the  $\text{Ca}^{2+}$  peaks nor the duration of the signal, suggesting a stereotypical neuronal  $\text{Ca}^{2+}$  response to stimulations (above the defined threshold). One could have expected an impact of anesthesia on the signal duration, given the fact that crucial  $\text{Ca}^{2+}$  extrusion mechanisms [ $\text{Na}^+/\text{Ca}^{2+}$  exchanger (NCX) and the plasma membrane  $\text{Ca}^{2+}$  ATPase (PMCA)] are potentially inhibited by volatile anesthesia. Corresponding studies however were mainly performed *in vitro* or *ex vivo* (Franks et al., 1995; Ay et al., 2005).

## Astroglial $\text{Ca}^{2+}$ Events Follow Neuronal Activation After Cortical Stimulation

To study astroglial  $\text{Ca}^{2+}$  responses after electrical stimulation, mice with astrocyte-specific GCaMP3 expression were used. The stimulation amplitude and anesthesia levels were varied. The rise of the  $\text{Ca}^{2+}$  transients started approximately 1.6 s to 2.6 s after stimulation onset and the maximum peak value was found between 3.5 s and 5.5 s, when the electrical stimulation was already terminated. Together with the delay time to the  $\text{Ca}^{2+}$  transient peaks of neurons (approximately 0.6 s to 1.2 s for neuropil and 2 s to 2.5 s for soma), the astroglial activation followed the neuronal activation, likely due to glial responses to the release of neurotransmitters (Araque, 2008; Volterra et al., 2014; Shigetomi et al., 2016; Guerra-Gomes et al., 2017). In addition, no dependency of the  $\text{Ca}^{2+}$  signal peak time to the anesthesia was found which was in line with the neuronal peak time. Similarly, astroglial  $\text{Ca}^{2+}$  peak amplitudes increased with augmenting stimulation intensity, as seen in neurons. However, this effect was less pronounced in astrocytes. Taken together with the observation of reduced delays to



peak amplitude with increasing stimulation strength exclusively in astrocytes, the integrative function of astrocytes following neuronal activation is highlighted (Araque et al., 2014; Caudal et al., 2020). In accordance with neuronal  $\text{Ca}^{2+}$  signal duration, astroglial signal duration was not significantly modulated by stimulation intensity or isoflurane levels. In contrast to neurons, astrocytes displayed longer  $\text{Ca}^{2+}$  events with higher variability ( $3.6 \pm 0.1$  s vs.  $8.4 \pm 0.5$  s; mean  $\pm$  SD). Previous studies revealed prominent depression of astroglial  $\text{Ca}^{2+}$  signaling under anesthesia (Nimmerjahn et al., 2009; Thrane et al., 2012). In contrast to our experimental setup, these studies focused on spontaneous or physiologically evoked astroglial  $\text{Ca}^{2+}$  activity, thus accounting for the discrepancies.

## Multichannel Surface Electrodes Enabled the Recording of Electrical Signals in the Cortex

Determining the brain activity state of mice during complex *in vivo* experimental procedures can be crucial for successful and comprehensive data acquisition, e.g., by quantifying the depth of anesthesia (Land et al., 2012). With the LCP surface electrode arrays (round-shaped electrode sites), acquisition of low noise ECoG recordings was achieved *via* standard bandpass (0.5 Hz to 250 Hz) and notch filtering (50 Hz). No further signal filtering like wavelet denoising was required (Schweigmann et al., 2018). A channel similarity study was performed for the LCP electrodes by calculating the correlation of the individual channels. The result indicated that there was a high similarity between adjacent channels in the awake as well as in the anesthetized mouse. However, for more distant electrode sites, some signal differences were detected by decreasing channel correlation. Moreover, the channel correlation was systematically reduced in awake compared to anesthetized mice, reflecting the asynchronous network activity in awake states. In a recent study, channel correlations performed in mice and humans could resolve local activity patterns even when ECoG recording sites were less than 1 mm apart (Rogers et al., 2019).

Our results offer a valuable starting point for experimental designs involving evoked potentials, where ECoG activity and its propagation could be linked to functional 2P-LSM, thereby offering new options to study microcircuits across different cell populations (Mohajerani et al., 2013).

## Combination of *In vivo* 2P-LSM and ECoG Recordings to Unravel Neuron-Glia Interactions

The successful combination of *in vivo* 2P-LSM and ECoG recording was demonstrated in experiments with astroglial GCaMP3 expression. After 35 days post electrode implantation, the optical window visibility was of good quality, and low noise ECoGs could be acquired, enabling the identification of anesthesia depth. Analysis of  $\text{Ca}^{2+}$  transients showed a variation in the number of  $\text{Ca}^{2+}$  events per time when the anesthetics' concentration was altered. Approximately 0.05–0.7  $\text{Ca}^{2+}$  events/s in the anesthetized (isoflurane 1.5%) and 2.5–3.9  $\text{Ca}^{2+}$  events/s in the awake mouse were detected.

Previously a 10-fold reduction of spontaneous somatic signals was described for astrocytes when the mouse was anesthetized (Thrane et al., 2012). Considering the different field of views and physiological variations, we found comparable results. Thereby, the ECoG recordings will help to understand the temporal-spatial pattern of  $\text{Ca}^{2+}$ -signals in future studies, which will link small ECoG changes with astroglial activity. Such experiments will be highly valuable to study neuron-glia interactions *in vivo*.

## Boundaries for Cortical Surface Electrode Application in Combination With 2P-LSM

Different technologies for the development of surface electrodes exist comprising various base materials like polyimide (Choi et al., 2010; Kuzum et al., 2014; Khodagholy et al., 2015; Vomero et al., 2020), parylene (Khodagholy et al., 2013; Park et al., 2014; Richner et al., 2014; Donahue et al., 2018) or less frequently LCP (Lee et al., 2009; Min et al., 2014). The use of LCP electrodes limited the visual access for 2P-LSM due to the non-transparent, white material, therefore one or several optical windows had to be integrated to enable successful access to the cortex. Another limitation of the selected technology was in the miniaturization of the electrode sites compared to other electrode technologies, where small electrode sites in the 20  $\mu\text{m}$  range could be achieved (Kuzum et al., 2014; Khodagholy et al., 2015; Donahue et al., 2018). Further miniaturization might enhance the acquisition of asynchronous network activity. However, the industrial series production of the electrodes enabled a cost-effective solution which could become more and more important in decoding cell behavior and interaction *in vivo*.

Previously, thin, flexible, and transparent surface electrodes based on parylene C (with 16 channels and graphene-coated electrode sides and interconnections) were introduced for recording and stimulation application (Park et al., 2014, 2018). Fluorescent imaging had been performed at the cortical surface with one-photon excitation (UV light) over a cortex area of  $4.6 \times 3.4 \text{ mm}^2$ , so that the entire electrode was visible. With a transparency of more than 90% (Park et al., 2014),  $\text{Ca}^{2+}$  signals could be recorded directly at the electrode sites (Park et al., 2018). Also, a comparison of parylene C electrodes and platinum electrode sites was presented. The metal structure blocked the visual access, but the electrode impedance [ $|Z(f = 10 \text{ Hz})| \approx 1 \text{ M}\Omega$ , 200  $\mu\text{m}$  in diameter] was at least one-order smaller than the impedance of the graphene electrodes [ $|Z(f = 10 \text{ Hz})| \approx 10 \text{ M}\Omega$ , 200  $\mu\text{m}$  in diameter; Park et al., 2018]. Here, our circular platinum electrode sites showed an impedance range of  $|Z(f = 10 \text{ Hz})| = 29\text{--}48 \text{ k}\Omega$  for an electrode diameter of 150  $\mu\text{m}$ . The  $\text{CSC}_C$  of the graphene electrodes was estimated to be approximately  $88 \mu\text{C}/\text{cm}^2$  (Park et al., 2018), whereas we achieved a  $\text{CSC}_C$  of 10,500  $\mu\text{C}/\text{cm}^2$  to 15,800  $\mu\text{C}/\text{cm}^2$ , indicating a higher current drive capability. A surface electrode made from PET, photoresist SU-8, gold electrode tracks, and graphene electrode sites was developed to use the transparent electrode for combined recording and deep tissue 2P-LSM (Thunemann et al., 2018). The impedance traces showed an impedance magnitude of  $|Z(f = 10 \text{ Hz})| \approx 10 \text{ M}\Omega\text{--}200 \text{ M}\Omega$  for the size of the squared



electrode sites of  $100\ \mu\text{m} \times 100\ \mu\text{m}$  (Thunemann et al., 2018). Again, the current drive capability of the graphene electrode site might be strongly limited.

Electrical recording and one photon or two-photon excitation in hippocampal tissue slices were combined using a polyimide electrode with graphene electrode sites (square-shaped  $25\ \mu\text{m} \times 25\ \mu\text{m}$ ; Kuzum et al., 2014). The transparency of the electrode was characterized for light wavelength in the range of 400 nm to 900 nm and showed a limitation by the polyimide (thickness 12.5  $\mu\text{m}$  and 25  $\mu\text{m}$ ) rather than graphene. For wavelengths above 600 nm, the transparency was 80% to 85% whereas between 600 nm and 450 nm it decreases down to 10% (Kuzum et al., 2014). This might be a major concern for deep tissue 2P-LSM where e.g., only weak signals (due to tissue scattering effects) can be acquired. Another recent study (Donahue et al., 2018) pointed out the result of the combination of an electrode array made from parylene C and gold interconnections with two-photon imaging. The square electrode sites had a size of  $25\ \mu\text{m} \times 25\ \mu\text{m}$ , and the width of the interconnection lines was around 20  $\mu\text{m}$  at the electrode head (Donahue et al., 2018). The routing of the interconnection line was selected in a way that the visual access through the inner area of the electrode head was maximized. With that design, heating and photoelectric effects were minimized (Donahue et al., 2018). However, this could cause the problem that metal structures within the optical field might be heated up by laser light adsorption. This problem could also occur with polyimide electrodes.

Currently, there does not seem to be any electrode technology that can be used without restrictions. With the high-level microsystem-produced electrodes, a high degree of miniaturization and improved flexibility would be possible. However, general transparency could be only achieved if the electrode contacts were also realized with transparent conductive materials. But these materials still seem to have deficits in electrode impedance and current transfer capability.

## CONCLUSION

We developed versatile, reliable, and cost-effective LCP surface electrodes, allowing the combination of *in vivo* 2P-imaging and electrophysiology in the mouse CNS. The pilot studies highlighted the biocompatibility and the new opportunities provided by the technology. Several types of LCP electrodes,

optimized for tissue stimulation and low noise ECoG recording, are available to study and modulate CNS function in health and disease.

## DATA AVAILABILITY STATEMENT

The original contributions presented in the study are included in the article, further inquiries can be directed to the corresponding author.

## ETHICS STATEMENT

The animal study was reviewed and approved by Landesamt für Gesundheit und Verbraucherschutz of Saarland state (license numbers: 71/2013, 36/2016).

## AUTHOR CONTRIBUTIONS

MS developed and optimized surface electrodes, performed imaging and recording, data analysis, wrote the initial manuscript, and conceived the study. LC performed the immunohistochemical assessment of biocompatibility, electrode implantation surgeries (optimization and preparation), imaging and recording, data analysis, wrote initial manuscript, and conceived the study. GS provided custom-made Matlab routines (MSparkles). AS and KK conceived the study and revised the manuscript. FK conceived the study, provided infrastructure, grant support, and finalized the manuscript. All authors contributed to the article and approved the submitted version.

## FUNDING

This project has received funding from the European Union's Horizon 2020 research and innovation programme under the Marie Skłodowska-Curie grant agreement No. 722053 (EU-GliaPhD), from the Deutsche Forschungsgemeinschaft (DFG) SPP 1757, DFG SFB894, DFG FOR2289, DFG SFB1158, H2020-FETPROACT-01-2016 Neurofibers, and from the Trier University of Applied Sciences (project MIRACLE).

## ACKNOWLEDGMENTS

We are grateful to Daniel Schauenburg for expert mouse maintenance and Frank Rhode for technical assistance.

## REFERENCES

- Araque, A. (2008). Astrocytes process synaptic information. *Neuron Glia Biol.* 4, 3–10. doi: 10.1017/S1740925X09000064
- Araque, A., Carmignoto, G., Haydon, P. G., Oliet, S. H., Robitaille, R., and Volterra, A. (2014). Gliotransmitters travel in time and space. *Neuron* 81, 728–739. doi: 10.1016/j.neuron.2014.02.007
- Araque, A., Parpura, V., Sanzgiri, R. P., and Haydon, P. G. (1999). Tripartite synapses: glia, the unacknowledged partner. *Trends Neurosci.* 22, 208–215. doi: 10.1016/s0166-2236(98)01349-6
- Arranz, A. M., and De Strooper, B. (2019). The role of astroglia in Alzheimer's disease: pathophysiology and clinical implications. *Lancet Neurol.* 18, 406–414. doi: 10.1016/S1474-4422(18)30490-3
- Ay, B., Wallace, D., Mantilla, C. B., and Prakash, Y. S. (2005). Differential inhibition of neuronal  $\text{Na}^+$ - $\text{Ca}^{2+}$  exchange versus store-operated  $\text{Ca}^{2+}$  channels by volatile anesthetics in pheochromocytoma (PC12) cells. *Anesthesiology* 103, 93–101. doi: 10.1097/0000542-200507000-00016
- Basser, P. J., and Roth, B. J. (2000). New currents in electrical stimulation of excitable tissues. *Annu. Rev. Biomed. Eng.* 2, 377–397. doi: 10.1146/annurev.bioeng.2.1.377
- Bazargani, N., and Attwell, D. (2016). Astrocyte calcium signaling: the third wave. *Nat. Neurosci.* 19, 182–189. doi: 10.1038/nn.4201
- Beckner, M. E. (2020). A roadmap for potassium buffering/dispersion via the glial network of the CNS. *Neurochem. Int.* 136:104727. doi: 10.1016/j.neuint.2020.104727

- Bernier, L. P., Bohlen, C. J., York, E. M., Choi, H. B., Kamyabi, A., Dissing-Olesen, L., et al. (2019). Nanoscale surveillance of the brain by microglia via cAMP-regulated filopodia. *Cell Rep.* 27, 2895.e4–2908.e4. doi: 10.1016/j.celrep.2019.05.010
- Beudel, M., and Brown, P. (2016). Adaptive deep brain stimulation in Parkinson's disease. *Parkinsonism Relat. Disord.* 22, S123–S126. doi: 10.1016/j.parkreldis.2015.09.028
- Blanck, T. J., and Thompson, M. (1982). Enflurane and isoflurane stimulate calcium transport by cardiac sarcoplasmic reticulum. *Anesth. Analg.* 61, 142–145. doi: 10.1213/00000539-198202000-00015
- Bojarskaite, L., Bjørnstad, D. M., Pettersen, K. H., Cunen, C., Hermansen, G. H., Åbjørnsbråten, K. S., et al. (2020). Astrocytic  $\text{Ca}^{2+}$  signaling is reduced during sleep and is involved in the regulation of slow wave sleep. *Nat. Commun.* 11:3240. doi: 10.1038/s41467-020-17062-2
- Brini, M., Cali, T., Ottolini, D., and Carafoli, E. (2014). Neuronal calcium signaling: function and dysfunction. *Cell. Mol. Life Sci.* 71, 2787–2814. doi: 10.1007/s00018-013-1550-7
- Burda, J. E., Bernstein, A. M., and Sofroniew, M. V. (2016). Astrocyte roles in traumatic brain injury. *Exp. Neurol.* 275, 305–315. doi: 10.1016/j.expneurol.2015.03.020
- Burda, J. E., and Sofroniew, M. V. (2014). Reactive gliosis and the multicellular response to CNS damage and disease. *Neuron* 81, 229–248. doi: 10.1016/j.neuron.2013.12.034
- Caudal, L. C., Gobbo, D., Scheller, A., and Kirchhoff, F. (2020). The paradox of astroglial  $\text{Ca}^{2+}$  signals at the interface of excitation and inhibition. *Front. Cell. Neurosci.* 14:399. doi: 10.3389/fncel.2020.609947
- Chen, Y., Rommelfanger, N. J., Mahdi, A. I., Wu, X., Keene, S. T., Obaid, A., et al. (2021). How is flexible electronics advancing neuroscience research? *Biomaterials* 268:120559. doi: 10.1016/j.biomaterials.2020.120559
- Chiang, C. H., Wang, C., Barth, K., Rahimpour, S., Trumpis, M., Duraivel, S., et al. (2021). Flexible, high-resolution thin-film electrodes for human and animal neural research. *J. Neural Eng.* 18:045009. doi: 10.1088/1741-2552/ac02dc
- Choi, J. H., Koch, K. P., Poppendieck, W., Lee, M., and Shin, H. S. (2010). High resolution electroencephalography in freely moving mice. *J. Neurophysiol.* 104, 1825–1834. doi: 10.1152/jn.00188.2010
- Cogan, S. F. (2008). Neural stimulation and recording electrodes. *Annu. Rev. Biomed. Eng.* 10, 275–309. doi: 10.1146/annurev.bioeng.10.061807.160518
- Collins, R. O., and Thomas, R. C. (2001). The effect of calcium pump inhibitors on the response of intracellular calcium to caffeine in snail neurones. *Cell Calcium* 30, 41–48. doi: 10.1054/ceca.2001.0209
- Covelo, A., and Araque, A. (2018). Neuronal activity determines distinct gliotransmitter release from a single astrocyte. *eLife* 7:e32237. doi: 10.7554/eLife.32237
- Cupido, A., Catalin, B., Steffens, H., and Kirchhoff, F. (2014). “Surgical procedures to study microglial motility in the brain and in the spinal cord by *in vivo* two-photon laser-scanning microscopy,” in *Confocal and Multiphoton Laser-Scanning Microscopy of Neuronal Tissue: Applications and Quantitative Image Analysis*, eds L. Bakota and R. Brandt (New York: Springer) 37–50.
- Deshpande, T., Li, T., Henning, L., Wu, Z., Müller, J., Seifert, G., et al. (2020). Constitutive deletion of astrocytic connexins aggravates kainate-induced epilepsy. *Glia* 68, 2136–2147. doi: 10.1002/glia.23832
- Donahue, M. J., Kaszas, A., Turi, G. F., Rózsa, B., Slézia, A., Vanzetta, I., et al. (2018). Multimodal characterization of neural networks using highly transparent electrode arrays. *eNeuro* 5:ENEURO.0187-18.2018. doi: 10.1523/ENEURO.0187-18.2018
- Donat, C. K., Scott, G., Gentleman, S. M., and Sastre, M. (2017). Microglial activation in traumatic brain injury. *Front. Aging Neurosci.* 9:208. doi: 10.3389/fnagi.2017.00208
- Durkee, C. A., and Araque, A. (2019). Diversity and specificity of astrocyte-neuron communication. *Neuroscience* 396, 73–78. doi: 10.1016/j.neuroscience.2018.11.010
- Englert, R., Rupp, F., Kirchhoff, F., Koch, K. P., and Schweigmann, M. (2017). Technical characterization of an 8 or 16 channel recording system to acquire electrocorticograms of mice. *Curr. Dir. Biomed. Eng.* 3, 595–598. doi: 10.1515/cdbme-2017-0124
- Evangelidis, G. D., and Psarakis, E. Z. (2008). Parametric image alignment using enhanced correlation coefficient maximization. *IEEE Trans. Pattern Anal. Mach. Intell.* 30, 1858–1865. doi: 10.1109/TPAMI.2008.113
- Franks, J. J., Horn, J. L., Janicki, P. K., and Singh, G. (1995). Stable inhibition of brain synaptic plasma membrane calcium ATPase in rats anesthetized with halothane. *Anesthesiology* 82, 118–128. doi: 10.1097/00000542-199501000-00016
- Franks, N. P., and Lieb, W. R. (1988). Volatile general anaesthetics activate a novel neuronal  $\text{K}^{+}$  current. *Nature* 333, 662–664. doi: 10.1038/333662a0
- Gómez-Gonzalo, M., Martín-Fernández, M., Martínez-Murillo, R., Mederos, S., Hernández-Vivanco, A., Jamison, S., et al. (2017). Neuron-astrocyte signaling is preserved in the aging brain. *Glia* 65, 569–580. doi: 10.1002/glia.23112
- Guerra-Gomes, S., Sousa, N., Pinto, L., and Oliveira, J. F. (2017). Functional roles of astrocyte calcium elevations: from synapses to behavior. *Front. Cell. Neurosci.* 11:427. doi: 10.3389/fncel.2017.00427
- Guo, Z. V., Hires, S. A., Li, N., O'Connor, D. H., Komiyama, T., Ophir, E., et al. (2014). Procedures for behavioral experiments in head-fixed mice. *PLoS One* 9:e88678. doi: 10.1371/journal.pone.0088678
- Guo, M., Wang, J., Zhao, Y., Feng, Y., Han, S., Dong, Q., et al. (2020). Microglial exosomes facilitate  $\alpha$ -synuclein transmission in Parkinson's disease. *Brain* 143, 1476–1497. doi: 10.1093/brain/awaa090
- Hannon, J. D., and Cody, M. J. (2002). Effects of volatile anesthetics on sarcoplasmic calcium transport and sarcoplasmic reticulum calcium content in isolated myocytes. *Anesthesiology* 96, 1457–1464. doi: 10.1097/00000542-200206000-00027
- Harada, K., Ito, M., Wang, X., Tanaka, M., Wongso, D., Konno, A., et al. (2017). Red fluorescent protein-based cAMP indicator applicable to optogenetics and *in vivo* imaging. *Sci. Rep.* 7:7351. doi: 10.1038/s41598-017-07820-6
- Heuser, K., Nome, C. G., Pettersen, K. H., Åbjørnsbråten, K. S., Jensen, V., Tang, W., et al. (2018).  $\text{Ca}^{2+}$  signals in astrocytes facilitate spread of epileptiform activity. *Cereb. Cortex* 28, 4036–4048. doi: 10.1093/cercor/bhy196
- International Multiple Sclerosis Genetics Consortium. (2019). Multiple sclerosis genomic map implicates peripheral immune cells and microglia in susceptibility. *Science* 365:eaav7188. doi: 10.1126/science.aav7188
- Jahn, H. M., Kasakow, C. V., Helfer, A., Michely, J., Verkhratsky, A., Maurer, H. H., et al. (2018). Refined protocols of tamoxifen injection for inducible DNA recombination in mouse astroglia. *Sci. Rep.* 8:5913. doi: 10.1038/s41598-018-24085-9
- Karus, C., Mondragão, M. A., Ziemens, D., and Rose, C. R. (2015). Astrocytes restrict discharge duration and neuronal sodium loads during recurrent network activity. *Glia* 63, 936–957. doi: 10.1002/glia.22793
- Khodagholy, D., Doublet, T., Quilichini, P., Gurfinkel, M., Leleux, P., Ghestem, A., et al. (2013). *in vivo* recordings of brain activity using organic transistors. *Nat. Commun.* 4:1575. doi: 10.1038/ncomms2573
- Khodagholy, D., Gelin, J. N., Thesen, T., Doyle, W., Devinsky, O., Malliaras, G. G., et al. (2015). NeuroGrid: recording action potentials from the surface of the brain. *Nat. Neurosci.* 18, 310–315. doi: 10.1038/nn.3905
- Kirsch, D. L., and Nichols, F. (2013). Cranial electrotherapy stimulation for treatment of anxiety, depression, and insomnia. *Psychiatr. Clin. North Am.* 36, 169–176. doi: 10.1016/j.psc.2013.01.006
- Kislin, M., Mugantseva, E., Molotkov, D., Kullesskaya, N., Khirug, S., Kirilkin, I., et al. (2014). Flat-floored air-lifted platform: a new method for combining behavior with microscopy or electrophysiology on awake freely moving rodents. *J. Vis. Exp.* 88:e51869. doi: 10.3791/51869
- Koyanagi, Y., Torturo, C. L., Cook, D. C., Zhou, Z., and Hemmings, H. C. (2019). Role of specific presynaptic calcium channel subtypes in isoflurane inhibition of synaptic vesicle exocytosis in rat hippocampal neurones. *Br. J. Anaesth.* 123, 219–227. doi: 10.1016/j.bja.2019.03.029
- Kuzum, D., Takano, H., Shim, E., Reed, J. C., Juul, H., Richardson, A. G., et al. (2014). Transparent and flexible low noise graphene electrodes for simultaneous electrophysiology and neuroimaging. *Nat. Commun.* 5:5259. doi: 10.1038/ncomms6259
- Land, R., Engler, G., Kral, A., and Engel, A. K. (2012). Auditory evoked bursts in mouse visual cortex during isoflurane anesthesia. *PLoS One* 7:e49855. doi: 10.1371/journal.pone.0049855
- Lee, S. W., Seo, J. M., Ha, S., Kim, E. T., Chung, H., and Kim, S. J. (2009). Development of microelectrode arrays for artificial retinal implants using liquid crystal polymers. *Invest. Ophthalmol. Vis. Sci.* 50, 5859–5866. doi: 10.1167/iops.09-3743
- Lissek, T., Obenhaus, H. A., Ditzel, D. A., Nagai, T., Miyawaki, A., Sprengel, R., et al. (2016). General anesthetic conditions induce network synchrony

- and disrupt sensory processing in the cortex. *Front. Cell. Neurosci.* 10:64. doi: 10.3389/fncel.2016.00064
- Majewska, A., Brown, E., Ross, J., and Yuste, R. (2000). Mechanisms of calcium decay kinetics in hippocampal spines: role of spine calcium pumps and calcium diffusion through the spine neck in biochemical compartmentalization. *J. Neurosci.* 20, 1722–1734. doi: 10.1523/JNEUROSCI.20-05-01722.2000
- Michelson, N. J., Eles, J. R., Vazquez, A. L., Ludwig, K. A., and Kozai, T. D. Y. (2019). Calcium activation of cortical neurons by continuous electrical stimulation: frequency dependence, temporal fidelity, and activation density. *J. Neurosci. Res.* 97, 620–638. doi: 10.1002/jnr.24370
- Min, K. S., Lee, C. J., Jun, S. B., Kim, J., Lee, S. E., Shin, J., et al. (2014). A liquid crystal polymer-based neuromodulation system: an application on animal model of neuropathic pain. *Neuromodulation* 17, 160–169. doi: 10.1111/ner.12093
- Minnikanti, S., Pereira, M. G., Jaraiedi, S., Jackson, K., Costa-Neto, C. M., Li, Q., et al. (2010). *in vivo* electrochemical characterization and inflammatory response of multiwalled carbon nanotube-based electrodes in rat hippocampus. *J. Neural Eng.* 7:16002. doi: 10.1088/1741-2560/7/1/016002
- Mohajerani, M. H., Chan, A. W., Mohsenvand, M., LeDue, J., Liu, R., McVea, D. A., et al. (2013). Spontaneous cortical activity alternates between motifs defined by regional axonal projections. *Nat. Neurosci.* 16, 1426–1435. doi: 10.1038/nn.3499
- Mori, T., Tanaka, K., Buffo, A., Wurst, W., Kühn, R., and Götz, M. (2006). Inducible gene deletion in astroglia and radial glia—a valuable tool for functional and lineage analysis. *Glia* 54, 21–34. doi: 10.1002/glia.20350
- Nikolic, L., Shen, W., Nobili, P., Virenque, A., Ulmann, L., and Audinat, E. (2018). Blocking TNF $\alpha$ -driven astrocyte purinergic signaling restores normal synaptic activity during epileptogenesis. *Glia* 66, 2673–2683. doi: 10.1002/glia.23519
- Nimmerjahn, A., Kirchhoff, F., and Helmchen, F. (2005). Resting microglial cells are highly dynamic surveillants of brain parenchyma *in vivo*. *Science* 308, 1314–1318. doi: 10.1126/science.1110647
- Nimmerjahn, A., Mukamel, E. A., and Schnitzer, M. J. (2009). Motor behavior activates Bergmann glial networks. *Neuron* 62, 400–412. doi: 10.1016/j.neuron.2009.03.019
- Obien, M. E., Deligkaris, K., Bullmann, T., Bakkum, D. J., and Frey, U. (2014). Revealing neuronal function through microelectrode array recordings. *Front. Neurosci.* 8:423. doi: 10.3389/fnins.2014.00423
- Park, D.-W., Ness, J. P., Brodnick, S. K., Esquibel, C., Novello, J., Atry, F., et al. (2018). Electrical neural stimulation and simultaneous *in vivo* monitoring with transparent graphene electrode arrays implanted in GCaMP6f mice. *ACS Nano* 12, 148–157. doi: 10.1021/acsnano.7b04321
- Park, D.-W., Schendel, A. A., Mikael, S., Brodnick, S. K., Richner, T. J., Ness, J. P., et al. (2014). Graphene-based carbon-layered electrode array technology for neural imaging and optogenetic applications. *Nat. Commun.* 5:5258. doi: 10.1038/ncomms6258
- Parpura, V., Basarsky, T. A., Liu, F., Jęftinija, K., Jęftinija, S., and Haydon, P. G. (1994). Glutamate-mediated astrocyte neuron signaling. *Nature* 369, 744–747. doi: 10.1038/369744a0
- Paukert, M., Agarwal, A., Cha, J., Doze, V. A., Kang, J. U., and Bergles, D. E. (2014). Norepinephrine controls astroglial responsiveness to local circuit activity. *Neuron* 82, 1263–1270. doi: 10.1016/j.neuron.2014.04.038
- Polikov, V. S., Tresco, P. A., and Reichert, W. M. (2005). Response of brain tissue to chronically implanted neural electrodes. *J. Neurosci. Methods* 148, 1–18. doi: 10.1016/j.jneumeth.2005.08.015
- Pologruto, T. A., Sabatini, B. L., and Svoboda, K. (2003). ScanImage: flexible software for operating laser scanning microscopes. *Biomed. Eng. Online* 2:13. doi: 10.1186/1475-925X-2-13
- Potter, K. A., Buck, A. C., Self, W. K., and Capadona, J. R. (2012). Stab injury and device implantation within the brain results in inversely multiphasic neuroinflammatory and neurodegenerative responses. *J. Neural Eng.* 9:046020. doi: 10.1088/1741-2560/9/4/046020
- Prinz, M., Jung, S., and Priller, J. (2019). Microglia biology: one century of evolving concepts. *Cell* 179, 292–311. doi: 10.1016/j.cell.2019.08.053
- Radman, T., Ramos, R. L., Brumberg, J. C., and Bikson, M. (2009). Role of cortical cell type and morphology in subthreshold and suprathreshold uniform electric field stimulation *in vitro*. *Brain Stimul.* 2, 215.e3–228.e3. doi: 10.1016/j.brs.2009.03.007
- Rattay, F. (1998). Analysis of the electrical excitation of CNS neurons. *IEEE Trans. Biomed. Eng.* 45, 766–772. doi: 10.1109/10.678611
- Richner, T. J., Thongpang, S., Brodnick, S. K., Schendel, A. A., Falk, R. W., Krugner-Higby, L. A., et al. (2014). Optogenetic micro-electrocorticography for modulating and localizing cerebral cortex activity. *J. Neural Eng.* 11:016010. doi: 10.1088/1741-2560/11/1/016010
- Rogers, N., Hermiz, J., Ganji, M., Kaestner, E., Kılıç, K., Hossain, L., et al. (2019). Correlation structure in micro-ECoG recordings is described by spatially coherent components. *PLoS Comput. Biol.* 15:e1006769. doi: 10.1371/journal.pcbi.1006769
- Ross, W., Fleidervish, I., and Lasser-Ross, N. (2013). Imaging sodium in axons and dendrites. *Cold Spring Harb. Protoc.* 2013, 433–437. doi: 10.1101/pdb.prot074310
- Rudolph, U., and Antkowiak, B. (2004). Molecular and neuronal substrates for general anaesthetics. *Nat. Rev. Neurosci.* 5, 709–720. doi: 10.1038/nrn1496
- Rusakov, D. A. (2015). Disentangling calcium-driven astrocyte physiology. *Nat. Rev. Neurosci.* 16, 226–233. doi: 10.1038/nrn3878
- Salatino, J. W., Ludwig, K. A., Kozai, T. D. Y., and Purcell, E. K. (2017). Glial responses to implanted electrodes in the brain. *Nat. Biomed. Eng.* 1, 862–877. doi: 10.1038/s41551-017-0154-1
- Schendel, A. A., Thongpang, S., Brodnick, S. K., Richner, T. J., Lindevig, B. D., Krugner-Higby, L., et al. (2013). A cranial window imaging method for monitoring vascular growth around chronically implanted micro-ECoG devices. *J. Neurosci. Methods* 218, 121–130. doi: 10.1016/j.jneumeth.2013.06.001
- Schweigmann, M., Koch, K. P., Auler, F., and Kirchhoff, F. (2018). Improving electrocorticograms of awake and anaesthetized mice using wavelet denoising. *Curr. Dir. Biomed. Eng.* 4, 469–472. doi: 10.1515/cdbme-2018-0112
- Shigetomi, E., Patel, S., and Khakh, B. S. (2016). Probing the complexities of astrocyte calcium signaling. *Trends Cell Biol.* 26, 300–312. doi: 10.1016/j.tcb.2016.01.003
- Shokouinejad, M., Park, D. W., Jung, Y. H., Brodnick, S. K., Novello, J., Dingle, A., et al. (2019). Progress in the field of micro-electrocorticography. *Micromachines* 10:62. doi: 10.3390/mi10010062
- Simons, M., and Nave, K.-A. (2015). Oligodendrocytes: myelination and axonal support. *Cold Spring Harb. Perspect. Biol.* 8:a020479. doi: 10.1101/cshperspect.a020479
- Sohal, H. S., Clowry, G. J., Jackson, A., O'Neill, A., and Baker, S. N. (2016). Mechanical flexibility reduces the foreign body response to long-term implanted microelectrodes in rabbit cortex. *PLoS One* 11:e0165606. doi: 10.1371/journal.pone.0165606
- Study, R. E. (1994). Isoflurane inhibits multiple voltage-gated calcium currents in hippocampal pyramidal neurons. *Anesthesiology* 81, 104–116. doi: 10.1097/00005542-199407000-00016
- Swire, M., and Ffrench-Constant, C. (2018). Seeing is believing: myelin dynamics in the adult CNS. *Neuron* 98, 684–686. doi: 10.1016/j.neuron.2018.05.005
- Thrane, A. S., Thrane, V. R., Zeppenfeld, D., Lou, N., Xu, Q., Nagelhus, E. A., et al. (2012). General anesthesia selectively disrupts astrocyte calcium signaling in the awake mouse cortex. *Proc. Natl. Acad. Sci. U S A* 109, 18974–18979. doi: 10.1073/pnas.1209448109
- Thunemann, M., Lu, Y., Liu, X., Kılıç, K., Desjardins, M., Vandenberghe, M., et al. (2018). Deep 2-photon imaging and artifact-free optogenetics through transparent graphene microelectrode arrays. *Nat. Commun.* 9:2035. doi: 10.1038/s41467-018-04457-5
- Timic Stamenic, T., Feseha, S., Valdez, R., Zhao, W., Klawitter, J., and Todorovic, S. M. (2019). Alterations in oscillatory behavior of central medial thalamic neurons demonstrate a key role of CaV3.1 isoform of T-channels during isoflurane-induced anesthesia. *Cereb. Cortex* 29, 4679–4696. doi: 10.1093/cercor/bhz002
- Traiffort, E., Kassoussi, A., Zahaf, A., and Laouarem, Y. (2020). Astrocytes and microglia as major players of myelin production in normal and pathological conditions. *Front. Cell. Neurosci.* 14:79. doi: 10.3389/fncel.2020.00079
- Verkhatsky, A., and Nedergaard, M. (2018). Physiology of astroglia. *Physiol. Rev.* 98, 239–389. doi: 10.1152/physrev.00042.2016
- Volterra, A., Liaudet, N., and Savtchouk, I. (2014). Astrocyte Ca<sup>2+</sup> signalling: an unexpected complexity. *Nat. Rev. Neurosci.* 15, 327–335. doi: 10.1038/nrn3725
- Vomero, M., Porto Cruz, M. F., Zucchini, E., Ciarpella, F., Delfino, E., Carli, S., et al. (2020). Conformable polyimide-based  $\mu$ ECoGs: bringing the

- electrodes closer to the signal source. *Biomaterials* 255:120178. doi: 10.1016/j.biomaterials.2020.120178
- Westphalen, R. I., and Hemmings, H. C. Jr. (2006). Volatile anesthetic effects on glutamate versus GABA release from isolated rat cortical nerve terminals: basal release. *J. Pharmacol. Exp. Ther.* 316, 208–215. doi: 10.1124/jpet.105.090647
- Woods, V., Trumpis, M., Bent, B., Palopoli-Trojani, K., Chiang, C. H., Wang, C., et al. (2018). Long-term recording reliability of liquid crystal polymer  $\Omega$ ECOG arrays. *J. Neural Eng.* 15:066024. doi: 10.1088/1741-2552/aae39d
- Xie, Z., Yang, Q., Song, D., Quan, Z., and Qing, H. (2020). Optogenetic manipulation of astrocytes from synapses to neuronal networks: a potential therapeutic strategy for neurodegenerative diseases. *Glia* 68, 215–226. doi: 10.1002/glia.23693
- Ye, H., and Steiger, A. (2015). Neuron matters: electric activation of neuronal tissue is dependent on the interaction between the neuron and the electric field. *J. Neuroeng. Rehabil.* 12:65. doi: 10.1186/s12984-015-0061-1
- Yeung, M. S. Y., Djelloul, M., Steiner, E., Bernard, S., Salehpour, M., Possnert, G., et al. (2019). Dynamics of oligodendrocyte generation in multiple sclerosis. *Nature* 566, 538–542. doi: 10.1038/s41586-018-0842-3
- Yun, S. P., Kam, T.-I., Panicker, N., Kim, S., Oh, Y., Park, J. S., et al. (2018). Block of A1 astrocyte conversion by microglia is neuroprotective in models of Parkinson's disease. *Nat. Med.* 24, 931–938. doi: 10.1038/s41591-018-0051-5
- Zhao, W., Zhang, M., Liu, J., Liang, P., Wang, R., Hemmings, H. C., et al. (2019). Isoflurane modulates hippocampal cornu ammonis pyramidal neuron excitability by inhibition of both transient and persistent sodium currents in mice. *Anesthesiology* 131, 94–104. doi: 10.1097/ALN.0000000000002753
- Ziemens, D., Oschmann, F., Gerkau, N. J., and Rose, C. R. (2019). Heterogeneity of activity-induced sodium transients between astrocytes of the mouse hippocampus and neocortex: mechanisms and consequences. *J. Neurosci.* 39, 2620–2634. doi: 10.1523/JNEUROSCI.2029-18.2019

**Conflict of Interest:** The authors declare that the research was conducted in the absence of any commercial or financial relationships that could be construed as a potential conflict of interest.

**Publisher's Note:** All claims expressed in this article are solely those of the authors and do not necessarily represent those of their affiliated organizations, or those of the publisher, the editors and the reviewers. Any product that may be evaluated in this article, or claim that may be made by its manufacturer, is not guaranteed or endorsed by the publisher.

Copyright © 2021 Schweigmann, Caudal, Stopper, Scheller, Koch and Kirchhoff. This is an open-access article distributed under the terms of the Creative Commons Attribution License (CC BY). The use, distribution or reproduction in other forums is permitted, provided the original author(s) and the copyright owner(s) are credited and that the original publication in this journal is cited, in accordance with accepted academic practice. No use, distribution or reproduction is permitted which does not comply with these terms.





# Neuronal and Astrocytic Regulations in Schizophrenia: A Computational Modelling Study

Lea Fritschi<sup>1</sup>, Johanna Hedlund Lindmar<sup>2</sup>, Florian Scheidl<sup>3</sup> and Kerstin Lenk<sup>4,5\*</sup>

<sup>1</sup> Department of Mathematics, ETH Zurich, Zurich, Switzerland, <sup>2</sup> Institute of Neuroinformatics, University of Zurich, ETH Zurich, Zurich, Switzerland, <sup>3</sup> Department of Computer Science, ETH Zurich, Zurich, Switzerland, <sup>4</sup> Computational Biophysics and Imaging Group (CBIG), Faculty of Medicine and Health Technology, BioMediTech, Tampere University, Tampere, Finland, <sup>5</sup> Institute of Neural Engineering, Graz University of Technology, Graz, Austria

## OPEN ACCESS

### Edited by:

Christian Lohr,  
University of Hamburg, Germany

### Reviewed by:

Bernhard J. Mitterauer,  
Independent Researcher, Salzburg,  
Austria

Yuriy Pankratov,  
University of Warwick,  
United Kingdom

### \*Correspondence:

Kerstin Lenk  
lenk.kerstin@gmail.com

### Specialty section:

This article was submitted to  
Non-Neuronal Cells,  
a section of the journal  
Frontiers in Cellular Neuroscience

**Received:** 31 May 2021

**Accepted:** 26 July 2021

**Published:** 26 August 2021

### Citation:

Fritschi L, Lindmar JH, Scheidl F and  
Lenk K (2021) Neuronal and Astrocytic  
Regulations in Schizophrenia: A  
Computational Modelling Study.  
Front. Cell. Neurosci. 15:718459.  
doi: 10.3389/fncel.2021.718459

According to the tripartite synapse model, astrocytes have a modulatory effect on neuronal signal transmission. More recently, astrocyte malfunction has been associated with psychiatric diseases such as schizophrenia. Several hypotheses have been proposed on the pathological mechanisms of astrocytes in schizophrenia. For example, post-mortem examinations have revealed a reduced astrocytic density in patients with schizophrenia. Another hypothesis suggests that disease symptoms are linked to an abnormality of glutamate transmission, which is also regulated by astrocytes (glutamate hypothesis of schizophrenia). Electrophysiological findings indicate a dispute over whether the disorder causes an increase or a decrease in neuronal and astrocytic activity. Moreover, there is no consensus as to which molecular pathways and network mechanisms are altered in schizophrenia. Computational models can aid the process in finding the underlying pathological malfunctions. The effect of astrocytes on the activity of neuron-astrocyte networks has been analysed with computational models. These can reproduce experimentally observed phenomena, such as astrocytic modulation of spike and burst signalling in neuron-astrocyte networks. Using an established computational neuron-astrocyte network model, we simulate experimental data of healthy and pathological networks by using different neuronal and astrocytic parameter configurations. In our simulations, the reduction of neuronal or astrocytic cell densities yields decreased glutamate levels and a statistically significant reduction in the network activity. Amplifications of the astrocytic ATP release toward postsynaptic terminals also reduced the network activity and resulted in temporarily increased glutamate levels. In contrast, reducing either the glutamate release or re-uptake in astrocytes resulted in higher network activities. Similarly, an increase in synaptic weights of excitatory or inhibitory neurons raises the excitability of individual cells and elevates the activation level of the network. To conclude, our simulations suggest that the impairment of both neurons and astrocytes disturbs the neuronal network activity in schizophrenia.

**Keywords:** computational psychiatry, computational model, neuron-astrocyte network, glutamate, schizophrenia, linear mixed effects models

# 1. INTRODUCTION

Astrocytes contribute to the complex cognitive function in humans (Santello et al., 2019), whereby they have structural, homeostatic, and metabolic roles. Astrocytes are connected to each other via gap junctions and form non-overlapping domains in complex networks. This glial cell type composes, together with a pre- and a postsynaptic neuron, the so-called tripartite synapse (Araque et al., 1999). They take up glutamate rapidly from the synaptic cleft to ensure a short glutamate exposition to the postsynaptic neuron for precise synaptic transmission. Subsequently, astrocytes respond to neuronal activity with intracellular calcium ( $\text{Ca}^{2+}$ ) elevations and release ions and transmitter molecules in return.

Seemingly neurons and astrocytes play a role in psychiatric diseases such as schizophrenia (SCZ) (Uhlhaas and Singer, 2010; Takahashi and Sakurai, 2013; Moraga-Amaro et al., 2014; Mei et al., 2018). SCZ is associated with positive (such as delusions and hallucinations), negative (such as social withdrawal and lack of motivation), and cognitive symptoms (difficulties in memory and attention).

Due to the success of first generation antipsychotics, the *dopamine hypothesis* of SCZ was formed. The underlying assumption of this hypothesis is that excessive transmission of subcortical dopamine causes the positive symptoms of SCZ (Grnder and Cumming, 2016). While research has found significant support of this hypothesis, it is not pathognomonic and does not sufficiently account for the negative symptoms of SCZ.

Post-mortem examinations, human induced pluripotent stem cell experiments, and animal studies have revealed a reduced astrocytic and neuronal synaptic density in SCZ patients (Cotter et al., 2001; Brennand et al., 2011; Dietz et al., 2020; Naujock et al., 2020). Cell death is associated with excitotoxicity due to excessive glutamate amounts and glutamate receptor activation (Drouin-Ouellet et al., 2011). However, the mechanisms and pathways of this developmental brain disorder are not well understood yet. Different studies reach conflicting conclusions. Some papers report an upregulation in glial fibrillary acidic protein (GFAP) in SCZ astrocytes (review by Moraga-Amaro et al., 2014), whereas in other studies, a reduced GFAP expression has been described (review by Takahashi and Sakurai, 2013).

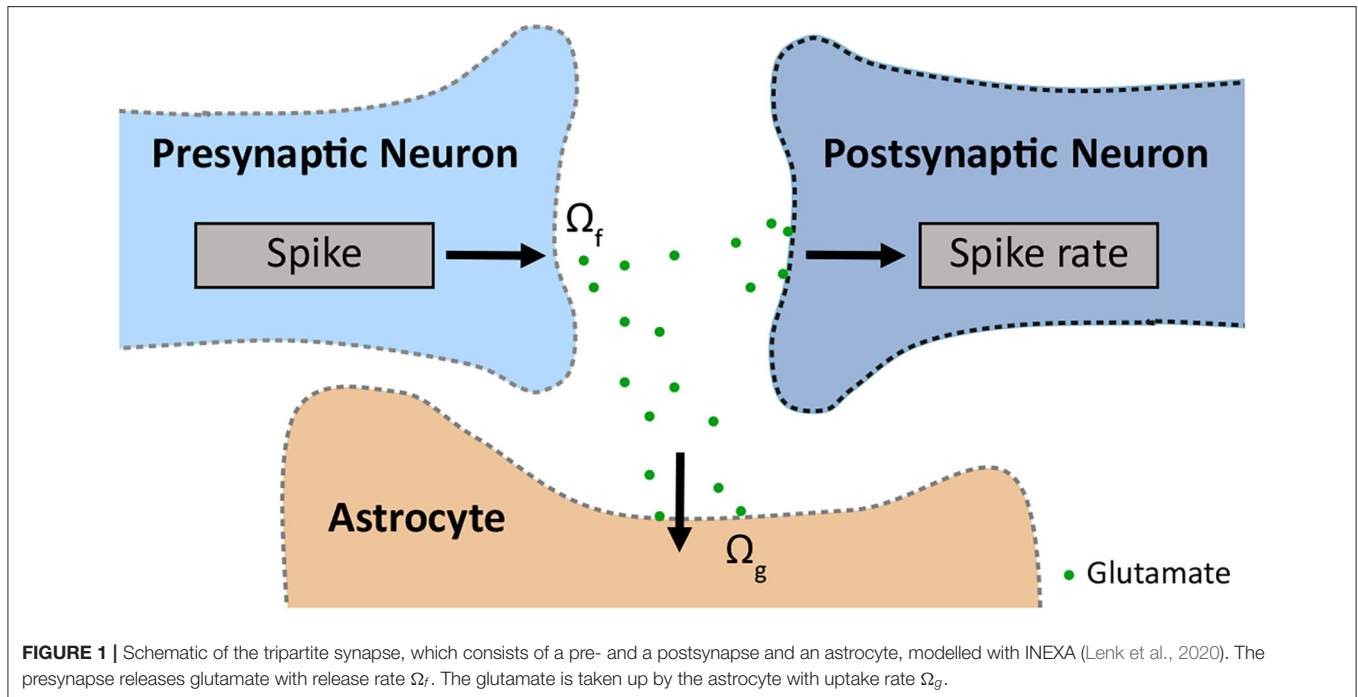
Koskivi et al. (2020) found that human stem cell-derived astrocytes from SCZ patients show highly sex-specific alterations in gene expression. The Gene Ontology pathways related to neuronal wiring and inflammation are altered in SCZ astrocytes. Healthy neurons co-cultured with SCZ astrocytes of either sex exhibited a significantly increased response to glutamate. Transplanted hiPSC-astrocyte progenitors from SCZ patients developed into matured astrocytes in a mouse model and led to subtle behavioural changes. Furthermore, they induced demyelination, synaptic dysfunction and affected the inflammation pathways (Koskivi et al., 2020). Several studies have shown that the expression of the metabotropic glutamate receptor (mGluR) type 5 is increased in astrocytes in the prefrontal cortex (Ohnuma et al., 1998; Kosten et al., 2016).

For neurons, the *glutamate hypothesis* of SCZ has been established (de Bartolomeis et al., 2005; Moghaddam and Javitt, 2012; Takahashi and Sakurai, 2013; Cohen et al., 2015; Mei et al., 2018): a hypofunction of NMDA receptors (NMDARs) leads to excessive glutamate release, mainly prevalent in the hippocampus and prefrontal cortex. However, the underlying mechanisms are not yet clarified. A decreased level of D-serine, which is mainly released by astrocytes, affects the NMDAR function in neurons. Both glutamate and either D-serine or glycine are co-agonists to the NMDAR binding sites. The astrocyte-derived NMDAR antagonist kynurenic acid (KYNA) shows increased levels in SCZ patients (Takahashi and Sakurai, 2013; Cohen et al., 2015). Interneurons might react to changes in NMDAR function with inhibition, leading to disinhibition and a hyperexcitation of glutamate levels in SCZ (Moghaddam and Javitt, 2012; Mei et al., 2018). Alternatively, Schobel et al. (2013) suggested that excess synaptic glutamate release results in a reduction of the interneuronal function and hippocampal disinhibition. The abnormality of glutamate transmission is also related to astrocytes since they regulate the glutamate uptake and release from and to the extracellular space (Danbolt, 2001; Kondziella et al., 2007). While the glutamate hypothesis is more recent and less well studied than the dopamine hypothesis, it has the advantage of being able to account for a wider range of SCZ symptoms (Hu et al., 2015; Mei et al., 2018).

A third hypothesis is that, instead, the excessive glutamate release leads to the NMDAR hypofunction. Higher glutamate levels may result in a rise of astrocytic  $\text{Ca}^{2+}$  levels. Subsequently, astrocytes may release higher concentrations of the gliotransmitter adenosine triphosphate (ATP). Lalo et al. (2016) suggested that the activation of postsynaptic purinergic P2X receptors (P2XRs) by ATP downregulates NMDARs.

These findings indicate that different neuronal and astrocytic malfunctions could lead to the same disease, despite different underlying mechanisms. This poses a major challenge to effective treatments for psychiatric diseases (Herman et al., 2012; Stephan et al., 2016). Computational models can complement or supersede experimental studies (Manninen et al., 2018; Oschmann et al., 2018), where the latter are not feasible or too expensive. They can guide experimental researchers to the relevant pathways that are altered in disease and thus predict pharmaceutical responses (Moran et al., 2016). Siekmeier and Hoffman (2002) proposed a computational model in which they reduced the number of synapses in a neuronal network. This synaptic pruning leads to semantic priming and difficulties in accessing memories in SCZ patients. Mahdavi et al. (2014) developed a tripartite synapse model focusing on the dysregulation of D-serine released by the astrocyte. To our best knowledge, no biophysical neuron-astrocyte network models have been published that explore the role of astrocytes in SCZ.

In this study, we investigate how changes in mechanisms and topology in neuron-astrocyte networks alter the functional state, i.e., spike and burst rate of neurons as well as glutamate levels in astrocytes, in health and SCZ. For this, we use the previously published computational model called INEXA (Lenk et al., 2020) to test the following four SCZ-related hypotheses: we alter (1) the number of neurons or astrocytes in the network,



(2) the effect of astrocytic ATP on the postsynaptic activity, (3) the release of glutamate from the presynapse and the uptake of glutamate by the astrocyte, and (4) the excitatory and/or inhibitory synaptic strength.

## 2. MATERIALS AND METHODS

To study the three aspects mentioned above in SCZ, we used the published model INEXA (Lenk et al., 2020) with the main components as shown in **Figure 1**. In section 2.1, we describe the governing equations of the INEXA model. In section 2.2, we explain how the model is used to simulate neuron-astrocyte networks in healthy and SCZ states. In sections 2.3, 2.4, the statistical analysis of the resulting neuronal and astrocytic activity is described.

### 2.1. Governing Equations of the INEXA Model

The phenomenological model INEXA (Lenk et al., 2020) includes both excitatory and inhibitory neurons and was initially developed to study the astrocytes' effect on neuronal firing rates in the cortex. The governing equation for simulating neurons is the one for the firing rate  $\lambda_i$  of a postsynaptic neuron  $i$  for each time step  $t_k$  of 5 ms:

$$\lambda_i(t_k) = \max \left( 0, c_i + \sum_j y_{ij} \cdot s_j(t_{k-1}) - \sum_j y_{\text{Astro}} \cdot A_{ija}(t_{k-1}) \right), \quad (1)$$

where  $c_i$  is the stochastic noise of neuron  $i$ . The term  $y_{ij}$  denotes the synaptic weight between the presynaptic neuron  $j$  and a postsynaptic neuron  $i$ , which can vary at each time step. The

synapse can be either excitatory ( $y_{ij} \in [0, 1]$ , representing glutamatergic neurons) or inhibitory ( $y_{ij} \in [-1, 0]$ , representing GABAergic interneurons). The parameter  $s_j$  is a binary term indicating whether neuron  $j$  transmitted a spike in the previous time step  $t_{k-1}$ . The second term in the equation denotes the depressing effect caused by astrocytes. The variable  $A_{ija}$  is binary, indicating whether a synapse  $ij$  is enclosed by astrocyte  $a$  and if astrocyte  $a$  was active at the previous time step. If this is the case, the astrocyte applies a depressing effect,  $y_{\text{Astro}}$ , on the synapse. Otherwise,  $A_{ija}$  is zero, removing the astrocytic effect on neuronal activity.

Due to limited experimental data on the interaction between GABAergic neurons and astrocytes, the INEXA model currently only connects astrocytes with glutamatergic synapses. These excitatory synapses release glutamate into the synaptic cleft with rate  $\Omega_f$ . The released glutamate binds to astrocytic mGluRs with rate  $\Omega_g$  causing the inositol 1,4,5-trisphosphate ( $\text{IP}_3$ )-mediated release of  $\text{Ca}^{2+}$  from the endoplasmic reticulum (ER) into the astrocytic cytoplasm (**Figure 1**).

The governing equation for astrocyte dynamics describes the intracellular calcium dynamics  $[\text{Ca}^{2+}]_{ija}$  in an astrocyte  $a$  that encloses the synapse  $ij$ :

$$[\text{Ca}^{2+}]_{ija}(t_k) = [\text{Ca}^{2+}]_{ija}(t_{k-1}) + \Omega_{\text{acc}} \cdot ([\text{IP}_3]_{ija}(t_k) - [\text{Ca}^{2+}]_{ija}(t_{k-1})). \quad (2)$$

The calcium concentration is composed of the calcium concentration left from the last time step ( $[\text{Ca}^{2+}]_{ija}(t_{k-1})$ ), the  $\text{IP}_3$ -mediated  $\text{Ca}^{2+}$ -induced  $\text{Ca}^{2+}$ -release from the ER stores, and the  $\text{Ca}^{2+}$  uptake back to the ER by the SERCA (sarco/endoplasmic reticulum  $\text{Ca}^{2+}$ -ATPase) pumps. To reflect the slow dynamics of the calcium release (which can take up to multiple seconds), we

**TABLE 1** | Used parameters for simulating healthy and SCZ neuron-astrocyte networks.

Parameter	Value	Unit	Definition
$Y_{\max}^+$	<b>0.7</b> ;0.8;0.9	-	Upper boundary for excitatory synaptic weights
$Y_{\max}^-$	0.1;0.5;0.6; <b>0.7</b>	-	Upper boundary for inhibitory synaptic weights
$\Omega_f$	<b>0.0020</b> ;0.0010;0.0005	$s^{-1}$	Rate of synaptic facilitation
$\Omega_g$	<b>0.0770</b> ;0.0385;0.0193	$s^{-1}$	Recovery rate of gliotransmitter receptors
$Y_{\text{Astro}}$	<b>0.01</b> ;0.025;0.05;0.075;0.1	-	Downregulation of NMDARs by P2XRs
Astrocytes	81; <b>107</b>	-	Number of astrocytes in the network
Neurons	187; <b>250</b>	-	Number of neurons in the network

Bold printed numbers refer to the values used in Lenk et al. (2020).

multiplied the ER term by the time scale  $\Omega_{acc}$ . A more detailed description of the INEXA model can be found in the original article (Lenk et al., 2020).

## 2.2. Simulated Experimental Setups

The topology and connectivity of the neuron-astrocyte network models were generated as described in Lenk et al. (2020) (see parameters in **Table 1**). Hence, 107 astrocytes and 250 neurons were placed uniformly at random on a planar area of  $750 \times 750 \times 10 \mu m^3$ , resembling the electrode field of an *in vitro* multielectrode array (MEA). Neurons and astrocytes within a distance of  $30 \mu m$  were reallocated to account for the cell sizes. Astrocyte-astrocyte connections were formed whenever the distance was smaller than  $100 \mu m$ . Neuron-neuron and astrocyte-neuron connections were created according to a truncated Gaussian distribution based on their distance.

To study the effects of various spatial network topologies and network connectivities, we generated three spatially different network topologies A, B, and C. For each network A, B, C, we computed three independent connectivity configurations (CC 1, 2, 3) according to the rules described above, resulting in a total of nine different networks. We considered those networks to represent the healthy, non-pathological baseline. Different topological properties of these initial networks are described in **Table 2**. The stochastic noise  $c_i$  was set to 0.02 in all simulations.

To simulate healthy, non-pathological neuron-astrocyte network activity, we tuned the parameters of the INEXA model so that they resemble *in vitro* MEA recordings. Thereby, we used a reference spike rate of 30–200 spikes per minute as measured from mouse neurons (Gramowski et al., 2006; Jenkinson et al., 2017) and human-derived neurons (Tukker et al., 2018; Kizner et al., 2019).

Based on hypotheses and experimental evidence about SCZ described in the Introduction, we modified four different sets of INEXA parameters and examined their effect on neuronal and astrocytic activity. More specifically, we simulated the following four pathological changes in the neuron-astrocyte interaction:

1. We stochastically removed 25% of astrocytes or 25% of neurons from premade network configurations to account for the reduced astrocytic and neuronal synaptic density in SCZ patients.
2. We amplified the depressing signal  $y_{\text{Astro}}$  of astrocytes to study the effect of astrocytic ATP on the postsynaptic activity.
3. We scaled the two parameters  $\Omega_f$  and  $\Omega_g$  by the factors 0.5 and 0.25, which control glutamate release from presynapses and glutamate uptake by astrocytes, respectively (**Figure 1**). Simulations were performed for each combination of the distorted and unmodified parameter values  $\Omega_f$  and  $\Omega_g$ .
4. We increased the maximal synaptic weight  $Y_{\max}^+$  and  $Y_{\max}^-$  for excitatory and inhibitory neurons, which both result in a higher excitability of the cells.

The latter two manipulations allowed us to simulate the excessive release of glutamate in excitatory neurons and astrocytes as well as the dysfunctional interneurons assumed in the *glutamate hypothesis* of SCZ. A summary of the modified parameters can be found in **Table 1**. All other model parameters not listed in this table were used as described in the original paper by Lenk et al. (2020). Each simulation consisted of  $T = 5 \text{ min}$  simulated time and was repeated 10 times to account for the statistical variability of our results.

## 2.3. Quantifying Neuronal and Astrocytic Activity Features

To analyze the neuronal activity, we calculated spike and burst describing features. Bursts are cascades of spikes (i.e., action potentials). The features were determined using a modified version of the cumulative moving average (CMA) algorithm (Kapucu et al., 2012; Välikki et al., 2017). Therewith, we calculated the *mean spike rate* in spikes per minute and the *mean burst rate* in bursts per minute across all neurons, respectively. Additionally, we quantified the astrocytic activity by calculating how often an astrocyte changes its state to 'active' during the simulated time  $T$  and denoted the count as *mean number of activations per astrocyte*. We will refer to these three features as response variables below. The results were depicted as box plots.

## 2.4. Testing the Effects of Different Neuronal and Astrocytic Dysfunctions

The objective of this section is twofold: we quantify the effects of the four simulated pathological changes in SCZ (see section 2.2) on the neuronal and astrocytic response variables and estimate how much the effects vary for different network configurations. In the previously described simulated experimental setups, there were two sources of stochasticity. One came from the stochastic nature of the INEXA model, e.g., when creating the excitatory and inhibitory synaptic weights and in the update equations. The other was due to the fact that neuron-neuron and astrocyte-neuron connections were formed stochastically in our setup. To estimate the average random effect from both sources of stochasticity, we performed all simulations on the nine initial networks, as described in section 2.2. We analysed the data with linear mixed-effects (LME) models using the lme4-package (Bates et al., 2015) in R, version 3.6.3 (2020-02-29). In order to



**TABLE 2 |** Different connectivity properties of the nine initial networks used in this paper.

Network & CC	Network connectivity [%]	Average number of gap junctions	Excitatory synapses w.o. astrocyte [%]
A 1	27.32	4.88	8.75
A 2	27.42	4.88	8.72
A 3	27.43	4.88	8.55
B 1	27.53	4.50	1.75
B 2	27.57	4.50	1.77
B 3	27.59	4.50	1.90
C 1	28.93	4.79	5.65
C 2	29.16	4.79	5.46
C 3	28.95	4.79	3.36

In the first column, A, B, C refer to three networks with the same topology features. The numbers indicate the varying neuron-neuron and astrocyte-neuron network connectivity configurations (CC 1, 2, 3). The network connectivity (second column) denotes the percentage of neuronal connections formed. The average number of gap junctions (third column) describes how many connections each astrocyte forms with other astrocytes on average. Since the astrocyte-astrocyte network connectivity is not probabilistic, this value is constant for each network with the same underlying spatial topology. Excitatory synapses without astrocyte (fourth column) expresses the percentage of excitatory neuronal synapses left without an astrocyte.

satisfy the LME model requirements, it was sometimes necessary to transform the response variable  $Z$  by some function  $\varphi: \mathbb{R} \rightarrow \mathbb{R}$ . In the following subsections, we decomposed the variance of  $\varphi(Z)$  into intra-network terms  $\Sigma$ , which capture the stochasticity from different network connectivity configurations, and the residual error variance  $\sigma^2$ . We note that these are the variance terms for the transformed response  $\varphi(Z)$ . If one is interested in prediction intervals for  $Z$ , these must first be computed for  $\varphi(Z)$  and then back-transformed.

#### 2.4.1. Hypothesis 1: Astrocyte or Neuron Removal

In the first set of simulated experiments, we quantified the average effect of stochastically removing 25% of the astrocytes or neurons, respectively. In order to estimate the random effect of different network configurations, we made three identical copies of each of the nine networks described in section 2.2 and **Table 2**. Then, we either randomly removed 25% of astrocytes or 25% of neurons including their connections to other cells, which resulted in 27 cell-reduced networks per cell type.

For all of these networks, we ran 10 simulations and fit the resulting data using an LME model with a fixed effect for cell removal and a random effect for different network configurations. Using contrasts to distinguish the full network from reduced networks (Oehlert, 2010) (see **Supplementary Material**), we then determined the average reduction  $\delta_{\text{rem}}$  of the response variables resulting from cell removal in percent. Moreover, we decomposed the variance of the transformed response  $\varphi(Z)$  into an inter-network term  $\sigma_{\text{rem}}^2$  and the residual error variance  $\sigma^2$ . For each response variable, we report the restricted maximum likelihood (REML) estimates, 95% confidence intervals (CIs) of  $\delta_{\text{rem}}$  as well as the  $p$ -value for the null-hypothesis that the mean response of reduced and default networks A, B and C coincides. We also

present the REML estimates and the 95% CIs for the standard deviations  $\sigma_{\text{rem}}/\hat{\mu}$  and  $\sigma/\hat{\mu}$ , which have been normalised by the mean  $\hat{\mu}$  of the transformed response  $\varphi(Z)$ , when no cells were removed. A more detailed description of the reported quantities mentioned in this section and the LME model can be found in the **Supplementary Material**.

#### 2.4.2. Hypothesis 2: Effect of Astrocytic ATP

In this part, we altered the impact of astrocytic ATP on the postsynaptic P2XR and NMDAR activity by modifying the parameter  $y_{\text{Astro}}$ . Therefore, we first performed 10 simulations with  $y_{\text{Astro}} \in \{0.01, 0.025, 0.05, 0.075, 0.1\}$  for each of the nine networks described in section 2.2. To analyze our simulated data, we used the LME model

$$\log(Z_{ij}) = (\mu + u_{i,\mu}) + (\beta_a + u_{i,a}) \cdot y_{\text{Astro}} + \beta_{a^2} \cdot y_{\text{Astro}}^2 + \varepsilon_{ij}, \quad (3)$$

where the index  $i$  enumerates the nine network configurations and  $j \in \{1, \dots, 10\}$  indices the 10 independent repetitions. The variable  $\mu$  is the average value of  $\log(Z)$  if  $y_{\text{Astro}}$  was equal to zero. The coefficients  $\beta_a, \beta_{a^2}$  correspond to the average increase of  $\log(Z)$  in dependence of  $y_{\text{Astro}}$  and  $y_{\text{Astro}}^2$ , respectively. Random effects are captured in the vectors  $u_i: = (u_{i,\mu}, u_{i,a})$  for each  $i$ , which are independent with multivariate Gaussian distribution  $u_i \sim \mathcal{N}(\mathbf{0}, \Sigma)$  with mean  $\mathbf{0}$  and diagonal covariance matrix  $\Sigma = \text{diag}(\sigma_{\mu}^2, \sigma_a^2) \in \mathbb{R}^{2 \times 2}$ . This means that we assumed the individual components to be independent. The stochasticity of the INEXA model and the residual error is captured in  $\varepsilon_{ij}$ , which we assumed to be normally distributed with mean 0, equal variance  $\sigma^2$  and independent of  $u_i$  for all indices  $i$ . We reported REML estimates and CIs for  $\mu, \beta_a, \beta_{a^2}, \Sigma$  and  $\sigma^2$ .

#### 2.4.3. Hypothesis 3: Glutamate Dynamics Parameters

Following the *glutamate hypothesis* of SCZ, we tested the effect of changing the parameters regulating the glutamate dynamics in neurons and astrocytes. The parameters  $w_f$  and  $w_g$  for the glutamate dynamics are defined as follows: running the LME model with parameter values  $w_f$  and  $w_g$  corresponds to the scaling of the presynaptic glutamate release rate by a factor  $w_f$  (equivalent to a multiplication of  $\Omega_f$  by  $w_f$ ) and scaling the astrocyte glutamate uptake rate by a factor  $w_g$  (equivalent to multiplying  $\Omega_g$  by  $w_g$ ) compared to the default rates of the INEXA model. For every response variable  $Z = Z(w_f, w_g)$ , we used the LME model

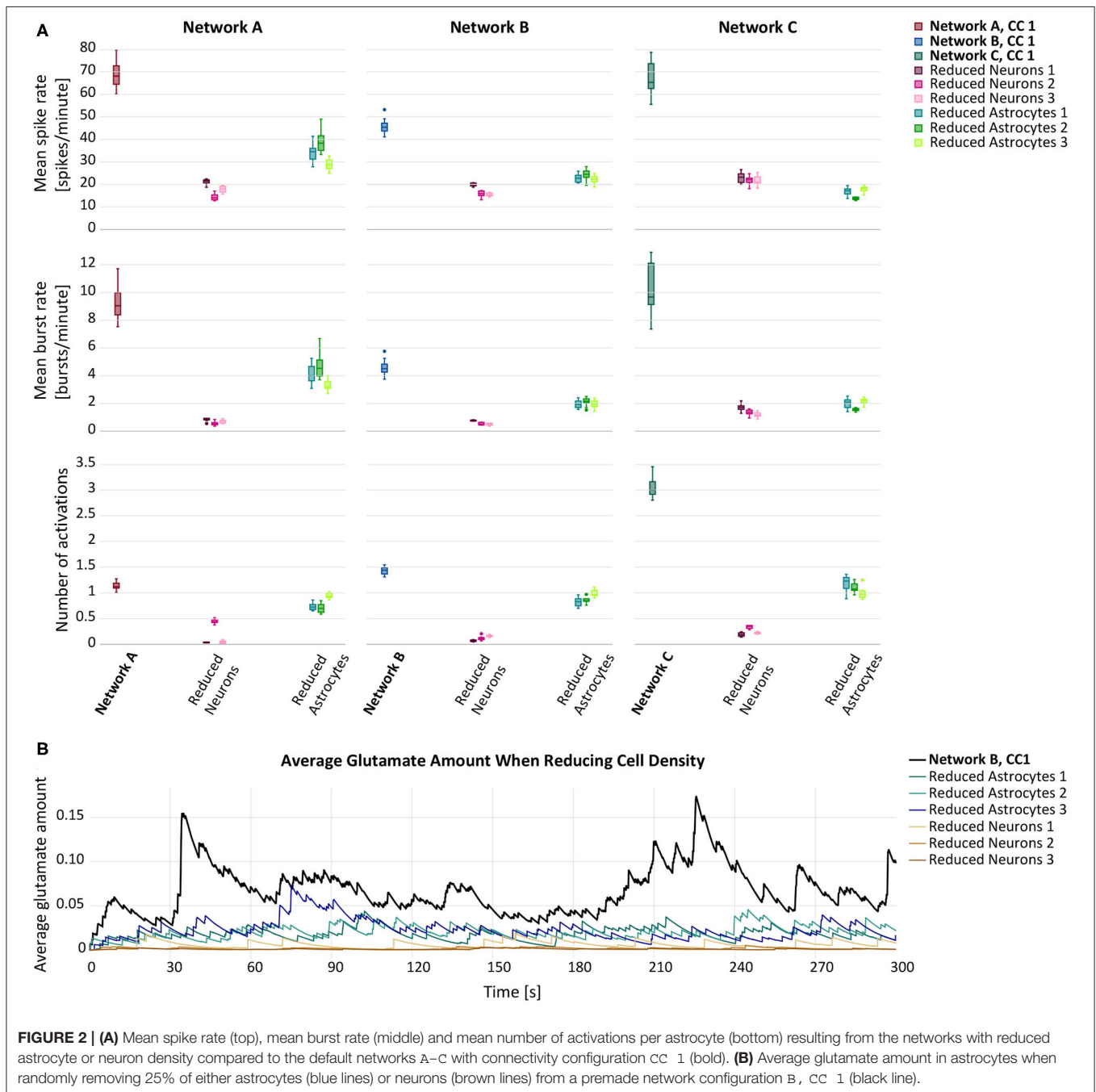
$$Z_{ij} = (\mu + u_{i,\mu}) + (\beta_f + u_{i,f})w_f + (\beta_g + u_{i,g})w_g + \beta_{f^2}w_f^2 + \beta_{g^2}w_g^2 + (\beta_{fg} + u_{i,fg})w_fw_g + \varepsilon_{ij}, \quad (4)$$

where the index  $i$  enumerates the nine network configurations described in section 2.2 and  $j \in \{1, \dots, 10\}$  denotes 10 independent repetitions. The variable  $\mu$  stands for the average value of the response  $Z$  if  $w_f$  and  $w_g$  were equal to zero. The coefficients  $\beta_f, \beta_g, \beta_{f^2}, \beta_{g^2}, \beta_{fg} \in \mathbb{R}$  correspond to the average increase of  $Z$  in dependence of the parameters they are multiplied by. Random effects were captured in vectors  $u_i: = (u_{i,\mu}, u_{i,f}, u_{i,g}, u_{i,fg})$ , which are independent with multivariate

Gaussian distribution  $u_i \sim \mathcal{N}(\mathbf{0}, \Sigma)$  with mean  $\mathbf{0}$  and covariance matrix  $\Sigma$ . We assumed  $\Sigma = \text{diag}(\sigma_\mu^2, \sigma_f^2, \sigma_g^2, \sigma_{fg}^2) \in \mathbb{R}^{4 \times 4}$  was a diagonal matrix with positive entries, which means that the individual components were assumed to be independent. The random effects  $u_i$  are specific to each network configuration  $i$ , however we assumed them to be identically distributed. The estimates for  $\sigma_\mu^2, \sigma_f^2, \sigma_g^2, \sigma_{fg}^2$  quantify the variance of  $Z$  as a stochastic function of parameter values  $w_f$  and  $w_g$ , considering the stochasticity from random network connectivities. The stochasticity of the INEXA model as well as the residual error was

captured in  $\varepsilon_{ij} \sim \mathcal{N}(0, \sigma^2)$ , which we assumed to be normally distributed with mean 0, equal variance  $\sigma^2$  and independent of  $u_i$  for all indices  $i$ .

We performed 10 simulations with the INEXA model for each of the nine networks described in section 2.2 and every combination of the parameter values  $w_f, w_g \in \{1, 1/2, 1/4\}$ . The corresponding values for  $\Omega_f, \Omega_g$  are listed in **Table 1**. Fitting this data in  $R$ , we reported the REML estimates and CIs for  $\mu, \beta_f, \beta_g, \beta_{f^2}, \beta_{g^2}, \beta_{fg}, \Sigma$ , and  $\sigma^2$ . We created contour plots for the response  $Z(w_f, w_g)$  as a function of  $w_f$  and  $w_g$  using the



estimates provided by the LME model fit and setting all stochastic terms equal to 0.

#### 2.4.4. Hypothesis 4: Changes in the Excitatory and Inhibitory Synaptic Weights

In this set of simulated experiments, we tested the dependency of neuronal and astrocytic activity on the inhibitory and excitatory synaptic weight boundaries  $Y_{\max}^-$  and  $Y_{\max}^+$  (see section 2.1). In our statistical LME model, we considered first and second order fixed effects of synaptic weight boundaries on the response variables as well as a random effect term to account for the variation caused by different network configurations. For ease of notation, let  $y_{\text{in}}$  and  $y_{\text{ex}}$  denote the parameter values for  $Y_{\max}^-$  and  $Y_{\max}^+$ , respectively. For every response variable  $Z = Z(y_{\text{in}}, y_{\text{ex}})$ , we assumed the statistical model

$$Z_{ij} = \mu + \beta_{\text{in}} y_{\text{in}} + \beta_{\text{ex}} y_{\text{ex}} + \beta_{\text{in}^2} y_{\text{in}}^2 + \beta_{\text{ex}^2} y_{\text{ex}}^2 + \beta_{\text{in,ex}} y_{\text{in}} y_{\text{ex}} + \gamma_i + \varepsilon_{ij}, \quad (5)$$

where the index  $i$  enumerates the nine network configurations described in section 2.2 and  $j \in \{1, \dots, 10\}$  denotes 10 independent repetitions. The variable  $\mu$  refers to the estimated mean of  $Z$  if  $y_{\text{in}}$  and  $y_{\text{ex}}$  were equal to zero. The coefficients  $\beta_{\text{in}}, \beta_{\text{ex}}, \beta_{\text{in}^2}, \beta_{\text{ex}^2}, \beta_{\text{in,ex}} \in \mathbb{R}$  correspond to the average increase of  $Z$  in dependence of the parameters they are multiplied by. Random effects were captured in the random variables  $\gamma_i$ , which we assumed to be independent with zero-mean Gaussian distribution and equal variance  $\sigma_{\text{net}}^2$ . The variance term  $\sigma_{\text{net}}^2$  quantifies how much the response varies between different stochastically chosen network connectivities if all other parameters are held constant. The residual error was captured in  $\varepsilon_{ij}$ , which we assumed to be normally distributed with mean 0, equal variance  $\sigma^2$  and independent of  $\gamma_i$  for all indices  $i$ .

We performed 10 simulations with the INEXA model for each of the nine networks described in section 2.2 and every combination of the parameter values for  $Y_{\max}^-, Y_{\max}^+$  listed in Table 1. Fitting this data in  $R$ , we reported the REML estimates and 95% CIs for  $\mu, \beta_{\text{in}}, \beta_{\text{ex}}, \beta_{\text{in}^2}, \beta_{\text{ex}^2}, \beta_{\text{in,ex}}, \sigma_{\text{net}}$  and  $\sigma$ . Moreover, we created contour plots for the response  $Z(y_{\text{in}}, y_{\text{ex}})$  as

a function of  $y_{\text{in}}$  and  $y_{\text{ex}}$  using the estimates provided by the LME model fit while setting all stochastic terms equal to 0.

### 3. RESULTS

#### 3.1. Hypothesis 1: Astrocyte or Neuron Removal Leads to Reduction of the Network Activity

In our first set of simulations, we reduced the cell density of either astrocytes or neurons by 25%. The cell removal resulted in a general decrease of mean spike rate, mean burst rate and mean number of astrocyte activations (Figure 2A). Overall, the decline of the response variables was larger when the neurons were removed from the network. In Figure 2B, the average amount of glutamate prevalent in astrocytes is shown at each time step. While both forms of reduction caused a decrease in astrocytic glutamate, the effect was more pronounced in the case of neuron removal. The  $p$ -values for the null-hypothesis that the mean response of reduced and default networks coincide were smaller than  $10^{-10}$  for all response variables and both simulated experiments.

The results of the LME model fit are listed in Table 3 for the astrocyte removal and in Table 3 for the neuron removal. They show that cell removal leads to statistically significant activity reduction. The 95% CIs of  $\delta_{\text{rem}}$  are tighter for the neuron removal than for astrocyte removal, indicating that the neuron removal data was fit more accurately by the LME model. The results highlight stark differences between the inter-network standard deviations  $\sigma_{\text{rem}}/\hat{\mu}$  of the transformed responses  $\varphi(Z)$ . While in the astrocyte removal experiments, the inter-network variance of the logarithm of the mean spike rate is relatively low, the standard deviation term for the logarithm of the mean number of astrocyte activations is estimated to be at around 50%. This shows that the robustness to changing network configurations varies significantly for the different response variables considered. Similarly, the standard deviation  $\sigma/\hat{\mu}$  of the residual error varies considerably between different response variables, but is consistently smaller than the inter-network standard deviation  $\sigma_{\text{rem}}/\hat{\mu}$ .

**TABLE 3 |** Estimates and 95% confidence intervals for the quantities estimated in the astrocyte (upper part) and neuron (lower) removal experiments in percent.

Transformation	Mean spike rate			Mean burst rate			Mean # astrocyte activations		
	$\varphi(\cdot) = \log(\cdot)$			$\varphi(\cdot) = \log(\cdot)$			$\varphi(\cdot) = \log(\cdot)$		
	Est	CI <sub>2.5</sub>	CI <sub>97.5</sub>	Est	CI <sub>2.5</sub>	CI <sub>97.5</sub>	Est	CI <sub>2.5</sub>	CI <sub>97.5</sub>
<b>ASTROCYTE REMOVAL</b>									
$\hat{\delta}_{\text{rem}} \cdot 100\%$	65.90	56.50	73.27	72.45	59.94	81.05	53.96	41.33	63.87
$\hat{\sigma}_{\text{rem}}/\hat{\mu} \cdot 100\%$	7.66	5.80	9.29	22.73	17.23	27.57	46.80	35.51	56.74
$\hat{\sigma}/\hat{\mu} \cdot 100\%$	2.42	2.25	2.62	7.29	6.77	7.89	13.02	12.08	14.09
<b>NEURON REMOVAL</b>									
$\hat{\delta}_{\text{rem}} \cdot 100\%$	72.07	65.88	77.14	91.04	86.91	93.87	93.27	86.63	97.60
$\hat{\sigma}_{\text{rem}}/\hat{\mu} \cdot 100\%$	6.30	4.77	7.64	23.03	17.46	27.92	28.73	21.82	34.81
$\hat{\sigma}/\hat{\mu} \cdot 100\%$	1.94	1.80	2.10	7.11	6.60	7.70	6.00	5.57	6.49

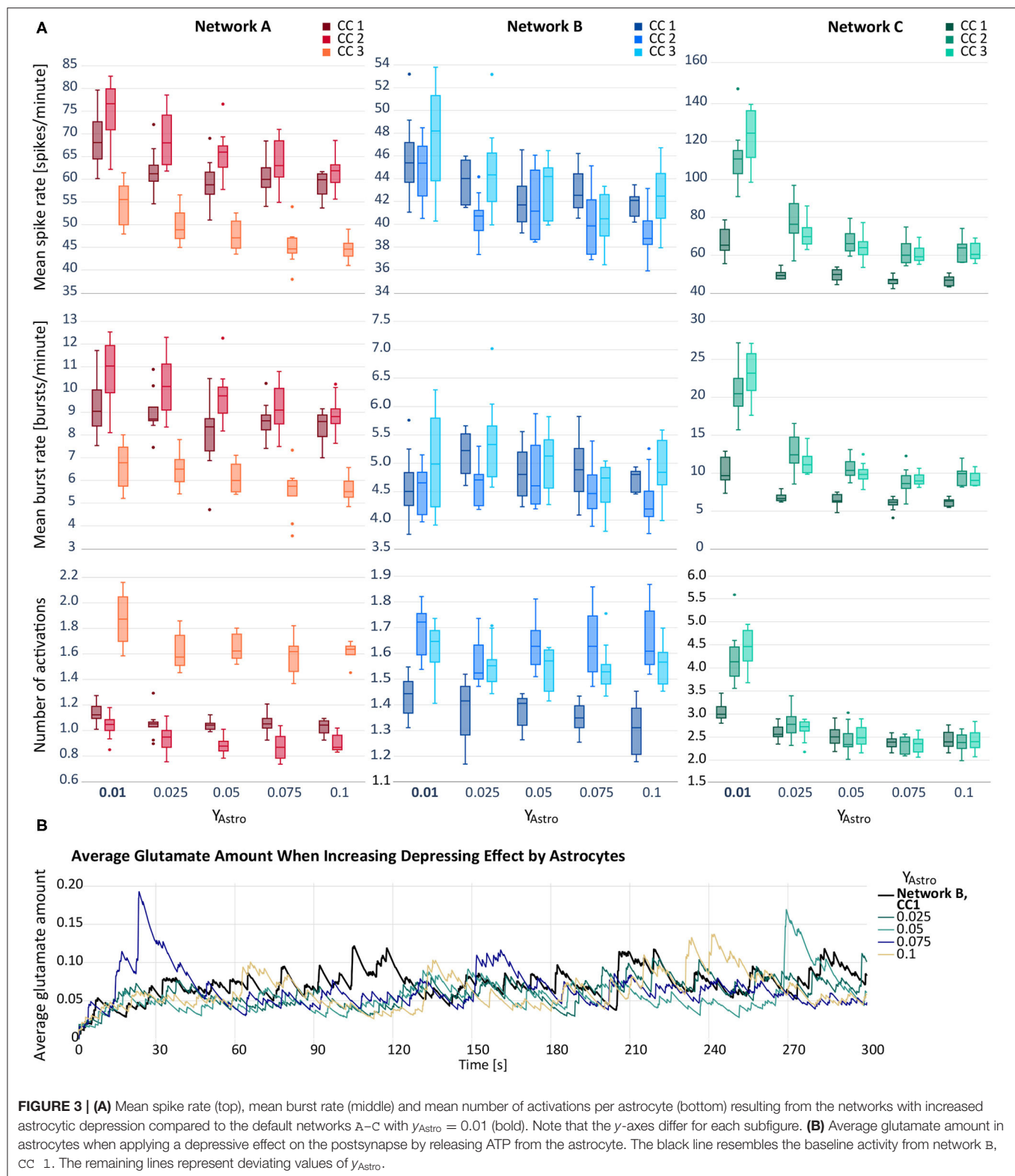


**FIGURE 3 | (A)** Mean spike rate (top), mean burst rate (middle) and mean number of activations per astrocyte (bottom) resulting from the networks with increased astrocytic depression compared to the default networks A–C with  $y_{Astro} = 0.01$  (bold). Note that the y-axes differ for each subfigure. **(B)** Average glutamate amount in astrocytes when applying a depressive effect on the postsynapse by releasing ATP from the astrocyte. The black line resembles the baseline activity from network B, CC 1. The remaining lines represent deviating values of  $y_{Astro}$ .

### 3.2. Hypothesis 2: Effect of Astrocytic ATP

For our second hypothesis, we increased the depressing effect of the astrocytic gliotransmitter ATP on excitatory postsynapses.

As can be seen in **Figure 3A**, the depressing effect results in a decreased mean spike rate. In networks A and C, the activity reduction can also be observed for the other two response



**TABLE 4** | Restricted maximum likelihood estimates, lower and upper ends of 95% confidence intervals for the astrocyte depressing effects experiment.

Transformation	Mean spike rate			Mean burst rate			Mean # astrocyte activations		
	log(-)			log(-)			log(-)		
	Est	CI <sub>2.5</sub>	CI <sub>97.5</sub>	Est	CI <sub>2.5</sub>	CI <sub>97.5</sub>	Est	CI <sub>2.5</sub>	CI <sub>97.5</sub>
$\hat{\sigma}_\mu$	0.31	0.20	0.51	0.51	0.32	0.82	0.48	0.30	0.78
$\hat{\sigma}_a$	1.90	1.15	3.13	2.98	1.81	4.92	1.96	1.19	3.23
$\hat{\sigma}$	0.10	0.09	0.11	0.15	0.14	0.16	0.10	0.09	0.11
$\hat{\mu}$	4.25	4.03	4.46	2.24	1.89	2.59	0.72	0.39	1.05
$\hat{\beta}_a$	-8.92	-10.67	-7.16	-9.39	-12.13	-6.64	-7.67	-9.47	-5.88
$\hat{\beta}_{a^2}$	57.12	46.01	68.23	57.93	40.66	75.20	52.53	41.34	63.73

variables, mean burst rate and astrocyte activity. The increase of the depression,  $\gamma_{\text{Astro}}$ , from 0.01 to 0.025 has the proportionally largest effect. In network B, the behaviour of the mean burst rate and the astrocyte activity follows no clear tendency. **Figure 3B** depicts the average amount of astrocytic glutamate ready for release in presence with an ATP release from the astrocyte. Compared to the baseline level, we observed temporary higher levels of glutamate when amplifying the depressing effect.

In **Table 4**, we listed the REML estimates and confidence intervals of the parameters of the LME model described in section 2.4.2. We observed a positive second order fixed effect ( $\hat{\beta}_{a^2}$ ) and a negative first-order one ( $\hat{\beta}_a$ ) for all logarithmically transformed responses  $\log(Z_{ij})$ . While we obtain tight confidence intervals for the baseline activity  $\hat{\mu}$ , the first and second order coefficients  $\hat{\beta}_a, \hat{\beta}_{a^2}$  have comparatively wider confidence intervals. The standard deviation term  $\hat{\sigma}_\mu$  of  $\log(Z_{ij})$  associated with  $\mu$  is considerably lower than the standard deviation term  $\hat{\sigma}_a$  associated with  $\hat{\beta}_a$ , moreover the confidence intervals of  $\hat{\sigma}_\mu$  are narrower than those of  $\hat{\sigma}_a$ , indicating that the first order term is difficult to fit by our model. The error standard deviation  $\hat{\sigma}$  is comparatively low and has tight confidence intervals for all responses.

### 3.3. Hypothesis 3: Reducing the Glutamate Release and Uptake Rate Results in Higher Network Activity

**Figure 4A** depicts the behaviour of the response variables with respect to varying rates of synaptic facilitation,  $\Omega_f$ , and varying recovery rates of the gliotransmitter receptors,  $\Omega_g$ . In general, a reduction in both,  $\Omega_g$  and  $\Omega_f$ , resulted in an elevation of the response variables. However, the increase between two consecutive values for  $\Omega_f$  was larger than between two values of  $\Omega_g$ . An exception was observed for network B, for which the modification of  $\Omega_g$  did not result in any considerable changes of the response variables.

We observed a similar behaviour for the average glutamate level when varying  $\Omega_f$  and  $\Omega_g$ . **Figure 4B** shows a larger effect of  $\Omega_g$  compared to the effect of  $\Omega_f$ . Decreasing either parameter resulted in elevated response variables compared to the default network. Also in this case, the effect of  $\Omega_f$  was larger compared to the effect of  $\Omega_g$ .

The results of the LME model fit are reported in **Table 5**. We observed that the average response  $\mu$  fitted for values  $w_f = w_g = 0$  (baseline activity) was difficult to estimate, indicated by the wide confidence intervals. Also the estimated standard deviation  $\hat{\sigma}_\mu$  of the baseline activity due to different network configurations was large relative to  $\mu$  for all response variables, particularly for the mean number of astrocyte activations. For most response variables, the estimated standard deviation  $\hat{\sigma}$  of the residual error was at around 10% of the baseline activity, significantly smaller than  $\hat{\sigma}_\mu$ .

The parameters  $\beta_f, \beta_{f^2}$  had tight confidence intervals, indicating that the estimates were reliable. We saw a strong negative first order effect of the rate of presynaptic glutamate uptake  $w_f$  on all responses and a positive second-order effect. For all responses, the standard deviation estimate  $\sigma_f$  of the first order effect was small relative to  $\hat{\beta}_f$ . Similarly, we found a negative first order and a positive second-order effect of the astrocyte glutamate uptake on all variables with small estimated standard deviation  $\hat{\sigma}_g$ . The corresponding 95% CIs for the parameters  $\beta_g, \beta_{g^2}$  were slightly wider than those of  $\beta_f$  and  $\beta_{f^2}$ . The first-order interaction coefficient  $\beta_{fg}$  of the parameters  $w_f$  and  $w_g$  was significant, but with a small effect for all responses. The fact that  $\hat{\sigma}_{fg}$  and  $\beta_{fg}$  lay in a similar range indicates that the interaction terms might vary considerably for different network configurations. However, these effects were all small compared to  $\beta_f$  or  $\beta_g$ . Contour plots of the response variables derived from the LME model fit are shown in **Figure 5**.

### 3.4. Hypothesis 4: Higher Network Activity When Increasing Synaptic Weight Parameters

In this section, we computationally investigated the neuronal and astrocytic response to synaptic perturbations caused by SCZ. **Figure 6A** depicts the behaviour of the three response variables while changing either the maximum inhibitory synaptic weight  $Y_{\text{max}}^-$  or in the maximum excitatory synaptic weight  $Y_{\text{max}}^+$ . Increases in  $Y_{\text{max}}^-$  and  $Y_{\text{max}}^+$  yielded in elevated response variables. The relationship between the parameter distortion and the effect on the observation variables were consistent among the three networks (A, B, C) and their corresponding connectivities (1, 2, 3). However, network B showed a comparatively reduced response to deviations in  $Y_{\text{max}}^-$ . The variance induced by

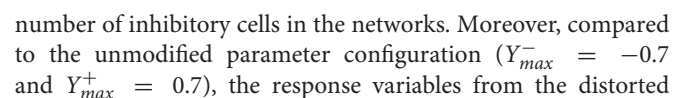


**TABLE 5 |** Restricted maximum likelihood estimates, lower and upper ends of 95% confidence intervals for the glutamate dynamics experiment.

Parameter	Mean spike rate			Mean burst rate			Mean # astrocyte activations		
	Est	CI <sub>2.5</sub>	CI <sub>97.5</sub>	Est	CI <sub>2.5</sub>	CI <sub>97.5</sub>	Est	CI <sub>2.5</sub>	CI <sub>97.5</sub>
$\hat{\sigma}_\mu$	24.97	15.31	41.57	7.57	4.70	12.57	1.14	0.69	1.90
$\hat{\sigma}_f$	45.08	27.13	73.45	9.84	5.80	16.07	2.61	1.60	4.25
$\hat{\sigma}_g$	23.38	12.57	39.18	5.61	2.89	9.44	1.39	0.80	2.31
$\hat{\sigma}_{fg}$	50.91	29.52	83.58	12.59	7.19	20.68	2.55	1.50	4.19
$\hat{\sigma}$	12.50	11.88	13.14	3.23	3.07	3.40	0.62	0.59	0.65
$\hat{\mu}$	281.19	262.43	299.95	68.72	63.14	74.30	15.26	14.39	16.12
$\hat{\beta}_f$	-151.58	-187.47	-115.69	-53.21	-61.46	-44.96	-16.12	-18.13	-14.12
$\hat{\beta}_g$	-41.36	-66.23	-16.49	-13.86	-20.11	-7.61	-2.82	-4.15	-1.48
$\hat{\beta}_{f2}$	3.64	-11.23	18.52	10.72	6.87	14.57	5.45	4.71	6.18
$\hat{\beta}_{g2}$	18.60	3.73	33.48	6.05	2.20	9.90	0.59	-0.15	1.32
$\hat{\beta}_{fg}$	-43.82	-79.56	-8.07	-8.97	-17.82	-0.12	-0.29	-2.08	1.51

parameter configurations showed higher variances in most of the cases.

In **Figure 6B**, the average glutamate amount in all astrocytes is plotted against time for varying  $Y_{max}^-$  and  $Y_{max}^+$ . We noted that a change in the glutamate behaviour was achieved by all deviation levels of  $Y_{max}^+$ . For  $Y_{max}^-$ , a large deviation from the default values was required to see a change in the average glutamate levels. The smaller deviations of  $Y_{max}^-$  did not yield a notable elevation of neither the response variables (**Figure 6A**) nor the time course of the average glutamate level (**Figure 6B**).

The parameter estimates of the corresponding statistical LME analysis are listed in **Table 6**. We refer to the average  $\mu$  of the response variable when setting parameter values  $y_{in}, y_{ex}$  to zero as the baseline activity. Comparing the parameter estimates in **Table 6** to the data in **Figure 6A**, we observe that the estimated baseline activity  $\hat{\mu}$  is significantly larger than the average response. This effect is compensated by large values of parameters  $\hat{\beta}_{in}, \hat{\beta}_{ex}, \hat{\beta}_{in^2}, \hat{\beta}_{ex^2}$  and  $\hat{\beta}_{in,ex}$ . Thus, to analyse the magnitude of the standard deviation terms, we refer to **Figure 6A**. We observed that the estimated residual standard deviation  $\hat{\sigma}$  was at around 1/10 to 1/2 of the average response value. The confidence intervals for  $\sigma_{net}$  were wide, so the random effect due to different network connectivities was not clear. However, across all experiments,  $\hat{\sigma}_{net}$  was estimated to be smaller than  $\hat{\sigma}$ . Thus, it is likely that on average, responses vary more significantly for different repetitions than between networks with different connectivities. Further, we observed relatively wide confidence intervals for all fitted coefficients, indicating that the model fit and the provided estimates have limited expressiveness. Contour plots of the response variables derived from the LME model fit are shown in **Figure 5**.

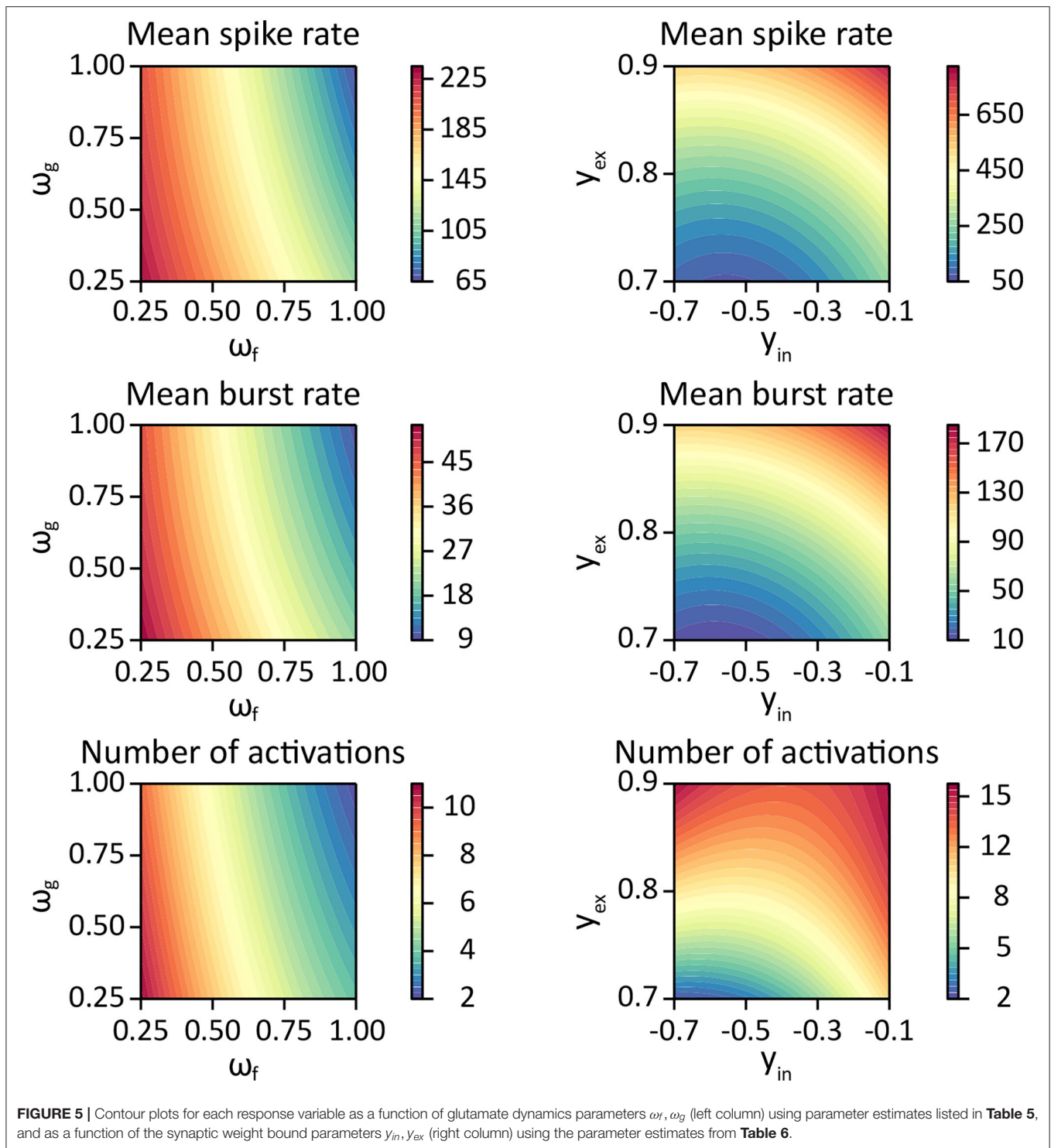
## 4. DISCUSSION

Schizophrenia is characterised by diverse dysregulations and malfunctions in neurons and astrocytes (Takahashi and Sakurai, 2013; Moraga-Amaro et al., 2014; Mei et al., 2018). In astrocytes, the pathology is among others indicated by a higher GFAP

expression, an altered morphology, loss of gap junctions between cells, and an elevated glutamate release (Mitterauer, 2009; Catts et al., 2014; Mei et al., 2018). In neurons, SCZ is indicated by morphological alterations, reductions in cell density, and excessive glutamate release, which is due to the hypofunction of NMDA receptors (Cotter et al., 2001; Mei et al., 2018). Spontaneous neuronal activity is a fine balance between excitation and inhibition (Lisman, 2012; Sohal and Rubenstein, 2019), which is between 30 and 200 spikes per minute in healthy human stem cell-derived neurons (Tukker et al., 2018; Kizner et al., 2019). However, it is disputed whether SCZ causes an increase or a decrease in neuronal and astrocytic activity (Mei et al., 2018; Naujock et al., 2020).

Computational models can support the understanding of biophysical pathways when experiments are not realisable or too expensive. So far, a multitude of biophysical (bottom-up) and symptom focused (top-down) models have been developed. According to the reviews by Rolls et al. (2008) and Valton et al. (2017), top-down models mostly support the *dopamine hypothesis*. For example, Hoffman and McGlashan (2006) explored the effects of neuronal pruning and excessive dopamine. Using a recurrent backpropagation model of working memory, they showed how neuron reduction or hyperdopaminergic systems can produce spontaneous percepts simulating hallucinated speech. Furthermore, they were able to provide an explanation for the onset of SCZ in late adolescence. For the *glutamate hypothesis*, only a few computational models are available (Valton et al., 2017). The models mostly focused on excitatory and inhibitory neurons, showing that deficits in glutamatergic or GABAergic activity lead to impairments in working-memory and other cognitive processing (Valton et al., 2017).

In the last few years, attempts were made to simulate SCZ using the Bayesian inference hypothesis. This hypothesis assumes that the brain combines sensory evidence together with prior knowledge and expectation to interpret a stimulus.

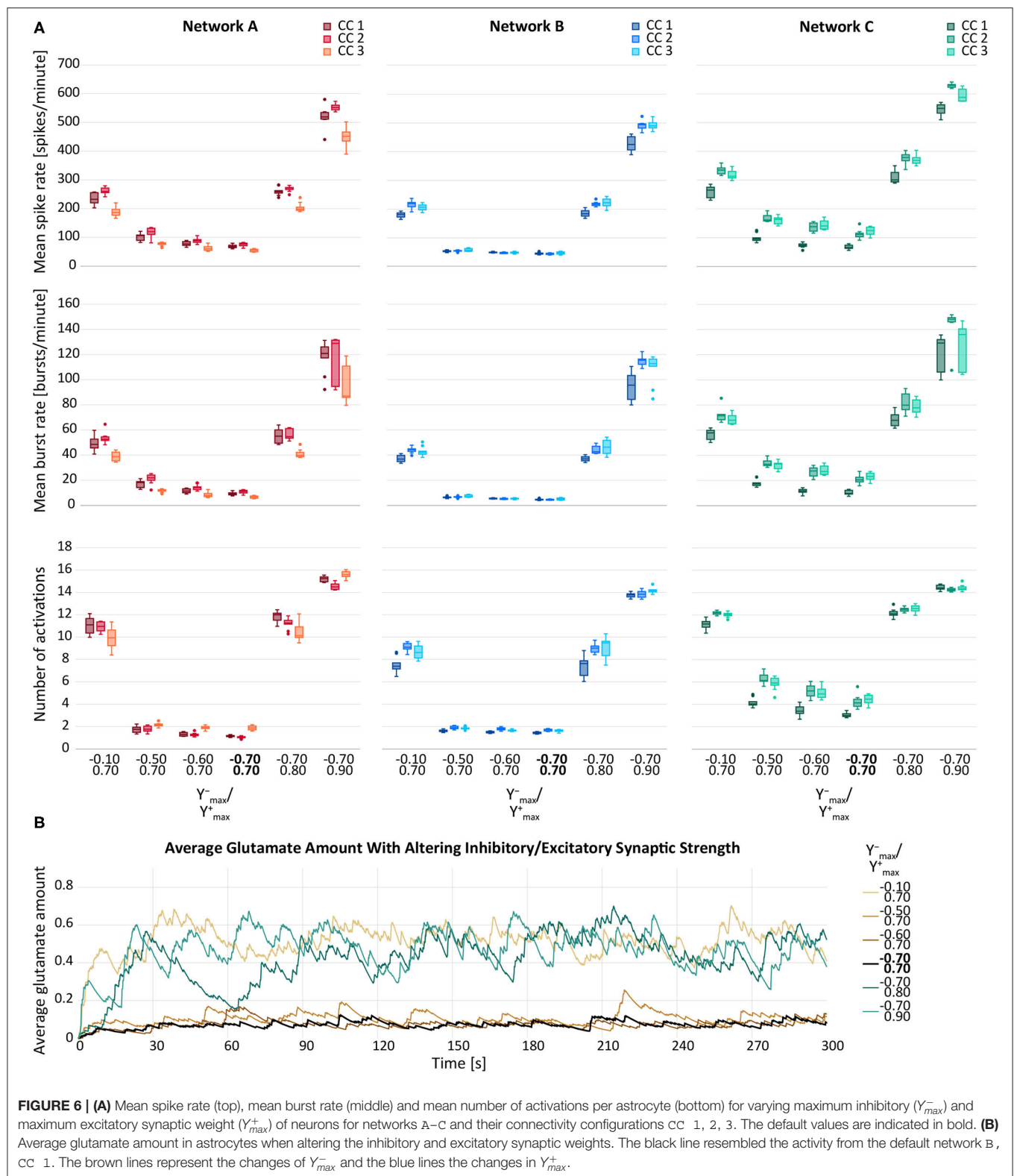


In SCZ, different delusions bias the expected value, leading to stronger perceptual biases in the future. So far, the hypothesis has mostly been tested for illusions (Valton et al., 2017). One of the first computational models in that area was made by Adams et al. (2013). Using a biological predictive coding scheme, they showed that psychosis in SCZ can be

accounted by an increased prior precision and trait abnormalities (e.g., abnormalities of smooth pursuit eye movements, event-related brain potentials or anhedonia) by a decrease in prior precision.

The loss of gap junctions in astrocytes can be a hallmark in SCZ (Mitterauer, 2009). Using the INEXA model, Genocchi





et al. (2020) studied the effect of gap junction uncoupling on the neuronal activity. Additionally, Lenk et al. (2021) showed that larger distances between astrocytes, and thus, less gap junctions,

seem to centralise the information transmission in astrocytes. The spike rate and burst rate increased until a cell-cell distance of 100  $\mu\text{m}$  and then decreased again.

**TABLE 6 |** Restricted maximum likelihood estimates, lower and upper ends of 95% confidence intervals for the synaptic weight parameter experiments.

Par	Mean spike rate			Mean burst rate			Mean # astrocyte activations.		
	Est	CI <sub>2.5</sub>	CI <sub>97.5</sub>	Est	CI <sub>2.5</sub>	CI <sub>97.5</sub>	Est	CI <sub>2.5</sub>	CI <sub>97.5</sub>
$\hat{\sigma}_{net}$	38.49	23.96	63.00	7.92	4.87	13.02	0.62	0.36	1.03
$\hat{\sigma}$	58.89	56.35	61.33	16.42	15.71	17.10	2.07	1.98	2.15
$\hat{\mu}$	2607.76	2129.18	3086.35	582.85	449.47	716.23	-64.05	-80.83	-47.27
$\hat{\beta}_{in}$	533.64	361.76	705.52	122.23	74.30	170.15	79.58	73.55	85.61
$\hat{\beta}_{ex}$	-7845.90	-9040.42	-6651.38	-1783.96	-2117.05	-1450.86	182.21	140.29	224.14
$\hat{\beta}_{in^2}$	7456.40	6628.56	8284.23	1582.80	1351.95	1813.64	183.75	154.69	212.80
$\hat{\beta}_{ex^2}$	6623.51	5879.52	7367.50	1519.87	1312.40	1727.33	-102.41	-128.52	-76.29
$\hat{\beta}_{in,ex}$	751.31	562.72	939.90	163.00	110.41	215.59	-67.54	-74.16	-60.92

In this paper, we investigated the effect resulting from four different hypotheses of SCZ on neuronal and astrocytic activity. Using the computational network model by Lenk et al. (2020), we separately examined the neuronal and astrocytic dynamics depending on (1) the neuron and astrocyte density in the network, (2) the depressing effect of astrocytes on excitatory neurons, (3) the glutamate release from the presynapse and the glutamate uptake by the adjacent astrocyte, and (4) the excitatory and/or inhibitory synaptic weight between neurons. Furthermore, we applied a set of statistical models to quantify the effect of these pathological changes.

Several studies report that the neuronal and astrocytic density decreases in several brain regions in SCZ (Cotter et al., 2001; Brennand et al., 2011; Williams et al., 2013), which may be caused by excessive glutamate levels (Drouin-Ouellet et al., 2011). Wagenaar et al. (2006) studied the effect of neuronal cell density on the spike and burst behaviour recorded with MEAs. They found that sparser cultures exhibit a lower spike rate as well as delayed network development. In our simulated experiments, we found that reducing the number of neurons or astrocytes by 25% (hypothesis (1)) causes a significant decrease in neuronal and astrocytic activity. In the original paper of our computational model (Lenk et al., 2020), the number of astrocytes was increased, which led to an elevation of the neuronal activity. Conversely, this means that when astrocytes and their connections are eliminated, neuronal activity also decreases. Astrocytes are assumed to have a homeostatic effect on neurons, they can both enhance and dampen neuronal activity (Santello et al., 2019). Additionally, we found that the effect of reducing astrocytes or neurons can vary significantly for different network connectivity configurations. While the effect on the mean spike rate is robust to varying network connectivity configurations, the mean burst rate and the number of astrocyte activations are not. This might be useful for relating the behaviours of networks with the same number of cells, but different or unknown network configurations.

Furthermore, we have studied the effect of ATP release from the astrocyte on the postsynapse [hypothesis (2)]. Lalo et al. (2016) have demonstrated that ATP activates postsynaptic P2XRs resulting in a downregulation of neuronal NMDARs. This negative feedback mechanism might prevent cell damage due to excessive  $Ca^{2+}$  and glutamate concentrations (Singh and

Abraham, 2017). By the regulation of NMDARs, P2XRs might also be involved in synaptic plasticity and long-term potentiation (LTP) (Moraga-Amaro et al., 2014; Lalo et al., 2016; Singh and Abraham, 2017). This receptor type could even have a protective role by avoiding excitotoxicity and excessive LTP (Lalo et al., 2016).

An increase in neuronal and astrocytic activity was observed when altering the rate of presynaptic facilitation and the recovery rate of mGluRs [hypothesis (3)]. The decreased facilitation rate increases the amount of neurotransmitters ready for release to the synaptic cleft, thereby increasing the release probability and spike rate. Similarly, decreasing the recovery rate of gliotransmitter receptors results in a higher presynaptic potentiation (Helen et al., 1992; Agulhon et al., 2008). Subsequently, this leads to an increase of the neuronal activity.

According to the *glutamate hypothesis of SCZ*, NMDARs undergo a hypofunction leading to an excessive glutamate release (Mei et al., 2018). The changes in the NMDAR function may be caused by D-serine (Takahashi and Sakurai, 2013; Cohen et al., 2015; Mei et al., 2018), which we implicitly modelled by increasing the excitatory synaptic weights. In the future, we aim to add D-serine explicitly to the INEXA model for investigating its role in long-term potentiation and thus memory (Henneberger et al., 2010). Furthermore, GABAergic interneurons (Uhlhaas and Singer, 2010) might be impacted by SCZ due to reaction to the alterations in the NMDARs and an impaired synthesis and reuptake of GABA into the cell (Uhlhaas and Singer, 2010; Moghaddam and Javitt, 2012; Mei et al., 2018). When investigating hypothesis (4), the results show a higher neuronal and astrocytic activity, when increasing the inhibitory or excitatory synaptic weights (both yields in a neuronal excitation).

Further experimental observations are coherent with our modelling results. In SCZ, glutamine synthetase, which catalyzes glutamate, was shown to have reduced activity leading to higher levels of intracellular astrocytic glutamate, and thus, result in a neuronal hyperexcitability (Hu et al., 2015; Mei et al., 2018). This observation is in agreement with the results of our simulated experiments from hypotheses (3) and (4). The accumulation of glutamate was most pronounced in simulated experiments with a decreased mGluR recovery rate. In these experiments,

glutamate accumulated quickly before stabilizing at an extremely high level. As to be expected, the neuronal activity increased with dysinhibition of the GABAergic neurons or the excitation of the glutamatergic neurons.

In the INEXA model, we mainly concentrated on the  $IP_3$ -dependent  $Ca^{2+}$  dynamics. Srinivasan et al. (2015) showed that somatic calcium is abolished in adult  $Ip3r2^{-/-}$  mice. In the future, we intend to extend the model by adding astrocytic NMDARs and  $\alpha$ -amino-3-hydroxy-5-methyl-4-isoxazolepropionic acid (AMPA) receptors as well as the glutamate transporter-dependent pathway to gain further insights into the possible dysfunctions in schizophrenia.

Dynamical causal modeling (DCM), a framework using Bayesian statistics to compare competing models (Friston et al., 2003), has given rise to differential diagnosis methods for psychiatric diseases (Stephan et al., 2017). In the future, we will apply Bayesian inference to obtain posterior distributions of certain astrocytic parameters from INEXA, building the basis for Bayesian model selection among competing disease mechanisms linked to astrocyte malfunction.

## DATA AVAILABILITY STATEMENT

The datasets for this study can be found in Github: [https://github.com/kerstinlenk/INEXA\\_SCZ/](https://github.com/kerstinlenk/INEXA_SCZ/).

## REFERENCES

- Adams, R., Stephan, K., Brown, H., Frith, C., and Friston, K. (2013). The computational anatomy of psychosis. *Front. Psychiatry* 4:47. doi: 10.3389/fpsy.2013.00047
- Agulhon, C., Petravic, J., McMullen, A. B., Sweager, E. J., Minton, S. K., Taves, S. R., et al. (2008). What is the role of astrocyte calcium in neurophysiology? *Neuron* 59, 932–946. doi: 10.1016/j.neuron.2008.09.004
- Araque, A., Parpura, V., Sanzgiri, R. P., and Haydon, P. G. (1999). Tripartite synapses: glia, the unacknowledged partner. *Trends Neurosci.* 22, 208–215. doi: 10.1016/S0166-2236(98)01349-6
- Bates, D., Mchler, M., Bolker, B., and Walker, S. (2015). Fitting linear mixed-effects models using lme4. *J. Stat. Softw. Articles* 67, 1–48. doi: 10.18637/jss.v067.i01
- Brennan, K. J., Simone, A., Jou, J., Gelboin-Burkhart, C., Tran, N., Sangar, S., et al. (2011). Modelling schizophrenia using human induced pluripotent stem cells. *Nature* 473, 221–225. doi: 10.1038/nature09915
- Catts, V. S., Wong, J., Fillman, S. G., Fung, S. J., and Shannon Weickert, C. (2014). Increased expression of astrocyte markers in schizophrenia: association with neuroinflammation. *Aust. N. Z. J. Psychiatry* 48, 722–734. doi: 10.1177/0004867414531078
- Cohen, S. M., Tsien, R. W., Goff, D. C., and Halassa, M. M. (2015). The impact of NMDA receptor hypofunction on GABAergic neurons in the pathophysiology of schizophrenia. *Schizophr. Res.* 167, 98–107. doi: 10.1016/j.schres.2014.12.026
- Cotter, D., Mackay, D., Landau, S., Kerwin, R., and Everall, I. (2001). Reduced glial cell density and neuronal size in the anterior cingulate cortex in major depressive disorder. *Arch. Gen. Psychiatry* 58, 545–553. doi: 10.1001/archpsyc.58.6.545
- Danbolt, N. C. (2001). Glutamate uptake. *Progr. Neurobiol.* 65, 1–105. doi: 10.1016/S0304-0082(00)00067-8
- de Bartolomeis, A., Fiore, G., and Iasevoli, F. (2005). Dopamine-glutamate interaction and antipsychotics mechanism of action: implication for new

## AUTHOR CONTRIBUTIONS

KL wrote the first draft of the manuscript. LF, JL, and FS collected simulation data. LF, FS, and KL visualized the results. FS designed and performed the statistical analysis. All authors designed and performed research and contributed to the manuscript writing and revision. In addition, they have read and approved the submitted version.

## FUNDING

KL was funded by the Academy of Finland (decision nos. 314647 and 326452).

## ACKNOWLEDGMENTS

We thank Barbara Priwitzer for the discussion about the statistical analysis. Furthermore, we want to thank the Statistical Consulting Service at ETH Zurich, especially Chiara Vanetta for her advice on the statistical models and their interpretation.

## SUPPLEMENTARY MATERIAL

The Supplementary Material for this article can be found online at: <https://www.frontiersin.org/articles/10.3389/fncel.2021.718459/full#supplementary-material>

- pharmacological strategies in psychosis. *Curr. Pharm. Des.* 11, 3561–3594. doi: 10.2174/138161205774414538
- Dietz, A. G., Goldman, S. A., and Nedergaard, M. (2020). Glial cells in schizophrenia: a unified hypothesis. *Lancet Psychiatry* 7, 272–281. doi: 10.1016/S2215-0366(19)30302-5
- Drouin-Ouellet, J., Brownell, A. L., Saint-Pierre, M., Fasano, C., Emond, V., Trudeau, L. E., et al. (2011). Neuroinflammation is associated with changes in glial mGluR5 expression and the development of neonatal excitotoxic lesions. *Glia* 59, 188–199. doi: 10.1002/glia.21086
- Friston, K., Harrison, L., and Penny, W. (2003). Dynamic causal modelling. *Neuroimage* 19, 1273–1302. doi: 10.1016/S1053-8119(03)00202-7
- Genocchi, B., Lenk, K., and Hyttinen, J. (2020). “Influence of astrocytic gap junction coupling on in silico neuronal network activity,” in *MEDICON 2019, IFMBE Proceedings* (Cham: Springer Nature Switzerland AG 2020), 480–487.
- Gramowski, A., Jügel, K., Jügel, K., Stuewe, S., Schulze, R., McGregor, G. P., et al. (2006). Functional screening of traditional antidepressants with primary cortical neuronal networks grown on multielectrode neurochips. *Eur. J. Neurosci.* 24, 455–465. doi: 10.1111/j.1460-9568.2006.04892.x
- Grnder, G., and Cumming, P. (2016). “Chapter 7-the dopamine hypothesis of schizophrenia: current status,” in *The Neurobiology of Schizophrenia*, eds T. Abel and T. Nickl-Jockschat (San Diego, CA: Academic Press), 109–124.
- Helen, C., Kastiris, C., Salm, A. K., and McCarthy, K. (1992). Stimulation of the P 2Y Purinergic Receptor on Type 1 astroglia results in inositol phosphate formation and calcium mobilization. *J. Neurochem.* 58, 1277–1284. doi: 10.1111/j.1471-4159.1992.tb11339.x
- Henneberger, C., Papouin, T., Oliet, S. H. R., and Rusakov, D. A. (2010). Long-term potentiation depends on release of d-serine from astrocytes. *Nature* 463, 232–236. doi: 10.1038/nature08673
- Herman, E., Bubser, M., Conn, P., and Jones, C. (2012). “Metabotropic glutamate receptors for new treatments in schizophrenia,” lems in psychiatry, in *Novel Antischizophrenia Treatments, Vol. 213 of Handbook of Experimental*

- Pharmacology*, eds M. A. Geyer and G. Gross (Berlin; Heidelberg: Springer Berlin Heidelberg), 297–365.
- Hoffman, R., and McGlashan, T. (2006). Using a speech perception neural network computer simulation to contrast neuroanatomic versus neuromodulatory models of auditory hallucinations. *Pharmacopsychiatry* 39(Suppl. 1), S54–S64. doi: 10.1055/s-2006-931496
- Hu, W., MacDonald, M. L., Elswick, D. E., and Sweet, R. A. (2015). The glutamate hypothesis of schizophrenia: evidence from human brain tissue studies. *Ann. N. Y. Acad. Sci.* 1338, 38–57. doi: 10.1111/nyas.12547
- Jenkinson, S. P., Grandgirard, D., Heidemann, M., Tschertner, A., Avondet, M.-A., and Leib, S. L. (2017). Embryonic stem cell-derived neurons grown on multi-electrode arrays as a novel *in vitro* bioassay for the detection of clostridium botulinum neurotoxins. *Front. Pharmacol.* 8:73. doi: 10.3389/fphar.2017.00073
- Kapucu, F., Tanskanen, J., Mikkonen, J. E., Ylä-Outinen, L., Narkilahti, S., and Hyttinen, J. A. K. (2012). Burst analysis tool for developing neuronal networks exhibiting highly varying action potential dynamics. *Front. Comput. Neurosci.* 6, 1–14. doi: 10.3389/fncom.2012.00038
- Kizner, V., Fischer, S., and Naujock, M. (2019). “Multielectrode Array (MEA)-based detection of spontaneous network activity in human iPSC-derived cortical neurons,” in *Cell-Based Assays Using iPSCs for Drug Development and Testing*, Vol. 1994, eds C. F. Mandenius and J. Ross (New York, NY: Springer Science+Business Media), 209–216.
- Kondziella, D., Brenner, E., Eyjolfsson, E. M., and Sonnewald, U. (2007). How do glial-neuronal interactions fit into current neurotransmitter hypotheses of schizophrenia? *Neurochem Int.* 50, 291–301. doi: 10.1016/j.neuint.2006.09.006
- Koskivi, M., Lehtonen, S., Trontti, K., Keuters, M., Wu, Y. C., Koivisto, H., et al. (2020). Patient iPSC-astrocytes show transcriptional and functional dysregulation in schizophrenia. *BioRxiv*, 1–45. doi: 10.1101/2020.10.23.350413
- Kosten, L., Verhaeghe, J., Verkerk, R., Thomae, D., De Picker, L., Wyffels, L., et al. (2016). Multiprobe molecular imaging of an NMDA receptor hypofunction rat model for glutamatergic dysfunction. *Psychiatry Res. Neuroimaging* 248, 1–11. doi: 10.1016/j.pscychres.2016.01.013
- Lalo, U., Palygin, O., Verkhatsky, A., Grant, S. G. N., and Pankratov, Y. (2016). ATP from synaptic terminals and astrocytes regulates NMDA receptors and synaptic plasticity through PSD-95 multi-protein complex. *Sci. Rep.* 6, 33609. doi: 10.1038/srep33609
- Lenk, K., Genocchi, B., Barros, M. T., and Hyttinen, J. A. (2021). Larger connection radius increases hub astrocyte number in a 3D neuron-astrocyte network model. *IEEE Trans. Mol. Biol. Multiscale Commun.* 7, 83–88. doi: 10.1109/TMBMC.2021.3054890
- Lenk, K., Satuvuori, E., Lallouette, J., Ladrón-de Guevara, A., Berry, H., and Hyttinen, J. A. K. A. (2020). A computational model of interactions between neuronal and astrocytic networks: the role of astrocytes in the stability of the neuronal firing rate. *Front. Comput. Neurosci.* 13:92. doi: 10.3389/fncom.2019.00092
- Lisman, J. (2012). Excitation, inhibition, local oscillations, or large-scale loops: what causes the symptoms of schizophrenia? *Curr. Opin. Neurobiol.* 22, 537–544. doi: 10.1016/j.conb.2011.10.018
- Mahdavi, A., Bahrami, F., and Janahmadi, M. (2014). “Studying the effect of dysregulation of NMDA receptors function in schizophrenia,” in *22nd Iranian Conference on Electrical Engineering, ICEE 2014, number ICEE* (Tehran: IEEE), 1990–1995.
- Manninen, T., Havela, R., and Linne, M.-L. (2018). Computational models for calcium-mediated astrocyte functions. *Front. Comput. Neurosci.* 12:14. doi: 10.3389/fncom.2018.00014
- Mei, Y.-Y., Wu, D. C., and Zhou, N. (2018). Astrocytic regulation of glutamate transmission in schizophrenia. *Front. Psychiatry* 9:544. doi: 10.3389/fpsy.2018.00544
- Mitterauer, B. (2009). Loss of function of glial gap junctions may cause severe cognitive impairments in schizophrenia. *Med. Hypotheses* 73, 393–397. doi: 10.1016/j.mehy.2009.04.003
- Moghaddam, B., and Javitt, D. (2012). From revolution to evolution: the glutamate hypothesis of schizophrenia and its implication for treatment. *Neuropsychopharmacology* 37, 4–15. doi: 10.1038/npp.2011.181
- Moraga-Amaro, R., Jerez-Baraona, J., Simon, F., and Stehberg, J. (2014). Role of astrocytes in memory and psychiatric disorders. *J. Physiol. Paris* 108, 240–251. doi: 10.1016/j.jphysparis.2014.08.005
- Moran, R., Stephan, K. E., Botvinick, M., Breakspear, M., Carter, C. S., Kalivas, P. W., et al. (2016). “Candidate examples for a computational approach to address practical problems in psychiatry,” in *Computational Psychiatry: New Perspectives on Mental Illness*, Vol. 20, Chapter 12, eds A. D. R. Gordon (Cambridge, MA: The MIT Press), 223–245.
- Naujock, M., Speidel, A., Fischer, S., Kizner, V., Dörner-Ciossek, C., and Gillardon, F. (2020). Neuronal differentiation of induced pluripotent stem cells from schizophrenia patients in two-dimensional and in three-dimensional cultures reveals increased expression of the Kv4.2 subunit DPP6 that contributes to decreased neuronal activity. *Stem. Cells Dev.* 29, 1577–1587. doi: 10.1089/scd.2020.0082
- Oehlert, G. W. (2010). *A First Course in Design and Analysis of Experiments*. University of Minnesota Digital Conservancy. Available online at: <https://hdl.handle.net/11299/168002>
- Ohnuma, T., Augood, S. J., Arai, H., McKenna, P. J., and Emson, P. C. (1998). Expression of the human excitatory amino acid transporter 2 and metabotropic glutamate receptors 3 and 5 in the prefrontal cortex from normal individuals and patients with schizophrenia. *Mol. Brain Res.* 56, 207–217. doi: 10.1016/S0169-328X(98)00063-1
- Oschmann, F., Berry, H., Obermayer, K., and Lenk, K. (2018). From *in silico* astrocyte cell models to neuron-astrocyte network models: a review. *Brain Res Bull.* 136, 76–84. doi: 10.1016/j.brainresbull.2017.01.027
- Rolls, E. T., Loh, M., Deco, G., and Winterer, G. (2008). Computational models of schizophrenia and dopamine modulation in the prefrontal cortex. *Nat. Rev. Neurosci.* 9, 696–709. doi: 10.1038/nrn2462
- Santello, M., Toni, N., and Volterra, A. (2019). Astrocyte function from information processing to cognition and cognitive impairment. *Nat. Neurosci.* 22, 154–166. doi: 10.1038/s41593-018-0325-8
- Schobel, S. A., Chaudhury, N. H., Khan, U. A., Paniagua, B., Styner, M. A., Asllani, I., et al. (2013). Imaging patients with psychosis and a mouse model establishes a spreading pattern of hippocampal dysfunction and implicates glutamate as a driver. *Neuron* 78, 81–93. doi: 10.1016/j.neuron.2013.02.011
- Siekmeier, P. J., and Hoffman, R. E. (2002). Enhanced semantic priming in schizophrenia: a computer model based on excessive pruning of local connections in association cortex. *Br. J. Psychiatry* 180, 345–350. doi: 10.1192/bjp.180.4.345
- Singh, A., and Abraham, W. C. (2017). Astrocytes and synaptic plasticity in health and disease. *Exp. Brain Res.* 235, 1645–1655. doi: 10.1007/s00221-017-4928-1
- Sohal, V. S., and Rubenstein, J. L. R. (2019). Excitation-inhibition balance as a framework for investigating mechanisms in neuropsychiatric disorders. *Mol. Psychiatry* 24, 1248–1257. doi: 10.1038/s41380-019-0426-0
- Srinivasan, R., Huang, B. S., Venugopal, S., Johnston, A. D., Chai, H., Zeng, H., et al. (2015). Ca<sup>2+</sup> signaling in astrocytes from *Ip3r2*<sup>-/-</sup> mice in brain slices and during startle responses *in vivo*. *Nat. Neurosci.* 18, 708–717. doi: 10.1038/nn.4001
- Stephan, K., Schlagenhauf, F., Huys, Q., Raman, S., Aponte, E., Brodersen, K., et al. (2017). Computational neuroimaging strategies for single patient predictions. *Neuroimage* 145, 180–199. doi: 10.1016/j.neuroimage.2016.06.038
- Stephan, K. E., Bach, D. R., Fletcher, P. C., Flint, J., Frank, M. J., Friston, K. J., et al. (2016). Charting the landscape of priority problems in psychiatry, part 1: classification and diagnosis. *Lancet Psychiatry* 3, 77–83. doi: 10.1016/S2215-0366(15)00361-2
- Takahashi, N., and Sakurai, T. (2013). Roles of glial cells in schizophrenia: Possible targets for therapeutic approaches. *Neurobiol. Dis.* 53, 49–60. doi: 10.1016/j.nbd.2012.11.001
- Tukker, A. M., Wijnolts, F. M., de Groot, A., and Westerink, R. H. (2018). Human iPSC-derived neuronal models for *in vitro* neurotoxicity assessment. *Neurotoxicology* 67, 215–225. doi: 10.1016/j.neuro.2018.06.007
- Uhlhaas, P. J., and Singer, W. (2010). Abnormal neural oscillations and synchrony in schizophrenia. *Nat. Rev. Neurosci.* 11, 100–113. doi: 10.1038/nrn2774
- Välkki, I. A., Lenk, K., Mikkonen, J. E., Kapucu, F. E., and Hyttinen, J. A. K. (2017). Network-wide adaptive burst detection depicts neuronal activity with improved accuracy. *Front. Comput. Neurosci.* 11:40. doi: 10.3389/fncom.2017.00040
- Valton, V., Romaniuk, L., Douglas Steele, J., Lawrie, S., and Seriès, P. (2017). Comprehensive review: computational modelling of schizophrenia. *Neurosci. Biobehav. Rev.* 83, 631–646. doi: 10.1016/j.neubiorev.2017.08.022



- Wagenaar, D. A., Pine, J., and Potter, S. S. M. (2006). An extremely rich repertoire of bursting patterns during the development of cortical cultures. *BMC Neurosci.* 7:11. doi: 10.1186/1471-2202-7-11
- Williams, M. R., Hampton, T., Pearce, R. K., Hirsch, S. R., Ansorge, O., Thom, M., et al. (2013). Astrocyte decrease in the subgenual cingulate and callosal genu in schizophrenia. *Eur. Arch. Psychiatry Clin. Neurosci.* 263, 41–52. doi: 10.1007/s00406-012-0328-5

**Conflict of Interest:** The authors declare that the research was conducted in the absence of any commercial or financial relationships that could be construed as a potential conflict of interest.

**Publisher's Note:** All claims expressed in this article are solely those of the authors and do not necessarily represent those of their affiliated organizations, or those of the publisher, the editors and the reviewers. Any product that may be evaluated in this article, or claim that may be made by its manufacturer, is not guaranteed or endorsed by the publisher.

Copyright © 2021 Fritschi, Lindmar, Scheidl and Lenk. This is an open-access article distributed under the terms of the Creative Commons Attribution License (CC BY). The use, distribution or reproduction in other forums is permitted, provided the original author(s) and the copyright owner(s) are credited and that the original publication in this journal is cited, in accordance with accepted academic practice. No use, distribution or reproduction is permitted which does not comply with these terms.



# Novel *in vitro* Experimental Approaches to Study Myelination and Remyelination in the Central Nervous System

Davide Marangon<sup>1</sup>, Nicolò Caporale<sup>2,3</sup>, Marta Boccazzi<sup>4</sup>, Maria P. Abbracchio<sup>1</sup>, Giuseppe Testa<sup>2,3</sup> and Davide Lecca<sup>1\*</sup>

<sup>1</sup> Laboratory of Molecular and Cellular Pharmacology of Purinergic Transmission, Department of Pharmaceutical Sciences, Università degli Studi di Milano, Milan, Italy, <sup>2</sup> Department of Oncology and Hemato-Oncology, University of Milan, Milan, Italy, <sup>3</sup> Human Technopole, Milan, Italy, <sup>4</sup> Laboratory of Molecular and Cellular Pharmacology of Purinergic Transmission, Department of Pharmacological and Biomolecular Sciences, Università degli Studi di Milano, Milan, Italy

## OPEN ACCESS

### Edited by:

Christian Lohr,  
University of Hamburg, Germany

### Reviewed by:

Timothy Edward Kennedy,  
McGill University, Canada  
Janos Groh,  
University Hospital Würzburg,  
Germany

### \*Correspondence:

Davide Lecca  
davide.lecca@unimi.it

### Specialty section:

This article was submitted to  
Non-Neuronal Cells,  
a section of the journal  
Frontiers in Cellular Neuroscience

**Received:** 28 July 2021

**Accepted:** 22 September 2021

**Published:** 14 October 2021

### Citation:

Marangon D, Caporale N, Boccazzi M, Abbracchio MP, Testa G and Lecca D (2021) Novel *in vitro* Experimental Approaches to Study Myelination and Remyelination in the Central Nervous System. *Front. Cell. Neurosci.* 15:748849. doi: 10.3389/fncel.2021.748849

Myelin is the lipidic insulating structure enwrapping axons and allowing fast saltatory nerve conduction. In the central nervous system, myelin sheath is the result of the complex packaging of multilamellar extensions of oligodendrocyte (OL) membranes. Before reaching myelinating capabilities, OLs undergo a very precise program of differentiation and maturation that starts from OL precursor cells (OPCs). In the last 20 years, the biology of OPCs and their behavior under pathological conditions have been studied through several experimental models. When co-cultured with neurons, OPCs undergo terminal maturation and produce myelin tracts around axons, allowing to investigate myelination in response to exogenous stimuli in a very simple *in vitro* system. On the other hand, *in vivo* models more closely reproducing some of the features of human pathophysiology enabled to assess the consequences of demyelination and the molecular mechanisms of remyelination, and they are often used to validate the effect of pharmacological agents. However, they are very complex, and not suitable for large scale drug discovery screening. Recent advances in cell reprogramming, biophysics and bioengineering have allowed impressive improvements in the methodological approaches to study brain physiology and myelination. Rat and mouse OPCs can be replaced by human OPCs obtained by induced pluripotent stem cells (iPSCs) derived from healthy or diseased individuals, thus offering unprecedented possibilities for personalized disease modeling and treatment. OPCs and neural cells can be also artificially assembled, using 3D-printed culture chambers and biomaterial scaffolds, which allow modeling cell-to-cell interactions in a highly controlled manner. Interestingly, scaffold stiffness can be adopted to reproduce the mechanosensory properties assumed by tissues in physiological or pathological conditions. Moreover, the recent development of iPSC-derived 3D brain cultures, called organoids, has made it possible to study key aspects of embryonic brain development, such as neuronal differentiation, maturation and network formation in temporal dynamics that

are inaccessible to traditional *in vitro* cultures. Despite the huge potential of organoids, their application to myelination studies is still in its infancy. In this review, we shall summarize the novel most relevant experimental approaches and their implications for the identification of remyelinating agents for human diseases such as multiple sclerosis.

**Keywords:** myelination, oligodendrocytes, co-cultures, hiPSCs, organoids, models, neurodegenerative diseases

## INTRODUCTION

Myelin is a very specialized lipidic insulating structure that allows rapid and efficient conduction of nerve impulses. During evolution, myelin has become a key requirement for the motor, sensory and cognitive functions in vertebrates (Zalc, 2006). Myelin sheath is the result of the complex packaging of multilamellar extensions generated by specialized glial cells, i.e., oligodendrocytes (OLs) in the central nervous system (CNS) and Schwann cells in the peripheral nervous system. Although anatomical and histological studies have described the existence of what now we call myelin since the 18th century, the structural and chemical complexity of myelin made the elucidation of its function elusive until recently (Boullerne, 2016).

Advances in understanding the physiology of myelination have been achieved only a few decades ago, when dissociated brain tissues from small mammals were cultured giving rise to the first primitive neuron-glia co-cultures (Bornstein and Murray, 1958; Kim, 1972). These studies paved the way to the modern myelinating *in vitro* models described in this review. In the CNS, the identification of OL precursor cells (OPCs) was the starting point for investigating oligodendroglia biology. OPCs, highly dividing cells during embryogenesis, become relatively quiescent (but not silent) during adulthood, when they still represent an important source of potential remyelinating OLs after injury (Nishiyama et al., 2021a). During their differentiation to mature myelinating cells, OPCs make contacts with other glial cells and neurons with which they can form synapses and gap junctions, and they continuously refine their intrinsic program based on extracellular cues and inputs received from contacted cells. Neurotransmitters, axonal signals, morphogens, cytokines, and extracellular matrix (ECM) proteins can all contribute to changing the fate of OPCs, modulating their maturation timing, promoting their local migration, or keeping them undifferentiated to maintain a pool of slowly proliferating cells (Nishiyama et al., 2021a). The cellular and molecular context make OPCs highly heterogeneous and plastic, both in time and space, with mechanisms that remain largely unknown. The recent development of 3D scaffolds and new materials with different stiffness has highlighted that, as any other cells, OPCs and OLs are also sensitive to the mechanical features of the extracellular environment. Thus, when grown on plastics, *in vitro* cultures may lead to more artifactual results than previously expected. For these reasons, isolation methods and culture conditions are a crucial issue to determine OPC behavior *in vitro*.

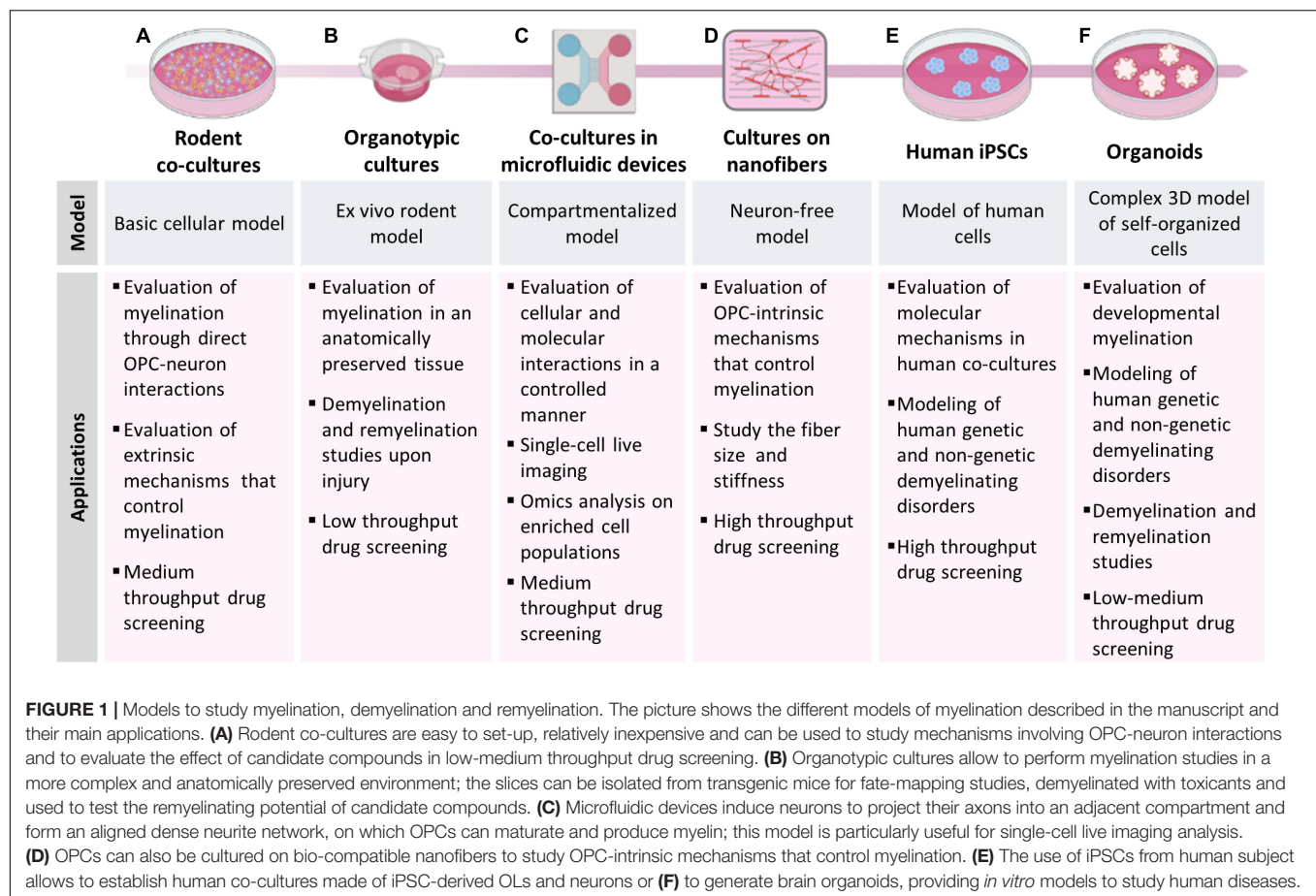
Although OPC monocultures recapitulate several features of OL differentiation and myelination, thus helping to elucidate myelin-related functions (Zuchero et al., 2015), they do not represent a proper myelination model, since in the absence of

axons or axon-like structures they show limited myelination abilities. Rodent OPC-neuron co-cultures, still representing the most widely used myelinating assays, have intrinsic limits due to the potential species-specific differences in both differentiation and myelination dynamics (Mabbott et al., 2006; Scantlebury et al., 2014). Indeed, although myelin plays the same role in humans and rodents, myelination kinetics are significantly different. In rodents, myelination takes place after birth and is resolved within postnatal day 60, whereas in humans it requires more than 20 years (Nakagawa et al., 1998; Giedd et al., 1999; Yeung et al., 2014). This very long time is likely due to the unique complexity of human connections. Intrinsic differences in oligodendroglia biology between humans and rodents is also reflected in differences in the OPC pool (Dietz et al., 2016). For this reason, cellular reprogramming from human derived cells (typically dermal fibroblasts) into induced pluripotent stem cells (iPSCs) and then into terminally differentiated OLs is increasingly becoming an important means to assess the effect of pharmacological agents on OPC maturation and axonal myelination both in physiological conditions and after insults. Induced humanized models are likely to mimic more accurately the behavior of human cells. iPSCs can be derived directly from patients to assess the importance of genetic and/or environmental cues in the pathogenesis of diseases, and offer the opportunity to generate personalized disease models. A few examples have been described also in demyelinating diseases such as leukodystrophies or multiple sclerosis (MS). Human iPSCs can be also grown as organoids, self-organizing 3D structures that recapitulate the developmental features of the organ of origin. Brain organoids have been used to study the formation of cortical layers maintaining the complex cell-to-cell interactions, with a strong focus on neurons, whereas OL and myelination dynamics have been mostly neglected.

In this review, we shall describe the classic methods used to study myelination and remyelination *in vitro*, we shall introduce some of the most recent methods, their limits, and their potential relevance in the field (**Figure 1**), and finally shall describe the most relevant implications in the identification of remyelinating agents for human diseases.

## CLASSIC *IN VITRO* METHODS AND MYELINATION ASSAYS

The first reports showing *in vitro* myelination date back to the late 1950s and made use of various CNS tissues from chicks, kittens or rodents broken up by chemical and mechanical digestion and then dissociated to obtain a mixed cell population



(Bornstein and Murray, 1958; Kim, 1972). The derived cultures were plated on collagen and cultured in high serum media giving rise to irregular myelination and to very variable experimental regimes. Subsequent improvements in culturing protocols of dissociated cells (e.g., development of defined media and usage of more compliant substrates) allowed to reduce variability and to greatly increase the control over experimental conditions. Moreover, technical advances allowed to define some fundamental aspects of myelination dynamics, such as the ability of OL processes to exclusively myelinate axons, the absolute need of neurons and of a continuous bidirectional crosstalk between neurons and OLs to allow a proper myelination, the synchronization of these processes, the importance of axonal density, the role of additional cells like astrocytes or microglia (Raffaele et al., 2021b) and the similarities and differences between *in vitro* and *in vivo* myelination (Lubetzki et al., 1993; Jarjour et al., 2012). Dissociated CNS cultures from different brain areas (e.g., hippocampus, spinal cord, cerebellum) allowed to identify, for the first time, region-specific differences in myelination dynamics (Baumann and Pham-Dinh, 2001; Thomson et al., 2006). Although dissociated CNS cultures are made by both neurons and glial cells, their common source does not allow to independently manipulate the different populations. Furthermore, the highly inconsistent neuron survival from study to study may lead to highly variable results.

Myelinating co-culture models in which neurons and OLs are independently isolated and then cultured together have been developed to overcome some of the limitations described above (Figure 1A). In these models, neurons are usually isolated from embryonic brain tissues, and then differentiated to reach morphological and functional maturation before adding oligodendroglial cells. On the contrary, OPCs are usually isolated after birth, before the end of the first postnatal week, when they reach the highest density (Nishiyama et al., 2021b), so that they can be expanded using mitogens (e.g., bFGF and PDGF) and then plated onto mature neurons. OLs and neurons can be obtained from different species, CNS regions, and tissues at different developmental stage, or they can be prepared using different methods (e.g., isolation from tissue explants or mixed glial cultures, immunopanning, magnetic or fluorescent-activated cell sorting). Moreover, both populations can be manipulated independently before setting up the co-culture. The co-culture of dissociated dorsal root ganglia neurons (DRGs) with primary oligodendroglial cells is one of the most used myelinating model in the last decades (Windebank et al., 1985; Xiao et al., 2009). In this model, DRGs from rodent embryos are removed from spinal nerves and maintained in culture until maturation (usually 3 weeks) and then OPCs from postnatal day 1–3 pups are added onto them. Recent refinements of the experimental protocols allowed to obtain myelinating fibers in 10–18 days after adding



OLs to neurons (Azevedo et al., 2018; Shimizu et al., 2018). Even though OPCs/OLs are exclusively CNS glia while DRGs are not CNS neurons, this mixed co-culture contributed to identify both secreted (e.g., neuregulins, ATP) and contact-mediated (e.g., integrins) axonal signals influencing oligodendroglial development and myelination. However, analogies between *in vivo* CNS myelination and findings obtained with this model may be questionable. Moreover, DRG survival depends on the presence of neurotrophins (e.g., nerve growth factor), which can negatively affect axon myelination (Chan et al., 2004). To address these major issues several co-culture models were developed taking advantage of different types of neurons (hippocampal, cortical, cerebellar) isolated from CNS tissues of rodent embryos.

A method to obtain hippocampal neuron/OL co-cultures in the absence of an astrocyte feeding layer was described for the first time in 2012 (Gardner et al., 2012). These co-cultures were used to study myelin-mediated regulation of ion channel trafficking (Gardner et al., 2012), the mechanism defining myelination-incompetent axon segments during neural development (Diez-Revuelta et al., 2017) and to develop assays for the evaluation of drugs promoting CNS axon regeneration (Gang et al., 2015). Hippocampus contains many myelinated axons projecting within the hippocampus (Arnold and Trojanowski, 1996), whose alterations may profoundly affect learning and memory. Hippocampal demyelination is a prominent feature of MS brain, and hippocampal atrophy correlates with cognitive decline in MS patients (Baltan et al., 2021). Nevertheless, it has been shown that CA1 neurons may survive demyelination and hibernate in a state that protects the demyelinated axon, facilitating functional recovery following remyelination. Hippocampal demyelination was also observed in Alzheimer's disease (Ota et al., 2019) and epilepsy (Drenthen et al., 2020), suggesting a contribution to the onset of several cognitive symptoms.

Analysis on MS post-mortem tissues highlighted signs of demyelination in many brain regions, including cortical and sub-cortical areas. Interestingly, in some cases, cortical demyelinated lesions did not show signs of immune cell infiltration, suggesting that neurodegenerative events may precede neuroinflammation and white matter demyelination (Trapp and Nave, 2008). In this context, cortical neuron/OL co-cultures may represent a useful system for studying the axo-myelinic neurotransmission and the evolution of MS lesions at cortical level. To date, this co-culture system has been used to investigate the myelin membrane trafficking pathways required for axon ensheathment (Feldmann et al., 2011) and the effect of OL-derived exosomes on neuronal firing rate, axonal transport, and signal transduction (Frohlich et al., 2014; Fruhbeis et al., 2020).

The co-culture models described above do represent a valuable tool for studying the fine mechanisms that regulate axon-OL interplay and myelination, but they do not consider either the three-dimensional structure of the CNS or the role of other CNS populations, which may affect the dynamics of myelination, demyelination and remyelination. On the contrary, animal models currently represent the most suitable available non-human models, but have limitations in terms of management, costs, feasibility of drug treatments and biotechnological manipulation. The golden mean between *in vitro* and *in vivo*

models of myelination are *ex vivo* cultures, in which the three-dimensional structure of the different brain areas is reproduced taking advantage of thin slices (**Figure 1B**). The advantage of this system is that it can be easily used as disease model, since brain slices can be isolated from different regions of animal models of disease such as transgenic mice, (Humpel, 2019) and they can be demyelinated *in vitro* exposing the cultures to toxicants. For example, lysolecithin-treated slices have been widely used to study early demyelination events, response of OPCs to demyelinating insults, remyelination and the role of other glial populations, and to evaluate the remyelinating potential of pharmacological and biotechnological interventions (Miron et al., 2010; Goudarzi et al., 2016; Marangon et al., 2020).

## NEW MATERIALS AND SUPPORTS FOR CELL CULTURES

The *in vitro* myelination models described above are made up by intricate networks of co-cultured cells, making it difficult to perform single-cell and large scales (omics) analyses on either neurons or myelinating cells. Microfluidic technology can be used to overcome these limitations by assembling multi-compartment cell culture devices in which microenvironmental conditions can be controlled spatially and temporally to better mimic *in vivo* conditions (**Figure 1C**). These devices allow the compartmentalization of neuronal cell bodies, axons and myelinating cells, and the generation of aligned dense networks in specific compartments that are physically isolated from neuronal somas, thus enabling single-cell live imaging, high-throughput and -omics analyses on highly enriched cell populations.

The first application of this technology to neuroscience dates back to 2005, when Taylor et al. (2005) isolated and directed the growth of CNS axons without neurotrophins by means of a microfluidic platform, providing a highly adaptable system to model many aspects of CNS physiopathology (Taylor et al., 2005). The culture chamber consisted of a polydimethylsiloxane (PDMS) mold containing a relief pattern of somal and axonal compartments (1.5-mm wide, 7-mm long, 100-mm high) connected by microgrooves (10-mm wide, 3-mm high), which guide axon growth into the axonal side. This method allowed to investigate the transport of axonal mRNAs in developing neurons, to test the role of soluble factors in axonal injury and regeneration, and to generate the first prototype of compartmentalized co-culture with oligodendroglial cells. However, only several years later this technology was successfully applied to study myelination, demyelination and remyelination.

For example, Vaquié et al. (2019) generated a lesion model of myelination suitable for high-resolution time-lapse imaging of neuron-glial cell interactions and transcriptomic analyses both in physiological conditions and after lesion (Vaquié et al., 2019). In this device, made of two chambers connected by microgrooves, dissociated DRGs were plated in the first chamber, from which neuronal cell bodies projected their axons to the second chamber where precursors of myelinating cells were plated. Authors showed that both OLs and Schwann cells were able to myelinate axons and that laser-induced axonal lesion in

the microgrooves led to demyelination in the second chamber. Interestingly, in response to VEGFR1 activation, Schwann cells were able to guide axonal regrowth, re-interact with regenerated axons and remyelinate them, whereas OLs, which did not upregulate VEGFR1 after axonal lesion, passively responded to demyelination either dying or remaining in their original myelinating state (Vaquié et al., 2019). The regenerative action of Schwann cells depends on the formation of “actin spheres,” which constrict axons until their disintegration, thereby accelerating the clearing of axonal debris after lesion. Of note, enforced expression of VEGFR1 in OLs induced axon fragmentation to a similar level as in neuron/SC cultures and promoted axonal regrowth.

The advantages of microfluidic devices can be also combined with those offered by embryonic stem cells (ESCs) and iPSCs (see section “Models to Study Human Oligodendrocytes in Physiology and Disease”). In this context, in 2015, Kerman et al. (2015) developed a custom semi-automated computer platform, called Computer-assisted Evaluation of Myelin formation, to quantify myelin in co-cultures of ESC-derived myelinating OLs and cortical neurons plated on compartmentalized microfluidics-based devices (Kerman et al., 2015). Unlike the original microfluidic device design by Taylor, which is characterized by low-height cell compartments enclosed within PDMS, authors adopted an open-well design, which, by reducing the capillary forces, allowed to increase the number of neurons remaining in the neuronal compartment and the density of axons growing into the myelination compartment. In this study, ESCs were firstly converted into neural precursor cells (NPCs) (Marchetto et al., 2008) and then differentiated into OLs by switching them firstly in OPC differentiation medium (N2/B27 supplemented with IGF1 and PDGF $\alpha$ ) and then in myelination medium (N2/B27 with CNTF, NT3 and T3), whereas neurons were differentiated from ESCs following a previously published protocol that enriched the cultures in cortical neurons (Gaspard et al., 2009). At 10–14 DIV, when neurons extended many axons into the myelination compartment, mature OLs were added to the device. Maintaining co-cultures in 40 ng/ml T3 significantly promoted myelination of axons. This assay allowed to follow the myelination process by real time imaging over several days and to clearly show that OLs sense the environment constantly extending and retracting their processes around and along axons before starting myelination.

Very recently, another group developed a new 3D printing-based fabrication method to produce repeatably PDMS-based microfluidics devices with an open compartment design (Ristola et al., 2019). These microfluidics devices were made by three sequential compartments: two neuronal soma compartments interconnected to a central compartment by forty 250  $\mu$ m-long microtunnels. This characteristic architecture allowed the growth of an aligned neurite network in which neurite-OL interactions and myelination could be easily analyzed. To obtain a myelinating culture, primary DRG neurons isolated from spinal cords of E15 rat embryos were first seeded in the neuronal soma compartments and, after 21 DIV, OPCs were seeded onto the neurite network compartment of the device. After 18 days in co-culture in SATO medium, OLs showed MBP-positive segments along the neurites in an aligned configuration. Interestingly, the

size of microtunnels and myelination compartments have been reported to influence both neurite outgrowth and myelination; indeed, neurons extended their neurites into the myelination compartment more efficiently in larger microtunnels (3.5- $\mu$ m high and 10- $\mu$ m wide) compared to smaller ones (1.5- $\mu$ m high and 5- $\mu$ m wide). Instead, a shorter myelination compartment (3-mm long) promoted the formation of more aligned and dense neurite networks with respect to larger one (5-mm long), facilitating myelination analysis.

Myelin wrapping is also closely related to axonal diameter. Large-diameter axons are preferentially myelinated over small-diameter ones, which remain unmyelinated (Voyvodic, 1989). However, understanding the exact contribution of axonal diameter to myelin formation by using co-culture systems remains complex, since the diameter-dependent mechanisms are barely distinguishable from those induced by the extrinsic cues deriving from axon-glia contacts. Several studies demonstrated that axonal signals mainly act as negative regulators of myelination, whereas the initiation of the process does not depend on axonal signals (Podbielska et al., 2013). Accordingly, OPCs seeded onto fixed axons differentiate and form compact myelin with the same timing and robustness of OPCs on live axons, demonstrating that dynamic interactions between OLs and axons are not required for either differentiation or myelination (Rosenberg et al., 2008). The same results were obtained several years later by using polystyrene nanofibers, inert structures designed to mimic CNS axons (Figure 1D). This important finding opened new horizons in exploring the autonomous OL cellular mechanisms that control myelination. In 2013, Lee et al. (2013) fabricated aligned fibers by electrospinning liquid polystyrene, a material commonly used for cell cultures, demonstrating that fibers with a  $>0.4$   $\mu$ m diameter represent a sufficient axonal cue for initiating myelin wrapping by OLs (Lee et al., 2013). Later, Bechler et al. (2015), taking advantage of parallel-aligned electrospun fibers composed of poly-L-lactic acid, showed that OLs do have the intrinsic capability to form compact sheaths that reflect their *in vivo* origin, demonstrating that OPCs acquire a regional identity prior to differentiation and that this identity determines sheath length (Bechler et al., 2015).

Thanks to advances in aligned electrospinning technology, nanofibers can now be rapidly fabricated, standardized, and configured into various densities and patterns as desired. OPC-nanofibers cultures can also be used to assess whether and how individual neuronal surface signals may modulate contact formation with OLs and their myelinating capacity. To this aim nanofibers are coated with signaling proteins of interest. OPCs plated on ephrin-A1-coated fibers exhibited a decreased maturation rate and generated fewer sheath-like structures per cell compared with poly-D-lysine-coated control fibers, suggesting that OL ephrin receptors are involved in regulating myelination by sensing inhibitory cues in the form of ephrins expressed on the axonal surface (Harboe et al., 2018).

A great advantage of the nanofiber system is that it facilitates the assessment of multiple biologically relevant parameters, providing key insight into which cellular process may be affected by any given treatment. Nevertheless, most existing

high-throughput systems prioritize the speed of analysis and allow only to acquire information on single parameters, such as MBP intensity, sheath length, g-ratio. In this context, automated high-throughput methods that combine micro-engineered nanofibers, automated microscopy, and analytic algorithms to extract detailed morphological properties from individual OLs can be exploited to remove bias and variability, facilitate massive increases in sample size and analytic speed and to accelerate the discovery of new therapeutics with promyelinating activity (Xu et al., 2019).

The advancement in electrospinning technology and production of new biodegradable and biocompatible materials may also have unprecedented applications in neural regeneration. In this context, polycaprolactone (PCL), and PCL-gelatin copolymer nanofibers, represent interesting materials. Both the nanofibers supported OPC growth, survival, and differentiation, but differentiated OLs formed significantly more myelinated nanofiber segments with PCL-gelatin than PCL-only nanofibers, demonstrating that fiber composition, biological function and hydrophilicity can affect the efficiency of OPC differentiation and fiber wrapping (Li et al., 2014).

Chemical, physical and mechanical properties of the macroenvironment strongly influence basic processes such as proliferation, maturation, migration, response to stimuli in a similar way to biochemical signals (Jagielska et al., 2012). This issue has been largely overlooked until recently. Brain tissues and axons have an extremely low mechanical stiffness (Young's elastic modulus  $E \sim 0.1\text{--}1\text{ kPa}$ ), which is approximately six orders of magnitude lower than silica glass, polystyrene, and PCL (Young's elastic modulus  $10^8\text{--}9\text{ Pa}$ ). Interestingly, stiffness of some regions of the brain have a significant linear correlation with age and sex, while others do not (Arani et al., 2015; Takamura et al., 2020). Espinosa-Hoyos et al. (2018) developed the first mechanically compliant axon-like fiber arrays, a model that replicates the physical cues of the glial cell microenvironment (Espinosa-Hoyos et al., 2018) and that allows to evaluate the effects of axon diameter, artificial axon stiffness and ligand coating on OL engagement and myelination. They have demonstrated that OLs were three times more likely to ensheath stiffer (140 kPa) artificial axons, compared to more compliant counterparts approximating the sub-kPa stiffness of biological axons (0.4 kPa). Furthermore, in line with previous findings, they found that laminin-coated artificial axons were more significantly ensheathed by OLs compared to poly-D-lysine-coated artificial axons and that OLs preferentially engaged 10- $\mu\text{m}$  diameter axons compared to 20- $\mu\text{m}$  ones, suggesting a maximum permissive diameter threshold above which full myelin wrapping may not proceed efficiently. This study revealed that both axon diameter and ligand type can play a role in OL response in the presence of axon-like mechanical stiffness and it may represent the basis for the generation of engineered environments that reflect key pathophysiological, mechanical, geometric, and biochemical components of the glial microenvironment for myelination assays.

The efficiency of OL differentiation and myelination depends on ECM stiffness as well. Indeed, a more rigid ECM results in significant reduction in OL branching complexity, which strongly

correlates with decreased expression of OPC differentiation markers (Urbanski et al., 2016). Thus, changes in the mechanical properties of the CNS following injury may play a prominent role in repair and remyelination. It has been recently shown that acutely demyelinated lesions, which can spontaneously remyelinate, present lower stiffness than healthy tissue in both the lysolecithin and cuprizone models, whereas tissues chronically exposed to cuprizone are stiffer than healthy white matter (Urbanski et al., 2019), suggesting that the increase of matrix rigidity observed in chronic MS lesions might be involved in remyelination failure. The effect of ECM stiffness on oligodendroglial functions has been recently studied during aging. OPC microenvironment stiffens with age and this mechanical change is sufficient to cause age-related loss of function of OPCs (Segel et al., 2019). Aged OPCs cultured on synthetic scaffolds, designed to mimic the stiffness of young brains, or transplanted into the prefrontal cortex of neonatal rats, were molecularly and functionally rejuvenated, whereas young progenitors transplanted into aged environments lost optimal regenerative properties, indicating that ECM aging contributes to the impairment of OPC functions. Interestingly, this age-related loss of function can be reversed also through inhibition of PIEZO1 (Segel et al., 2019), a mechanosensitive ion channel which regulates cell density and stem-cell activation. Piezo1 knockdown in aged mice after lysolecithin-induced demyelination markedly improved the regenerative capacity of OPCs, whereas its knockdown in pups increased the total density of OPCs, suggesting that PIEZO1-mediated mechanical signaling is essential for OPCs during growth and development, but then becomes non-compliant to regeneration with aging.

## UNRAVELING OLIGODENDROGLIAL HETEROGENEITY WITH SINGLE-CELL OMICS

The recent development of single-cell omics represents a unique opportunity to quantify simultaneously a high number of molecular states for each cell of a complex organ. It is now possible to genome-wide profile, at different degrees of sensitivity, accuracy and scalability, RNA, DNA, histone modifications, chromatin accessibility, DNA methylation, nuclear lamina interactions, chromosomal contacts, and the protein signatures of individual cells. Among these, single cell RNA seq is at the forefront because of the higher throughput and accuracy, and its application to the clinics is now closer (Tanay and Regev, 2017; Chappell et al., 2018). These advances have opened the possibility to overcome the inherent limitations associated with the averaged readout of bulk sequencing for mixtures of heterogeneous cell populations and thereby unveil how cell-types expressing the same canonical markers may instead comprise more diverse subpopulations than previously thought.

For a long time, OPCs have been considered as a functionally homogeneous population in the adult CNS. However, as highlighted above, when looking at the whole oligodendroglial lineage, they show significant differences in terms of proliferation, differentiation, myelination, migration



capabilities and energetic metabolism. Moreover, a large fraction of OPCs does not differentiate, but instead remains in a progenitor state throughout adulthood, suggesting the existence of sub-populations with different functions. OPCs from different brain regions express distinct ion channel profiles, which lend unique electrical properties (Spitzer et al., 2019). Conditional loss of OPCs in specific brain regions led to unexpected outcomes, such as depressive-like behavior, persistent weight-gain, and leptin insensitivity. Moreover, in specific conditions, OPCs can also display immunomodulatory properties, upregulating the antigen presentation machinery and cytokine production (Fernandez-Castaneda et al., 2020). The dynamic role of OPCs in the adult CNS was recently investigated by exploring adult OPC diversity in the mouse brain at transcriptional level (Beiter et al., 2020). OPCs from the adult mouse brain clustered into three distinct subpopulations characterized by specific transcriptional signatures and Gene Ontology profiles. Interestingly, OPC cluster 1 (OPC1) and 3 (OPC3) expressed a unique subset of common OPC markers, suggesting that they may not be critical to OPC functioning as previously thought. OPC1 expressed high levels of Clusterin, a gene found upregulated in both Alzheimer's disease and MS, suggesting that these cells may play an active role in these diseases. OPC cluster 2 showed enrichment in multiple proteins involved in ECM organization and cytokine mediated signaling, whereas OPC3 showed significant upregulation of the G protein-coupled receptor (GPR17), a promising target for remyelination therapies (Bonfanti et al., 2020; Parravicini et al., 2020; Angelini et al., 2021) and up-regulation of several genes related to neuronal differentiation and synapse organization.

Mature OLs are heterogeneous as well. This was recently highlighted analyzing more than 5,000 individual cell transcriptomes expressing markers from the OL lineage, isolated from 10 distinct regions of the anterior-posterior and dorsal-ventral axis of the mouse juvenile and adult CNS (Marques et al., 2016). Biclustering analysis, hierarchical clustering, and differential expression analysis led to the identification of six distinct populations of mature OLs (MOL) and two populations of myelin-forming OLs. However, despite some mature OL populations were found enriched in certain regions in juvenile mice, they disappeared in adulthood, suggesting that each brain region optimizes its circuitries by a unique proportion and combination of mature OLs during development. Differentially and equally expressed genes among these populations indicated segregation of MOL1-4, enriched in lipid biosynthesis and myelination genes, from MOL5-6 clusters, enriched for synapse components.

In addition to advancing our understanding of the molecular mechanisms underlying OL functions, single cell omics studies represent a powerful tool for studying the pathogenesis of OL disorders. Single cell transcriptomic analysis of the OL lineage in mice recently allowed to pinpoint an active role of OLs in the paradigmatic case of MS. On one hand, Falcao et al. (2018) discovered that during disease, OLs express genes of the major histocompatibility complex class I and II (MHC-I and -II), and a substantial number of susceptibility genes for MS, so far mainly associated with immune cells. Indeed, they next showed that OPCs can phagocytose and activate memory and effector CD4-positive T cells (Falcao et al., 2018). On the

other hand, Moyon et al. (2015) found that adult OPCs revert to a neonatal-like transcriptome when activated during MS, by increasing innate immune system genes, IL1 $\beta$  and CCL2, and producing cytokines that increase their capacity to migrate to areas of demyelination and thus have an impact on the process of remyelination (Moyon et al., 2015).

One of the most interesting potentials of single-cell omics data analysis is the reconstruction and analysis of developmental trajectories. Single cell transcriptomes can be projected, after dimensionality reduction, in a common analytical space through different algorithms that can define a distance between the single cells coming from a complex tissue based on the similarity of their transcriptomes, thus defining a new temporal concept defined as pseudotime (Haghverdi et al., 2016; Tritschler et al., 2019). This is recently acquiring even a dynamic spin, with the introduction of the concept of RNA velocity, which models the derivative of mRNA abundance through an estimate of spliced vs. unspliced transcripts, and thus infers the direction of transcriptional regulation between cells in the pseudotime trajectory (La Manno et al., 2018; Gorin et al., 2020). Jakel et al. (2019) took advantage of snRNA-seq and Single-cell Near-Neighbor Network Embedding analysis, which places transcriptionally similar clusters close to each other on a tree, to identify new oligodendroglial populations in pseudotime in the human white matter of control subjects and progressive MS patients. Thanks to this approach, OL lineage cells were segregated into 7 oligodendroglial (Oligo 1–6 and imOL, immune oligodendroglia), one OPC and one committed OL precursor clusters (Jakel et al., 2019). Pseudotime analysis identified Oligo6 as an intermediate stage between OPCs and mature OLs, and Oligo1 and Oligo5 as end-states. Interestingly, the transcriptional network of the latter relates cell-cell adhesion and viability, whereas they did not present high expression of myelin genes (as Oligo3 and Oligo4 cluster), suggesting that not all mature OLs maintain a strongly active transcriptional machinery for myelination. The intermediate Oligo6 cells, which are extremely enriched in Opalin, and Oligo1, were found significantly reduced in MS, both in normal-appearing white matter and lesions, adding evidence to the concept that normal-appearing white matter is indeed not “normal” (de Groot et al., 2013; Angelini et al., 2021). On the contrary, Oligo2, Oligo3, Oligo5 and imOLs, which are closely associated with microglia, have been found enriched in MS, suggesting that MS pathophysiology may not be strictly associated with a global failure of differentiation, but rather with a skew in specific subpopulations.

Specifically, single cell analysis has also enabled fundamental advances of our understanding of human OL development, suggesting a higher cellular heterogeneity than previously thought, with defined subpopulations and cell states associated with different stages of lineage progression and functional states (van Bruggen et al., 2017).

As a matter of fact, single-cell transcriptome profiling of cortical lobes and pons during human embryonic and fetal development allowed to capture the developmental trajectory of OL lineage cells until the human mid-fetal stage, revealing that (i) OPCs were more similar than neurons when comparing the anatomical origin (cortex vs. pons), and (ii) four oligo cell clusters were characterized, represented by



proliferating OPCs (PDGFR $\alpha$ <sup>+</sup>/CDK1<sup>+</sup>), OPCs that exited cell cycle (PDGFR $\alpha$ <sup>+</sup>/CDK1<sup>-</sup>), OPCs starting to express APOD (apolipoprotein D), and newly formed OLs (NFOs) expressing MOG, ITPR2, and PDGFA. These cell clusters followed a stepwise developmental path with NFOs enriched by the end of the second trimester. Similar to mice, OLIG1 was expressed throughout OL development, PDGFR $\alpha$  was specifically expressed in OPCs, and myelination proteins such as MBP appeared when OPCs differentiated into OLs (Fan et al., 2020). A further elucidation of the developmental landscape of human early OPC was recently shown, using engineered knock-in hESC-reporter lines, with a tag under the endogenous, OPC-specific, PDGFR $\alpha$  promoter. Time-course sc RNA-sequencing of purified OPCs uncovered transcriptional heterogeneity of PDGFR $\alpha$ <sup>+</sup> OPCs; pseudotime analysis allowed to identify two distinct developmental trajectories for OLs vs. astrocytes differentiation from OPCs, and highlighted mTOR and cholesterol biosynthesis as key signaling pathways in the maturation of OLs from OPCs (Chamling et al., 2021). Moreover, in another study, authors applied sc RNA sequencing to OL-lineage cells isolated from surgical tissues over second-trimester fetal, 2-year-old pediatric, 13-year-old adolescent, and adult donors, thereby covering advanced developmental stages including time of peak myelination. Three distinct cellular subpopulations were identified, including an early OPC group, enriched for the premyelinating fetal group of cells, a late OPC group (l-OPC) and a mature OL group, two cell clusters present in both the pediatric and adult age group. However, single cell analysis revealed that while pediatric vs. adult l-OPCs differ significantly for their molecular features, mature OLs are very similar across age groups (Perlman et al., 2020).

## MODELS TO STUDY HUMAN OLIGODENDROCYTES IN PHYSIOLOGY AND DISEASE

Before the advent of the hiPSCs technology 15 years ago establishing valid and reproducible methods to culture human cells *in vitro* presented major difficulties. In the case of the CNS, these difficulties were amplified by the anatomically difficult access to human brain tissue; studies were therefore almost exclusively limited to either postmortem or “normally appearing” cerebral samples from surgeries. Besides the problem related to the unpredictability of sampling timing, studies performed with such samples suffered from unsurmountable tissue degradation and low reproducibility of results, and their relevance was highly limited to specific pathophysiological conditions. Moreover, in these studies, it was difficult to provide the appropriate control tissue from healthy individuals, nor it was possible to follow the development of a disease in the same patient longitudinally or to predict how his/her brain would respond to therapies. The only alternatives were represented by immortalized human CNS cell lines, or by a very limited repertoire of human primary cell cultures. These two options also have significant issues; in the former, the *in vitro* “immortalization” procedures (that necessarily included the use of oncogenes) can induce

unpredictable changes of cell behavior, whereas, in the latter, human primary cells invariably underwent aging when placed in culture and could rarely be kept in culture for more than a few passages. All these difficulties have severely hampered progress of knowledge in human OL biology.

## Deriving Human Oligodendrocytes From Pluripotent Stem Cells

A first progress was made with the discovery of ESCs, pluripotent cells directly extracted from embryos, which could be committed to neural progenitors and then differentiated *in vitro* into astrocytes, neurons or OLs. Despite human ESCs have been widely used to unravel fundamental questions of OL development and to shed light on the mechanisms driving CNS cell differentiation and behavior, their application has been profoundly limited by ethical concerns associated to their origin, their scarce availability, low reproducibility of the published protocols, also across different hESC lines, and from their low efficiency to generate mature myelinating OLs (Alsanie et al., 2013). In this context, the introduction of the iPSCs technology, namely the possibility of reprogramming somatic cells into pluripotent cells by transduction using a defined set of transcription factors (Teshigawara et al., 2017), and their subsequent *in vitro* differentiation to the desired cell phenotype, greatly improved the molecular and functional characterization of human OLs and, more in general, it opened the unexpected opportunity to study the unique behavior of any cell type in a personalized way, acquiring information on how diseases develop in every single individual, and allowing the identification of the very appropriate cure for that disease in that specific patient (Figure 1E).

Since the discovery of iPSC, several groups have developed specific protocols to obtain hiPSC-derived OLs by adopting protocols previously used to derive hESC-derived OLs. These protocols were exclusively based on different chemically defined media supplemented with mitogens (e.g., bFGF, PDGF and EGF) or differentiation promoting factors (e.g., RA, T3) at proper time intervals in the attempts to recapitulate *in vitro* the developmental cues that occur *in vivo* during oligodendrogenesis (Jang et al., 2011; Pouya et al., 2011). Indeed, sequential induction steps allow to obtain embryoid bodies, to acquire a neural phenotype and finally to drive their differentiation through the oligodendroglial lineage. However, these medium-based protocols have a limited efficiency, require long culture periods (42 days were necessary to obtain immature O4<sup>+</sup> cells from hiPSCs, and other 3–4 weeks to further differentiate them into MBP<sup>+</sup> cells (Figures 2A,B) and have been tested on a reduced number of hiPSCs lines. Based on these earlier studies, more recent papers have developed more robust differentiation protocols (Figures 2C,D), in which, despite the still long differentiation times (70–100 DIV to generate functional OPCs/OLs from hiPSCs) the results were more consistent and were validated on an higher number of lines (Wang et al., 2013; Douvaras et al., 2014; Douvaras and Fossati, 2015).

Novel approaches based on the ectopic over-expression of transcription factors (TFs) completely changed the view of

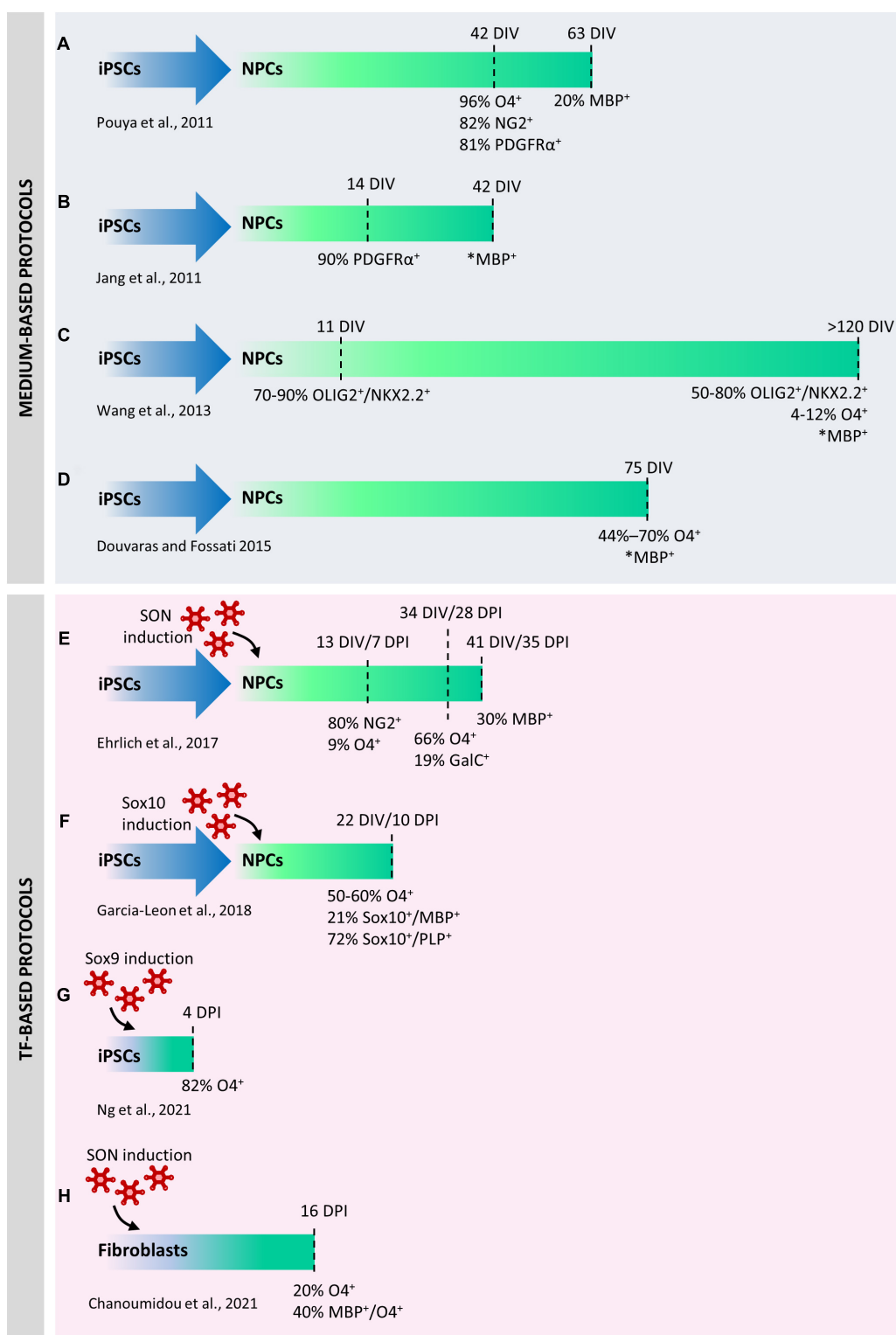


**FIGURE 2 |** Comparison between protocols used to differentiate human induced pluripotent stem cells (iPSCs) into oligodendrocytes (iOLs). The first published protocols were exclusively based on chemically defined media supplemented with mitogens or differentiation promoting factors (**A–D**). Medium-based protocols were progressively refined to increase their robustness and reproducibility in a higher number of lines. Direct differentiation by ectopic expression of selected transcription factors has significantly accelerated the differentiation of neural precursor cells (NPCs) into iOLs and increased the reprogramming efficiency (**E–G**). In one case, direct conversion of iPSCs into iOLs has been described (**H**). DIV, days *in vitro*; DPI, days post induction. \*Percentage not available.

hiPSC reprogramming to OLs. A first protocol published in 2017 was based on the conversion of hiPSC-derived neural progenitor cells (hiNPCs) into hiOLs by transducing them with a “SON construct” consisting in the combination of three typical oligodendroglial TFs, namely SOX10, OLIG2, and NKX6.2 (Ehrlich et al., 2017). This approach yielded up to 70% O4<sup>+</sup> OLs within 28 days of differentiation and 30% of the O4<sup>+</sup> cells further differentiated into mature MBP<sup>+</sup> OLs within seven additional days (**Figure 2E**). In a subsequent study (Garcia-Leon et al., 2018), the expression of SOX10 alone led to the production of approximately 50%–60% of O4<sup>+</sup> cells and 21% of MBP<sup>+</sup> mature hiOLs in 22 days from hiPSC stage (**Figure 2F**). Global gene-expression profiling and RNA-sequencing (RNA-seq) performed on SON- and SOX10-induced O4<sup>+</sup> cells demonstrated that hiOLs generated by TF overexpression resemble primary human adult OLs at the transcriptome level. O4<sup>+</sup> hiOLs were also able to myelinate axons both *in vivo* after transplantation into Shi/Shi Rag2<sup>-/-</sup> dysmyelinating immunodeficient mice and *in vitro* when co-cultured with neurons derived from hiPSCs or nanofibers (Ehrlich et al., 2017; Garcia-Leon et al., 2018, 2020).

Very recently, a seminal paper identified 241 TFs whose ability to induce cell differentiation had never been previously investigated (Ng et al., 2021). Several of them were virtually able to downregulate the expression of pluripotency markers in a few days. Among them, authors demonstrated that ATOH1, NKX3-1, ETV2 and SOX9 were able to directly reprogram hiPSCs into neurons, fibroblasts, vascular endothelial-like cells and OLs, respectively, only in 4 days (**Figure 2G**). In addition to the incomparable speed of the protocol, full cell reprogramming can be achieved in serum-free media without any supplements, soluble factors, or mechanical cues, thus allowing the parallel programming of hiPSCs into two or three defined cell types in the same culture. Four days after Sox9 infection, 82% of the cells were O4<sup>+</sup> and, similarly to what observed with Sox10- and SON-mediated induction, their transcriptomic signature was similar to primary OLs. Parallel induction of OLs and neurons in the same plate demonstrated that these co-cultures could form compact myelin after 30 days.

Finally, another outstanding paper (Chanoumidou et al., 2021) has described a robust and highly reproducible protocol for the direct conversion of human young, adult, and old-aged fibroblasts into OLs by overexpressing the SON construct for 16 days (**Figure 2H**). From 9 days post infection on, directly converted human induced OL-like cells (dc-hiOLs) progressively acquired a branched morphology upon medium enrichment with differentiation factors (including NT3, insulin-like growth factor 1, and dibutyryl cyclic). Flow-cytometry and immunocytochemistry analyses revealed that O4<sup>+</sup> cells were already detectable 8 days post-infection and their number increased progressively until day 16 (as well MBP<sup>+</sup> cells), reaching an average percentage of 20% between cells derived from young, adult and old-aged fibroblast. Similarly to hiOLs derived from the transduction of NPCs with SON (Ehrlich et al., 2017), dc-hiOLs were able to ensheath synthetic nanofibers as well as neuronal processes of hiPSCs derived neurons.

Apart from the different protocol length, the hiOLs generated in these studies showed similar properties and

myelinating capability. The discrepancy in the time needed to achieve an efficient re-programming could be explained by the differences in the infected cells (NPCs vs. iPSCs) and the concomitant different number, type and role of TFs used in the different protocols (three vs. one TF and Sox10 vs. Sox9). Indeed, whereas Sox9 has a central role in the specification of OPCs and continues to be expressed until terminal differentiation, Sox10 appears immediately after specification, and plays an essential function in the induction and execution of the terminal differentiation and myelination program (Reiprich et al., 2017).

The use of TFs in cell reprogramming to generate human OLs is a relatively new approach, and it is likely that different combinations of TFs will enable to further improve the generation of hiOLs not only in terms of yield, but also to reproduce the functional heterogeneity of OLs and their precursors.

## Modeling Human Diseases Using Induced Pluripotent Stem Cells-Derived Oligodendrocytes

The studies described above represented an important proof of concept of the broad and paramount applications of these cells in pre-clinical research and paved the way for their applications in high-throughput screening for drug discovery (see section “Applications of Induced Pluripotent Stem Cells-Derived Cells and Cerebral Organoids to Drug Discovery: Advantages and Challenges”) and in modeling human demyelinating diseases, in particular those with a genetic component. This is the case of the Pelizaeus-Merzbacher disease (PMD), an X-linked leukodystrophy characterized by developmental delay, ataxia, spasticity, and nystagmus. Different signs of the disease are due to a constellation of different mutations in the Proteolipid Protein 1 (PLP1) gene that encodes for one of the major myelin proteins. Aberrant expression or misfolding of this protein leads to its accumulation in OLs and eventually to apoptosis and demyelination in many areas of the CNS (Nobuta et al., 2019).

Despite several efforts have been made to identify a common pathogenic process underlying this disease, no direct links between an individual's unique PLP1 mutation and the etiology or course of their disease have been found.

Immunocytochemistry and flow cytometry analysis on hiOL cultures derived from PMD-hiPSCs (Douvaras et al., 2014; Douvaras and Fossati, 2015) allowed to get insights into cellular and molecular defects underlying the disease (Nevin et al., 2017). The hiOPC number was strikingly reduced in most cultures, suggesting that, at least in a subset of individuals, defects at the OPC stage anticipate dysmyelination. Moreover, despite OPC deficits, most PMD cultures (10 out of 12) were still able to produce O4<sup>+</sup> OLs, but these immature cells were noticeably defective in process extension and branching. In the cultures in which PLP was detectable, the accumulation was always in the ER (Nevin et al., 2017). Different missense mutations showed accumulation and mis-localization of PLP to the ER, increased ER stress, apoptosis and decreased myelination,

consistent with the different level of clinical severity of the subjects (Numasawa-Kuroiwa et al., 2014).

Mutant iOLs also showed lipid peroxidation, abnormal iron metabolism, and hypersensitivity to free iron (Nobuta et al., 2019) when compared to line-specific isogenic controls obtained by correcting the PLP1<sup>G74E</sup> mutation in patient's iPSCs, thus suggesting a causal link between ferroptosis and PMD pathogenesis. This hypothesis was further confirmed by the observation that treatment with deferoxamine (DFO), deferiprone (DFP), two Food and Drug Administration (FDA)-approved iron chelators, and apotransferrin (apo-TF) rescued mutant OL apoptosis, survival and differentiation *in vitro*. Human mutant O4<sup>+</sup> cells pre-treated with apo-TF or DFO during *in vitro* differentiation and transplanted into the cerebellum of immunocompromised Shi mice or placed on human fetal brain slice cultures showed also a substantially improved differentiation (Nobuta et al., 2019). The efficacy of DFP in enhancing OL survival and promoting new myelin formation was finally demonstrated in Jimpy mice, a PMD mouse model that harbors a Plp1 point mutation and causes a very aggressive disease.

Thus, this article highlighted an additional cardinal feature of hiOLs, namely their translational importance in paving the way to the discovery of new effective drugs for still incurable CNS diseases.

The iPSC technology has been instrumental to study OL behavior also in non-genetic diseases, such as MS. Myelin-forming OLs can be derived *via* hiPSCs from both relapsing-remitting (RRMS) (Song et al., 2012) and primary progressive (PPMS) MS patients. However, their maturation and myelination capabilities do not seem to be significantly different from those of healthy OLs (Song et al., 2012; Douvaras et al., 2014; Garcia-Leon et al., 2018; Mozafari et al., 2020; Starost et al., 2020). Conversely, supernatants from both polarized human microglia or activated peripheral blood mononuclear cells (PBMCs) significantly inhibited hiOL differentiation, highlighting a role for immune regulators as extrinsic key players in MS pathogenesis and potentially responsible of repair failure (Hess et al., 2020; Starost et al., 2020). In addition, hiPSC-NPCs from patients with PPMS were less able to provide neuroprotection to myelin injury or support OPC differentiation *in vitro* compared to control iPSC-NPCs, probably due to their aberrant cellular senescence (Nicaise et al., 2017, 2019). Since cellular senescence can be associated with a proinflammatory and paracrine effect exerted by the cells on surrounding tissue, this can be a further extrinsic mechanism contributing to the not permissive environment within white matter lesions, leading to remyelination impairment.

Thanks to hiPSCs, it has been possible to highlight OL involvement in diseases such as amyotrophic lateral sclerosis (ALS), schizophrenia, and frontotemporal dementia with Parkinsonism, in which demyelination is not traditionally a key feature (Chanoumidou et al., 2020).

Amyotrophic lateral sclerosis is characterized by the progressive loss of motor neurons (MNs) in the brain cortex and spinal cord, leading to muscle atrophy and death by respiratory paralysis within 3–5 years after the first symptoms (Brown and Al-Chalabi, 2017). Recent studies on mouse models of ALS have

shown that OLs are also involved in the non-cell-autonomous nature of the disease contributing to disease progression by triggering or aggravating damage to MNs (Kang et al., 2013; Philips et al., 2013) [for extensive review, see Raffaele et al. (2021a)]. Analysis on hiOLs derived from human sporadic and familial ALS patients carrying mutations in SOD1, TARDBP, C9orf72, and FIG4 allowed to demonstrate that, while these cells were able to differentiate and mature similarly to matched controls, they exerted toxic effects on mouse motor neurons *in vitro*, partially due to defective lactate production and release by hiOLs. However, addition of lactate to cocultures only partially reversed the ALS-hiOLs mediated toxicity, suggesting that MN survival also requires additional insoluble factors and/or cell-to-cell contacts (Ferraiuolo et al., 2016).

## BRAIN ORGANIDS AS NEW EXPERIMENTAL SYSTEMS FOR *IN VITRO* MYELINATION STUDIES

The interest for recapitulating *in vitro* the complexity of human brain development ushered the development of organoids, 3D structures grown from stem cells and consisting of organ-specific cell types that self-organizes and can be maintained in culture over extended periods of time (Di Lullo and Kriegstein, 2017; Lopez-Tobon et al., 2020). Brain organoids can be derived from both pluripotent stem cells, ESCs and iPSCs. Starting from the pluripotent state, most of the organoid protocols are characterized by the generation of embryoid bodies (EBs) as a first step: monolayers of pluripotent stem cells growing on a matrix are dissociated at single cell level, and a precise number is replated into ultra-low attachment wells. This enables the cells to aggregate and form EBs that grow in suspension and are subsequently patterned toward the lineages of differentiation of interest. There are several approaches that aim at recapitulating different regions and/or complexity of the CNS development, each of which is better suited for addressing specific biological questions. However, there are common aspects to all brain organoid protocols, which include (i) the formation of self-organizing structures, in particular rosettes which resemble the embryonic stratification of the epithelium of the neural tube with apico-basal polarity and are subdivided into proliferative and differentiating zones, (ii) the generation of different subpopulations of progenitors usually absent in the 2D counterparts and (iii) a considerable degree of basic compartmentalization at the extracellular level that includes the production of their own rudimentary ECM (Kelava and Lancaster, 2016; Quadrato et al., 2016; Di Lullo and Kriegstein, 2017; Giandomenico and Lancaster, 2017; Kyrousi and Cappello, 2020).

Different brain organoids can be on the other hand very different in their specificity to recapitulate either whole brain or specific brain regions such as cortex, hippocampus, thalamus or hypothalamus (Qian et al., 2016; Birey et al., 2017; Lancaster et al., 2017; Xiang et al., 2019; Ozaki et al., 2021). In case of cerebral cortex, it is possible to differentiate the most dorsal part of the forebrain (the pallium), that gives rise to glutamatergic



neurons, or the ventral one (the subpallium) that gives origin to GABAergic interneurons (Bagley et al., 2017; Birey et al., 2017). In this way, 3D differentiation of hiPSCs into cortical brain organoids can recapitulate the physiological emergence of the six distinctive neuronal layers of the cortex, along with astrocytes (Sloan et al., 2017), and the outer radial glia subset of progenitors that underlies the specific expansion of the human neocortex (Bershteyn et al., 2017; Pollen et al., 2019). Brain organoids reproduce the cell diversity of human brain, they show patterns of electrical activities whose oscillations resemble the prenatal human electroencephalography (Trujillo et al., 2019), and, when transplanted in mouse, they establish functional connections with different regions of the host brain (Mansour et al., 2018) and innervate dissected mouse spinal cord inducing muscle contraction (Giandomenico et al., 2019).

Brain organoids have been used to study the molecular basis of human corticogenesis (Lopez-Tobon et al., 2019), to develop new disease models (Birey et al., 2017; Caporale and Testa, 2019; Klaus et al., 2019; Cheroni et al., 2020; Khan et al., 2020), and to study evolution (Kanton et al., 2019; Pollen et al., 2019) usually focusing on neurons and on astrocytes. The OL lineage remained underrepresented because, up to 2018, no protocol has yielded reproducible generation and maturation of OLs. Despite the neural origin of OPCs (Naruse et al., 2017), organoids that are patterned toward the dorsal pallium do not generate OPCs in a robust way, and, consequently, they have never been used to study myelination. This paradigm changed after the optimization of protocols in which cortical brain organoids were patterned toward the dorsal telencephalon (Pasca et al., 2015), through timely exposure to platelet-derived growth factor AA (PDGF-AA) and insulin-like growth factor 1 (IGF-1) to drive the expansion of native OPC populations, followed by thyroid hormone (T3) to induce OL differentiation (Madhavan et al., 2018; Marton et al., 2019). All these protocols (**Figures 3A,B**) were validated across different hiPSC lines and characterized at the level of single cell omics to identify the stages and trajectories of OL differentiation, showing similar expression patterns compared to human primary cells.

In the rodent brain, the OL first wave of differentiation derives from the ventral regions, but dorsal-derived OLs are the ones required for proper myelination in the brain cortex. The analogous developmental processes and timing in humans was unknown until recently, when Kim et al. (2019) took advantage of OLIG2-GFP knock-in hiPSC reporter lines to follow oligodendrogenesis in forebrain organoids patterned toward the ventral and the dorsal pallium (**Figure 3C**). With this approach, they identified distinct temporal expression patterns in the two lineages, even though OLs could be differentiated in both systems, after neuronal maturation. When assembling ventral and dorsal organoids, dorsally derived oligodendroglial cells outcompete ventrally derived oligodendroglia and become dominant after long-term culture (Kim et al., 2019). These results are in line with recent observations about the specific impact of ventral OPCs on the migration and maturation of mouse cortical interneurons (Lepiemme et al., 2021). These pioneering studies demonstrated that generating brain organoids with myelinating OLs is indeed possible, however, they require

very long protocols (from 110 to 210 days) to produce myelinated fibers. Interestingly, it has been shown that pre-patterning of NSCs with FGF2, PDGF-AA, and purmorphamine, leads to the production of OLIG2 and NKX2.2-expressing neurospheres (**Figure 3D**) and facilitates glial specification during organoid development (Yun et al., 2020). These OPC-derived spheroids were used to validate the effect of benzotropine and miconazole, two promyelinating drugs *in vivo* (Deshmukh et al., 2013). Both drugs dramatically enhanced the MBP<sup>+</sup>/SOX10<sup>+</sup> populations compared to DMSO-treated organoids after 12 weeks in culture, while miconazole also showed a 15% increase in terms of myelinating OLs compared to T3-treated organoids. Recently, Shaker et al. (2021) developed a protocol to generate brain organoids containing OLs capable of myelinate endogenously produced cortical neurons in only 42 days (**Figure 3E**), through the exposure to a cocktail of growth factors and small molecules. This contains T3, neurotrophin NT3, hepatocytes growth factor, IGF-1, and PDGF-AA to pattern the differentiation toward the oligodendroglial lineage and to foster the proliferation of OPCs, B27 without vitamin A and cAMP to drive the maturation of OPCs to myelinating OL, biotin and BME to increase the survival of the maturing OLs, as well as N2, insulin, and non-essential amino acids to promote the co-differentiation of neurons and astrocytes (Shaker et al., 2021).

As mentioned above, regional identity of developing OLs is another important factor that may influence the timing and the myelinating properties of OLs during organoid formation. During development, MBP<sup>+</sup> forebrain-derived OLs emerge at gestational week 17–20, but myelination starts several months later, in the postnatal phase (Jakovcevski et al., 2009). In contrast, the emergence of ventral spinal cord-derived OLs occurs much earlier, around gestational week 10, and is followed by the appearance of myelinated fibers 4 weeks later (Weidenheim et al., 1993). Similarly, organoids generated from the ventral spinal cord showed earlier myelination (**Figure 3F**). Moreover, electron microscopy revealed that in these organoids, called “myelinoids,” myelin thickness, compaction and assembly at the paranodal junction are comparable to those observed *in vivo* (James et al., 2021), whereas forebrain-patterned organoids demonstrated sparse myelination and lacked the typical architecture of myelinated axons. These parameters are crucial to model myelin physiology and to recapitulate myelin function. Myelinoids were also used to investigate the concept of adaptive myelination, according to which OLs modulate myelin structure in response to changes in neuronal activity. Myelinoids chronically treated with tetanus toxin, which blocks synaptic vesicles release, showed a 20% reduction in the number of sheaths made by individual OLs and a 38% reduction in myelin volume. Due to their spinal origin, myelinoids may not be optimal to recapitulate myelination kinetics or neurological conditions typical of the brain, but, indeed, they represent an important proof-of-concept in the field.

As shown for iPSCs, human brain organoids can be exploited to study cellular pathology and dysfunction associated to genetic mutations, with the advantage of having a complex architecture. Oligocortical spheroids generated from iPSC lines with different PMD-related mutations (PLP1 deletion, duplication and point-mutation) have shown PLP1 levels and PLP1 localization

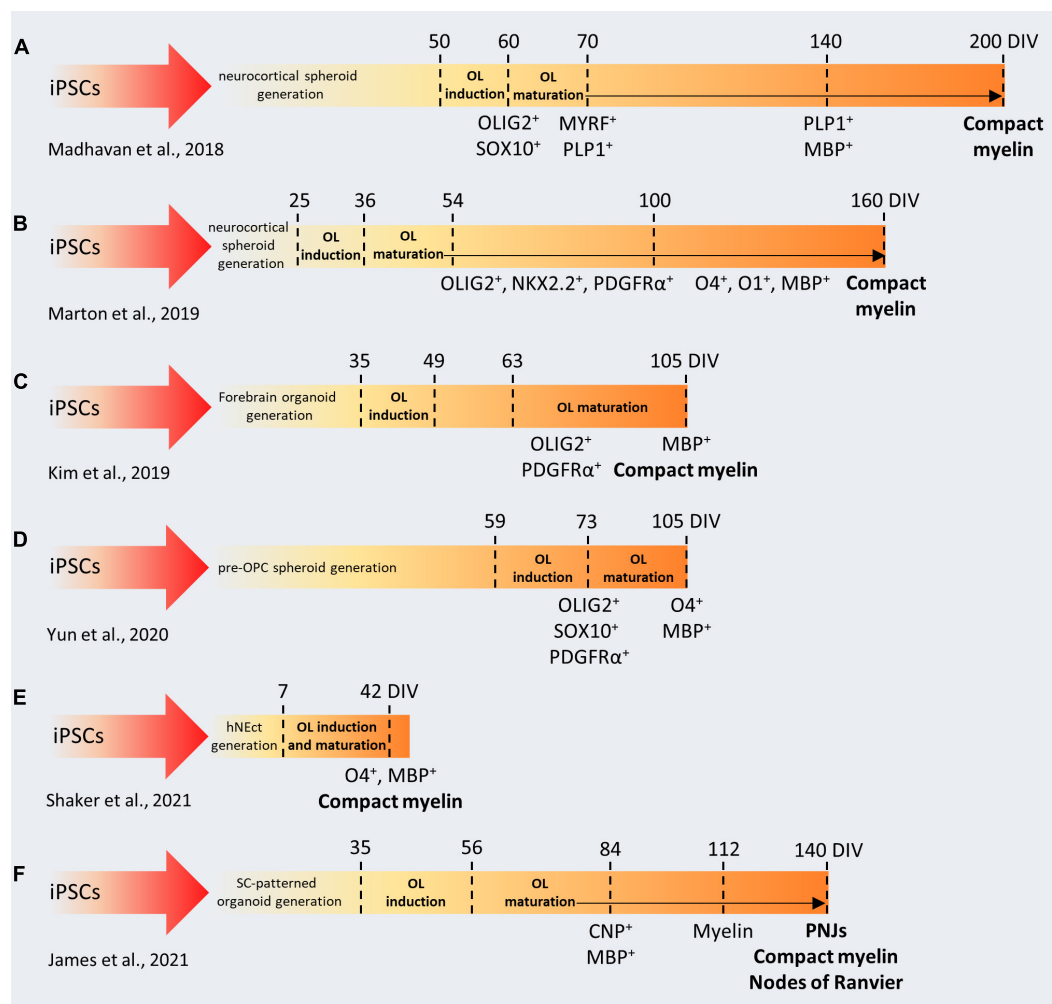


**FIGURE 3 |** Comparison between protocols used to generate brain organoids containing myelinating oligodendrocytes. (A–F) In the first phase of each protocol, iPSCs are cultured and patterned to generate 3D brain-like structures (forebrain, spinal cord, neuroectoderm). Then, OL induction and maturation is achieved by using specific soluble factors (e.g., PDGF-AA, IGF1, FGF2, T3). iPSCs, induced pluripotent stem cells; DIV, days *in vitro*; OL, oligodendrocyte; OPC, oligodendrocyte precursor cell; SC, spinal cord; hNect, human neuroectodermal layer; PNJs, paranodal axoglial junctions.

correlated with the different genetic status of the donors and alteration in the number of differentiating OLs (Madhavan et al., 2018). Interestingly, CRISPR correction of the PLP1 point mutation in iPSCs prior to spheroid generation restored PLP1 mobilization and OL number. OLs in brain organoids are also susceptible to lyssolecithin (Marton et al., 2019), suggesting that they can be used to study OL loss or injury in disorders affecting CNS myelination.

The examples described above indicate that, although the application of brain organoids to myelination studies is still in its infancy, further optimization of this technology could allow the development of totally new experimental platforms to better understand human myelin biology, to investigate the basis of adaptive myelination, to generate new *in vitro* demyelination/remyelination models, to study patient-specific genetic background as an intrinsic trigger of myelin dysfunction and to perform drug screening (Figure 1F).

## APPLICATIONS OF INDUCED PLURIPOTENT STEM CELLS-DERIVED CELLS AND CEREBRAL ORGANOIDS TO DRUG DISCOVERY: ADVANTAGES AND CHALLENGES

Due to their capability to recapitulate several pathophysiological aspects of the bona fide human cells, one of the most obvious applications of hiOLs has been their use as a tool for phenotypic drug screening, thus allowing to validate data previously obtained on either rodent OLs or more limited human OL models. For example, Ehrlich et al. (2017) cultured hiOL in the presence of miconazole, clobetasol, benztropine, indometacin, clemastine, and oxybutynin, six FDA-approved drugs used for the treatment of various diseases and acting with different mechanisms of actions, that have been recently described to

promote differentiation or myelination of rodent OLs, thus highlighting their potential in drug repositioning (Deshmukh et al., 2013; Mei et al., 2014; Najm et al., 2015). However, only miconazole, clobetasol and benztropine did increase the percentage of MBP<sup>+</sup> mature hiOLs after 21 days in culture, suggesting that species-specific differences could be relevant for drug screening (Ehrlich et al., 2017). Accordingly, benztropine and clemastine enhanced the terminal differentiation and maturation also of hiOLs derived from direct conversion of fibroblast with SON construct, while miconazole showed a milder but still significant effect (Chanoumidou et al., 2021). High-throughput screening (HTS) applied to human iPSC-derived neurons and OLs co-culture also demonstrated enhanced myelination after treatment with miconazole, clobetasol and pranlukast (Garcia-Leon et al., 2018). Interestingly, drugs previously shown to promote oligodendroglial differentiation failed to restore impaired hiOL differentiation induced by PBMC supernatants, whereas immunomodulatory treatments on PBMCs partly restored hiOL differentiation, indicating that more complex models are needed to mimic the inflammatory environment typical of MS lesions (Starost et al., 2020).

Thus, one first conclusion that can be drawn from these data is that drug screening on human iOL (and more in general on human iPSC-derived cells) can help surmounting species related differences in pharmacological responses, which is not a trivial issue.

Second, generating patient-specific terminally differentiated cell types offers the possibility to conduct *in vitro* “clinical trials” (McNeish et al., 2015), in which drugs can be tested for both efficacy and toxicity. This can guide the choice of the most appropriate treatment for each patient and overcome problems related to individual susceptibility to develop side effects, although, of course, caution should be placed on the issue that differentiated iPSC-derived cell systems cannot reveal propensity to side effects related to individual drug metabolism and excretion. Moreover, *in vitro* clinical trials can lead to improved patients’ stratification and lower compound attrition rates. Certainly, the availability of a model allowing “personalized” drug screening will greatly facilitate the drug discovery process that normally takes more than 10 years to go from the discovery of a new molecule to its approval.

Third, besides the development and screening of new drugs, iPSC-based models can be used to identify already marketed drugs (or drugs for which safety studies on humans are already available) to be repurposed for the treatment of orphan diseases with high medical need. As an example, ezogabine, an anti-epileptic drug, showed efficacy in iPSC-derived motor neurons to model ALS, leading to the subsequent initiation of clinical trials (McNeish et al., 2015).

However, there are still issues to be solved. The first is related to the molecular maturity of iPSC-derived cells, which exhibit immature characteristics comparable to embryonal or fetal cells. This is particularly important for modeling late-onset diseases, where maturity is a critical aspect, like Alzheimer’s and Parkinson’s disease. In order to simulate aging *in vitro*, scientists are tackling this problem using chemical and pharmacological approaches reproducing some of the features typical of aged

tissues, for example by employing specific culture medium formulations inducing mitochondrial stress, inhibiting protein catabolism, or overexpressing progerin, a truncated version of the premature aging protein lamin A (Doss and Sachinidis, 2019).

A second issue is that, inevitably, drug screening performed on iPSC-derived OLs does not consider the contribution of other cell types to drug response (see also above) raising the need of setting up more complex models, where all the cell types of the living brain are present and interact with each other.

In this respect, cerebral organoids (COs) show substantial potential, and, as underlined above, accumulating data are validating organoids as a reliable model. Recently, a human CO model of prion disease was used for evaluating the effectiveness of putative drugs in inhibiting prion accumulation (Groverman et al., 2021). Another recent study generated 1,300 iPSC-derived COs from 11 sporadic AD patients to identify FDA-approved drugs as candidates for drug repositioning (Park et al., 2021). Cocultures of motor neuron spheroids from a patient with sporadic ALS and 3D muscle fiber bundles were used to reproduce ALS pathology and to test the efficacy of candidate drugs already used in phase 1 and 2 clinical trials (Osaki et al., 2018).

However, there still remain several challenges that are currently being addressed by academic and industrial researchers in order to fully exploit this technology to the discovery of new CNS drugs, including new myelinating therapeutic agents (Salick et al., 2021). Here, we summarize some of them.

A first issue relates to the need of generating *automated systems* to overcome the very high experimental variability between different cerebral organoids preparations. There is a need to develop fully integrated end-to-end cell culture systems (incubator and imaging platforms) that can maintain, passage and differentiate cells to generate uniform cerebral organoids in an automated manner to reduce the variability introduced by multiple human hands. A second issue relates to the need of *high resolution and potent imaging systems*, which, differently from monolayered cells, are essential in the case of organoids, both to check their expected 3D conformation and to assess the effects of drugs and other treatments on organoids’ 3D organization. Traditional fluorescence microscopes are not suited for performing high resolution imaging of 3D samples deeper than few micrometers, mainly due to the obscuring effects of light scatter. This limitation can be overcome by different strategies: (i) clearing techniques have been developed to ensure a uniform density of the sample (through a combination of delipidation, decolourization, decalcification, and refractive index matching) so that all wavelengths of light can pass through the tissue (Richardson and Lichtman, 2015; Ueda et al., 2020). These approaches are often combined with light sheet microscopes for rapid, high-resolution imaging of large volumes, indeed they have been successfully applied to organoids, achieving imaging of large and thick samples with subcellular resolution (Boutin and Hoffman-Kim, 2015; Dekkers et al., 2019; Albanese et al., 2020). However, they are not suited for live imaging applications that are essential to study key neurodevelopmental processes; (ii) computational methods such as 3D deconvolution can assist 3D resolution, but there are still difficulties in deconvolving complex samples because widefield microscopy deconvolution

provides limited penetration due to high background and light scattering (McNally et al., 1999); (iii) spinning disk confocal microscopy and resonant scanning microscopy have significantly improved point scanning microscopy, but while such systems enable to observe thick living samples at increased depth and speed, they all result in substantial phototoxicity, due to out-of-focus illumination (Jemielita et al., 2013); (iv) multiphoton excitation allows to acquire deep planes from thick samples with reduced phototoxicity because there is no absorption above and below the plane of focus and indeed is considered the best solution for imaging deep layers in the organoids when clearing cannot be performed (Dekkers et al., 2019). Deleterious effects are occasionally observed with two-photon excitation of certain fluorophores and imaging is relatively time consuming and may lead to photobleaching since it is still based on a point scanning approach.

Thus, proper microscopy systems maintaining high resolution, low phototoxicity and photobleaching, while increasing speed, depth, and size of the field of view, still need to be developed.

Finally, the *scale of experiments* required for high-throughput drug screening is an additional challenge for the cerebral organoid field. Biotech and pharma industry are just starting to explore this new area (Shah et al., 2020), but work is still ongoing to uncover the full potential of cerebral organoids in target and drug discovery.

## CONCLUSION

Myelination is a crucial process in vertebrates and its complexity has made the elucidation of the underlying mechanisms extremely challenging. The discoveries in the physiology of myelination have been possible only thanks to the advances in the *in vitro* technologies. The new frontiers are now humanized models, increasingly reproducing human physiology and pathology. However, human iPSCs are only a starting

point. Indeed, hiOLs are sensitive to the environment, and their behavior can be influenced by the cells and cell structures they take contact with, including glia, vessels, axons, ECM, by cell culture media and growth factors, and by the mechanical properties of the culture supports. Brain organoids recapitulate the developmental trajectories of neural cells, circuits, and connection and are likely to become a new powerful tool to study myelination, demyelination and remyelination dynamics in the next few years. Myelinating/demyelinating models based on human iPSC-derived cells should be consolidated to become a new gold standard and progressively reduce the use of animal models. The development of new technologies for data analysis, automation, miniaturization and HTS will pave the way for new reliable drug screening platforms.

## AUTHOR CONTRIBUTIONS

DM and MB prepared the figures. DL combined the contributions and revised the manuscript. All authors contributed to conception and writing of the present review and read, revised, and approved the submitted version.

## FUNDING

This research was supported by Italian Ministry of University and Research (MUR); PRIN - Progetti di Ricerca di Interesse Nazionale (MA; Grant no. 2017NSXP8J); FISM—Fondazione Italiana Sclerosi Multipla—cod. 2017/R/1, the EU Horizon 2020 ENDpoiNTs project (GT; Grant no. 825759), the University of Milan and “Fondazione Romeo ed Enrica Invernizzi”—sponsored Human Organoid Models Integrative Center (HOMIC) (GT and NC), and financed or co-financed with the “5 per mille” public funding to MA. MB is currently supported by a fellowship from the Italian Multiple Sclerosis Foundation (FISM; 2019\_BS\_006).

## REFERENCES

- Albanese, A., Swaney, J. M., Yun, D. H., Evans, N. B., Antonucci, J. M., Velasco, S., et al. (2020). Multiscale 3D phenotyping of human cerebral organoids. *Sci. Rep.* 10:21487. doi: 10.1038/s41598-020-78130-7
- Alsanie, W. F., Niclis, J. C., and Petratos, S. (2013). Human embryonic stem cell-derived oligodendrocytes: protocols and perspectives. *Stem Cells Dev.* 22, 2459–2476. doi: 10.1089/scd.2012.0520
- Angelini, J., Marangon, D., Raffaele, S., Lecca, D., and Abbracchio, M. P. (2021). The Distribution of GPR17-Expressing Cells Correlates with White Matter Inflammation Status in Brain Tissues of Multiple Sclerosis Patients. *Int. J. Mol. Sci.* 22:4574. doi: 10.3390/ijms22094574
- Arani, A., Murphy, M. C., Glaser, K. J., Manduca, A., Lake, D. S., Kruse, S. A., et al. (2015). Measuring the effects of aging and sex on regional brain stiffness with MR elastography in healthy older adults. *Neuroimage* 111, 59–64. doi: 10.1016/j.neuroimage.2015.02.016
- Arnold, S. E., and Trojanowski, J. Q. (1996). Human fetal hippocampal development: I. Cytoarchitecture, myeloarchitecture, and neuronal morphologic features. *J. Comp. Neurol.* 367, 274–292. doi: 10.1002/(SICI)1096-9861(19960401)367:2<274::AID-CNE9<3.0.CO;2-2
- Azevedo, M. M., Domingues, H. S., Cordelieres, F. P., Sampaio, P., Seixas, A. I., and Relvas, J. B. (2018). Jmy regulates oligodendrocyte differentiation via modulation of actin cytoskeleton dynamics. *Glia* 66, 1826–1844. doi: 10.1002/glia.23342
- Bagley, J. A., Reumann, D., Bian, S., Levi-Strauss, J., and Knoblich, J. A. (2017). Fused cerebral organoids model interactions between brain regions. *Nat. Methods* 14, 743–751. doi: 10.1038/nmeth.4304
- Baltan, S., Jawaid, S. S., Chomyk, A. M., Kidd, G. J., Chen, J., Battapady, H. D., et al. (2021). Neuronal hibernation following hippocampal demyelination. *Acta Neuropathol. Commun.* 9:34. doi: 10.1186/s40478-021-01130-9
- Baumann, N., and Pham-Dinh, D. (2001). Biology of oligodendrocyte and myelin in the mammalian central nervous system. *Physiol. Rev.* 81, 871–927. doi: 10.1152/physrev.2001.81.2.871
- Bechler, M. E., Byrne, L., and Ffrench-Constant, C. (2015). CNS Myelin Sheath Lengths Are an Intrinsic Property of Oligodendrocytes. *Curr. Biol.* 25, 2411–2416. doi: 10.1016/j.cub.2015.07.056
- Beiter, R. M., Fernandez-Castaneda, A., Rivet-Noor, C., Merchak, A., Bai, R., Slogar, E., et al. (2020). Evidence for oligodendrocyte progenitor cell heterogeneity in the adult mouse brain. *bioRxiv* [preprint]. doi: 10.1101/2020.03.06.981373
- Bershteyn, M., Nowakowski, T. J., Pollen, A. A., Di Lullo, E., Nene, A., Wynshaw-Boris, A., et al. (2017). Human iPSC-Derived Cerebral Organoids Model Cellular Features of Lissencephaly and Reveal Prolonged Mitosis of Outer Radial Glia. *Cell Stem Cell* 20, 435–449.e4. doi: 10.1016/j.stem.2016.12.007



- Birey, F., Andersen, J., Makinson, C. D., Islam, S., Wei, W., Huber, N., et al. (2017). Assembly of functionally integrated human forebrain spheroids. *Nature* 545, 54–59. doi: 10.1038/nature22330
- Bonfanti, E., Bonifacio, T., Raffaele, S., Milanese, M., Morgante, E., Bonanno, G., et al. (2020). Abnormal Upregulation of GPR17 Receptor Contributes to Oligodendrocyte Dysfunction in SOD1 G93A Mice. *Int. J. Mol. Sci.* 21:2395. doi: 10.3390/ijms21072395
- Bornstein, M. B., and Murray, M. R. (1958). Serial observations on patterns of growth, myelin formation, maintenance and degeneration in cultures of newborn rat and kitten cerebellum. *J. Biophys. Biochem. Cytol.* 4, 499–504. doi: 10.1083/jcb.4.5.499
- Boullenger, A. I. (2016). The history of myelin. *Exp. Neurol.* 283, 431–445. doi: 10.1016/j.expneurol.2016.06.005
- Boutin, M. E., and Hoffman-Kim, D. (2015). Application and assessment of optical clearing methods for imaging of tissue-engineered neural stem cell spheres. *Tissue Eng. Part C Methods* 21, 292–302. doi: 10.1089/ten.TEC.2014.0296
- Brown, R. H., and Al-Chalabi, A. (2017). Amyotrophic Lateral Sclerosis. *N. Engl. J. Med.* 377, 162–172. doi: 10.1056/NEJMra1603471
- Caporale, N., and Testa, G. (2019). “At the Intersection of Epigenetics and Regeneration: An Analysis of the Experimental Outlook of Organoid Technology,” in *Epigenetics and Regeneration*, ed. D. Palacios (Amsterdam: Elsevier), 385–402.
- Chamling, X., Kallman, A., Fang, W., Berlinicke, C. A., Mertz, J. L., Devkota, P., et al. (2021). Single-cell transcriptomic reveals molecular diversity and developmental heterogeneity of human stem cell-derived oligodendrocyte lineage cells. *Nat. Commun.* 12:652. doi: 10.1038/s41467-021-20892-3
- Chan, J. R., Watkins, T. A., Cosgaya, J. M., Zhang, C., Chen, L., Reichardt, L. F., et al. (2004). NGF controls axonal receptivity to myelination by Schwann cells or oligodendrocytes. *Neuron* 43, 183–191. doi: 10.1016/j.neuron.2004.06.024
- Chanoumidou, K., Hernandez-Rodriguez, B., Windener, F., Thomas, C., Stehling, M., Mozafari, S., et al. (2021). One-step Reprogramming of Human Fibroblasts into Oligodendrocyte-like Cells by SOX10, OLIG2, and NKX6.2. *Stem Cell Rep.* 16, 771–783. doi: 10.1016/j.stemcr.2021.03.001
- Chanoumidou, K., Mozafari, S., Baron-Van Evercooren, A., and Kuhlmann, T. (2020). Stem cell derived oligodendrocytes to study myelin diseases. *Glia* 68, 705–720. doi: 10.1002/glia.23733
- Chappell, L., Russell, A. J. C., and Voet, T. (2018). Single-Cell (Multi)omics Technologies. *Annu. Rev. Genomics Hum. Genet.* 19, 15–41. doi: 10.1146/annurev-genom-091416-035324
- Cheroni, C., Caporale, N., and Testa, G. (2020). Autism spectrum disorder at the crossroad between genes and environment: contributions, convergences, and interactions in ASD developmental pathophysiology. *Mol. Autism* 11:69. doi: 10.1186/s13229-020-00370-1
- de Groot, M., Verhaaren, B. F., de Boer, R., Klein, S., Hofman, A., van der Lugt, A., et al. (2013). Changes in normal-appearing white matter precede development of white matter lesions. *Stroke* 44, 1037–1042. doi: 10.1161/STROKEAHA.112.680223
- Dekkers, J. F., Alieva, M., Wellens, L. M., Ariese, H. C. R., Jamieson, P. R., Vonk, A. M., et al. (2019). High-resolution 3D imaging of fixed and cleared organoids. *Nat. Protoc.* 14, 1756–1771. doi: 10.1038/s41596-019-0160-8
- Deshmukh, V. A., Tardif, V., Lyssiotis, C. A., Green, C. C., Kerman, B., Kim, H. J., et al. (2013). A regenerative approach to the treatment of multiple sclerosis. *Nature* 502, 327–332. doi: 10.1038/nature12647
- Di Lullo, E., and Kriegstein, A. R. (2017). The use of brain organoids to investigate neural development and disease. *Nat. Rev. Neurosci.* 18, 573–584. doi: 10.1038/nrn.2017.107
- Dietz, K. C., Polanco, J. J., Pol, S. U., and Sim, F. J. (2016). Targeting human oligodendrocyte progenitors for myelin repair. *Exp. Neurol.* 283, 489–500. doi: 10.1016/j.expneurol.2016.03.017
- Diez-Revelta, N., Higuero, A. M., Velasco, S., Penas-de-la-Iglesia, M., Gabius, H. J., and Abad-Rodriguez, J. (2017). Neurons define non-myelinated axon segments by the regulation of galectin-4-containing axon membrane domains. *Sci. Rep.* 7:12246. doi: 10.1038/s41598-017-12295-6
- Doss, M. X., and Sachinidis, A. (2019). Current Challenges of iPSC-Based Disease Modeling and Therapeutic Implications. *Cells* 8:403. doi: 10.3390/cells8050403
- Douvaras, P., and Fossati, V. (2015). Generation and isolation of oligodendrocyte progenitor cells from human pluripotent stem cells. *Nat. Protoc.* 10, 1143–1154. doi: 10.1038/nprot.2015.075
- Douvaras, P., Wang, J., Zimmer, M., Hanchuk, S., O’Bara, M. A., Sadiq, S., et al. (2014). Efficient generation of myelinating oligodendrocytes from primary progressive multiple sclerosis patients by induced pluripotent stem cells. *Stem Cell Rep.* 3, 250–259. doi: 10.1016/j.stemcr.2014.06.012
- Drenth, G. S., Backes, W. H., Aldenkamp, A. P., Vermeulen, R. J., Klinkenberg, S., and Jansen, J. F. A. (2020). On the merits of non-invasive myelin imaging in epilepsy, a literature review. *J. Neurosci. Methods* 338:108687. doi: 10.1016/j.jneumeth.2020.108687
- Ehrlich, M., Mozafari, S., Glatza, M., Starost, L., Velychko, S., Hallmann, A. L., et al. (2017). Rapid and efficient generation of oligodendrocytes from human induced pluripotent stem cells using transcription factors. *Proc. Natl. Acad. Sci. U. S. A.* 114, E2243–E2252. doi: 10.1073/pnas.1614412114
- Espinosa-Hoyos, D., Jagielska, A., Homan, K. A., Du, H., Busbee, T., Anderson, D. G., et al. (2018). Engineered 3D-printed artificial axons. *Sci. Rep.* 8:478. doi: 10.1038/s41598-017-18744-6
- Falcao, A. M., van Bruggen, D., Marques, S., Meijer, M., Jakel, S., Agirre, E., et al. (2018). Disease-specific oligodendrocyte lineage cells arise in multiple sclerosis. *Nat. Med.* 24, 1837–1844. doi: 10.1038/s41591-018-0236-y
- Fan, X., Fu, Y., Zhou, X., Sun, L., Yang, M., Wang, M., et al. (2020). Single-cell transcriptome analysis reveals cell lineage specification in temporal-spatial patterns in human cortical development. *Sci. Adv.* 6:eaa2978. doi: 10.1126/sciadv.aaz2978
- Feldmann, A., Amphornrat, J., Schonherr, M., Winterstein, C., Mobius, W., Ruhwedel, T., et al. (2011). Transport of the major myelin proteolipid protein is directed by VAMP3 and VAMP7. *J. Neurosci.* 31, 5659–5672. doi: 10.1523/JNEUROSCI.6638-10.2011
- Fernandez-Castaneda, A., Chappell, M. S., Rosen, D. A., Seki, S. M., Beiter, R. M., Johanson, D. M., et al. (2020). The active contribution of OPCs to neuroinflammation is mediated by LRP1. *Acta Neuropathol.* 139, 365–382. doi: 10.1007/s00401-019-02073-1
- Ferraiuolo, L., Meyer, K., Sherwood, T. W., Vick, J., Likhite, S., Frakes, A., et al. (2016). Oligodendrocytes contribute to motor neuron death in ALS via SOD1-dependent mechanism. *Proc. Natl. Acad. Sci. U. S. A.* 113, E6496–E6505. doi: 10.1073/pnas.1607496113
- Frohlich, D., Kuo, W. P., Fruhbeis, C., Sun, J. J., Zehendner, C. M., Luhmann, H. J., et al. (2014). Multifaceted effects of oligodendroglial exosomes on neurons: impact on neuronal firing rate, signal transduction and gene regulation. *Philos. Trans. R. Soc. Lond. B Biol. Sci.* 369:20130510. doi: 10.1098/rstb.2013.0510
- Fruhbeis, C., Kuo-Elsner, W. P., Muller, C., Barth, K., Peris, L., Tenzer, S., et al. (2020). Oligodendrocytes support axonal transport and maintenance via exosome secretion. *PLoS Biol.* 18:e3000621. doi: 10.1371/journal.pbio.3000621
- Gang, L., Yao, Y. C., Liu, Y. F., Li, Y. P., Yang, K., Lu, L., et al. (2015). Co-culture of oligodendrocytes and neurons can be used to assess drugs for axon regeneration in the central nervous system. *Neural. Regen. Res.* 10, 1612–1616. doi: 10.4103/1673-5374.167759
- Garcia-Leon, J. A., Garcia-Diaz, B., Eggermont, K., Caceres-Palomo, L., Neyrinck, K., Madeiro da Costa, R., et al. (2020). Generation of oligodendrocytes and establishment of an all-human myelinating platform from human pluripotent stem cells. *Nat. Protoc.* 15, 3716–3744. doi: 10.1038/s41596-020-0395-4
- Garcia-Leon, J. A., Kumar, M., Boon, R., Chau, D., One, J., Wolfs, E., et al. (2018). SOX10 Single Transcription Factor-Based Fast and Efficient Generation of Oligodendrocytes from Human Pluripotent Stem Cells. *Stem Cell Rep.* 10, 655–672. doi: 10.1016/j.stemcr.2017.12.014
- Gardner, A., Jukkola, P., and Gu, C. (2012). Myelination of rodent hippocampal neurons in culture. *Nat. Protoc.* 7, 1774–1782. doi: 10.1038/nprot.2012.100
- Gaspard, N., Bouschet, T., Herpoel, A., Naeije, G., van den Amele, J., and Vanderhaeghen, P. (2009). Generation of cortical neurons from mouse embryonic stem cells. *Nat. Protoc.* 4, 1454–1463. doi: 10.1038/nprot.2009.157
- Giandomenico, S. L., and Lancaster, M. A. (2017). Probing human brain evolution and development in organoids. *Curr. Opin. Cell Biol.* 44, 36–43. doi: 10.1016/j.celb.2017.01.001
- Giandomenico, S. L., Mierau, S. B., Gibbons, G. M., Wenger, L. M. D., Masullo, L., Sit, T., et al. (2019). Cerebral organoids at the air-liquid interface generate diverse nerve tracts with functional output. *Nat. Neurosci.* 22, 669–679. doi: 10.1038/s41593-019-0350-2
- Giedd, J. N., Blumenthal, J., Jeffries, N. O., Castellanos, F. X., Liu, H., Zijdenbos, A., et al. (1999). Brain development during childhood and adolescence: a longitudinal MRI study. *Nat. Neurosci.* 2, 861–863. doi: 10.1038/13158

- Gorin, G., Svensson, V., and Pachter, L. (2020). Protein velocity and acceleration from single-cell multiomics experiments. *Genome Biol.* 21:39. doi: 10.1186/s13059-020-1945-3
- Goudarzi, S., Rivera, A., Butt, A. M., and Hafizi, S. (2016). Gas6 Promotes Oligodendrogenesis and Myelination in the Adult Central Nervous System and After Lysolecithin-Induced Demyelination. *ASN Neuro* 8:1759091416668430. doi: 10.1177/1759091416668430
- Groveman, B. R., Ferreira, N. C., Foliaki, S. T., Walters, R. O., Winkler, C. W., Race, B., et al. (2021). Human cerebral organoids as a therapeutic drug screening model for Creutzfeldt-Jakob disease. *Sci. Rep.* 11:5165. doi: 10.1038/s41598-021-84689-6
- Haghverdi, L., Buttner, M., Wolf, F. A., Buettner, F., and Theis, F. J. (2016). Diffusion pseudotime robustly reconstructs lineage branching. *Nat. Methods* 13, 845–848. doi: 10.1038/nmeth.3971
- Harboe, M., Torvund-Jensen, J., Kjaer-Sorensen, K., and Laursen, L. S. (2018). Ephrin-A1-EphA4 signaling negatively regulates myelination in the central nervous system. *Glia* 66, 934–950. doi: 10.1002/glia.23293
- Hess, K., Starost, L., Kieran, N. W., Thomas, C., Vincenten, M. C. J., Antel, J., et al. (2020). Lesion stage-dependent causes for impaired remyelination in MS. *Acta Neuropathol.* 140, 359–375. doi: 10.1007/s00401-020-02189-9
- Humpel, C. (2019). Organotypic Brain Slices of ADULT Transgenic Mice: a Tool to Study Alzheimer's Disease. *Curr. Alzheimer Res.* 16, 172–181. doi: 10.2174/1567205016666181212153138
- Jagielska, A., Norman, A. L., Whyte, G., Vliet, K. J., Guck, J., and Franklin, R. J. (2012). Mechanical environment modulates biological properties of oligodendrocyte progenitor cells. *Stem Cells Dev.* 21, 2905–2914. doi: 10.1089/scd.2012.0189
- Jakel, S., Agirre, E., Mendanha Falcao, A., van Bruggen, D., Lee, K. W., Knuesel, I., et al. (2019). Altered human oligodendrocyte heterogeneity in multiple sclerosis. *Nature* 566, 543–547. doi: 10.1038/s41586-019-0903-2
- Jakovcevski, I., Filipovic, R., Mo, Z., Rakic, S., and Zecevic, N. (2009). Oligodendrocyte development and the onset of myelination in the human fetal brain. *Front. Neuroanat.* 3:5. doi: 10.3389/neuro.05.005.2009
- James, O. G., Selvaraj, B. T., Magnani, D., Burr, K., Connick, P., Barton, S. K., et al. (2021). iPSC-derived myelinoids to study myelin biology of humans. *Dev. Cell* 56, 1346–1358.e1346. doi: 10.1016/j.devcel.2021.04.006
- Jang, J., Kang, H. C., Kim, H. S., Kim, J. Y., Huh, Y. J., Kim, D. S., et al. (2011). Induced pluripotent stem cell models from X-linked adrenoleukodystrophy patients. *Ann. Neurol.* 70, 402–409. doi: 10.1002/ana.22486
- Jarjour, A. A., Zhang, H., Bauer, N., French-Constant, C., and Williams, A. (2012). In vitro modeling of central nervous system myelination and remyelination. *Glia* 60, 1–12. doi: 10.1002/glia.21231
- Jemielita, M., Taormina, M. J., Delaurier, A., Kimmel, C. B., and Parthasarathy, R. (2013). Comparing phototoxicity during the development of a zebrafish craniofacial bone using confocal and light sheet fluorescence microscopy techniques. *J. Biophotonics* 6, 920–928. doi: 10.1002/jbio.201200144
- Kang, S. H., Li, Y., Fukaya, M., Lorenzini, I., Cleveland, D. W., Ostrow, L. W., et al. (2013). Degeneration and impaired regeneration of gray matter oligodendrocytes in amyotrophic lateral sclerosis. *Nat. Neurosci.* 16, 571–579. doi: 10.1038/nn.3357
- Kanton, S., Boyle, M. J., He, Z., Santel, M., Weigert, A., Sanchis-Calleja, F., et al. (2019). Organoid single-cell genomic atlas uncovers human-specific features of brain development. *Nature* 574, 418–422. doi: 10.1038/s41586-019-1654-9
- Kelava, I., and Lancaster, M. A. (2016). Stem Cell Models of Human Brain Development. *Cell Stem Cell* 18, 736–748. doi: 10.1016/j.stem.2016.05.022
- Kerman, B. E., Kim, H. J., Padmanabhan, K., Mei, A., Georges, S., Joens, M. S., et al. (2015). In vitro myelin formation using embryonic stem cells. *Development* 142, 2213–2225. doi: 10.1242/dev.116517
- Khan, T. A., Revah, O., Gordon, A., Yoon, S. J., Krawisz, A. K., Goold, C., et al. (2020). Neuronal defects in a human cellular model of 22q11.2 deletion syndrome. *Nat. Med.* 26, 1888–1898. doi: 10.1038/s41591-020-1043-9
- Kim, H., Xu, R., Padmashri, R., Dunaevsky, A., Liu, Y., Dreyfus, C. F., et al. (2019). Pluripotent Stem Cell-Derived Cerebral Organoids Reveal Human Oligodendrogenesis with Dorsal and Ventral Origins. *Stem Cell Rep.* 12, 890–905. doi: 10.1016/j.stemcr.2019.04.011
- Kim, S. U. (1972). Formation of synapses and myelin sheaths in cultures of dissociated chick embryonic spinal cord. *Exp. Cell Res.* 73, 528–530. doi: 10.1016/0014-4827(72)90087-0
- Klaus, J., Kanton, S., Kyrrousi, C., Ayo-Martin, A. C., Di Giaimo, R., Riesenberger, S., et al. (2019). Altered neuronal migratory trajectories in human cerebral organoids derived from individuals with neuronal heterotopia. *Nat. Med.* 25, 561–568. doi: 10.1038/s41591-019-0371-0
- Kyrrousi, C., and Cappello, S. (2020). Using brain organoids to study human neurodevelopment, evolution and disease. *Wiley Interdiscip. Rev. Dev. Biol.* 9:e347. doi: 10.1002/wdev.347
- La Manno, G., Soldatov, R., Zeisel, A., Braun, E., Hochgerner, H., Petukhov, V., et al. (2018). RNA velocity of single cells. *Nature* 560, 494–498. doi: 10.1038/s41586-018-0414-6
- Lancaster, M. A., Corsini, N. S., Wolfinger, S., Gustafson, E. H., Phillips, A. W., Burkard, T. R., et al. (2017). Guided self-organization and cortical plate formation in human brain organoids. *Nat. Biotechnol.* 35, 659–666. doi: 10.1038/nbt.3906
- Lee, S., Chong, S. Y., Tuck, S. J., Corey, J. M., and Chan, J. R. (2013). A rapid and reproducible assay for modeling myelination by oligodendrocytes using engineered nanofibers. *Nat. Protoc.* 8, 771–782. doi: 10.1038/nprot.2013.039
- Lepiemme, F., Mazzucchi, G., Silva, C. G., and Nguyen, L. (2021). Oligodendrocyte precursor cells guide the migration of cortical interneurons by unidirectional contact repulsion. *bioRxiv* [Preprint]. doi: 10.1101/2021.05.27.446000
- Li, Y., Ceylan, M., Shrestha, B., Wang, H., Lu, Q. R., Asmatulu, R., et al. (2014). Nanofibers support oligodendrocyte precursor cell growth and function as a neuron-free model for myelination study. *Biomacromolecules* 15, 319–326. doi: 10.1021/bm401558c
- Lopez-Tobon, A., Caporale, N., Trattaro, S., and Testa, G. (2020). “Three-dimensional models of human brain development,” in *Stem Cell Epigenetics*, eds E. Meshorer and G. Testa (Amsterdam: Elsevier), 257–278.
- Lopez-Tobon, A., Villa, C. E., Cheroni, C., Trattaro, S., Caporale, N., Conforti, P., et al. (2019). Human Cortical Organoids Expose a Differential Function of GSK3 on Cortical Neurogenesis. *Stem Cell Rep.* 13, 847–861. doi: 10.1016/j.stemcr.2019.09.005
- Lubetzki, C., Demerens, C., Anglade, P., Villarroya, H., Frankfurter, A., Lee, V. M., et al. (1993). Even in culture, oligodendrocytes myelinate solely axons. *Proc. Natl. Acad. Sci. U. S. A.* 90, 6820–6824. doi: 10.1073/pnas.90.14.6820
- Mabbott, D. J., Noseworthy, M., Bouffet, E., Laughlin, S., and Rockel, C. (2006). White matter growth as a mechanism of cognitive development in children. *Neuroimage* 33, 936–946. doi: 10.1016/j.neuroimage.2006.07.024
- Madhavan, M., Nevin, Z. S., Shick, H. E., Garrison, E., Clarkson-Paredes, C., Karl, M., et al. (2018). Induction of myelinating oligodendrocytes in human cortical spheroids. *Nat. Methods* 15, 700–706. doi: 10.1038/s41592-018-0081-4
- Mansour, A. A., Goncalves, J. T., Bloyd, C. W., Li, H., Fernandes, S., Quang, D., et al. (2018). An in vivo model of functional and vascularized human brain organoids. *Nat. Biotechnol.* 36, 432–441. doi: 10.1038/nbt.4127
- Marangon, D., Boda, E., Parolisi, R., Negri, C., Giorgi, C., Montarolo, F., et al. (2020). In vivo silencing of miR-125a-3p promotes myelin repair in models of white matter demyelination. *Glia* 68, 2001–2014. doi: 10.1002/glia.23819
- Marchetto, M. C., Muotri, A. R., Mu, Y., Smith, A. M., Cezar, G. G., and Gage, F. H. (2008). Non-cell-autonomous effect of human SOD1 G37R astrocytes on motor neurons derived from human embryonic stem cells. *Cell Stem Cell* 3, 649–657. doi: 10.1016/j.stem.2008.10.001
- Marques, S., Zeisel, A., Codeluppi, S., van Bruggen, D., Mendanha Falcao, A., Xiao, L., et al. (2016). Oligodendrocyte heterogeneity in the mouse juvenile and adult central nervous system. *Science* 352, 1326–1329. doi: 10.1126/science.aaf6463
- Marton, R. M., Miura, Y., Sloan, S. A., Li, Q., Revah, O., Levy, R. J., et al. (2019). Differentiation and maturation of oligodendrocytes in human three-dimensional neural cultures. *Nat. Neurosci.* 22, 484–491. doi: 10.1038/s41593-018-0316-9
- McNally, J. G., Karpova, T., Cooper, J., and Conchello, J. A. (1999). Three-dimensional imaging by deconvolution microscopy. *Methods* 19, 373–385. doi: 10.1006/meth.1999.0873
- McNeish, J., Gardner, J. P., Wainger, B. J., Woolf, C. J., and Eggan, K. (2015). From Dish to Bedside: lessons Learned While Translating Findings from a Stem Cell Model of Disease to a Clinical Trial. *Cell Stem Cell* 17, 8–10. doi: 10.1016/j.stem.2015.06.013
- Mei, F., Fancy, S. P. J., Shen, Y. A., Niu, J., Zhao, C., Presley, B., et al. (2014). Micropillar arrays as a high-throughput screening platform for therapeutics in multiple sclerosis. *Nat. Med.* 20, 954–960. doi: 10.1038/nm.3618

- Miron, V. E., Ludwin, S. K., Darlington, P. J., Jarjour, A. A., Soliven, B., Kennedy, T. E., et al. (2010). Fingolimod (FTY720) enhances remyelination following demyelination of organotypic cerebellar slices. *Am. J. Pathol.* 176, 2682–2694. doi: 10.2353/ajpath.2010.091234
- Moyon, S., Dubessy, A. L., Aigrot, M. S., Trotter, M., Huang, J. K., Dauphinot, L., et al. (2015). Demyelination causes adult CNS progenitors to revert to an immature state and express immune cues that support their migration. *J. Neurosci.* 35, 4–20. doi: 10.1523/JNEUROSCI.0849-14.2015
- Mozafari, S., Starost, L., Manot-Saillet, B., Garcia-Diaz, B., Xu, Y. K. T., Roussel, D., et al. (2020). Multiple sclerosis iPSC-derived oligodendroglia conserve their properties to functionally interact with axons and glia in vivo. *Sci. Adv.* 6:eabc6983. doi: 10.1126/sciadv.abc6983
- Najm, F. J., Madhavan, M., Zaremba, A., Shick, E., Karl, R. T., Factor, D. C., et al. (2015). Drug-based modulation of endogenous stem cells promotes functional remyelination in vivo. *Nature* 522, 216–220. doi: 10.1038/nature14335
- Nakagawa, H., Iwasaki, S., Kichikawa, K., Fukusumi, A., Taoka, T., Ohishi, H., et al. (1998). Normal myelination of anatomic nerve fiber bundles: MR analysis. *AJNR Am. J. Neuroradiol.* 19, 1129–1136.
- Naruse, M., Ishizaki, Y., Ikenaka, K., Tanaka, A., and Hitoshi, S. (2017). Origin of oligodendrocytes in mammalian forebrains: a revised perspective. *J. Physiol. Sci.* 67, 63–70. doi: 10.1007/s12576-016-0479-7
- Nevin, Z. S., Factor, D. C., Karl, R. T., Douvaras, P., Laukka, J., Windrem, M. S., et al. (2017). Modeling the Mutational and Phenotypic Landscapes of Pelizaeus-Merzbacher Disease with Human iPSC-Derived Oligodendrocytes. *Am. J. Hum. Genet.* 100, 617–634. doi: 10.1016/j.ajhg.2017.03.005
- Ng, A. H. M., Khoshakhlagh, P., Rojo Arias, J. E., Pasquini, G., Wang, K., Swiersy, A., et al. (2021). A comprehensive library of human transcription factors for cell fate engineering. *Nat. Biotechnol.* 39, 510–519. doi: 10.1038/s41587-020-0742-6
- Nicaise, A. M., Banda, E., Guzzo, R. M., Russomanno, K., Castro-Borrero, W., Willis, C. M., et al. (2017). iPSC-derived neural progenitor cells from PPMS patients reveal defect in myelin injury response. *Exp. Neurol.* 288, 114–121. doi: 10.1016/j.expneurol.2016.11.012
- Nicaise, A. M., Wagstaff, L. J., Willis, C. M., Paisie, C., Chandok, H., Robson, P., et al. (2019). Cellular senescence in progenitor cells contributes to diminished remyelination potential in progressive multiple sclerosis. *Proc. Natl. Acad. Sci. U. S. A.* 116, 9030–9039. doi: 10.1073/pnas.1818348116
- Nishiyama, A., Serwanski, D. R., and Pfeiffer, F. (2021a). Many roles for oligodendrocyte precursor cells in physiology and pathology. *Neuropathology* 41, 161–173. doi: 10.1111/neup.12732
- Nishiyama, A., Shimizu, T., Sherafat, A., and Richardson, W. D. (2021b). Life-long oligodendrocyte development and plasticity. *Semin. Cell Dev. Biol.* 116, 25–37. doi: 10.1016/j.semcdb.2021.02.004
- Nobuta, H., Yang, N., Ng, Y. H., Marro, S. G., Sabeur, K., Chavali, M., et al. (2019). Oligodendrocyte Death in Pelizaeus-Merzbacher Disease Is Rescued by Iron Chelation. *Cell Stem Cell* 25, 531–541.e6. doi: 10.1016/j.stem.2019.09.003
- Numasawa-Kuroiwa, Y., Okada, Y., Shibata, S., Kishi, N., Akamatsu, W., Shoji, M., et al. (2014). Involvement of ER stress in dysmyelination of Pelizaeus-Merzbacher Disease with PLP1 missense mutations shown by iPSC-derived oligodendrocytes. *Stem Cell Rep.* 2, 648–661. doi: 10.1016/j.stemcr.2014.03.007
- Osaki, T., Uzel, S. G. M., and Kamm, R. D. (2018). Microphysiological 3D model of amyotrophic lateral sclerosis (ALS) from human iPSC-derived muscle cells and optogenetic motor neurons. *Sci. Adv.* 4:eaat5847. doi: 10.1126/sciadv.aat5847
- Ota, M., Sato, N., Kimura, Y., Shigemoto, Y., Kunugi, H., and Matsuda, H. (2019). Changes of Myelin Organization in Patients with Alzheimer's Disease Shown by q-Space Myelin Map Imaging. *Dement. Geriatr. Cogn. Dis. Extra* 9, 24–33. doi: 10.1159/000493937
- Ozaki, H., Suga, H., and Arima, H. (2021). Hypothalamic-pituitary organoid generation through the recapitulation of organogenesis. *Dev. Growth Differ.* 63, 154–165. doi: 10.1111/dgd.12719
- Park, J. C., Jang, S. Y., Lee, D., Lee, J., Kang, U., Chang, H., et al. (2021). A logical network-based drug-screening platform for Alzheimer's disease representing pathological features of human brain organoids. *Nat. Commun.* 12:280. doi: 10.1038/s41467-020-20440-5
- Parravicini, C., Lecca, D., Marangon, D., Coppolino, G. T., Daniele, S., Bonfanti, E., et al. (2020). Development of the first in vivo GPR17 ligand through an iterative drug discovery pipeline: a novel disease-modifying strategy for multiple sclerosis. *PLoS One* 15:e0231483. doi: 10.1371/journal.pone.0231483
- Pasca, A. M., Sloan, S. A., Clarke, L. E., Tian, Y., Makinson, C. D., Huber, N., et al. (2015). Functional cortical neurons and astrocytes from human pluripotent stem cells in 3D culture. *Nat. Methods* 12, 671–678. doi: 10.1038/nmeth.3415
- Perlman, K., Couturier, C. P., Yaqubi, M., Tanti, A., Cui, Q. L., Pernin, F., et al. (2020). Developmental trajectory of oligodendrocyte progenitor cells in the human brain revealed by single cell RNA sequencing. *Glia* 68, 1291–1303. doi: 10.1002/glia.23777
- Philips, T., Bento-Abreu, A., Nonneman, A., Haack, W., Staats, K., Geelen, V., et al. (2013). Oligodendrocyte dysfunction in the pathogenesis of amyotrophic lateral sclerosis. *Brain* 136, 471–482. doi: 10.1093/brain/awt339
- Podbielska, M., Banik, N. L., Kurowska, E., and Hogan, E. L. (2013). Myelin recovery in multiple sclerosis: the challenge of remyelination. *Brain Sci.* 3, 1282–1324. doi: 10.3390/brainsci3031282
- Pollen, A. A., Bhaduri, A., Andrews, M. G., Nowakowski, T. J., Meyerson, O. S., Mostajo-Radji, M. A., et al. (2019). Establishing Cerebral Organoids as Models of Human-Specific Brain Evolution. *Cell* 176, 743–756.e17. doi: 10.1016/j.cell.2019.01.017
- Pouya, A., Satarian, L., Kiani, S., Javan, M., and Baharvand, H. (2011). Human induced pluripotent stem cells differentiation into oligodendrocyte progenitors and transplantation in a rat model of optic chiasm demyelination. *PLoS One* 6:e27925. doi: 10.1371/journal.pone.0027925
- Qian, X., Nguyen, H. N., Song, M. M., Hadiono, C., Ogden, S. C., Hammack, C., et al. (2016). Brain-Region-Specific Organoids Using Mini-bioreactors for Modeling ZIKV Exposure. *Cell* 165, 1238–1254. doi: 10.1016/j.cell.2016.04.032
- Quadrato, G., Brown, J., and Arlotta, P. (2016). The promises and challenges of human brain organoids as models of neuropsychiatric disease. *Nat. Med.* 22, 1220–1228. doi: 10.1038/nm.4214
- Raffaele, S., Gelosa, P., Bonfanti, E., Lombardi, M., Castiglioni, L., Cimino, M., et al. (2021b). Microglial vesicles improve post-stroke recovery by preventing immune cell senescence and favoring oligodendrogenesis. *Mol. Ther.* 29, 1439–1458. doi: 10.1016/j.ymthe.2020.12.009
- Raffaele, S., Boccazzi, M., and Fumagalli, M. (2021a). Oligodendrocyte Dysfunction in Amyotrophic Lateral Sclerosis: mechanisms and Therapeutic Perspectives. *Cells* 10:565. doi: 10.3390/cells10030565
- Reiprich, S., Cantone, M., Weider, M., Baroti, T., Wittstatt, J., Schmitt, C., et al. (2017). Transcription factor Sox10 regulates oligodendroglial Sox9 levels via microRNAs. *Glia* 65, 1089–1102. doi: 10.1002/glia.23146
- Richardson, D. S., and Lichtman, J. W. (2015). Clarifying Tissue Clearing. *Cell* 162, 246–257. doi: 10.1016/j.cell.2015.06.067
- Ristola, M., Sukki, L., Azevedo, M. M., Seixas, A. I., Relvas, J. B., Narkilahti, N., et al. (2019). A compartmentalized neuron-oligodendrocyte co-culture device for myelin research: design, fabrication and functionality testing. *J. Micromech. Microeng.* 6, 1–13. doi: 10.1088/1361-6439/ab16a7
- Rosenberg, S. S., Kelland, E. E., Tokar, E., De la Torre, A. R., and Chan, J. R. (2008). The geometric and spatial constraints of the microenvironment induce oligodendrocyte differentiation. *Proc. Natl. Acad. Sci. U. S. A.* 105, 14662–14667. doi: 10.1073/pnas.0805640105
- Salick, M. R., Lubeck, E., Riesselman, A., and Kaykas, A. (2021). The future of cerebral organoids in drug discovery. *Semin. Cell Dev. Biol.* 111, 67–73. doi: 10.1016/j.semcdb.2020.05.024
- Scantlebury, N., Cunningham, T., Dockstader, C., Laughlin, S., Gaetz, W., Rockel, C., et al. (2014). Relations between white matter maturation and reaction time in childhood. *J. Int. Neuropsychol. Soc.* 20, 99–112. doi: 10.1017/S1355617113001148
- Segel, M., Neumann, B., Hill, M. F. E., Weber, I. P., Viscomi, C., Zhao, C., et al. (2019). Niche stiffness underlies the ageing of central nervous system progenitor cells. *Nature* 573, 130–134. doi: 10.1038/s41586-019-1484-9
- Shah, K., Bedi, R., Rogozhnikov, A., Ramkumar, P., Tong, Z., Rash, B., et al. (2020). Optimization and scaling of patient-derived brain organoids uncovers deep phenotypes of disease. *bioRxiv* [Preprint]. doi: 10.1101/2020.08.26.251611 preprint
- Shaker, M. R., Pietrogrande, G., Martin, S., Lee, J. H., Sun, W., and Wolvetang, E. J. (2021). Rapid and Efficient Generation of Myelinating Human Oligodendrocytes in Organoids. *Front. Cell Neurosci.* 15:631548. doi: 10.3389/fncel.2021.631548
- Shimizu, S., Ishino, Y., Tohyama, M., and Miyata, S. (2018). NDE1 positively regulates oligodendrocyte morphological differentiation. *Sci. Rep.* 8:7644. doi: 10.1038/s41598-018-25898-4



- Sloan, S. A., Darmanis, S., Huber, N., Khan, T. A., Birey, F., Caneda, C., et al. (2017). Human Astrocyte Maturation Captured in 3D Cerebral Cortical Spheroids Derived from Pluripotent Stem Cells. *Neuron* 95, 779–790.e6. doi: 10.1016/j.neuron.2017.07.035
- Song, B., Sun, G., Herszfeld, D., Sylvain, A., Campanale, N. V., Hirst, C. E., et al. (2012). Neural differentiation of patient specific iPSCs as a novel approach to study the pathophysiology of multiple sclerosis. *Stem Cell Res.* 8, 259–273. doi: 10.1016/j.scr.2011.12.001
- Spitzer, S. O., Sitnikov, S., Kamen, Y., Evans, K. A., Kronenberg-Versteeg, D., Dietmann, S., et al. (2019). Oligodendrocyte Progenitor Cells Become Regionally Diverse and Heterogeneous with Age. *Neuron* 101, 459–471.e5. doi: 10.1016/j.neuron.2018.12.020
- Starost, L., Lindner, M., Herold, M., Xu, Y. K. T., Drexler, H. C. A., Hess, K., et al. (2020). Extrinsic immune cell-derived, but not intrinsic oligodendroglial factors contribute to oligodendroglial differentiation block in multiple sclerosis. *Acta Neuropathol.* 140, 715–736. doi: 10.1007/s00401-020-02217-8
- Takamura, T., Motosugi, U., Sasaki, Y., Kakegawa, T., Sato, K., Glaser, K. J., et al. (2020). Influence of Age on Global and Regional Brain Stiffness in Young and Middle-Aged Adults. *J. Magn. Reson. Imaging* 51, 727–733. doi: 10.1002/jmri.26881
- Tanay, A., and Regev, A. (2017). Scaling single-cell genomics from phenomenology to mechanism. *Nature* 541, 331–338. doi: 10.1038/nature21350
- Taylor, A. M., Blurton-Jones, M., Rhee, S. W., Cribbs, D. H., Cotman, C. W., and Jeon, N. L. (2005). A microfluidic culture platform for CNS axonal injury, regeneration and transport. *Nat. Methods* 2, 599–605. doi: 10.1038/nmeth777
- Teshigawara, R., Cho, J., Kameda, M., and Tada, T. (2017). Mechanism of human somatic reprogramming to iPSC cell. *Lab. Invest.* 97, 1152–1157. doi: 10.1038/labinvest.2017.56
- Thomson, C. E., Hunter, A. M., Griffiths, I. R., Edgar, J. M., and McCulloch, M. C. (2006). Murine spinal cord explants: a model for evaluating axonal growth and myelination in vitro. *J. Neurosci. Res.* 84, 1703–1715. doi: 10.1002/jnr.21084
- Trapp, B. D., and Nave, K. A. (2008). Multiple sclerosis: an immune or neurodegenerative disorder? *Annu. Rev. Neurosci.* 31, 247–269. doi: 10.1146/annurev.neuro.30.051606.094313
- Tritschler, S., Buttner, M., Fischer, D. S., Lange, M., Bergen, V., Lickert, H., et al. (2019). Concepts and limitations for learning developmental trajectories from single cell genomics. *Development* 146:dev170506. doi: 10.1242/dev.170506
- Trujillo, C. A., Gao, R., Negraes, P. D., Gu, J., Buchanan, J., Preissl, S., et al. (2019). Complex Oscillatory Waves Emerging from Cortical Organoids Model Early Human Brain Network Development. *Cell Stem Cell* 25, 558–569.e7. doi: 10.1016/j.stem.2019.08.002
- Ueda, H. R., Erturk, A., Chung, K., Gradinaru, V., Chedotal, A., Tomancak, P., et al. (2020). Publisher Correction: tissue clearing and its applications in neuroscience. *Nat. Rev. Neurosci.* 21:298. doi: 10.1038/s41583-020-0291-5
- Urbanski, M. M., Brendel, M. B., and Melendez-Vasquez, C. V. (2019). Acute and chronic demyelinated CNS lesions exhibit opposite elastic properties. *Sci. Rep.* 9:999. doi: 10.1038/s41598-018-37745-7
- Urbanski, M. M., Kingsbury, L., Moussouros, D., Kassim, I., Mehjabeen, S., Paknejad, N., et al. (2016). Myelinating glia differentiation is regulated by extracellular matrix elasticity. *Sci. Rep.* 6:33751. doi: 10.1038/srep33751
- van Bruggen, D., Agirre, E., and Castelo-Branco, G. (2017). Single-cell transcriptomic analysis of oligodendrocyte lineage cells. *Curr. Opin. Neurobiol.* 47, 168–175. doi: 10.1016/j.conb.2017.10.005
- Vaquí, A., Sauvain, A., Duman, M., Nocera, G., Egger, B., Meyenhofer, F., et al. (2019). Injured Axons Instruct Schwann Cells to Build Constricting Actin Spheres to Accelerate Axonal Disintegration. *Cell Rep.* 27, 3152–3166.e7. doi: 10.1016/j.celrep.2019.05.060
- Voyvodic, J. T. (1989). Target size regulates calibre and myelination of sympathetic axons. *Nature* 342, 430–433. doi: 10.1038/342430a0
- Wang, S., Bates, J., Li, X., Schanz, S., Chandler-Militello, D., Levine, C., et al. (2013). Human iPSC-derived oligodendrocyte progenitor cells can myelinate and rescue a mouse model of congenital hypomyelination. *Cell Stem Cell* 12, 252–264. doi: 10.1016/j.stem.2012.12.002
- Weidenheim, K. M., Epshteyn, I., Rashbaum, W. K., and Lyman, W. D. (1993). Neuroanatomical localization of myelin basic protein in the late first and early second trimester human foetal spinal cord and brainstem. *J. Neurocytol.* 22, 507–516. doi: 10.1007/BF01189039
- Windebank, A. J., Wood, P., Bunge, R. P., and Dyck, P. J. (1985). Myelination determines the caliber of dorsal root ganglion neurons in culture. *J. Neurosci.* 5, 1563–1569. doi: 10.1523/JNEUROSCI.05-06-01563.1985
- Xiang, Y., Tanaka, Y., Cakir, B., Patterson, B., Kim, K. Y., Sun, P., et al. (2019). hESC-Derived Thalamic Organoids Form Reciprocal Projections When Fused with Cortical Organoids. *Cell Stem Cell* 24, 487–497.e7. doi: 10.1016/j.stem.2018.12.015
- Xiao, J., Wong, A. W., Willingham, M. M., Kaasinen, S. K., Hendry, I. A., Howitt, J., et al. (2009). BDNF exerts contrasting effects on peripheral myelination of NGF-dependent and BDNF-dependent DRG neurons. *J. Neurosci.* 29, 4016–4022. doi: 10.1523/JNEUROSCI.3811-08.2009
- Xu, Y. K. T., Chitsaz, D., Brown, R. A., Cui, Q. L., Dabarno, M. A., Antel, J. P., et al. (2019). Deep learning for high-throughput quantification of oligodendrocyte ensheathment at single-cell resolution. *Commun. Biol.* 2:116. doi: 10.1038/s42003-019-0356-z
- Yeung, M. S., Zdunek, S., Bergmann, O., Bernard, S., Salehpour, M., Alkass, K., et al. (2014). Dynamics of oligodendrocyte generation and myelination in the human brain. *Cell* 159, 766–774. doi: 10.1016/j.cell.2014.10.011
- Yun, W., Kim, I. Y., Song, G., and You, S. (2020). Rapid induction of gliogenesis in OLIG2 and NKX2.2-expressing progenitors-derived spheroids. *Stem Cells Transl. Med.* 9, 1643–1650. doi: 10.1002/sctm.19-0455
- Zalc, B. (2006). The acquisition of myelin: a success story. *Novartis Found Symp.* 276, 15–21. doi: 10.1002/9780470032244.ch3
- Zuchero, J. B., Fu, M. M., Sloan, S. A., Ibrahim, A., Olson, A., Zaremba, A., et al. (2015). CNS myelin wrapping is driven by actin disassembly. *Dev. Cell* 34, 152–167. doi: 10.1016/j.devcel.2015.06.011

**Conflict of Interest:** The authors declare that the research was conducted in the absence of any commercial or financial relationships that could be construed as a potential conflict of interest.

**Publisher's Note:** All claims expressed in this article are solely those of the authors and do not necessarily represent those of their affiliated organizations, or those of the publisher, the editors and the reviewers. Any product that may be evaluated in this article, or claim that may be made by its manufacturer, is not guaranteed or endorsed by the publisher.

Copyright © 2021 Marangon, Caporale, Boccazzi, Abbracchio, Testa and Lecca. This is an open-access article distributed under the terms of the Creative Commons Attribution License (CC BY). The use, distribution or reproduction in other forums is permitted, provided the original author(s) and the copyright owner(s) are credited and that the original publication in this journal is cited, in accordance with accepted academic practice. No use, distribution or reproduction is permitted which does not comply with these terms.





# Novel Toolboxes for the Investigation of Activity-Dependent Myelination in the Central Nervous System

Jack Kent Heflin and Wenjing Sun\*

Department of Neuroscience, Wexner Medical Center, The Ohio State University, Columbus, OH, United States

## OPEN ACCESS

### Edited by:

Francesca Boscia,  
University of Naples Federico II, Italy

### Reviewed by:

Maria Kukley,  
Achucarro Basque Center for  
Neuroscience, Spain  
Rafael Góis Almeida,  
University of Edinburgh,  
United Kingdom  
Ben Emery,  
Oregon Health and Science  
University, United States

### \*Correspondence:

Wenjing Sun  
Wenjing.Sun@osumc.edu

### Specialty section:

This article was submitted to  
Non-Neuronal Cells,  
a section of the journal  
Frontiers in Cellular Neuroscience

**Received:** 02 September 2021

**Accepted:** 06 October 2021

**Published:** 02 November 2021

### Citation:

Heflin JK and Sun W (2021) Novel  
Toolboxes for the Investigation of  
Activity-Dependent Myelination in the  
Central Nervous System.  
*Front. Cell. Neurosci.* 15:769809.  
doi: 10.3389/fncel.2021.769809

Myelination is essential for signal processing within neural networks. Emerging data suggest that neuronal activity positively instructs myelin development and myelin adaptation during adulthood. However, the underlying mechanisms controlling activity-dependent myelination have not been fully elucidated. Myelination is a multi-step process that involves the proliferation and differentiation of oligodendrocyte precursor cells followed by the initial contact and ensheathment of axons by mature oligodendrocytes. Conventional end-point studies rarely capture the dynamic interaction between neurons and oligodendrocyte lineage cells spanning such a long temporal window. Given that such interactions and downstream signaling cascades are likely to occur within fine cellular processes of oligodendrocytes and their precursor cells, overcoming spatial resolution limitations represents another technical hurdle in the field. In this mini-review, we discuss how advanced genetic, cutting-edge imaging, and electrophysiological approaches enable us to investigate neuron-oligodendrocyte lineage cell interaction and myelination with both temporal and spatial precision.

**Keywords:** activity-dependent myelination, local stimulation, AMPA receptor, glutamate uncaging, time-lapse imaging

## INTRODUCTION

Myelination refers to the process of wrapping axons with compact layers of the plasma membrane, and it occurs primarily postnatally (Foran and Peterson, 1992; Baumann and Pham-Dinh, 2001; Nishiyama et al., 2009). The presence of myelin sheaths drastically increases the conduction velocity along axons. As the conduction velocity can be fine-tuned by myelin thickness and sheath length (Ford et al., 2015; Etxeberria et al., 2016), myelin is also pivotal in maintaining precise spatiotemporal activity patterns in neuronal circuits. Several recent studies particularly highlighted the importance of myelination for proper neuronal circuit activities and cognitive function in health and diseases (Pan et al., 2020; Steadman et al., 2020; Chen et al., 2021). Myelin sheaths in the central nervous system (CNS) are exclusively formed by oligodendrocytes that are generated from the differentiation of oligodendrocyte precursor cells (OPCs). Oligodendrocytes have the innate capability to wrap fibrous structures (Lee et al., 2012; Bechler et al., 2015). With the development of various pharmacological and genetic tools, it became clear that oligodendrogenesis and myelin formation are regulated by both intrinsic programs and extrinsic factors

(Li and Richardson, 2016; Mayoral and Chan, 2016; Fletcher et al., 2018). Accumulating evidence has shown that social interaction (Liu et al., 2012; Makinodan et al., 2012), experience (Hughes et al., 2018), sensory inputs (Mangin et al., 2012; Hill et al., 2014), and motor learning activities (McKenzie et al., 2014; Bacmeister et al., 2020) modulate myelin adaptation and oligodendrocyte lineage cell behavior. Recent studies using state-of-the-art optogenetic (Gibson et al., 2014) and chemogenetic (Mitew et al., 2018) techniques showed that stimulating neuronal firing increased myelin thickness along the axons and oligodendrogenesis within the stimulated region. However, our understanding of the mechanisms underlying “activity-dependent myelination” is still limited.

For the past two decades, the development of various transgenic fluorescence reporter mouse lines has enabled us to directly visualize oligodendrocyte lineage cells at different stages (Mallon et al., 2002; Yuan et al., 2002; Karram et al., 2008; Zhu et al., 2008; Hughes et al., 2013). Genetic fate mapping studies using OPC specific Cre or CreER lines crossed with Cre-reporter mice have also generated vast information regarding oligodendrocyte lineage plasticity in both physiological and pathological conditions across multiple CNS regions (Lappe-Siefke et al., 2003; Rivers et al., 2008; Kang et al., 2010; Zhu et al., 2011; Tognatta et al., 2017; Huang et al., 2019). More recent studies have focused on manipulating the oligodendroglial-specific expression of key molecules in regulating oligodendroglial lineage plasticity or neuron-oligodendroglial communication. Together with the development of novel electrophysiological and optical techniques, we now have more comprehensive tools to study the underlying mechanisms for activity-dependent myelination.

## MANIPULATING THE EXPRESSION OF POSTSYNAPTIC NEUROTRANSMITTER RECEPTORS IN OLIGODENDROCYTE LINEAGE CELLS

The discovery of neuron-OPC synaptic contacts (Bergles et al., 2000) has inspired the myelin research field for the last 2 decades. The prevalence of such synapses across different CNS regions (Lin and Bergles, 2004; Jabs et al., 2005; Lin et al., 2005; Ge et al., 2006; Káradóttir et al., 2008; Kukley et al., 2008; Mangin et al., 2008; Vélez-Fort et al., 2010), including the white matter (Kukley et al., 2007; Ziskin et al., 2007), and the fact that synaptic contacts enable neuron-OPC communication with both temporal and spatial precision position them as an ideal candidate to instruct activity-dependent myelination. Novel genetic mouse models that specifically silence or overexpress different postsynaptic neurotransmitter receptors in oligodendrocyte lineage cells can manipulate neuron-OPC synaptic transmission without interfering with neuron-neuron communication, thereby providing in-depth insights into the functional implications of these neuron-OPC synapses.

Glutamatergic postsynaptic currents in OPCs exhibit fast kinetics and are primarily mediated through AMPA receptors. In a recent study, Kougioumtzidou et al. (2017)

created several murine transgenic lines to reduce or eliminate AMPA receptor-mediated postsynaptic responses by crossing Sox10-Cre line and Rosa-YFP reporter line with different combinations of *Gria2<sup>flox/flox</sup>* line, *Gria4<sup>flox/flox</sup>* line, and *Gria3* null line. Triple knock-out of *GluA2–4* showed almost no AMPA receptor-mediated spontaneous synaptic responses (Figure 1A) and exhibited reduced numbers of mature oligodendrocytes within the corpus callosum in mice at both P14 and P53, while the proliferation of OPCs remained unaltered (Kougioumtzidou et al., 2017). Similar results in oligodendrocyte lineage were observed with *Gria2<sup>-/-</sup>Gria3* null double transgenic mice, where the AMPA receptor-mediated currents were reduced by half (Kougioumtzidou et al., 2017). However, neither single transgenic Sox10-Cre: *Gria2<sup>flox/flox</sup>* nor germline *Gria3* null mice alone displayed any phenotype in oligodendrocyte lineage development and myelination, suggesting that there might be compensatory mechanisms between the expression of AMPA receptor subunits (Kougioumtzidou et al., 2017).

Among *GluA1–4* subunits, *GluA2* determines the  $\text{Ca}^{2+}$  permeability such that only receptors lacking *GluA2* are  $\text{Ca}^{2+}$  permeable. Previous studies demonstrated that OPCs express  $\text{Ca}^{2+}$  permeable AMPA receptors in the hippocampus (Bergles et al., 2000; Ge et al., 2006). In the corpus callosum,  $\text{Ca}^{2+}$  permeable AMPA receptors can only be detected in OPCs during adulthood (Ziskin et al., 2007), but not in the early postnatal period (Kukley et al., 2007). One emerging question is whether  $\text{Ca}^{2+}$  permeability through AMPA receptors regulates oligodendrocyte lineage plasticity and activity-dependent myelination. Different genetic strategies have been utilized to address this question. In the study mentioned above, Kougioumtzidou et al. (2017) did not observe any changes in oligodendrocyte lineage development and myelination from the corpus callosum at P14 using the Sox10-Cre: *Gria2<sup>flox/flox</sup>* line to increase  $\text{Ca}^{2+}$  permeability by deleting *GluA2* in OPCs (Figure 1B). Conversely, Khawaja et al. (2021) recently generated an inducible *GluA2* overexpression line (Sox10-CreER: Ai14:R26-Gria2) where the decreases in  $\text{Ca}^{2+}$  permeability through AMPA receptors (Figure 1C) resulted in an increase in OPCs only in the adult mice. Myelination in younger mice from the same line was not affected by *GluA2* overexpression when 4-Hydroxytamoxifen was injected early postnatally (Khawaja et al., 2021).

Besides transgenic mouse lines, viral gene delivery approaches are routinely used for transgene expression *in vivo*. Although most adeno-associated viruses (AAV) serotypes exhibit dominance in neuronal tropism with constitutive promoters driving the gene expression (Burger et al., 2004; Cearley and Wolfe, 2006), several studies successfully drove oligodendrocyte-specific gene expression *in vivo* using AAVs with oligodendrocyte-specific promoters, such as myelin basic protein or myelin-associated glycoprotein (Chen et al., 1998; Lawlor et al., 2009; Von Jonquieres et al., 2016), or packaging AAV vectors with a novel oligotropic capsid (Powell et al., 2016; Weinberg et al., 2017). However, so far, AAV particles rarely transduce OPCs in a specific and consistent fashion

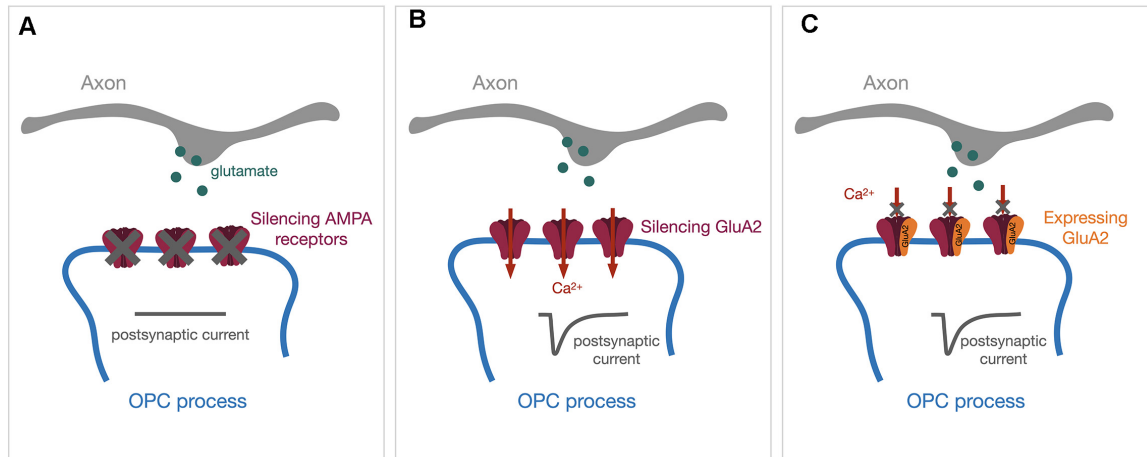


**FIGURE 1 |** Genetic approaches to manipulate the expression of AMPA receptors in OPCs. Synaptic vesicles containing glutamate (green dots) will be released upon the arrival of action potentials. The release of glutamate will activate post-synaptic AMPA receptors and evoke a post-synaptic current (dark gray traces). **(A)** Genetically silencing all AMPA receptor subunits will diminish AMPA receptor-mediated postsynaptic currents. **(B)** Silencing the GluA2 subunit alone will increase  $\text{Ca}^{2+}$  permeability through AMPA receptors. **(C)** Expressing the GluA2-containing AMPA receptor will block the  $\text{Ca}^{2+}$  entry through AMPA receptors. OPCs, oligodendrocyte precursor cells.

*in vivo*. Instead, the retrovirus is a good alternative as it only transfects dividing cells (Van Praag et al., 2002), and OPCs are the major source of proliferating cells in the postnatal CNS (Dawson et al., 2003). While also aiming at manipulating AMPA receptor-dependent  $\text{Ca}^{2+}$  permeability, Chen et al. (2018) modified OPC-expressed AMPA receptors *in vivo* using retroviral vectors early postnatally. They delivered retroviral vectors expressing either full-length GluA2 with point mutations or truncated GluA2 into the corpus callosum during postnatal 2–3 weeks and reported that ~95% of transduced cells belong to oligodendrocyte lineage (Chen et al., 2018). This study showed that GluA2 point mutations increasing the AMPA receptor  $\text{Ca}^{2+}$  permeability enhanced OPC proliferation and suppressed their differentiation. Perturbing the trafficking of GluA2-containing AMPARs by expressing the cytoplasmic C-terminal of the GluA2 subunit decreased the OPC differentiation without affecting the proliferation during myelin development (Chen et al., 2018). While the two studies mentioned above used transgenic lines to manipulate GluA2 expression in the total OPC population, this study only targeted proliferating OPCs, which may explain the difference in their observations.

OPCs gradually lose synaptic contacts with neurons during their differentiation into oligodendrocytes, accompanied by a downregulation of ionotropic glutamate receptors (De Biase et al., 2010; Kukley et al., 2010). Nevertheless, Evonuk et al. (2020) crossed the PLP-CreER line with *Gria4<sup>tm1Mony</sup>* mice (Fuchs et al., 2007) to specifically knock-out GluA4 in more mature PLP<sup>+</sup> oligodendroglial cells. They reported that deleting GluA4 ameliorated myelin degeneration and axonal damage in a mouse model of multiple sclerosis (Evonuk et al., 2020). Oligodendrocyte lineage cells also express NMDA receptors (Kárádóttir et al., 2005, 2008; Salter and Fern, 2005; Micu et al., 2006). These NMDA receptors are reported to be involved in mediating myelin responses after CNS

injuries (Kárádóttir et al., 2005; Micu et al., 2006, 2007). It has been suggested that remyelination after white matter injury is NMDA receptor-dependent (Lundgaard et al., 2013). Genetic models that specifically delete NMDA receptor subunit NR1 in OPCs exhibited normal myelination and did not show obvious alteration in survival or proliferation of OPCs (De Biase et al., 2011; Guo et al., 2012). However, Saab et al. (2016) recently reported that oligodendroglial NMDA receptors regulate GLUT1-mediated glucose import into the myelin compartment, and the deletion of NR1 in CNP<sup>+</sup> oligodendroglial cells led to a delay in myelin development.

GABAergic interneuron-OPC synapses primarily activate  $\text{Cl}^-$ -permeable GABA<sub>A</sub> receptors in OPCs. Instead of hyperpolarizing the membrane potential, the activation of GABA<sub>A</sub> receptor depolarizes the post-synaptic membrane due to high intracellular  $\text{Cl}^-$  concentration (Lin and Bergles, 2004; Passlick et al., 2013). GABAergic synaptic inputs in OPCs are therefore not electrically “inhibitory”. While direct GABAergic synaptic contacts in OPCs persist through the development to adulthood in the mouse hippocampus (Lin and Bergles, 2004), in the cortex those direct synaptic activities start decreasing after the second postnatal week and gradually switch to the volume transmission mode mediated by the extra-synaptic activation of GABA<sub>A</sub> receptors (Vélez-Fort et al., 2010). In the neocortex, OPCs are highly connected with fast-spiking parvalbumin (PV) interneurons, and  $\gamma 2$  subunits of GABA<sub>A</sub> receptors are exclusively expressed at post-synaptic sites of PV interneuron-OPC synapses (Ordaz et al., 2015). Balia et al. (2017) bred NG2creERT2:GCamp3:  $\gamma 2^{\text{fl/fl}}$  mice to specifically inactivate  $\gamma 2$ - GABA<sub>A</sub> receptor-mediated synapses in OPCs early postnatally. They reported no alteration in OPC proliferation or differentiation, but a decrease in OPC density at P30 compared to control mice, suggesting that  $\gamma 2$ - GABA<sub>A</sub> receptors play a role in OPC self-maintenance

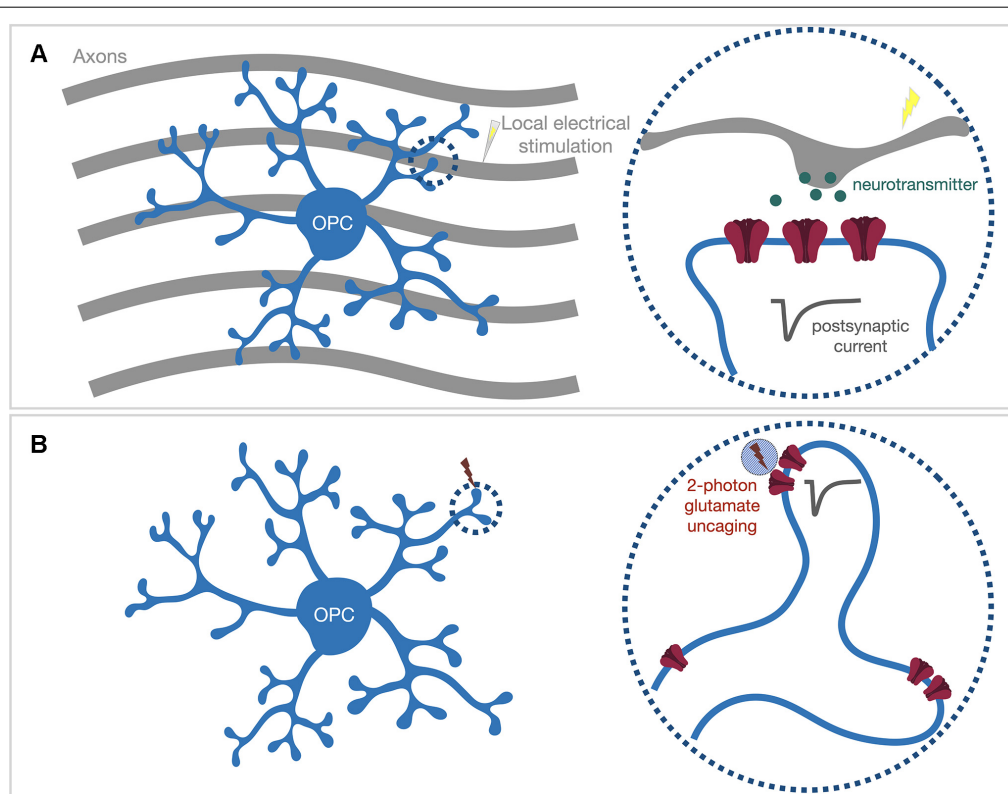


**FIGURE 2 |** Locally activate postsynaptic receptors within OPC processes via either **(A)** local electrical stimulation or **(B)** 2-photon glutamate uncaging. **(A)** The mono-polar stimulating electrode can be placed in close proximity ( $\sim 5 \mu\text{m}$ ) to the target OPC process (dash circle) to only stimulate the axons passing the process segment. **(B)** Acute brain slices are bathed with caged-glutamate containing bath solution. The 2-photon uncaging laser ( $\sim 720 \text{ nm}$ ) is pointed to the target locations by galvo scan mirrors inside the scan head. A brief uncaging laser pulse (0.6–1 ms) will uncage the caged-glutamate compound within the 2-photon excitation volume (blue shaded circle) and evoke an electrical response from post-synaptic neurotransmitter receptors (dark gray trace).

(Balía et al., 2017). In a more recent study from the same group, Benamer et al. (2020) further characterized this transgenic line and revealed that  $\gamma 2$  mutant mice exhibited abnormal axonal morphology and myelin distribution in PV interneurons, along with increased nodal and internodal lengths of myelinated PV axons. Those observed myelin defects decreased the firing frequency of PV interneurons and their connectivity with excitatory neurons, leading to the impairment of sensory function in  $\gamma 2$  mutant mice (Benamer et al., 2020). It will be interesting for future studies to investigate the functional role of synaptic contacts between other types of interneurons and OPCs, perhaps with genetic models that specifically delete  $\text{GABA}_A$  receptors in OPCs in general.

## ELICITING LOCAL POSTSYNAPTIC RESPONSES WITHIN OPC PROCESSES

Accumulating data have suggested that neuronal activity-induced downstream signaling often occurs locally within the thin processes of oligodendroglial cells. Axonal stimulation using electrical, optogenetic, or chemogenetic strategies has been shown to induce local myelin basic protein synthesis

within OPC processes (Wake et al., 2011) and increase myelin thickness of stimulated axons (Gibson et al., 2014; Mitew et al., 2018). Confocal time-lapse imaging studies have demonstrated that cellular processes of oligodendrocyte lineage cells actively contact and form initial ensheathment with axons, but the stabilization and elongation of formed myelin sheaths are regulated by neuronal activity (Hines et al., 2015; Mensch et al., 2015; Koudelka et al., 2016). Thus far, it is not clear whether the single contacted axon's activity is sufficient to trigger downstream signaling cascades within OPC processes locally, or whether activities from a large group of axons are required to initiate global signaling that spreads out to the whole OPC process architecture. To tease apart these two scenarios, we need to use experimental paradigms that will only activate one or just a few synapses within a spatially confined region. We previously applied local electrical stimulation by placing a mono-polar stimulating electrode approximately  $5 \mu\text{m}$  away from the target OPC process segment (Figure 2A; Sun et al., 2016). When combining electrophysiology recording with 2-photon  $\text{Ca}^{2+}$  imaging, we observed that such a local stimulus is sufficient to trigger  $\text{Ca}^{2+}$  entry within the local compartment with similar kinetics as the global voltage-gated  $\text{Ca}^{2+}$  channel (VGCC)-mediated



$\text{Ca}^{2+}$  entry induced by current injection (Sun et al., 2016). The somatic depolarization upon local stimulation was well below the activation threshold for VGCCs, and we did not observe a widespread global  $\text{Ca}^{2+}$  signal upon local stimulation. Our results suggest that only a limited number of axons passing the target OPC process were activated upon local stimulation, and also indicate a substantial attenuation along the OPC processes, as suggested by our previous theoretical simulation (Sun and Dietrich, 2013). Our observation also suggests the expression of voltage-gated ion channels within OPC processes (Sun et al., 2016). Therefore, the local synaptic response can be amplified or dampened through the activation of ion channels within processes. Since myelin basic protein, and likely other myelin proteins could be synthesized within the OPC processes (Wake et al., 2011), future studies could utilize local electrical stimulation together with advanced *in situ* hybridization techniques, such as RNAscope (Wang et al., 2012), to address remaining questions like whether local synaptic inputs are sufficient to initialize the transport, local expression, and translation of myelin-specific mRNAs.

Nevertheless, the spatial resolution of local electrical stimulation is not sufficient to accurately identify which nearby synapses are activated, especially when there is no optical tool available to visualize where synapses are located along OPC processes. To circumvent this limitation, the alternative approach is to optically activate postsynaptic neurotransmitter receptors on OPC processes with high optical resolution (Figure 2B). 2-photon glutamate uncaging generates an optically controlled transient release of glutamate by brief photolysis of caged-glutamate within the diffraction-limited 2-photon excitation volume (Matsuzaki et al., 2001). A single uncaging pulse applied at the dendritic spine head of neurons can produce an AMPA receptor-mediated current response similar to a synaptic response (Matsuzaki et al., 2001). We reported that the same strategy could be used to map AMPA receptors in OPCs (Sun et al., 2016). Although OPC processes are not equipped with spine structures that clearly indicate the clustering of AMPA receptors, we demonstrated that AMPA receptors are expressed along the process (Sun et al., 2016). The fact that the same uncaging pulse (720 nm, 0.65 ms, ~35–45 mW at the surface of the specimen; Sun et al., 2016) produced variable response sizes along a process segment suggests that AMPA receptors do not distribute homogeneously, but instead, might cluster in “hot spots”. However, whether those AMPA receptor “hot spots” represent locations of neuron-OPC synapses needs further investigation.

Beyond mapping AMPA receptor distribution, 2-photon glutamate uncaging may be useful to explore the functional implication of neuron-OPC synapses. For example, it can be used to study how OPCs integrate neuronal inputs from different synaptic contact sites and initialize downstream signaling cascades. Various electrophysiological studies characterized different voltage-gated ion channel expression in OPCs (Steinhäuser et al., 1994; Kressin et al., 1995; Akopian et al., 1996; Chittajallu et al., 2004; Tong et al., 2009; De Biase

et al., 2010; Kukley et al., 2010; Haberlandt et al., 2011), and many of those ion channels, e.g., calcium and potassium channels, are likely expressed on the membrane of thin processes (Sun et al., 2016). The fact that voltage signals strongly attenuate along the OPC process (Sun and Dietrich, 2013) highlights the importance of understanding how these locally expressed ion channels respond to inputs from multiple synapses and shape the post-synaptic membrane potentials within OPC process compartments. The size of integrated local post-synaptic membrane potential might determine whether downstream signaling cascades can be triggered, e.g., whether  $\text{Ca}^{2+}$  channels can be activated and elicit a local  $\text{Ca}^{2+}$  transient. While local electrical stimulation cannot accurately determine how many synapses will be activated and where those activated synapses are located, 2-photon uncaging pulses can be pointed to multiple spatially apart spots with a minimal switching time (0.6–1 ms per uncaging pulse plus 0.1 ms laser switching time; Sun et al., 2016). Therefore, when combined with  $\text{Ca}^{2+}$  imaging and patch-clamp recording, 2-photon uncaging is an ideal tool to investigate the voltage integration of synaptic inputs from different sites and the subsequent  $\text{Ca}^{2+}$  signaling within a local process compartment. Glutamate uncaging is also suited to study activity-dependent synaptic or morphological plasticity. Ge et al. (2006) reported  $\text{Ca}^{2+}$  permeable AMPA receptor-mediated long-term potentiation (persistent strengthening of synaptic transmission) in OPCs from the murine hippocampus. Thus far, it is unclear whether such plasticity and potentially other types of synaptic plasticity exist at an individual synapse level and whether those types of synaptic plasticity are required for local translation of myelin proteins. Additionally, it is known that OPCs are motile and have filopodia-like protrusions constantly extending and retracting (Hughes et al., 2013). Understanding whether synaptic inputs can guide those dynamic protrusion movements to form initial contact with axons will be an important direction for future investigations. Indeed, a similar approach has been used in neuronal studies to demonstrate the occurrence of long-term potentiation at individual spines (Matsuzaki et al., 2004) and repetitive uncaging pulses-induced formation of new functional spines (Kwon and Sabatini, 2011). Taken together, 2-photon glutamate uncaging combined with other techniques is a powerful tool to tackle important questions like whether local synaptic integration is functionally meaningful and whether any specific neuronal activity patterns are preferred for initiation of myelin wrapping.

## CAPTURING THE DYNAMICS OF THE MYELIN FORMATION WITH TIME-LAPSE IMAGING

Myelination is a multi-step process that involves the proliferation and differentiation of oligodendrocyte precursor cells followed by the initial contact and ensheathment of axons by mature oligodendrocytes. The whole process spans a long temporal window, and conventional end-point studies cannot capture

the dynamics during the whole process. Recent studies have employed time-lapse imaging techniques based on confocal microscopy in the zebrafish model and generated crucial information about the initial myelin sheath formation along axons (Hines et al., 2015; Mensch et al., 2015; Koudelka et al., 2016). Those studies changed our previous knowledge or assumption that oligodendrocytes only select the electrically active axons to make the initial contact and subsequently start the wrapping process to form a sheath segment. Instead, oligodendrocytes constantly make contacts with axons and form initial myelin sheath segments, but at the same time, also often retract some formed sheaths. Therefore, the stabilization of those established sheaths is the key, and this step is heavily dependent on axonal vesicle release (Hines et al., 2015). Moreover, neuronal activity also influences the length of the sheaths (Hines et al., 2015) and the number of myelin sheaths each oligodendrocyte makes (Mensch et al., 2015). It is worth mentioning that to visualize oligodendrocyte lineage cells in different stages, those studies generated transgenic lines that express fluorescence protein under promoters (e.g., Sox10) that are widely expressed at almost all stages within oligodendrocyte lineage. In addition, they often chose to express membrane-anchored fluorescence protein instead of cytoplasm-expressing ones for the better visualization of myelin sheaths. Using synaptic protein-expressing transgenic zebrafish models, several studies further demonstrated the relationship between axonal vesicle exocytosis and myelin sheath formation through *in vivo* time-lapse imaging (Hughes and Appel, 2019; Almeida et al., 2021). To investigate how oligodendrocyte lineage cells react to axonal activity or vesicle release, recent studies also used genetically encoded  $\text{Ca}^{2+}$  indicators and showed that various myelin sheaths movements are accompanied by  $\text{Ca}^{2+}$  transients with different duration and frequencies within oligodendrocyte processes (Baraban et al., 2018; Krasnow et al., 2018; Hughes and Appel, 2020). By combining  $\text{Ca}^{2+}$  imaging with the single-cell RNA sequencing technique, Marisca et al. (2020) also demonstrated that subgroups of OPCs exhibited widespread heterogeneity in eliciting  $\text{Ca}^{2+}$  responses and initiating proliferation or differentiation upon neuronal activities.

The zebrafish larva as the animal model clearly shows the advantage of *in vivo* imaging due to its transparency. When looking at imaging techniques that can be applied *in vivo* for mouse models, the multi-photon laser scanning system surpasses the confocal system as it penetrates deeper into the tissue with less scattering and phototoxicity. However, it is worth mentioning that 2-photon microscopy generally does not reach more than 500  $\mu\text{m}$  deep in the brain. Imaging deeper brain structures often involves tissue removal and the embedment of a gradient index lens (Jung et al., 2004). Future studies employing adaptive optical correction (Wang et al., 2015) or utilizing 3-photon *in vivo* imaging (Horton et al., 2013; Hontani et al., 2021) might partially overcome this limitation. Recent studies utilizing *in vivo* 2-photon imaging demonstrated how OPCs maintain hemostasis (Hughes et al., 2013), exhibit experience-dependent oligodendrogenesis and

myelin adaptation (Hughes et al., 2018), and undergo adaptive remodeling during motor learning activities (Bacmeister et al., 2020). Choosing the appropriate time interval between the consecutive acquisition sessions is critical for these studies because the interval represents the temporal resolution. One must carefully set this parameter to obtain sufficient details about the target cellular event without generating a vast number of images. For example, we now know that OPCs are highly motile and can translocate to a new position within 2–3 days, even in adulthood (Hughes et al., 2013). Therefore, the interval between imaging sessions needs to be set much shorter than 2–3 days to follow the same group of cells over the whole imaging period. Longitudinal *in vivo* imaging studies take over days to weeks and involve re-anesthetizing the animal and re-identifying the exact imaging area between imaging sessions. Setting the imaging area with easily identified landmarks, e.g., visible blood vessels, is often helpful. Imaging processing and analysis are also challenging for *in vivo* time-lapse imaging studies, and it usually requires algorithms to correct moving artifacts and align all images taken at different time points. Due to technical difficulties such as motion artifacts caused by heartbeat and breathing, fewer studies employed time-lapse *in vivo* imaging for the spinal cord than the brain. However, the development of implantable spinal cord windows (Farrar et al., 2012; Tedeschi et al., 2016) may allow future studies to follow the dynamic communication between axons and oligodendroglial cells within the murine spinal cord. Miniaturized microscopes, also called miniscopes, can be directly head-mounted in freely moving animals and allow optical recording over an extended period (Ghosh et al., 2011). However, the conventional miniscope has lower optical resolution than the 2-photon scanning system and therefore cannot resolve finer cellular structures like dendritic spines (Silva, 2017). The ongoing development of 2-photon miniscopes (Zong et al., 2017) might overcome this problem and provide *in vivo* imaging in freely behaving animals with greater optical resolution. Miniscope platforms might be suited for future studies investigating longitudinal changes in oligodendroglial plasticity and myelin formation in various behavioral paradigms.

Besides imaging oligodendroglial cells and myelin sheaths with genetically labeled fluorescence proteins, a couple of label-free *in vivo* myelin imaging techniques have also been developed during the last decade. Coherent anti-Stokes Raman scattering (CARS) microscopy utilizes the intrinsic  $\text{CH}_2$  symmetric stretching vibration of the enriched lipid structure to image myelin sheaths (Wang et al., 2005; Fu et al., 2008). Meanwhile, spectral confocal reflectance microscopy (SCoRe; Schain et al., 2014) generates label-free myelin images by capturing the highly reflective signals from lipids using several lasers with different wavelengths. In combination with *in vivo* fluorescence microscopy (Schain et al., 2014), those novel label-free techniques can image dynamics between axons and myelin sheaths with great resolution and reduce the dependence on genetic models for *in vivo* imaging of myelin. The long-term stability and phototoxicity of these label-free imaging techniques still need to

be characterized for time-lapse *in vivo* imaging studies spanning multiple days.

## CONCLUDING REMARKS

We have now reached a widely accepted notion that neuronal activity positively regulates myelin development and adaptation during adulthood. It is clear that activity-dependent myelination is a fairly dynamic process, and future studies will require the design of specific experimental paradigms to capture the dynamics with great temporal and spatial precision. Future studies using a multidisciplinary approach addressing whether inputs from just a few synapses are sufficient to initialize the expression and translation of myelin-specific mRNAs within OPC processes and whether there is any preferred neuronal firing pattern for initiating downstream cellular events will enhance our understanding of the functional role of neuron-OPC synapses. Additionally, monitoring oligodendroglial cellular behavior and tracing key intracellular signaling molecule's activity *in vivo* in various behavioral paradigms will offer

further insights into the mechanisms that control activity-dependent myelination.

## AUTHOR CONTRIBUTIONS

JH and WS wrote the manuscript. WS conceived the project and supervised the overall progress. All authors contributed to the article and approved the submitted version.

## FUNDING

This work was supported by the start-up fund from Wexner Medical Center at The Ohio State University (to WS).

## ACKNOWLEDGMENTS

We thank Dr. Andrea Tedeschi and Dr. Maria Kukley for the helpful discussion and comments. We also thank Haven Rodocker and Alaina Scavuzzo for proofreading.

## REFERENCES

- Akopian, G., Kressin, K., Derouiche, A., and Steinhauser, C. (1996). Identified glial cells in the early postnatal mouse hippocampus display different types of  $\text{Ca}^{2+}$  currents. *Glia* 17, 181–194. doi: 10.1002/(SICI)1098-1136(199607)17:3<181::AID-GLIA1>3.0.CO;2-4
- Almeida, R. G., Williamson, J. M., Madden, M. E., Early, J. J., Voas, M. G., Talbot, W. S., et al. (2021). Myelination induces axonal hotspots of synaptic vesicle fusion that promote sheath growth. *Curr. Biol.* 31, 3743–3754.e5. doi: 10.1016/j.cub.2021.06.036
- Bacmeister, C. M., Barr, H. J., McClain, C. R., Thornton, M. A., Nettles, D., Welle, C. G., et al. (2020). Motor learning promotes remyelination *via* new and surviving oligodendrocytes. *Nat. Neurosci.* 23, 819–831. doi: 10.1038/s41593-020-0637-3
- Balia, M., Benamer, N., and Angulo, M. C. (2017). A specific GABAergic synapse onto oligodendrocyte precursors does not regulate cortical oligodendrogenesis. *Glia* 65, 1821–1832. doi: 10.1002/glia.23197
- Baraban, M., Koudelka, S., and Lyons, D. A. (2018).  $\text{Ca}^{2+}$  activity signatures of myelin sheath formation and growth *in vivo*. *Nat. Neurosci.* 21, 19–23. doi: 10.1038/s41593-017-0040-x
- Baumann, N., and Pham-Dinh, D. (2001). Biology of oligodendrocyte and myelin in the mammalian central nervous system. *Physiol. Rev.* 81, 871–927. doi: 10.1152/physrev.2001.81.2.871
- Bechler, M. E., Byrne, L., and Ffrench-Constant, C. (2015). CNS myelin sheath lengths are an intrinsic property of oligodendrocytes. *Curr. Biol.* 25, 2411–2416. doi: 10.1016/j.cub.2015.07.056
- Benamer, N., Vidal, M., Balia, M., and Angulo, M. C. (2020). Myelination of parvalbumin interneurons shapes the function of cortical sensory inhibitory circuits. *Nat. Commun.* 11:5151. doi: 10.1038/s41467-020-18984-7
- Bergles, D. E., Roberts, J. D., Somogyi, P., and Jahr, C. E. (2000). Glutamatergic synapses on oligodendrocyte precursor cells in the hippocampus. *Nature* 405, 187–191. doi: 10.1038/35012083
- Burger, C., Gorbatyuk, O. S., Velardo, M. J., Peden, C. S., Williams, P., Zolotukhin, S., et al. (2004). Recombinant AAV viral vectors pseudotyped with viral capsids from serotypes 1, 2, and 5 display differential efficiency and cell tropism after delivery to different regions of the central nervous system. *Mol. Ther.* 10, 302–317. doi: 10.1016/j.ymthe.2004.05.024
- Cearley, C. N., and Wolfe, J. H. (2006). Transduction characteristics of adeno-associated virus vectors expressing cap serotypes 7, 8, 9, and Rh10 in the mouse brain. *Mol. Ther.* 13, 528–537. doi: 10.1016/j.ymthe.2005.11.015
- Chen, T.-J., Kula, B., Nagy, B., Barzan, R., Gall, A., Ehrlich, I., et al. (2018). *in vivo* regulation of oligodendrocyte precursor cell proliferation and differentiation by the AMPA-receptor subunit GluA2. *Cell Rep.* 25, 852–861.e7. doi: 10.1016/j.celrep.2018.09.066
- Chen, J.-F., Liu, K., Hu, B., Li, R.-R., Xin, W., Chen, H., et al. (2021). Enhancing myelin renewal reverses cognitive dysfunction in a murine model of Alzheimer's disease. *Neuron* 109, 2292–2307.e5. doi: 10.1016/j.neuron.2021.05.012
- Chen, H., McCarty, D. M., Bruce, A. T., Suzuki, K., and Suzuki, K. (1998). Gene transfer and expression in oligodendrocytes under the control of myelin basic protein transcriptional control region mediated by adeno-associated virus. *Gene Ther.* 5, 50–58. doi: 10.1038/sj.gt.3300547
- Chittajallu, R., Aguirre, A., and Gallo, V. (2004). NG2-positive cells in the mouse white and grey matter display distinct physiological properties. *J. Physiol.* 561, 109–122. doi: 10.1113/jphysiol.2004.074252
- Dawson, M. R., Polito, A., Levine, J. M., and Reynolds, R. (2003). NG2-expressing glial progenitor cells: an abundant and widespread population of cycling cells in the adult rat CNS. *Mol. Cell. Neurosci.* 24, 476–488. doi: 10.1016/s1044-7431(03)00210-0
- De Biase, L. M., Kang, S. H., Baxi, E. G., Fukaya, M., Pucak, M. L., Mishina, M., et al. (2011). NMDA receptor signaling in oligodendrocyte progenitors is not required for oligodendrogenesis and myelination. *J. Neurosci.* 31, 12650–12662. doi: 10.1523/JNEUROSCI.2455-11.2011
- De Biase, L. M., Nishiyama, A., and Bergles, D. E. (2010). Excitability and synaptic communication within the oligodendrocyte lineage. *J. Neurosci.* 30, 3600–3611. doi: 10.1523/JNEUROSCI.6000-09.2010
- Etxeberria, A., Hokanson, K. C., Dao, D. Q., Mayoral, S. R., Mei, F., Redmond, S. A., et al. (2016). Dynamic modulation of myelination in response to visual stimuli alters optic nerve conduction velocity. *J. Neurosci.* 36, 6937–6948. doi: 10.1523/JNEUROSCI.0908-16.2016
- Evonuk, K. S., Doyle, R. E., Moseley, C. E., Thornell, I. M., Adler, K., Bingaman, A. M., et al. (2020). Reduction of AMPA receptor activity on mature oligodendrocytes attenuates loss of myelinated axons in autoimmune neuroinflammation. *Sci. Adv.* 6:eaa5936. doi: 10.1126/sciadv.aax5936
- Farrar, M. J., Bernstein, I. M., Schlafer, D. H., Cleland, T. A., Fetcho, J. R., and Schaffer, C. B. (2012). Chronic *in vivo* imaging in the mouse spinal cord using an implanted chamber. *Nat. Methods* 9, 297–302. doi: 10.1038/nmeth.1856
- Fletcher, J. L., Murray, S. S., and Xiao, J. (2018). Brain-derived neurotrophic factor in central nervous system myelination: a new mechanism to promote myelin plasticity and repair. *Int. J. Mol. Sci.* 19:4131. doi: 10.3390/ijms19124131

- Foran, D. R., and Peterson, A. C. (1992). Myelin acquisition in the central nervous system of the mouse revealed by an MBP-Lac Z transgene. *J. Neurosci.* 12, 4890–4897. doi: 10.1523/JNEUROSCI.12-12-04890.1992
- Ford, M. C., Alexandrova, O., Cossell, L., Stange-Marten, A., Sinclair, J., Kopp-Scheinflug, C., et al. (2015). Tuning of Ranvier node and internode properties in myelinated axons to adjust action potential timing. *Nat. Commun.* 6:8073. doi: 10.1038/ncomms9073
- Fu, Y., Huff, T. B., Wang, H.-W., Wang, H., and Cheng, J.-X. (2008). *Ex vivo* and *in vivo* imaging of myelin fibers in mouse brain by coherent anti-Stokes Raman scattering microscopy. *Opt. Express* 16, 19396–19409. doi: 10.1364/oe.16.019396
- Fuchs, E. C., Zivkovic, A. R., Cunningham, M. O., Middleton, S., Lebeau, F. E., Bannerman, D. M., et al. (2007). Recruitment of parvalbumin-positive interneurons determines hippocampal function and associated behavior. *Neuron* 53, 591–604. doi: 10.1016/j.neuron.2007.01.031
- Ge, W.-P., Yang, X.-J., Zhang, Z., Wang, H.-K., Shen, W., Deng, Q.-D., et al. (2006). Long-term potentiation of neuron-glia synapses mediated by  $\text{Ca}^{2+}$ -permeable AMPA receptors. *Science* 312, 1533–1537. doi: 10.1126/science.1124669
- Ghosh, K. K., Burns, L. D., Cocker, E. D., Nimmerjahn, A., Ziv, Y., Gamal, A. E., et al. (2011). Miniaturized integration of a fluorescence microscope. *Nat. Methods* 8, 871–878. doi: 10.1038/nmeth.1694
- Gibson, E. M., Purger, D., Mount, C. W., Goldstein, A. K., Lin, G. L., Wood, L. S., et al. (2014). Neuronal activity promotes oligodendrogenesis and adaptive myelination in the mammalian brain. *Science* 344:1252304. doi: 10.1126/science.1252304
- Guo, F., Maeda, Y., Ko, E. M., Delgado, M., Horiuchi, M., Soulika, A., et al. (2012). Disruption of NMDA receptors in oligodendroglial lineage cells does not alter their susceptibility to experimental autoimmune encephalomyelitis or their normal development. *J. Neurosci.* 32, 639–645. doi: 10.1523/JNEUROSCI.4073-11.2012
- Haberlandt, C., Derouiche, A., Wyczynski, A., Haseleu, J., Pohle, J., Karraam, K., et al. (2011). Gray matter NG2 cells display multiple  $\text{Ca}^{2+}$ -signaling pathways and highly motile processes. *PLoS One* 6:e17575. doi: 10.1371/journal.pone.0017575
- Hill, R. A., Patel, K. D., Goncalves, C. M., Grutzendler, J., and Nishiyama, A. (2014). Modulation of oligodendrocyte generation during a critical temporal window after NG2 cell division. *Nat. Neurosci.* 17, 1518–1527. doi: 10.1038/nn.3815
- Hines, J. H., Ravanelli, A. M., Schwindt, R., Scott, E. K., and Appel, B. (2015). Neuronal activity biases axon selection for myelination *in vivo*. *Nat. Neurosci.* 18, 683–689. doi: 10.1038/nn.3992
- Hontani, Y., Xia, F., and Xu, C. (2021). Multicolor three-photon fluorescence imaging with single-wavelength excitation deep in mouse brain. *Sci. Adv.* 7:eabf3531. doi: 10.1126/sciadv.abf3531
- Horton, N. G., Wang, K., Kobat, D., Clark, C. G., Wise, F. W., Schaffer, C. B., et al. (2013). *in vivo* three-photon microscopy of subcortical structures within an intact mouse brain. *Nat. Photonics* 7, 205–209. doi: 10.1038/nphoton.2012.336
- Huang, W., Guo, Q., Bai, X., Scheller, A., and Kirchhoff, F. (2019). Early embryonic NG2 glia are exclusively gliogenic and do not generate neurons in the brain. *Glia* 67, 1094–1103. doi: 10.1002/glia.23590
- Hughes, A. N., and Appel, B. (2019). Oligodendrocytes express synaptic proteins that modulate myelin sheath formation. *Nat. Commun.* 10:4125. doi: 10.1038/s41467-019-12059-y
- Hughes, A. N., and Appel, B. (2020). Microglia phagocytose myelin sheaths to modify developmental myelination. *Nat. Neurosci.* 23, 1055–1066. doi: 10.1038/s41593-020-0654-2
- Hughes, E. G., Kang, S. H., Fukaya, M., and Bergles, D. E. (2013). Oligodendrocyte progenitors balance growth with self-repulsion to achieve homeostasis in the adult brain. *Nat. Neurosci.* 16, 668–676. doi: 10.1038/nn.3390
- Hughes, E. G., Orthmann-Murphy, J. L., Langseth, A. J., and Bergles, D. E. (2018). Myelin remodeling through experience-dependent oligodendrogenesis in the adult somatosensory cortex. *Nat. Neurosci.* 21, 696–706. doi: 10.1038/s41593-018-0121-5
- Jabs, R., Pivneva, T., Hüttmann, K., Wyczynski, A., Nolte, C., Kettenmann, H., et al. (2005). Synaptic transmission onto hippocampal glial cells with hGFAP promoter activity. *J. Cell Sci.* 118, 3791–3803. doi: 10.1242/jcs.02515
- Jung, J. C., Mehta, A. D., Aksay, E., Stepnoski, R., and Schnitzer, M. J. (2004). *in vivo* mammalian brain imaging using one- and two-photon fluorescence microendoscopy. *J. Neurophysiol.* 92, 3121–3133. doi: 10.1152/jn.00234.2004
- Kang, S. H., Fukaya, M., Yang, J. K., Rothstein, J. D., and Bergles, D. E. (2010). NG2<sup>+</sup> CNS glial progenitors remain committed to the oligodendrocyte lineage in postnatal life and following neurodegeneration. *Neuron* 68, 668–681. doi: 10.1016/j.neuron.2010.09.009
- Kárádóttir, R., Cavalier, P., Bergersen, L. H., and Attwell, D. (2005). NMDA receptors are expressed in oligodendrocytes and activated in ischaemia. *Nature* 438, 1162–1166. doi: 10.1038/nature04302
- Kárádóttir, R., Hamilton, N. B., Bakiri, Y., and Attwell, D. (2008). Spiking and nonspiking classes of oligodendrocyte precursor glia in CNS white matter. *Nat. Neurosci.* 11, 450–456. doi: 10.1038/nn2060
- Karram, K., Goebbels, S., Schwab, M., Jennissen, K., Seifert, G., Steinhauser, C., et al. (2008). NG2-expressing cells in the nervous system revealed by the NG2-EYFP knockin mouse. *Genesis* 46, 743–757. doi: 10.1002/dvg.20440
- Khawaja, R. R., Agarwal, A., Fukaya, M., Jeong, H.-K., Gross, S., Gonzalez-Fernandez, E., et al. (2021). GluA2 overexpression in oligodendrocyte progenitors promotes postinjury oligodendrocyte regeneration. *Cell Rep.* 35:109147. doi: 10.1016/j.celrep.2021.109147
- Koudelka, S., Voas, M. G., Almeida, R. G., Baraban, M., Soetaert, J., Meyer, M. P., et al. (2016). Individual neuronal subtypes exhibit diversity in CNS myelination mediated by synaptic vesicle release. *Curr. Biol.* 26, 1447–1455. doi: 10.1016/j.cub.2016.03.070
- Kougioumtzidou, E., Shimizu, T., Hamilton, N. B., Tohyama, K., Sprengel, R., Monyer, H., et al. (2017). Signalling through AMPA receptors on oligodendrocyte precursors promotes myelination by enhancing oligodendrocyte survival. *eLife* 6:e28080. doi: 10.7554/eLife.28080
- Krasnow, A. M., Ford, M. C., Valdivia, L. E., Wilson, S. W., and Attwell, D. (2018). Regulation of developing myelin sheath elongation by oligodendrocyte calcium transients *in vivo*. *Nat. Neurosci.* 21, 24–28. doi: 10.1038/s41593-017-0031-y
- Kressin, K., Kuprijanova, E., Jabs, R., Seifert, G., and Steinhauser, C. (1995). Developmental regulation of  $\text{Na}^{+}$  and  $\text{K}^{+}$  conductances in glial cells of mouse hippocampal brain slices. *Glia* 15, 173–187. doi: 10.1002/glia.440150210
- Kukley, M., Capetillo-Zarate, E., and Dietrich, D. (2007). Vesicular glutamate release from axons in white matter. *Nat. Neurosci.* 10, 311–320. doi: 10.1038/nn1850
- Kukley, M., Kiladze, M., Tognatta, R., Hans, M., Swandulla, D., Schramm, J., et al. (2008). Glial cells are born with synapses. *FASEB J.* 22, 2957–2969. doi: 10.1096/fj.07-090985
- Kukley, M., Nishiyama, A., and Dietrich, D. (2010). The fate of synaptic input to NG2 glial cells: neurons specifically downregulate transmitter release onto differentiating oligodendroglial cells. *J. Neurosci.* 30, 8320–8331. doi: 10.1523/JNEUROSCI.0854-10.2010
- Kwon, H.-B., and Sabatini, B. L. (2011). Glutamate induces de novo growth of functional spines in developing cortex. *Nature* 474, 100–104. doi: 10.1038/nature09986
- Lappe-Siefke, C., Goebbels, S., Gravel, M., Nicksch, E., Lee, J., Braun, P. E., et al. (2003). Disruption of Cnp1 uncouples oligodendroglial functions in axonal support and myelination. *Nat. Genet.* 33, 366–374. doi: 10.1038/ng1095
- Lawlor, P. A., Bland, R. J., Mouravlev, A., Young, D., and During, M. J. (2009). Efficient gene delivery and selective transduction of glial cells in the mammalian brain by AAV serotypes isolated from nonhuman primates. *Mol. Ther.* 17, 1692–1702. doi: 10.1038/mt.2009.170
- Lee, S., Leach, M. K., Redmond, S. A., Chong, S. Y., Mellon, S. H., Tuck, S. J., et al. (2012). A culture system to study oligodendrocyte myelination processes using engineered nanofibers. *Nat. Methods* 9, 917–922. doi: 10.1038/nmeth.2105
- Li, H., and Richardson, W. D. (2016). Evolution of the CNS myelin gene regulatory program. *Brain Res.* 1641, 111–121. doi: 10.1016/j.brainres.2015.10.013
- Lin, S.-C., and Bergles, D. E. (2004). Synaptic signaling between GABAergic interneurons and oligodendrocyte precursor cells in the hippocampus. *Nat. Neurosci.* 7, 24–32. doi: 10.1038/nn1162
- Lin, S.-C., Huck, J. H., Roberts, J. D., Macklin, W. B., Somogyi, P., and Bergles, D. E. (2005). Climbing fiber innervation of NG2-expressing glia in



- the mammalian cerebellum. *Neuron* 46, 773–785. doi: 10.1016/j.neuron.2005.04.025
- Liu, J., Dietz, K., Deloyht, J. M., Pedre, X., Kelkar, D., Kaur, J., et al. (2012). Impaired adult myelination in the prefrontal cortex of socially isolated mice. *Nat. Neurosci.* 15, 1621–1623. doi: 10.1038/nn.3263
- Lundgaard, I., Luzhynskaya, A., Stockley, J. H., Wang, Z., Evans, K. A., Swire, M., et al. (2013). Neuregulin and BDNF induce a switch to NMDA receptor-dependent myelination by oligodendrocytes. *PLoS Biol.* 11:e1001743. doi: 10.1371/journal.pbio.1001743
- Makinodan, M., Rosen, K. M., Ito, S., and Corfas, G. (2012). A critical period for social experience-dependent oligodendrocyte maturation and myelination. *Science* 337, 1357–1360. doi: 10.1126/science.1220845
- Mallon, B. S., Shick, H. E., Kidd, G. J., and Macklin, W. B. (2002). Proteolipid promoter activity distinguishes two populations of NG2-positive cells throughout neonatal cortical development. *J. Neurosci.* 22, 876–885. doi: 10.1523/JNEUROSCI.22-03-00876.2002
- Mangin, J.-M., Kunze, A., Chittajallu, R., and Gallo, V. (2008). Satellite NG2 progenitor cells share common glutamatergic inputs with associated interneurons in the mouse dentate gyrus. *J. Neurosci.* 28, 7610–7623. doi: 10.1523/JNEUROSCI.1355-08.2008
- Mangin, J. M., Li, P., Scafidi, J., and Gallo, V. (2012). Experience-dependent regulation of NG2 progenitors in the developing barrel cortex. *Nat. Neurosci.* 15, 1192–1194. doi: 10.1038/nn.3190
- Marisca, R., Hoche, T., Agirre, E., Hoodless, L. J., Barkey, W., Auer, F., et al. (2020). Functionally distinct subgroups of oligodendrocyte precursor cells integrate neural activity and execute myelin formation. *Nat. Neurosci.* 23, 363–374. doi: 10.1038/s41593-019-0581-2
- Matsuzaki, M., Ellis-Davies, G. C., Nemoto, T., Miyashita, Y., Iino, M., and Kasai, H. (2001). Dendritic spine geometry is critical for AMPA receptor expression in hippocampal CA1 pyramidal neurons. *Nat. Neurosci.* 4, 1086–1092. doi: 10.1038/nn736
- Matsuzaki, M., Honkura, N., Ellis-Davies, G. C., and Kasai, H. (2004). Structural basis of long-term potentiation in single dendritic spines. *Nature* 429, 761–766. doi: 10.1038/nature02617
- Mayoral, S. R., and Chan, J. R. (2016). The environment rules: spatiotemporal regulation of oligodendrocyte differentiation. *Curr. Opin. Neurobiol.* 39, 47–52. doi: 10.1016/j.conb.2016.04.002
- McKenzie, I. A., Ohayon, D., Li, H., De Faria, J. P., Emery, B., Tohyama, K., et al. (2014). Motor skill learning requires active central myelination. *Science* 346, 318–322. doi: 10.1126/science.1254960
- Mensch, S., Baraban, M., Almeida, R., Czopka, T., Ausborn, J., El Manira, A., et al. (2015). Synaptic vesicle release regulates myelin sheath number of individual oligodendrocytes *in vivo*. *Nat. Neurosci.* 18, 628–630. doi: 10.1038/nn.3991
- Micu, I., Jiang, Q., Coderre, E., Ridsdale, A., Zhang, L., Woulfe, J., et al. (2006). NMDA receptors mediate calcium accumulation in myelin during chemical ischaemia. *Nature* 439, 988–992. doi: 10.1038/nature04474
- Micu, I., Ridsdale, A., Zhang, L., Woulfe, J., McClintock, J., Brantner, C. A., et al. (2007). Real-time measurement of free  $\text{Ca}^{2+}$  changes in CNS myelin by two-photon microscopy. *Nat. Med.* 13, 874–879. doi: 10.1038/nm1568
- Mitew, S., Gobijs, I., Fenlon, L. R., McDougall, S. J., Hawkes, D., Xing, Y. L., et al. (2018). Pharmacogenetic stimulation of neuronal activity increases myelination in an axon-specific manner. *Nat. Commun.* 9:306. doi: 10.1038/s41467-017-02719-2
- Nishiyama, A., Komitova, M., Suzuki, R., and Zhu, X. (2009). Polydendrocytes (NG2 cells): multifunctional cells with lineage plasticity. *Nat. Rev. Neurosci.* 10, 9–22. doi: 10.1038/nrn2495
- Orduz, D., Maldonado, P. P., Balia, M., Velez-Fort, M., De Sars, V., Yanagawa, Y., et al. (2015). Interneurons and oligodendrocyte progenitors form a structured synaptic network in the developing neocortex. *eLife* 4:e06953. doi: 10.7554/eLife.06953
- Pan, S., Mayoral, S. R., Choi, H. S., Chan, J. R., and Kheirbek, M. A. (2020). Preservation of a remote fear memory requires new myelin formation. *Nat. Neurosci.* 23, 487–499. doi: 10.1038/s41593-019-0582-1
- Passlick, S., Grauer, M., Schafer, C., Jabs, R., Seifert, G., and Steinhauser, C. (2013). Expression of the gamma2-subunit distinguishes synaptic and extrasynaptic GABA<sub>A</sub> receptors in NG2 cells of the hippocampus. *J. Neurosci.* 33, 12030–12040. doi: 10.1523/JNEUROSCI.5562-12.2013
- Powell, S. K., Khan, N., Parker, C. L., Samulski, R. J., Matsushima, G., Gray, S. J., et al. (2016). Characterization of a novel adeno-associated viral vector with preferential oligodendrocyte tropism. *Gene Ther.* 23, 807–814. doi: 10.1038/gt.2016.62
- Rivers, L. E., Young, K. M., Rizzi, M., Jamen, F., Psachoulia, K., Wade, A., et al. (2008). PDGFRA/NG2 glia generate myelinating oligodendrocytes and piriform projection neurons in adult mice. *Nat. Neurosci.* 11, 1392–1401. doi: 10.1038/nn.2220
- Saab, A. S., Tzvetavona, I. D., Trevisiol, A., Baltan, S., Dibaj, P., Kusch, K., et al. (2016). Oligodendroglial NMDA receptors regulate glucose import and axonal energy metabolism. *Neuron* 91, 119–132. doi: 10.1016/j.neuron.2016.05.016
- Salter, M. G., and Fern, R. (2005). NMDA receptors are expressed in developing oligodendrocyte processes and mediate injury. *Nature* 438, 1167–1171. doi: 10.1038/nature04301
- Schain, A. J., Hill, R. A., and Grutzendler, J. (2014). Label-free *in vivo* imaging of myelinated axons in health and disease with spectral confocal reflectance microscopy. *Nat. Med.* 20, 443–449. doi: 10.1038/nm.3495
- Silva, A. J. (2017). Miniaturized two-photon microscope: seeing clearer and deeper into the brain. *Light Sci. Appl.* 6:e17104. doi: 10.1038/lsa.2017.104
- Steadman, P. E., Xia, F., Ahmed, M., Mocle, A. J., Penning, A. R. A., Geraghty, A. C., et al. (2020). Disruption of oligodendrogenesis impairs memory consolidation in adult mice. *Neuron* 105, 150–164.e6. doi: 10.1016/j.neuron.2019.10.013
- Steinhäuser, C., Kressin, K., Kuprijanova, E., Weber, M., and Seifert, G. (1994). Properties of voltage-activated  $\text{Na}^{+}$  and  $\text{K}^{+}$  currents in mouse hippocampal glial cells *in situ* and after acute isolation from tissue slices. *Pflügers Arch.* 428, 610–620. doi: 10.1007/BF00374585
- Sun, W., and Dietrich, D. (2013). Synaptic integration by NG2 cells. *Front. Cell. Neurosci.* 7:255. doi: 10.3389/fncel.2013.00255
- Sun, W., Matthews, E. A., Nicolas, V., Schoch, S., and Dietrich, D. (2016). NG2 glial cells integrate synaptic input in global and dendritic calcium signals. *eLife* 5:e16262. doi: 10.7554/eLife.16262
- Tedeschi, A., Dupraz, S., Laskowski, C. J., Xue, J., Ulas, T., Beyer, M., et al. (2016). The calcium channel subunit  $\alpha\text{2delta2}$  suppresses axon regeneration in the adult CNS. *Neuron* 92, 419–434. doi: 10.1016/j.neuron.2016.09.026
- Tognatta, R., Sun, W., Goebbels, S., Nave, K. A., Nishiyama, A., Schoch, S., et al. (2017). Transient Cnp expression by early progenitors causes Cre-Lox-based reporter lines to map profoundly different fates. *Glia* 65, 342–359. doi: 10.1002/glia.23095
- Tong, X.-P., Li, X.-Y., Zhou, B., Shen, W., Zhang, Z.-J., Xu, T.-L., et al. (2009).  $\text{Ca}^{2+}$  signaling evoked by activation of  $\text{Na}^{+}$  channels and  $\text{Na}^{+}/\text{Ca}^{2+}$  exchangers is required for GABA-induced NG2 cell migration. *J. Cell Biol.* 186, 113–128. doi: 10.1083/jcb.200811071
- Van Praag, H., Schinder, A. F., Christie, B. R., Toni, N., Palmer, T. D., and Gage, F. H. (2002). Functional neurogenesis in the adult hippocampus. *Nature* 415, 1030–1034. doi: 10.1038/4151030a
- Vélez-Fort, M., Maldonado, P. P., Butt, A. M., Audinat, E., and Angulo, M. C. (2010). Postnatal switch from synaptic to extrasynaptic transmission between interneurons and NG2 cells. *J. Neurosci.* 30, 6921–6929. doi: 10.1523/JNEUROSCI.0238-10.2010
- Von Jonquieres, G., Fröhlich, D., Klugmann, C. B., Wen, X., Harasta, A. E., Ramkumar, R., et al. (2016). Recombinant human myelin-associated glycoprotein promoter drives selective AAV-mediated transgene expression in oligodendrocytes. *Front. Mol. Neurosci.* 9:13. doi: 10.3389/fnmol.2016.00013
- Wake, H., Lee, P. R., and Fields, R. D. (2011). Control of local protein synthesis and initial events in myelination by action potentials. *Science* 333, 1647–1651. doi: 10.1126/science.1206998
- Wang, F., Flanagan, J., Su, N., Wang, L.-C., Bui, S., Nielson, A., et al. (2012). RNAscope: a novel *in situ* RNA analysis platform for formalin-fixed, paraffin-embedded tissues. *J. Mol. Diagn.* 14, 22–29. doi: 10.1016/j.jmoldx.2011.08.002
- Wang, H., Fu, Y., Zickmund, P., Shi, R., and Cheng, J.-X. (2005). Coherent anti-stokes Raman scattering imaging of axonal myelin in live spinal tissues. *Biophys. J.* 89, 581–591. doi: 10.1529/biophysj.105.061911

- Wang, K., Sun, W., Richie, C. T., Harvey, B. K., Betzig, E., and Ji, N. (2015). Direct wavefront sensing for high-resolution *in vivo* imaging in scattering tissue. *Nat. Commun.* 6:7276. doi: 10.1038/ncomms8276
- Weinberg, M. S., Criswell, H. E., Powell, S. K., Bhatt, A. P., and Mccown, T. J. (2017). Viral vector reprogramming of adult resident striatal oligodendrocytes into functional neurons. *Mol. Ther.* 25, 928–934. doi: 10.1016/j.ymthe.2017.01.016
- Yuan, X., Chittajallu, R., Belachew, S., Anderson, S., Mcbain, C. J., and Gallo, V. (2002). Expression of the green fluorescent protein in the oligodendrocyte lineage: a transgenic mouse for developmental and physiological studies. *J. Neurosci. Res.* 70, 529–545. doi: 10.1002/jnr.10368
- Zhu, X., Bergles, D. E., and Nishiyama, A. (2008). NG2 cells generate both oligodendrocytes and gray matter astrocytes. *Development* 135, 145–157. doi: 10.1242/dev.004895
- Zhu, X., Hill, R. A., Dietrich, D., Komitova, M., Suzuki, R., and Nishiyama, A. (2011). Age-dependent fate and lineage restriction of single NG2 cells. *Development* 138, 745–753. doi: 10.1242/dev.047951
- Ziskin, J. L., Nishiyama, A., Rubio, M., Fukaya, M., and Bergles, D. E. (2007). Vesicular release of glutamate from unmyelinated axons in white matter. *Nat. Neurosci.* 10, 321–330. doi: 10.1038/nn1854
- Zong, W., Wu, R., Li, M., Hu, Y., Li, Y., Li, J., et al. (2017). Fast high-resolution miniature two-photon microscopy for brain imaging in freely behaving mice. *Nat. Methods* 14, 713–719. doi: 10.1038/nmeth.4305

**Conflict of Interest:** The authors declare that the research was conducted in the absence of any commercial or financial relationships that could be construed as a potential conflict of interest.

**Publisher's Note:** All claims expressed in this article are solely those of the authors and do not necessarily represent those of their affiliated organizations, or those of the publisher, the editors and the reviewers. Any product that may be evaluated in this article, or claim that may be made by its manufacturer, is not guaranteed or endorsed by the publisher.

Copyright © 2021 Heflin and Sun. This is an open-access article distributed under the terms of the Creative Commons Attribution License (CC BY). The use, distribution or reproduction in other forums is permitted, provided the original author(s) and the copyright owner(s) are credited and that the original publication in this journal is cited, in accordance with accepted academic practice. No use, distribution or reproduction is permitted which does not comply with these terms.

# Advantages of publishing in Frontiers



## OPEN ACCESS

Articles are free to read  
for greatest visibility  
and readership



## FAST PUBLICATION

Around 90 days  
from submission  
to decision



## HIGH QUALITY PEER-REVIEW

Rigorous, collaborative,  
and constructive  
peer-review



## TRANSPARENT PEER-REVIEW

Editors and reviewers  
acknowledged by name  
on published articles

## Frontiers

Avenue du Tribunal-Fédéral 34  
1005 Lausanne | Switzerland

Visit us: [www.frontiersin.org](http://www.frontiersin.org)

Contact us: [frontiersin.org/about/contact](http://frontiersin.org/about/contact)



## REPRODUCIBILITY OF RESEARCH

Support open data  
and methods to enhance  
research reproducibility



## DIGITAL PUBLISHING

Articles designed  
for optimal readership  
across devices



## FOLLOW US

@frontiersin



## IMPACT METRICS

Advanced article metrics  
track visibility across  
digital media



## EXTENSIVE PROMOTION

Marketing  
and promotion  
of impactful research



## LOOP RESEARCH NETWORK

Our network  
increases your  
article's readership